Zebrafish left-right organizer : multi-scale analysis of cilia behaviors and flow-sensing mechanism for symmetry-breaking

Rita Rua Ferreira

UNIVERSITÉ DE STRASBOURG

ÉCOLE DOCTORALE DES SCIENCES DE LA VIE ET DE LA SANTE

Institut de Génétique et de Biologie Moléculaire et Cellulaire (IGBMC)

THÈSE

présentée par :

Rita RUA FERREIRA

soutenue le : **31 mars 2017**

pour obtenir le grade de : **Docteur de l'Université de Strasbourg**

Discipline/ Spécialité : Biologie du Développement

Etude du mécanisme de la sensation du flux ciliaire dans l'organiseur droite gauche du poisson zébre

Zebrafish left-right organizer: multi-scale analysis of cilia behaviors and flow-sensing mechanism for symmetry-breaking

THÈSE dirigée par :
Docteur VERMOT Julien — DR2, Université de Strasbourg - IGBMC, FR

RAPPORTEURS:
Professeur BLUM Martin — Professeur, Universität Hohenheim, DE
Docteur SPASSKY Nathalie — DR1, IBENS-ENS, FR

AUTRES MEMBRES DU JURY:
Docteur CHARVIN Gilles — CR1, IGBMC, FR

“It always seems impossible until it’s done” – Nelson Mandela

Acknowledgments/Remerciements/Agradecimentos

First, I would like to thank the members of my jury, Professor Martin Blum, Doctor Nathalie Spassky and Doctor Gilles Charvin for accepting to evaluate my PhD work. In particular, I would like to thank Professor Blum and Doctor Spassky for coming to Strasbourg for my Viva. Finally, I would like to thank Doctor Charvin for all the nice discussions we had during the seminars I have had the chance to give at IGBMC during my PhD and also for being a member of my mid-thesis committee. I would also like to thank Geraldine Schverer for all the help dealing with the paperwork from the Doctoral School.

Next, I would like to thank Julien, my supervisor, for several reasons but first for selecting me for this amazing project. I confess that I was not expecting to pass the interview with the jury panel for the International PhD program, let alone to make you think I was the right person for the task (given I am not even a biologist by training). However, things went pretty well and finally we ended up working together. Thank you for supporting me when things were difficult, especially for always believing that I would be able to finish the project (much more than I believed it myself most of the time). Thanks for all the opportunities to go abroad for courses, workshops and to attend several conferences that made me a much more confident person to talk openly about the project and about science in general. Thank you for your supervision on the project during the last four years - if the project kept being exciting it was also because of your input. Even maybe without noticing, thanks for letting me take the lead in organizing things in your laboratory, as it was something I really enjoyed doing. Thanks for everything, it was great to work with you ☺

This project would not have been possible without Willy. I have to say, during my Masters back in the days in Lisbon when I was reading Willy's papers with Julien, I was always curious to meet him because I was truly fascinated by his work on the Kupffer's vesicle. It was part of the reason I applied to Julien's laboratory - because I wanted to become part of their "team" ☺ With Willy I learnt a lot, much more that I could have imagined when I started. Thank you ever so much for your patience, training me for the cilia analysis and explaining all the details about image and data processing. I really appreciated your effort in making me understand why things were done like the way they were instead of just giving me the results. It was a pleasure to meet you and to work with you. Also, thanks for taking some time to proofread this PhD manuscript. Recently, Guillaume Pakula joined us as a PhD student in Willy's laboratory and he is also a great asset to the team. Thanks a lot for your patience in trying to give me the kind of graphs I needed and in explaining to me very basic concepts when I was super stressed about it. Wish you all the luck with the rest of your PhD ☺

Thanks also to the biggest smile on our team, Andrej Vilfan. Despite being an amazing scientist and making the best numerical models that I have ever seen, he is such a nice person. Even when there were periods when we were all crazy and stressed, Andrej was always smiling on our chats on Skype. Thanks a lot for that Andrej, for keeping us positive and believing that things will always eventually end up OK, and, of course, thanks for all the nice discussions about the physics side of the project. I have learnt so much with you as well, a whole new way of seeing the world. I really enjoyed working with you, thank you ever so much ☺

Also would like to thank Rita Fior, my Professor at the University during my Masters, for showing me the amazing world of Developmental Biology that was totally unknown for me at that time. A big hug for my Masters supervisor Susana Lopes, than more than accepting me in her lab, trusted me since day zero that I was able to do a biophysic-related project. Thanks to her I got familiar with Julien's work in the left-right field and that is also why I am here today. In addition, thanks for your friendship during all this time. Obrigada ☺

I would like to thank the IGBMC Imaging platform, especially Marc K. and Pascal K. Most of the things I know about microscopy I have learnt at IGBMC with Marc and Pascal and I have to say that for several times I bothered both of them with text messages and phone calls complaining about the

errors the confocal microscopes were giving. That's why I have to thank both of them for always giving me the freedom to call and to try to at least do something to fix the microscope remotely. Also, thank you guys for the nice environment and laughing afternoons we had together at the Imaris station ☺ Merci!

I would also would like to thank the Department of Development and Stem Cells of IGBMC, all the groups for the nice discussions over the years and especially France Chivaille, who took care of all the details related with my Viva and made my life easier during such a stressfull period ☺ Merci!

J'aimerais aussi remercier Sandrine, Sylvie et, plus récemment Norbert, pour leur incroyable travail à l'animalerie. Cela demande beaucoup d'efforts pour que tout fonctionne parfaitement et pour que les poissons soient aussi "heureux" que possible et vous avez tous fait ça comme des pros. Merci beaucoup pour toutes les fois où j'ai dû vous appeler pour vous demander de l'aide lorsque le tram avait des soucis et que je ne pouvais pas arriver à l'heure. Aussi, désolée pour les fois où j'avais du retard dans le maintien de mes lignées, mais quelques fois le travail au labo demandait toute mon attention pendant des journées entières. Sans vous, rien n'aurait été possible, alors je vous remercie énormément pour votre travail à l'animalerie, nous en sommes très reconnaissant.

I will like to thank all the members of the Lab Vermot for the nice discussions from which I have learnt so much. Good thing about having a side project in the lab is that I also now know a lot about heart and valve development and you guys are doing top research. Wish you all the best and I have no doubts amazing findings will come out of your work. I will hear great things about you guys for sure ☺

I would especially like to thank Lhéanna. She started in the lab as my student during her Masters and since day one we worked perfectly as a team. Afterwards, she stayed with us and I have to say it was a gift Julien gave me. Without her, none of the ISH and genotyping would have been ready on time for this manuscript. She always did more than what I asked her while keeping a smile on her face. I will never be able to thank you as you deserve and I just want to say that you are a great person and an excellent colleague, in all aspects. Also, I want to apologize if I sometimes pushed you too much – I can imagine how hard it was to deal with me during the last months, I tried my best to keep the stress inside me but I am sure here and there I might have said something inappropriate or made you feel unhappy working with me. I am really sorry about that - you are excellent and never let anyone tell you otherwise. I will always recommend you because you are really, really great, and we have something in common that made it one of the best things ever sharing a bench with you. Wish you all the best Lhéanna you deserve it. Hope we will keep in touch ☺

I also have to thank Stéphane immensely for being with me since the first day in the lab. He was the first person I met at IGBMC in the day of the interview and since then I know that if there is anything I need I can go to him and he will fix it or knows someone that can help. Thank you ever so much for doing this and helping every time it is needed. Also, managing the fish facility is something you do perfectly and that's the base of our work! Merci beaucoup ☺

I would also like to thank Jacky, the first person I have worked in the lab and taught me so many things. Thanks for sharing your time and knowledge with me and for all the guidance during the period we had together in the lab. It was a great pleasure to work with you and being part of your project. All the best for your future ☺

I would like to thank warmly the "*compi* network": Pedro, Emily, Caroline, Francesco, Marina…Remember all the good moments we had together in the lab makes me miss you even more. We had so much fun (and cakes, and cookies, and biscuits, and cakes…. and cakes) and you made my days in the lab just HAPPY!! There is a word that only exists in Portuguese that really says what I felt since you guys left to other adventures: SAUDADE! There is no translation in any other language but it really describes the feeling of missing something or someone… and sometimes we are really happy in the small details and we do not know it. Even now, I find myself thinking, Emily will show up and ask if anyone wants a "cup of tea", or Francesco will call saying "5min and I am ready for lunch" when Pedro has already been waiting ages for him… or remembering when Caroline was trying to teach French to Francesco, oh my goodness, one of the best videos we ever made. Time will not come back and I am truly happy we keep all being friends and you guys left for very good and exciting adventures (of course I've already visited you, couldn't stay away for long), but that for me was really the best period of the whole PhD… and from all the competences I gained, none is comparable to the people I have met and I am lucky to call friends. Will never forget Francesco's stories and his food. Cooking pasta was never the same after meeting you– I have to go to Cambridge and check if you still manage to do it so well ☺ I would also like to thank Paola for all the nice "discussions" with Francesco that made us laugh so much over lunch time. Better than one Italian in the lab, is having two ☺

Caro, I stole your fish!!! Missing you like crazy in the lab!! Hope we will see each other soon and I will keep my promise, I will bring Maurice to the Viva, provided that nobody accidentally trashes him in the lab move. He is still "alive" and grown up…it's been three years now ☺ thanks a lot for all the good things you taugh me and all the "older" PhD student-advices!! Prepared me a lot for what was coming AHAH ☺ hope to have the chance to visit you soon!!! Bisous!!

To Emily, there is not much more to say, you are part of my family, you know it. I think our epic moment will always be your last day when we both cried in the street in Strasbourg (to be honest me much much much more than you) but apart from not having tea together every day (that is a real shame, Skype should provide that functionality), it was good that after a year nothing changed and whatsapp has kept you closer. Missing you and Mark a lot. Hopefully we have plenty of plans together coming this year ☺ Looking forward to seeing you at my Viva xx

Compi Marina, muchas gracias por todos los buenos momentos que pasamos cuando vivimos juntas. Sigo pensando que deberíamos escribir un libro sobre todas esas historias (OK, Cervantes Institute was too long ago so no more Spanish for you). Thank you compi for all your support during the several times you were in the lab…and good luck for the future, you will do great ☺ and by the way, I am not applying for EMBL, and there is a lot of Pokémon's in my neighborhood in Lisbon so you can always come and visit again ☺

Would like to give a big OBRIGADO to Pedro and Marta, you guys are just awesome. Thanks a lot for everything - you both made my life here easier with all your experienced comments about science (but life in general) and mainly for the company. Muito obrigada por tudo, por serem uns queridos e terem paciência para me aturar, por me darem a oportunidade de estar com a vossa Laurinha (que para mim já é sobrinha), e por terem estado sempre lá quando eu precisei. Nunca vos vou poder agradecer o suficiente. Foi mesmo um prazer conhecer-vos e espero que um dia nos encontremos todos em Portugal, a viver no melhor país do mundo ☺

Furthermore, I would like to thank you guys ever so much for carefully proofreading my PhD manuscript. Emily, Pedro and Marta, I will never be able to thank you enough. All your comments made this manuscript much better than it was before, and I can only hug you very hard next time I see you ☺

A big thank you to Adam, Joanna, Ana, Helena, André, Poonam, Maria-Elena… all former members of teams from IGBMC with whom I had so much fun with. Hope to see you all soon ☺

Also, to Paulo, former PhD coordinator of IGBMC for all his advice and especially for the time he took to sit down with me and other students to chat and see our problems from other people's perspectives. Obrigada Paulo ☺

Big thanks as well to my talented cousin, who is a graphical designer and who made the zebrafish cartoon I have after the cover page. With two sentences she really understood my point and I love it. Obrigada Inês ☺

I would also like to thank my friend Marta Lourenço, who started her PhD in the same week as me in Berlin and despite being one of the funniest people I have ever meet, always had the best comments and advice to give me regarding the problems I was facing during the last years. It is impossible to translate but have to say this girl has a natural talent to make people laugh ☺ Obrigada por tudo Martinha, sem ti nunca tinha aguentado isto até ao final…força nisso que também estás quase!!! E "biba a Póboa, carago" ☺ (sim, acabei de escrever isto na tese!!! ahahah)

Queria também agradecer à Nádia e à Susete porque mesmo tão recentes, foram umas amigas do caraças neste último ano, obrigada por tudo, aproveitem bem a vida meninas e já sabem…se algo correr mal por aqui vamos todos para Pinhel que lá é seguro ☺

Ao meu namorado Humberto (Beko) obrigada por todo o apoio ao longo destes últimos anos, mesmo nos dias em que eu mal me aturava tu conseguias sempre aturar-me…isso é um dom que devias explorar ☺ Admiro muito o que fizeste para vires para cà e ainda mais o que deixaste de fazer para que eu pudesse continuar a trabalhar, não deve ser fácil viver com alguém que raramente desliga do trabalho. Prometo que isso vai melhorar!! Esta tese também é tua porque se alguém me fazia sair da cama nos piores dias eras tu, e quem me amparou o choro muitas vezes foste tu…sempre tu… obrigada zéquinha ☺

Para terminar, queria agradecer à minha família e aos meus amigos que mesmo longe estiveram sempre comigo. À Rita e à Sara por estarem sempre do outro lado do telefone e por todos os esforços em nos vermos o máximo de tempo quando eu estava de visita. Foram um apoio incondicional e sem vocês não teria conseguido. Obrigada por terem vindo cá também, foi tão divertido, nunca me hei-de esquecer da nossa ida à Disneyland…temos de voltar agora com o Mi ☺

Aos meus irmãos que apesar de não ligarem (eheheh sempre a dar a dica ☺) sei que estão sempre comigo para o que eu precisar e isso é o que verdadeiramente importa, e eu estarei sempre com e para vocês.

Aos meus tios Marcelinos que por whatsapp foram animando os meus dias, foi muito bom ter a vossa companhia e de certa forma estar em Portugal no vosso dia-a-dia.

Aos meus tios João e Maria João que sei que sabem mais que ninguém o que é passar por isto e sabem que não é fácil, obrigada pelas palavras de coragem sempre que estávamos juntos. Um muito obrigada ao meu tio emprestado Pedro Marques, por todas as mensagens de apoio e bons convivios durante as minhas visitas a casa.

Ao meu padrinho João Luis, um grande exemplo para mim, que esteve sempre cá atrás no meu subconsciente a dizer que eu era capaz e que se não era doutora de uma maneira seria de outra ☺

Aos meus queridos avós, que me viram entrar na escola e depois de…. Sei lá… mais de 20 anos…me veem a conseguir o ultimo diploma! São todos um exemplo de força para mim. Obrigada pelos abraços apertados e pelas comidinhas boas que me foram fazendo matar as saudades. Vocês são o meu pilar, gosto tanto de vocês!!

Por fim, aos meus pais e ao João que sempre sempre estiveram ao meu lado, quando eu quis vir para cá, quando eu quis desistir, quando eu quis voltar e agora que está a acabar…e talvez precise de um cantinho lá em casa de novo ☺ Obrigada do fundo do meu coraçao! Um obrigada também aos meus cães mais bons que sem saberem transmitem-me tanto.

Gosto muito muito de todos vocês, mesmo que o meu feitio não o permita dizer quando devia! ☺
Aguardo ansiosamente ver-vos no auditorio em Março para que eu possa finalmente dizer **c'est fini**!!!!

Por fim, queria agradecer a todos, mesmo todos, os que me apoiaram nesta aventura tão difícil. Aqueles que me disseram que ia conseguir « nas calmas », aos que me disseram que ao fim de um mês estava de volta a casa…e àqueles que nada disseram mas que sorriram porque sabiam que nunca deixo nada por fazer, quando tem de ser feito. Um muito obrigada!!!

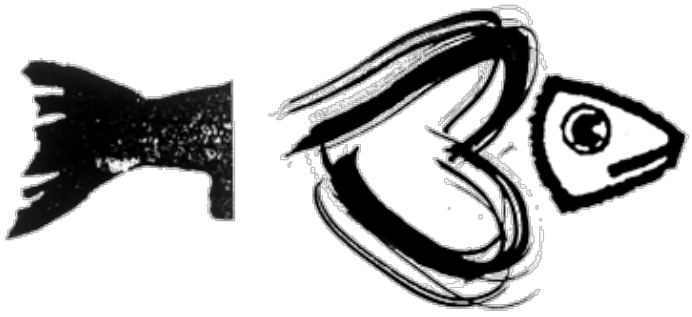

List of publications, posters and oral communications

(Chronological order)

Publications

- **Origins of meridional tilt in the zebrafish left-right organizer**.

Ferreira RR, Klaeyle L., Pakula G., Supatto W., Vermot, J.

(in preparation)

- **3D-Cilia Map: a live, high content imaging method to link cilia biophysical features with left-right symmetry breaking**

Supatto W., Pakula G., Ferreira RR, Vermot, J.

(in preparation)

- **Physical limits of flow sensing in the left-right organizer**.

Ferreira R.R., Vilfan A., Julicher, F., Supatto W., Vermot, J.

(in revision)

- **The balancing roles of mechanical forces during left-right patterning and asymmetric morphogenesis.**

Ferreira RR, Vermot J.

Mech Dev. 2017 Apr;144(Pt A):71-80. doi: 10.1016/j.mod.2016.11.001. Epub 2016 Nov 5. (R*eview*)

- **Developmental Alterations in Heart Biomechanics and Skeletal Muscle Function in Desmin Mutants Suggest an Early Pathological Root for Desminopathies.**

Ramspacher C., Steed E., Boselli F., Ferreira R., Faggianelli N., Roth S., Spiegelhalter C., Messaddeq N., Trinh L., Liebling M., Chacko N., Tessadori F., Bakkers J., Laporte J., Hnia K., Vermot J.

Cell Rep. 2015 doi: 10.1016/j.celrep.2015.05.010.

- **Endothelial cilia mediate low flow sensing during zebrafish vascular development.**

Goetz JG, Steed E, Ferreira RR, Roth S, Ramspacher C, Boselli F, Charvin G, Liebling M, Wyart C, Schwab Y, Vermot J.

Cell Rep. 2014 doi: 10.1016/j.celrep.2014.01.032.

Posters

- **9th European Zebrafish Meeting, Oslo, 28-June 2-July 2016**

Title: Order and coherence of 3D cilia positioning in the left-right organizer.

Authors: Ferreira RR, Vilfan A., Julicher, F., Supatto W., Vermot J.

- **CILIA 2014, Paris, 18-21 November 2014** (Prize for best poster)

Title: Order and coherence of 3D cilia positioning in the left-right organizer.

Authors: Ferreira RR, Supatto W., Vermot J.

- **GRD meeting, Monte Sainte Odile, 3-5 November 2014**

Title: Order and coherence of cilia distribution within the left-right organizer.

Authors: Ferreira RR, Supatto W., Monduc F., Vilfan A., Vermot J.

- **Workshop on Mechanics and growth of tissues, Paris, 13-16 January 2014**

Title: Order and coherence of 3D cilia positioning in the zebrafish left-right organizer.

Authors: Ferreira RR, Vilfan A., Julicher, F., Supatto W., Vermot J.

Oral communications

- **Physics and Biological Systems 2016, Palaiseau, 24-26 October 2016** (Invited speaker)

Title: Order and coherence of 3D cilia positioning in the left-right organizer.

Authors: Ferreira RR, Vilfan A., Julicher, F., Supatto W., Vermot J.

- **EMBO Conference CILIA 2016, Amsterdam, 4-7 October 2016**

Title: Multiscale analysis of the left-right organizer reveals the governing biophysical features behind cilia mediated symmetry breaking.

Authors: Ferreira RR, Vilfan A., Julicher, F., Supatto W., Vermot J.

- **9th French Congress of Cilia, Flagella and Centrosomes, Strasbourg, October 2015**
  (Prize for best talk for junior scientist)

Title: Order and coherence of 3D cilia positioning in the left-right organizer.

Authors: Ferreira RR, Supatto W., Vermot J.

- **2nd Tri-Regional Stem Cell and Developmental Biology Meeting, Freiburg, October 2015**

Title: Left-right patterning: Order and coherence of the left-right organizer.

Authors: Ferreira RR, Supatto W., Vermot. J.

- **7th Regional Meeting on Fish Genetics and Development, Castle Landeck, October 2013**

Title: Order and coherence of the left-right organizer in zebrafish.

Authors: Ferreira RR, Supatto W., Vermot. J.

Table of contents

List of figures, tables and movies

Introduction

Manuscript 2

Manuscript 3

List of abbreviations

2PEF: two-photon excitation fluorescence microscopy
AD: anterior-dorsal
AP: anteroposterior
BMPs: Bone Morphogenic Proteins
cAct-RIIa: activing type IIa receptor
Car: *caronte*
Cerl-2: (Cerberus-like protein 2)
CHD: congenital heart defects
CP: central pair
DFCs: dorsal forerunner cells
DRC: dynein regulatory complex
DV: dorsoventral
ECVs: extra-cellular vesicles
FGF: fibroblast growth factor
GJC: gap junction communication
GRP: gastrocoel roof plate
HH: Hedgehog
HNF3β: Hepatocyte nuclear factor 3-beta
Hpf: hours post-fertilization
IFT: intraflagellar transport
Ipk1: inositol 1,3,4,5,6-pentakisphospate 2-kinase
ISH: *in situ* hybridization
iv: *inversus viscerum*
KO: knock out
KV: Kupffer's vesicle
LPM: lateral plate mesoderm
LR: left-right
LRD: *left-right dynein*
LRDR: *left-right dynein-related*
LRO: left-right organizer
LRR: Leucine-rich repeats
LRRC50: Leucine-rich repeat-containing protein 50
MO: morpholino
MTOC: microtubule-organizing center
NVPs: nodal vesicular parcels
PC2: Polycystin 2
PCD: primary ciliary dyskinesia
PCP: planar cell polarity
PKD1L1: polycystic kidney disease 1 –like 1
PKD2/Trpp2: Polycystic kidney disease 2/ *Transient receptor potential Polycystic2-like*
RA: retinoic acid
Re: Reynolds number
Rock2b: Rho-associated, coiled-coil cointaining protein kinase 2b
SELI: self-enhancement and laterality inhibition
SEM: scanning electron micrograph
SEM: standard error of the mean
Shh: *Sonic Hedgehog*
SS: somite-stage
TGFβ: Transforming Growth Factor Beta
Vangl2: *Van Gogh*-like 2
WISH: whole mount *in situ* hybridization
WT: wild-type

Introduction

1. Left-right asymmetries and laterality defects

All vertebrates, including Humans, look bilaterally symmetrical from the outside. However, most visceral organs and associated vasculature are asymmetrically positioned within the body cavity. This constitutes an embryonic axis called the left-right (LR) axis. In a normal arrangement of *situs*, called *situs solitus*, the heart apex, the stomach and the spleen lie on the left slide of the body, while the liver on the right side. The lungs are also asymmetrical since the right lung has more lobes than the left **(Fig. 1)**. However, 1 in about 10 000 individuals present a complete mirror-image reversal of the LR asymmetry, a situation called *situs inversus* (Fliegauf et al., 2007; Ramsdell, 2005; Shapiro et al., 2014; Sutherland and Ware, 2009) **(Fig. 2)**. This mirror-image orientation usually carries little or no clinical consequence, unless it occurs as part of a syndrome affecting other parts of the body (Peeters and Devriendt, 2006). *Situs ambiguus*, also called *heterotaxy*, is a much broader category that defines any combination of abnormal LR asymmetries that cannot be strictly classified as *situs solitus* or *situs inversus* (Fliegauf et al., 2007; Ramsdell, 2005; Shapiro et al., 2014; Sutherland and Ware, 2009) **(Fig. 2)**. Individuals with heterotaxy have complex birth defects affecting the heart, lungs, liver, spleen, intestines, other organs and the related vasculature (Brueckner, 2007; Ramsdell, 2005; Sutherland and Ware, 2009). Heterotaxy syndrome alters the structure of the heart and related vessels, the structure of the lungs, but also can lead to asplenia (absence of spleen) or polysplenia (multiple but poorly functioning spleens), among other defects in the visceral organs **(Fig. 2)**. Complex congenital heart defects (CHDs) are very frequently present in individuals with *situs ambiguus* (greater than 90%) (Li et al., 2015)(reviewed in (Ramsdell, 2005)).

The condition of *situs inversus* was firstly described in 1793 by a Scottish physician called Matthew Baillie, but it was only in 1933 the pulmologist Kartagener reported cases with a triad of symptoms (called Kartagener triad) including sinusitis, bronchiectasis and *situs inversus* (Kartagener, 1933). The first link between LR abnormalities and ciliary problems was only made late in the 70s by Afzelius, which reported that half of his patients showed signs of infertility, as a result of defective sperm flagella and immotile oviduct cilia, and also pathologies described in the Kartagener's triad (Afzelius, 1976). Only decades later, this condition was recognized as Kartagener's syndrome.

Motile cilia and flagella machinery are specialized in generating fluid-flow or simply move fluids. Failure of these mechanisms compromises mucus clearance, causing chronic airway diseases, which are associated with defects of laterality and fertility (Kartagener's syndrome) and brain development (Badano et al., 2006; Mitchison and Valente, 2017). Through the years, multiple functions of cilia have been uncovered during development and cilia defects are cause of multiple human diseases generally known as Ciliopathies **(Fig. 3)** (Fliegauf et al., 2007; Goetz and Anderson, 2010; Hildebrandt et al., 2011; Marshall and Kintner, 2008). Thus, motile ciliopathies are characterized by the dysfunction of tissues, organs, and gametes that have specialized cilia (Mitchison and Valente, 2017). The hallmark disease of motile cilia is Primary Ciliary Dyskinesia (PCD). It is a rare, usually inherited, autosomal disease with a recessive pattern - estimated prevalence of 1:15.000 (Mitchison and Valente, 2017;

Sutherland and Ware, 2009; Theegarten and Ebsen, 2011). Includes a group of diseases that present alterations in the motility of respiratory cilia, and the coexistence of PCD and *situs inversus* is now recognized as Kartagener's syndrome (Afzelius, 1976; Kartagener, 1933; Mitchison and Valente, 2017; Norris, 2012; Schwabe et al., 2008; Theegarten and Ebsen, 2011). PCD can also coexist with heterotaxy, indicating that loss of cilia motility can also result in ambiguous LR asymmetry and not only total reversal of laterality (Li et al., 2016; Shapiro et al., 2014). Importantly, not all Ciliopathies are related to motile cilia. Some are based on defects occurring in primary cilia, such as Polycystic Kidney Disease, *Bardet−Biedl* syndrome, *Joubert* Syndrome, *Alström* syndrome or *Meckel Gruber* syndrome (Fliegauf et al., 2007; Vincensini et al., 2011; Ware et al., 2011) **(Fig. 3B)**. In the past years, primary cilia have gain more and more attention from the medical and scientific community, given many reports have been showing primary cilia can act as a signaling center for many important pathways for the cells (Malicki and Johnson, 2017; Singla and Reiter, 2006).

Given the variety of Ciliopathies and pathways involved in the etiology of this group of pathologies, a detailed and accurate knowledge of cilia biology and function is thus critical to better understand the mechanisms behind the disease and propose more efficient diagnosis and treatment for these patients.

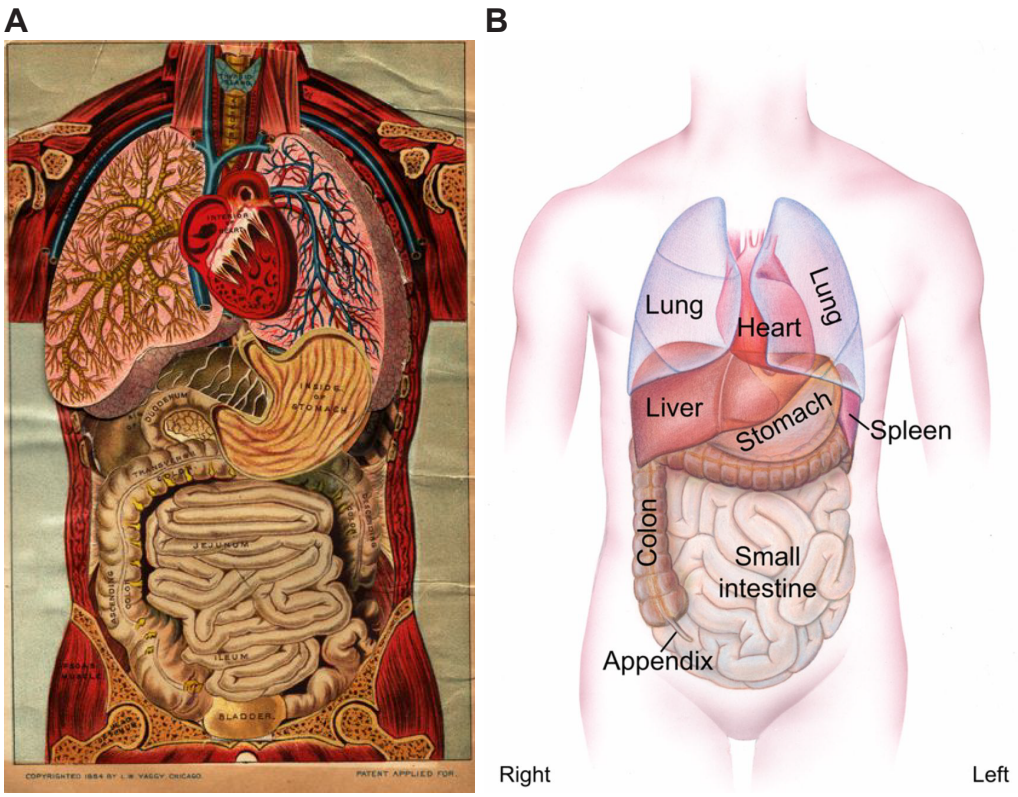

Fig. 1: Bilateral symmetrical from the outside vs. visceral organ asymmetry. In a normal arrangement of *situs*, called *situs solitus*, the heart apex, the stomach and the spleen lie on the left slide of the body, while the liver on the right side. The lungs are also asymmetrical since the right lung has more lobes than the left. **(A)** Adapted from https://www.flickr.com/photos/opheliachong/311436270/in/pool-86365505@N00/ and **(B)** Adapted from (Blum et al., 2014a).

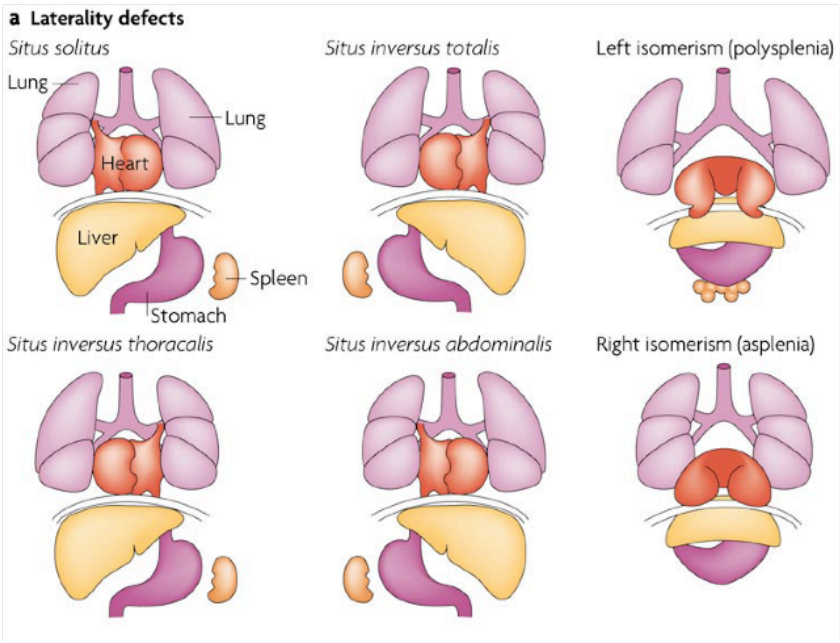

Fig. 2: Human laterality disorders: schematic illustration of normal left–right body asymmetry (*situs solitus*) and five laterality defects that affect the lungs, heart, liver, stomach and spleen. Adapted from (Fliegauf et al., 2007).

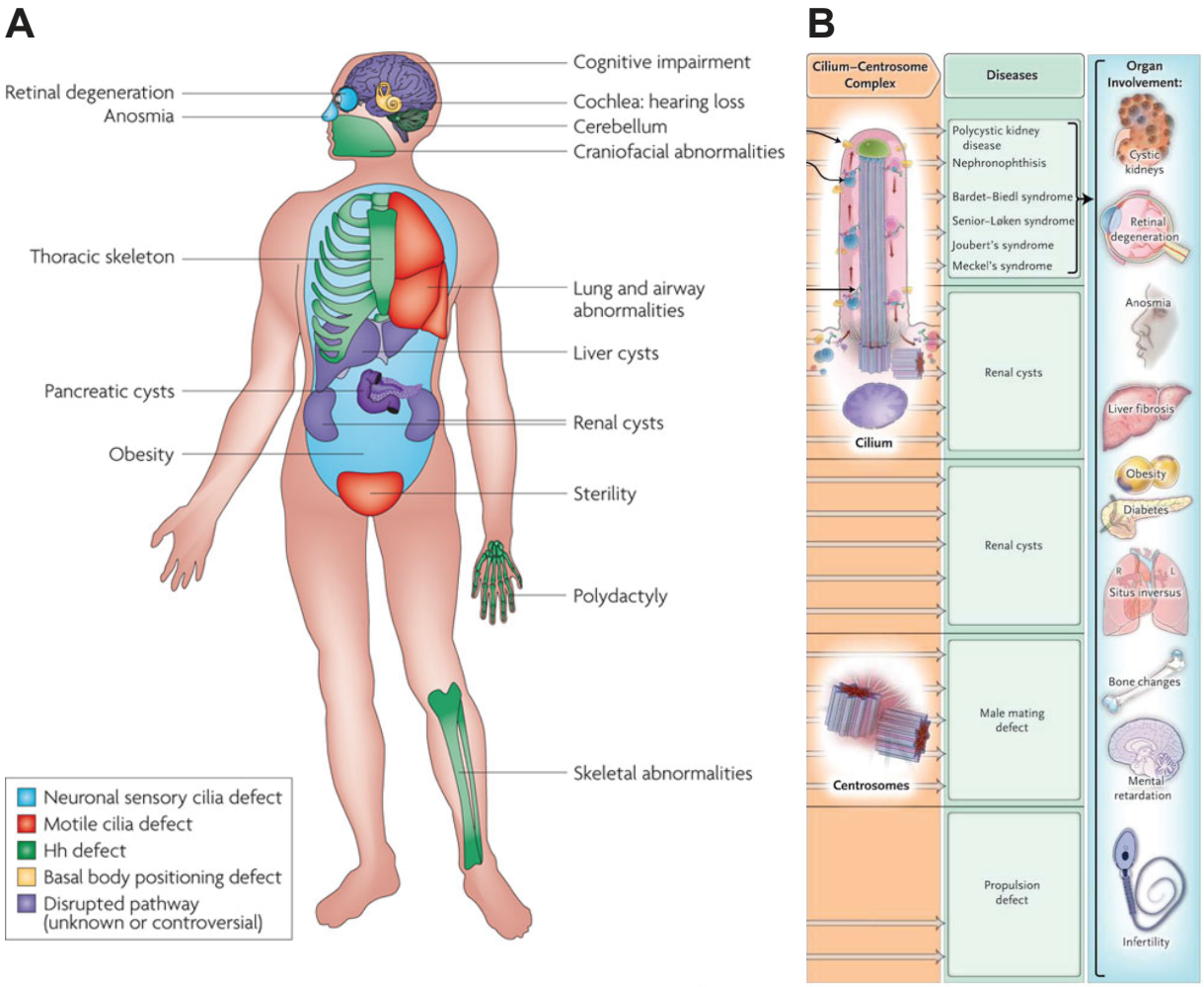

Fig. 3: Organs affected in human Ciliopathies: (**A-B**) Numerous pleiotropic human disorders have been attributed to defects in cilia formation. Some aspects of these syndromes have been attributed to defective hedgehog (Hh) signalling. Others to defective specialized cilia. Infertility observed in patients with ciliopathies is the result of defective sperm flagella and motile oviduct cilia. **(A)** Adapted from (Goetz and Anderson, 2010) and **(B)** adapted from (Hildebrandt et al., 2011)

2. Cilia ultrastructure and classification

Cilia and flagella are ubiquitous antenna-like organelles observed from protists to mammals that protrude out of nearly all vertebrate non-dividing cells (Fliegauf et al., 2007; Mitchison and Valente, 2017; Vincensini et al., 2011). The distinction between cilia and flagella is mostly historical, as both organelles display a common architecture (Bloodgood, 2010; Lodish H, 2000). Cilia and flagella number, length and disposition can be highly variable from one cell type to another. Pioneering studies carried out in the unicellular green alga *Chlamydomonas reinhardtii* established the link between cilia and several genetic diseases. Nowadays several other models are used to study cilia biology and function, such as vertebrates (mouse, zebrafish, Xenopus), ciliated protists (*Paramecium, Tetrahymena*, *Trypanosoma* or *Leishmania*), or invertebrates (*Caenorhabditis elegans* and *Drosophila melanogaster*). All in all, each one of these models have specific advantages for cilia studies regarding its ultrastructure and biological function (Vincensini et al., 2011).

The cilium consists of a microtubule-based core structure, called axoneme, which is covered by a specialized plasma membrane, and protrudes into the extracellular space **(Fig. 4)**. It is assembled from a basal body (microtubule-organizing center (MTOC) derived from the mother centriole), which docks the cilium at the cell surface (Hildebrandt et al., 2011; Ishikawa and Marshall, 2011). The axoneme is constructed from nine parallel doublet microtubules known as outer doublets, which elongate from the basal body, that may or may not contain two central microtubules, called central pair (9+2 or 9+0 axoneme, respectively) **(Fig. 4A)** (Bisgrove and Yost, 2006; Ishikawa and Marshall, 2011). The space between the junction of the basal body and the ciliary axoneme is called “transition zone” **(Fig. 4)**. It is enriched in Y-shaped fibers, which extend from the microtubule outer doublets to the ciliary membrane, and it is thought to function as a selective filter, regulating which molecules can pass into or out of the cilium **(Fig. 4B)**. The distal tips of cilia are also structurally and functionally complex microtubule-capping structures, which link the ends of the axonemal microtubules to the ciliary membrane (Sloboda, 2005)(reviewed in (Bisgrove and Yost, 2006; Hildebrandt et al., 2011; Ishikawa and Marshall, 2011). Overall, most of these structural features can influence the fluid flow generated by motile cilia (Hilfinger and Julicher, 2008).

During the process of cilia growth, named ciliogenesis, and even after its conclusion, cilium remains a highly dynamic structure. Motor proteins transport cargo proteins along the ciliary axoneme, and vice-versa, in a process known as intraflagellar transport (IFT) **(Fig. 5)**. This bidirectional movement along the axoneme is made by the molecular motors kinesins and dyneins, which bring IFT particles/cargo towards the tip or back to the basal body and the cell, respectively **(Fig. 4B** and **5)** (Ishikawa and Marshall, 2011).

Cilia are classified according to their internal molecular arrangement and their ability to move, and generically two cilia types can be defined: primary and motile cilia. A single primary cilium is found on the apical surface of the majority of cells in the human body, including epithelial cells, fibroblasts and

neurons (Bisgrove and Yost, 2006; Fliegauf et al., 2007; Vincensini et al., 2011). According to the internal arrangement, primary cilia have a 9+0 axoneme (no central microtubule pair) and lack of dynein arms and radial spokes (Ishikawa and Marshall, 2011) **(Fig. 4A'')**. They are generally shorter and immotile, but they can sense physical and biochemical extracellular signals (Berbari et al., 2009; Singla and Reiter, 2006), being even considered as a complex signaling center for various pathways (Malicki and Johnson, 2017; Singla and Reiter, 2006). Thus, its functional importance has been highlighted in the past years also by the discovery of the numerous pathologies caused by defects at the level of the primary cilium **(Fig. 3)** (Ware et al., 2011). The only exception are the 9+0 cilia from the mouse left-right organizer (LRO), that even if they lack a central pair of microtubules, they beat producing a vortical motion (Nonaka et al., 1998). In contrast, motile cilia are present in large numbers at the surface of epithelial cells, in regions such as the respiratory tract, trachea and oviduct **(Fig. 6A-B)**. They cooperatively beat in synchronized wave-like pattern to generate and direct fluid movement (reviewed in (Supatto and Vermot, 2011; Vincensini et al., 2011). To drive their bending motion, motile cilia have a central pair of microtubules, attached to outer and inner dynein arms and radial spokes, that make a link between the nine peripheral doublet microtubules and the central pair (9+2 axoneme) **(Fig. 4A** and **6C)** (Ishikawa and Marshall, 2011; Lindemann and Lesich, 2010). Cilia motility is accomplished by dynein motor activity, which slides the microtubule doublets relative to one another **(Fig. 6C)** (Hilfinger and Julicher, 2008; King, 2016; Lindemann and Lesich, 2010; Theegarten and Ebsen, 2011). Cilia are chiral organelles giving the internal handedness of the molecular motors composing its ultrastructure (i.e. distinct from their mirror image). This particularity is thought to determine the directed rotation of the beating cilia (Ferreira and Vermot, 2017; Hilfinger and Julicher, 2008). Mutants in the radial spokes and a complex of proteins called the dynein regulatory complex (DRC) revealed its critical role for cilia motility (Castleman et al., 2009; Colantonio et al., 2009). Both the radial spokes and the DRC are known to contain calcium-binding proteins, which allows cilia and flagella to respond to free calcium and thus altering their beating pattern (Lindemann and Lesich, 2010).

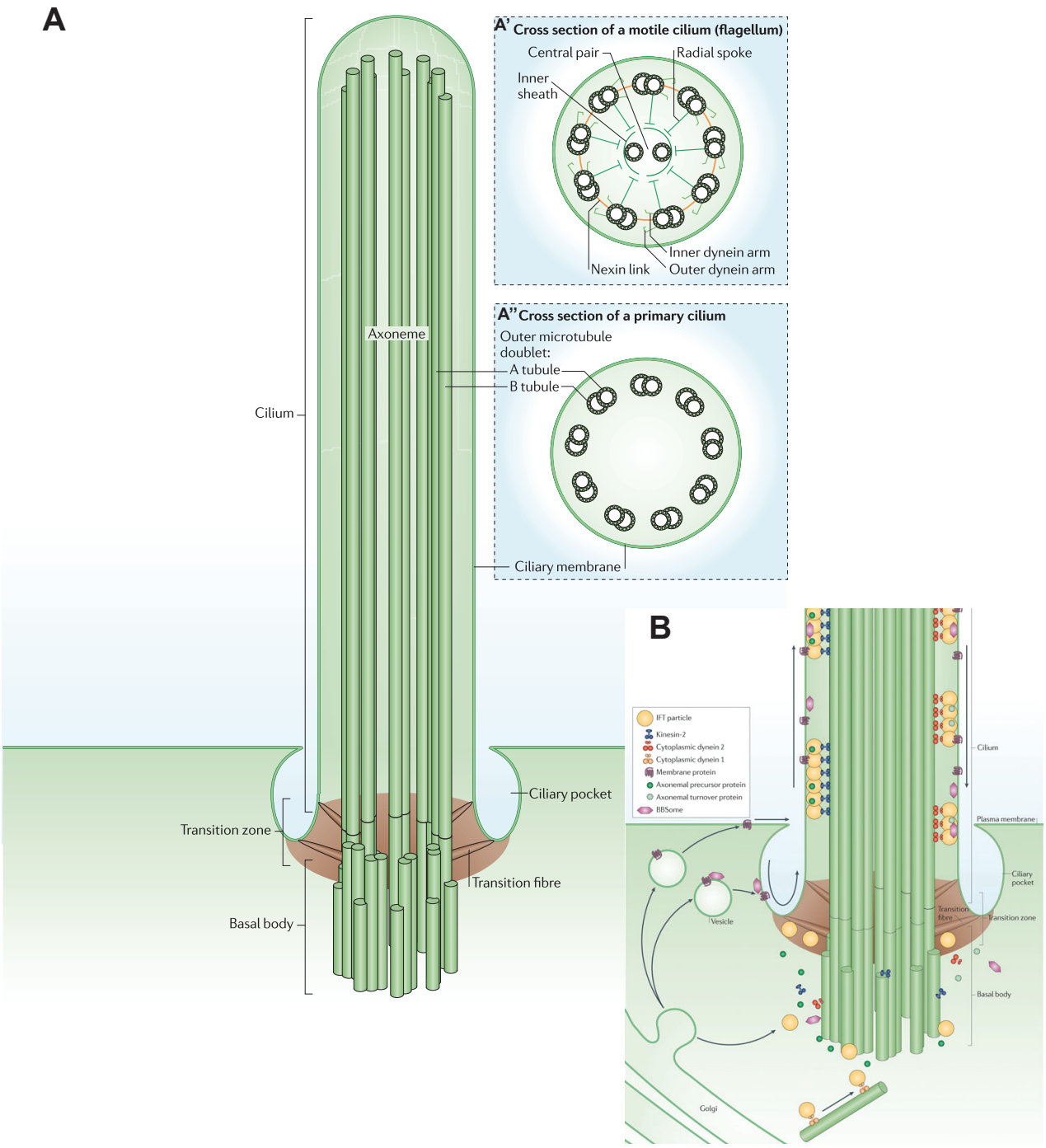

Fig. 4: The architecture of cilia: Schematic diagram of the primary cilium (**A-B**): (**A'**) Cross-section diagrams of a typical motile cilium and a non-motile primary cilium (**A''**). (**B**) Representation of the transition zone that forms a selectivity barrier at the base of the cilium. Proteins pass through this barrier either directly from the cytoplasm, or via lateral motion in the membrane following the docking and fusion of Golgi-derived vesicles near the ciliary base. Adapted from (Ishikawa and Marshall, 2011).

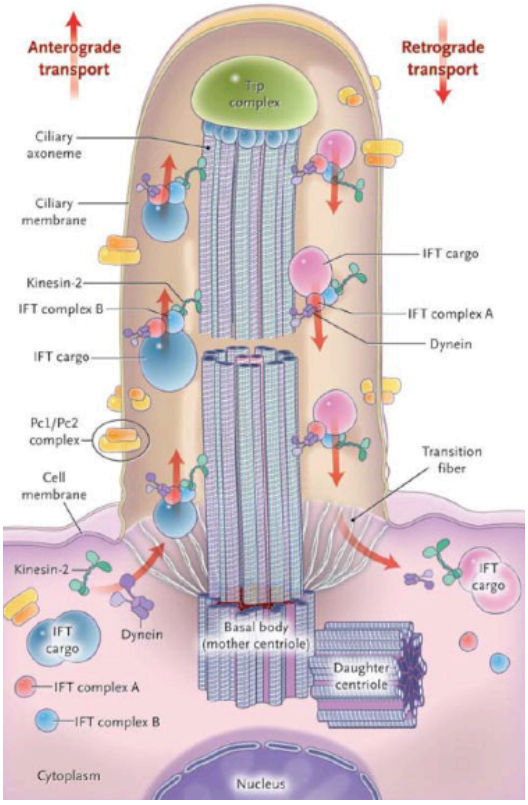

Fig.5: Structure of the Cilium and Intraflagellar Transport: The cilium consists of a microtubule-based axoneme covered by a specialized plasma membrane, which is assembled from the basal body, or mother centriole. Transition fibers act as a filter for molecules passing into or out of the cilium. Axonemal and membrane components are transported by means of intraflagellar transport (IFT) along the axonemal doublet microtubules toward the tip by proteins called kinesins and down back to the cell body (retrograde transport) by means of motor proteins called dyneins. Adapted from (Hildebrandt et al., 2011).

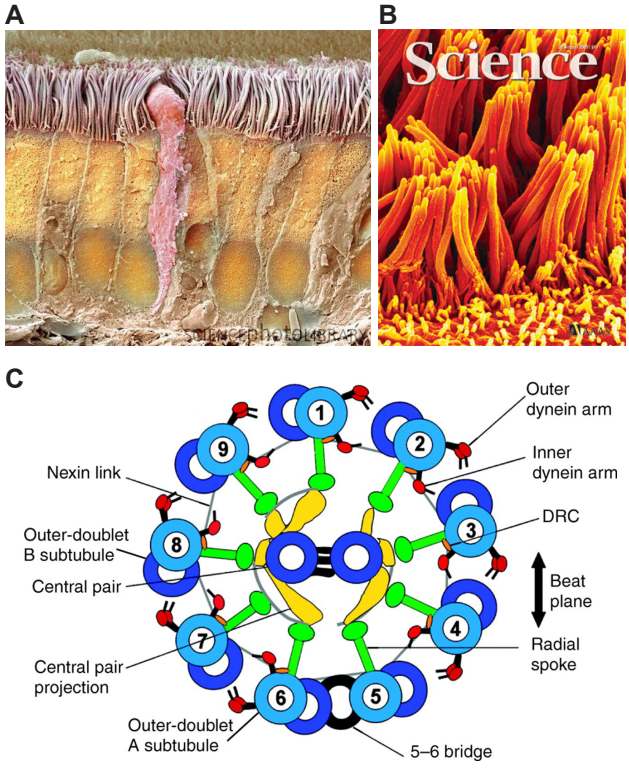

Fig.6: Motile cilia in the epithelial airways and its ultrastructure:
(A) Colored scanning electron micrograph (SEM) of a section through the trachea: The lining consists of mucus secreting goblet cells (pink) and epithelial cells that are covered in cilia.
Source: https://fr.pinterest.com/source/sciencephotolibrary.tumblr.com

(B) Science journal cover with a colored SEM (magnification ~34,000x) of the surface of mouse airway epithelia showing cilia protruding from epithelial cells Source: Science journal – Image from Tom Moninger and Data from Phil Karp.

(C) Schematic diagram of the flagellar/motile cilium axoneme in cross-section: The axoneme of a motile cilium is composed by nine parallel doublet microtubules known as outer doublets, which elongate from the basal body that contains two central microtubules, called central pair (CP). To drive their bending motion, the CP is attached to outer and inner dynein arms and radial spokes, which make a link between the nine peripheral doublet microtubules and the CP. Also, dynein motor proteins slide on the microtubule doublets to allow cilia movement. Radial spokes and a complex of proteins called the dynein regulatory complex (DRC) it is also critical for cilia motility. Adapted from (Lindemann and Lesich, 2010).

3. Left-right axis determination

The determination of the three body axes during early development is key for the organization of the vertebrate body plan. The anteroposterior (AP) and dorsoventral (DV) axes are established through precise morphogen signaling pathways. Although distinct mechanisms are behind the patterning of the AP and DV axes, both are patterned concomitantly in space and time (Hamada and Tam, 2014; Tuazon and Mullins, 2015). The left-right (LR) axis arises only after the DV and the AP axes have been defined. The role of cilia in a number of physiological processes has been long recognized, but especially in development, in which both motile and immotile cilia play important roles for LR determination (Kramer-Zucker et al., 2005; Nakamura et al., 2006). In vertebrates it occurs during early stages of embryonic development through a complex process involving epigenetic and genetic mechanisms (Capdevila et al., 2000; Hamada et al., 2002; Pourquie, 2011).

Furthermore, the use of animal models has been crucial to uncover the role of cilia in the LR development. Until a couple of decades ago our knowledge about the molecular and genetic mechanisms behind LR asymmetric morphogenesis was very poor, with no genes identified as being asymmetrically expressed on the LR axis. The earliest groundbreaking advances in the research field of LR were made possible by the use of chick embryos as a model organism. The first breakthrough was the identification of a genetic cascade asymmetrically expressed present in the developing chick embryo during gastrulation (Levin et al., 1995).

While LR symmetry breaking in several vertebrates involves cilia-mediated directional flows and asymmetric expression of nodal in the lateral plate mesoderm (LPM) (Levin et al., 1995; Lowe et al., 1996; Rebagliati et al., 1998a), chick embryos seem to use a modified symmetry breaking mechanism. Currently, the process by which LR asymmetry is established can be divided into four main steps during early development **(Fig. 7A)** (Hamada et al., 2002; Hirokawa et al., 2012; Mercola, 2003; Mercola and Levin, 2001). The first step is the initial LR symmetry-breaking event, which occurs in or near the embryonic node, as a consequent of the leftward extracellular fluid flow that is generated by the movement of motile cilia. The second step is characterized by the transduction of the newly generated asymmetric information to the left LPM, through the asymmetric expression of signaling molecules, such as the Nodal and Lefty proteins. Asymmetric expression of Nodal induces the expression of the transcription factor Pitx2c, starting then the third phase of the process. During the last phase, proteins such as Pitx2c control localized changes in cell migration, shape, proliferation and survival in order to drive the morphogenesis of various asymmetric visceral organs(Ferreira and Vermot, 2017). The establishment of the LR breaking process as described is based on studies of different vertebrates, such as zebrafish, frog, chick and mouse. Although the asymmetric patterns of gene expression differ among species, a conserved feature is the production of Nodal (or a Nodal homologue) in the left LPM. All the work developed by many groups in all vertebrates has led to the identification of the central components in the LR pathway, such as Nodal, Lefty1 and Lefty2, and the homeobox gene Pitx2 **(Fig. 7B)** (Hamada et al., 2002; Mercola, 2003). This strongly conserved LR

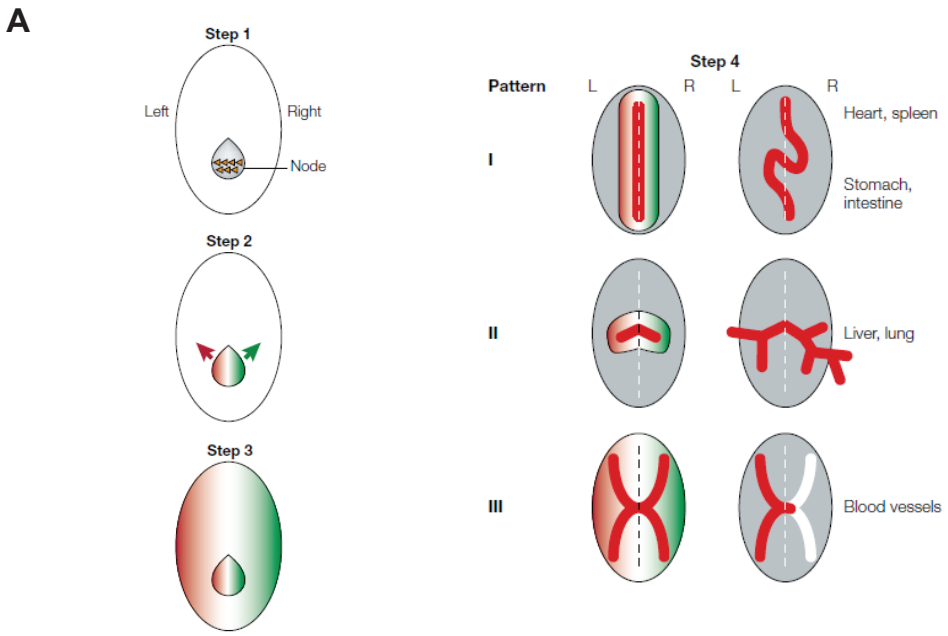

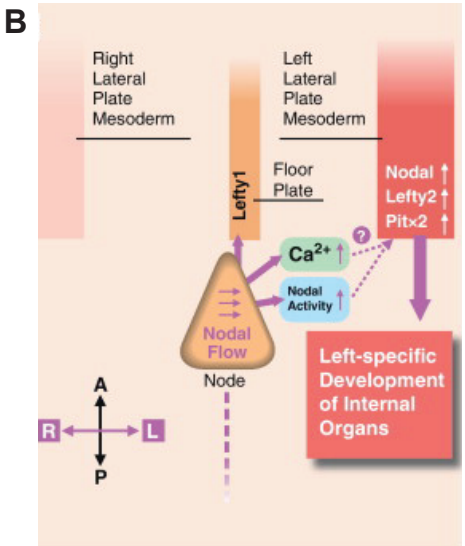

Fig.7: Four steps of left-right asymmetric morphogenesis. (A) The first step is the initial LR symmetry-breaking event, which occurs in or near the embryonic node; the second step is characterized by the transduction of the newly generated asymmetric information to the left lateral plate mesoderm (LPM) through the asymmetric expression of signaling molecules; the third step is the induction of the transcription factor Pitx2c. The last phase, proteins such as Pitx2c control localized changes in cell migration, shape, proliferation and survival in order to drive the morphogenesis of various asymmetric visceral organs. Adapted from (Hamada et al., 2002). **(B)** Readouts of nodal flow in the mouse node: according to the direction of the nodal flow, the left side of the floor plate expresses *Lefty1* and the left LPM expresses *Nodal*, *Lefty2* and *Pitx2*, possibly through a calcium elevation and *nodal* activation on the left periphery of the node. Adapted from (Hirokawa et al., 2012).

pathway throughout the vertebrate lineage, argues for its ancient origin that has been conserved through evolution (Blum et al., 2014a; Norris, 2012).

3.1 Step 1: initial LR symmetry-breaking event

It is of crucial relevance studying the Nodal-related signaling pathways and subsequent related gene cascade, but it is also important to address the knowledge gap about the event that turns nodal asymmetrically expressed in the first place. The two mutually exclusive current models will be presented in this section: one that relies on cilia-driven flows and the LROs as the "birth" of asymmetric signal, while other trusts that early determinants defined the LR axis in a cilia and LRO-independent manner.

3.1.1 LROs and cilia-driven flows

The fact that the earliest asymmetrically expressed genes are active at the node (Levin, 2005) drew attention to this structure as a location where the initial LR decision might occur. The leftward flow responsible for LR symmetry breaking was first identified in mouse by Nonaka and colleagues (Nonaka et al., 2002; Nonaka et al., 1998), and named "nodal flow". Subsequently, the role of cilia motility and the resulting nodal flow was observed in many other vertebrates like rabbit, Xenopus, and fish (Essner et al., 2005; Essner et al., 2002; Hojo et al., 2007; Kramer-Zucker et al., 2005; Nonaka et al., 1998; Okada et al., 2005; Schweickert et al., 2007), and proven to be highly conversed and required for the establishment of the LR axis in vertebrates. In this section, the LROs of mouse, zebrafish and Xenopus will be described in detail.

Mouse Node

The structure that acts as the LRO of the mouse embryo is called the node **(Fig. 8)** (Hamada and Tam, 2014; Nonaka et al., 1998; Norris, 2012; Okada et al., 2005). The mouse node can be found at the rostral end of the primitive streak of a mouse embryo at 8.25 days of development (6 somite) **(Fig. 8A)** (Hamada and Tam, 2014; Lee and Anderson, 2008; Norris, 2012). The ventral node, is constituted of a columnar epithelium that is localized between the anterior notochord and the primitive streak in the midline of the embryo (Blum et al., 2007; Lee and Anderson, 2008). Most of the cells lining the central region of the ventral node (also called pit cells) have a motile cilium **(Fig. 8A-B)** (Sulik et al., 1994). These cilia are polarized with respect to the AP axis **(Fig. 8G)** (Hashimoto et al., 2010) and by rotating in a clockwise direction, drive the nodal flow leftwards in the node (Essner et al., 2002; Hirokawa et al., 2012; Nonaka et al., 1998) **(Fig. 8D-F)**. At present it is thought that 9+0 node cilia are motile and produce a vortical motion **(Fig. 8C-F)** (Nonaka et al., 1998). However, the existence of 9+2 cilia in the node has also being reported (Caspary et al., 2007; Odate et al., 2016), even though in a much lower fraction than the 9+0 cilia and without any side biased distribution (Odate et al., 2016). Interestingly, it has been shown that nodal 9+0 cilia ultrastructure can be altered with a brief exposure to Taxol (a microtubule-stabilizing drug), in contrast with 9+2 cilia that were unaltered. This report concludes that even though the absence of central pair and radial spokes in node cilia allows them to

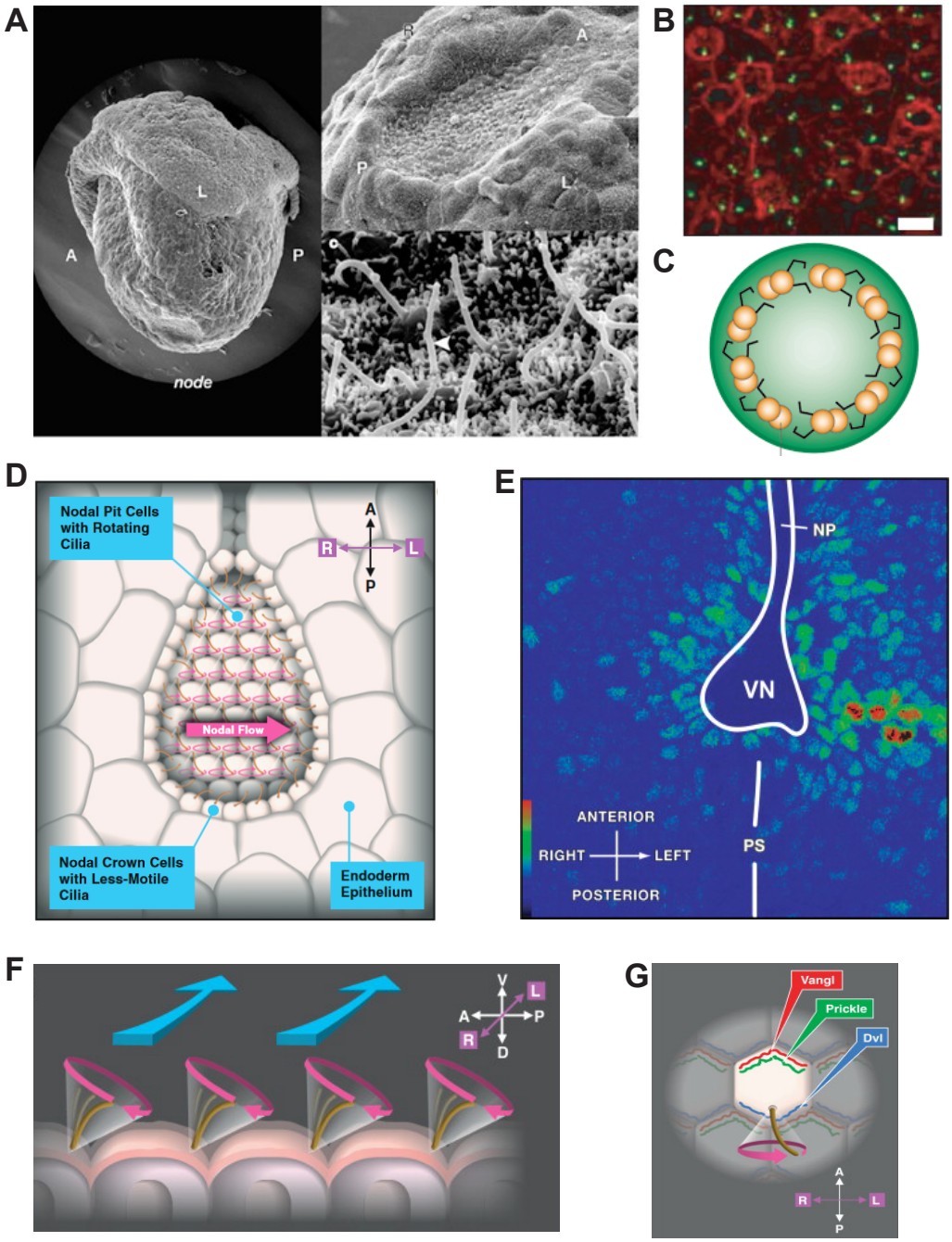

Fig.8: The mouse LRO – the Node: (A) The node localization in the embryos and its monocilia: arrowhead shows the monocilia by scanning electron micrograph (SEM) in a 8.0 days post coitum (dpc) mouse embryo. The anteroposterior (AP) and left–right (LR) axes are indicated. Adapted from (Hamada et al., 2002). **(B)** Posterior positioning of the cilia represented by immunofluorescence microscopy: in red the cell margins and in green the cilia – upper in anterior. Adapted from (Hirokawa et al., 2012). **(C)** Schematics of the ultrastructure of a 9+0 cilia that are found in early mouse embryos. Even being 9+0 these cilia are motile. Adapted from (Hamada et al., 2002). **(D)** Ventral view of the mouse node showing the two populations of cilia that composed the mouse node: nodal pit cells with rotating cilia in the middle and nodal crown cells with led motile cilia at the periphery. Motile cilia generate a flow called nodal flow. Adapted from (Hirokawa et al., 2012). **(E)** Calcium is elevated on the left side of the node in response to the nodal flow. Ventral view of a 7.5 dpc mouse embryo stained by Fluo3-AM (to detect calcium) is shown in a pseudocolor image. NP, notochordal plate; VN, ventral node; PS, primitive streak. VN, NP, and PS are traced by white lines. Adapted from (Hirokawa et al., 2006). **(F)** Cilia tilted rotation generate the leftward flow (ventral view). This tilted rotation allows cilia to generate a net flow over time, since the recovery and active strokes have different phases. Adapted from (Hirokawa et al., 2012). **(G)** Schematic representation of PCP signaling in the nodal pit cells. *Vangl* is in red and *Prickle* in green in the anterior pole and *Dishevelled* is depicted in blue in the posterior pole. This pathway may polarize the nodal pit cells along the AP axis, resulting in a posterior tilt. Adapted from (Hirokawa et al., 2012)

perform a unidirectional rotation, as a trade-off, it makes their ultrastructure more fragile (Shinohara et al., 2015). In contrast to the pit cells, the crown cells located at the edge of the node have immotile cilia **(Fig. 8D)** (Yoshiba and Hamada, 2014; Yoshiba et al., 2012). Thus, in the node, two populations of cilia were described based on the presence/absence of *left-right dynein-related* (*lrdr*) expression (McGrath et al., 2003; Supp et al., 1997): motile lrd-positive cilia at the center (pit cells), and a population of immotile lrd-negative cilia at the periphery (crown cells) (McGrath et al., 2003). The latter was suggested to be capable of sensing the mechanical stress of the stronger leftward flow (mechanosensory cilia), whereas the motile cilia movement drives a leftward fluid-flow over the mouse LRO **(Fig. 8D)** (McGrath et al., 2003; Tabin and Vogan, 2003). Lrd gene mutations in mice (*inversus viscerum* – iv) result in immotile cilia in the node (Lowe et al., 1996; Okada et al., 1999; Schreiner et al., 1993; Singh et al., 1991; Supp et al., 1999; Supp et al., 1997), and as a consequence absence of nodal flow and randomized LR axis. Lrd-related expression can be found also in chick, Xenopus and in zebrafish gastrulating embryos (Essner et al., 2002). Experiments in which mouse laterality has been reversed when an artificial rightward flow was imposed on the node (Nonaka et al., 2002), or proper laterality was restored in mutants with no flow - *inversus viscerum* (iv) - just by artificially provide to their nodes a leftward flow (Nonaka et al., 2002; Okada et al., 1999), are supportive that the directional flow provides the asymmetric cue needed to determine the LR axis.

Downstream of nodal flow, asymmetric calcium (Ca^{2+}) signaling is observed at the periphery of the node, with stronger signaling on the left side compared to the right **(Fig. 8E)**. This rising in calcium is thought to occur through the function of target genes, such as polycystic kidney disease 2 (Pkd2) and polycystic kidney disease 1-like1 (Pkd1l1), that encodes a Ca^{2+} channel and the putative molecule for force sensing (Ferreira and Vermot, 2017; McGrath and Brueckner, 2003; Tabin and Vogan, 2003).

Zebrafish Kupffer's vesicle

In zebrafish and other teleost fishes, Kupffer's vesicle (KV) is believed to be the functional equivalent to the mouse ciliated node in the LR axis determination (Amack, 2014; Brummett and Dumont, 1978; Dasgupta and Amack, 2016; Essner et al., 2002), and thus called the zebrafish LRO. Firstly described by *Kupffer* in 1868, only with morphological studies using electron microscopy in the bait fish *Fundulus heteroclitus*, it was revealed that KV cells were monociliated (Brummett and Dumont, 1978). In zebrafish, the precursor cells of the KV are called dorsal forerunner cells (DFCs) that migrate at the leading edge of the embryonic shield during gastrulation (Cooper and D'Amico, 1996; Melby et al., 1996) **(Fig. 9A-B)**. In contrast to other cells in this region, DFCs do not involute during gastrulation, but remain at the leading edge of epibolic movements (Cooper and D'Amico, 1996; Melby et al., 1996; Oteiza et al., 2008). By the end of gastrulation, DFCs migrate deeper into the embryo and organize to form the KV at the end of epiboly **(Fig. 9B)** (Amack et al., 2007; Oteiza et al., 2008). During subsequent somite stages, KV constitute a small but distinctive epithelial closed vesicle containing fluid, located mid-ventrally posterior to the yolk cell or its extension, and transiently present during most of the segmentation period **(Fig. 9C)** (Kimmel et al., 1995; Kramer-Zucker et al., 2005). The monociliated epithelium of the KV is composed of 9+2 cilia **(Fig. 9D)** (Ferrante et al., 2009; Kramer-Zucker et al., 2005; Kreiling et al., 2007). As in the mouse node (Cartwright et al., 2004), KV monocilia

have a rotational motion with a tilted axis of rotation **(Fig. 9E-G)** (Borovina et al., 2010; Supatto et al., 2008). Little is known about the potential factors that could control cilia beat frequency and cilia length. Notch signaling pathway was been involved in cilia length control (Lopes et al., 2010) and *foxj1* (winged-helix domain-containing transcription factor) in cilia motility (Hellman et al., 2010; Yu et al., 2008). Furthermore, it has been reported a role for the inositol 1,3,4,5,6-pentakisphosphate 2-kinase (Ipk1) in ciliary beating and length maintenance (Sarmah et al., 2005; Sarmah and Wente, 2010). By beating, cilia are thus responsible for the production of an asymmetric flow in the KV in the DV axis **(Fig. 9F)** (Essner et al., 2005; Kramer-Zucker et al., 2005; Supatto et al., 2008). This flow is thought to trigger an asymmetric calcium response on the left side of the cavity **(Fig. 9H)** (Francescatto et al., 2010; Sarmah et al., 2005; Yuan et al., 2015), which is critical to establish the left-sided expression of genes involved in providing left identity, such as *southpaw* and *pitx2* (Kramer-Zucker et al., 2005). However, how the flow is interpreted and then converted into LR asymmetric gene expression is still unknown.

Several studies confirmed ciliated cells are not equally distributed in KV, given the existence of a cluster of ciliated-cells in the anterior-dorsal (AD) region of the KV (Kramer-Zucker et al., 2005; Kreiling et al., 2007; Okabe et al., 2008). This denser region of ciliated cells it thought to be a potential source of the driving force behind the strong directional flow **(Fig. 9G)** (Kramer-Zucker et al., 2005; Kreiling et al., 2007; Okabe et al., 2008; Sampaio et al., 2014; Supatto et al., 2008; Wang et al., 2011; Wang et al., 2012). Recent studies suggested that a highly regulated organization of the LRO is dependent on cellular forces and thus crucial for the proper determination of the LR axis **(Fig. 9I)** (Compagnon et al., 2014; Ferreira and Vermot, 2017; Wang et al., 2011; Wang et al., 2012).

Xenopus Gastrocoel roof plate

Motile cilia also generate unidirectional fluid flow in the LRO of Xenopus embryos, in the gastrocoel roof plate (GRP) during neurulation, prior asymmetric nodal transcription starts in the left LPM (Blum et al., 2014a; Schweickert et al., 2007). The ciliated gastrocoel roof plate (GRP), where leftward flow develops during neurulation, is derived from the superficial mesoderm of the gastrula, in close contact with Spemann's organizer during early gastrulation **(Fig. 10A-D)** (Blum et al., 2014b).

Experiments injecting methylcellulose to prevent the leftward flow, resulted in laterality defects, demonstrating the key role of the flow for the asymmetric gene expression and organ *situs* (Schweickert et al., 2007). Structural and molecular characterization studies of cilia demonstrated the homology between the LRO of Xenopus, mouse and zebrafish. Like others, *Xenopus* embryos revealed a cilia-driven fluid flow at comparable developmental stages, in homologous embryological structures, and also in timed-transient organs before the induction of asymmetric *nodal* transcription in the left LPM **(Fig. 10E-G)** (Schweickert et al., 2007). Although, flow velocities generated within the LRO of fish, mice and Xenopus (Blum et al., 2009; Blum et al., 2014a; Blum et al., 2014b; Schweickert et al., 2007; Supatto and Vermot, 2011), are much lower when compared to other organs in zebrafish (Anton et al., 2013; Cartwright et al., 2008; Cartwright et al., 2009; Ferreira and Vermot, 2017; Goetz et al., 2014; Hove et al., 2003; Supatto and Vermot, 2011), that could be due to the physical environment of the LROs **(Table 1)**.

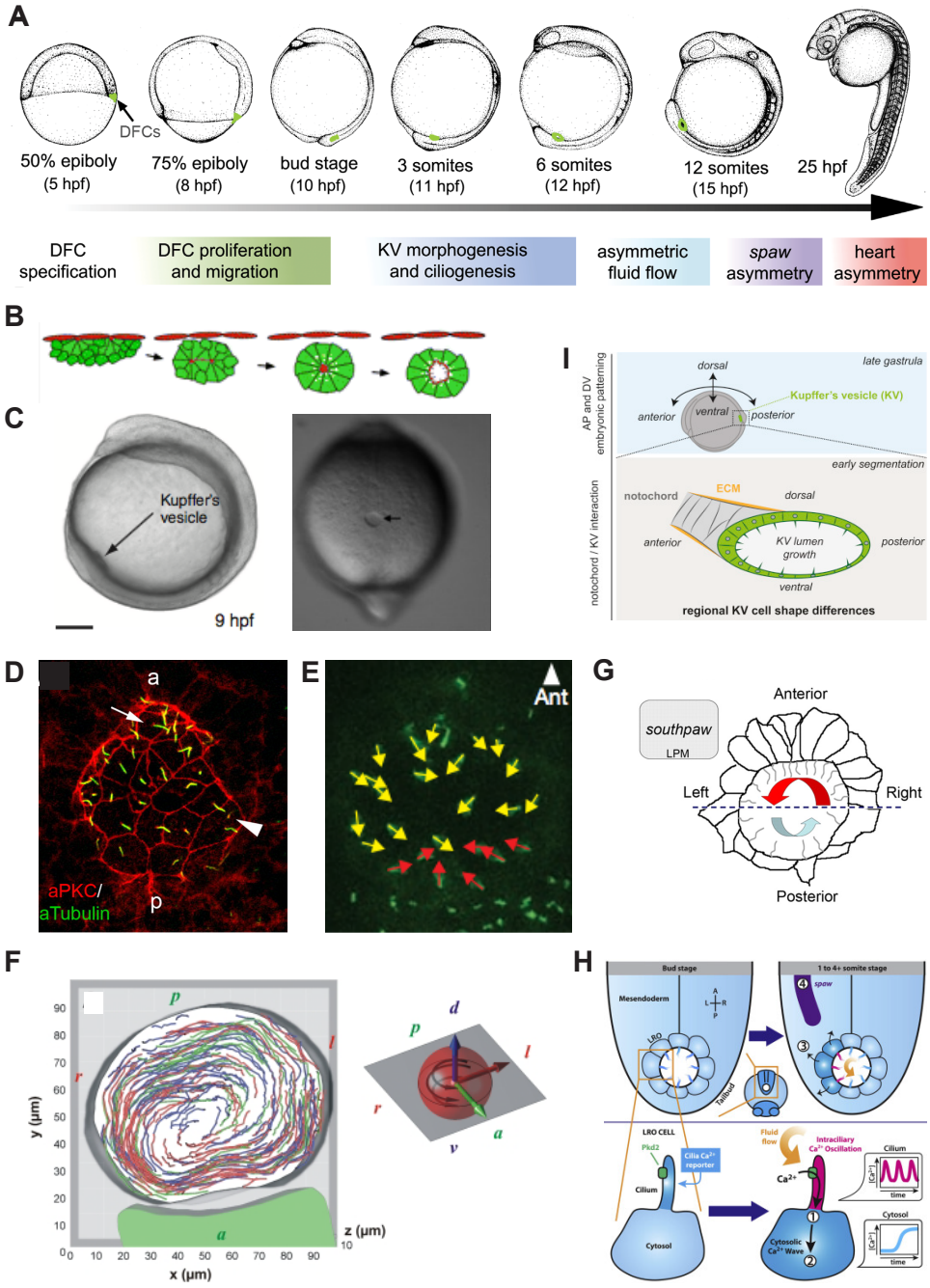

Fig.9: The zebrafish LRO – the Kupffer's vesicle (KV): (A) Timeline of zebrafish developmental events critical for LR axis determination and embryo patterning. In green are depicted the dorsal forerunner cells (DFCs), precursors of the KV. Adapted from (Gokey et al., 2016). **(B)** Schematic representation of KV lumen formation from the DFCs cluster. Adapted from (Oteiza et al., 2008). **(C)** Brightfield side and tail views of a 10 hours post-fertilization (hpf) zebrafish embryo, black arrows highlight the KV: (A) Adapted from (Supatto and Vermot, 2011) and (B) adapted from (Kreiling et al., 2007). **(D)** Fluorescent immunostaining of KV cells at 8-SS with aPKC (red) and acetylated tubulin (green) antibodies. "a" = anterior and "p" = posterior. Adapted from (Wang et al., 2011). **(E)** Z-stack confocal projections through the floor and wall of *Arl13b–GFP* (green) labelled embryo showing a posterior tilt in the KV. Anterior is up. Adapted from (Borovina et al., 2010). **(F)** KV rotational flow extracted from fluorescence data. (*A*) Particle tracks indicating the fluid streamlines of the steady-state flow within the KV. The particles exhibit a circular motion around the DV axis (panel on the left). Schematics of the spatial orientation of the KV (AP, DV and LR are represented in *green*, *blue*, and *red*, respectively). The black arrows indicate the counterclockwise rotation of the flow (when viewed from the dorsal side) (panel on the right). Adapted from (Supatto et al., 2008). **(G)** Schematics of the AP gradient of ciliated cells in the KV: a dense packing of elongated ciliated cells in the anterior half of KV (delineated by the dashed line) drives strong leftward flow (red arrow), and fewer cilia in the posterior half of KV move fluid rightward at a slower velocity (blue arrow). This flow is thought to trigger the asymmetric *spaw* expression in left LPM. Adapted from (Wang et al., 2011). **(I)** Regional KV cell shape differences, the mechanism behind: the notochord induces regional differences in cell shape within KV by triggering extracellular matrix (ECM) accumulation adjacent to anterior-dorsal (AD) regions of KV. This localized ECM deposition restricts apical expansion of lumen-lining epithelial cells in AD regions of KV during lumen growth. Adapted from (Compagnon et al., 2014). **(H)** Intraciliary calcium was described to be crucial to initiate the LR development, in parallel with cilia motility and flow. Adapted from (Yuan et al., 2015).

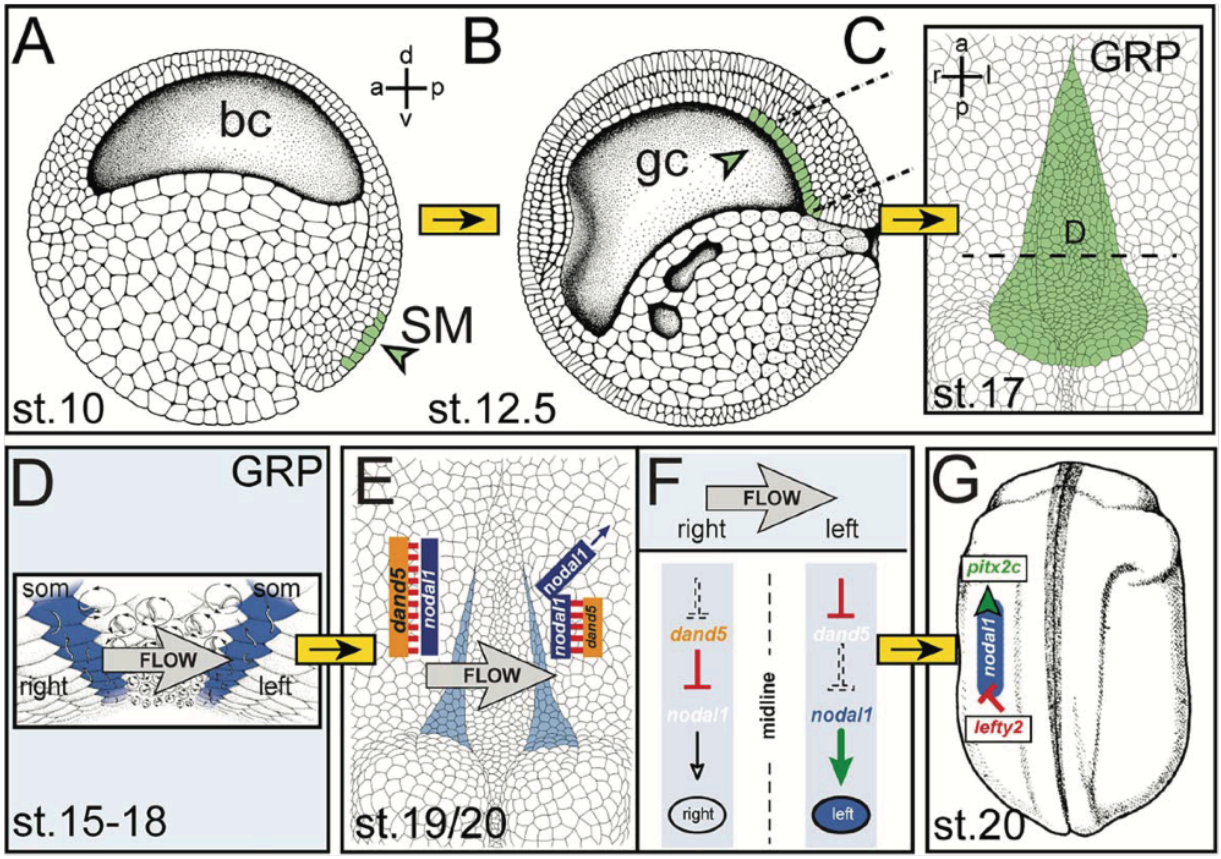

Fig.10: The Xenopus LRO – the gastrocoel roof plate (GRP): symmetry breaking mechanism dependent on cilia and cilia-driven flow. (A-C) The ciliated GRP develops from the superficial mesoderm (SM), which expresses the motile cilia transcription factor *foxj1*, and which invaginates during gastrulation. **(D)** Polarized cilia at the center of the GRP produce a leftward flow of extracellular fluids. **(E)** Leftward flow will represse the Nodal antagonist *dand5/coco* in the lateral GRP cells, and de-repress the co-expressed *Nodal* (F), thus inducing an asymmetric Nodal signaling cascade in the left LPM **(G)**. Adapted from (Tisler et al., 2017).

Table 1: Table summarizing the cilia properties of various embryonic models. Adapted from (Supatto and Vermot, 2011)

Species	Organ	Structure	Mono- or multiciliated cells	Frequency (Hz)	Length (μm)	Rotation direction (view from the cilium tip)	θ (deg)	ψ (deg)	Directional flow velocity (μm s^{-1})
Zebrafish	Left–right organizer (Kupffer's vesicle)	9 + 2[a]	Mono[a]	29.7 ± 0.3[b] 26.2 ± 1.6[a]	3.3 ± 1.1[a] 3.7 ± 0.8[c]	Clockwise[b,d,e] Counterclockwise[a]	30[f]		10–50[f]
	Inner ear	9 + 2 9 + 0 (this study)	Mono[g]	34 ± 6[g]	5.9 ± 0.2[g]		~90[h]		~10–50[h]
	Central canal spinal cord	9 + 0[a]	Mono[a]	12.3 ± 3.4[a]	2.1 ± 0.7[a]				0.45 ± 0.03[a]
	Pronephric ducts	9 + 2[a]	Mono and multi[a]	20.0 ± 3.2[a]	8.8 ± 2[a]	Clockwise[a]			
Mouse	Left–right organizer (node)	9 + 0[d]	Mono[d]	10.7 ± 2.8[i]	5.5[i]	Clockwise[i]	35–40[i]	40–50[i]	4 (leftward)[i] −2 (rightward)[i] 50[j]
	Brain ventricles		Multi[k]	12–17[k]	8–10[k]	Wave pattern[k]			
Medaka	Left–right organizer (Kupffer's vesicle)	9 + 2[l]	Mono[l]	42.7 ± 2.6[i]	5[i]	Clockwise[i]	35–40[i]	40–50[i]	7.4 ± 3.6[i]
Xenopous	Gastrocoel roof plate			20–25[m]	3–5[m]	Clockwise[m]			3.5 (leftward)[m]

Cilia are characterized by their internal microtubule structure, by their number at the cell surface (mono- or multiciliated), their beating frequency, length, direction, and rotation direction. ψ and θ give a good indication about the ability of cilia to generate a directional flow. When divergent informations are reported in the literature, several indications are present in the same box. For example, both clockwise and counterclockwise rotation directions have been reported in zebrafish.

[a] Kramer-Zucker *et al.* (2005).
[b] Okabe *et al.* (2008).
[c] Lopes *et al.* (2010).
[d] Nonaka *et al.* (1998).
[e] Okada *et al.* (1999).
[f] Supatto *et al.* (2008).
[g] Colantonio *et al.* (2009).
[h] Wu *et al.* (2011).
[i] Okada *et al.* (2005).
[j] Nonaka *et al.* (2002).
[k] Hirota *et al.* (2010).
[l] Kobayashi *et al.* (2010).
[m] Schweickert *et al.* (2007).

Chick Hensen's node

While LR symmetry breaking in several vertebrates involves cilia-mediated directional flows and asymmetric expression of nodal in the LPM (Levin et al., 1995; Lowe et al., 1996; Rebagliati et al., 1998a), chick embryos seem to use a modified symmetry breaking mechanism, in which no ciliary flow is produced, even though the Hensen's node is ciliated (Essner et al., 2002; Manner, 2001). The chick uses a different strategy for symmetry breaking that relies on asymmetric cell rearrangements that generate a leftward migration of cells around the Hensen's node (Cui et al., 2009; Essner et al., 2002; Ferreira and Vermot, 2017; Gros et al., 2009; Manner, 2001; Mendes et al., 2014; Pagan-Westphal and Tabin, 1998; Tsikolia et al., 2012).

3.1.2 Prevailing models of LR symmetry breaking based on cilia-driven flows

Even though a lot have been done in the last decades with several animal models, the mechanism by which nodal flow is sensed and induces a subsequent asymmetric gene cascade is not totally clear and thus remains the major unanswered question in the LR patterning field (Hamada, 2008; Hamada and Tam, 2014; Marshall and Kintner, 2008). Some hypotheses are currently in debate, either suggesting the asymmetric distribution of signaling molecules (morphogens or membrane-bounded vesicles), or an asymmetric mechanical influence sensed by immotile cilia in the node **(Fig. 11A-C)** (Ferreira and Vermot, 2017).

The asymmetric distribution of signaling molecules in the LRO, can be divided in two hypothesis: the "morphogen hypothesis" **(Fig. 11A)** and the "nodal vesicular parcel hypothesis" **(Fig. 11B)**. The first argues that a short-lived molecule becomes enriched on the left side of the node by the action of the leftward flow, creating a LR asymmetric signal and could be detected on the left side of the node – gradient of concentration (Nonaka et al., 1998). Both computational and experimental experiments argued that such asymmetric molecule gradient is possible but only for molecules between 15 and 50 kDa in size (Cartwright et al., 2004; Norris, 2012; Okada et al., 2005). Yet, the nature of the hypothetical morphogen and its receptors are completely unknown. The second hypothesis relies on the existence of membrane-bounded vesicles that are carried leftwards by the action of the nodal flow, where they burst and release their cargoes asymmetrically (Tanaka et al., 2005). It has been shown *fibroblast growth factor* (FGF) signaling triggers the secretion of little membrane-vesicles (0.3–5μm) termed "nodal vesicular parcels" (NVPs), that carry *Sonic hedgehog* (Shh) and *retinoic acid* (RA) (Tanaka et al., 2005). The movement of NVPs across the mouse node was mathematically modeled (Cartwright et al., 2007) and it was demonstrated that the flow can indeed cause the vesicles to accumulate on the left side, in line with what it was shown for the morphogen hypothesis (Cartwright et al., 2004). However, according to this numerical model the biophysical properties of node (such as high viscosity) do not allow the mechanism of NVP breaking in the vicinity of cilia or by the action of flow (Cartwright et al., 2007). More studies would have to be done to give more insights about the mechanism by which the rupture of the NVPs could happen on the left-side of the node.

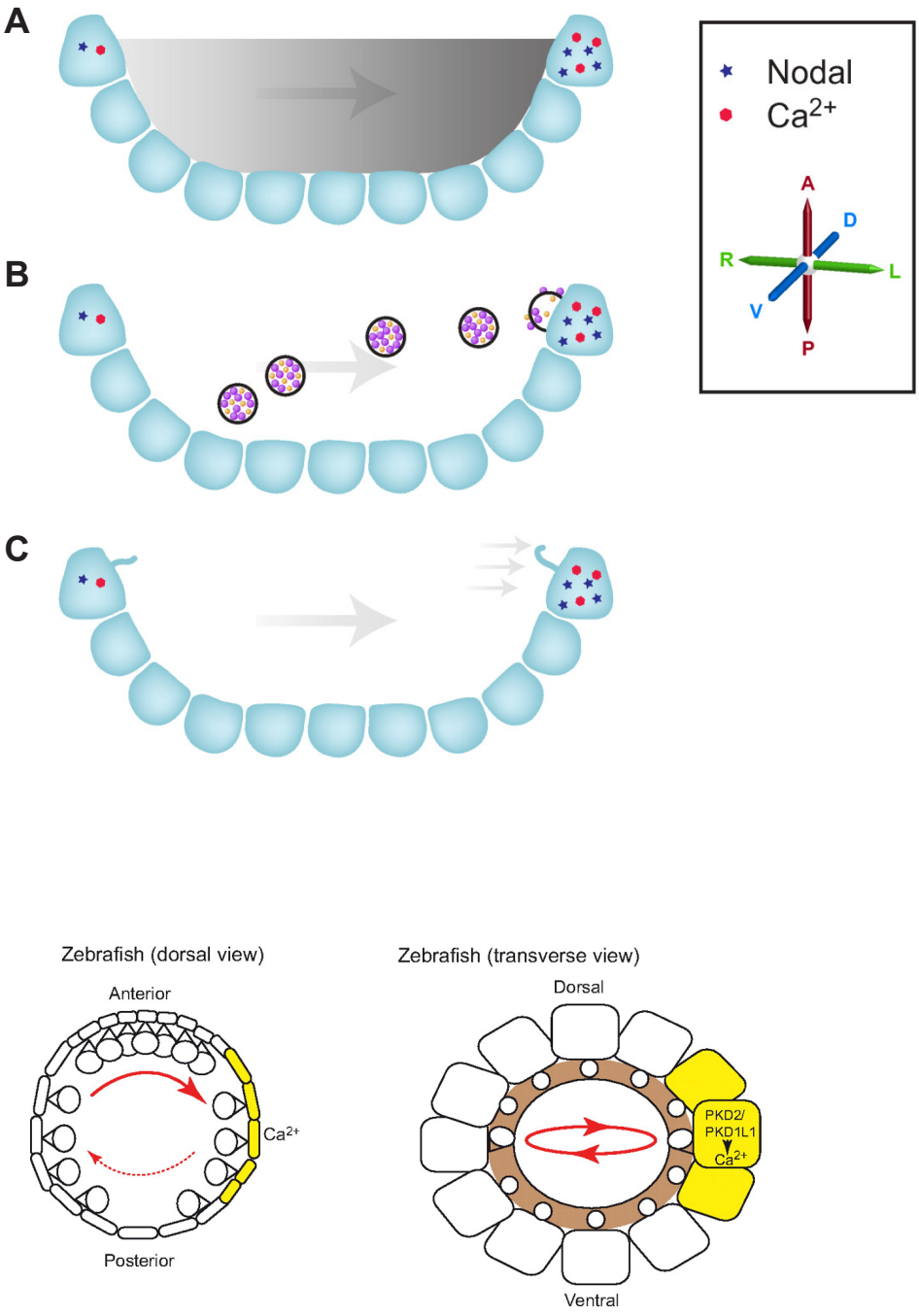

Fig.11: Three potential models of how flow breaks symmetry at the node: side view of the node with the legend in the inset. The node is represented in section, with the axes rotated by 90° from Figure 1; the axes are marked. **(A)** The morphogen hypothesis posits that a morphogen produced within the node becomes asymmetrically localized in response to flow (depicted as a gray gradient). **(B)** The nodal vesicular parcel (NVP) hypothesis implies that morphogen-containing vesicles are carried leftwards by nodal flow, breaking in contact with cilia on the left side of the node. **(C)** The two-cilia hypothesis argues that flow itself is detected on the left side of the node by mecnhanically deforming cilia-containing mechanosensory channels, that would release calcium. In fact, all three hypothesis release calcium and activate Nodal-cascade on the left side of the node. Adapted from (Norris, 2012). **(D)** Cilia-driven flows in the left-right organizer of zebrafish (KV): rotational flow in the KV lead to an asymmetric calcium response on the left embryonic side (yellow) through the calcium channels PKD2 and PKDL1. Although asymmetric calcium signaling is well characterized, no gradient or NVPs have been identified so far. However, chaotic flow has been demonstrated in vivo (represented in brown). Adapted from (Freund et al., 2012).

The mechanical sensed hypothesis is called the 'two-cilia model' **(Fig. 11C)** and is based on the discovery that two populations of cilia coexist in the node as described previously. One of motile cilia identifiable by left-right dynein (*Lrd*), and other of immotile cilia capable of sensing the mechanical stress generated by the leftward flow (also called sensory cilia), only on the left side of the node (McGrath et al. 2003; Tabin & Vogan 2003). It has been proposed that the mechanosensory cilia trigger a left-sided calcium signal through the action of *Polycystic kidney disease 2/Transient receptor potential Polycystic2-like* (Pkd2/Trpp2) channels localized on the cilia axoneme **(Fig. 11D)**. Pkd2 is known to form a functional calcium channel that is thought to sense the bending of primary cilia induced by urine flow in the renal tubule, thus functioning as a mechanosensor (Nauli et al., 2003). *Polycystic kidney disease 1 - like 1* (*Pkd1l1*) is the functional partner of Pkd2 **(Fig. 11D)**. Pkd1l1-Pkd2 colocalize on motile cilia in the medaka KV where all cilia are thought to be motile (Kamura et al., 2011). Same reported showed flow can activate cilia that are chemosensory on the left side of the embryo (Kamura et al., 2011). Both *Pkd2* and *Pkd1l1* are involved in LR patterning, being needed for the embryo to respond to nodal flow (Field et al., 2011; Pennekamp et al., 2002). However, how only the immotile cilia on the left would sense the pulling force exerted by the flow and not the ones on the right has been questioned and is still a matter of debate regarding the "two-cilia model" hypothesis (Ferreira and Vermot, 2017; Pennekamp et al., 2015; Supatto and Vermot, 2011).

The current hypothesis is that all cilia may have sensory functions. Motile cilia of the mammalian respiratory epithelium have been reported to exhibit both mechanosensitivity and chemosensitivity (reviewed in (Bloodgood, 2010)). Recently, it was also reported an unexpected demonstration of chemoreception by the localization of different members of the bitter taste-receptor family to motile cilia of airway epithelial cells (Shah et al., 2009). Indeed, bitter compounds induce a rise in intracellular-calcium concentration in ciliated cells corresponding to an increase in the cilia beat frequency (Shah et al., 2009).

Indeed, for all these hypotheses, the outcome is an asymmetric left-sided Ca^{2+} signal at the LRO **(Fig. 11)** (McGrath et al., 2003; Yuan et al., 2015), and currently only the two-cilia hypothesis through the known function of Pkd1l1/Pkd2 provides a mechanism to explain how this signal might be generated (reviewed in (Ferreira and Vermot, 2017; Norris, 2012; Pennekamp et al., 2015). Clearly, more studies will be needed to clarify all these hypotheses and their physical limitations in the process of LR breaking of symmetry.

3.1.3 More than cilia: other players in the establishment of the initial asymmetry.

It has been proposed that cilia-driven leftward flow purely acts as an amplification step for a LR asymmetry that exists prior to the directional fluid flow, at least in Xenopus, chick and fish (Vandenberg et al., 2013). The so called "ion flux" hypothesis **(Fig. 12)** predicts that the asymmetry defined by ion-flux should be present in the absence of flow, and thus LR determination depends on a very early differential ion flux created by H+/K+-ATPase activity. In *Xenopus*, an asymmetrically localized ion flux is set up through an H+/K+ ATPase transporter and it has been shown that maternal

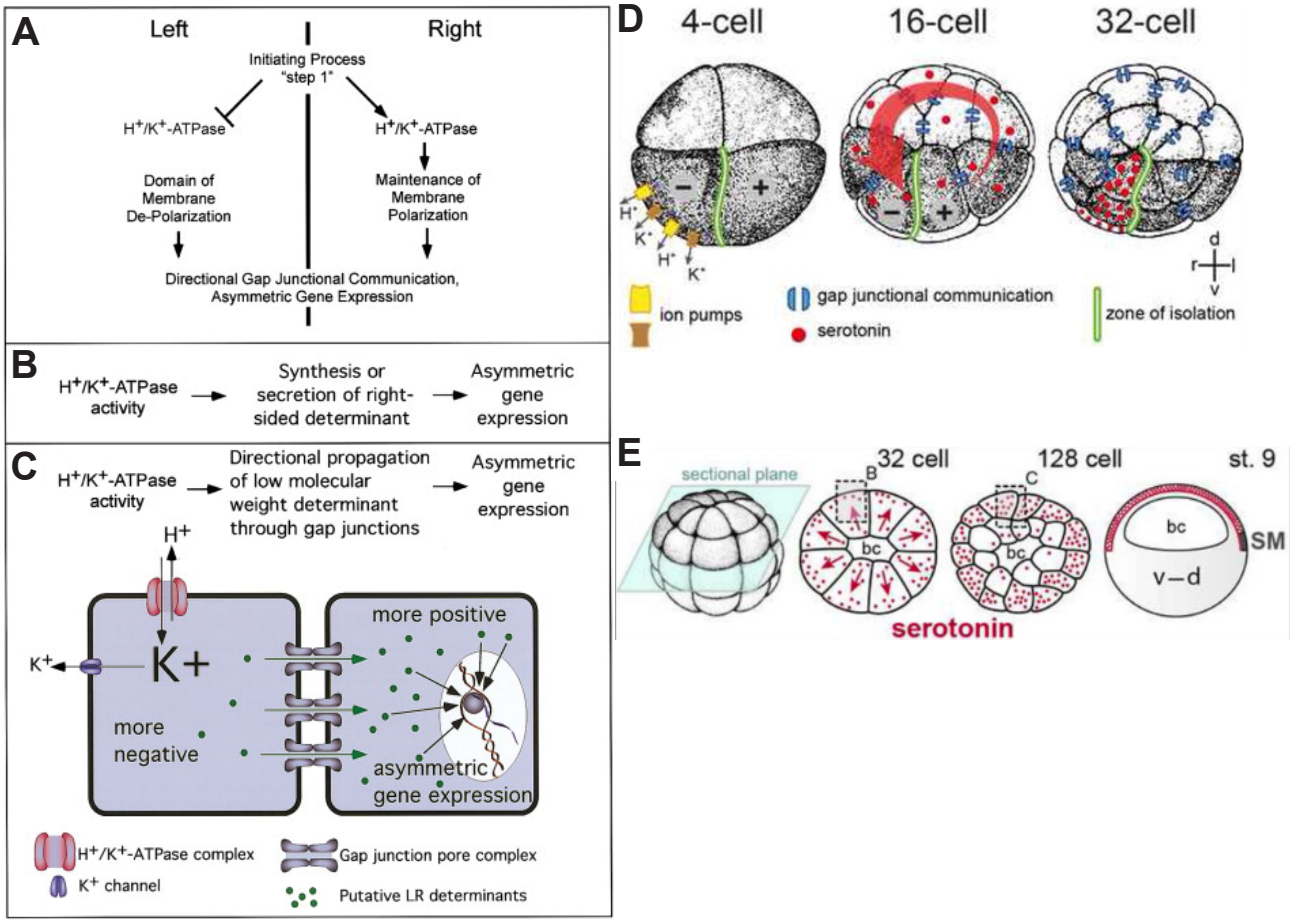

Fig.12: Alternative symmetry breaking mechanisms ("ion-flux" model): (A-C) Models for Involvement of H^+/K^+-ATPase in Early LR Asymmetry. **(A)** H^+/K^+-ATPase activity is localized to the right side of early *Xenopus* and chick embryos. **(B)** H^+/K^+-ATPase function might directly regulate the secretion of an early determinant of asymmetric gene expression. **(C)** H^+/K^+-ATPase might influence the propagation of unknown, low molecular weight LR determinants (green dots) between cells. Unidirectional propagation might rely simply on electrophoresis of charged determinants through open gap junction channels (depicted) or connexin gating. The segregation of determinants triggers asymmetric expression of genes in multicellular fields. Adapted from (Levin et al., 2002). **(D)** Asymmetrically expressed ion pumps create a voltage gradient in the 4-cell embryo which initiates the electrogenic transfer of serotonin through gap junctional communication (GJC) to the ventral-right lineage at the 32-cell stage. Serotonin accumulates in this lineage because the ventral midline is devoid of GJC. Adapted from (Blum et al., 2014b). **(E)** Schematic serotonin accumulation in the epithelial layer of the blastocoel roof before the onset of gastrulation. Transversal sections of 32- and 128-cell embryos (plane indicated in light blue) and sagittal (animal-vegetal) section of stage 9 blastula embryo. Adapted from (Blum et al., 2014b).

H+/K+-ATPase mRNA is symmetrically expressed in the 1-cell embryo but becomes localized during the first two cell divisions, demonstrating that asymmetry is generated (Levin et al., 2002; Vandenberg et al., 2013). Moreover, the use of H+/K+-ATPase inhibitors perturb the normal left-sidedness of asymmetric gene expression and organ heterotaxia in Xenopus (Levin et al., 2002; Vandenberg et al., 2013). Same report suggested cytoskeletal motor proteins asymmetrically transport a maternal deposit of the ion pump ATP4 (as mRNA and/or translated protein), changing its distribution from symmetric to asymmetric, and thus generating an intracellular pH and voltage gradient. Moreover, the small charged molecule – potentially serotonin (Fukumoto et al., 2005) -, would be driven to the left side by gap junction communication channels (GJC) **(Fig. 12)** (Levin and Mercola, 1998b; Levin et al., 2002; Vandenberg et al., 2013). This biased distribution of serotonin is proposed to repress Nodal activity on the right side, thus activating it on the left in both *Xenopus* and chick embryos (Levin and Mercola, 1998b, 1999; Levin et al., 2002; Vandenberg et al., 2013). Although H^+/K^+-ATPase subunit mRNAs are symmetrically localized in chick embryos, in contrast with frog embryos, an endogenous difference in membrane voltage potential exists between the left and right sides of the primitive streak in these embryos. Inhibition of GJC channels also induces heterotaxia in *Xenopus* and chick (Levin and Mercola, 1998b, 1999; Levin et al., 2002; Vandenberg et al., 2013). Furthermore, in zebrafish it was shown the LR axis can be also determined by the early activity of an H+/K+ ATPase pump, even without affecting cilia or KV fluid flow (Kawakami et al., 2005). The function of another proton pump, the H+-V-ATPase, was also been reported to determine the LR axis in *Xenopus*, fish and chick, and particularly in zebrafish ciliogenesis in the KV was affected (Adams et al., 2006).

Even though the evidences described previously, different reports have shown experimental data confirming the inherent importance of the LRO for breaking the initial symmetry of the embryos. When the medaka fish KV was mechanically destroyed, severe laterality defects occurred (Bajoghli et al., 2007). Similar outcomes were described when the precursor cells of the LROs of the Xenopus gastrula (Blum et al., 2009) and zebrafish embryo (Essner et al., 2005) were removed or ablated, but also, when the viscous properties of the flow were disrupted, preventing the induction of the Nodal cascade when flow is hampered (Schweickert et al., 2007; Shinohara et al., 2012). Based in all this work, it is also plausible that LROs and its motile cilia break the initial symmetry, and not act as amplifiers of some earlier laterality signals.

Although the fluid flow generated by cilia seems to be the first symmetry-breaking event in mouse, it may not be the initial event in other organisms where it is more likely to serve as an amplification mechanism of the LR decision made earlier in development. In zebrafish, X*enopus* and chick, different mechanisms seem to act prior to the leftward flow initiation but so far, evidences for both models of breaking the initial symmetry seem plausible, even if the models are mutually exclusive. Only future work will give more insights about the true mechanism in place, even though different organisms could have adapted their symmetry-breaking event throughout evolution.

3.2 Step 2: Mechanism of *nodal* induction and nodal-related gene cascade

Before visible morphological LR asymmetries can be observed in the vertebrate embryo, a conserved cascade of asymmetrically expressed genes, called the Nodal cascade is activated at the onset of gastrulation (reviewed in (Lourenço, 2010)). As mentioned before in this introduction, many groundbreaking advances in the LR asymmetry came from studies in chick embryos. The first breakthrough was the identification of a cascade of asymmetrically expressed signals present in the developing chick embryo during gastrulation (Levin et al., 1995; Pagan-Westphal and Tabin, 1998). By using *in situ* hybridization techniques, the chick embryos allowed the analysis of gene expression patterns, long before asymmetric morphogenesis occur (Levin et al., 1995). Given its simple geometry during gastrulation stages compared with other models like mouse, frog or fish made the chick embryo an outstanding model to study gene expression at the time. It was back in 1995, Levin and colleagues discovered a number of genes asymmetrically expressed in the developing chick embryo (Levin et al., 1995), which included *Activin type IIa Receptor* (cAct-RIIa), *Sonic hedgehog* (Shh), *Nodal* (known as *cNR-1*), and *Hepatocyte nuclear factor 3-beta* (HNF3β). Shh protein was the first asymmetric signal identified in the chick node (Levin et al., 1995; Pagan-Westphal and Tabin, 1998). Further downstream in the pathway are the left-specific genes nodal, *lefty-1*, *lefty-2* and *Pitx2* (Levin et al., 1995; Logan et al., 1998; Meno et al., 1998; Ryan et al., 1998). On the right body side, a supposed Activin-like signal (expression of cActRIIa) (Levin et al., 1995; Levin et al., 1997) simultaneously induces the transcription of FGF-8 (Boettger et al., 1999), thus limiting the expression of *Shh*, *Nodal* and *Pitx2* on the left side of the node (Boettger et al., 1999; Levin et al., 1995) **(Fig. 13)**.

Although the Nodal cascade is conserved among vertebrates, the mechanisms of initiation and control of nodal expression in the node in the first place and then in the left LPM reveals some variances between vertebrates. Nodal signals belong to the transforming growth factor-beta (TGF-β) superfamily and are essential for the induction of mesoderm and endoderm and the determination of the LR axis (reviewed in (Schier, 2009)). *Cerberus*/DAN and *Cerberus-like* proteins, play a role as TGF-β antagonist proteins. Although there is only one Nodal gene in mouse (Zhou et al., 1993), there are three in zebrafish (*Cyclops*, *Squint*, and *Southpaw*) (Erter et al., 1998; Feldman et al., 1998; Long et al., 2003; Rebagliati et al., 1998a; Rebagliati et al., 1998b; Sampath et al., 1998) and five in Xenopus (*Xnr1, 2, 4-6*) (Jones et al., 1995; Joseph and Melton, 1997; Takahashi et al., 2000)(reviewed in (Schier, 2009)). Extracellular inhibitors such as members of the Lefty and Cerberus/DAN families can antagonize Nodal signaling by binding to Nodal itself or to its receptors (reviewed in (Schier, 2009)). Thus, the so-called Nodal signaling cascade consists in the asymmetric expression of signaling molecules from the TGF-β family, such as Nodal, its secreted feedback repressor *Lefty* (also known as *Antivin*) and the homeodomain transcription factor Pitx2 (Marjoram and Wright, 2011; Schier, 2009; Shen, 2007). Asymmetric expression of the transcription factor Pitx2c controls localized changes in cell migration, shape, proliferation and survival in order to drive the morphogenesis of various

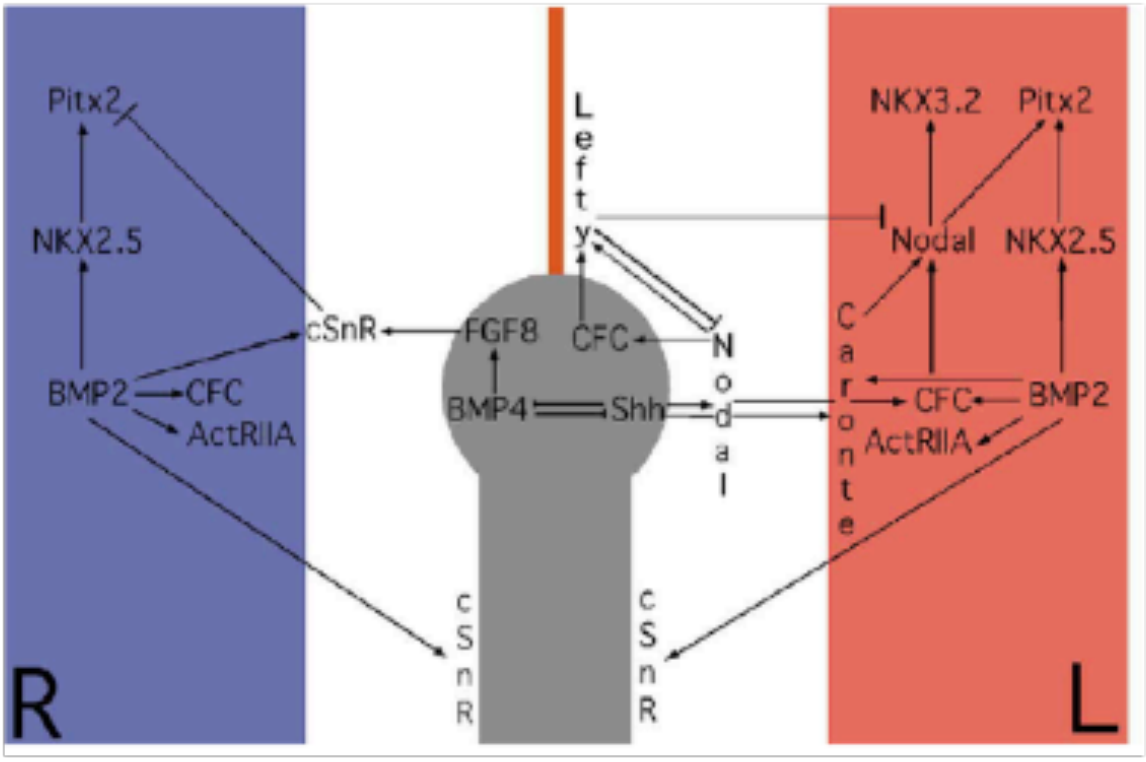

Fig.13: Pathway to establish the LR axis in the chick embryo during gastrulation.
Within the LRO of the ckick, the Hensen's node, antagonistic interactions between *Shh* and *BMP4* result in the formation of an asymmetric signaling center that ultimately leads to the lateralization of the LPM. *Shh* induces *Nodal* in a small domain adjacent to the left side of node. *Nodal* establishes the expression of *Lefty* in the midline, and for this induction, the presence of the co-factor CFC is required. *Lefty* is involved in limiting *Nodal* expression and prevents the spreading of left-sided signals to the right side. *Nodal* probably with the help of *Caronte* traverses the paraxial and intermediate mesoderm and reaches the LPM which is competent to respond to *Nodal* signaling due to the expression of CFC and ActRHA. Nodal is upregulated within the LPM and induces the expression of *Pitx2* and *NKX3.2*. Subsequently, Nodal is downregulated and Pitx2 expression is maintained by Nkx2.5. BMP2 is required for maintaining Caronte, CFC, ActRHA, and Nkx2.5 expression in the LPM. On the right side, FGF8 is asymmetrically expressed within the node and upregulates the expression of cSnR . This antagonist prevents the expression of *Pitx2* and thus, the establishment of left identity on the right, in addition *cSnR* is also symmetrically expressed in the paraxial mesoderm. Both expression domains require the presence of BMP signals. Adapted from (Brand, 2003)

asymmetric visceral organs (Blum et al., 2014a; Ferreira and Vermot, 2017; Hamada et al., 2002; Hirokawa et al., 2012).

Mouse *Cerl2*

In mouse, the first gene to show asymmetric expression around de node is *cerl-2* (*Cerberus-like protein 2*), a Nodal antagonist (Belo et al., 2009). *Cerl-2* was firstly detected as being bilateral in the peri-nodal crown-cells until the two somites stage, as for Nodal **(Fig. 14A)**. Around early somitogenesis, *Cerl-2* displays an asymmetric expression on the right side of the mouse LRO (Marques et al., 2004), assuming a complementary expression pattern to that of Nodal, that is mainly expressed on the left side (Collignon et al., 1996). Therefore it has been shown that *cerl-2* inhibits Nodal on the same side it is expressed, keeping Nodal signaling restricted to the left half of the embryo (Kawasumi et al., 2011; Marques et al., 2004). C*erl-2* knockout (KO) mice display laterality defects in the LPM, revealing its importance in LR determination in the mouse gastrula (Marques et al., 2004). The biased distribution of *Cerl2* transcripts on the right half of the embryo was associated with a preferential mRNA decay on the left side, which could be a consequence of both flow and *Wnt-Cerl2* signaling feedback loops **(Fig. 14B)** (Nakamura et al., 2012). For several years the question was how an apparently subtle fluid-flow can create an asymmetric signal capable of keeping an asymmetry in the whole embryo. A mechanism called Self-Enhancement and Laterality Inhibition (SELI) system has being proposed, and relies on the fact the asymmetric signal of Nodal generated in the node, would create an amplified expression in the LPM, hence resulting in an exclusively left-sided pattern of expression (Nakamura et al., 2006). Adding up to the SELI system in the LPM, the *Wnt-Cerl2* feedback loops observed in the node itself (Nakamura et al., 2012), ensures that it would not be necessary to have a strong and stable Nodal signal to break the initial symmetry in the whole embryo. A more recent report has shown the accumulation of *Cerl2* protein on the right side at early stages on the node moves to the left side later on. Furthermore, this movement has been shown to be strongly dependent on the nodal flow (Inacio et al., 2013). It has to prevent Nodal activity on the right LPM per se, but also it has to later stop Nodal activity on the left-side of the node and left LPM, to keep the LR signaling balance in the mouse (Inacio et al., 2013) **(Fig. 14C)**. Given the importance of the leftward nodal flow generated by cilia in the node, and the straight genetic balance between Nodal and its antagonist Cerl-2, it is clear that in the mouse the initial LR asymmetry is controlled by both mechanisms to ensure a proper LR determination in the mouse embryos.

Zebrafish *Charon*

Zebrafish *Charon* is expressed in the cells that line the posterior domain of the KV region **(Fig. 15A)** (Hashimoto et al., 2004; Lopes et al., 2010) at 10-somite stage, expression pattern that resembles the one from Cerl-2 at initial stages in the mouse embryo (Marques et al., 2004). *Charon* can work as an inhibitor of the three Nodal-related molecules in zebrafish **(Fig. 15B)** (*southpaw*, *cyclops* and *squint*) (Long et al., 2003; Rebagliati et al., 1998b; Sampath et al., 1998). *Southpaw*, is the first gene asymmetrically expressed in the LPM, but around the KV is expressed bilaterally in two domains that are kept even when the propagation in the LPM starts (Hashimoto et al., 2004; Long et al., 2003;

Lopes et al., 2010; Wang and Yost, 2008). Similarly to the phenotype of *Cerl-2* KO mice, *charon* knockdown experiments showed defects in the LR axis determination, either on gene expression patterns in the LPM or in heart development (Hashimoto et al., 2004), confirming a crucial role in the LR patterning in zebrafish. These phenotypes were similar to those related to defects in Nodal signaling expression or overexpression of Nodal inhibitors, confirming that *charon* can act in zebrafish as an antagonist of Nodal-related genes (*southpaw*), as in mouse (Hashimoto et al., 2004). Some years after, *charon* expression was suggested to be the first asymmetric flow genetic target event in zebrafish, and also to be a target of the Notch signaling pathway (Lopes et al., 2010). Furthermore, it has been described that *charon* expression in a wild-type zebrafish KV is initially symmetric and then becomes clearly asymmetric on the right side from eight-somite stage onwards **(Fig. 15A)** (Lopes et al., 2010). A more recent study proposed cilia-driven flow in the KV predicts *charon* expression and organ *situs*, in which *charon* expression would be inversely proportional to high local flow in the KV: *charon* would be stronger on the right side of the KV, where the local flow is weaker, and *vice versa* **(Fig. 15C)** (Sampaio et al., 2014).

Xenopus *Coco*

Furthermore it has been reported that *Xenopus Coco/dand5* - a secreted antagonist of TGF-β signaling like *charon* and *cerl-2* (Bell et al., 2003) - has an essential role in regulating the LR axis determination in the *Xenopus* embryo (Vonica and Brivanlou, 2007). *Coco* is expressed bilaterally in the posterior paraxial mesoderm at neurula stage, where it shares the same expression pattern with the TGF-β ligands *Xnr1* and *derriére*. It has been shown that *Coco* is required exclusively on the right side and *Xnr1* on the left side, for proper LR patterning (Vonica and Brivanlou, 2007). Another report revealed *coco* expression to be the first asymmetric flow target genetic event also in *Xenopus (Schweickert et al., 2010). Their model stands on the fact the leftward flow represses Coco on the le*ft margin of the LRO, which in turn releases the repression of Nodal **(Fig. 10E-G)** (Schweickert et al., 2010).

Chick Caronte

In the chick embryo, LR asymmetric patterns of gene expression in the LPM are initiated by signals located in and around the Hensen's node. It has been shown that *Caronte* (Car), a secreted protein encoded by a member of the *Cerberus/Dan* gene family, mediates the *Sonic hedgehog* (Shh)-dependent induction of left-specific genes in the LPM (Yokouchi et al., 1999). Asymmetric expression of *Shh* on the left side of the chick embryo, which induced expression of Nodal, first in a small domain adjacent to the Hensen's Node and subsequently in the left LPM. Mechanistically, *car* is induced by *Shh* and repressed by fibroblast growth factor-8 (*FGF-8*), and consequently *car* activates nodal expression by playing as an antagonist for bone morphogenic proteins (BMPs), known to repress nodal activity (Yokouchi et al., 1999) **(Fig. 13)**. To sum up, in the chick embryo, there is a complex network of antagonistic molecular interactions between several components that cooperate to control LR asymmetry (Raya and Izpisua Belmonte, 2004b).

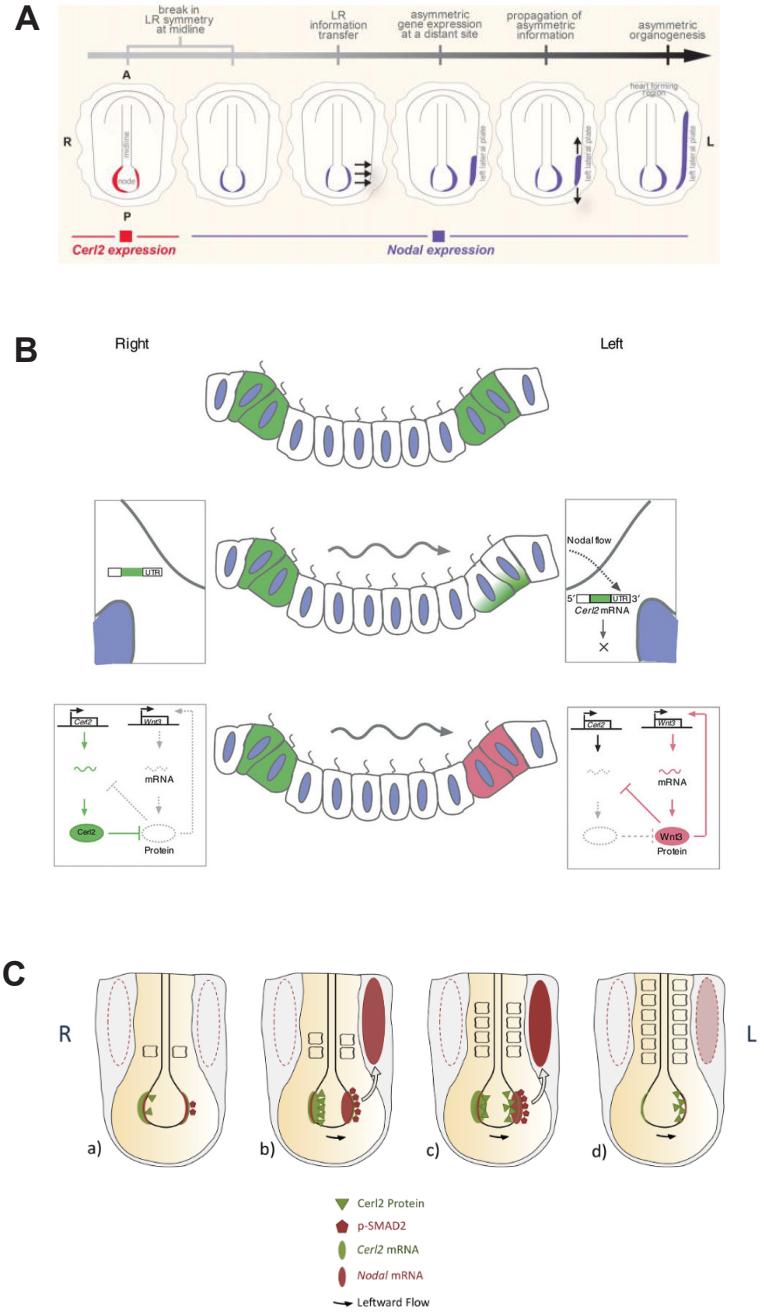

Fig.14: Summary of the symmetry-breaking events that occurs in the node during early somitogenesis. (A) Schematics of the dynamic sequential spatio-temporal localization of *Nodal* gene expression in the mouse embryo. Initially *Nodal* expression in the periphery of the node is "U" shaped as it encompasses the posterior half of the node. Expression subsequently splits and a bilateral pattern arises. The asymmetry of *Nodal* expression at the mouse node appears to be synchronized with its activation in the left LPM. Adapted from (Saijoh et al., 2014). **(B)** Schematics of the decay of *Cerl2* mRNA summarizing the mechanism that converts the signal transmitted by nodal flow into robust asymmetry of *Cerl2* expression, with both Flow and Wnt Signals Promoting its mRNA decay. Adapted from (Nakamura et al., 2012). **(C)** Schematics of the sequential Nodal activity in the mouse node. *Nodal* expression is represented in light red oval, and *Cerl2* expression in light green oval. The dynamic behavior of Cerl2 protein is illustrated in green triangles, and the readout of nodal signaling, pSmad2, is indicated in red pentagons. The asymmetric expression of *Nodal* in the left-LPM of mouse embryos is represented by the filled red oval. At early stages, Cerl2 protein localizes and prevents the activation of *Nodal* genetic cascade on the right side. Later, due to nodal flow, Cerl2 right-to-left translocation shutdowns Nodal activity in the node and consequently affects the activity of Nodal in the LPM. The arrows represent the nodal signal transfer across the node. Adapted from (Inacio et al., 2013).

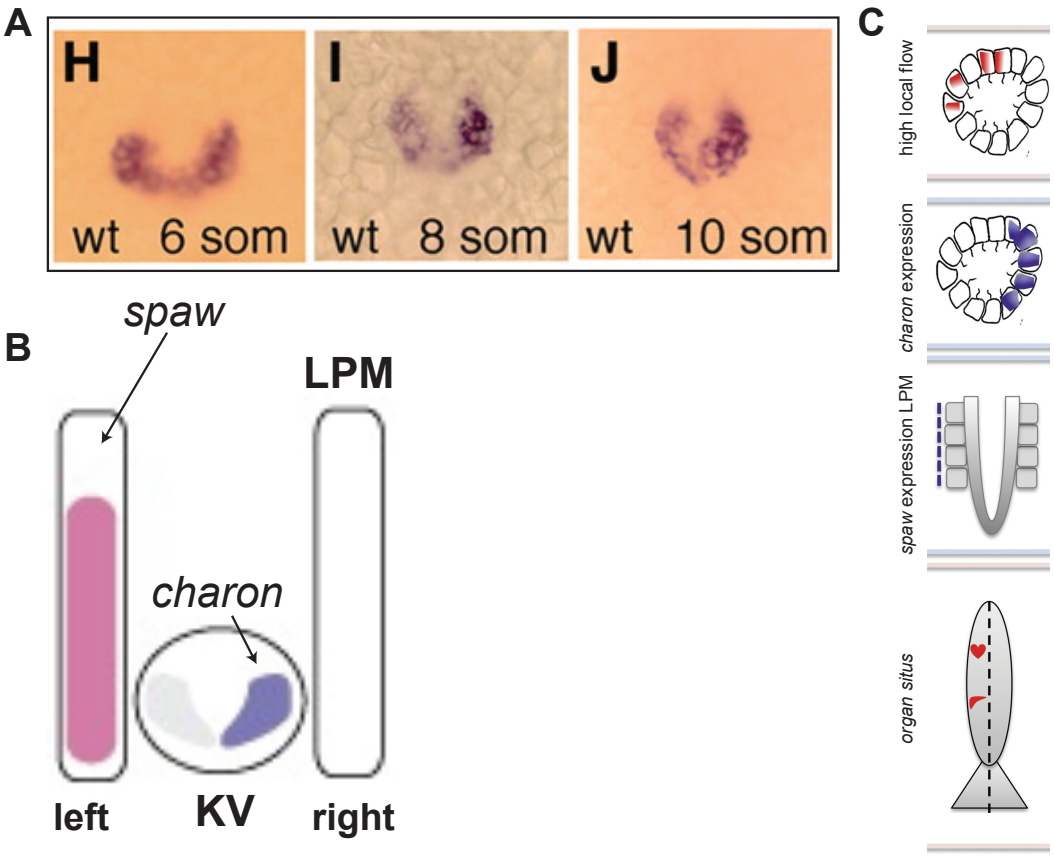

Fig.15: Interaction between KV flow, *charon* and *spaw* expression. (A) *charon* expression pattern is symmetrical at 6-SS and is asymmetrical afterwards. Adapted from (Lopes et al., 2010). **(B)** Schematics of the interaction between *spaw* (Nodal-related gene) and *charon*, its antagonist. Adapted from (Hojo et al., 2007). **(C)** Model for the biological bignificance of KV cilia-driven flow and the interaction between flow-*charon* and *spaw* to promote organ *situs*. When ciliated cells positioned both anteriorly and on the left side of KV are stimulated by higher local flows (top panel), then *charon* expression (blue cells) gets stronger on the right side of the KV, meaning *charon* expression is degraded by local strong flow (second panel). Consequently, *spaw* expression will be stronger on the left LPM (third panel), generating *situs solitus* as the most likely outcome (lower panel). Adapted from (Sampaio et al., 2014).

Summarizing, although mouse *Cerl-2*, zebrafish *Charon and* Xenopus *Coco* have revealed distinct expression patterns, this molecular cascade of activity from the leftward flow to the down-regulation of *Cerl2/Coco/Charon* mRNA on the left side with concomitant enhancement of Nodal activity in the left side of the LRO is highly conserved among fish, frog and mouse. Also, for chick, even though its symmetry-breaking process is not mediated by an asymmetric flow, it reveals the molecular and genetic cascade of events is similar. The proteins encoded by those genes seem to be part of an evolutionary conserved mechanism that plays a role as Nodal antagonists in the vertebrate embryo, crucial for restricting Nodal signaling to the left half of the embryo, and thus LR determination (Belo et al., 2009; Blum et al., 2014a; Hamada and Tam, 2014; Raya and Izpisua Belmonte, 2004a; Schier, 2009).

4. Mechanical forces during left-right patterning and asymmetric morphogenesis

Giving mechanical forces are emerging as a key input in the different steps of left-right (LR) axis determination, from the initial event of symmetry breaking to the asymmetric morphogenesis, we thought to write a comprehensive review on the topic. We reviewed the molecular and sub-cellular basis of mechanical and biochemical pathways activated during LR patterning and asymmetric morphogenesis. Throughout the review, we discuss the potential mechanosensors involved and the mechanical forces generated at cellular and tissue scale, which special attention to cell chirality.

The review (Ferreira and Vermot, 2017) is attached in the following pages on this section and it is part of the Introduction chapter on this PhD thesis.

Mechanisms of Development 144 (2017) 71–80

Contents lists available at ScienceDirect

Mechanisms of Development

journal homepage: www.elsevier.com/locate/mod

Review

The balancing roles of mechanical forces during left-right patterning and asymmetric morphogenesis

Rita R. Ferreira, Julien Vermot *

Institut de Génétique et de Biologie Moléculaire et Cellulaire, Illkirch, France
Centre National de la Recherche Scientifique, UMR7104, Illkirch, France
Institut National de la Santé et de la Recherche Médicale, U964, Illkirch, France
Université de Strasbourg, Illkirch, France

ARTICLE INFO

Article history:
Received 1 August 2016
Accepted 3 November 2016
Available online 5 November 2016

ABSTRACT

Left-right patterning and asymmetric morphogenesis arise from a complex set of molecular and cellular interactions that are particularly dynamic and associated with mechanical forces. How do mechanical forces translate into tissular asymmetries? Are these forces asymmetrical *de novo*, or do they build up from pre-existing asymmetries? Advances in developmental genetics, live imaging and cell biology have recently shed light on the origins of mechanical forces generated at the cell scale and their implication in asymmetric patterning and morphogenesis is now emerging. Here we ask when and how, molecular asymmetries and mechanical forces contribute to left-right patterning and organ asymmetries.

Contents

1. Introduction

Mechanical forces are ubiquitous and can modulate the developmental program of plants and animals (Mammoto and Ingber, 2010; Mirabet et al., 2011). Mechanical forces are influent in many steps of embryonic development, from gastrulation to organogenesis (Hamada, 2015; Heisenberg and Bellaiche, 2013; Mammoto and Ingber, 2010). Gastrulation (Behrndt et al., 2012; Farge, 2003; Hiramatsu et al., 2013; Maitre et al., 2012), kidney morphogenesis (Kramer-Zucker et al., 2005), inner ear and otolith formation (Colantonio et al., 2009; Wu et al., 2011), neuron migration (Sawamoto et al., 2006), cardiovascular development (Boselli et al., 2015; Freund et al., 2012; Peralta et al., 2013), haematopoiesis (Pardanaud and Eichmann, 2009), and left-right symmetry breaking (Nonaka et al., 1998) are all mediated by mechanical stresses and force mediated signaling (Zhang and Labouesse, 2012). Prominent mechanical forces-related diseases include cancer (Fernandez-Sanchez et

* Corresponding author.
E-mail address: julien@igbmc.fr (J. Vermot).

http://dx.doi.org/10.1016/j.mod.2016.11.001

al., 2015; Fernandez-Sanchez et al., 2010), ciliopathies (Hildebrandt et al., 2011) and cardiovascular diseases such as atherosclerosis (Hahn and Schwartz, 2009).

Despite the long recognition of the importance of mechanical forces in development, an understanding of how mechanical forces impact development has, until recently, remained elusive. Technological advances in recent years have allowed researchers to study the effects of physical forces on cell behaviors at unprecedented resolution (Ladoux et al., 2016; Lecuit et al., 2011). The results of these studies have led to a paradigm, where in its most extreme form, holds the idea that physical forces, independently of gene expression, can affect tissue development and growth by directly modulating cell behavior (Savin et al., 2011). Mechanical forces have also been shown to act as a key component in the coordination of cell behaviors at the tissue scale, in particular during tissue folding (Striedter et al., 2015). As a consequence, it is now clear that mechanical forces constitute an essential element in multiple aspects of the morphogenetic program (LeGoff and Lecuit, 2016; Zhang et al., 2010).

Forces can be sensed at the molecular and cellular scale through mechanosensitive proteins (Vogel and Sheetz, 2006). A major focus of research is now to define the molecules and signaling pathways associated with mechanotransduction and work from many different fields has now shown that pressure-sensitive membrane proteins, cytoskeletal elements, and extracellular matrix (ECM) components can participate in the interchange between mechanical forces and biochemical signals at the cellular scale (Mammoto et al., 2012; Vogel and Sheetz, 2006). Although much has been done in the study of biomechanical signaling at the cellular scale, the effects of forces at a tissue scale level have emerged only recently (Grill, 2011; Lecuit et al., 2011; Mammoto and Ingber, 2010). The field strongly benefits from concepts and formulation developed by physicists, which promoted the identification and quantification of the relevant forces through unifyed approaches (Grill, 2011). Recent advances in cell biology and live imaging are now allowing researchers to directly assess the distribution of tissue forces, thus helping them to have a better view of how mechanical forces can impact development (Sugimura et al., 2016). This, combined with the discoveries of novel mechanosensitive proteins and pathways, are consistently changing our view of how mechanical forces can impact development.

Left-right patterning and asymmetric morphogenesis is one of the most fascinating aspects of developmental biology. Both the symmetry and asymmetries of the body plan require a number of processes that need to be carefully controlled through a genetic program (Capdevila et al., 2000; Hamada et al., 2002; Pourquie, 2011). Being asymmetric certainly constitutes an advantage in the process of organ packing and positioning in a restrained space. Accordingly, most of our internal organs are asymmetrically positioned within the body cavity. Recent studies in the field of the left-right signaling and asymmetric tissue morphogenesis are now clarifying and reinforcing the interest in the field of mechanical forces and morphogenesis. Examples of tissue asymmetry can be seen in heart tube loop, brain folding, airway branching (Yashiro et al., 2007) and gut looping (Savin et al., 2011). Here, we review the molecular and sub-cellular basis of mechanical and biochemical pathways activated during left-right patterning and asymmetric morphogenesis. Throughout the review, we discuss the potential mechanosensors involved and the mechanical forces generated at cellular and tissue scale.

2. Left-right symmetry breaking mediated by cilia mediated flow forces

Fluid motion is usually mediated by motile cilia in the body. Motile cilia are organelles that protrude from nearly all vertebrate cells with typical lengths between 3 and 10 μm in growing tissues (Avasthi and Marshall, 2012; Ishikawa and Marshall, 2014; Keeling et al., 2016; Vincensini et al., 2011). In vertebrates, cilia are commonly thought to function as chemical and/or mechanical sensors. Motile cilia move fluids, and in doing so they participate in controlling several key developmental processes, such as chemical gradient formation, biomineralization or tubulogenesis (Cartwright et al., 2009). Left-right (LR) specification in vertebrates occurs in the left-right organizer (LRO), which is defined by a group of specialized cells located within the presomitic mesoderm. The cells delineating the LRO are ciliated and contain motile cilia that generate a slow-moving flow (the nodal flow) involved in the initial step of symmetry breaking (Nonaka et al., 1998) (Fig. 1A). Additionally, an intercellular amplification of the asymmetric signals occurs through genetic feedback mechanism near and around the LRO (Nakamura et al., 2006). The prominent models explaining symmetry breaking within the LRO suggests either an asymmetric chemical gradient (Okada et al., 2005), or that the LRO cells can mechanically sense flow due to a particular type of sensory cilia located in the periphery of the LRO, dictates the asymmetry (McGrath et al., 2003; Tabin and Vogan, 2003). While it is possible that these two mechanisms work together, a number of elements are still lacking for our complete understanding of the process (Pennekamp et al., 2015). Importantly, symmetry breakage occurs even in mutant mice with only two motile cilia (Shinohara et al., 2012). Experimental data using a mutant of the Notch signaling pathway and simulations of fluid flow dynamics in the zebrafish LRO revealed a threshold of approximately 30 motile cilia to get a proper LR symmetry breakage (Sampaio et al., 2014). This suggests that the flow detection apparatus is extremely efficient. When considering the flow velocities generated within the LRO of fish, mice and xenopus (Blum et al., 2009; Blum et al., 2014; Schweickert et al., 2007; Supatto and Vermot, 2011), it appears that they are much lower when compared to other organs - for example, they are 3 to 10 times lower than the hemodynamics generated in the vascular network even at its earliest embryonic stages (Anton et al., 2013; Cartwright et al., 2009; Goetz et al., 2014; Hove et al., 2003; Supatto and Vermot, 2011).

The mechanosensory hypothesis has been favored by the discovery that Trpp2 (PKD2 or polycystic kidney disease protein 2) is key for LR patterning (Field et al., 2011; Kamura et al., 2011; McGrath et al., 2003; Pennekamp et al., 2002; Schottenfeld et al., 2007; Yuan et al., 2015). Trrp2 is a potent mechanosensory protein (Patel et al., 2010; Sharif-Naeini et al., 2010) both in kidney and vasculature (Goetz et al., 2014; Nauli et al., 2003; Nauli et al., 2008) that acts in combination with Pkd1 at the cell membrane. In zebrafish, Trpp2 is necessary for the genesis of asymmetric calcium release around the LRO, which is initiated within cilia (Yuan et al., 2015). Mutant protein of Trpp2 that cannot bind to the membrane cannot rescue Trpp2 loss of function in the LRO and lead to LR symmetry defects (Yoshiba et al., 2012). Trpp2 belongs to the big family of transient receptor potential proteins (TRP) that contain a number of mechanosensitive channels. Yet, Trpp2 is not a 'canonical' stretch sensitive channel and its biology is extremely complex and cell type specific (Giamarchi et al., 2006): it is part of a multiprotein complex involved in transducing Ca^{2+}-dependent information. It localizes to primary cilia of renal epithelial cells, where it seems involved in mechanosensitive transduction signals (Nauli et al., 2003; Pazour et al., 2002; Yoder et al., 2002), but it has been observed at the cell membrane and in the ER. Trpp2 has been shown to inhibit the response of stretch activated cation channels in smooth muscle cells, suggesting that it can modulate mechanotransduction without being a mechanosensor itself (Sharif-Naeini et al., 2009). Recently, the group of David Clapham showed that intraciliary calcium increase is not observed in the mouse LRO in response to flow forces, suggesting that the primary function of TRP channels, including Trpp2, is not to modulate intraciliary calcium in response to cilia bending, and, as a consequence, do not act as mechanosensor in this context (Delling et al., 2016). In that aspect, it is worth mentioning that Pkd2 mutants do not present apparent defects in intracellular calcium levels in the node (Yoshiba et al., 2012). Importantly, Trpp2 frequently acts in combination with other mechanosensitive proteins such as Trpv4 (Du et al., 2014; Heckel et al., 2015; White et al., 2016), Pkd1 (Hanaoka et al.,

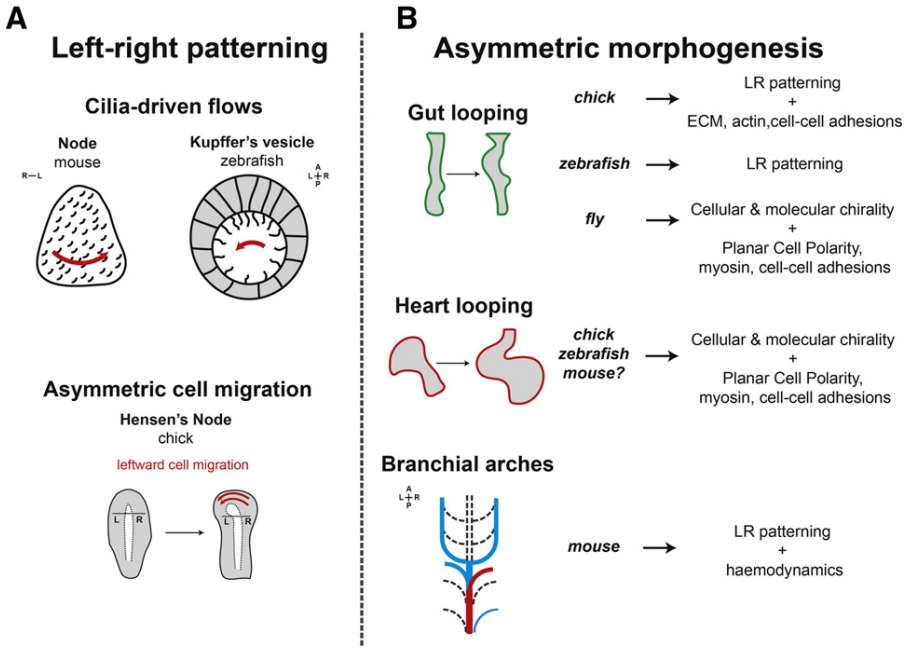

Fig. 1. Summary of left-right patterning and asymmetric morphogenesis: (A) Left-right (LR) specification in vertebrates occurs in LR organizers (top left: mouse Node; top right: zebrafish Kupffer's vesicle; down: chick Hensen's node). The cells delineating the mouse and zebrafish LR organizers are ciliated and contain motile cilia that generate a cilia-driven slow-moving flow (the nodal flow – red arrow) involved in the initial step of symmetry breaking. The chick embryos do not seem to rely on cilia-driven flow but on asymmetric cell migration to break LR symmetry. During development, the cells around the Hensen's node (bottom left) experiences an asymmetric cell migration with changes in adhesion, thus interfering with the LR patterning of chick embryos. (B) Asymmetric morphogenesis of internal organs in different model systems required not only LR patterning but also depend on cellular and molecular chirality, as well as tissue intrinsic properties such as cell-cell adhesion, cytoskeleton components like actin and myosin, among others. In panel B, we summarize gut and heart looping in the different animal models as well as branchial arch formation in the mouse embryo.

2000; Nauli et al., 2003) or Pkd1l1 (Grimes et al., 2016; Kamura et al., 2011) to mediate the calcium flux. During left-right patterning, the partner of Trpp2 is Pkd1l1, Pkdl1 physically interacts with Trpp2 (Field et al., 2011) and is necessary for LR patterning in mouse and medaka fish (Field et al., 2011; Grimes et al., 2016; Kamura et al., 2011). Additionally, Pkd1l1 might be sensitive to proteoglycan distribution (Superina et al., 2014) and it is suspected that the ECM can alter Pkd1l1 biological activity at the cell surface. All in all, these recent results suggest that TRP channels might act as a mechanosensor in the LRO, yet the mechanism by which they operate remains mysterious. Along the same line, how do cilia sense flow and whether non-ciliary sensory mechanisms are involved in the LR breaking are crucial questions to answer for our understanding of the mechanism of symmetry breaking. When considering the pkd1/trpp2 complex, it seems that the couple Pkd1/Trpp2 also has non-mechanosensitive signaling properties. For example, it looks like Pkd1 can act as a prototypical membrane receptor that concordantly regulates Pkd2 channels and G-proteins in neurons and kidney cells (Delmas et al., 2004). Interestingly, Pkd1 proteins can be activated by potent signaling molecules, such as Wnt ligands (Kim et al., 2016), to activate intracellular calcium signaling. Considering the multiplicity of outcomes trpp2/pkd1 interactions and activations can lead to, a better understanding of the targets of mechanism of action of Trpp2 and Pkd1l1 at the cell membrane and cilia will be key to figure out the mechanism initiating asymmetric gene expression in the LRO. Most importantly, it will help to understand if (and how) mechanotransduction is indeed at work in the LRO.

3. Left-right symmetry breaking mediated *via* asymmetric cell migration and adhesion

A few vertebrate species do not seem to rely on cilia mediated flow (Blum et al., 2009; Gros et al., 2009) but depend on asymmetric cell migration to break left-right (LR) symmetry. Intrinsically, cells are chiral and naturally spread with a chiral order when plated on a dish (Chen et al., 2012; Tee et al., 2015). Additionally, cells tend to migrate with directionality which is dictated by the substrate (Caballero et al., 2015; Comelles et al., 2014) suggesting that cell migration directionality is mechanosensitive. Importantly, the position of the centrosome, which can be considered as the actin and microtubule organizer of the cells, is also dictated by cellular force distribution in cell culture (Farina et al., 2016; Pitaval et al., 2010). A good example of how asymmetric cell migration and adhesion play a role in the patterning of embryos during development concerns the cell movements around the Hensen's node. It was shown that asymmetric cell rearrangements take place within the node of chick embryos, thus creating a transient leftward movement of cells around it (Cui et al., 2009; Gros et al., 2009), which later stops (Fig. 1A). The migration of cells away from the midline to the left side consequently deform the shape of the node. Thus, these leftward movements lead to the asymmetric expression of *shh* (Sonic Hedgehog) and *fgf8* (fibroblast growth factor 8). *Shh* is initially expressed bilaterally at the rostral side of the node and later becomes restricted to the left. Moreover, the *fgf8* bilateral expression in the primitive streak results in an asymmetric expression on the right side of the node (Cui et al., 2009; Gros et al., 2009). To understand how the leftward movement of cells occurs in the chick, Gros and colleagues (Gros et al., 2009) studied the driving force for cell rearrangements and how they could disrupt it (and which consequences will arise from it). Their work has shown that by impairing the myosin-II pathway, as well as, by physically blocking cell movements in the node, the leftward movement of cells was no longer seen. Likewise, the chick node lost its asymmetrical shape on the LR axis, when compared to control embryos (Gros et al., 2009). In addition to the disruption of the leftward movement of cells, Gros and colleagues have reported the bilateral gene expression of *shh* and *fgf8*, thus suggesting the leftwards cell movements are required to initiate the LR asymmetric expression domains in the chick embryo (Gros et al., 2009). Nevertheless, until recently, there was no answer

for the question of how this transient leftward movement of cells in the chick node was controlled in a time-dependent manner. In other words, it was not clear how the transient movement would stop once the asymmetry has been established. Based on the evidence that N-cadherin is asymmetrically expressed in a time-dependent fashion in the node and its inhibition gives rise to heart misplacement (Garcia-Castro et al., 2000), Mendes and colleagues have recently proposed N-cadherin as a good candidate to stop the transient leftward movements, possibly *via* an asymmetric cell-cell adhesion mechanism (Mendes et al., 2014). This study combined a photoconvertible fluorescent protein (*Kaede*) with *in vivo* microscopy to track single cell movements in the node of the chick embryo, and in this way investigated the migratory behaviors in the node region in response to N-cadherin perturbations. They concluded that N-cadherin is important to stabilize the molecular asymmetries established earlier in the node, so that the correct asymmetric information is transferred to the lateral plate mesoderm (LPM) and the proper asymmetric looping of the heart is achieved (Garcia-Castro et al., 2000; Mendes et al., 2014). Since cadherin proteins are known mechanosensitive proteins (Huveneers and de Rooij, 2013; Ladoux et al., 2010; Lecuit and Yap, 2015; Weber et al., 2012), it would be interesting to assess if the process of asymmetric cell migration is in itself driven by mechanical forces or by the intrinsic cell chirality often observed *in vitro*.

4. Cell contractility and forces associated with left-right organizer formation

Recent studies have identified regulators of the actomyosin cytoskeleton (Wang et al., 2011; Wang et al., 2012) and components of the extracellular matrix (ECM) (Compagnon et al., 2014) as mediators of cell positioning in the zebrafish left-right organizer (LRO) (called Kupffer's vesicle (KV)), important for the breaking symmetry event. The ECM is thought not only to provide a structure to support organs but also to control cell-cell communication, proliferation, differentiation, and migration.

The KV in zebrafish is formed by a group of nearly two-dozen cells, known as dorsal forerunner cells (DFCs), which migrate deep into the embryo through development. These cells undergo a mesenchymal-to-epithelial transition (MET) to form the KV in a vesicle-like structure with a mono-ciliated epithelium (Essner et al., 2005). Several studies confirmed the existence of a cluster of ciliated-cells in the anterior-dorsal (AD) region of the KV (Kramer-Zucker et al., 2005; Kreiling et al., 2007; Okabe et al., 2008), suggesting this higher density of cilia (as a consequence of a higher cell density) can cause the strong directional flow observed in the KV (Kramer-Zucker et al., 2005; Kreiling et al., 2007; Okabe et al., 2008; Sampaio et al., 2014; Wang et al., 2011; Wang et al., 2012) (Fig. 1A).

The knowledge gap about the molecular and cellular mechanisms regulating the asymmetries in cell density within the KV has only recently started to be filled. Wang and colleagues started by proposing a model of cell remodeling that would allow an initially symmetric organ to acquire anterior-posterior (AP) asymmetry. In this model, anterior KV cells would be more tightly packed than posterior cells, as a consequence of the gradient of cell tension in the AP axis (Wang et al., 2011; Wang et al., 2012). They have identified Rock2b (Rho kinase protein) as a key regulator of KV remodeling (Wang et al., 2011). Depletion of the Rock2b-Myosin II pathway resulted in the disruption of the cell cluster in the AD region, changes in cell morphology and impairment of the asymmetric cilia-driven flow, which then impacts the proper establishment of the left-right (LR) axis (Wang et al., 2011; Wang et al., 2012). Making use of mathematical simulations, they proposed a model in which the Rock2b-Myosin II pathway regulates cell–cell interfacial tension during KV remodeling, by regulating cell contractility and cell adhesion (Wang et al., 2012).

More recently, by studying endogenous and ectopically induced KV, Compagnon and colleagues proposed that local differences in the shape of KV ciliated-cells are the result of localized ECM deposition at the surface of the adjacent notochord. This accumulation of ECM would restrict the apical expansion of the lumen-lining KV epithelial cells within the AD region, in response to lumen growth during the development of the KV (Compagnon et al., 2014). In this work, they have shown that laminin and fibronectin strongly accumulate at the axial-paraxial boundary adjacent to the AD region of the KV highly packed with ciliated-cells. Furthermore, interfering with these ECM components result in the impairment of the KV remodeling process important for the breaking of LR symmetry, suggesting that ECM-dependent cell shape changes are critical for KV function (Compagnon et al., 2014).

These studies suggest that a highly regulated organization of the LRO is dependent on cellular forces. Proper modulation of these forces is thus crucial for generating an architectural asymmetry within the organ, thus playing a key role for its function as LRO in zebrafish.

5. Molecular and subcellular chirality in the process of left-right patterning

At the molecular scale, asymmetries of sub cellular components has long been thought to provide the initial asymmetry necessary to initiate an asymmetric gene cascade (Brown and Wolpert, 1990; Levin and Mercola, 1998). Interestingly, this hypothesis fits when considering the molecular architecture of the internal organization of motile cilia, which is chiral (Figs. 2 and 3). The body of the cilium is made of a chiral alignement of microtubule (as well as its basal body) such that the direction of cilia rotation has been proposed to be determined by the structural interaction of their protein building blocks sliding, which has to be chiral as well (Hilfinger and Julicher, 2008). Flow in the LRO can thus been considered as a way to convey the molecular chirality to an asymmetric flow (Levin, 2005). In this model, the obtained cilia mediated flow allows to scale up the molecular asymmetries to the LRO (Fig. 2).

However, the direction of cilia motility is not enough to drive a directional flow. Cilia need to be posteriorly tilted in order to generate a directional flow, and this in turn depends on the proper positioning and orientation of the cilia at the posterior side of cell surface of the LRO (Hashimoto and Hamada, 2010; Supatto and Vermot, 2011). The molecular mechanisms that set this orientation depends on the Planar Cell Polarity (PCP) pathway (Borovina et al., 2010; Hashimoto et al., 2010; Song et al., 2010). This process is dynamic, as it seems that cilia move towards caudal side of the node in response to the PCP (Hashimoto et al., 2010). The gradual posterior positioning of the basal body correlates with increase flow in the node, which suggests that the posterior tilt increases accordingly. Interestingly, it has been shown that the process of cilia positioning in multiciliated cells is force dependent - flow itself has been shown to modulate cilia orientation in brain ependymal cilia (Guirao et al., 2010) and is mediated by Pkd1 and Pkd2 (Ohata et al., 2015). This mechanism, though, does not seem at work in the node where cells are monociliated, since pkd2 mouse mutants do have normal nodal flow (Yoshiba et al., 2012). In addition, exogenous strain polarizes apical microtubules, and align stable components of the PCP pathway orthogonal to the axis of strain in the developing skin of xenopus (Chien et al., 2015). Thus, it seems that oriented tissue strain can play a role in determining the global axis of planar polarity *in vivo* (Chien et al., 2015). It will be interesting to test if tissue strain is oriented in the node and if cilia orientation can be affected as a consequence of strain, and, potentially, mechanotransduction. Furthermore, the mechanism that position the cilium is thought to be microtubule dependent, but the role of actin might have been understudied. The recent discovery that the centrosome also acts as an actin organizer might trigger more effort in that direction of research (Farina et al., 2016).

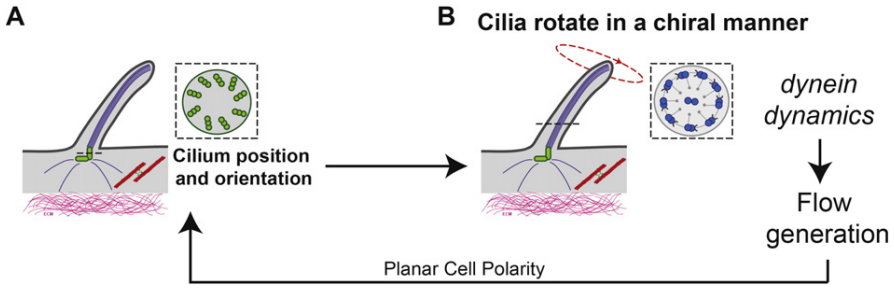

Fig. 2. Cilia position and orientation is important for cilia-driven flow generation in the left-right organizers (LRO): (A) the cilium orientation is initially determined by its basal body (green struture). A cross section on the basal body (inset) shows its nine-fold symmetric organization. The basal body dictates at some extent the degree to which cilia are tilted at the cell surface and thus, could be linked to the correct direction of cilia-driven fluid flow in the LRO. (B) Cilia in LRO rotate in a chiral manner, depending on the way the motor dyneins crosslink with the set of microtubules inside the cilium (inset). Different structures can be found in the motile cilia of the LRO: in the mouse Node, the motile cilia have a typical 9 + 0 structure (absence of central pair), whereas in the zebrafish Kupffer's vesicle the central pair is present (9 + 2 structure as shown in the inset). Cilia rotation set the forces to generating a chiral fluid flow, capable to break the symmetry of many vertebrates. Furthermore, cilia-driven flow generated in connection with the cell cytoskeleton (red:actin and green:myosin), and in addition to an expected contribution of the Planar Cell Polarity pathway, can employ a potent organization on the orientation of the basal body itself.

6. Cell and tissue chirality in the process of asymmetric morphogenesis

The translation of molecular asymmetry into mechanical forces is certainly best known from the work perfomed in cultured cells and, more recently, in *C. elegans* under the impulsion of biophysicists. Their work mainly focuses on the actomyosin network, which corresponds to the key effector of the molecular motors that drive cell shape and migration. Together, this work suggests that the entire actin network at the cellular scale can have a chiral behavior in response to the rotational forces produced at the focal adhesion of the cells (Naganathan et al., 2016; Tee et al., 2015). Recent studies provide new insights on the chiral organization of the actin network (Chen et al., 2012; Naganathan et al., 2014; Tee et al., 2015). Chen and colleagues have shown that when vascular mesenchymal cells grow until confluency on micro-patterned stripes, they align in a constant chiral fashion, which could be disrupted by drug treatments for myosin II or Rho signaling (Chen et al., 2012) (Fig. 3B). Also, for single fibroblasts plated onto round micro-patterns, it was shown that the actin cytoskeleton self-organizes in a chiral pattern, revealing an unusual transition from a radially symmetric pattern to another that is chiral (Tee et al., 2015). Interestingly, the handedness of the chiral pattern can be changed by a single protein, the alpha actinin 1, suggesting that cell chirality can be turned on and off by a single protein (Tee et al., 2015). In another study using *C. elegans*, Naganathan and colleagues quantitatively demonstrated that the generation of active chiral torques by the actomyosin cortex facilitates chiral symmetry breaking along the antero-posterior axis of the embryo (Naganathan et al., 2014). Also, they have shown that active torques are dependent on myosin activity, and can be altered by modulating Rho signaling (Naganathan et al., 2014). Taken together, these studies argue for the idea that chirality of cells and tissues might be dependent on the proper alignment of molecular torques generated by the actomyosin activity. While still early, it is tempting to extend this concept to chiral morphogenetic rearrangements that have been observed at other stages in *C. elegans* development (Pohl and Bao, 2010) and during the first cleavage (Schonegg et al., 2014; Singh and Pohl, 2014).

In summary, interesting hypotheses are now emerging in order to explain the role of subcellular asymmetries at the embryonic scale in organisms possessing a left-right organizer. An intriguing possibility is that cell chirality could be used as an additional element to provide the embryo with handedness, forcing tissue asymmetries independently of the canonical left-right signaling pathway (McDowell et al., 2016) (Figs. 1 and 3).

6.1. Gut looping chirality

One of the most striking examples of asymmetric organ morphogenesis in response to left-right (LR) positional cues (Burdine and Schier,

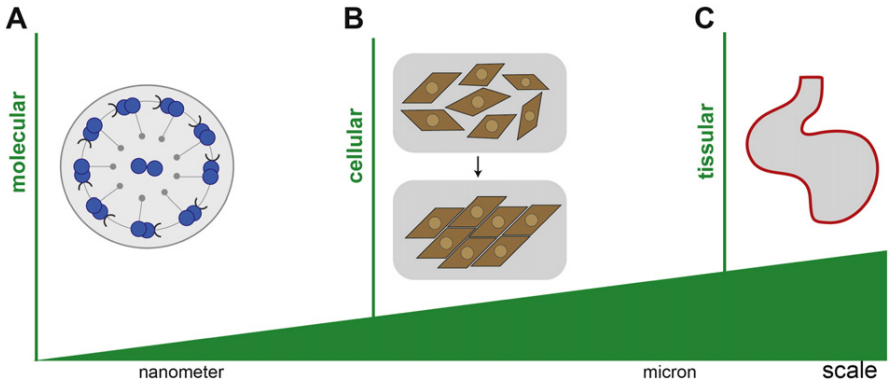

Fig. 3. Different scales of chiral organization: from molecular to tissular level: (A) Cross section of a motile cilium, characterized by an axoneme, which consists of a regular cylindrical arrangement of microtubules (in blue), crosslinked in a chiral fashion by motor proteins called dyneins (in dark grey). Inside the axoneme of the cilium, it is the action of crosslinking dyneins (and other) proteins, that generate internal forces that localy slide the microtubules, leading in turn to the bending of the cilium. (B) At the cellular level, various types of cells are chiral and naturally spread with a chiral order when plated on a dish. The chiral organization of the actin network itself may explain this behavior is then translated to the cell. In this schematics, confluent vascular mesenchymal cells (in brown) grow until confluency on fibronectin plates (in grey), and then align in a constant chiral fashion, in an actin-dependant fashion. (C) An example of an internal organ whose formation and morphogenesis is dependent on cellular and molecular chiralities is the embryonic heart.

2000; Levin, 2005; Tabin and Vogan, 2003) is the gut, in which the liver is positioned on the left side, whereas the pancreas remains on the right side of the body plan. Also the intestine rotates and folds in a complex pattern to facilitate its packing in the abdominal cavity (Horne-Badovinac et al., 2003). In vertebrates, the embryonic gut tube forms the intestines through a characteristic looping after an initial 270° rotation (Savin et al., 2011). Savin and colleagues analyzed the effects of forces at a tissue scale level during the gut morphogenesis in chick embryos (Savin et al., 2011). They have proposed that homogeneous and isotropic forces, which arise from the relative growth between the gut tube and the dorsal mesentery (DM) could be at the origin of the gut loop formation in the chick embryo (Savin et al., 2011). Based on their experimental observations, after physical separation of the DM from the gut, the intestine uncoils into a straight tube, indicating that it was under compression, whereas the unconstrained DM contracts, indicating that was under tension. Thus the gut–DM complex is essential to maintain the mature loops in the gut (Savin et al., 2011). Their theoretical model captured the key properties of the looping patterns, strongly suggesting the gut looping pattern is established by the balance of forces induced by the relative growth between the gut-DM complex (Savin et al., 2011).

Yet, the mechanism that drive asymmetric positioning of the gut is not only mechanical but follows asymmetric cues acting downstream of the canonical left-right pathway. Visceral organs are surrounded by a basement membrane (specialized ECM) that mediates mesoderm-endoderm interactions critical for organogenesis. Work done in chick and mouse (Davis et al., 2008; Kurpios et al., 2008) has shown that the looping direction of the gut is established by modifications both in the ECM and in the adhesion of mesenchymal cells. *In silico* data proposed that mesenchymal cells are more densely packed on the left side, and this can be a consequence of LR asymmetries in both ECM and cell-cell adhesion (Kurpios et al., 2008). These asymmetries are regulated by the asymmetrically expressed *Nodal*-induced transcription factors *Pitx2*, *Isl1* (both left) and *Tbx18* (right) (Davis et al., 2008; Kurpios et al., 2008). Both *Pitx2* and *Isl1* up-regulate N-cadherin activity on the left DM, thus changing the morphology of epithelial cells and increasing the aggregation level of mesenchymal cells on the left DM (Kurpios et al., 2008). Both cell changes promote a tilt in the developing midgut that provides the LR bias needed to later induce the counterclockwise gut rotation, and failure to do so leads to defects in gut rotation (Davis et al., 2008; Kurpios et al., 2008). Even though *Pitx2* has a major role is the gut development, its cellular targets that drive asymmetric morphogenesis are not known. Welsh and colleagues have shown that *Pitx2*-specific effectors mediate Wnt signaling and that Wnt pathway components were asymmetrically expressed according to the LR axis (Welsh et al., 2013). Their work established a link between actin dynamics and cadherin-based junctions, which culminate in the asymmetric cell behaviors seen during gut morphogenesis in chick embryos (Davis et al., 2008; Kurpios et al., 2008; Welsh et al., 2013). Also, Mahadevan and colleagues have shown that the process of arteriogenesis in the DM begins during gut rotation and continues strictly on the left side, and is dependent on the *Pitx2* target gene *Cxcl12*. The same work revealed that gut lymphangiogenesis starts on the left DM, in a process dependent on gut arteriogenesis. Thus, they have proposed that the *Pitx2* LR-pathway drives arterial and lymphatic vessels development in the gut (Mahadevan et al., 2014) (Fig. 1B).

In zebrafish, the gut tube originates from a solid rod of endodermal cells that forms a lumen as the cells polarize (Ng et al., 2005; Ober et al., 2003; Wallace and Pack, 2003). During the looping of the gut, the left and right LPM migrate separately, dorsal and ventrolateral to the gut, respectively (Horne-Badovinac et al., 2003). This asymmetric migration displaces the gut to the left. It occurs specifically within the gut-looping region and requires functional LR gene expression and establishment of epithelial polarity within the LPM (Horne-Badovinac et al., 2003). Mutations that disrupt the epithelial structure of the LPM perturb this asymmetric migration and inhibit gut looping. Asymmetric LPM migration still occurs when the endoderm is ablated from the gut-looping region, suggesting that the LPM can autonomously provide a motive force for gut displacement (Horne-Badovinac et al., 2003). Work from Yin and colleagues gave new insights about the role of the ECM remodeling during the asymmetric migration of the LPM during zebrafish gut looping (Yin et al., 2010). They have shown that a localized reduction of laminin deposition is necessary for the asymmetric cell rearrangements within the LPM, as a consequence of the degradation of the basement membrane at the LMP-gut boundary. Thus, it was revealed that such LPM-ECM interaction is crucial for the asymmetric migration of the LPM during gut-looping (Yin et al., 2010). Hochgreb-Hagele and colleagues continued exploring the role of laminin in this context (Hochgreb-Hagele et al., 2013). Using laminin mutants, they observed that due to the lack of basement membrane at the LPM-gut boundary, some LPM cells escape from the LPM and protrude into the gut. Such cell behavior disrupts the normal communication between the LPM cells and stops the collective migration of the LPM (Hochgreb-Hagele et al., 2013). Therefore, there is now enough evidence supporting the important role of the ECM during the establishment of LR axis during the organogenesis of visceral organs. Furthermore, it is established that the epithelial LPM determines the chirality of gut looping and thus the asymmetric position of the digestive organs in several vertebrates (Davis et al., 2008; Hochgreb-Hagele et al., 2013; Kurpios et al., 2008).

In invertebrates, LR asymmetries can be also observed. Several tissues in the fruit fly *Drosophila melanogaster* display LR asymmetries and chiral morphogenesis, like the brain, Malpighian tubules, genitalia and gut (Geminard et al., 2014). The discovery of the conserved *myosin ID* gene (MyoIC and MyoID) as being a main element of LR asymmetry revealed a novel pathway involving actin cytoskeleton and adherens junctions (Hozumi et al., 2006; Speder et al., 2006). MyoID is a dextral determinant for the orientation of all *Drosophila* LR visceral organs (Hozumi et al., 2006; Speder et al., 2006). Mutants for MyoID show reversed lateralization of the internal organs (Hozumi et al., 2006; Speder et al., 2006; Speder and Noselli, 2007). Furthermore, knockdown of myoID in a specific tissue lead to abnormal LR phenotypes exclusively in the affected tissue, without disturbing the laterality of other organs (Speder et al., 2006). This suggests the existence of additional tissue-specific LR organizers (LRO) that remain to be characterized. Furthermore, in these LROs, it was shown that beta-catenin and DE-cadherins (*Drosophila* E-cadherin homolog) play an important role (Hozumi et al., 2006; Petzoldt et al., 2012; Speder et al., 2006), since asymmetric distribution of DE-cadherin dictates the coiling direction of the embryonic hindgut in *Drosophila* (Taniguchi et al., 2011).

Also, the work of Okumura and colleagues have identified *zipper*, which encodes a *Drosophila* non-muscle myosin II heavy chain, as an essential gene for the biased positioning of the embryonic anterior midgut (Okumura et al., 2010). They found myosin II was involved in the two major events in the LR patterning of the embryonic anterior midgut, concerning the biased positioning of the circular visceral muscle cells (that cover the midgut epithelium) and the rotation of the midgut itself. They have proposed that myosin II is responsible for the generation of force needed to lead to a LR biased morphogenesis (Okumura et al., 2010). Later, the work of González-Morales and colleagues showed that a molecular link between myoID and the Planar Cell Polarity atypical cadherin Dachsous (Ds). MyoID interacts with the intracellular domain of Ds, an essential link for the dextral polarity of neighboring hindgut progenitors and required for organ looping in *Drosophila* (Gonzalez-Morales et al., 2015). Taken together, it was shown in *Drosophila* that adherens junctions, myosin and PCP are important to connect LR asymmetry and cell and organ polarity. Also, it seems *Drosophila* has a unique mechanism to establish the LR through different organizers, since in vertebrates it is more or less established that a single developmental event is sufficient to determine LR patterning for all internal organs (Geminard et al., 2014).

6.2. Heart chiral looping

Another example of an internal organ whose formation is dependent on mechanical forces is the embryonic heart (Forouhar et al., 2006; Hove et al., 2003; Voronov et al., 2004) (Fig. 1B). Noel and colleagues, by using an *ex-vivo* heart culture system, have shown the dextral heart looping is a tissue-intrinsic process that requires the activity of actin and myosin (Noel et al., 2013). They have also demonstrated that *Nodal* signaling regulates *α-actin1b* gene expression asymmetricaly, suggesting that asymmetric *Nodal* signaling may enhance a cytoskeleton-based tissue-intrinsic mechanism of heart looping. Thus, this work supports the idea that chiral heart looping is a tissue-intrinsic process that could be controlled by both *Nodal*-dependent and -independent mechanisms (Noel et al., 2013).

Work done in the developing mouse heart (Linask et al., 2003; Linask et al., 2002; Lu et al., 2008) has shown that non-muscle myosin heavy chains IIA and IIB are asymmetrically expressed in the embryonic heart tube, and also, that their position seems to be strictly correlated with the direction of heart looping regardless of the expression of *Pitx2*. Moreover, when myosin-based tension generation is disrupted during the initial stages of heart looping, the whole process of cardiac morphogenesis is impaired (Wei et al., 2002). It does not seem that the constant variation of tension associated with heart contraction is important for heart looping as the heart still loops properly in the absence of contraction (Noel et al., 2013; Sehnert et al., 2002). Thus, it seems that tissue scale tension generated by differential cell shape is involved in providing the force for proper looping. Additional mechanical cues provided by the pericardial cavity might also be important (Bayraktar and Manner, 2014). Studies of heart looping biomechanics in chick embryos have produced interesting models to explain heart looping (Bayraktar and Manner, 2014; Shi et al., 2014). Bayraktar and Männer used a physical model to show that differential growth of the heart and pericardial cavity could contribute to a compressive load that provides extrinsic determinants for heart looping mechanics. Simulations of the growing heart tube constrained within the cavity buckle into a helical shape consistent with the shape of the c-looped heart tube (Bayraktar and Manner, 2014). In contrast to the "growth-induced buckling hypothesis" suggested by Bayraktar and Manner, Shi and colleagues proposed a model in which the differential hypertrophic growth of the myocardium acts as the main force responsible for bending the heart tube. Furthermore, they explore the fact that other regional growth and cytoskeletal contractions, as well as external compressive loads, drive the biased torsion of the heart tube. Here, the bending would be driven mainly by forces generated within the heart tube, while torsion would be caused by external loads (Shi et al., 2014). Even though biomechanical modeling of the embryonic heart is a powerful approach, there are still a number of parameters, such as the contribution of bending and torsion to the looping of the heart tube, that still remain difficult to assess experimentally making the current models difficult to validate.

6.3. Forces modulating branchial arch artery system asymmetry

Sometimes altered distribution of mechanical forces can provide surprising outcomes in the process of asymmetric development. The work of Yashiro and colleagues probably illustrate this the best. They showed that ablation of the unilateral asymmetric *Pitx2* expression impairs asymmetric remodeling of the branchial arch artery system, causing the aortic arch to develop with randomized laterality (Yashiro et al., 2007). They proposed a model in which *Pitx2* induces a regional morphological change that consequently generates an asymmetric blood flow in that region. The uneven distribution of blood flow induces a differential response of growth factors, leading to the maintenance of the left branchial arch artery and regression of its right counterpart, forming this way a left-sided aortic arch (Yashiro et al., 2007). Considering vascular morphogenesis is dependent on hemodynamics (Boselli et al., 2015; Freund et al., 2012), it is possible that the same flow responsive gene network involved in angiogenesis is at work in this process (Fig. 1B). In particular, it seems likely that a feedback loop involving stretch sensitive channels, such as Piezo 1 (Li et al., 2014; Ranade et al., 2014) could be involved in modulating endothelial cell response to forces and alter branchial arches morphogenesis. Interestingly, the homolog of klf2, a transcription factor whose expression is controlled by shear stress *in vivo* (Dekker et al., 2002; Lee et al., 2006), klf2a in zebrafish, has been shown to control branchial arches morphogenesis in response to flow forces (Nicoli et al., 2010).

7. Conclusion

It is now clear that mechanical forces constitute an essential element to include for our understanding of left-right patterning and asymmetric morphogenesis. At both the cellular or tissue scales, a number of unexpected asymmetric inputs can be provided by mechanical forces. They finally translate into asymmetric cell migration, directional flow mediated by beating cilia or chiral spreading of the cells. Together, it seems that mechanical forces can be used to balance or modulate the strong inputs of genetic signals in order to refine or reinforce the cell or tissue movements that are associated with asymmetric development. Not surprisingly, a number of these forces depend on cell contractility and actomyosin modulators. We predict that a lot will be gained from *in vitro* studies and biophysical studies aiming for the identification of the origins of the cellular chirality and how they are connected with the structural component of actomyosin proteins to generate the rotational forces at the base of the chiral organization of the actin network. Obviously, identifying the mechanism activating or inibiting chiral torque generation mediated by the actin cytoskeleton will be necessary to clarify the role of cytoskeletal chirality during left-right patterning and morphogenesis. We foresee key inputs coming from studies of self organising explants systems such as gastruloids, where axis patterning and nodal function start to be unravelled (Turner et al., 2016). Furthermore, quantifying the asymmetric forces generated within the LRO and during asymmetric morphogenesis will help to identify what are the relevant forces and what potential mechanosensors are involved. Finally, the array of mechanosensors at work in each system remain to be studied, and animal models like zebrafish, xenopus and chicken will help a lot in that quest because of their accessibility to experimentation and the possibility to directly impose forces on the embryo. Alternatives including organoids and the use 3D scaffolds should help in that quest as well (Clevers, 2016).

Acknowledgements

We thank Renée Chow and the Vermot lab for discussion and thoughtful comments on the manuscript. JV was supported by HFSP (CDA00032/2010-C), INSERM (Avenir 2008), AFM (14983 and 16852), FRM (DEQ20140329553), the Seventh Framework Program (MC-IRG256549), ANR (ANR-12-ISV2-0001, ANR-11-EQPX-0029, ANR-2010-JCJC-1510-01), EMBO YIP (2014), and by the grant ANR-10-LABX-0030-INRT, a French State fund managed by the Agence Nationale de la Recherche under the frame program Investissements d'Avenir labeled ANR-10-IDEX-0002-02. R.R.F. was supported by the IGBMC International PhD program (LABEX-INRT).

References

Anton, H., Harlepp, S., Ramspacher, C., Wu, D., Monduc, F., Bhat, S., Liebling, M., Paoletti, C., Charvin, G., Freund, J.B., et al., 2013. Pulse propagation by a capacitive mechanism drives embryonic blood flow. Development 140, 4426–4434.

Avasthi, P., Marshall, W.F., 2012. Stages of ciliogenesis and regulation of ciliary length. Differentiation 83, S30–S42.

Bayraktar, M., Manner, J., 2014. Cardiac looping may be driven by compressive loads resulting from unequal growth of the heart and pericardial cavity. Observations on a physical simulation model. Front. Physiol. 5, 112.

Behrndt, M., Salbreux, G., Campinho, P., Hauschild, R., Oswald, F., Roensch, J., Grill, S.W., Heisenberg, C.P., 2012. Forces driving epithelial spreading in zebrafish gastrulation. Science 338, 257–260.
Blum, M., Beyer, T., Weber, T., Vick, P., Andre, P., Bitzer, E., Schweickert, A., 2009. Xenopus, an ideal model system to study vertebrate left-right asymmetry. Dev. Dyn. 238, 1215–1225.
Blum, M., Feistel, K., Thumberger, T., Schweickert, A., 2014. The evolution and conservation of left-right patterning mechanisms. Development 141, 1603–1613.
Borovina, A., Superina, S., Voskas, D., Ciruna, B., 2010. Vangl2 directs the posterior tilting and asymmetric localization of motile primary cilia. Nat. Cell Biol. 12, 407–412.
Boselli, F., Freund, J.B., Vermot, J., 2015. Blood flow mechanics in cardiovascular development. Cell. Mol. Life Sci. 72, 2545–2559.
Brown, N.A., Wolpert, L., 1990. The development of handedness in left/right asymmetry. Development 109, 1–9.
Burdine, R.D., Schier, A.F., 2000. Conserved and divergent mechanisms in left-right axis formation. Genes Dev. 14, 763–776.
Caballero, D., Voituriez, R., Riveline, D., 2015. The cell ratchet: interplay between efficient protrusions and adhesion determines cell motion. Cell Adhes. Migr. 9, 327–334.
Capdevila, J., Vogan, K.J., Tabin, C.J., Izpisua Belmonte, J.C., 2000. Mechanisms of left-right determination in vertebrates. Cell 101, 9–21.
Cartwright, J.H., Piro, O., Tuval, I., 2009. Fluid dynamics in developmental biology: moving fluids that shape ontogeny. HFSP J. 3, 77–93.
Chen, T.H., Hsu, J.J., Zhao, X., Guo, C., Wong, M.N., Huang, Y., Li, Z., Garfinkel, A., Ho, C.M., Tintut, Y., et al., 2012. Left-right symmetry breaking in tissue morphogenesis via cytoskeletal mechanics. Circ. Res. 110, 551–559.
Chien, Y.H., Keller, R., Kintner, C., Shook, D.R., 2015. Mechanical strain determines the axis of planar polarity in ciliated epithelia. Curr. Biol. 25, 2774–2784.
Clevers, H., 2016. Modeling development and disease with organoids. Cell 165, 1586–1597.
Colantonio, J.R., Vermot, J., Wu, D., Langenbacher, A.D., Fraser, S., Chen, J.N., Hill, K.L., 2009. The dynein regulatory complex is required for ciliary motility and otolith biogenesis in the inner ear. Nature 457, 205–209.
Comelles, J., Caballero, D., Voituriez, R., Hortiguela, V., Wollrab, V., Godeau, A.L., Samitier, J., Martinez, E., Riveline, D., 2014. Cells as active particles in asymmetric potentials: motility under external gradients. Biophys. J. 107, 1513–1522.
Compagnon, J., Barone, V., Rajshekar, S., Kottmeier, R., Pranjic-Ferscha, K., Behrndt, M., Heisenberg, C.P., 2014. The notochord breaks bilateral symmetry by controlling cell shapes in the zebrafish laterality organ. Dev. Cell 31, 774–783.
Cui, C., Little, C.D., Rongish, B.J., 2009. Rotation of organizer tissue contributes to left-right asymmetry. Anat. Rec. (Hoboken) 292, 557–561.
Davis, N.M., Kurpios, N.A., Sun, X., Gros, J., Martin, J.F., Tabin, C.J., 2008. The chirality of gut rotation derives from left-right asymmetric changes in the architecture of the dorsal mesentery. Dev. Cell 15, 134–145.
Dekker, R.J., van Soest, S., Fontijn, R.D., Salamanca, S., de Groot, P.G., VanBavel, E., Pannekoek, H., Horrevoets, A.J., 2002. Prolonged fluid shear stress induces a distinct set of endothelial cell genes, most specifically lung Kruppel-like factor (KLF2). Blood 100, 1689–1698.
Delling, M., Indzhykulian, A.A., Liu, X., Li, Y., Xie, T., Corey, D.P., Clapham, D.E., 2016. Primary cilia are not calcium-responsive mechanosensors. Nature 531, 656–660.
Delmas, P., Nauli, S.M., Li, X., Coste, B., Osorio, N., Crest, M., Brown, D.A., Zhou, J., 2004. Gating of the polycystin ion channel signaling complex in neurons and kidney cells. FASEB J. 18, 740–742.
Du, J., Ma, X., Shen, B., Huang, Y., Birnbaumer, L., Yao, X., 2014. TRPV4, TRPC1, and TRPP2 assemble to form a flow-sensitive heteromeric channel. FASEB J. 28, 4677–4685.
Essner, J.J., Amack, J.D., Nyholm, M.K., Harris, E.B., Yost, H.J., 2005. Kupffer's vesicle is a ciliated organ of asymmetry in the zebrafish embryo that initiates left-right development of the brain, heart and gut. Development 132, 1247–1260.
Farge, E., 2003. Mechanical induction of twist in the *Drosophila* foregut/stomodeal primordium. Curr. Biol. 13, 1365–1377.
Farina, F., Gaillard, J., Guerin, C., Coute, Y., Sillibourne, J., Blanchoin, L., Thery, M., 2016. The centrosome is an actin-organizing centre. Nat. Cell Biol. 18 (65-+).
Fernandez-Sanchez, M.E., Serman, F., Ahmadi, P., Farge, E., 2010. Mechanical induction in embryonic development and tumor growth integrative cues through molecular to multicellular interplay and evolutionary perspectives. Methods Cell Biol. 98, 295–321.
Fernandez-Sanchez, M.E., Barbier, S., Whitehead, J., Bealle, G., Michel, A., Latorre-Ossa, H., Rey, C., Fouassier, L., Claperon, A., Brulle, L., et al., 2015. Mechanical induction of the tumorigenic beta-catenin pathway by tumour growth pressure. Nature 523, 92–95.
Field, S., Riley, K.L., Grimes, D.T., Hilton, H., Simon, M., Powles-Glover, N., Siggers, P., Bogani, D., Greenfield, A., Norris, D.P., 2011. Pkd1l1 establishes left-right asymmetry and physically interacts with Pkd2. Development 138, 1131–1142.
Forouhar, A.S., Liebling, M., Hickerson, A., Nasiraei-Moghaddam, A., Tsai, H.J., Hove, J.R., Fraser, S.E., Dickinson, M.E., Gharib, M., 2006. The embryonic vertebrate heart tube is a dynamic suction pump. Science 312, 751–753.
Freund, J.B., Goetz, J.G., Hill, K.L., Vermot, J., 2012. Fluid flows and forces in development: functions, features and biophysical principles. Development 139, 1229–1245.
Garcia-Castro, M.I., Vielmetter, E., Bronner-Fraser, M., 2000. N-cadherin, a cell adhesion molecule involved in establishment of embryonic left-right asymmetry. Science 288, 1047–1051.
Geminard, C., Gonzalez-Morales, N., Coutelis, J.B., Noselli, S., 2014. The myosin ID pathway and left-right asymmetry in *Drosophila*. Genesis 52, 471–480.
Giamarchi, A., Padilla, F., Coste, B., Raoux, M., Crest, M., Honore, E., Delmas, P., 2006. The versatile nature of the calcium-permeable cation channel TRPP2. EMBO Rep. 7, 787–793.
Goetz, J.G., Steed, E., Ferreira, R.R., Roth, S., Ramspacher, C., Boselli, F., Charvin, G., Liebling, M., Wyart, C., Schwab, Y., et al., 2014. Endothelial cilia mediate low flow sensing during zebrafish vascular development. Cell Rep. 6, 799–808.
Gonzalez-Morales, N., Geminard, C., Lebreton, G., Cerezo, D., Coutelis, J.B., Noselli, S., 2015. The atypical cadherin Dachsous controls left-right asymmetry in *Drosophila*. Dev. Cell 33, 675–689.
Grill, S.W., 2011. Growing up is stressful: biophysical laws of morphogenesis. Curr. Opin. Genet. Dev. 21, 647–652.
Grimes, D.T., Keynton, J.L., Buenavista, M.T., Jin, X., Patel, S.H., Kyosuke, S., Vibert, J., Williams, D.J., Hamada, H., Hussain, R., et al., 2016. Genetic analysis reveals a hierarchy of interactions between polycystin-encoding genes and genes controlling cilia function during left-right determination. PLoS Genet. 12, e1006070.
Gros, J., Feistel, K., Viebahn, C., Blum, M., Tabin, C.J., 2009. Cell movements at Hensen's node establish left/right asymmetric gene expression in the chick. Science 324, 941–944.
Guirao, B., Meunier, A., Mortaud, S., Aguilar, A., Corsi, J.M., Strehl, L., Hirota, Y., Desoeuvre, A., Boutin, C., Han, Y.G., et al., 2010. Coupling between hydrodynamic forces and planar cell polarity orients mammalian motile cilia. Nat. Cell Biol. 12, 341–350.
Hahn, C., Schwartz, M.A., 2009. Mechanotransduction in vascular physiology and atherogenesis. Nat. Rev. Mol. Cell Biol. 10, 53–62.
Hamada, H., 2015. Role of physical forces in embryonic development. Semin. Cell Dev. Biol. 47-48, 88–91.
Hamada, H., Meno, C., Watanabe, D., Saijoh, Y., 2002. Establishment of vertebrate left-right asymmetry. Nat. Rev. Genet. 3, 103–113.
Hanaoka, K., Qian, F., Boletta, A., Bhumia, A.K., Piontek, K., Tsiokas, L., Sukhatme, V.P., Guggino, W.B., Germino, G.G., 2000. Co-assembly of polycystin-1 and-2 produces unique cation-permeable currents. Nature 408, 990–994.
Hashimoto, M., Hamada, H., 2010. Translation of anterior-posterior polarity into left-right polarity in the mouse embryo. Curr. Opin. Genet. Dev. 20, 433–437.
Hashimoto, M., Shinohara, K., Wang, J., Ikeuchi, S., Yoshiba, S., Meno, C., Nonaka, S., Takada, S., Hatta, K., Wynshaw-Boris, A., et al., 2010. Planar polarization of node cells determines the rotational axis of node cilia. Nat. Cell Biol. 12, 170–176.
Heckel, E., Boselli, F., Roth, S., Krudewig, A., Belting, H.G., Charvin, G., Vermot, J., 2015. Oscillatory flow modulates mechanosensitive klf2a expression through trpv4 and trpp2 during heart valve development. Curr. Biol. 25, 1354–1361.
Heisenberg, C.P., Bellaiche, Y., 2013. Forces in tissue morphogenesis and patterning. Cell 153, 948–962.
Hildebrandt, F., Benzing, T., Katsanis, N., 2011. Ciliopathies. N. Engl. J. Med. 364, 1533–1543.
Hilfinger, A., Julicher, F., 2008. The chirality of ciliary beats. Phys. Biol. 5, 016003.
Hiramatsu, R., Matsuoka, T., Kimura-Yoshida, C., Han, S.W., Mochida, K., Adachi, T., Takayama, S., Matsuo, I., 2013. External mechanical cues trigger the establishment of the anterior-posterior axis in early mouse embryos. Dev. Cell 27, 131–144.
Hochgreb-Hagele, T., Yin, C., Koo, D.E., Bronner, M.E., Stainier, D.Y., 2013. Laminin beta1a controls distinct steps during the establishment of digestive organ laterality. Development 140, 2734–2745.
Horne-Badovinac, S., Rebagliati, M., Stainier, D.Y., 2003. A cellular framework for gut-looping morphogenesis in zebrafish. Science 302, 662–665.
Hove, J.R., Koster, R.W., Forouhar, A.S., Acevedo-Bolton, G., Fraser, S.E., Gharib, M., 2003. Intracardiac fluid forces are an essential epigenetic factor for embryonic cardiogenesis. Nature 421, 172–177.
Hozumi, S., Maeda, R., Taniguchi, K., Kanai, M., Shirakabe, S., Sasamura, T., Speder, P., Noselli, S., Aigaki, T., Murakami, R., et al., 2006. An unconventional myosin in *Drosophila* reverses the default handedness in visceral organs. Nature 440, 798–802.
Huveneers, S., de Rooij, J., 2013. Mechanosensitive systems at the cadherin-F-actin interface. J. Cell Sci. 126, 403–413.
Ishikawa, H., Marshall, W.F., 2014. Mechanobiology of ciliogenesis. Bioscience 64, 1084–1091.
Kamura, K., Kobayashi, D., Uehara, Y., Koshida, S., Iijima, N., Kudo, A., Yokoyama, T., Takeda, H., 2011. Pkd1l1 complexes with Pkd2 on motile cilia and functions to establish the left-right axis. Development 138, 1121–1129.
Keeling, J., Tsiokas, L., Maskey, D., 2016. Cellular mechanisms of ciliary length control. Cell 5.
Kim, S., Nie, H., Nesin, V., Tran, U., Outeda, P., Bai, C.X., Keeling, J., Maskey, D., Watnick, T., Wessely, O., et al., 2016. The polycystin complex mediates Wnt/Ca(2+) signalling. Nat. Cell Biol. 18, 752–764.
Kramer-Zucker, A.G., Olale, F., Haycraft, C.J., Yoder, B.K., Schier, A.F., Drummond, I.A., 2005. Cilia-driven fluid flow in the zebrafish pronephros, brain and Kupffer's vesicle is required for normal organogenesis. Development 132, 1907–1921.
Kreiling, J.A., Prabhat Williams, G., Creton, R., 2007. Analysis of Kupffer's vesicle in zebrafish embryos using a cave automated virtual environment. Dev. Dyn. 236, 1963–1969.
Kurpios, N.A., Ibanes, M., Davis, N.M., Lui, W., Katz, T., Martin, J.F., Izpisua Belmonte, J.C., Tabin, C.J., 2008. The direction of gut looping is established by changes in the extracellular matrix and in cell:cell adhesion. Proc. Natl. Acad. Sci. U. S. A. 105, 8499–8506.
Ladoux, B., Anon, E., Lambert, M., Rabodzey, A., Hersen, P., Buguin, A., Silberzan, P., Mege, R.M., 2010. Strength dependence of cadherin-mediated adhesions. Biophys. J. 98, 534–542.
Ladoux, B., Mege, R.M., Trepat, X., 2016. Front-rear polarization by mechanical cues: from single cells to tissues. Trends Cell Biol. 26, 420–433.
Lecuit, T., Yap, A.S., 2015. E-cadherin junctions as active mechanical integrators in tissue dynamics. Nat. Cell Biol. 17, 533–539.
Lecuit, T., Lenne, P.F., Munro, E., 2011. Force generation, transmission, and integration during cell and tissue morphogenesis. Annu. Rev. Cell Dev. Biol. 27, 157–184.
Lee, J.S., Yu, Q., Shin, J.T., Sebzda, E., Bertozzi, C., Chen, M., Mericko, P., Stadtfeld, M., Zhou, D., Cheng, L., et al., 2006. Klf2 is an essential regulator of vascular hemodynamic forces in vivo. Dev. Cell 11, 845–857.
LeGoff, L., Lecuit, T., 2016. Mechanical forces and growth in animal tissues. Cold Spring Harb. Perspect. Biol. 8, a019232.

Levin, M., 2005. Left-right asymmetry in embryonic development: a comprehensive review. Mech. Dev. 122, 3–25.
Levin, M., Mercola, M., 1998. The compulsion of chirality: toward an understanding of left-right asymmetry. Genes Dev. 12, 763–769.
Li, J., Hou, B., Tumova, S., Muraki, K., Bruns, A., Ludlow, M.J., Sedo, A., Hyman, A.J., McKeown, L., Young, R.S., et al., 2014. Piezo1 integration of vascular architecture with physiological force. Nature 515, 279–282.
Linask, K.K., Yu, X., Chen, Y., Han, M.D., 2002. Directionality of heart looping: effects of Pitx2c misexpression on flectin asymmetry and midline structures. Dev. Biol. 246, 407–417.
Linask, K.K., Han, M.D., Linask, K.L., Schlange, T., Brand, T., 2003. Effects of antisense misexpression of CFC on downstream flectin protein expression during heart looping. Dev. Dyn. 228, 217–230.
Lu, W., Seeholzer, S.H., Han, M., Arnold, A.S., Serrano, M., Garita, B., Philp, N.J., Farthing, C., Steele, P., Chen, J., et al., 2008. Cellular nonmuscle myosins NMHC-IIA and NMHC-IIB and vertebrate heart looping. Dev. Dyn. 237, 3577–3590.
Mahadevan, A., Welsh, I.C., Sivakumar, A., Gludish, D.W., Shilvock, A.R., Noden, D.M., Huss, D., Lansford, R., Kurpios, N.A., 2014. The left-right Pitx2 pathway drives organ-specific arterial and lymphatic development in the intestine. Dev. Cell 31, 690–706.
Maitre, J.L., Berthoumieux, H., Krens, S.F., Salbreux, G., Julicher, F., Paluch, E., Heisenberg, C.P., 2012. Adhesion functions in cell sorting by mechanically coupling the cortices of adhering cells. Science 338, 253–256.
Mammoto, T., Ingber, D.E., 2010. Mechanical control of tissue and organ development. Development 137, 1407–1420.
Mammoto, A., Mammoto, T., Ingber, D.E., 2012. Mechanosensitive mechanisms in transcriptional regulation. J. Cell Sci. 125, 3061–3073.
McDowell, G., Rajadurai, S., Levin, M., 2016. From cytoskeletal dynamics to organ asymmetry: a nonlinear, regulative pathway underlies left-right patterning. Philos. Trans. R. Soc. Lond. B. Biol. Sci. 371.
McGrath, J., Somlo, S., Makova, S., Tian, X., Brueckner, M., 2003. Two populations of node monocilia initiate left-right asymmetry in the mouse. Cell 114, 61–73.
Mendes, R.V., Martins, G.G., Cristovao, A.M., Saude, L., 2014. N-cadherin locks left-right asymmetry by ending the leftward movement of Hensen's node cells. Dev. Cell 30, 353–360.
Mirabet, V., Das, P., Boudaoud, A., Hamant, O., 2011. The role of mechanical forces in plant morphogenesis. Annu. Rev. Plant Biol. 62, 365–385.
Naganathan, S.R., Furthauer, S., Nishikawa, M., Julicher, F., Grill, S.W., 2014. Active torque generation by the actomyosin cell cortex drives left-right symmetry breaking. Elife 3, e04165.
Naganathan, S.R., Middelkoop, T.C., Furthauer, S., Grill, S.W., 2016. Actomyosin-driven left-right asymmetry: from molecular torques to chiral self-organization. Curr. Opin. Cell Biol. 38, 24–30.
Nakamura, T., Mine, N., Nakaguchi, E., Mochizuki, A., Yamamoto, M., Yashiro, K., Meno, C., Hamada, H., 2006. Generation of robust left-right asymmetry in the mouse embryo requires a self-enhancement and lateral-inhibition system. Dev. Cell 11, 495–504.
Nauli, S.M., Alenghat, F.J., Luo, Y., Williams, E., Vassilev, P., Li, X., Elia, A.E., Lu, W., Brown, E.M., Quinn, S.J., et al., 2003. Polycystins 1 and 2 mediate mechanosensation in the primary cilium of kidney cells. Nat. Genet. 33, 129–137.
Nauli, S.M., Kawanabe, Y., Kaminski, J.J., Pearce, W.J., Ingber, D.E., Zhou, J., 2008. Endothelial cilia are fluid shear sensors that regulate calcium signaling and nitric oxide production through polycystin-1. Circulation 117, 1161–1171.
Ng, A.N., de Jong-Curtain, T.A., Mawdsley, D.J., White, S.J., Shin, J., Appel, B., Dong, P.D., Stainier, D.Y., Heath, J.K., 2005. Formation of the digestive system in zebrafish: III. Intestinal epithelium morphogenesis. Dev. Biol. 286, 114–135.
Nicoli, S., Standley, C., Walker, P., Hurlstone, A., Fogarty, K.E., Lawson, N.D., 2010. MicroRNA-mediated integration of haemodynamics and Vegf signalling during angiogenesis. Nature 464, 1196–1200.
Noel, E.S., Verhoeven, M., Lagendijk, A.K., Tessadori, F., Smith, K., Choorapoikayil, S., den Hertog, J., Bakkers, J., 2013. A nodal-independent and tissue-intrinsic mechanism controls heart-looping chirality. Nat. Commun. 4, 2754.
Nonaka, S., Tanaka, Y., Okada, Y., Takeda, S., Harada, A., Kanai, Y., Kido, M., Hirokawa, N., 1998. Randomization of left-right asymmetry due to loss of nodal cilia generating leftward flow of extraembryonic fluid in mice lacking KIF3B motor protein. Cell 95, 829–837.
Ober, E.A., Field, H.A., Stainier, D.Y., 2003. From endoderm formation to liver and pancreas development in zebrafish. Mech. Dev. 120, 5–18.
Ohata, S., Herranz-Perez, V., Nakatani, J., Boletta, A., Garcia-Verdugo, J.M., Alvarez-Buylla, A., 2015. Mechanosensory genes Pkd1 and Pkd2 contribute to the planar polarization of brain ventricular epithelium. J. Neurosci. 35, 11153–11168.
Okabe, N., Xu, B., Burdine, R.D., 2008. Fluid dynamics in zebrafish Kupffer's vesicle. Dev. Dyn. 237, 3602–3612.
Okada, Y., Takeda, S., Tanaka, Y., Izpisua Belmonte, J.C., Hirokawa, N., 2005. Mechanism of nodal flow: a conserved symmetry breaking event in left-right axis determination. Cell 121, 633–644.
Okumura, T., Fujiwara, H., Taniguchi, K., Kuroda, J., Nakazawa, N., Nakamura, M., Hatori, R., Ishio, A., Maeda, R., Matsuno, K., 2010. Left-right asymmetric morphogenesis of the anterior midgut depends on the activation of a non-muscle myosin II in *Drosophila*. Dev. Biol. 344, 693–706.
Pardanaud, L., Eichmann, A., 2009. Stem cells: the stress of forming blood cells. Nature 459, 1068–1069.
Patel, A., Sharif-Naeini, R., Folgering, J.R., Bichet, D., Duprat, F., Honore, E., 2010. Canonical TRP channels and mechanotransduction: from physiology to disease states. Pflugers Arch. 460, 571–581.
Pazour, G.J., San Agustin, J.T., Follit, J.A., Rosenbaum, J.L., Witman, G.B., 2002. Polycystin-2 localizes to kidney cilia and the ciliary level is elevated in orpk mice with polycystic kidney disease. Curr. Biol. 12, R378–R380.
Pennekamp, P., Karcher, C., Fischer, A., Schweickert, A., Skryabin, B., Horst, J., Blum, M., Dworniczak, B., 2002. The ion channel polycystin-2 is required for left-right axis determination in mice. Curr. Biol. 12, 938–943.
Pennekamp, P., Menchen, T., Dworniczak, B., Hamada, H., 2015. Situs inversus and ciliary abnormalities: 20 years later, what is the connection? Cilia 4, 1.
Peralta, M., Steed, E., Harlepp, S., Gonzalez-Rosa, J.M., Monduc, F., Ariza-Cosano, A., Cortes, A., Rayon, T., Gomez-Skarmeta, J.L., Zapata, A., et al., 2013. Heartbeat-driven pericardiac fluid forces contribute to epicardium morphogenesis. Curr. Biol. 23, 1726–1735.
Petzoldt, A.G., Coutelis, J.B., Geminard, C., Speder, P., Suzanne, M., Cerezo, D., Noselli, S., 2012. DE-cadherin regulates unconventional myosin ID and myosin IC in *Drosophila* left-right asymmetry establishment. Development 139, 1874–1884.
Pitaval, A., Tseng, Q., Bornens, M., Thery, M., 2010. Cell shape and contractility regulate ciliogenesis in cell cycle-arrested cells. J. Cell Biol. 191, 303–312.
Pohl, C., Bao, Z., 2010. Chiral forces organize left-right patterning in *C. elegans* by uncoupling midline and anteroposterior axis. Dev. Cell 19, 402–412.
Pourquie, O., 2011. Vertebrate segmentation: from cyclic gene networks to scoliosis. Cell 145, 650–663.
Ranade, S.S., Qiu, Z., Woo, S.H., Hur, S.S., Murthy, S.E., Cahalan, S.M., Xu, J., Mathur, J., Bandell, M., Coste, B., et al., 2014. Piezo1, a mechanically activated ion channel, is required for vascular development in mice. Proc. Natl. Acad. Sci. U. S. A. 111, 10347–10352.
Sampaio, P., Ferreira, R.R., Guerrero, A., Pintado, P., Tavares, B., Amaro, J., Smith, A.A., Montenegro-Johnson, T., Smith, D.J., Lopes, S.S., 2014. Left-right organizer flow dynamics: how much cilia activity reliably yields laterality? Dev. Cell 29, 716–728.
Savin, T., Kurpios, N.A., Shyer, A.E., Florescu, P., Liang, H., Mahadevan, L., Tabin, C.J., 2011. On the growth and form of the gut. Nature 476, 57–62.
Sawamoto, K., Wichterle, H., Gonzalez-Perez, O., Cholfin, J.A., Yamada, M., Spassky, N., Murcia, N.S., Garcia-Verdugo, J.M., Marin, O., Rubenstein, J.L., et al., 2006. New neurons follow the flow of cerebrospinal fluid in the adult brain. Science 311, 629–632.
Schonegg, S., Hyman, A.A., Wood, W.B., 2014. Timing and mechanism of the initial cue establishing handed left-right asymmetry in *Caenorhabditis elegans* embryos. Genesis 52, 572–580.
Schottenfeld, J., Sullivan-Brown, J., Burdine, R.D., 2007. Zebrafish curly up encodes a Pkd2 ortholog that restricts left-side-specific expression of southpaw. Development 134, 1605–1615.
Schweickert, A., Weber, T., Beyer, T., Vick, P., Bogusch, S., Feistel, K., Blum, M., 2007. Cilia-driven leftward flow determines laterality in *Xenopus*. Curr. Biol. 17, 60–66.
Sehnert, A.J., Huq, A., Weinstein, B.M., Walker, C., Fishman, M., Stainier, D.Y., 2002. Cardiac troponin T is essential in sarcomere assembly and cardiac contractility. Nat. Genet. 31, 106–110.
Sharif-Naeini, R., Folgering, J.H., Bichet, D., Duprat, F., Lauritzen, I., Arhatte, M., Jodar, M., Dedman, A., Chatelain, F.C., Schulte, U., et al., 2009. Polycystin-1 and -2 dosage regulates pressure sensing. Cell 139, 587–596.
Sharif-Naeini, R., Folgering, J.H., Bichet, D., Duprat, F., Delmas, P., Patel, A., Honore, E., 2010. Sensing pressure in the cardiovascular system: Gq-coupled mechanoreceptors and TRP channels. J. Mol. Cell. Cardiol. 48, 83–89.
Shi, Y., Yao, J., Young, J.M., Fee, J.A., Perucchio, R., Taber, L.A., 2014. Bending and twisting the embryonic heart: a computational model for c-looping based on realistic geometry. Front. Physiol. 5, 297.
Shinohara, K., Kawasumi, A., Takamatsu, A., Yoshiba, S., Botilde, Y., Motoyama, N., Reith, W., Durand, B., Shiratori, H., Hamada, H., 2012. Two rotating cilia in the node cavity are sufficient to break left-right symmetry in the mouse embryo. Nat. Commun. 3, 622.
Singh, D., Pohl, C., 2014. Coupling of rotational cortical flow, asymmetric midbody positioning, and spindle rotation mediates dorsoventral axis formation in *C. elegans*. Dev. Cell 28, 253–267.
Song, H., Hu, J., Chen, W., Elliott, G., Andre, P., Gao, B., Yang, Y., 2010. Planar cell polarity breaks bilateral symmetry by controlling ciliary positioning. Nature 466, 378–382.
Speder, P., Noselli, S., 2007. Left-right asymmetry: class I myosins show the direction. Curr. Opin. Cell Biol. 19, 82–87.
Speder, P., Adam, G., Noselli, S., 2006. Type ID unconventional myosin controls left-right asymmetry in *Drosophila*. Nature 440, 803–807.
Striedter, G.F., Srinivasan, S., Monuki, E.S., 2015. Cortical folding: when, where, how, and why? Annu. Rev. Neurosci. 38:291–307. http://dx.doi.org/10.1146/annurev-neuro-071714-034128 (Jul. 8).
Sugimura, K., Lenne, P.F., Graner, F., 2016. Measuring forces and stresses in situ in living tissues. Development 143, 186–196.
Supatto, W., Vermot, J., 2011. From cilia hydrodynamics to zebrafish embryonic development. Curr. Top. Dev. Biol. 95, 33–66.
Superina, S., Borovina, A., Ciruna, B., 2014. Analysis of maternal-zygotic ugdh mutants reveals divergent roles for HSPGs in vertebrate embryogenesis and provides new insight into the initiation of left-right asymmetry. Dev. Biol. 387, 154–166.
Tabin, C.J., Vogan, K.J., 2003. A two-cilia model for vertebrate left-right axis specification. Genes Dev. 17, 1–6.
Taniguchi, K., Maeda, R., Ando, T., Okumura, T., Nakazawa, N., Hatori, R., Nakamura, M., Hozumi, S., Fujiwara, H., Matsuno, K., 2011. Chirality in planar cell shape contributes to left-right asymmetric epithelial morphogenesis. Science 333, 339–341.
Tee, Y.H., Shemesh, T., Thiagarajan, V., Hariadi, R.F., Anderson, K.L., Page, C., Volkmann, N., Hanein, D., Sivaramakrishnan, S., Kozlov, M.M., et al., 2015. Cellular chirality arising from the self-organization of the actin cytoskeleton. Nat. Cell Biol. 17, 445–457.
Turner, D.A., Glodowski, C.R., Luz, A.C., Baillie-Johnson, P., Hayward, P.C., Collignon, J., Gustavsen, C., Serup, P., Schröter, C., Martinez Arias, A., 2016. Interactions between Nodal and Wnt signalling Drive Robust Symmetry Breaking and Axial Organisation in Gastruloids (Embryonic Organoids). bioRxiv, 051722 http://dx.doi.org/10.1101/051722.

Vincensini, L., Blisnick, T., Bastin, P., 2011. 1001 model organisms to study cilia and flagella. Biol. Cell. 103, 109–130.
Vogel, V., Sheetz, M., 2006. Local force and geometry sensing regulate cell functions. Nat. Rev. Mol. Cell Biol. 7, 265–275.
Voronov, D.A., Alford, P.W., Xu, G., Taber, L.A., 2004. The role of mechanical forces in dextral rotation during cardiac looping in the chick embryo. Dev. Biol. 272, 339–350.
Wallace, K.N., Pack, M., 2003. Unique and conserved aspects of gut development in zebrafish. Dev. Biol. 255, 12–29.
Wang, G., Cadwallader, A.B., Jang, D.S., Tsang, M., Yost, H.J., Amack, J.D., 2011. The Rho kinase Rock2b establishes anteroposterior asymmetry of the ciliated Kupffer's vesicle in zebrafish. Development 138, 45–54.
Wang, G., Manning, M.L., Amack, J.D., 2012. Regional cell shape changes control form and function of Kupffer's vesicle in the zebrafish embryo. Dev. Biol. 370, 52–62.
Weber, G.F., Bjerke, M.A., DeSimone, D.W., 2012. A mechanoresponsive cadherin-keratin complex directs polarized protrusive behavior and collective cell migration. Dev. Cell 22, 104–115.
Wei, L., Imanaka-Yoshida, K., Wang, L., Zhan, S., Schneider, M.D., DeMayo, F.J., Schwartz, R.J., 2002. Inhibition of Rho family GTPases by Rho GDP dissociation inhibitor disrupts cardiac morphogenesis and inhibits cardiomyocyte proliferation. Development 129, 1705–1714.
Welsh, I.C., Thomsen, M., Gludish, D.W., Alfonso-Parra, C., Bai, Y., Martin, J.F., Kurpios, N.A., 2013. Integration of left-right Pitx2 transcription and Wnt signaling drives asymmetric gut morphogenesis via Daam2. Dev. Cell 26, 629–644.
White, J.P., Cibelli, M., Urban, L., Nilius, B., McGeown, J.G., Nagy, I., 2016. TRPV4: molecular conductor of a diverse orchestra. Physiol. Rev. 96, 911–973.
Wu, D., Freund, J.B., Fraser, S.E., Vermot, J., 2011. Mechanistic basis of otolith formation during teleost inner ear development. Dev. Cell 20, 271–278.
Yashiro, K., Shiratori, H., Hamada, H., 2007. Haemodynamics determined by a genetic programme govern asymmetric development of the aortic arch. Nature 450, 285–288.
Yin, C., Kikuchi, K., Hochgreb, T., Poss, K.D., Stainier, D.Y., 2010. Hand2 regulates extracellular matrix remodeling essential for gut-looping morphogenesis in zebrafish. Dev. Cell 18, 973–984.
Yoder, B.K., Hou, X., Guay-Woodford, L.M., 2002. The polycystic kidney disease proteins, polycystin-1, polycystin-2, polaris, and cystin, are co-localized in renal cilia. J. Am. Soc. Nephrol. 13, 2508–2516.
Yoshiba, S., Shiratori, H., Kuo, I.Y., Kawasumi, A., Shinohara, K., Nonaka, S., Asai, Y., Sasaki, G., Belo, J.A., Sasaki, H., et al., 2012. Cilia at the node of mouse embryos sense fluid flow for left-right determination via Pkd2. Science 338, 226–231.
Yuan, S., Zhao, L., Brueckner, M., Sun, Z., 2015. Intraciliary calcium oscillations initiate vertebrate left-right asymmetry. Curr. Biol. 25, 556–567.
Zhang, H., Labouesse, M., 2012. Signalling through mechanical inputs: a coordinated process. J. Cell Sci. 125, 3039–3049.
Zhang, H., Gally, C., Labouesse, M., 2010. Tissue morphogenesis: how multiple cells cooperate to generate a tissue. Curr. Opin. Cell Biol. 22, 575–582.

5. Fluid mechanics at low Reynolds number and cilia tilt

Essentially, the main function of motile cilia is to generate fluid flow at the micrometer scale. However, physical laws that govern fluid dynamics at this scale are not trivial and the resultant fluid flow presents features that are not completely intuitive **(Fig. 16A)** (Freund et al., 2012; Supatto and Vermot, 2011). In fluid mechanics, the *Reynolds* number (Re) is a dimensionless number that characterizes the nature of a fluid flow and the relative contribution of inertia and viscous dissipation. The cilia-driven flow involved in the zebrafish development is characterized by Re << 1 **(Fig. 16B)**. More generally, fluid dynamics involved in most microscopic biological systems (Purcell, 1977) works at low Re. From a modeling perspective, the low values of Re allows the simplification of the Navier–Stokes flow equation, which is the general model governing fluid dynamics. In case Re << 1, viscous forces dominate inertial forces and the Navier–Stokes flow equation can be simplified to a Stokes flow equation **(Fig. 16A)** (reviewed in (Freund et al., 2012; Supatto and Vermot, 2011).

The LRO of the vertebrate embryos is typically a low Re environment. In such environment, a key question has been to understand how to obtain a net flow, regarding that in the absence of inertia, the flow velocity would be only proportional to the force applied by the cilium to the fluid. Importantly, the Stokes flow equation reveals that there is no time reversibility in at low Re environment, meaning time asymmetries would not be sufficient to create a net flow (Purcell, 1977). Thus, in order to generate a directional flow at low Re, cilia need to beat in a spatially asymmetric fashion, with a tilted conical motion **(Fig. 17A-B)** (Satir and Christensen, 2007; Supatto et al., 2008; Supatto and Vermot, 2011). In this case, the spatial symmetry of the cilium is broken even without bending, because the rotation axis of the cilium is not orthogonal to the cell surface, but tilted with an angle θ, towards the normal of the cell surface (Cartwright et al., 2004; Smith et al., 2008; Supatto et al., 2008; Supatto and Vermot, 2011; Vilfan, 2012; Vilfan and Julicher, 2006). Giving this, the cycle of rotation of a tilted cilium would consists of an effective stroke, during which the cilium is far from the cell membrane moving the maximum amount of fluid, and a recovery stroke when swings along the surface **(Fig. 17C)** (Freund et al., 2012; Marshall and Kintner, 2008; Supatto and Vermot, 2011). As both phases of the rotation cycle are defined by the interaction between the cilium and the cell surface, the direction of the generated-flow depends on the cilium tilt in relation with the cell. Thus, the direction of the flow would be perpendicular to the direction of the cilium tilt and parallel to the cell surface **(Fig. 17C)**. Importantly, spatial orientation is a key functional feature of motile cilia involved in LR symmetry breaking, as it determines the strength and directionality of the induced flow.

The model predictions of a cilium tilt first suggested by Cartwright and colleagues (Cartwright et al., 2004) and further investigated by demonstrating the importance of the cell surface and the no-slip boundary condition to obtain efficient and recovery strokes (Smith et al., 2008; Smith et al., 2007; Vilfan and Julicher, 2006), have been experimentally confirmed *in vivo* in mouse **(Fig. 17D)** (Nonaka et al., 2005; Okada et al., 2005) and in zebrafish **(Fig. 17E)** (Supatto et al., 2008). In the mouse node, the observed leftward flow (Nonaka et al., 1998; Nonaka et al., 2005) is a result of the posterior tilt of

cilia (Nonaka et al., 2005; Okada et al., 2005; Shiratori and Hamada, 2006). The basal bodies of the motile cilia are located on the posterior side of the node cells and the cilia are tilted towards the posterior side of the node due to the intrinsic dome-shape of these cells **(Fig. 17D)** (Hashimoto et al., 2010). The polarized location of the motile cells may be driven by the activity of the planar cell polarity (PCP) pathway revealed by the different distribution of PCP factors (e.g. Prickle2, Vangl1 and Dishevelled) to the anterior and posterior sides of the ventral node cells **(Fig. 8G)** (Song et al., 2010). Mutant mice have shown cilium tilt is controlled by the biased positioning of the basal body in the posterior region of the node cells, which is regulated by PCP pathway (Antic et al., 2010; Hashimoto et al., 2010; Okada et al., 2005; Song et al., 2010). Posterior projection of LR cilia has also been observed in Xenopus (Schweickert et al., 2007) and medaka fish (Okada et al., 2005). PCP also controls the apical docking and the planar polarization of basal bodies in multiciliated epithelial cells (Park et al., 2008).

Different types of cilia tilt have been observed *in vivo* for zebrafish: posterior tilt **(Fig. 17F)** (Borovina et al., 2010), dorsal tilt **(Fig. 17E)** (Supatto et al., 2008), or a mix of the two (Okabe et al., 2008). Given experiments have shown the cilia-generated flow in the KV is rotational around the DV axis, in theory this cannot be due to a posterior tilt but to a dorsal tilt (Supatto et al., 2008). Moreover, a dorsal tilt was observed in vivo in the KV (Supatto et al., 2008). The posterior tilt previously observed in mouse and in zebrafish involves elements of the PCP pathway (Borovina et al., 2010; Hashimoto et al., 2010; Song et al., 2010) as well as the flow itself (Guirao et al., 2010). We further discuss this issue in Manuscript 3 (Ferreira RR et al. – in revision).

To sum up, it is assumed the zebrafish KV is an analogous functional structure to the mouse node in terms of LRO determination (Essner et al., 2005). Yet, while the ciliated surface of the mouse node is relatively flat, the zebrafish KV is a spherical ciliated structure (Kreiling et al. 2007; Amack et al. 2007). Different topologies are thought to have an impact on the flow profiles observed (Supatto and Vermot, 2011). A circular flow is thus generated in the mouse node, very much like in fish. Yet, the backward motion observed in mouse spins around the AP axis contrary to the DV axis in fish (Supatto et al., 2008). However, the evident similarities with the mouse node, the role of the continuous flow circulating around the DV axis within the KV (Supatto et al., 2008) in the determination of the LR asymmetry is not so straightforward to interpret as for the mouse, and so requires further investigation (Supatto and Vermot, 2011). Thus, this PhD project aims to study the diversity of cilia orientation and fluid mechanics in the zebrafish embryo.

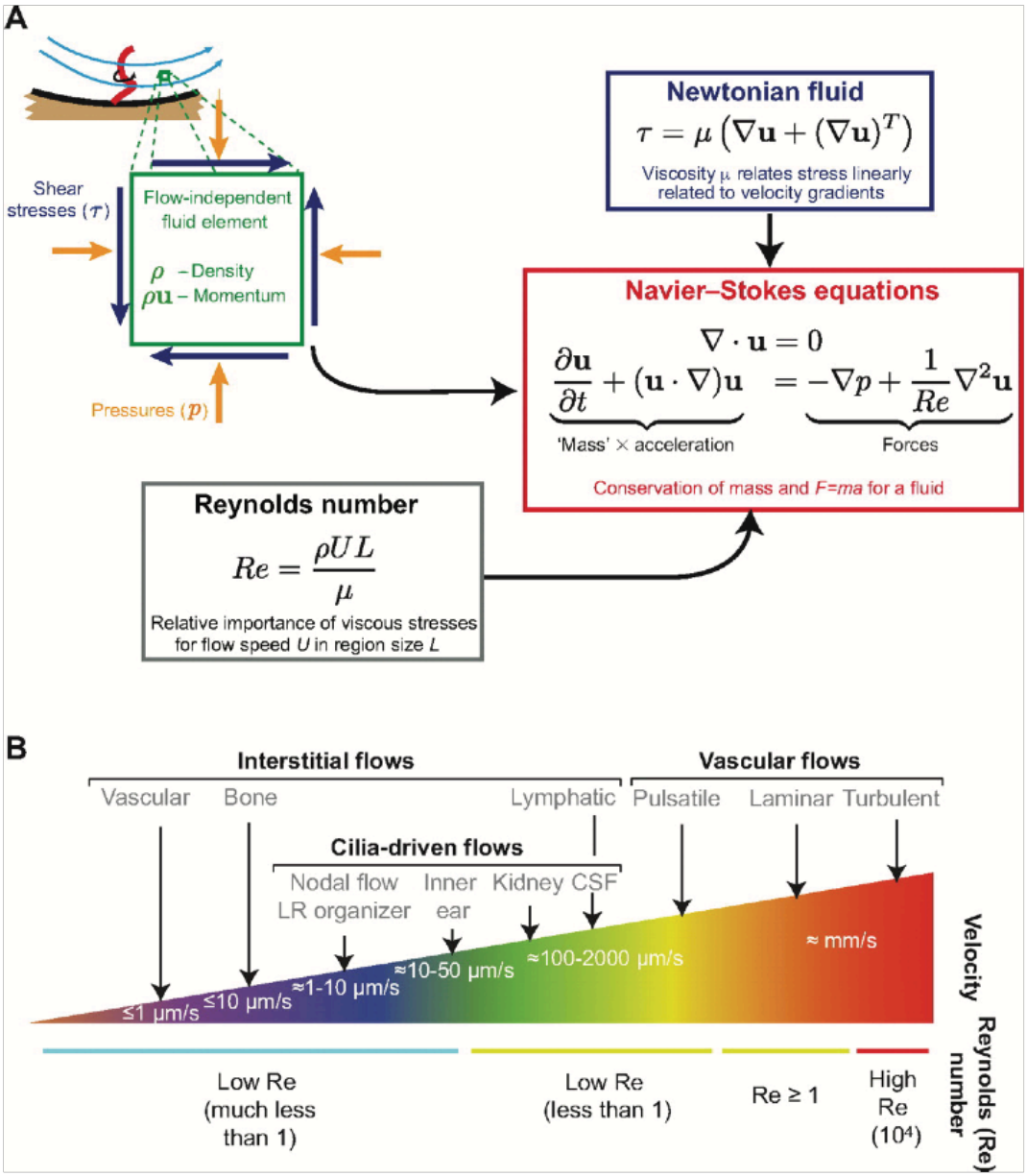

Fig.16: The equations that govern fluid flow in the physical environment of a LRO: (A) The Navier–Stokes equations describe the motion of fluids and can be developed by considering the conservation laws (mass and momentum) applied to a general small fluid element (depicted here by a green square) subject to pressures (orange arrows) and shear stresses (blue arrows), in this case those that have been generated by the movement of a cilium (red). **(B)** Schematics classifying the various types of flows encountered *in vivo* based on their average velocity and Reynolds number (Re). Adapted from (Freund et al., 2012).

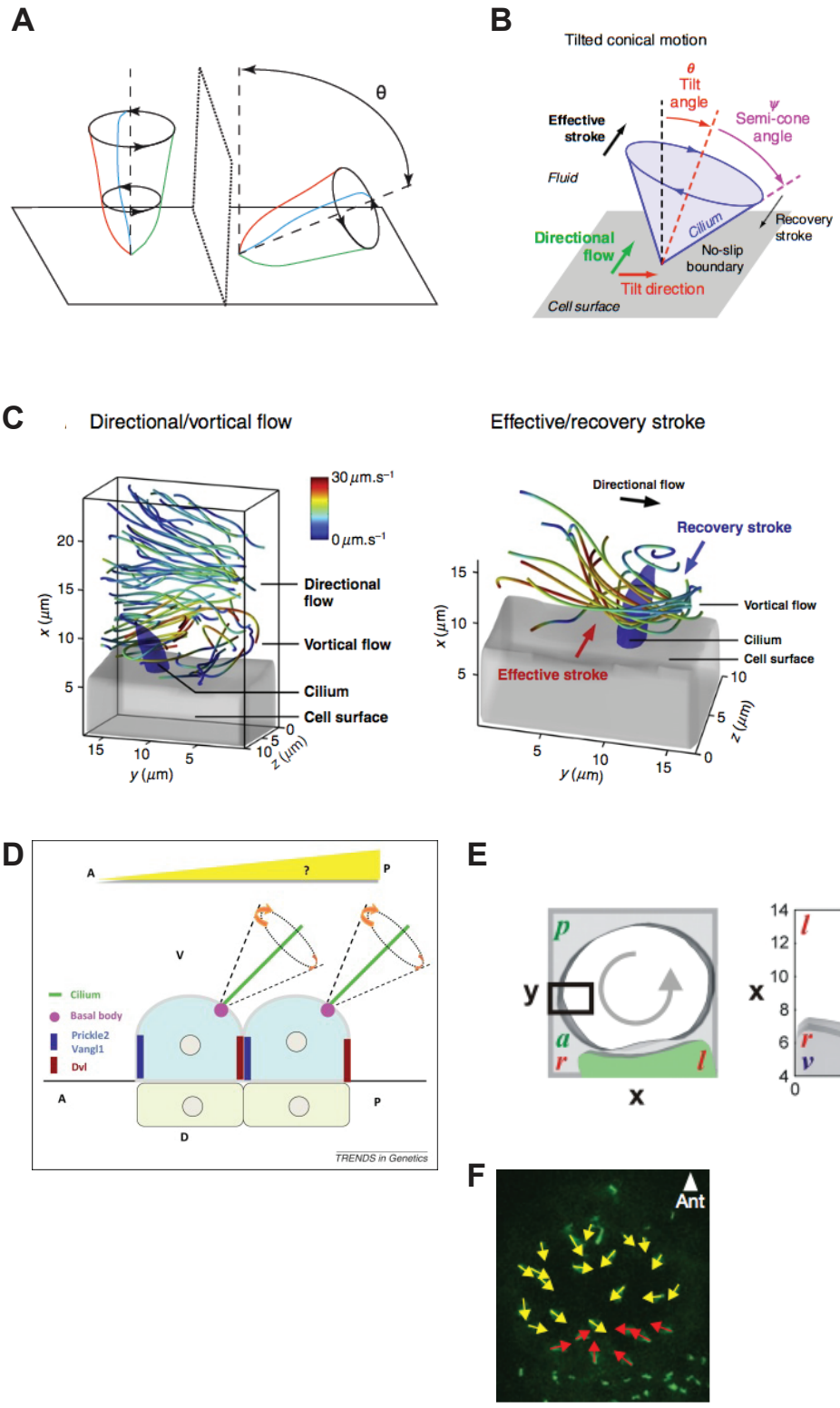

Fig.17: Cilia tilt characteristics. (A) Cilia with an angle of tilt (θ) of 90° or 35° displaying circular motion. Adapted from (Freund et al., 2012). **(B)** Cilium with a tilted conical motion: spatial symmetry can be broken without bending of the cilium if the rotation axis of the cilium is not perpendicular to the cell membrane, but tilted with an angle θ toward the normal of this surface. Adapted from (Supatto and Vermot, 2011). **(C)** The flow in the KV is vortical close to the cilium and the cell membrane and directional far away (left panel). Effective and recovery strokes are identified in the flow surrounding a beating cilium with faster velocity on one side and slower velocity on the other (right panel). Adapted from (Supatto and Vermot, 2011). **(D)** Cilium from node cells have a posterior tilt. Polarized localization within node cells is shown for the basal body of the cilium and for PCP core proteins. The basal body is positioned at the posterior side of node cells, which results in tilting of the motile cilium toward the posterior side. *Prickle2* and *Vangl1* proteins are localized to the anterior side of the cells, whereas the *Dvl* protein is on the posterior side. Adapted from (Yoshiba and Hamada, 2014). **(E)** Schematics representing the rotational flow in the DV axis observed in the KV (left panel) and a posterior view showing the 30° dorsal tilt of the beating axis (right panel). Adapted from (Supatto et al., 2008). **(F)** Z-stack confocal projections through the floor and wall of *Arl13b–GFP* (green) labelled embryo showing a posterior tilt in the KV. Anterior is up. Adapted from (Borovina et al., 2010).

PhD thesis outline

PhD thesis outline

Both motile and immotile cilia play important roles in left-right (LR) axis determination in several vertebrates. Establishment of the LR axis generally involves cilia-mediated directional flows in organized structures (LR organizers, LRO) in which the LR symmetry is broken, thus driving asymmetric organogenesis in the developing embryos. However, many steps of this complex mechanism are still not understood. In my PhD project we aimed to explore the connection between the biophysical basis of directional flow generation and the biological mechanism that controls LR symmetry breaking and cilia implantation in the zebrafish LRO, the Kupffer's vesicle (KV). More specifically, we aimed to analyze the three-dimensional organization of ciliary implantation in order to extract the key parameters modulating the directional flow involved in breaking the axis of symmetry in the KV. This work will contribute to a better understanding of cilia functions and the mechanical forces involved during the process of early embryonic axis establishment.

To achieve this aim, we defined the following objectives:

- To developed a live-imaging methodology and an image analysis protocol to enable the extraction of information regarding the cilia biophysical features (3D orientation and density) that influence the establishment of a directional flow.
- To analyze cilia behaviors at a multi-scale level by mapping the biophysical parameters of cilia across the entire KV in wild-type embryos at three distinct embryonic stages and extract the key parameters of cilia implantation leading to the directional flow observed in the KV.
- To determine a possible correlation between cilia orientation and LR axis determination in the zebrafish KV.

These objectives are reflected in the structure of this thesis as follows:

1. **Manuscript 2** (*Methods Chapter*) describes the experimental workflow of the multiscale analysis pipeline that we developed in collaboration with the group of Dr Supatto (Ecole Polytechnique, Palaiseau, France), called *3D-Cilia Map*. First I optimized the *3D-Cilia Map* experimental workflow (Objective 1). It is to note that the LRO is not easily accessible for *in vivo* experiments either because of its location deep inside the embryo and because it requires difficult *ex vivo* culture systems. To circumvent this issue we focused on the zebrafish KV, which allows *in vivo* imaging without altering the integrity of the embryo and its native environment.

2. **Manuscript 3** (*Results Chapter I*) presents our multi-scale analysis of the biophysical parameters of cilia across the entire KV in wild-type embryos at three distinct embryonic stages in order to extract the behaviors of cilia orientation through time. This quantitative description of the KV morphology and cilia in the wild-type condition allowed us to generate accurate quantitative data, *in vivo*, and to feed mathematical models permitting the simulation of the flow profiles generated within the KV. Also, by integrating our experimental data into a physical study of flow generation, we tested the efficiency of

the cilia features in propagating the asymmetric signals responsible for the symmetry-breaking mechanism (Objective 2).

3. **Manuscript 4** (*Results Chapter II*) describes how, using *3D-Cilia Map,* we analyzed a group of pre-selected conditions (knock-downs, mutants and drug-treatments) known to impact the LR axis determination. In doing so, we further validated the *3D-Cilia Map* methodology and discovered new insights into the link between cilia orientation and LR axis determination (Objective 3)

In this multidisciplinary PhD project, I optimized the imaging protocol for live imaging of the KV using 2-photon microscopy and performed all embryo manipulations. I designed experiments and generated all experimental data (live imaging, left-right characterization experiments and maintenance of the zebrafish wild-type and mutant lines), and analyzed it using IMARIS software implementing methodologies developed in collaboration with Dr. Supatto. Dr. Willy Supatto and Guillaume Pakula developed the custom MatLab scripts for the data analyses. The theory for the numerical simulations of the flow patterns were performed in collaboration with Dr. Andrej Vilfan and Dr. Franck Jülicher, this step was crucial to generate predictions that can then be tested experimentally or conversely to do *in silico* experiments that could not be done *in vivo* due to limitations of the system.

The work presented here represents an important contribution to our current understanding of cilia behaviors and flow-sensing mechanisms in the establishment of the left-right axis in the zebrafish LRO.

Method: *Manuscript 2*

3D-Cilia Map: a live, high content imaging method to link cilia biophysical features with left-right symmetry breaking

Willy Supatto[1,*], Guillaume Pakula[1], Rita R. Ferreira[2,3,4,5] and Julien Vermot[2,3,4,5,*]

[1]Laboratory for Optics and Biosciences, Ecole Polytechnique, Centre National de la Recherche Scientifique (UMR7645), Institut National de la Santé et de la Recherche Médicale (U1182) and Paris Saclay University, Palaiseau, France
[2]Institut de Génétique et de Biologie Moléculaire et Cellulaire, Illkirch, France
[3]Centre National de la Recherche Scientifique, UMR7104, Illkirch, France
[4]Institut National de la Santé et de la Recherche Médicale, U964, Illkirch, France
[5]Université de Strasbourg, Illkirch, France

*contacts: willy.supatto@polytechnique.edu, julien@igbmc.fr

Abstract

To explore the connection between the biophysical basis of directional flow generation and the biological mechanism that controls left-right symmetry breaking and cilia implantation in the zebrafish LRO, the Kupffer's vesicle (KV), we developed *3D-Cilia Map*, a high-content 3D Mapping of Cilia Features. This methodology is a live-imaging based data analysis pipeline, for the mapping of cilia biophysical parameters in 3D geometry. Such approach addresses questions related with 3D orientation of motile cilia in the KV. Here we describe the experimental workflow of *3D-Cilia Map* that combines 3D live imaging, image processing and data registration to quantify, display and compare the biophysical features of the KV and cilia. *3D-Cilia Map* is a powerful and rigorous quantitative multiscale analysis of the biophysical features of cilia that could be used in the study of other ciliated spherical systems.

Introduction

Cilia motility in the left-right organizer (LRO) is a common feature for generating the directional flow necessary for symmetry breaking in vertebrates. However vertebrate LROs are highly diverse in shape and size. As there is a strong dependency between three dimensional (3D) physical environment and flow profiles, we hypothesized that an evolutionary diversification exists in the function of motile cilia for the efficient propagation of asymmetric cues amongst organizers. To provide quantitative arguments to this hypothesis, we developed high-content 3D Mapping of Cilia Features (*3D-Cilia Map*), a live-imaging based data analysis pipeline, for the mapping of biophysical parameters of cilia in a 3D geometry. It was designed to quantify parameters, such as Kupffer's vesicle (KV) size, shape and volume, as well as cilia motility, spatial distribution, surface density or orientation of rotational axis. Experimental data from different embryos is combined to perform statistical analyses and compare experimental conditions. 3D-Cilia Map is based on streamlined live imaging protocols optimized for cilia imaging enabling visualization of all endogenous cilia in the 50 to 80 cells constituting the KV in live zebrafish embryos at the developmental stages the KV is visible in the embryo (1- to 14-somite stage (SS)), allowing for accurate spatial cilia mapping in large sample sets. The approach uses a zebrafish line where cilia are fluorescently labelled (Borovina et al., 2010), 3D image acquisition using two-photon excited fluorescence microscopy, image processing and data registration as well as a high-content image analysis pipeline. *3D-Cilia Map* resolves inherent KV shape variability through post-acquisition registration algorithms, and generates an accurate ciliotopic map through spherical coordinate reconstruction based on sample orientation in 3D. In the custom designed analysis pipeline, the experimental features are used to feed a mathematical model of cilia dynamics and fluid flow generation to obtain additional information, such as the flow profile generated within the KV on a single-embryo basis, or the force generated by individual cilia.

Experimental workflow

The experimental workflow of *3D-Cilia Map* can be divided in six-steps described below.

Step 1. 3D live imaging of the KV

For live imaging, each embryo from the transgenic line *(actb2:Mmu.Arl13b-GFP)* (Borovina et al., 2010) was soaked in Bodipy TR (Molecular Probes), in order to obtain 3D image acquisition with two color channels (cilia in green and cytoplasm in red). For each embryo imaged, we perform two types of 3D image acquisition: first, the entire embryo was imaged with a large field-of-view acquisition at low spatial resolution (typically 600x600x150 µm3 volume with 1.15x1.15x5 μm^3 voxel size); secondly, the KV was imaged with a smaller field-of-view at high spatial resolution (typically 100x100x50 µm3 volume with 0.2x0.2x0.8 μm^3 voxel size). This first acquisition is crucial to estimate the body axes (**Fig.1A**) while the second is used to quantify cilia distribution and orientation in 3D (**Fig.1B**). For the study we developed 3D-Cilia Map, the acquisition parameters were optimized to obtain cilia traces in 3D based on the scanning artefact described previously in (Supatto and Vermot, 2011).

Step 2. Estimation of body plan reference frame at the KV location

We use the large field-of-view image of the embryo (**Fig.1A1**) and 3D visualisation (Imaris) to adjust three orthogonal slicers in 3D such that the intersection point is located inside the KV (**Fig.1A2**). The position of these planes is adjusted using structural landmarks, such as the embryonic midline and the outer surface of the embryo. The intersection of the planes corresponds to the body axis of the embryo (posterior to anterior, right to left, or ventral to dorsal). We defined these axes by drawing 3D vectors as shown in **Fig.1A3**.

Step 3. Cilia position and orientation

We use the high spatial resolution image of the embryo (**Fig.1B1**) and 3D visualisation (Imaris) to manually segment the cilia bases at the surface of the KV as represented with gray spots in **Fig.1B2-B3**. The 3D orientation of the rotation axis of each cilium is then estimated (**Fig.1B4**) based on the scanning artifact traces. We use a custom-made ImarisXT function in Matlab to automatically estimate the cilium orientation from the segmented base (**Fig.1B5-B6**). This function projects the green fluorescence signal on a local sphere surrounding each individual cilium base and fits a *von Mises–Fisher* distribution on the projected signal. The mean direction of this distribution is used as an estimation of the axis of rotation of the cilium. We then manually checked and corrected (if necessary) the direction represented by a gray vector from the cilium base to its tip (**Fig.1B6**). Cilia individual features are annotated at this step. When cilia are not beating, its orientation is simply the main direction of the cilium body. In addition, as the image quality is not homogeneous within the field-of-view, in rare instances the rotation axis is not possible to estimate (example from Manuscript 3: 13% of 1438 cilia investigated). As a consequence, we annotate the cilia in four experimental categories: motile cilia with clear orientation, motile cilia with unclear orientation, immotile cilia with clear orientation, and unclear cilia for which both beating and orientation are not clear (**Fig.1B4**).

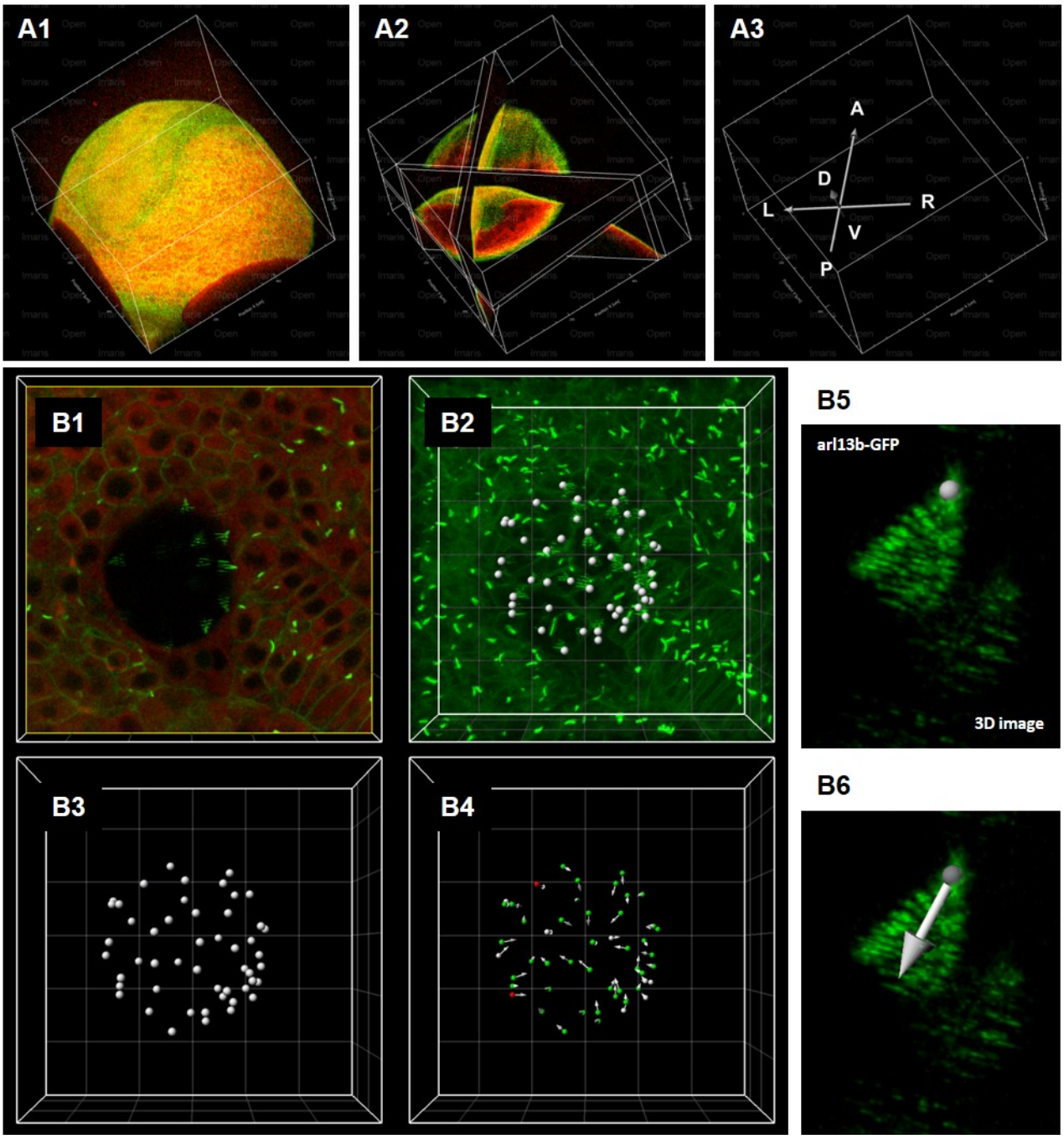

Manuscript 2 - Fig. 1: Live imaging and image processing to extract cilia position and orientation: To image deep enough into the zebrafish embryo and capture the entire Kupffer's vesicle (KV), each live embryo was imaged using 2PEF microscopy with a SP8 direct microscope (Leica Inc.) at 930nm wavelength (Chameleon Ultra laser, Coherent Inc.) using a low magnification high numerical aperture (NA) water immersion objective (Leica, 25x, 0.95 NA). We used the transgenic embryos (actb2:Arl13b-GFP) (Borovina et al., 2010) soaked for 60 minutes in Bodipy TR (Molecular Probe) prior the live imaging step: The fluorescence signal was collected using Hybrid internal detectors at 493-575 nm and 594-730 nm in order to discriminate the GFP signal labelling cilia from the signal labelling the KV cell surface. (**A1**) The entire embryo was imaged at low spatial resolution to estimate the embryonic axes: volume of 600µm×600µm×150µm comprising the midline and the KV from top to bottom with a voxel size of 1.15µm laterally and 5µm axially. The estimation of the body plan reference frame at the KV location was performed using the imaging shown in (**A1**) and the three orthogonal slicers were adjusted in 3D using Imaris (Bitplane), which intersection point is within the KV (**A2**). In the intersection of each two orthogonal slicers was used to design 3D vectors (**A3**). (**B1-2** and **B5-6**) The KV was imaged at high spatial resolution to quantify cilia distribution and orientation in 3D: 100x100x50 μm^3 3D-stacks with 0.2x0.2x0.8 μm^3 voxel size and 2.4 µs pixel dwell time were typically acquired in order to maximize the scanning artefact allowing to properly reconstruct cilia orientation in 3D (Supatto and Vermot, 2011). Cilia bases were manually segmented from the surface of the KV cells (gray spots in **B2-B3**), and its 3D orientation estimated (**B4**). Making use of a custom-made ImarisXT function in Matlab, cilium orientation was automatically estimated from the segmented base (**B5-B6**).

Step 4. 3D spatial registration: body plan reference frame and ellipsoid fitting

To register the 3D position and orientation of cilia, we first transform the spatial coordinates in accordance to the embryonic body plan determined using the large field-of-view image of the embryo (**Fig.1A1**). To achieve this, we transfer the estimations of body plan reference frame, cilia position and orientation vectors from Imaris to Matlab. Then fit an orthogonal basis to the manually estimated body plan reference frame and use the resulting orthogonal reference frame to register cilia position and orientation using body plan spatial coordinates. As a result, we can display the spatial distribution of cilia position in the body plan reference frame, as shown in **Fig. 2A1**. This distribution systematically follows an oblate spheroid shape (ellipsoid of revolution about its minor axis) with its minor axis aligned with the dorso-ventral axis of the embryo. To register data from different embryos on the same frame, we fit an oblate spheroid on the distribution of cilia bases (**Fig. 2A2**) using the Ellipsoid fit Matlab script from *Yury Petrov* (Northeastern University, Boston, MA). We then orthogonally project them at the surface of the fitted spheroid (**Fig. 2A3**). The fitting residue root mean square was 2.1±0.6 µm, meaning that the error on the spheroid fit is below the cell size.

Step 5. 3D cilia orientation angles θ and φ: estimate and histogram display

The fitted spheroid provides an estimation of the KV surface. We then define a local orthogonal basis (e_f, e_n, e_m) at each point of the spheroid surface. This local basis has a biological meaning: e_n is a vector normal (or orthogonal) to the KV surface and pointing towards the center of the vesicle; e_f is a vector along the surface and othogonal to the KV dorso-ventral axis: it defines a parallel of the spheroid (red line in **Fig. 2B1**) and it is oriented in the same direction as the rotational flow generated within the KV; and e_m is aligned along a meridian from the ventral to the dorsal pole of the KV (blue line in **Fig. 2B1**), pointing towards the dorsal pole. We define cilia vector components in this local basis and quantified the cilia orientation angles θ (cilium tilt angle respective to the surface normal) and φ (cilium orientation on the KV surface), as shown in **Fig. 2B2**. θ and φ are critical cilia features controlling the amplitude and direction of the flow generated within the KV. The θ tilt is the spatial asymmetry allowing the beating cilium to generate directional flow at low Reynolds number. The amplitude of the flow is proportional to sin(θ). A θ tilt of zero results in no directional flow. In the case of a non-zero θ tilt, the φ angle will determine the orientation of the flow generated by the cilium. φ can also modulate the flow amplitude: for instance, if two cilia have the same θ tilt but opposite φ angles, the flows generated by each cilium cancel each other, resulting in no net flow. The experimental values from different embryos can then be combined and displayed in rosette histograms using Matlab (0 to 360° rosette for φ, and 0 to 90° rosette for θ, such as in **Fig. 2C1** and **Fig. 2C2**, respectively).

Step 6. 2D map of cilia features and measurement of cilia surface density

To display cilia features on 2D maps and estimate cilia local density, we finally transform the spheroid into a sphere with surface density conservation (**Fig. 3A1-A2**). Such transformation allows us to define cilia positions using a spherical coordinate system (alpha, beta) and plot on a common 2D map the cilia features from different embryos that have different KV sizes and shapes. For instance, cilia motility status from different embryos are displayed in **Fig. 3B** (motile and immotile cilia represented

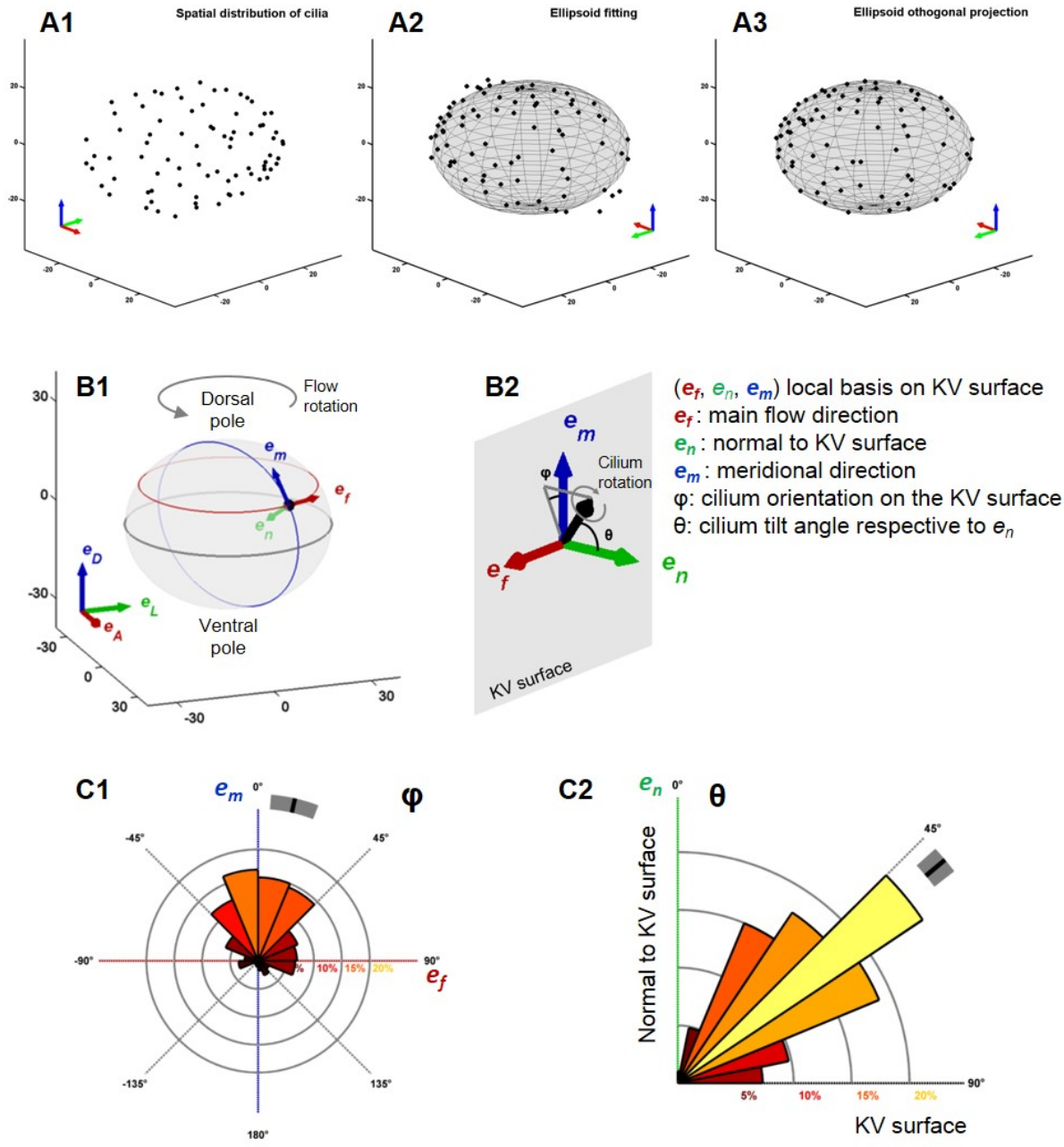

Manuscript 2 - Fig. 2: Estimation of cilia orientation angle φ and θ: Transformation of the spatial coordinates in accordance to the embryonic body plan (**A1-A3**): display of the spatial distribution of cilia position in the body plan reference frame (**A1**); fitting an oblate spheroid on the distribution of cilia bases, in order to register KV data from different embryos on the same frame (**A2**); orthogonal projection of cilia at the surface of the fitted spheroid (**A3**). Local orthogonal basis definition (e_f, e_n, e_m) at each point of the surface of the spheroid (**B1**), and φ and θ angles definition (**B2**). Data combination from different embryos and displayed in rosette histograms using Matlab: 0 to 360° rosette for φ (**C1**) and 0 to 90° rosette for θ (**C2**). Reference frames in **A1-A3** are the same as in **B1**: e_D, e_L, and e_A.
e_D= dorsal direction; e_L= left direction; e_A= anterior direction

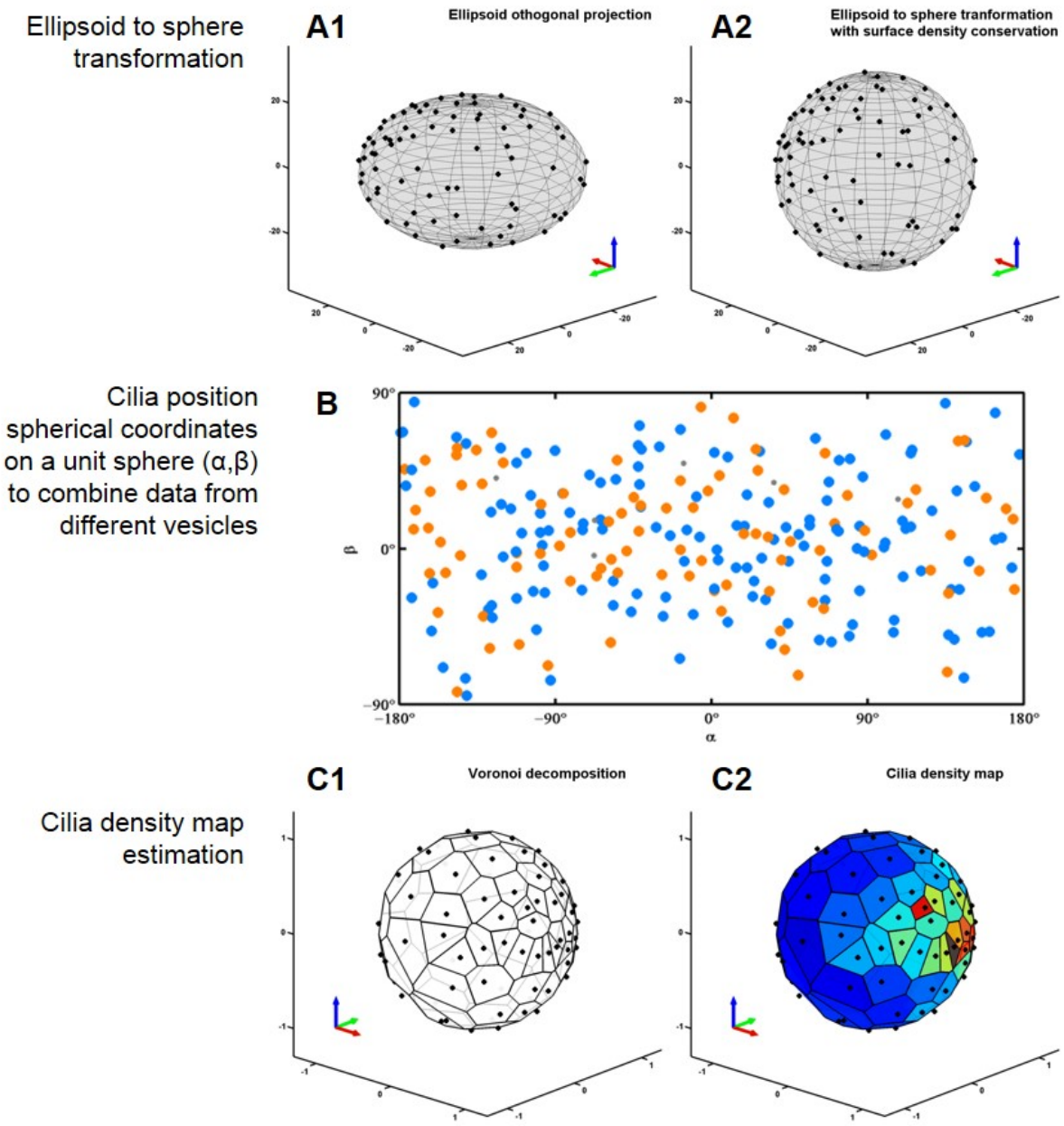

Manuscript 2 - Fig. 3: Data registration and spherical *Voronoi* diagram computation to combine cilia features from different embryos and estimate the cilia density map. (**A1-A2**) Ellipsoid to sphere transformation: Ellipsoid orthogonal projection (**A1**) and the actual transformation with surface density conservation (**A2**). (**B**) Cilia motility status from different embryos is displayed in a 2D map (motile and immotile cilia represented with blue and orange spots, respectively). (**C1-2**) Cilia density map estimation: Computation of a spherical *Voronoi* diagram of cilia distribution (**C1**) from which it was estimated the surface area occupied by individual cilium and obtained the local cilia density (**C2**).
Reference frames in **A1-A2** and **C1-C2**: e_D (blue), e_L (green), and e_A (red). e_D= dorsal direction; e_L= left direction; e_A= anterior direction

with blue and orange spots, respectively). We also use the spherical transformation to compute a spherical Voronoi diagram of cilia distribution (**Fig. 3C1**), from which we estimate the surface area occupied by individual cilium and obtained the local cilia density (**Fig. 3C2**). To compute the Voronoi diagram of points on the surface of the unit sphere in 3D, we use the *sphere_voronoi Matlab* package from John Burkardt (Department of Scientific Computing, Florida State University, https://people.sc.fsu.edu/~jburkardt/).

Discussion

In order to address the mechanism of left-right (LR) symmetry breaking quantitatively, *in vivo* and in three dimensions (3D) of space, we developed *3D-Cilia Map*, a live imaging-based method for the 3D quantitative mapping of cilia features in the zebrafish left-right organizer (LRO), the Kupffer's vesicle (KV). This methodology enables us to quantify cilia spatial distribution and orientation across the entire LRO, to combine and compare experimental data from different embryos, and to perform statistical analyses highlighting the regional differences of these parameters. *3D-Cilia Map* data could be also used to feed mathematical modeling, in order to evaluate the efficiency of the obtained 3D-cilia maps in propagating both mechanical and chemical signals asymmetrically that lead to the symmetry-breaking event (Manuscript 3). In sum, *3D-Cilia Map* is a powerful and rigorous quantitative multiscale analysis of the biophysical features of cilia (3D orientation, spatial localization and density), that could be used in the study of other ciliated spherical systems.

References

Borovina, A., Superina, S., Voskas, D., and Ciruna, B. (2010). Vangl2 directs the posterior tilting and asymmetric localization of motile primary cilia. Nat Cell Biol 12, 407-412.

Supatto, W., and Vermot, J. (2011). From cilia hydrodynamics to zebrafish embryonic development. Curr Top Dev Biol 95, 33-66.

Acknowledgements

We thank E. Beaurepaire and the Vermot lab for discussion and thoughtful comments on the manuscript. We thank B. Ciruna for providing fish stocks. We thank the IGBMC fish facility (S. Geschier and S. Gredler) and the IGBMC imaging center, in particular B. Gurchenkov, P. Kessler, M. Koch and D. Hentsch. This work was supported by HFSP, INSERM, AFM, FRM (DEQ20140329553), the seventh framework program (MC-IRG256549 and MC-IRG268379), ANR (ANR-12-ISV2-0001, ANR-11-EQPX-0029, ANR-2010-JCJC-1510-01) and by the grant ANR-10-LABX-0030-INRT, a French State fund managed by the Agence Nationale de la Recherche under the frame program Investissements d'Avenir labeled ANR-10-IDEX-0002-02. R.R.F. was supported by the IGBMC International PhD program (LABEX).

Results Chapter I:

Manuscript 3

Physical limits of flow sensing in the left-right organizer

Rita R. Ferreira[1,2,3,4], Andrej Vilfan[5,*] , Frank Jülicher[6], Willy Supatto[7,#,*], and Julien Vermot[1,2,3,4,#,*]

[1]Institut de Génétique et de Biologie Moléculaire et Cellulaire, Illkirch, France
[2]Centre National de la Recherche Scientifique, UMR7104, Illkirch, France
[3]Institut National de la Santé et de la Recherche Médicale, U964, Illkirch, France
[4]Université de Strasbourg, Illkirch, France
[5]J. Stefan Institute, Ljubljana, Slovenia
[6]Max-Planck-Institute for the Physics of Complex Systems, Dresden, Germany
[7]Laboratory for Optics and Biosciences, Ecole Polytechnique, Centre National de la Recherche Scientifique (UMR7645), Institut National de la Santé et de la Recherche Médicale (U1182) and Paris Saclay University, Palaiseau, France

Co-senior authors
*contacts: andrej.vilfan@ijs.si, willy.supatto@polytechnique.edu, julien@igbmc.fr

Abstract

Fluid flows generated by motile cilia are guiding the establishment of the left-right asymmetry of the body in the vertebrate left-right organizer. Competing hypotheses have been proposed: the direction of flow is sensed either through mechanosensation, or via the detection of chemical signals transported in the flow. We investigated the physical limits of flow detection in order to clarify which mechanisms could be reliably used for symmetry breaking. We integrated parameters describing cilia distribution and orientation obtained *in vivo* in zebrafish into a multiscale physical study of flow generation and detection. Our results show that the number of immotile cilia is too small to ensure robust left and right determination by mechanosensing, given the large spatial variability of the flow. However, motile cilia could sense their own motion by a yet unknown mechanism. Finally, transport of chemical signals by the flow can provide a simple and reliable mechanism of asymmetry establishment.

Introduction

Chirality describes the asymmetry between an object and its mirror image. How chiral asymmetries arise in Physics and Biology is a fundamental question that has fascinated researchers for many years (Morrow et al., 2017; Wagnière). A number of independent mechanisms of chirality establishment at multiple scales have been identified in living systems, ranging from subcellular with the establishment of chiral cortical flows (Naganathan et al., 2014) to the cellular scale during the process of cell fate specification (Gomez-Lopez et al., 2014) and to the tissue scale during the process of left-right (LR) axis specification (Blum et al., 2014b; Coutelis et al., 2014; Dasgupta and Amack, 2016; Hamada and Tam, 2014; Levin, 2005). Similar concepts also exist in the plant kingdom, suggesting widespread mechanisms of chirality transfer (Wang et al., 2013). Biological symmetry breaking is often associated with the internal handedness or chirality of molecular motors (Ferreira and Vermot, 2017; Inaki et al., 2016; Naganathan et al., 2016). One of the most striking examples of biological symmetry breaking is the mechanism of LR axis determination in the developing embryo, which is crucial for the asymmetric internal organ positioning. In most of the vertebrate species, LR axis determination is set by a symmetry biasing event which is under the control of a directional flow generated by the chiral beating pattern of motile cilia (Hirokawa et al., 2009; Nakamura and Hamada, 2012). To date, even though the molecular mechanisms of LR axis determination are highly conserved from fish, amphibians to mammals (Blum et al., 2014a), many steps of this process are not yet understood (Ferreira and Vermot, 2017; Shinohara and Hamada, 2017; Wolpert, 2014).

Prevailing models of LR specification in most vertebrates (Blum et al., 2009; Gros et al., 2009) involve groups of cells (the LR organizer, LRO) within the presomitic mesoderm (the segmental plate) coordinating asymmetry establishment through the control of a slow-moving flow (the nodal flow) (Nonaka et al., 1998) and an intercellular amplification of the asymmetric signals within and around the LRO cells (Nakamura et al., 2006). This slow-moving flow is produced by rotation of multiple, motile cilia located at the cell surface of the LRO. This flow leads to a collective cell response that occurs specifically on the left embryonic side of the LRO and is associated with an asymmetric intracellular calcium release (McGrath et al., 2003; Yuan et al., 2015). The LRO is a transient structure and its function is required for a limited period of time. In zebrafish, the LRO is visible between 10 hours after fertilization (3-somite stage) and 16 hours after fertilization (14-somite stage) (Essner et al., 2005; Yuan et al., 2015).

Cilia generate a directed flow by beating in a spatially asymmetric fashion (Satir and Christensen, 2007). Their cycle consists of a working stroke, during which a cilium is stretched away from the surface in order to move the maximum amount of fluid, and a recovery stroke, during which it swipes along the surface, thus reducing the backflow (Marshall and Kintner, 2008). Cilia in the LRO are relatively short and their beating pattern resembles rotation along the mantle of a tilted cone (Hirokawa et al., 2006; Nonaka et al., 2005; Okada et al., 2005). This tilt effectively makes one part of the cycle act as a working stroke and the other part as a recovery stroke. Spatial orientation is, therefore, a key functional feature of motile cilia involved in LR symmetry breaking, as it determines the strength and

directionality of the induced flow (Cartwright et al., 2004). The molecular mechanisms that set this orientation involve elements of the Planar Cell Polarity (PCP) pathway (Borovina et al., 2010; Hashimoto et al., 2010; Song et al., 2010) as well as flow itself (Guirao et al., 2010). At the molecular scale, the chirality of biomolecules has been proposed to provide some of the asymmetrical cues for LR symmetry breaking (Brown and Wolpert, 1990; Levin and Mercola, 1998a). This paradigm works well with cilia, as the sense of cilia rotation is determined by the chirality of the structure of their protein building blocks (Hilfinger and Julicher, 2008).

To accurately discriminate left from right, cells need to robustly sense a signal over the noise associated with flow and cilia beat. Two hypotheses have been proposed for asymmetric flow detection. According to the chemosensing hypothesis, the directional flow establishes a LR asymmetric chemical gradient that is detected by signaling systems which leads to LR asymmetric gene expression and cell responses in the LRO (Okada et al., 2005). The mechanosensing hypothesis, on the other hand, proposes that the LRO cells can detect the mechanical effects of flow. It has been suggested that this mechanosensing is mediated by a particular type of sensory cilia that is able to trigger a local, asymmetric response of the so-called crown cells which are located at the periphery of the node (mouse LRO) (McGrath et al., 2003; Tabin and Vogan, 2003). In the zebrafish LRO (also called Kupffer's vesicle or KV), the model for cilia-mediated mechanotransduction suggests that sensing cilia are immotile and will activate a cellular response due to physical asymmetries generated by the flow (Sampaio et al., 2014). The flow detection apparatus needs to be remarkably efficient, as demonstrated by the observation that, despite wild-type mice having hundreds of motile cilia in their LRO, proper asymmetry establishment occurs even in mutant mice with only two motile cilia in the LRO (Shinohara et al., 2012). Similarly, although wild-type zebrafish usually have around 50-60 motile cilia in the KV, correct asymmetry establishment occurs in zebrafish mutants with only 30 motile cilia (Sampaio et al., 2014). Considering that motile cilia might be chemosensors (Shah et al., 2009), LR symmetry breaking could rely on a combination of both mechanosensory and chemosensory mechanisms that could work in parallel. To date, however, several issues with both hypotheses have emerged: the molecular nature of a possible diffusing compound involved is still not known (Freund et al., 2012; Shinohara and Hamada, 2017) and cilia-mediated mechanotransduction in the mouse node has recently been experimentally challenged (Delling et al., 2016). In many aspects, these debates remain open because the sensitivity of mechanical and chemical detection mechanisms has not yet been assessed quantitatively from a physical standpoint based on properties of cilia and the flows they generate.

To test the sensitivity of the detection mechanisms, we investigated the physical limits of the system to discriminate left and right in the presence of flow irregularities and noise. We analyzed the system from the level of individual cilia to the scale of the entire organ using live imaging in order to determine the physical features controlling the flow. We used these experimental datasets to calculate the flow in unprecedented detail and assess its robustness. We show that the flow velocities and their local variability impose crucial constraints on potential mechanosensing by cilia and investigate the question

whether the small number of non-motile cilia can be sufficient to reliably distinguish between the left and the right side of KV. Furthermore, we use the calculated flow profile to simulate the directed diffusive motion of chemical signals and determine the limit on particle diffusivity for which the mechanism is reliable. Our results show that the physical limits to the reliability of mechanical sensing of flow are stronger than the ones associated with chemical sensing and suggest that chemosensation is the key mechanism for LR axis determination.

Results

Theoretical analysis of cilia generated flows patterns

In the current models, cilia-mediated left-right (LR) symmetry breaking is driven by a chiral flow pattern. In the zebrafish embryo, the directional flow corresponds to an anti-clockwise rotation around the dorsoventral (DV) axis when viewed from the dorsal pole of the Kupffer's vesicle (KV) (Figure 1A) (Essner et al., 2005; Kramer-Zucker et al., 2005). Motile cilia are the driver of the flow whose directionality mainly depends on two features: cilia density and spatial orientation. Several studies have focused on cilia orientation and density to explain the flow directionality in mouse and fish (Borovina et al., 2010; Cartwright et al., 2004; Montenegro-Johnson et al., 2016; Nonaka et al., 2005; Okabe et al., 2008; Okada et al., 2005; Sampaio et al., 2014; Smith et al., 2008) in order to understand the principles underlying flow generation. These studies led to contradicting conclusions by proposing different types of cilia orientation, such as posterior tilt (Borovina et al., 2010), dorsal tilt (Supatto et al., 2008), or a mix of the two (Okabe et al., 2008). To solve this issue, we used a theoretical approach and developed a simplified biophysical model that can be tested *in vivo*.

In order to gain insight into the mechanism of flow generation, we first use a simplified model, which does not consider the small scale inhomogeneities of the flow around individual cilia. This simplification is valid in the limit in which both the cilia length (*L*) and the characteristic distance between cilia are shorter than the distance at which we observe the flow. The latter distance is characterized by the radius of the KV (*R*). The cilia layer can then effectively be represented by a net slip velocity at the surface (Vilfan, 2012). With typical parameters L=6µm, R=35µm and a characteristic distance between cilia of 10µm, these conditions are roughly satisfied when observing the flows in the center of the KV. Calculations with a detailed hydrodynamic model shown later (section "Single vesicle analysis reveals a significant variability between embryos") confirm uniform flows in the center, but they also show a significant velocity variability near the KV surface, which is not captured by the simplified model.

The effective surface-slip velocity, which replaces the individual cilia in the simplified model, can be calculated from the cilia parameters as follows. We consider cilia covering a surface with area density ρ and rotating with the angular velocity ω along the mantle of a cone with a semi-cone angle ψ, tilted by the angle θ in a direction $\vec{e}_t$. The direction of rotation is clockwise as seen from the distal end towards the KV wall. They induce a net flow velocity above the ciliated layer in the direction perpendicular to the tilt direction (Smith et al., 2008; Vilfan, 2012)

$$\vec{v} = \frac{C_N \omega L^3}{6\eta} \rho \sin(\theta) \sin^2(\psi)\ \vec{e}_n \times \vec{e}_t \qquad (1)$$

where $\vec{e}_n$ is a unit vector normal to the vesicle surface, × is the vector product, $C_N \approx 1.2\pi\eta$ denotes the drag coefficient and η the fluid viscosity (see Figure 1C). This contribution results from the fact that a

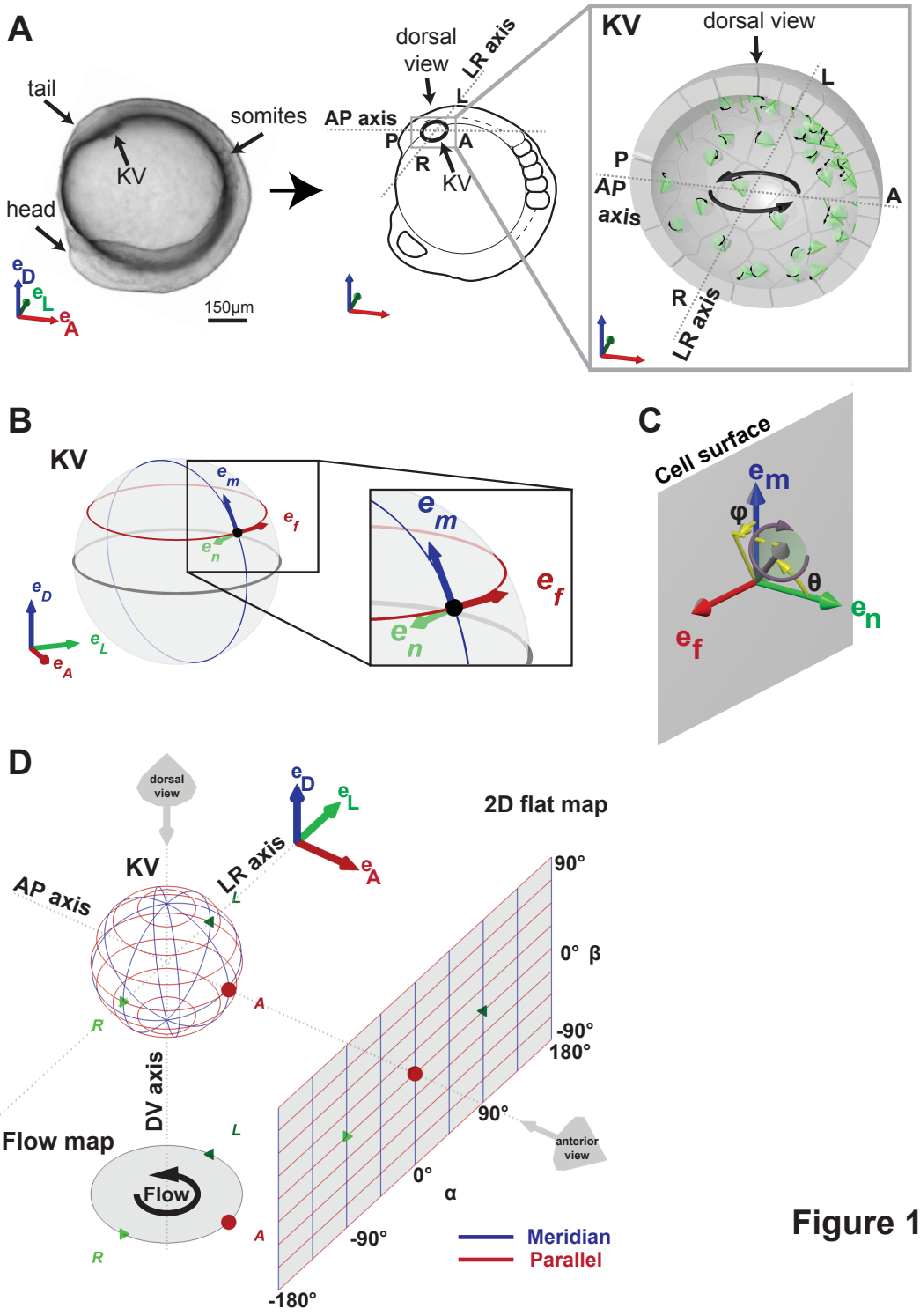

Figure 1

Manuscript 3 - Figure 1: Definition of coordinate systems of the Kupffer's vesicle (KV). (A) Side view of a zebrafish embryo at 5-somite stage (left panel) and its schematic drawing (middle panel), highlighting the KV localization (grey box). The zoom-up box (right panel) shows the schematic transverse section of the KV, depicting the cilia (in green), their rotational orientation (black curved arrows) and the directional flow (thick black arrows). **(B)** e_m, e_n, e_f is the local basis on the ellipsoid, which is used to define cilia orientation. The vector e_m is aligned along a meridian (blue) from the ventral to the dorsal pole; e_f follows a parallel (red) in the direction of the typical directional flow within the vesicle; e_n is the vector normal to the KV surface and pointing towards the center of the vesicle (green). **(C)** Cilia 3D orientation is quantified by two angles: θ (tilt angle from the surface normal e_n) and φ (angle between the surface projection of the cilia vector and the meridional direction). **(D)** 2D flat map representation of the KV surface with coordinates α and β. The origin is set in the anterior pole.
The embryonic body plan directions are marked as A (anterior), P (posterior), L (left), R (right), D (dorsal) and V (ventral). The body plan reference frame is defined as vectors e_D, e_L, e_A.
The following figure supplement is available for Manuscript 3 - Figure 1:
Figure supplement 1: Multiscale analysis from individual cilia to 3D modeling of the KV.

cilium moves more fluid during its working stroke, when it is further away from the surface, than during the recovery stroke, when it is closer. At the same time, even without a tilt (i.e. when the rotation axis is orthogonal to the cell surface), a rotating cilium induces a rotary flow with the amplitude $\sim 3\ \mathrm{C_N}\omega L^4 / (16\pi\eta)\sin^2(\psi)\cos(\psi)$. Although a surface (or a cavity) lined with untilted rotating cilia at a uniform density does not produce a long-range flow, non-uniformities in surface density ρ do lead to an effective slip velocity

$$\vec{v} = \frac{C_N \omega L^4}{8\eta}\sin^2(\psi)\cos(\psi)\,\vec{e}_n \times \vec{\nabla}\rho \qquad (2)$$

The flow observed inside the KV, which is, as a first approximation, characterized by uniform rotation (the fluid moves like a rotating rigid sphere) with the angular velocity Ω and the surface velocity $\vec{v} = \Omega R\cos(\beta)\,\vec{e}_f$ (see Figure 1B for the definition of the local basis $(\vec{e}_f, \vec{e}_n, \vec{e}_m)$ and Figure 1D for the definition of β) can be achieved in two ways (or a combination thereof):

1) Scenario 1: Dorsoventral gradient of cilia density (Figure 2A).
   No cilia tilt, $\theta = 0$, and a density profile $\rho = \rho_0\ (1 + \sin(\beta))\ /\ 2$ such that the density reaches its maximum at the dorsal pole.

2) Scenario 2: Meridional tilt (Figure 2B).
   Constant surface density $\rho = \rho_0$ and a meridional tilt $\theta > 0$ obeying $\sin(\theta) = \sin(\theta_0)\cos(\beta)$, i.e., cilia oriented along a meridian, which is the projected line from the ventral to the dorsal pole (blue line in Figure 1B,D).

Both scenarios or a combination of both are possible. However, the fluid velocity achieved with scenario 1 is smaller by a factor of $(3L/8R)\cos(\psi)\ /\ \sin(\theta_0) \approx 0.1$ as compared to scenario 2. This theoretical analysis shows that the directional flow depends on two main topological features of the vesicle: a profile of cilia density and a cilia orientation pattern following a meridional tilt in the KV.

3D-Cilia Map reveals multiple gradients of cilia density

In order to test whether scenario 1 (the cilia density gradient scenario, Figure 2A) or 2 (the meridional tilt scenario, Figure 2B) leads to the directional flow observed *in vivo*, we developed a live imaging-based method called 3D-Cilia Map (Figure 1-figure supplement 1 and Movie 1). 3D-Cilia Map is designed to quantify experimental features, such as KV size and shape, as well as the spatial distribution, surface density, motility and orientation of cilia (Figure 1-figure supplement 1). Developing zebrafish embryos can be accurately staged using the number of somites (blocks of presomitic mesoderm tissue that regularly form along both sides of the neural tube during the segmentation period) (Kimmel et al., 1995) (Figure 1A). We performed our analysis between 8- and 14- somite stages (SS), when the directional flow in the KV is well established (Essner et al., 2005; Kramer-Zucker et al., 2005; Long et al., 2003; Lopes et al., 2010). We analyzed the cilia density in 3D because

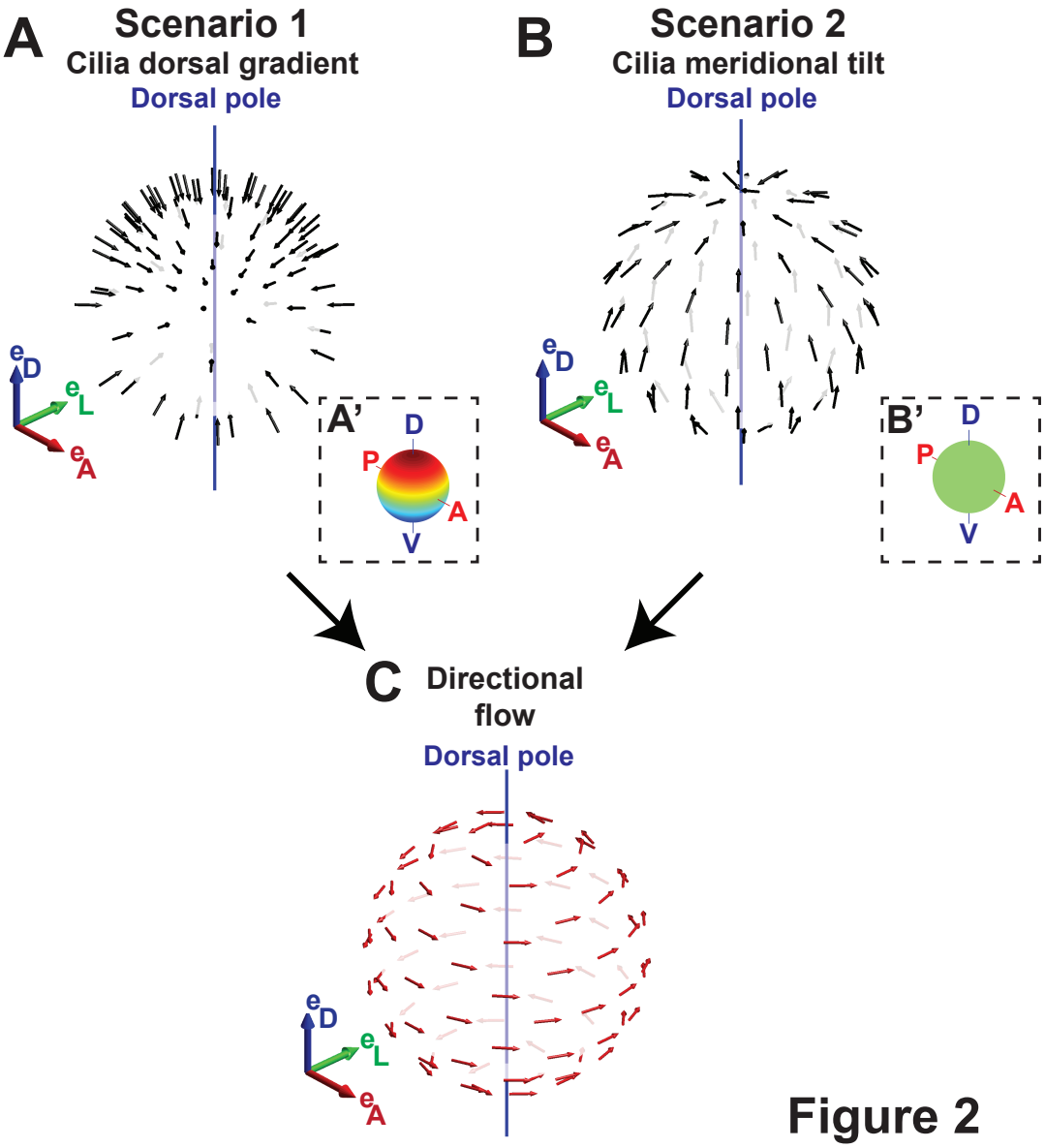

Figure 2

Manuscript 3 - Figure 2: Two scenarios for the origin of directional flow. (A) Scenario 1 – dorsal gradient: cilia unit vectors (black) are orthogonal to the surface, but the cilia density increases from the ventral to the dorsal pole. **(B)** Scenario 2 – meridional tilt: cilia are tilted along the meridians towards the dorsal pole. The insets in **(A'-B')** show the density maps on the sphere: a linear dorsal gradient for scenario 1 **(A')** and a uniform density for scenario 2 **(B')** (color map from blue to red representing low to high cilia density). **(C)** Both scenarios can theoretically account for the directional flow (red arrows) rotating about the dorsoventral axis observed experimentally. See Figure 1 for the definition of the body plan reference frame and coordinates systems.

it has previously been reported to vary along the anteroposterior (AP) axis (Borovina et al., 2010; Kreiling et al., 2007; Okabe et al., 2008; Supatto et al., 2008; Wang et al., 2011; Wang et al., 2012). In order to extract average features, the density maps from 20 vesicles with a total of 1197 cilia were averaged and represented either on the average vesicle spheroid (Figure 3A) or on a 2D flat map (Figure 3B). We found that the average density of cilia did not display any significant differences between left and right sides of the KV (Figure 3B). As expected from previous studies (Wang et al., 2011; Wang et al., 2012), a steep density gradient was observed along the AP axis, with increasing density towards the anterior pole of the vesicle (about 4 times denser than posterior) (Figure 3A,B). Interestingly, a gradient of cilia density was also seen along the DV axis, albeit shallower (dorsal being 2 times denser than ventral) (Figure 3B). Together, these results rule out scenario 1, since the dominant AP density gradient would lead to a significant contribution to directional flows around the AP axis which are not observed (Supatto et al., 2008).

KV motile cilia exhibit a meridional tilt

To test the scenario 2 (the meridional tilt scenario, Figure 2B) *in vivo*, we mapped cilia orientation in embryos between 8- and 14-SS. We defined the orientation of a cilium with a unit vector along the axis of the conical cilia movement and decomposed it in a local orthogonal basis ($\vec{e}_f, \vec{e}_n, \vec{e}_m$) on the KV surface as defined in Figure 1B, where:

- θ (tilt) is the angle of the cilium with respect to the KV surface normal (0° for a cilium orthogonal to the KV surface and 90° for parallel, Figure 1C).

- φ angle is the orientation of the cilium projected on the KV surface (0° for a cilium pointing in a meridional direction towards the dorsal pole, Figure 1C).

A meridional tilt would then correspond to θ > 0° and φ close to 0°. Among the 1197 cilia in 20 vesicles, we could determine their orientation and motility status for 86% and 89% of them, respectively. Less than 5% of the cilia were immotile at these stages. Together, we quantified the orientation of 1013 motile cilia (corresponding to 85% of all cilia). We plotted cilia unit vectors in the same local basis (black arrows in Figure 3C) and the average cilium as the 3D mean resultant vector (Berens, 2009) (gray arrow in Figure 3C). The resultant vector length r quantifies the spherical spread (the closer r is to one, the more cilia are concentrated around the mean direction). Despite a relatively broad distribution of cilia orientations ($r = 0.76$), we found that the θ tilt of the average cilium is near 46° and the average cilium has a 14° φ angle (Figure 3C). The resultant vector length and angles (r, θ, φ) from individual vesicles are listed in Table 1. In total, 65% of all motile cilia exhibited a φ angle between -45° and +45° (meridional quadrant). In addition, no specific spatial distribution of this orientation was detected (red in Figure 3D). These data demonstrate that motile cilia are oriented on average with a meridional tilt and support scenario 2 (Figure 2B), in which cilia meridional tilt is the dominant mechanism generating the directional flow within the KV (Figure 2C). Note that the meridional tilt results in dorsal cilia orientation on the equator and in posterior cilia orientation in the

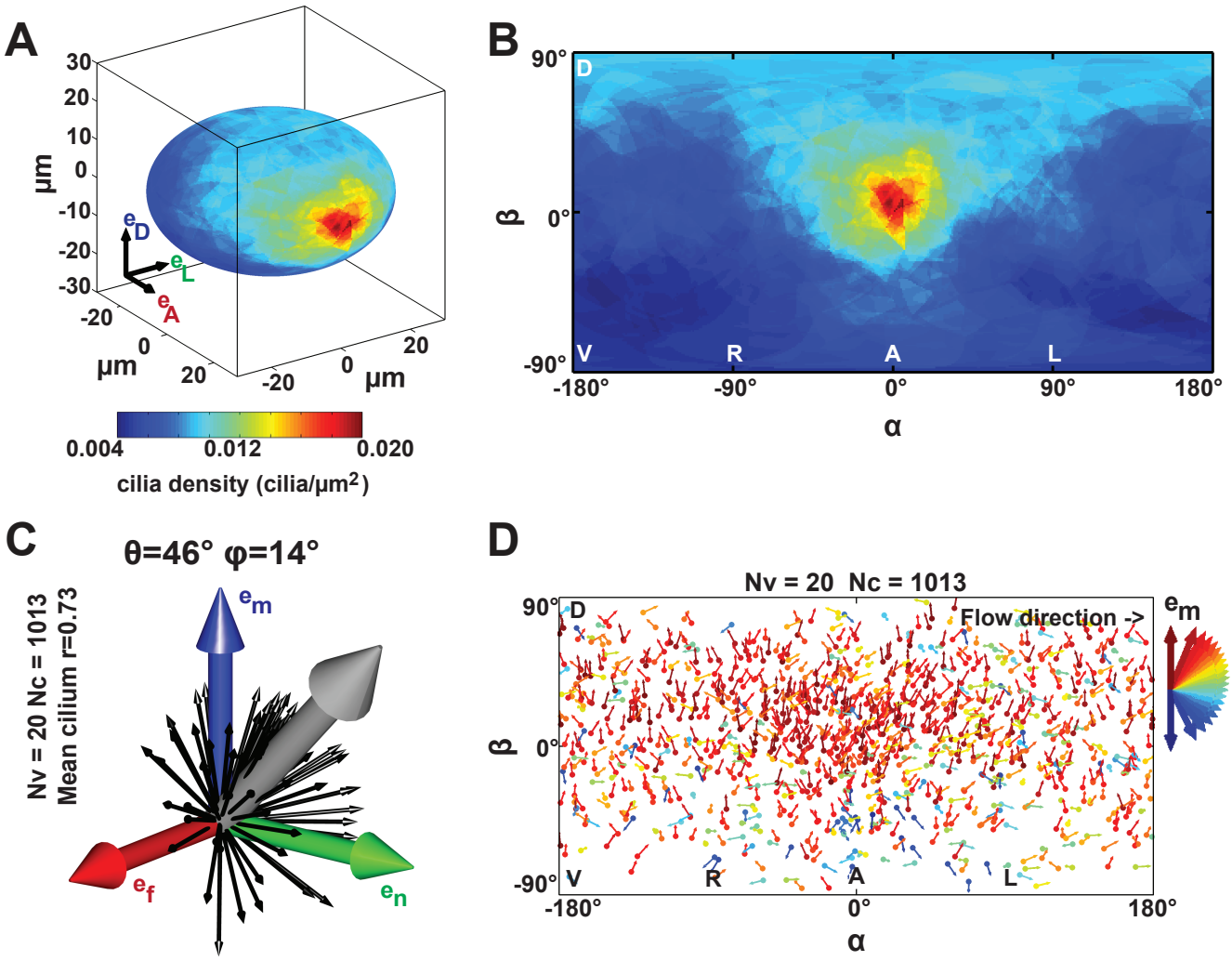

Figure 3

Manuscript 3 - Figure 3: Anterior gradient of cilia density and cilia meridional tilt in the Kupffer's vesicle (KV) at 8- to 14-somite stage (SS): (A-B) Averaged cilia density obtained from 20 vesicles represented on a 3D KV map **(A)** or on a 2D flat map **(B)** revealing a steep density gradient along the anteroposterior (AP) axis and the resulting enrichment at the anterior pole (in red). **(B)** Besides the enrichment at the anterior pole ($\alpha = 0°, \beta = 0°$), a density gradient along the dorsoventral (DV) axis is also visible ($\beta \geq 0°$ vs $\beta \leq 0°$). **(C)** Orientations of the 1013 motile cilia analyzed in the local basis (e_m, e_n, e_f) on the ellipsoid: the grey vector (not to scale) shows the vector average of all motile cilia orientations ($\theta = 46°$ and $\varphi = 14°$; $r = 0.73$); for the sake of clarity, only cilia orientations from one representative vesicle are shown by black vectors. **(D)** Cilia orientations (φ angles) on a 2D flat map. The majority of cilia point in the meridional direction (e_m in red). N_v = number of vesicles; N_c = number of cilia; r = resultant vector length
The following source data file is available for Manuscript 3 - Figure 3:
Figure 3-source data 1: LoadingKVdataSample.m **–** Matlab script describing the structure of KVdata.mat information (see script comments) and displaying a sample figure of cilia distribution in a vesicle to show how to use this MAT-file.

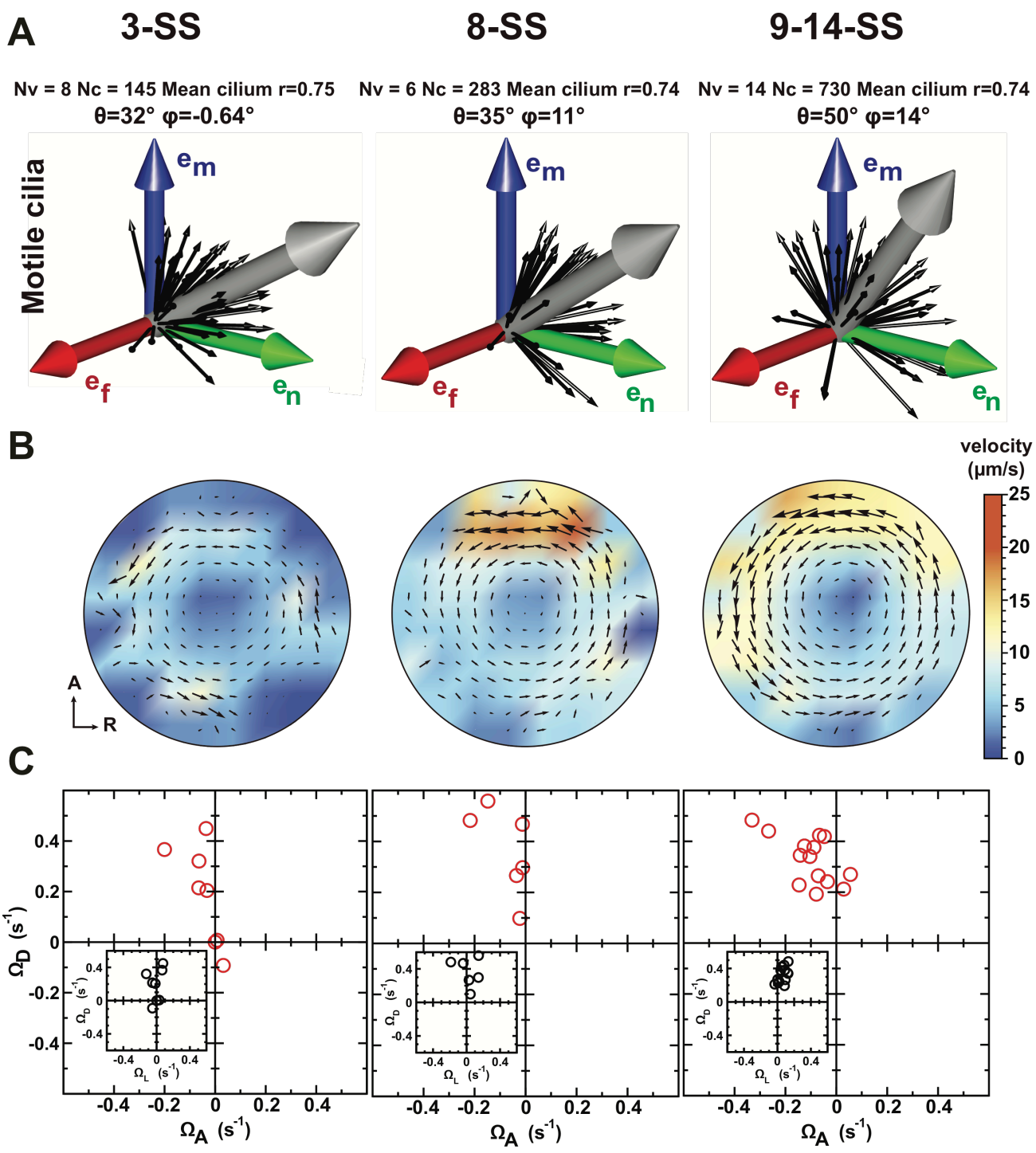

Figure 4

Manuscript 3 - Figure 4: Development of flow profiles and cilia orientations over time from 3- to 9-14 somite stage (SS): (A) Cilia orientation in the local basis (e_m, e_n, e_f) over time (see Figure 3C). Black vectors show cilia orientations from one representative vesicle. **(B)** Average flow in the equatorial plane of the Kupffer's vesicle (KV) calculated from cilia maps at each developmental stage. The average flow is rotational about the dorsoventral (DV) axis at all stages, getting stronger anteriorly from 8-SS onwards. A 3D visualization of these flows is shown in Movie 2. **(C)** Effective angular velocity ($\vec{\Omega}$) as a measure of rotational flow within a KV over time. Right view of the $\vec{\Omega}$ vector is shown in the main diagrams, posterior view in insets.
The following figure supplements are available for Figure 4:
Manuscript 3 – Figure 4-figure supplement 1: Quantification of KV and cilia features comparing the 3-, 8- and 9-14-SS and Figure 4-figure supplement 2: Changes in cilia spatial distribution and orientation over time.

anterior part of the dorsal KV. This might explain why several studies reported different orientation of the cilia in the KV (Borovina et al., 2010; Okabe et al., 2008; Supatto et al., 2008). With such a meridional tilt, all motile cilia can contribute to the directional flow around the DV axis, wherever they are located within the KV.

Variation in cilia surface density over time affects flow amplitude but not its direction

Current models for symmetry breaking are not taking into account the dynamics of cilia spatial distribution during the process. Nevertheless, the process of LR patterning occurs in a dynamic organ (Compagnon et al., 2014; Wang et al., 2012; Yuan et al., 2015), which might be associated with changes in the spatial distribution and orientation of cilia during the course of LR patterning. Previous reports have shown that the first signs of asymmetric cell response in the KV are observed between 3- and 8-SS (Francescatto et al., 2010; Sarmah et al., 2005; Yuan et al., 2015). To obtain accurate information about these dynamics, we map cilia positioning within the KV in three pools of embryos: early (3-SS), mid (8-SS) and late (9-14-SS) (Figure 4A). During this developmental time window, the KV size drastically changes with an average volume increasing from 17 pl at early to 45 pl and 82 pl at mid and late stages. The average number of cilia per vesicle also increases from 30 at early, to 52 and 63 at mid and late stages (Figure 4-figure supplement 1 and Table 1). Not surprisingly, the ratio of motile versus non-motile cilia also changes along with the total number, as previously observed by (Yuan et al., 2015). The fraction of motile cilia increases with time (44% of immotile cilia per vesicle on average at 3-SS vs. 2% at 8-SS) (Figure 4-figure supplement 1, Figure 4-figure supplement 2A and Table 1). At mid and late stages we observed a steep gradient of cilia surface density along the AP axis, which is not yet established at 3-SS (Figure 4-figure supplement 2B). Instead, a DV gradient of cilia density is present at 3-SS.

We next investigated the emergence of cilia motility and orientation by comparing early, mid and late stages. We observed that the spread around the average motile cilium is constant over time (resultant vector length r = 0.74 or 0.75) (Figure 4A). Additionally, it seems that the average orientation angle q of the motile cilia increases over time (from 32° to 50°, Figure 4A). When focusing on 3-SS embryos, we found that motile cilia at this stage already exhibit a clear meridional tilt, as the angle φ of the average motile cilium is close to 0° (57% of all cilia exhibited a φ angle in the meridional quadrant [-45°,+45°]) and θ is high (32°) (Figure 4A). Together these data suggest that the few motile cilia at 3-SS are already well oriented and generate a flow of low amplitude but in the proper direction.

We suspected that the increasing number of motile cilia and the changes in their spatial distribution would significantly alter the flow profile between 3- and 8-SS. To test this, we used our 3D cilia maps to numerically calculate the flow they generate at the different developmental stages (Figure 4B and Movie 2). We first validated our flow simulation by comparing it with experimentally measured flow profiles along the AP axis (Figure 5). As expected, due to the increase in anterior cilia density, the flow amplitude increases over time (Figure 4B and Figure 6A) with the most pronounced increase in the anterior region. We quantified the directionality of the flow by calculating the effective angular velocity

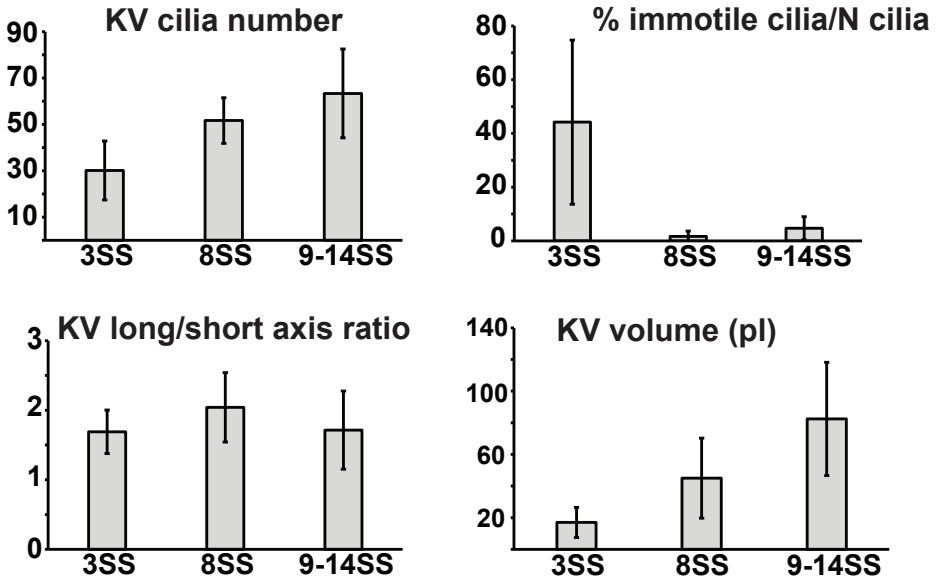

p value	KV cilia number		% immotile cilia		KV long/short axis ratio		KV volume (pl)	
	8SS	9-14SS	8SS	9-14SS	8SS	9-14SS	8SS	9-14SS
3SS	0.041	0.001	0.047	0.011	0.327	0.363	0.08	8.6×10^{-4}
8SS		0.018		0.1		0.079		0.009

Figure 4-figure supplement 1

Manuscript 3 - Figure 4-figure supplement 1: Quantification of KV and cilia features comparing the 3-, 8- and 9-14-somite stage (SS). Table p-values (see more features in Table 1).

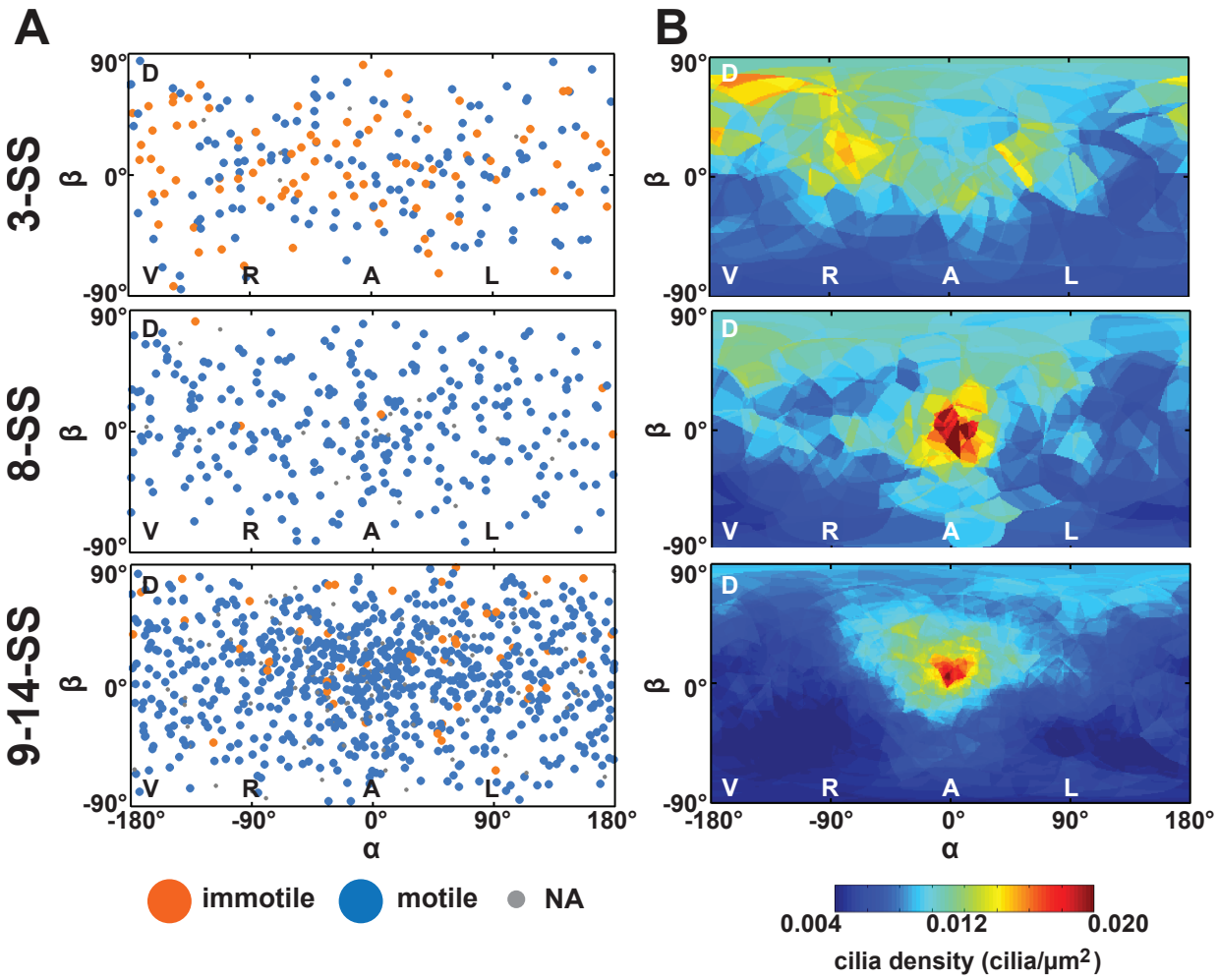

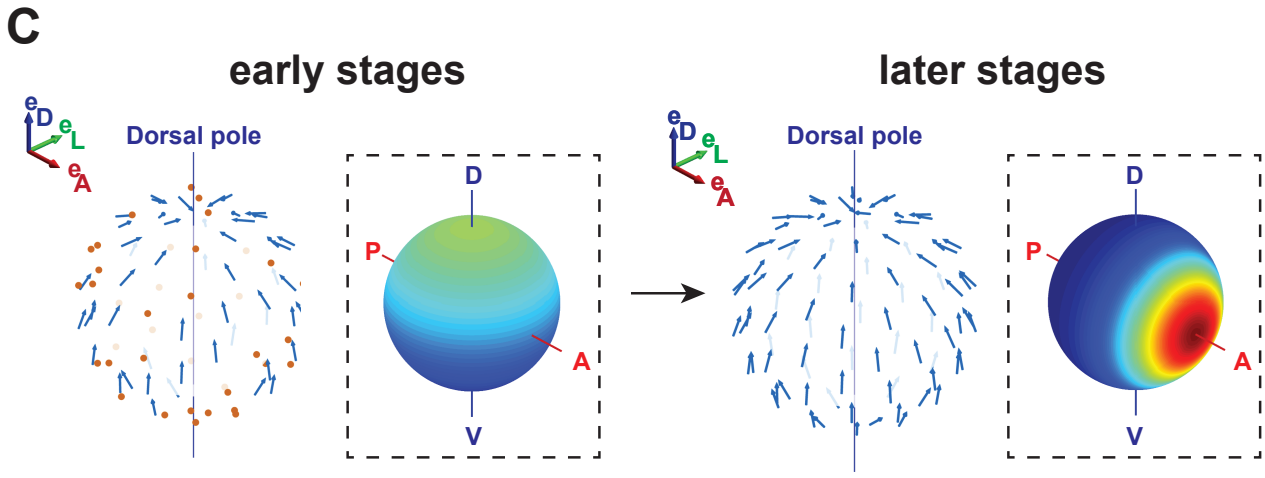

Figure 4-figure supplement 2

Manuscript 3 - Figure 4-figure supplement 2: Changes in cilia spatial distribution and orientation over time: (A) Spatial distribution in 2D maps of immotile (blue) and motile (orange) cilia. Between 3- and 9-14-somite stage (SS), the proportion of immotile cilia decreases from 44% to 5% (see also Table 1). **(B)** Cilia density maps show an enrichment at the anterior pole ($\alpha = 0°$) that accumulates over time (from 3- to 9-14-SS). **(C)** Scheme summarizing the main differences in cilia 3D orientation and density map (dashed boxes) between early (3-SS, left) and late (9- to 14-SS, right) stages of development: while early vesicles contain many immotile cilia (red), motile cilia (blue) always exhibit a meridional tilt at both early and late stages. The cilia density map is first dominated by a dorsal gradient before exhibiting a strong anterior gradient at late stages (color map from blue to red representing low to high cilia density). See Figure 1 for the definition of the body plan reference frame and coordinates systems.

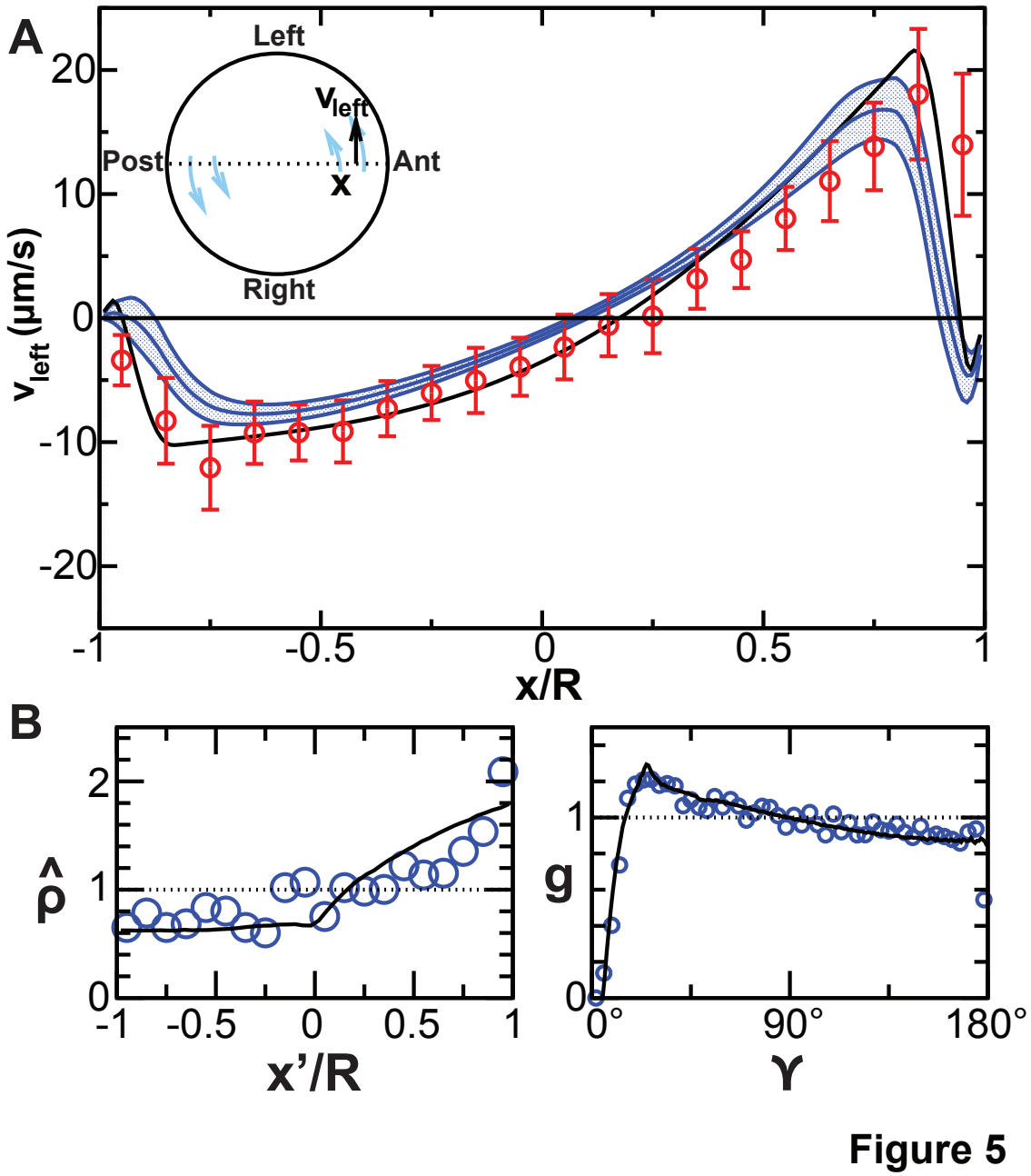

Figure 5

Manuscript 3 - Figure 5: Validation of calculated flow profiles. (A) Velocity profile along the anteroposterior (AP) axis (anterior: $x/R = 1$; posterior: $x/R = -1$), positive values indicate leftward flow. Red: experimental values obtained with particle tracking (Supatto et al., 2008). Blue: calculated flows using observed cilia distributions from vesicles from stages 8-somite stage (SS) to 14-SS (mean ± std. error; $N_v = 20$). Black: simulations using randomly generated cilia distributions. **(B)** Statistical features used to generate cilia distributions (blue circles: experimental distributions, black line: model). Left panel: normalized surface density as a function of the position along the tilted AP axis ($x' = 1$ at the point with maximum density, $(\alpha, \beta) = (0, 15°)$); right panel: pair correlation function as a function of the angular distance between two cilia. N_v = number of vesicles

$\vec{\Omega}$, defined as the angular velocity of a uniformly rotating sphere with the same angular momentum as the circulating fluid in the vesicle (Figure 4C and Table 1). Our results consistently show that in 8-SS and 9-14-SS embryos, the rotational flow persistently points in one direction. Most importantly, in 5 out of 8 vesicles, the flow direction is already set at 3-SS (Figure 4C and Figure 6-figure supplement 1A), suggesting that directional flow can emerge as early as 3-SS, even though the flow is of low amplitude (Movie 2). As a consequence, the establishment of an AP gradient of cilia from 3- to 8-SS does not affect the flow direction, which further supports cilia meridional tilt as the dominant mechanism used to generate directional flow within the KV.

Single vesicle analysis reveals a significant variability between embryos

An additional element to consider in the physical mechanisms of symmetry breaking is its robustness. Given that 90-95% of the zebrafish embryos have a properly positioned left axis (Gokey et al., 2016), the mechanism eliciting LR bias has to be highly robust even though the KV size, which affects LR patterning, is variable across embryos (Gokey et al., 2016). We sought to directly probe for the robustness of the biophysical features of the cilia through single vesicle analysis. We first analyzed cilia density in individual vesicles and found that cilia density and orientation are very variable from embryo to embryo (Figure 6B-D, Figure 6-figure supplement 1A-C and Table 1). Making use of the cilia maps observed in individual KV and our model of 3D flows, we determined the expected flow profiles. We assessed the general amplitude of the flow and found strong variability in the local flow velocities between individual vesicles at every developmental stage (Figure 6B-D and Figure 6-figure supplement 1A-C). In particular, the calculated profiles reveal a high level of variability of the difference between left and right flow amplitudes, without a persistent bias (Figure 6-figure supplement 1A-C). Similarly, we found the maximum velocity at the anterior and posterior poles of the KV is variable from embryo to embryo (Figure 6B-D and Figure 6-figure supplement 1A-C). We conclude that the local flow amplitude itself cannot be a good indicator of the embryonic side and is too variable to serve as a robust predictor of the left and right side of the vesicle. By contrast, the strength of the rotational flow characterized by the effective angular velocity $\vec{\Omega}$ appears robust (Figure 4C). Thus, while the average vesicle highlights a highly stereotyped organization, single vesicle analysis uncovers a high diversity of densities, orientations and local flow profiles. This identifies the directional flow as the most robust left-right asymmetric feature in the vesicle.

Comparing flow-mediated transport of signaling molecules and mechanical flow sensing as mechanisms for symmetry breaking in the KV

The hypotheses for the mechanisms of LR symmetry breaking are usually divided into two competing classes, independently of the topological differences amongst species: asymmetric distribution of signaling molecules (Hirokawa et al., 2006; Okada et al., 2005) or asymmetric mechanical influence (Hamada and Tam, 2014; Yoshiba and Hamada, 2014). Making use of the information gained from 3D-Cilia Map and numerically calculated flow profiles, we developed numerical simulations based on specific arrangements of cilia in order to corroborate or refute different hypotheses for symmetry

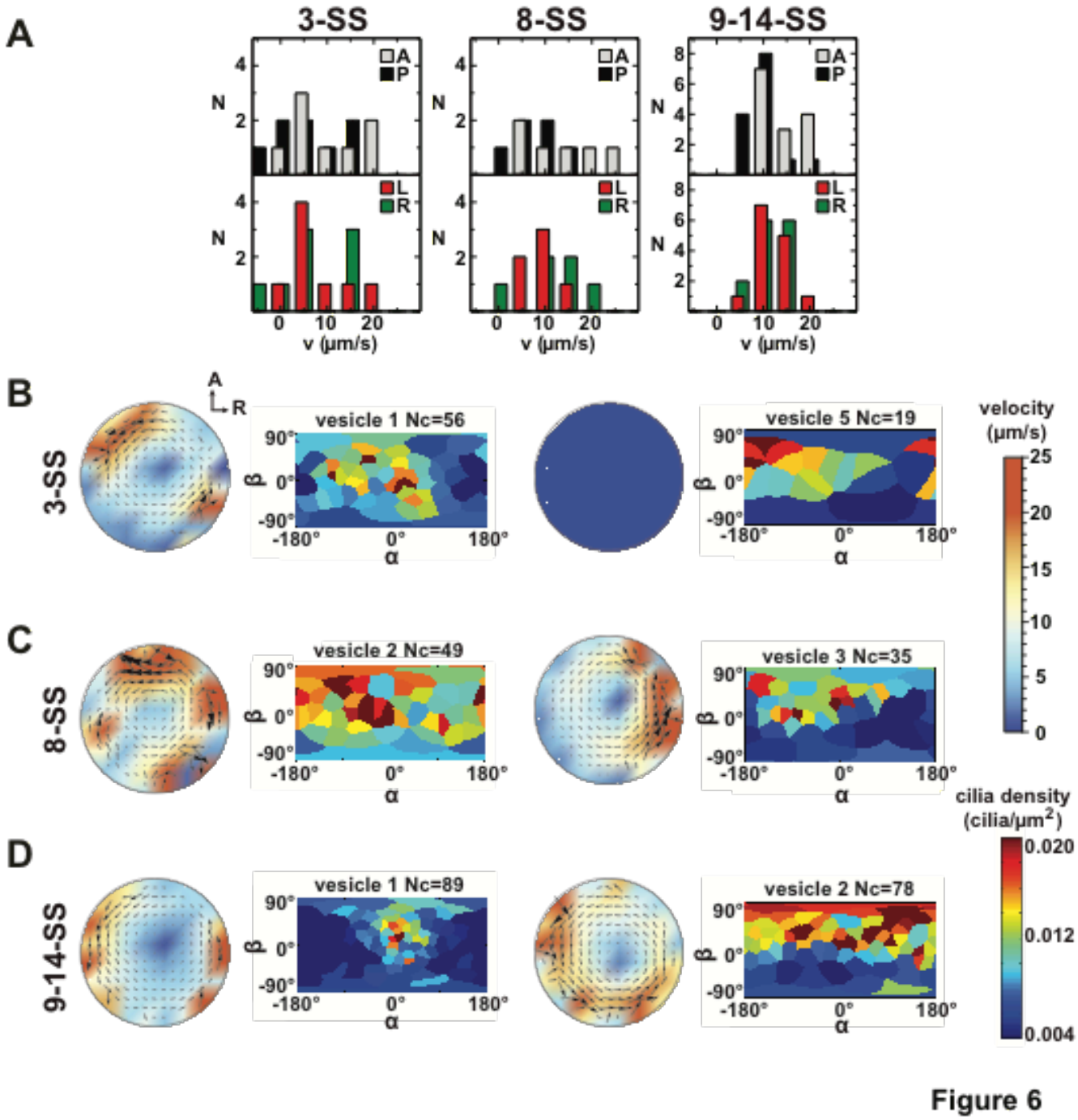

Figure 6

Manuscript 3 - Figure 6: Variability in cilia distributions and flow profiles between individual Kupffer's vesicle (KV) at 3-, 8- and 9-14- somite stage (SS): (A) Distributions of flow velocities in individual KV at 3-, 8- and 9-14-SS. The upper panel shows the mean velocities in the regions around the anterior (A) and posterior (P) poles and the lower panel around the left (L) and right (R) poles. **(B-D)** Flow profiles and 2D cilia density maps for two representative KV at 3-SS **(B)**, 8-SS **(C)** and 9-14-SS **(D)** (see Figure 6-supplement 1 for all individual KV).
The following figure supplement is available for Manuscript 3 - Figure 6:
Figure supplement 1: Flow profiles and 2D cilia density maps for all KV analyzed at 3-SS, 8-SS and 9-14-SS.

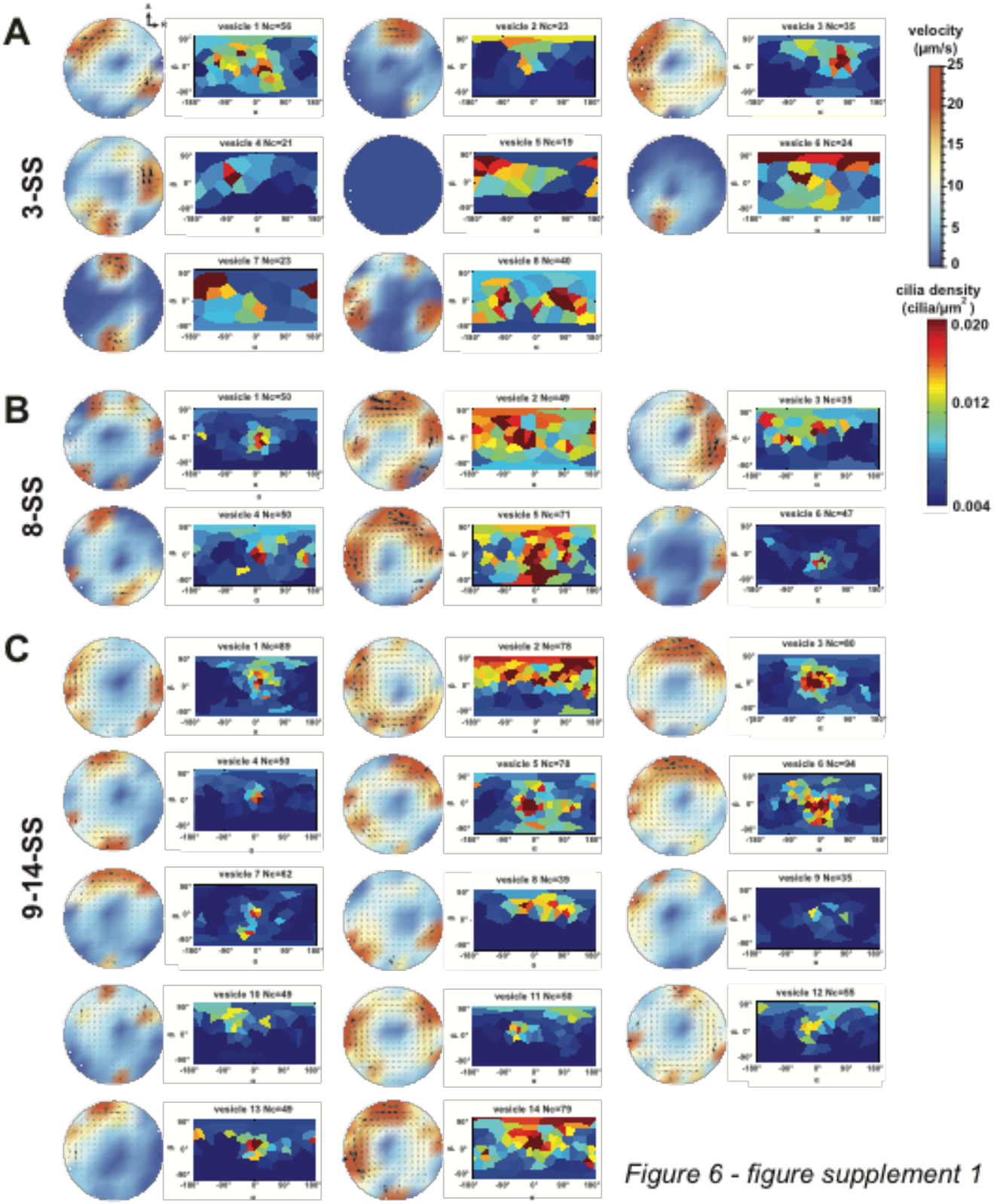

Figure 6 - figure supplement 1

Manuscript 3 - Figure 6-figure supplement 1: Flow profiles and 2D cilia density maps for all Kupffer's vesicles (KV) analyzed at 3-somite stage (SS) **(A)**, 8-SS **(B)** and 9-14-SS **(C)**, showing a great variability between embryos.

breaking in the LRO. In particular, we took into account the variability between embryos that we observed experimentally.

Mechanosensory mechanism 1: Directional flow sensing

We first evaluated the '*Directional flow-sensing mechanism'* where the left side is detected by sensing the directionality of the circular flow. Such a mechanism implies that cells need to distinguish between a fluid moving from anterior (A) towards posterior (P) (on the left side) and a fluid moving from P towards A (right side), and the cilium needs to sense the direction of flow. It also has to overcome the following obstacles: 1) The strong temporal variation associated with beating cilia overlays the directional flow to be detected. 2) In addition, the flow fields of adjacent cilia also perturb the static component of the directional flow. 3) The cilia would need a detection threshold sufficiently low to detect the relatively weak flows in the KV. Using our computational modeling, we tested the feasibility of criteria 1-3.

We used the cilia distributions from 20 analyzed vesicles, as well as a larger number of randomly generated vesicles with the same density profiles and interciliary distance distributions (see Methods). In each vesicle, we randomly chose 3 immotile cilia on each side and calculated the torque acting on them. The torques acting at the base of a cilium are calculated using the numerically determined force distributions along its length. The torque component that could potentially serve as the LR determinant is the meridional one, bending the cilium towards A or P (Figure 7A). In order to estimate the fraction of cilia that measure the torque in the correct direction above a certain threshold, we plotted cumulative distributions of the meridional component of the torque vector (Figure 7B,C). The instantaneous torques (dotted lines) show a broad distribution and have a direction opposite to that of the directional flow in about 25% of the cases. These fluctuations are caused by the beating of adjacent cilia, which induces on average an oscillating torque with an r.m.s amplitude of 9×10^{-19} Nm. Additionally, the torques are of a similar order of magnitude as the thermal fluctuations acting on the cilium, whose r.m.s. amplitude we estimate as 2×10^{-19} Nm (Appendix B). A simple estimate shows that both the thermal and oscillatory noise can be suppressed by temporal averaging (low-pass filtering) the signal with a time constant longer than 2 s. The distribution of time-averaged torques is shown by dashed lines in Figure 7B and C. A sensitivity threshold of 2×10^{-19} Nm would be sufficient to achieve a reliability of 95% (less than 5% of the immotile cilia on the left side would not detect the posterior-directed flow) in vesicles with the generated distributions (Figure 7B, dashed lines), but the greater variability of experimentally characterized vesicles does not allow this level of reliability (about 10% of the cilia are subject to flows of the opposite directionality, Figure 7C, dashed lines). A sufficient reliability can only be achieved by additionally averaging the torques detected on all 3 cilia on one side (solid lines). In this case the required detection threshold is 10^{-19} Nm. For comparison with other flow sensing cilia, we calculated the uniform shear rate required to exert the same torque. We find that for a 6 µm long cilium the threshold torque corresponds to a shear rate of 0.5 s^{-1} (shear stress 0.5 mPa). In renal cilia, Rydholm and colleagues (Rydholm et al., 2010) observed calcium signals with shear stresses of 20 mPa and higher. These results indicate that the mechanosensory detection of flow

would require cilia with an ability of direction-sensitive flow detection with a threshold 1-2 orders of magnitude lower than known comparable mechanosensory cilia. Moreover, many KV have fewer than 3 immotile cilia on each side, the number that would be needed for ensemble-averaging to overcome spatial inhomogeneities of the flow. The number of immotile cilia is higher at 3-SS, but the weaker and less regular flow excludes reliable side detection at that stage (Figure 7- figure supplement 1). Together, these results suggest that flow sensing in itself is difficult as the flow is weak and masked both by spatial and temporal fluctuations. We thus expect that such a mechanism of sensing would lack the robustness necessary for setting the LR axis accurately.

Mechanosensory mechanism 2: cells sense the motion of their own cilia

An attractive possibility based on mechanosensing is that cells '*detect the motion of their own cilia relative to already established body axes'*. In this case, the rotating cilium provides a cell the necessary chirality information, while the directional flow in KV would only appear as an epiphenomenon. The tip velocity of a beating cilium (400 µm/s) is significantly higher than the typical flow velocity (10 µm/s), which implies that in a motile cilium the torques caused by its own motion largely surpass those caused by the directional flow. Using the mobility matrix of a model cilium (see Methods) we calculated the torque components acting on the base of an isolated dorsally tilted motile cilium, positioned either on the left or on the right side (Figure 7D). The dashed lines show the time averages of the 3 torque components. The average torque caused by an active cilium's motion is about 20 times higher than the torque caused by the directional flow (*Mechanosensory mechanism 1*). If a cell could discriminate between a torque towards A or P exerted at the base of its motile cilium, the time-averaged meridional component of the torque vector (blue line), which has a magnitude of about 10^{-17} Nm, could serve as a side discriminator. Thus, cells sensing the torque direction generated by their own cilia to is a possible mechanism for an asymmetric response in the KV.

Flow-mediated transport of a signaling molecule

As the third mechanism, we investigated the possibility of '*flow-mediated transport of a secreted signaling molecule*' in the KV. It is known that classical motile cilia also contain receptors to detect the external chemical environment (Shah et al., 2009). We propose that cilia on the left and on the right side (45º around LR axis, representing the areas where the first asymmetric responses have been observed (Francescatto et al., 2010; Sarmah et al., 2005), act as detectors that absorb small particles in contact with their surface. Because the first asymmetric signal was observed on the left (Yuan et al., 2015), we propose that these particles are secreted in the anterior region (30º around the anterior pole) and that cells in this region do not absorb them (Figure 7E and Movie 3). As a rough estimate, we expect that flow-mediated transport requires a Péclet number $Pe = vR\,/\,D > 1$, which states that advection dominates over diffusion. With $\Omega = 0.5$ s^{-1}, we get $Pe = \Omega R^2 6\pi\eta r_{\text{Stokes}}\,/(k_B T) = r_{\text{Stokes}}\,/\,0.4\,\text{nm}$. The condition $Pe > 1$ is thus fulfilled for particles above nanometer size. To assess the feasibility of flow-mediated transport quantitatively, we simulated the diffusion of small particles in the flow fields calculated before (Figure 7F). We propose that asymmetry is detected based on the cumulative number of particles detected on each side. Therefore, the time course of particle secretion

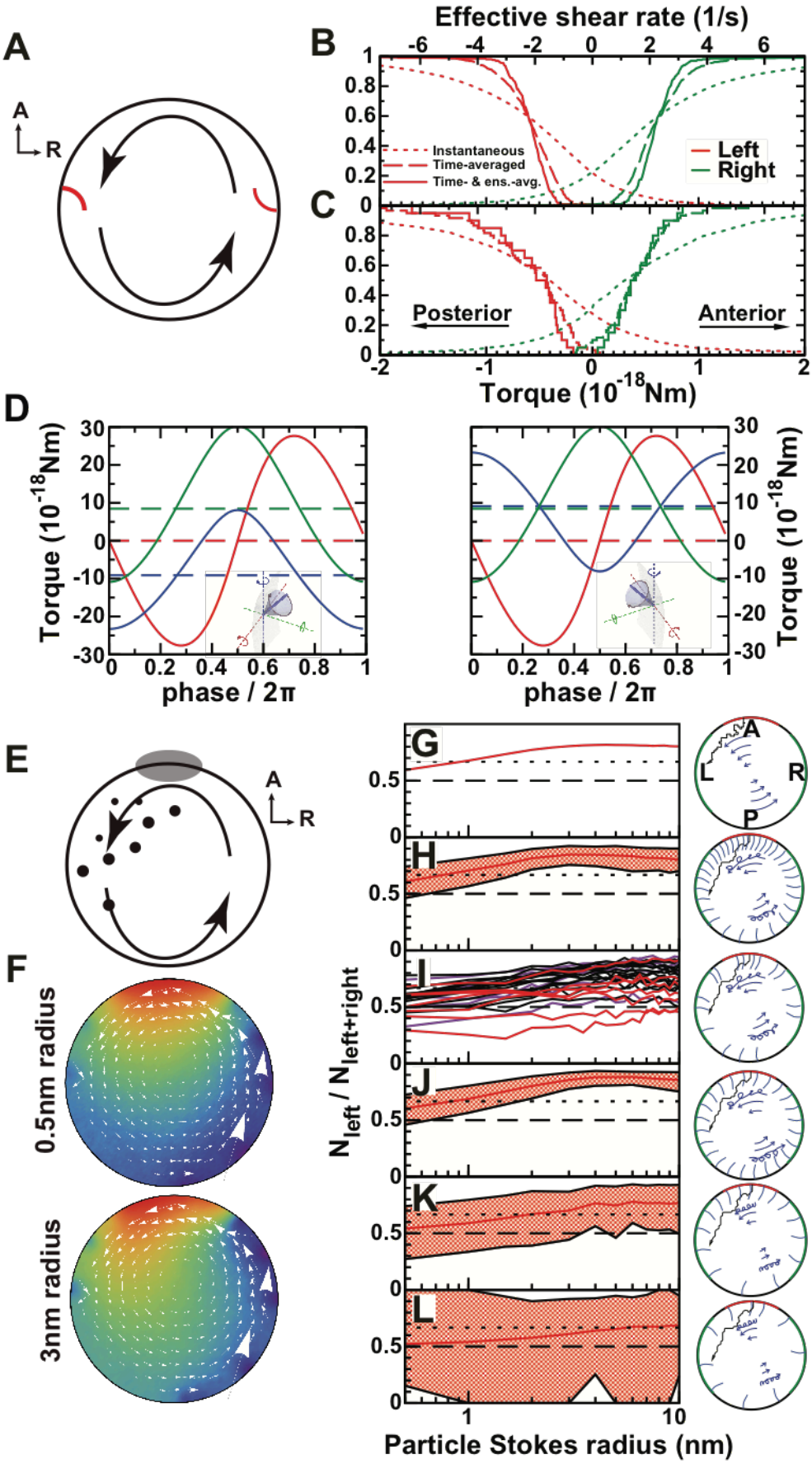

Figure 7

(Figure legend in the next page)

Manuscript 3 - Figure 7: Physical limits of possible side detection mechanisms. (A) Mechanosensory mechanism 1: directional flow sensing. Sensory cilia (red) on the left (L) and on the right (R) side are deflected by the rotational flow (arrows). They must be able to distinguish between anterior- and posterior-directed flows. **(B-C)** Cumulative fraction of cilia with the anterior acting force below (right, green) or above (left, red) the value on the abscissa. The dotted lines show instantaneous values (blurred by oscillatory flows of adjacent cilia), dashed lines show the temporal average, and the continuous line the temporal and ensemble average of 3 immotile cilia on each side. The diagrams show the results on randomly generated (B) and experimentally characterized (C) vesicles. The results show that reliable detection (<5% error) would need a sensitivity threshold of 1×10^{-19} Nm. The upper scale shows the effective flow shear rate above a planar surface that induces the equivalent torque on an isolated passive cilium of the same length. **(D)** Mechanosensory mechanism 2: detection of a cilium's own movement. According to this mechanism a cell can sense the torque components caused by the motion of its active cilium through the viscous fluid. The lines show the meridional component towards posterior (blue), parallel component towards dorsal (red), and normal component (green). The meridional component shows a temporal average of 10^{-17} Nm that could potentially allow discrimination between left (left panel) and right (right panel) side. **(E)** Chemosensory mechanism, based on flow mediated transport of a signaling molecule. Particles are secreted from a region 30° around the anterior (A) pole and then travel diffusively through the rotating fluid. They get absorbed upon encounter with any cilium outside the anterior region. Eventually, particles absorbed in a 45° region around left-right poles are counted. **(F)** Average particle concentration (arbitrary units) in the equatorial plane for particles where diffusion dominates fluid circulation (Stokes radius = 0.5nm, top) and those with drift dominating (3 nm, bottom). In the latter case an asymmetry in the distribution is clearly visible (Movie 3). **(G-L)** Fraction of particles counted on the left among the total count of left and right for different scenarios. The dotted line shows a proposed detection threshold with a left to right ratio of 2:1. The red line shows the average vesicle and the shadowed region the interval between the 5th and the 95th percentile. **(G)** Continuous model with uniform circulation (Ω=0.5s^{-1}). **(H)** Randomly generated cilia distributions with natural parameters. **(I)** Simulation on individual vesicles at 3-SS (red), 8-SS (indigo) and 9-14-SS (black). **(J)** Same as H, but homogeneous cilia distribution. **(K)** Same as H, but reduced number of cilia ($N_c = 35$). **(L)** Further reduced number of cilia ($N_c = 20$). N_c = number of cilia.
The following figure supplement is available for Manuscript 3 - Figure 7:
Figure supplement 1: Cumulative torque distributions on immotile cilia as in Figure 7C, but using cilia maps at 3-somite stage.

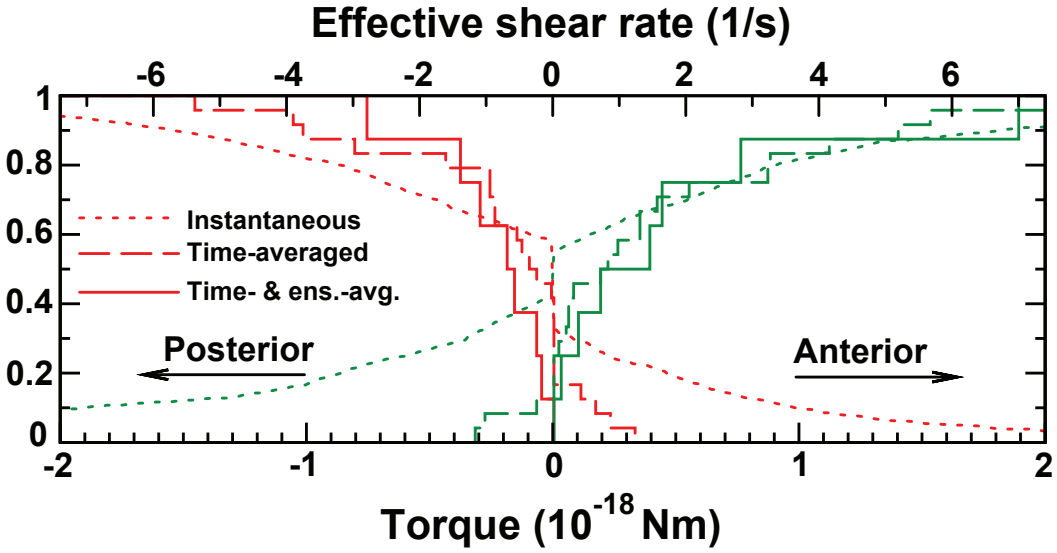

Figure 7 - figure supplement 1

Manuscript 3 - Figure 7-figure supplement 1: Cumulative torque distributions on immotile cilia as in Figure 7C, but using cilia maps at 3-somite stage.

is not important for our arguments. As a measure of asymmetry, we used the number of particles detected on the left side N_{left}, divided by the total number detected on the left and right combined ($N_{left+right}$) (Figure 7G-L). We estimate that the difference is detectable if the ratio between left and right is at least 2:1, i.e., if the fraction is higher than 2/3 (Figure 7G-L). Computational results on 20 vesicles are shown in Figure 7I. For signaling particles with a Stokes radius of 2 nm we obtain a robust asymmetric readout in 18 of 20 vesicles. In addition, we performed the computation on a larger number of randomly generated vesicles and see that, for particle sizes of 2-10 nm, more than 95% of the vesicles fulfill the asymmetry requirement. In order to elucidate the requirements on the arrangement of cilia needed for robust asymmetry establishment we also simulated vesicles with alternative distributions. Figure 7J shows a scenario with cilia distributed homogenously around the whole vesicle, which is equally efficient. It is therefore unclear whether the increased cilia density in the anterior region fulfills a purpose with regard to symmetry breaking. It is possible, however, that it becomes beneficial for different secretion scenarios. Since it was previously shown that there is a minimum number of motile cilia required to achieve LR patterning *in vivo* (Sampaio et al., 2014), we tested the model with a smaller number of motile cilia. With half the number of cilia ($N_c = 35$, Figure 7K) the vesicles still show sufficient average asymmetry, but fail to achieve 95% reliability. Interestingly, the mechanism becomes dysfunctional with 20 motile cilia, which is very close to the minimum observed *in vivo* by (Sampaio et al., 2014) (Figure 7L). This indicates that '*flow-mediated transport of a secreted signaling molecule*' is plausible in the KV and that the KV contains enough motile cilia to allow robust symmetry establishment through asymmetric transport of signaling molecules, but not much more than needed.

Discussion

Here, we have investigated physical mechanisms that could underlie the left-right (LR) symmetry breaking of the vertebrate body plan. We have combined microscopy and large-scale cilia mapping in living animals with theory to analyze the physical limits of the generation and detection of LR asymmetric flows. The experimental analysis of cilia patterns over time allowed us to generate a comprehensive map of complex *in vivo* cilia behaviors at key stages of LR symmetry breaking. We used this approach to assess the reliability by which asymmetric cues can be detected by cells in the process of the determination of the LR axis of the vertebrate body plan.

Recent work in fish and mice has highlighted two possible ways to mechanically sense the directional flow: asymmetric flow velocity sensing (Sampaio et al., 2014) and/or flow direction sensing (McGrath et al., 2003). Our results argue against asymmetric velocity sensing because no robust asymmetries in the flow amplitude were observed in the KV*,* as previously suggested (Smith et al., 2014). The calculated flow pattern obtained when using cilia parameters collected *in vivo* shows that its directionality is the most robust sign of chirality in the organizer. Another level of complexity, which is shared between mouse and fish, is the presence of beating cilia in the near vicinity of the immotile cilia. It has been suggested that these cilia detect the flow direction (Yoshiba et al., 2012). Indeed, the average distance from one cilium to its nearest neighbor is under 8 µm in the KV. At such a distance, the strong local flow perturbations have been shown to be chaotic (Supatto et al., 2008). In addition, the required sensitivity is of the same order of magnitude as thermal fluctuations. Both cilia beating and the thermal fluctuations could theoretically be overcome by time averaging if mechanosensitive cilia acted as low-pass filters. The observed average velocities are still below the detection threshold found in other mechanosensitive cilia (Delling et al., 2016; Goetz et al., 2014; Nauli et al., 2008; Rydholm et al., 2010) and we are not aware of systems that detect static forces with such sensitivity. Hair bundles are known to achieve remarkable sensitivity thresholds close to the level of thermal noise, but the majority of them detect stimuli at higher frequencies and therefore act as high- or band-pass filters (Muller et al., 2016). A notable exception is the utricular otolith, which acts as a low-pass filter, but senses significantly higher forces (Inoue et al., 2013). We conclude that small flow velocities are a major challenge to the reliable sensing of directionality. Moreover, the hypothesis that cilia are capable of directional flow sensing remains untested *in vivo* (Shinohara and Hamada, 2017).

In addition, we showed that due to spatial inhomogeneities resulting from the cilia distribution, temporal averaging within a single cilium could not be sufficient for robust side determination via detection of flow direction. Signals from several cilia on each side would need to be ensemble-averaged. For robust flow sensing, we found that three cilia on each side are necessary.

We observed *in vivo* that the number of immotile cilia decreases over time along with an increase in the number of motile cilia, resulting in a stronger flow velocity and directionality. Nevertheless, the stage at which the number of immotile cilia is high corresponds to the stage where flow is the lowest and the least robust. At later stages, when its directionally is established, we observed that only 5% of

cilia were immotile, less than 3 on each side. The number of immotile cilia is therefore too low to sense the flow direction. Combined with the related finding that cilia from isolated mouse cells do not bend significantly in response to flow applied at endogenous flow amplitudes (Delling et al., 2016), we conclude that a mechanism of symmetry breaking based solely on mechanical sensing of directional flow appears incompatible with our *in vivo* analysis.

These physical limitations led us to reconsider mechanosensing in the framework of LR symmetry breaking. Mechanosensing could, for instance, occur through the sensing of the cilia's own motion. The mean torque exerted by the fluid on a meridionally tilted beating cilium has the opposite direction from the torque exerted by the directional flow on an immotile cilium. A prediction of this auto-sensing hypothesis is therefore that an artificially induced counter-rotating flow (clockwise in dorsal view) would enhance, rather than reverse, the LR difference. Results in the mouse node (Nonaka et al., 2002) showing that externally imposed flow of opposite directionality can cause asymmetry reversal, contradict this view. Another observation in Xenopus that cannot be explained by the auto-sensing hypothesis is that the laterality mechanism breaks down when the fluid is made viscoelastic, which brings the directional flow to a halt, even though the cilia are still motile (Schweickert et al., 2007).

Conversely, our numerical simulations show that asymmetric transport of signaling molecules in the KV is a much more robust strategy than sensing mechanical cues. We characterize here the physical limit on the size of the signaling molecule for its reliable asymmetric distribution. Our calculations show that such mechanism requires the particle size to be bigger than 2 nm in order to work. Interestingly, this is in the size range of Membrane-bound Extra Cellular Vesicles (ECVs). ECVs play important roles in intercellular communication and may mediate a wide range of physiological and pathological processes (Cocucci et al., 2009; Hogan et al., 2009; Raposo and Stoorvogel, 2013; Wood et al., 2013).

In summary, we analyzed the physical limits of mechanisms that have been proposed for asymmetry establishment in zebrafish. Combining large-scale *in vivo* imaging with fluid dynamics calculations we were able to map the biophysical features of cilia in the KV and the flows they generate in unprecedented detail. This allowed us to quantitatively test the physical limits of flow detection mechanisms. We show that the small number of immotile cilia found in the KV cannot be sufficient to robustly detect the direction of the flow given its high local variability. Motile cilia could sense the torques exerted by the fluid as a result of their own motion, which largely surpass the influence of the directional flow. However, we show that this mechanism is incompatible with findings in other vertebrate species in which laterality establishment was suppressed in viscoelastic fluids and reversed with an artificial flow (Nonaka et al., 2002; Schweickert et al., 2007). Finally, we show that a chemosensory mechanism in which a LR gradient is established by combining directional flow around the dorsoventral axis with asymmetric particle secretion in the anterior region could explain the observed robust LR asymmetry establishment, provided that the particle size is above the lower limit of about 2 nm. Although the molecular nature of the flow detection mechanism remains obscure, our

analysis of physical limitations of two proposed mechanisms rules out directional flow sensing. It also allows us to predict the minimum size of the signaling particle, which will eventually facilitate the search for it.

Material and Methods

Zebrafish strains

The zebrafish transgenic line used in the study is *actb2:Mmu.Arl13b*-GFP (Borovina et al., 2010). Embryos were raised at 32°C in the dark. For imaging, embryos were soaked in with Bodipy TR (Molecular Probes) for 60 minutes prior to the desired developmental stage and were subsequently embedded in 0.8% low melting point agarose (Sigma Aldrich) in Danieau solution. Embryos were imaged between 3- and 14-somite stages (SS).

2-photon excitation fluorescence microscopy (2PEF)

To image deep enough into the zebrafish embryo and capture the entire Kupffer's vesicle (KV), each live embryo (n = 28) was imaged using 2PEF microscopy with a TCP SP5 or SP8 direct microscope (Leica Inc.) at 930 nm wavelength (Chameleon Ultra laser, Coherent Inc.) using a low magnification high numerical aperture (NA) water immersion objective (Leica, 25x, 0.95 NA). We imaged the KV of embryos labeled with both *Arl13b*-GFP and BodipyTR between 3- and 14-SS: 100x100x50 μm^3 3D-stacks with 0.2x0.2x0.8 μm^3 voxel size and 2.4 µs pixel dwell time were typically acquired in order to maximize the scanning artefact allowing to properly reconstruct cilia orientation in 3D (Figure 1-figure supplement 1E) as described in (Supatto and Vermot, 2011). The fluorescence signal was collected using Hybrid internal detectors at 493-575 nm and 594-730 nm in order to discriminate the GFP signal labeling cilia from the signal labeling the KV cell surface. To uncover the orientation of the KV within the body axes, the midline was also imaged. We typically imaged a volume of 600 µm×600 µm×150 µm comprising the midline and the KV from top to bottom with a voxel size of 1.15 µm laterally and 5 µm axially.

3D-Cilia Map: quantitative 3D cilia feature mapping

We devised 3D-Cilia Map, a quantitative imaging strategy to visualize and quantify the 3D biophysical features of all endogenous cilia in the 50 to 80 cells constituting the KV in live zebrafish embryos from 3- to 14-SS (Figure 1-figure supplement 1). We used Imaris (Bitplane Inc., RRID:SCR_007370) and custom-made scripts in Matlab (The MathWorks Inc., RRID:SCR_001622) to perform image processing, registration, and analysis, and to extract the following features: KV size, shape and volume, cilia motility, number of cilia per KV, cilia spatial distribution, orientation of rotational axis and surface density (Figure 1-figure supplement 1 and Table 1). Cilia motility, position, and orientation in 3D, as well as the reference frame of the body axes, were obtained from 2PEF images and exported from Imaris to Matlab using ImarisXT (Figure 1-figure supplement 1D,E). Since our analysis relies on the fluorescence signal from the cilia, we discarded embryos with levels of GFP expression too low to analyze them. Similarly, a few cilia per vesicle could be discarded when the signal or the spatial resolution was too low to accurately determine motility (11%) or orientation (14%). Each cilium was defined as a unit vector from its base to its tip (Figure 1-figure supplement 1E). Cilia positions were registered in the body plan reference frame. To estimate the KV surface, we fitted an oblate spheroid to the distribution of cilia bases using the Ellipsoid fit Matlab script by Yury Petrov (Northeastern University, Boston, MA) (see fitting residues in Table 1). We used cilia vector components in the local

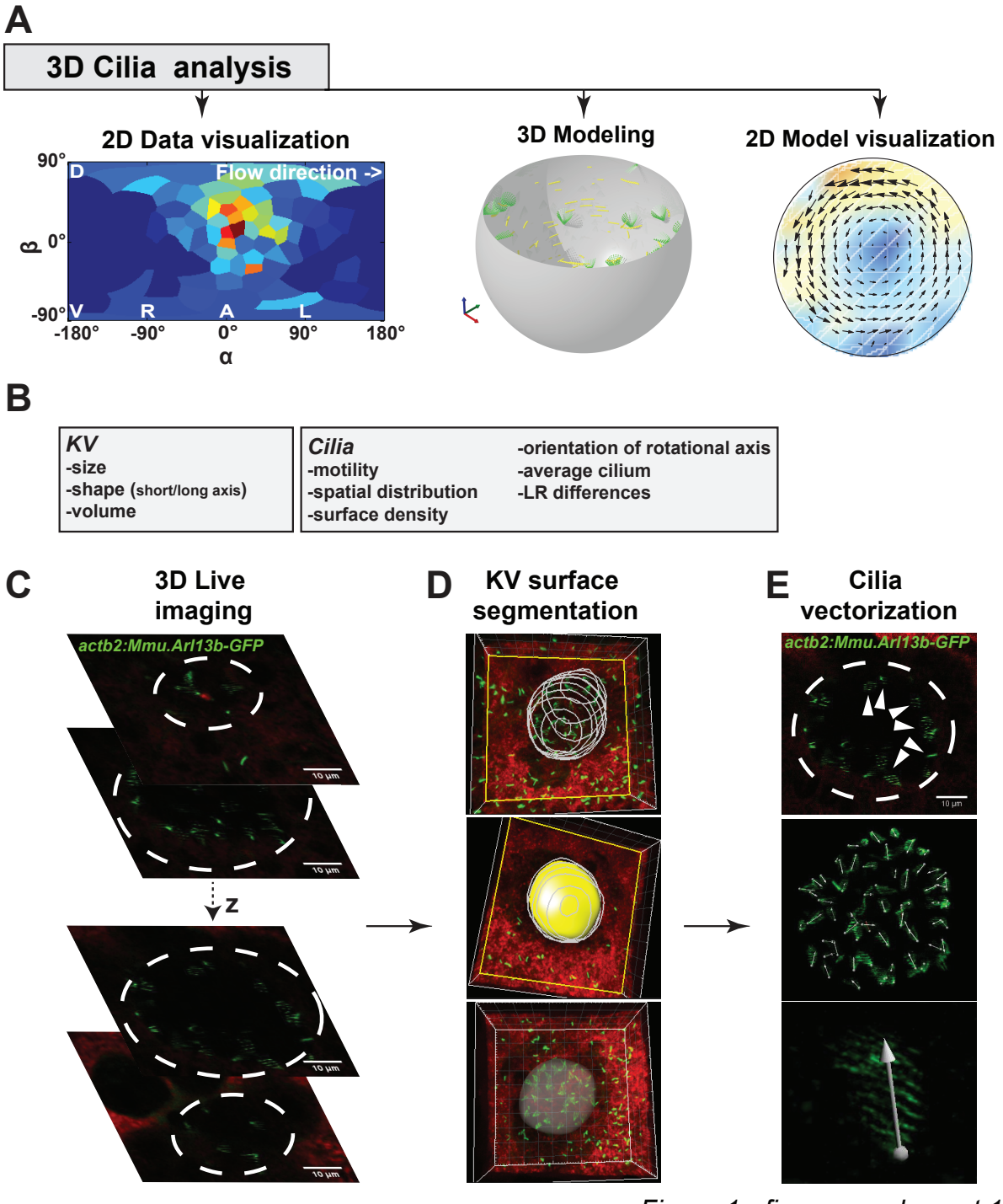

Figure 1 - figure supplement 1

Manuscript 3 - Figure 1-figure supplement 1: Multiscale analysis from individual cilia to 3D modeling of the Kupffer's vesicle (KV). (A) 3D-CiliaMap workflow pipeline: 3D live imaging with cilia analysis, followed by 2D visualization of cilia maps, 3D flow calculation based on live datasets, and flow visualization. **(B)** List of the KV and cilia features extracted using 3D-CiliaMap. **(C-E)** Successive steps forming the 3D-CiliaMap workflow from 3D live imaging to cilia vectorization (see also Movie 1): **(C)** 3D live imaging of the total volume of the KV, using *Tg* (*actb2:Mmu.Arl13b*-GFP*)* (Borovina et al., 2010) embryos soaked for 60 minutes in Bodipy TR (Molecular Probe) - dashed white lines underline the KV. **(D)** Using Imaris (Bitplane Inc.), the KV surface is manually segmented in order to reveal only the cilia belonging to the surface of the KV cells. **(E)** Slow acquisition speed with standard laser scanning microscopy allows detecting the cilia orientation in the KV using the *Tg* (*actb2:Mmu.Arl13b*-GFP*)* line: dashed white lines underline the KV (upper panel); dorsal view of the whole vesicle showing the vectors obtained from the GFP signal (middle panel); high magnification of a cilium with a vector corresponding to its rotational axis orientation (bottom panel).

stage	KV number	N cilia	% immotile cilia	Ellipsoid Axis a (µm)	Ellipsoid Axis b (µm)	ratio axis a / b	Volume (pl)	Average motile cilium: r	Average motile cilium: θ (°)	Average motile cilium: φ (°)	Ellipsoid fit RMS residue (µm)	Ω (s^{-1})
3-SS	1	56	11%	27	12	2.3	35	0.8	37	6	2.07	0.423
	2	23	39%	21	12	1.8	21	0.8	44	2	1.56	0.207
	3	35	3%	23	12	1.9	27	0.8	42	-11	2.38	0.457
	4	21	33%	18	11	1.6	15	0.8	22	12	2.14	0.350
	5	19	100%	15	9	1.7	8	NA	NA	NA	1.5	0.000
	6	24	54%	15	10	1.5	9	0.7	28	3	1.78	0.230
	7	23	61%	14	12	1.2	10	0.8	18	-46	1.92	0.110
	8	40	53%	18	11	1.6	16	0.7	8	22	2.05	0.034
	mean ± SD	**30±13**	**44% ± 31%**	**19 ± 5**	**11 ± 1**	**1.7 ± 0.3**	**17 ± 10**	**0.8 ± 0.1**	**28 ± 13**	**-2 ± 22**	**1.9 ± 0.3**	**0.226 ± 0.173**
8-SS	1	50	4%	29	18	1.6	64	0.8	37	-14	1.2	0.270
	2	49	2%	22	8	2.8	15	0.8	35	6	1.1	0.595
	3	43	0%	25	11	2.3	30	0.7	46	12	2.3	0.561
	4	50	4%	27	12	2.3	39	0.7	41	16	2.5	0.329
	5	71	0%	26	13	2.0	36	0.8	35	16	1.8	0.469
	6	47	0%	30	22	1.4	85	0.7	21	39	1.7	0.110
	mean ± SD	**52 ± 10**	**2% ± 2%**	**26 ± 3**	**14 ± 5**	**2.0 ± 0.5**	**45 ± 25**	**0.7 ± 0.1**	**36 ± 8**	**13 ± 17**	**1.7 ± 0.5**	**0.389 ± 0.186**
9-14-SS	1	89	16%	37	31	1.2	174	0.7	49	12	2.1	0.271
	2	78	6%	27	15	1.8	47	0.7	46	18	2.0	0.600
	3	80	3%	33	20	1.7	93	0.8	54	13	2.2	0.412
	4	50	0%	33	20	1.7	91	0.7	47	14	2.6	0.290
	5	78	6%	31	17	1.8	70	0.7	36	20	2.0	0.393
	6	94	4%	36	21	1.7	111	0.8	52	10	1.7	0.424
	7	62	11%	34	26	1.3	124	0.8	46	11	1.8	0.216
	8	39	3%	24	20	1.2	48	0.7	54	36	4.4	0.378
	9	35	0%	31	13	2.4	52	0.8	50	10	2.6	0.245
	10	49	4%	32	17	1.9	74	0.8	53	2	2.3	0.275
	11	50	2%	30	22	1.4	82	0.9	64	3	2.9	0.433
	12	55	2%	30	23	1.3	85	0.8	61	11	2.6	0.388
	13	49	4%	33	10	3.3	47	0.7	40	32	2.1	0.224
	14	79	5%	27	19	1.4	56	0.7	51	22	1.8	0.521
	mean ± SD	**63 ± 19**	**5% ± 4%**	**31 ± 4**	**19 ± 5**	**1.7 ± 0.6**	**82 ± 36**	**0.8 ± 0.05**	**50 ± 7**	**15 ± 10**	**2.3 ± 0.7**	**0.362 ± 0.114**

Manuscript 3 - Table 1: Statistical properties of all KV analyzed. Table summarizing some of the cilia features collected from the 3D-CiliaMap for individual KV at 3-, 8- and 9-14- somite stage (SS). The following source data file is available for Manuscript 3 - Table 1: Table1 – source data 1: KVdata.mat : Matlab MAT-file containing the cilia distribution and vectors from the 1438 cilia in 28 vesicles analyzed in this work. It includes cilia categories (motility and clear/unclear orientation), vesicle stage, position and vector coordinates in different reference frames.

Symbol	Description	From 3D-CiliaMap	Value: standardized vesicle
$(\vec{e}_m, \vec{e}_f, \vec{e}_n)$	Cilium's coordinate system	+	
$(\vec{e}_A, \vec{e}_L, \vec{e}_D)$	KV coordinate system	+	
α	Coordinate	+	
β	Coordinate	+	
θ	Cilium tilt	+	$0 - 60°$
φ	Cilium orientation on the cell surface	+	0
ψ	Cilium, semi-cone angle		$25°$
ω	Cilium, angular frequency		$25 \times 2\pi\ s^{-1}$
L	Cilium, length		6 µm
R	KV radius	+	35 µm
a	KV ellipsoid, equatorial radius	+	R
b	KV ellipsoid, height	+	R
N_c	Number of cilia	+	70
ρ	Surface density of cilia	+	
$\hat{\rho}$	Normalized surface density of cilia	+	See Figure 5
$g(\gamma)$	Cilia distribution, pair correlation	+	See Figure 5
η	Fluid viscosity	0.001 Pa s	
r_{Stokes}	Diffusive particle Stokes radius	$0.5 - 10$ nm	
D	Particle diffusion constant	$k_B T/(6\pi\eta\, r_{\text{Stokes}})$	
$\vec{v}(\vec{x})$	Fluid velocity inside KV	calculated	
$\vec{\Omega}$	Effective flow angular velocity	calculated	
$N_{\text{left}}, N_{\text{right}}$	Number of particles captured on the left/right	simulated	

Manuscript 3 - Table 2: List of symbols: Quantities and their values with sources where applicable.

orthogonal basis ($\vec{e}_f, \vec{e}_n, \vec{e}_m$) defined at each cilium position on the spheroid surface to quantify cilia orientation angles θ (cilium tilt angle respective to the surface normal) and φ (cilium orientation on the KV cell surface), as shown in (Figure 1C). The experimental values were combined from different embryos and displayed in rosette histograms using Matlab. Finally, to estimate the local cilia density we transformed the spheroid into a sphere with surface density conservation and computed a spherical Voronoi diagram of cilia distribution based on the sphere_voronoi Matlab package by John Burkardt (Department of Scientific Computing, Florida State University, https://people.sc.fsu.edu/~jburkardt/).

Flow calculation

When calculating the flow in a KV we first approximate it with a sphere of equal volume. We describe each cilium as a chain of 10 spheres (radius $a = 0.2$ µm) with a total length of $L = 6$ µm , circling clockwise along a tilted cone with a frequency of 25 Hz. The phases were chosen randomly under the constraint that collisions between cilia were prevented (in rare cases, when inconsistencies in datasets led to unavoidable collisions, a randomly chosen cilium was removed). The mobility matrix M of the system was calculated using the Green's function for point forces inside a spherical cavity as described in (Maul and Kim, 1994). For the diagonal elements (self-mobility of a particle) we used the expressions

$$\begin{aligned} \mathrm{M}_{\mathrm{ii}}^{\mathrm{rr}} &= \frac{1}{6\pi\eta \mathrm{a}}\left(1 - \frac{9}{4}\frac{\mathrm{a}}{\mathrm{R}}\frac{1}{1-\vec{\mathrm{x}}_{\mathrm{i}}^2/\mathrm{R}^2}\right) \\ \mathrm{M}_{\mathrm{ii}}^{\mathrm{tt}} &= \frac{1}{6\pi\eta \mathrm{a}}\left(1 - \frac{9}{8}\frac{\mathrm{a}}{\mathrm{R}}\left(\frac{1}{1-\vec{\mathrm{x}}_{\mathrm{i}}^2/\mathrm{R}^2} + 1 - \frac{1}{2}\frac{\vec{\mathrm{x}}_{\mathrm{i}}^2}{\mathrm{R}^2}\right)\right) \end{aligned} \qquad (3)$$

where M^{rr} denotes radial and M^{tt} the tangential mobility. $\vec{x}_i$ is the position of particle *i* relative to the center of the KV. In each step the forces on the particles representing points on cilia were calculated by solving the linear equation system $\vec{v}_i = \sum_j \mathrm{M}_{ij}\vec{F}_j$ and the fluid velocities subsequently from the Green's function.

The 2D flow profiles (e.g., Figure 4B) were created by averaging the velocity over time, over cilia phases, as well as across a layer between $z = -0.1R$ and $0.1R$. The flow profiles along the AP axis (Figure 5) were averaged over time, phases and a region between $y = -0.05R$ ... $0.05R$ and $z = -0.05R$ ... $0.05R$.

As a simple and well-defined measure to characterize the intensity and directionality of the flow, we introduced the effective angular velocity

$$\vec{\Omega} = \frac{5}{2\,VR^2}\int \vec{x}\times\vec{v}(\vec{x})dV\,, \qquad (4)$$

i.e., the angular velocity of a uniformly rotating sphere with the same angular momentum as the fluid in the KV (shown in Figure 4C). Note that the angular momentum is used solely as a velocity measure since the fluid inertia is negligible. $\vec{\Omega}$ can be calculated directly from the force distribution as

$$\vec{\Omega} = \frac{3}{16\pi\eta R^3}\sum_i (1 - \vec{x}_i^2/R^2)\ \vec{x}_i \times \vec{F}_i, \tag{5}$$

thus omitting the need for spatial integration. This non-trivial expression can be derived from the following considerations. From symmetry arguments, we know that the effective angular velocity caused by a point force $\vec{F}$ acting at point $\vec{x}$ inside the cavity can only have the form

$$\vec{\Omega} = w(|\vec{x}|)\ \vec{x} \times \vec{F} \tag{6}$$

with an unknown scalar function $w(r)$. We now consider a distribution of forces on a concentric sphere with radius r_i such that the velocity inside is

$$\vec{v}(\vec{x}) = \vec{\Omega}_0 \times \vec{x} \begin{cases} 1, & |\vec{x}| \le r_i \\ \frac{|\vec{x}|^{-3} - R^{-3}}{r_i^{-3} - R^{-3}}, & |\vec{x}| > r_i \end{cases}. \tag{7}$$

Using definition (4), the effective angular velocity of this distribution can be obtained by spatial integration with the result

$$\vec{\Omega} = \vec{\Omega}_0 \frac{3}{2}\left(1 - \frac{r_i^2}{R^2}\right)\left(\frac{R^3}{r_i^3} - 1\right)^{-1}. \tag{8}$$

At the same time, the force density at the inner sphere that maintains the velocity profile (7), is

$$\vec{f} = \vec{\Omega}_0 \times \vec{x}\ \ \frac{3\eta}{r_i}\left(1 - \frac{r_i^3}{R^3}\right)^{-1}. \tag{9}$$

Inserting this force density into equation (6) and integrating over the inner sphere gives

$$\vec{\Omega} = \vec{\Omega}_0 w(r_i) 8\pi\eta R^3 \left(\frac{R^3}{r_i^3} - 1\right)^{-1}. \tag{10}$$

The expressions (8) and (10) become equivalent when $w(r_i) = \frac{3}{16\pi\eta R^3}\left(1 - \frac{r_i^2}{R^2}\right)$, which leads to the equation (5) for the effective angular velocity.

Randomly generated vesicles

In addition to the available datasets, we extended our analysis to randomly generated cilia distributions that shared the main features with those observed in real KV. The vesicles were assigned a radius $R = 35\,\mu m$. We randomly distributed $N_c = 70$ cilia with a density function r that had its maximum at $(\alpha, \beta) = (0\,, 15°)$ and a pair correlation function g(γ) resembling the measured one (Figure 4C). All cilia were tilted meridionally (towards dorsal) with a tilt angle $\theta = 60° \times \cos\beta$. The randomly generated distributions allowed us to study the reliability of the proposed flow sensing hypotheses without being limited by the number of vesicles analyzed experimentally. In each simulation with randomly generated vesicles, 200 vesicles were simulated in order to obtain stable results.

Torques

To test the mechanosensing mechanism, we chose 3 immotile cilia situated in the left region of the KV (up to 45º away from the left pole), and 3 cilia situated in the right region of the KV (up to 45º away from the right pole). In case the number of immotile cilia in one region was insufficient we randomly assigned additional cilia as immotile. To test the case with maximum sensitivity the passive cilia were set normal to the surface ($\theta = 0$). After determining the forces on all cilia, the meridional component (in the direction of $\vec{e}_m$ on the left and $-\vec{e}_m$ on the right) of the torque vector was evaluated around the base of a cilium. Figure 7B,C shows the cumulative distributions of instantaneous values of these torques, their temporal average, as well as the temporal and ensemble average for a group of 3 cilia on each side.

Particle diffusion

We evaluated the model based on diffusion of signaling particles with a Langevin-dynamics simulation in the fluid velocity field evaluated before (Movie 3). We assumed that the particles are secreted from random points in a region 30º around anterior and captured whenever they encounter a cilium elsewhere. The simulation step was 0.001 s and the number of particles traced 1000. The diffusion constant of a particle was determined as $D = k_B T / (6\pi\eta\, r_{\text{Stokes}})$ with the fluid viscosity $\eta = 0.001\ \text{Pa s}$. Particles captured by cilia in the left and right region (up to 45º away from the left/right direction) were counted and the average ratio $N_{\text{left}} / N_{\text{left+right}}$, as well as its 5$^{\text{th}}$ and 95$^{\text{th}}$ percentile were plotted.

Statistical Analyses

We did not compute or predict the number of samples necessary for statistical differences because the standard deviation of our study's population was not known before starting our analysis. Biological replicate corresponds to the analysis of different embryos of the same stage. Technical replicate corresponds to the analysis of the same embryo imaged the same way. The sample size (replicate and number) to use was as defined by our ability to generate our datasets. We routinely analyze 5 to 10 embryos at each considered stage. Both the mean and the SD (Figure 4-figure supplement 1 and Table 1) were calculated for several of the KV and cilia features measured. For analyses between two groups of embryos, differences were considered statistically significant when the p-value < 0.05, as

determined using a two-tailed and paired Student's t-test. Circular statistics (resultant vector length r and 95% confidence intervals on the estimation of the mean angle) where computed using the CircStat Matlab toolbox (Berens, 2009). Descriptive statistics (cilia density maps) were displayed using Matlab custom scripts.

Appendix A

Derivation of the fluid velocity above a cilia layer with a density gradient

In order to derive the expression for the fluid velocity above an inhomogeneous layer of short cilia (Eq. 2), we look into the equivalent problem with a planar boundary condition. A symmetrically rotating cilium (no tilt) located at $\vec{X}$ is surrounded by a vortical flow with a far-field velocity profile

$$\vec{v}(\vec{x}) = \frac{3C_N\omega L^4}{16\pi\eta}\sin^2(\psi)\cos(\psi)\, z\, \frac{\vec{x}-\vec{X}}{|\vec{x}-\vec{X}|^5}\times\vec{e}_n \qquad (11)$$

where z is the height above the surface (Vilfan, 2012). A cilia carpet with surface density $\rho(\vec{X})$ then produces the flow

$$\vec{v}(\vec{x}) = \frac{C_N\omega L^4}{16\pi\eta}\sin^2(\psi)\cos(\psi)\int \rho(\vec{X}) z \left(\vec{\nabla}_X \frac{1}{|\vec{x}-\vec{X}|^3}\right)\times\vec{e}_n\, dS \qquad (12)$$

By applying partial integration the expression can also be written as

$$\vec{v}(\vec{x}) = -\frac{C_N\omega L^4}{16\pi\eta}\sin^2(\psi)\cos(\psi)\int \vec{\nabla}\rho(\vec{X})\times\vec{e}_n \frac{z}{|\vec{x}-\vec{X}|^3}\, dS \qquad (13)$$

For a small z, the integral yields $2\pi\vec{\nabla}\rho\times\vec{e}_n$ and we obtain Eq. (2). Because we assumed $L \ll R$, the derivation is equally valid for a non-planar (e.g., spherical) boundary condition. Thus, the effective slip velocity only depends on the density gradient. An infinite surface, uniformly lined with rotating cilia, does not produce any far-field flow.

Appendix B

Thermal noise on an elastic cilium

To estimate the thermal noise on a cilium, we treat it as an elastic beam with a flexural rigidity of $EI = 3{\times}10^{-23}\mathrm{Nm}^2$ (Battle et al., 2015). For cilia of this length, the dynamics is dominated by the fundamental bending mode and the cilium can be treated as a damped harmonic oscillator. The tip of the cilium then acts as an elastic spring with a spring constant $K = 3\,EI/L^3$. From the equipartition theorem it follows that the r.m.s. tip deflection is $\sqrt{k_B T/K}$, which corresponds to a torque measured at the base of the cilium ($\tau = K\,L\,\sqrt{k_B T/K} = \sqrt{3k_B T\,EI\,/\,L} = 2.5{\times}10^{-19}$ Nm). The relaxation rate of the cilium is $\Gamma = EI\,k_1^4/(C_N\,L^4)$ with $k_1 \approx 1.89$ (Battle et al., 2015), which gives Γ=80 s^{-1} and also determines the corner frequency of thermal noise. The spectral density of the force fluctuations is therefore

$$\langle \tau^2(\omega) \rangle = \frac{2}{\pi}\, k_B T\, KL^2\, \frac{\frac{1}{\Gamma}}{1+\frac{\omega^2}{\Gamma^2}}\,. \qquad (14)$$

A low pass filter with a time constant *T* reduces the spectral density at frequency ω by a factor $1/(1+(\omega T)^2)$. The total noise amplitude after filtering is given by the integral over the frequency spectrum

$$\langle \tau_f^2 \rangle = \int_0^\infty \frac{\langle \tau^2(\omega) \rangle}{1+(\omega T)^2}\, d\omega = \frac{\langle \tau^2 \rangle}{1+\Gamma T}\,. \qquad (15)$$

To reduce the detected r.m.s. amplitude of thermal noise to $2{\times}10^{-20}$ Nm, well below the proposed threshold for flow sensing, a time constant *T*=2 s is necessary.

In a similar way, we can estimate the effect of low-pass filtering on the noise that is caused by the beating of adjacent cilia. The flow calculation on mid- and late stage KV yields an average r.m.s. amplitude of the oscillatory torque $\tau_{osc}=9{\times}10^{-19}$ Nm, mostly with the ciliary beating frequency $\omega_0 = 2\,\pi{\times}25\ \mathrm{s}^{-1}$ (although higher harmonics are present). After filtering, the amplitude is reduced to $\tau_{\mathrm{osc-f}} = \tau_{\mathrm{osc}}/\sqrt{1+(\omega_0 T)^2}$. The filtered amplitude can be brought down to the same level ($\tau_{\mathrm{osc-f}} = 2{\times}10^{-20}\ \mathrm{Nm}$) with a time constant *T*=0.3 s.

The estimate shows that temporal averaging with a time constant longer than 2 s suppresses both the thermal and the oscillatory noise well below the estimated detection threshold. Spatial variability of the flow, on the other hand, still requires averaging over several immotile cilia.

Acknowledgements

We thank C. Wyart, C. Norden, M. Blum, D. Riveline, E. Beaurepaire, G. Pakula and the Vermot lab for discussion and thoughtful comments on the manuscript, in particular R. Chow for her help with editing. We thank the Lopes group and the Furthauer group for sharing data prior to publication. We thank B. Ciruna for providing fish stocks. We thank the IGBMC fish facility (S. Geschier and S. Gredler) and the IGBMC imaging center, in particular B. Gurchenkov, P. Kessler, M. Koch and D. Hentsch. This work was supported by HFSP, INSERM, AFM, FRM (DEQ20140329553), the European seventh framework program (MC-IRG256549 and MC-IRG268379), ANR (ANR-12-ISV2-0001, ANR-11-EQPX-0029, ANR-2010-JCJC-1510-01) and by the grant ANR-10-LABX-0030-INRT, a French State fund managed by the Agence Nationale de la Recherche under the frame program Investissements d'Avenir labeled ANR-10-IDEX-0002-02. R.R.F. was supported by the IGBMC International PhD program (LABEX). A.V. acknowledges support from the Slovenian Research Agency (grant J1-5437).

Movies

Movie 1: Visualization of the 3D-Cilia Map processing using raw data. The movie shows the 3D-Cilia Map processing workflow from 3D live imaging to Kupffer's vesicle (KV) surface segmentation and cilia vectorization. Firstly, one embryo from the *Tg* (*actb2:Mmu.Arl13b*-GFP) (Borovina et al., 2010) line soaked for 60 minutes in Bodipy TR (Molecular Probe) is imaged using 2PEF microscopy at 930 nm wavelength. A full z-stack of the KV can be seen. Subsequently, using Imaris (Bitplane Inc.), z-stacks are rendered into 3D volume and the KV cell surface is manually segmented so that only cilia at the cell surface surrounding the KV are visible. At the end we show the cilia vectorized in the whole volume imaged after 2PEF acquisition.

Movie 2: Display of the average flow in 3D at 3-, 8-, 9-14-somite stage (SS).
3D visualization of the calculated average flows at 3-SS (left), 8-SS (center) and 9-14-SS (right). See Figure 4B for the velocity color scale. The axes show the direction of anterior (red), left (green) and dorsal (blue). At all stages the average flow is directional around the dorsoventral (DV) axis, but the flow velocity increases between 3- and 9-14-SS. The flow profiles in the anteroposterior (AP)-left-right (LR) plane are shown in Figure 4B.

Movie 3: Simulated transport of signaling molecules in the Kupffer's vesicle (KV).
Panoramic view of the KV as seen from the center. The cilia distribution is obtained from vesicle 1 at 9-14-somite stage (Figure 6 – figure supplement 1C). Cilia shown in blue are motile and those in red immotile or undetermined. Signaling particles ($r_{\mathrm{Stokes}} = 5$ nm, not to scale), secreted from anterior (yellow), are subject to Brownian motion biased by the leftward flow until they are absorbed by a cilium (shown yellow after particle capture). 10s of video represent 1s real time.
Link for 360° video: https://youtu.be/1caSzBIe5rA

References

Battle, C., Ott, C.M., Burnette, D.T., Lippincott-Schwartz, J., and Schmidt, C.F. (2015). Intracellular and extracellular forces drive primary cilia movement. Proc Natl Acad Sci U S A *112*, 1410-1415.

Berens, P. (2009). CircStat: A MATLAB Toolbox for Circular Statistics. Journal of Statistical Software *31*.

Blum, M., Beyer, T., Weber, T., Vick, P., Andre, P., Bitzer, E., and Schweickert, A. (2009). Xenopus, an ideal model system to study vertebrate left-right asymmetry. Dev Dyn *238*, 1215-1225.

Blum, M., Feistel, K., Thumberger, T., and Schweickert, A. (2014a). The evolution and conservation of left-right patterning mechanisms. Development *141*, 1603-1613.

Blum, M., Schweickert, A., Vick, P., Wright, C.V., and Danilchik, M.V. (2014b). Symmetry breakage in the vertebrate embryo: when does it happen and how does it work? Dev Biol *393*, 109-123.

Borovina, A., Superina, S., Voskas, D., and Ciruna, B. (2010). Vangl2 directs the posterior tilting and asymmetric localization of motile primary cilia. Nat Cell Biol *12*, 407-412.

Brown, N.A., and Wolpert, L. (1990). The development of handedness in left/right asymmetry. Development *109*, 1-9.

Cartwright, J.H., Piro, O., and Tuval, I. (2004). Fluid-dynamical basis of the embryonic development of left-right asymmetry in vertebrates. Proc Natl Acad Sci U S A *101*, 7234-7239.

Cocucci, E., Racchetti, G., and Meldolesi, J. (2009). Shedding microvesicles: artefacts no more. Trends Cell Biol *19*, 43-51.

Compagnon, J., Barone, V., Rajshekar, S., Kottmeier, R., Pranjic-Ferscha, K., Behrndt, M., and Heisenberg, C.P. (2014). The notochord breaks bilateral symmetry by controlling cell shapes in the zebrafish laterality organ. Dev Cell *31*, 774-783.

Coutelis, J.B., Gonzalez-Morales, N., Geminard, C., and Noselli, S. (2014). Diversity and convergence in the mechanisms establishing L/R asymmetry in metazoa. EMBO Rep *15*, 926-937.

Dasgupta, A., and Amack, J.D. (2016). Cilia in vertebrate left-right patterning. Philos Trans R Soc Lond B Biol Sci *371*.

Delling, M., Indzhykulian, A.A., Liu, X., Li, Y., Xie, T., Corey, D.P., and Clapham, D.E. (2016). Primary cilia are not calcium-responsive mechanosensors. Nature *531*, 656-660.

Essner, J.J., Amack, J.D., Nyholm, M.K., Harris, E.B., and Yost, H.J. (2005). Kupffer's vesicle is a ciliated organ of asymmetry in the zebrafish embryo that initiates left-right development of the brain, heart and gut. Development *132*, 1247-1260.

Ferreira, R.R., and Vermot, J. (2017). The balancing roles of mechanical forces during left-right patterning and asymmetric morphogenesis. Mech Dev *144*, 71-80.

Francescatto, L., Rothschild, S.C., Myers, A.L., and Tombes, R.M. (2010). The activation of membrane targeted CaMK-II in the zebrafish Kupffer's vesicle is required for left-right asymmetry. Development *137*, 2753-2762.

Freund, J.B., Goetz, J.G., Hill, K.L., and Vermot, J. (2012). Fluid flows and forces in development: functions, features and biophysical principles. Development *139*, 1229-1245.

Goetz, J.G., Steed, E., Ferreira, R.R., Roth, S., Ramspacher, C., Boselli, F., Charvin, G., Liebling, M., Wyart, C., Schwab, Y.*, et al.* (2014). Endothelial cilia mediate low flow sensing during zebrafish vascular development. Cell Rep *6*, 799-808.

Gokey, J.J., Ji, Y., Tay, H.G., Litts, B., and Amack, J.D. (2016). Kupffer's vesicle size threshold for robust left-right patterning of the zebrafish embryo. Dev Dyn *245*, 22-33.

Gomez-Lopez, S., Lerner, R.G., and Petritsch, C. (2014). Asymmetric cell division of stem and progenitor cells during homeostasis and cancer. Cell Mol Life Sci *71*, 575-597.

Gros, J., Feistel, K., Viebahn, C., Blum, M., and Tabin, C.J. (2009). Cell movements at Hensen's node establish left/right asymmetric gene expression in the chick. Science *324*, 941-944.

Guirao, B., Meunier, A., Mortaud, S., Aguilar, A., Corsi, J.M., Strehl, L., Hirota, Y., Desoeuvre, A., Boutin, C., Han, Y.G.*, et al.* (2010). Coupling between hydrodynamic forces and planar cell polarity orients mammalian motile cilia. Nat Cell Biol *12*, 341-350.

Hamada, H., and Tam, P.P. (2014). Mechanisms of left-right asymmetry and patterning: driver, mediator and responder. F1000Prime Rep *6*, 110.

Hashimoto, M., Shinohara, K., Wang, J., Ikeuchi, S., Yoshiba, S., Meno, C., Nonaka, S., Takada, S., Hatta, K., Wynshaw-Boris, A.*, et al.* (2010). Planar polarization of node cells determines the rotational axis of node cilia. Nat Cell Biol *12*, 170-176.

Hilfinger, A., and Julicher, F. (2008). The chirality of ciliary beats. Phys Biol *5*, 016003.

Hirokawa, N., Tanaka, Y., and Okada, Y. (2009). Left-right determination: involvement of molecular motor KIF3, cilia, and nodal flow. Cold Spring Harb Perspect Biol *1*, a000802.

Hirokawa, N., Tanaka, Y., Okada, Y., and Takeda, S. (2006). Nodal flow and the generation of left-right asymmetry. Cell *125*, 33-45.

Hogan, M.C., Manganelli, L., Woollard, J.R., Masyuk, A.I., Masyuk, T.V., Tammachote, R., Huang, B.Q., Leontovich, A.A., Beito, T.G., Madden, B.J.*, et al.* (2009). Characterization of PKD protein-positive exosome-like vesicles. J Am Soc Nephrol *20*, 278-288.

Inaki, M., Liu, J., and Matsuno, K. (2016). Cell chirality: its origin and roles in left-right asymmetric development. Philos Trans R Soc Lond B Biol Sci *371*.

Inoue, M., Tanimoto, M., and Oda, Y. (2013). The role of ear stone size in hair cell acoustic sensory transduction. Sci Rep *3*, 2114.

Kimmel, C.B., Ballard, W.W., Kimmel, S.R., Ullmann, B., and Schilling, T.F. (1995). Stages of embryonic development of the zebrafish. Dev Dyn *203*, 253-310.

Kramer-Zucker, A.G., Olale, F., Haycraft, C.J., Yoder, B.K., Schier, A.F., and Drummond, I.A. (2005). Cilia-driven fluid flow in the zebrafish pronephros, brain and Kupffer's vesicle is required for normal organogenesis. Development *132*, 1907-1921.

Kreiling, J.A., Prabhat, Williams, G., and Creton, R. (2007). Analysis of Kupffer's vesicle in zebrafish embryos using a cave automated virtual environment. Dev Dyn *236*, 1963-1969.

Levin, M. (2005). Left-right asymmetry in embryonic development: a comprehensive review. Mech Dev *122*, 3-25.

Levin, M., and Mercola, M. (1998). The compulsion of chirality: toward an understanding of left-right asymmetry. Genes Dev *12*, 763-769.

Long, S., Ahmad, N., and Rebagliati, M. (2003). The zebrafish nodal-related gene southpaw is required for visceral and diencephalic left-right asymmetry. Development *130*, 2303-2316.

Lopes, S.S., Lourenco, R., Pacheco, L., Moreno, N., Kreiling, J., and Saude, L. (2010). Notch signalling regulates left-right asymmetry through ciliary length control. Development *137*, 3625-3632.

Marshall, W.F., and Kintner, C. (2008). Cilia orientation and the fluid mechanics of development. Curr Opin Cell Biol *20*, 48-52.

Maul, C., and Kim, S. (1994). Image systems for a Stokeslet inside a rigid spherical container Physics of Fluids *6*, 2221-2223.

McGrath, J., Somlo, S., Makova, S., Tian, X., and Brueckner, M. (2003). Two populations of node monocilia initiate left-right asymmetry in the mouse. Cell *114*, 61-73.

Montenegro-Johnson, T.D., Baker, D.I., Smith, D.J., and Lopes, S.S. (2016). Three-dimensional flow in Kupffer's Vesicle. J Math Biol.

Morrow, S.M., Bissette, A.J., and Fletcher, S.P. (2017). Transmission of chirality through space and across length scales. Nat Nanotechnol *12*, 410-419.

Muller, M., Heeck, K., and Elemans, C.P. (2016). Semicircular Canals Circumvent Brownian Motion Overload of Mechanoreceptor Hair Cells. PLoS One *11*, e0159427.

Naganathan, S.R., Furthauer, S., Nishikawa, M., Julicher, F., and Grill, S.W. (2014). Active torque generation by the actomyosin cell cortex drives left-right symmetry breaking. Elife *3*, e04165.

Naganathan, S.R., Middelkoop, T.C., Furthauer, S., and Grill, S.W. (2016). Actomyosin-driven left-right asymmetry: from molecular torques to chiral self organization. Curr Opin Cell Biol *38*, 24-30.

Nakamura, T., and Hamada, H. (2012). Left-right patterning: conserved and divergent mechanisms. Development *139*, 3257-3262.

Nakamura, T., Mine, N., Nakaguchi, E., Mochizuki, A., Yamamoto, M., Yashiro, K., Meno, C., and Hamada, H. (2006). Generation of robust left-right asymmetry in the mouse embryo requires a self-enhancement and lateral-inhibition system. Dev Cell *11*, 495-504.

Nauli, S.M., Kawanabe, Y., Kaminski, J.J., Pearce, W.J., Ingber, D.E., and Zhou, J. (2008). Endothelial cilia are fluid shear sensors that regulate calcium signaling and nitric oxide production through polycystin-1. Circulation *117*, 1161-1171.

Nonaka, S., Shiratori, H., Saijoh, Y., and Hamada, H. (2002). Determination of left-right patterning of the mouse embryo by artificial nodal flow. Nature *418*, 96-99.

Nonaka, S., Tanaka, Y., Okada, Y., Takeda, S., Harada, A., Kanai, Y., Kido, M., and Hirokawa, N. (1998). Randomization of left-right asymmetry due to loss of nodal cilia generating leftward flow of extraembryonic fluid in mice lacking KIF3B motor protein. Cell *95*, 829-837.

Nonaka, S., Yoshiba, S., Watanabe, D., Ikeuchi, S., Goto, T., Marshall, W.F., and Hamada, H. (2005). De novo formation of left-right asymmetry by posterior tilt of nodal cilia. PLoS Biol *3*, e268.

Okabe, N., Xu, B., and Burdine, R.D. (2008). Fluid dynamics in zebrafish Kupffer's vesicle. Dev Dyn *237*, 3602-3612.

Okada, Y., Takeda, S., Tanaka, Y., Izpisua Belmonte, J.C., and Hirokawa, N. (2005). Mechanism of nodal flow: a conserved symmetry breaking event in left-right axis determination. Cell *121*, 633-644.

Raposo, G., and Stoorvogel, W. (2013). Extracellular vesicles: exosomes, microvesicles, and friends. J Cell Biol *200*, 373-383.

Rydholm, S., Zwartz, G., Kowalewski, J.M., Kamali-Zare, P., Frisk, T., and Brismar, H. (2010). Mechanical properties of primary cilia regulate the response to fluid flow. Am J Physiol Renal Physiol *298*, F1096-1102.

Sampaio, P., Ferreira, R.R., Guerrero, A., Pintado, P., Tavares, B., Amaro, J., Smith, A.A., Montenegro-Johnson, T., Smith, D.J., and Lopes, S.S. (2014). Left-right organizer flow dynamics: how much cilia activity reliably yields laterality? Dev Cell *29*, 716-728.

Sarmah, B., Latimer, A.J., Appel, B., and Wente, S.R. (2005). Inositol polyphosphates regulate zebrafish left-right asymmetry. Dev Cell *9*, 133-145.

Satir, P., and Christensen, S.T. (2007). Overview of structure and function of mammalian cilia. Annu Rev Physiol *69*, 377-400.

Schweickert, A., Weber, T., Beyer, T., Vick, P., Bogusch, S., Feistel, K., and Blum, M. (2007). Cilia-driven leftward flow determines laterality in Xenopus. Curr Biol *17*, 60-66.

Shah, A.S., Ben-Shahar, Y., Moninger, T.O., Kline, J.N., and Welsh, M.J. (2009). Motile cilia of human airway epithelia are chemosensory. Science *325*, 1131-1134.

Shinohara, K., and Hamada, H. (2017). Cilia in Left-Right Symmetry Breaking. Cold Spring Harb Perspect Biol.

Shinohara, K., Kawasumi, A., Takamatsu, A., Yoshiba, S., Botilde, Y., Motoyama, N., Reith, W., Durand, B., Shiratori, H., and Hamada, H. (2012). Two rotating cilia in the node cavity are sufficient to break left-right symmetry in the mouse embryo. Nat Commun *3*, 622.

Smith, D.J., Blake, J.R., and Gaffney, E.A. (2008). Fluid mechanics of nodal flow due to embryonic primary cilia. J R Soc Interface *5*, 567-573.

Smith, D.J., Montenegro-Johnson, T.D., and Lopes, S.S. (2014). Organized chaos in Kupffer's vesicle: how a heterogeneous structure achieves consistent left-right patterning. Bioarchitecture *4*, 119-125.

Song, H., Hu, J., Chen, W., Elliott, G., Andre, P., Gao, B., and Yang, Y. (2010). Planar cell polarity breaks bilateral symmetry by controlling ciliary positioning. Nature *466*, 378-382.

Supatto, W., Fraser, S.E., and Vermot, J. (2008). An all-optical approach for probing microscopic flows in living embryos. Biophys J *95*, L29-31.

Supatto, W., and Vermot, J. (2011). From cilia hydrodynamics to zebrafish embryonic development. Curr Top Dev Biol *95*, 33-66.

Tabin, C.J., and Vogan, K.J. (2003). A two-cilia model for vertebrate left-right axis specification. Genes Dev *17*, 1-6.

Vilfan, A. (2012). Generic flow profiles induced by a beating cilium. Eur Phys J E Soft Matter *35*, 72.

Wagnière, G.H. On Chirality and the Universal Asymmetry: Reflections on Image and Mirror Image

Wang, G., Cadwallader, A.B., Jang, D.S., Tsang, M., Yost, H.J., and Amack, J.D. (2011). The Rho kinase Rock2b establishes anteroposterior asymmetry of the ciliated Kupffer's vesicle in zebrafish. Development *138*, 45-54.

Wang, G., Manning, M.L., and Amack, J.D. (2012). Regional cell shape changes control form and function of Kupffer's vesicle in the zebrafish embryo. Dev Biol *370*, 52-62.

Wang, J.S., Wang, G., Feng, X.Q., Kitamura, T., Kang, Y.L., Yu, S.W., and Qin, Q.H. (2013). Hierarchical chirality transfer in the growth of Towel Gourd tendrils. Sci Rep *3*, 3102.

Wolpert, L. (2014). Revisiting the F-shaped molecule: is its identity solved? Genesis *52*, 455-457.

Wood, C.R., Huang, K., Diener, D.R., and Rosenbaum, J.L. (2013). The cilium secretes bioactive ectosomes. Curr Biol *23*, 906-911.

Yoshiba, S., and Hamada, H. (2014). Roles of cilia, fluid flow, and Ca2+ signaling in breaking of left-right symmetry. Trends Genet *30*, 10-17.

Yoshiba, S., Shiratori, H., Kuo, I.Y., Kawasumi, A., Shinohara, K., Nonaka, S., Asai, Y., Sasaki, G., Belo, J.A., Sasaki, H.*, et al.* (2012). Cilia at the node of mouse embryos sense fluid flow for left-right determination via Pkd2. Science *338*, 226-231.

Yuan, S., Zhao, L., Brueckner, M., and Sun, Z. (2015). Intraciliary calcium oscillations initiate vertebrate left-right asymmetry. Curr Biol *25*, 556-567.

Results Chapter II:

Manuscript 4

Origins of meridional tilt in the zebrafish left-right organizer

Rita R. Ferreira[1,2,3,4], Lhéanna Klaeyle[1,2,3,4], Guillaume Pakula[5], Willy Supatto[5,#,*] and Julien Vermot[1,2,3,4,#,*]

[1]Institut de Génétique et de Biologie Moléculaire et Cellulaire, Illkirch, France
[2]Centre National de la Recherche Scientifique, UMR7104, Illkirch, France
[3]Institut National de la Santé et de la Recherche Médicale, U964, Illkirch, France
[4]Université de Strasbourg, Illkirch, France
[5]Laboratory for Optics and Biosciences, Ecole Polytechnique, Centre National de la Recherche Scientifique (UMR7645), Institut National de la Santé et de la Recherche Médicale (U1182) and Paris Saclay University, Palaiseau, France

Co-senior authors
***contacts:** willy.supatto@polytechnique.edu, julien@igbmc.fr

Abstract

Spatial orientation is a key functional feature of the motile cilia involved in LR symmetry breaking. The crucial role of the cilia angles phi (φ) and theta (θ), as determinants of the strength and directionality of the induced flow, raise the question of its origin *in vivo*. To understand the potential mechanism(s) behind the meridional tilt observed *in vivo* using the *3D-Cilia Map* methodology, we performed a comprehensive analysis of the main biophysical parameters of cilia, in a group of pre-selected conditions known to impact LR determination. Altogether, our results demonstrate most of the pre-selected conditions studied had no impact on the meridional tilt. In conditions in which cilia motility was impaired, however, the meridional tilt was strikingly lost. Furthermore, our study also suggests that cilia motility is needed to properly orient cilia during development of the KV. For the first time we reveal a surprising trend of asymmetric cilia implantation after 3-SS that increases with time. By performing the most comprehensive study to date of cilia orientation in the KV, we present new insights on the role of motile cilia during LR determination in zebrafish.

Introduction

Cilia driven flows organize the left-right (LR) embryonic axis in most vertebrates. These cilia mediated flows operate in the so-called LR organizer (LRO) – a ciliated cavity present in most vertebrates – to control and maintain the establishment of the internal organ asymmetric polarity. In zebrafish, the LRO is called the Kupffer's vesicle (KV) (**Fig.1A**). The cilia-generated flow triggers an asymmetric calcium response on the left side of the cavity (Francescatto et al., 2010; Sarmah et al., 2005; Yuan et al., 2015), and consequently a left-biased asymmetric pattern of gene expression (Essner et al., 2005; Kramer-Zucker et al., 2005).

Spatial orientation is a key functional feature of the motile cilia involved in LR symmetry breaking. The crucial role of the cilia angles *phi* (φ) and *theta* (θ), as determinants of the strength and directionality of the induced flow (Supatto et al., 2008; Supatto and Vermot, 2011), raises the question of their origins *in vivo*. In the mouse, cilia tilt seems to be dependent on the planar cell polarity (PCP) pathway and the shape of the node cells (Hashimoto et al., 2010; Marshall and Kintner, 2008). Another example of a clear coupling between cilia orientation and directional flow has been shown in ependymal cilia (Guirao et al., 2010). However the mechanism that sets the cilia tilt in the zebrafish LRO is not completely clear. Making use of *3D-Cilia Map* (Manuscript 2), we tried to elucidate the mechanism behind the meridional tilt observed *in vivo* in the zebrafish KV (Manuscript 3).

The zebrafish KV is an asymmetric organ, regarding the distribution of ciliated cells in the anterior-posterior (AP) axis (Kreiling et al., 2007; Okabe et al., 2008; Wang et al., 2011; Wang et al., 2012)(reviewed in (Ferreira and Vermot, 2017). The positioning of more ciliated cells in the anterior region of the KV is thought to be a critical step to drive a stronger leftward fluid flow across the anterior pole, capable of triggering the left-biased expression of LR markers in the lateral plate mesoderm (LPM), which is dependent on Myosin II activity and its activation by the Rock2b (Rho kinase) protein (Wang et al., 2012). The current model proposes Rock2b regulates Myosin II activity, which then controls cell-cell tension during the KV morphogenesis. In addition, actomyosin contractility is also required for basal body migration to the apical surface of cells to form cilia (Hong et al., 2015; Pitaval et al., 2010) All these evidences raise the possibility that the rock2b-Myosin II pathway might influence the biophysical parameters of cilia in the KV, more specifically the meridional tilt.

Cilia motility has also been shown to be critical for the development and function of several organs (Colantonio et al., 2009; Jaffe et al., 2016). Given the LR symmetry-breaking fluid-flow is generated by motile cilia in the zebrafish KV, defects in cilia motility are closely linked with LR abnormalities (Essner et al., 2005; Kramer-Zucker et al., 2005). Cilia motility is highly dependent on the presence of dynein arms, which are attached to the microtubules, and radial spokes (Colantonio et al., 2009; Jaffe et al., 2016; Lindemann and Lesich, 2010). Recently, it was reported cilia motility and cilia polarization could be linked, in the zebrafish kidney cells and Xenopus skin (Jaffe et al., 2016), however the role of motility in cilia orientation at the level of the KV remains unknown. In zebrafish, *lrdr1* (*left-right dynein related-1*) is expressed in the KV precursor cells (dorsal forerunner cells, DFCs) and in the KV itself

(Essner et al., 2005; Essner et al., 2002). In the mouse Node, *lrdr1* is required for cilia motility (Kawakami et al., 2005) and proper development of an asymmetric fluid-flow (Essner et al., 2005). On the other hand, LRRC50 (leucine-rich repeat (LRR) containing protein 50) is a 562 amino acid protein, which in zebrafish is expressed in tissues that contain motile cilia (Jaffe et al., 2016; Sullivan-Brown et al., 2008). A mutant allele within one of the LRR domains affects its ability to interact with specific targets important for cilia motility (Sullivan-Brown et al., 2008). Lrrc50 mRNA is provided maternally and thus expressed at KV stages (Sullivan-Brown et al., 2008). The role of cilia motility in the establishment of the meridional tilt in the KV, however, remains unstudied.

PCP proteins, initially identified in *Drosophila melanogaster*, are required to establish cell polarity within tissues across a large variety of animal species. Zebrafish embryos carrying mutations in several of the Wnt/PCP pathway core components exhibit a characteristic morphogenetic phenotype, due to impaired convergent extension movements (Heisenberg et al., 2000; Kilian et al., 2003; Marlow et al., 1998). The zebrafish *trilobite* locus encodes a Van Gogh/Strabismus homologue, Van gogh-like 2 (*Vangl2*), which is essential for PCP signaling (Jessen and Solnica-Krezel, 2004). *Vangl2* function is required for the posterior tilt observed in KV cilia, and anomalies in cilia orientation disrupt the cilia-driven flow and thus LR determination (Borovina et al., 2010). Still, the involvement of PCP pathway in setting the meridional tilt remains unclear.

The “two-cilia model” for the mechanism of LR symmetry-breaking argues that immotile cilia present in the LRO detect and respond to the nodal flow through a Pkd2 (polycystic kidney disease-2 or Trpp2)-mediated mechanism, which is consistent with Polycystin 2 (PC2) having a role upstream of asymmetric Nodal gene transcription (Field et al., 2011; Kamura et al., 2011; McGrath et al., 2003; Pennekamp et al., 2002; Schottenfeld et al., 2007; Yoshiba et al., 2012; Yuan et al., 2015). Human PKD2 encodes a Ca^{2+}-activated, non-specific cation channel, named PC2 (Gonzalez-Perrett et al., 2001; Hanaoka et al., 2000; Vassilev et al., 2001), and mutations in PKD2 cause autosomal dominant polycystic kidney disease in humans (reviewed in (Boucher and Sandford, 2004; Wu and Yu, 2016)). In the mouse LRO, endogenous Trpp2 is localized in the two populations of ciliated cells in the node, however the PC2 is required specifically in the peripheral cells for sensing the nodal flow (Yoshiba et al., 2012) and trigger a left-specific intracellular calcium release in the node. In zebrafish, *pkd2/trpp2* has been shown to be key for the origin of the intra-ciliary asymmetric calcium oscillations in the KV (Yuan et al., 2015). Recently a contradictory report has demonstrated that intra-ciliary calcium oscillations are not observed in the mouse node in response to flow forces, questioning the role of Trpp2 as mechanosensor in this context (Delling et al., 2016) (reviewed in (Ferreira and Vermot, 2017)). Nevertheless, mouse and zebrafish mutants for Pkd2/Trpp2 have strong laterality defects (Pennekamp et al., 2002; Schottenfeld et al., 2007). Therefore, the involvement of the potential flow sensing mechanism in setting up the meridional tilt remains elusive.

The Nodal asymmetric signaling cascade initiates in the left LPM and dictates asymmetric organ morphogenesis. Expression of Nodal-related genes is both necessary and sufficient to induce the

correct asymmetric position of internal organs (*situs solitus*) (reviewed in (Ferreira and Vermot, 2017; Hamada et al., 2002; Hirokawa et al., 2012). *Southpaw* (*spaw*), a zebrafish nodal-related gene, is the first gene asymmetrically expressed in the LPM and is thought to establish the LR asymmetry through the induction of *pitx2*, another nodal-related gene, on the left LPM (Long et al., 2003). Loss-of-function experiments have shown that *spaw* is required for the establishment of visceral LR asymmetry, such as cardiac (both heart jogging and looping) and gut (Long et al., 2003). How 3D cilia orientation might be linked to the downstream LR gene cascade has not yet been studied.

To understand the potential mechanism(s) behind the establishment of the meridional tilt observed *in vivo* using *3D-Cilia Map* (Manuscript 3), we performed a comprehensive analysis of the main biophysical parameters of cilia (such as cilia density and 3D orientation), in a group of pre-selected conditions known to impact LR determination **(Fig.1B-C)**. Doing so, we not only further validated the *3D-Cilia Map* methodology but also generated the most comprehensive study up to date of cilia orientation in the zebrafish KV.

Altogether, our results demonstrate that most of the pre-selected conditions studied kept the meridional tilt. Only in the conditions in which cilia motility was impaired, was the meridional tilt lost. Furthermore, we revealed a surprising potential trend of asymmetric cilia implantation after 3-SS that increases with time.

Results

Here, we used our *3D-Cilia Map* methodology to analyze key biophysical parameters of KV cilia (such as cilia density and 3D orientation), in a group of pre-selected candidate conditions previously reported to impact LR determination **(Fig.1B-C)**. Based on previous reports indicating their involvement in LR symmetry breaking, we pre-selected candidates from the following signaling pathways: Rock2b-Myosin II, cilia motility (*lrdr1* and *lrrc50*), PCP (*Vangl2*), cilia mechanosensation (*pkd2/trpp2*) and Nodal-related gene cascade (*spaw*). For this study we took advantage of different analysis tools to impair gene expression and protein function, from morpholino-based (MO) knock-downs, to drug treatments and knock-out mutant lines **(Fig.1C)**. All the analyses of 3D cilia orientation were performed using embryos at 8-somite stage (SS), when flow in the KV is well established (Essner et al., 2005; Kramer-Zucker et al., 2005; Long et al., 2003; Lopes et al., 2010).

Validation of LR defects in pre-selected candidates

Before studying the biophysical parameters of cilia, we confirmed that all pre-selected candidates resulted in LR axis defects in our hands **(Fig.1C)**. For that purpose we examined the gene expression of *southpaw* (*spaw*) in the LPM in embryos between 17- to 19-SS (Long et al., 2003) by *in situ* hybridization (ISH) **(Supplemental Fig.1A)**. Heart and gut laterality were assessed in the same embryos, at 48- and 53-hours post-fertilization (hpf) respectively. The heart looping could be observed using bright-field imaging, and the gut laterality by ISH against *foxA3* (Monteiro et al., 2008) **(Supplemental Fig.1B)**. For simplicity, we merged the laterality information of heart and gut looping and described it according to the clinical terminology used: *situs solitus* (describes the normal condition: heart with a rightward loop and the gut showing the liver is on the left and the pancreas on the right), *situs inversus* (pathological condition characterized by a complete reversal of the organ laterality) and *heterotaxy* (pathological condition described by any combination of abnormal LR asymmetries that cannot be strictly classified as *situs solitus* or *situs inversus*) (Fliegauf et al., 2007; Ramsdell, 2005; Shapiro et al., 2014; Sutherland and Ware, 2009).

Only the *rock2b*$^{-/-}$ embryos did not show LR defects and was excluded from the 3D cilia orientation analysis. We are currently analyzing this *rock2b* mutant allele in more detail. All the other pre-selected conditions reveled laterality defects regarding either the expression pattern of *spaw* in the LPM or the internal organ *situs*, in comparison with wild-type transgenic embryos (**Fig. 2**, **Supplemental Fig. 2-6** and **Supplemental Table 1**, see figure legends for more details). These results confirmed the role of the pre-selected conditions in LR determination. Next we addressed their involvement in 3D cilia orientation using the *3D-Cilia Map* methodology.

Morphological parameters of the KV are extremely variable between embryos

As demonstrated in Manuscript 3 for wild-type embryos, we used the *3D-Cilia Map* methodology to analyze the biophysical parameters of KV cilia (such as cilia density and 3D orientation), but also to

study the general characteristics of the KV morphology for each embryo, such as size, volume, cilia number and cilia motility.

To assess the potential role of cilia meridional tilt in the LR defects observed in the candidates studied, we asked if the morphological parameters of the KV were affected following loss or depletion of candidate function. For that purpose, we measured the small and long axis of the oblate spheroid of the KV (**Supplemental Fig. 7A-B**) and its volume (**Supplemental Fig. 7C**). We also analyzed the total cilia number and density (**Supplemental Fig. 7D-E**). All parameters measured were extremely variable between embryos within the same developmental stage, even though the average values of all embryos per condition were similar to the wild-type at 8-SS **(Supplemental Tables 2-4).** This strong variability between embryos can be observed by the large distribution around the average value for each parameter measured (**Supplemental Fig. 7**). As demonstrated in Manuscript 3, cilia motility increases over time while the KV matures. Overall, for all candidates at 8-SS, the number of immotile cilia is almost insignificant (**Supplemental Fig. 8B-B'** and **Supplemental Tables 2-4)**. Only wild-type embryos at 3-SS had a significant number of immotile cilia (≈40%, **Supplemental Fig. 8B-B'**, and **Supplemental Table 2**). Conversely, in the cases in which cilia motility was disrupted, the number of motile cilia was reduced to zero (**Supplemental Fig. 8A-A', Supplemental Table 3** and **Movie 1**).

Despite the individual variability in the morphological parameters of the KV, the average embryo per pre-selected condition presented similar values as the wild-type at the same developmental stage, and thus we conclude that potential differences in 3D cilia orientation do not arise due to defects of the overall KV morphogenesis.

Disruption of the anterior cluster in *spaw*$^{-/-}$ embryos

Knowing cilia density is one of the key biophysical parameters to obtain a proper directional flow in the KV we decided to study the spatial distribution of cilia *in vivo*. Previous reports have shown cilia density varies along the anteroposterior (AP) axis, with the existence of an anterior cluster of ciliated cells in the KV (Borovina et al., 2010; Kreiling et al., 2007; Okabe et al., 2008; Supatto et al., 2008; Wang et al., 2011; Wang et al., 2012). In our previous work (Manuscript 3), we also observed a steep increase in cilia density in the anterior pole of the KV (about 4 times denser than posterior). Thus, we analyzed cilia spatial distribution in 3D for each pre-selected candidate in comparison with wild-type embryos at 8-SS. For all the conditions studied in this manuscript, only the two conditions from the Rock2b-Myosin II pathway were previously reported to disrupt the anterior cluster of ciliated cells (Wang et al., 2011; Wang et al., 2012). Concordantly, our results showed that blebbistatin-treated and *rock2b* morphant embryos (**Fig. 3**) seemed to lose, to some extent, the anterior cluster of ciliated cells. Analysis of both *lrrc50*$^{-/-}$/*lrrc50*$^{+/-}$ and *cup*$^{-/-}$/*non-cup* a clear cluster of cilia in the anterior pole of the KV, similar to that of wild-type embryos (**Fig. 3**). Surprisingly we also found a clear disruption of the cluster of ciliated cells in the *situs inversus*$^{-/-}$ (*spaw*) embryos (**Fig. 3**). Considering that *spaw* is thought to only act downstream of the fluid-flow for LR axis determination, this link with KV morphogenesis could open a new discussion on additional roles in this system. Furthermore, we found that for all candidates

A

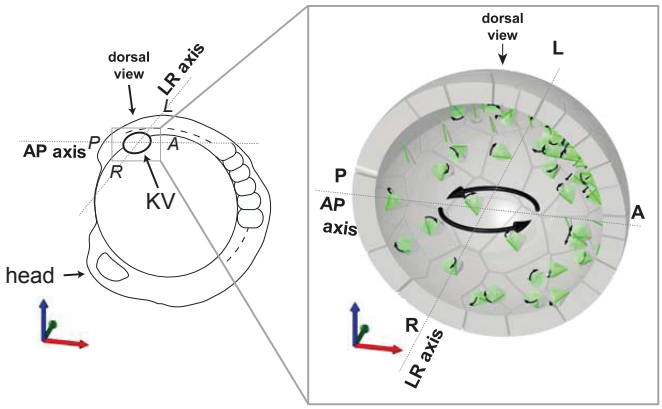

B

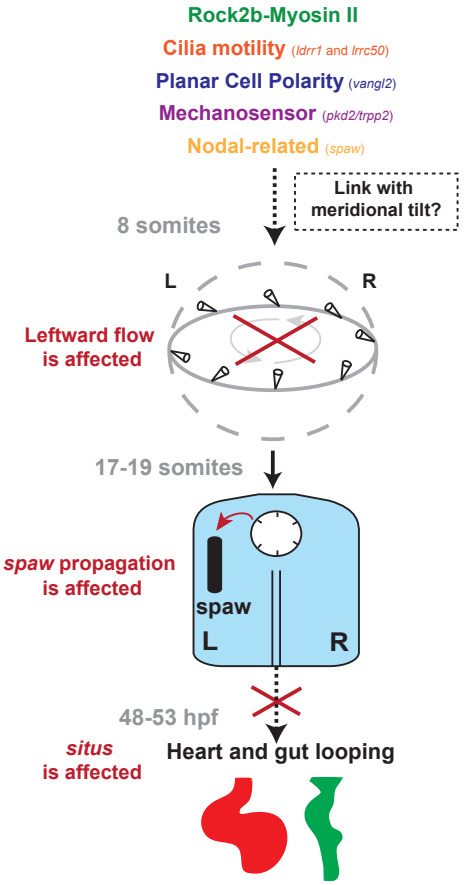

C

pre-selected conditions	Analysis tools		References
rock2b-Myosin II	*rock2b*-MO	MO designed to block the *rock2b* RNA splicing site	Wang et al., 2011
	blebbistatin drug	used to inhibit the ATPase activity of Myosin II	Wang et al., 2012
	rock2b mutant line	*rock2b* (Sa17708: point mutation)	Kettleborough et al., 2013
Cilia motility	*lrdr1*-MO	MO targeted against *dnah9* (*lrdr1*-MO) - motor dynein involved in cilia motility	Essner et al., 2005
	lrrc50 mutant line	*lrrc50* (tm317b: point mutation) - outer dynein subunit required for cilia motility	Sullivan-Brown et al., 2008 ; van Rooijen et al., 2008
Planar cell polarity	*trilobite/Vangl2* mutant line	Wnt/PCP mutants for *Vangl2*	Heisenberg et al., 2000
Cilia mechanosensor	*pkd2/trpp2* mutant line	*Pkd2/Trpp2*, called cup (tc241:point mutation)	Schottenfeld et al., 2007
Nodal-related gene	situs inversus/*spaw* mutant line	*spaw* (s457:point mutation)	Beis et al., 2005; Kalogirou et al., 2014

Manuscript 4 - Fig. 1: Schematics regarding the main question of my PhD project and the analysis tools used during the manuscript: (A) Schematics of the position of the KV in the embryo, of a transverse section of the KV and of the 3 main axes used to locate cilia positions in 3D (AP, DV and LR) and in 2D – adapted from Manuscript 3 **(B)** Schematic representation of the LR axis determination pathway within the scope of our study: the pre-selected candidate pathways are known to be involved in the LR determination, by affecting several steps of this pathways. All have been shown to affect the cilia-driven leftward flow in the KV that would consequently affect the left-sided spaw expression in the LPM and the asymmetric position of the internal organs. A possible link of these pathways with the meridional tilt observed in the KV remains unknown and is the main question we would like to address in this manuscript. **(C)** Table summarizing the pre-selected candidate pathways and the tools we used to address each pathway, with the respective references.
AP= anterior-posterior; LR= left-right; hpf= hours post-fertilization; L=left, R=right; MO=morpholino

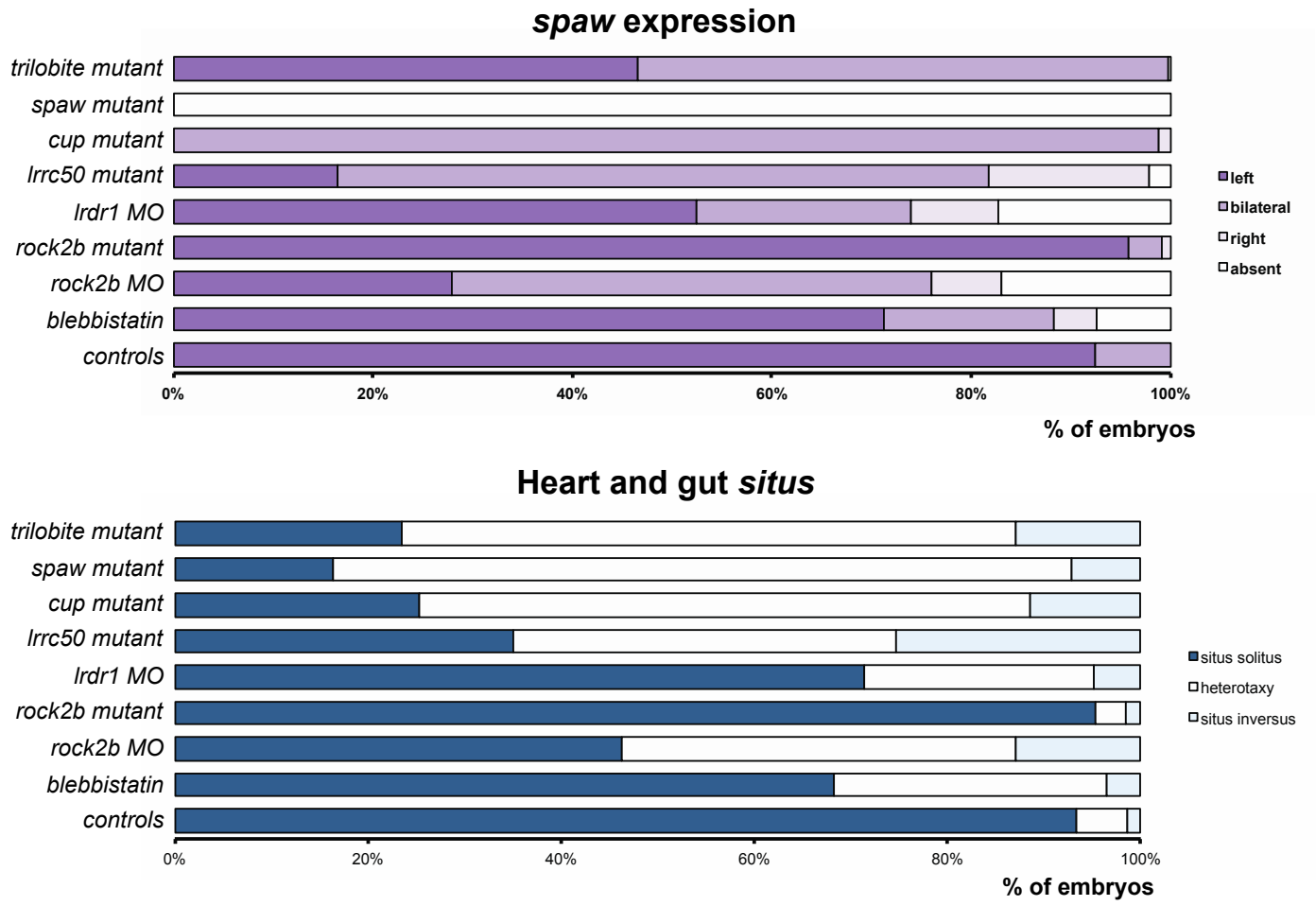

Manuscript 4 - Fig. 2: Quantification of the *spaw* expression patterns in the LPM and heart and gut *situs* in the pre-selected candidates. 2D 100% stacked bar plots depicting the expression patterns of *spaw* in the LPM (upper panel) and the *situs* phenotype (lower panel). Only the morpholino-based (MO) knock-downs, drug treatments and knock-out mutant lines are displayed in both bar plots in comparison with the wild-type transgenic controls. All the specific controls of each of the conditions can be found in the Supplemental Figures 2-6. Except for the *rock2b* mutant embryos, all the other pre-selected conditions revealed laterality defects regarding either the expression pattern of spaw in the LPM or the internal organ *situs*, in comparison with wild-type transgenic controls. The percentage of embryos can be read on the X axis. *Spaw* expression patterns in the LPM can be divided in left, bilateral, right or absent (Supplemental Figures 1). *Situs* phenotypes can be divided in *situs solitus*, *heterotaxy* and *situs inversus*, the clinical terminology.

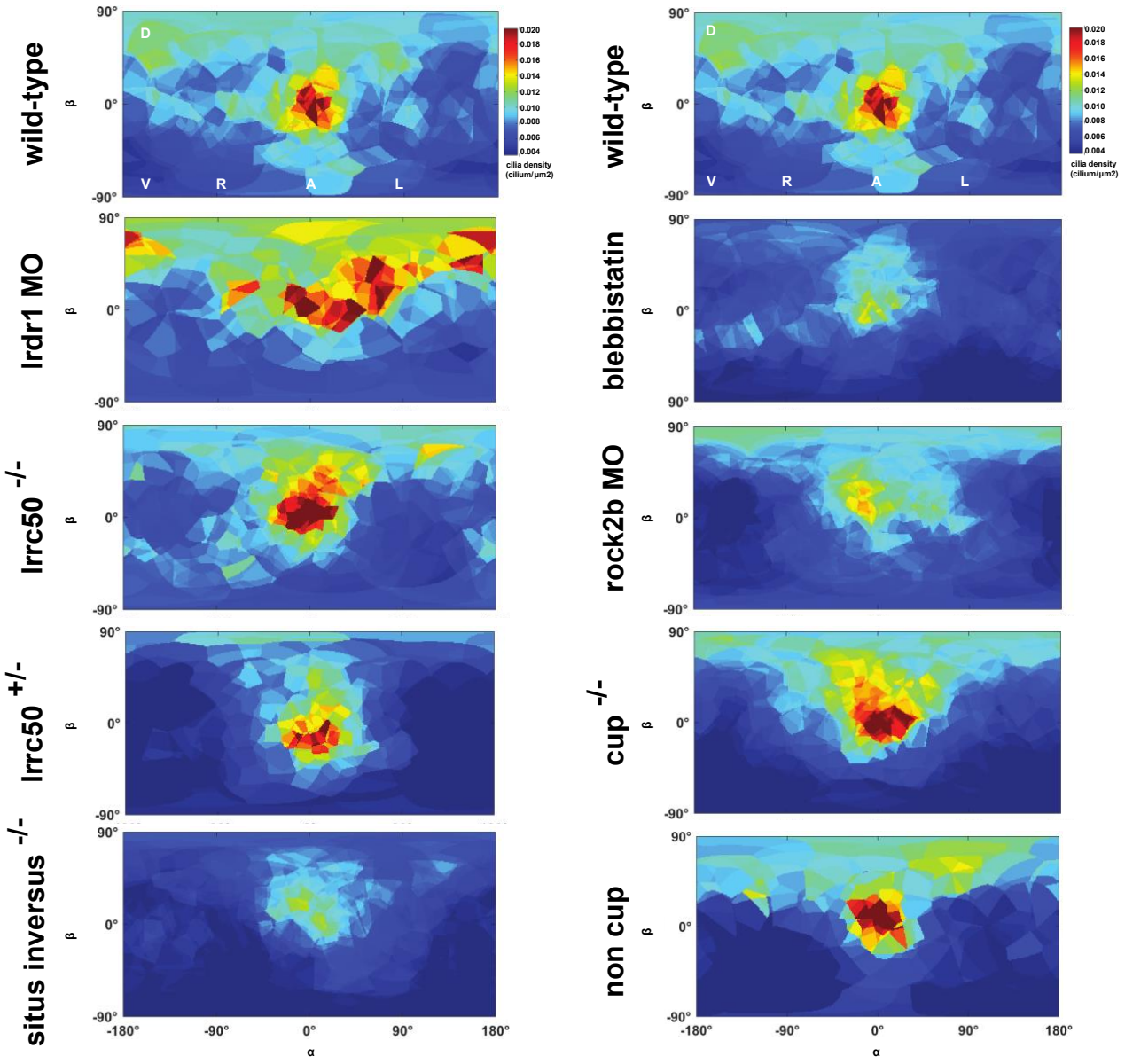

Manuscript 4 - Fig. 3: Averaged cilia density distribution for embryos at 8-SS, represented on a 2D flat map (cilia density in cilium/µm^2). Density maps from all vesicles per condition were averaged and represented on a 2D flat map with spherical coordinates. All maps have the same colour code. It is considered to have a ciliated cluster anteriorly when red in the region α=0° and β=0°. Blebbistatin-treated, *rock2b*-morphants and situs inversus$^{-/-}$ (*spaw*) mutants do not present the anterior cluster of ciliated cells. All the other conditions have an anterior cluster as the wild-type embryos. Cases code: lrdr1 MO = lrdr1-morphant; rock2b MO = rock2b-morphant; cup = cup$^{-/-}$; non cup = cup$^{+/+}$ or cup$^{+/-}$ siblings; situs inversus = spaw$^{-/-}$

studied, the average density of cilia did not display differences between the left and right hemispheres of the KV, as in wild-type controls (**Fig. 3**). *Lrdr1*-morphant embryos displayed the strongest phenotype with disruption of the normal AP and dorsoventral (DV) gradients of ciliated cells and smaller KVs (**Fig. 3**), even though embryos are viable until at least 53hpf (the latest time point studied), without obvious morphological defects.

These results show that both rock2b-Myosin II pathway candidates and, surprisingly, *spaw*$^{-/-}$ mutants disrupted the normal morphogenesis of the KV, more precisely the "KV remodeling" mechanism described by (Wang et al., 2012), in which the ciliated cluster is formed anteriorly in the KV during its morphogenesis. The other pre-selected candidates appear to have no direct role in the formation of the anterior ciliated cluster.

Cilia motility is crucial to set the meridional tilt

The cilia 3D orientation is key to generate a directional flow in the KV. As demonstrated in Manuscript 3, the flow generated by cilia within the KV is mainly governed by their tilted orientation, and the main angles that characterize cilia orientation are *theta* (θ) and *phi* (φ). In a local orthogonal basis $(\vec{e}_f, \vec{e}_n, \vec{e}_m)$ on the KV surface (**Fig. 4A-B**), θ (tilt) is the angle of the cilium respective to the KV surface normal (0° for a cilium orthogonal to the KV surface and 90° for parallel), and φ angle is the orientation of the cilium projected on the KV surface (0° for a cilium pointing in a meridional direction towards the dorsal pole (**Fig. 4A-B**). To have a first estimation of the cilia orientation in the KV, we measured θ and φ distributions and displayed the results in rosette-like plots (**Fig. 5-6,** see figure legends for details). Considering the physical environment of the KV (low *Reynolds* number in which inertia can be neglected) and the linearity of the *Stokes* equations, we can assume that the amplitude and direction of the average flow velocity will result from the average cilium for each KV. We defined the average cilium of each vesicle as the 3D mean resultant vector of all cilia unit vectors in the same local basis $(\vec{e}_f, \vec{e}_n, \vec{e}_m)$ (**Fig. 4A-B**) and the resultant vector length and angles (r, θ, φ) were quantified in individual vesicles. In the local basis $(\vec{e}_f, \vec{e}_n, \vec{e}_m)$, the average flow amplitude is then proportional to $r\sin(\theta)$ and its direction parallel to the cell surface in the φ +90° direction (**Fig. 4C**). The average cilium for each condition was displayed using K plots, in which θ and φ of the average cilium per vesicle can be seen in the same graph, but also the average θ and φ per condition studied (**Fig. 4C**), more details in the Figure legend). Studying the average cilium improved the inter-case comparisons on cilia orientation between controls and the pre-selected candidates (**Fig. 4C**) since both angles can be compared simultaneously in the same graph for the different conditions. Towards a more comprehensive analysis of 3D cilia orientation we first measured θ and φ distributions and then obtained the θ and φ values of the average cilium.

For all the candidates studied, the θ angle distributions showed an average value of θ that was always higher than zero (**Fig. 5** and **Supplemental Fig. 9A** and **Supplemental Tables 2-4**), a pre-requisite for the meridional tilt (by definition: θ > 0°). However, when cilia motility was impaired the outcomes were different: while in *Irrc50*$^{-/-}$ the average value of θ was similar to that of the *Irrc50*$^{+/-}$ siblings and

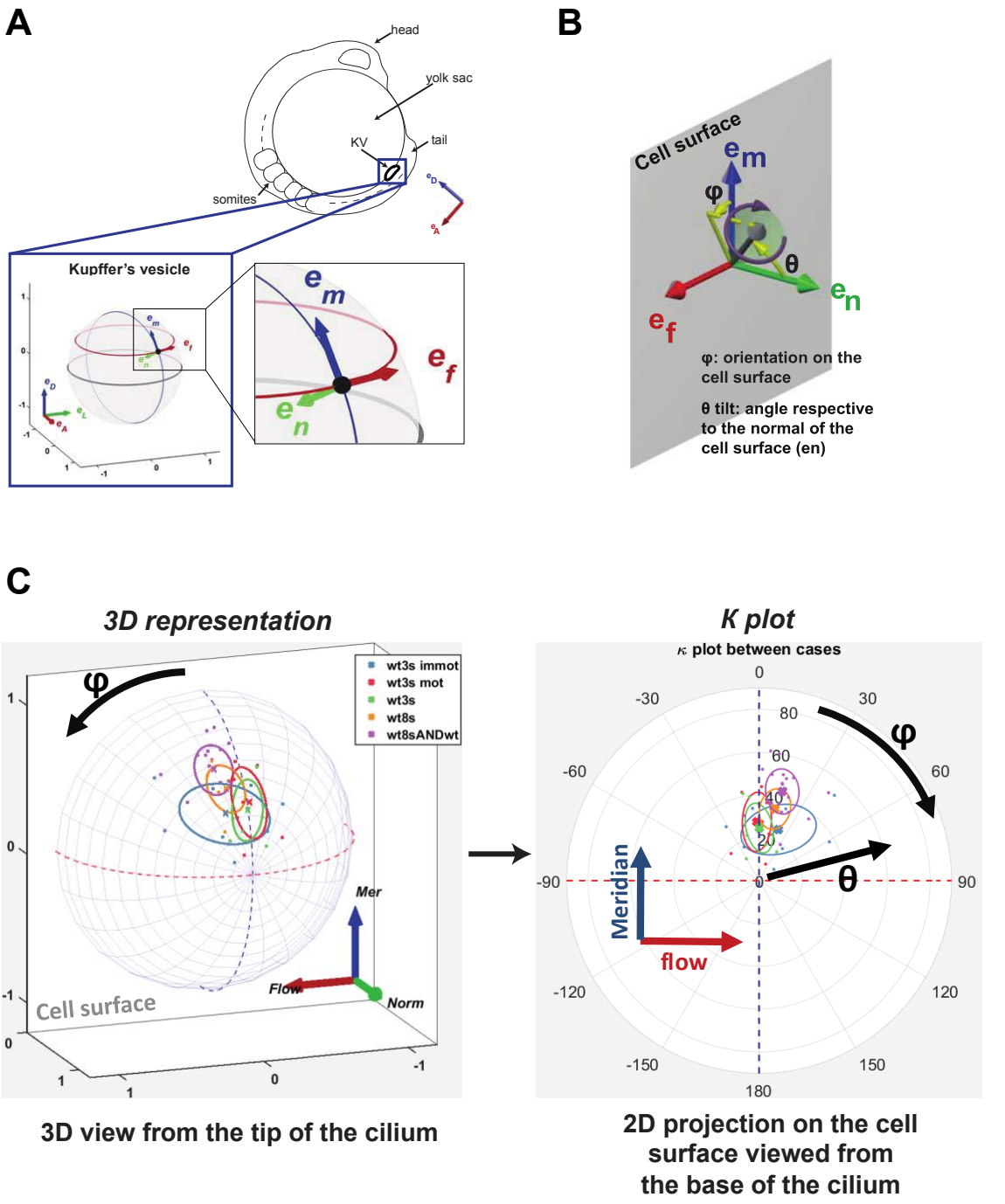

Manuscript 4 - Fig. 4: Reference frames used to analyse 3D cilia orientation in the KV and new display of the average cilium (K plots): (A) Side view of a schematic drawing of a zebrafish embryo at 5-SS, highlighting the Kupffer's vesicle (KV) localization (inside the blue box) and its orientation according to the reference frame (e_D and e_A). The zoom-up box (lower panel) shows the schematics of the two coordinate systems used (e_D, e_L, and e_A; e_m, e_n and e_f). The second zoom-up shows the local basis on the ellipsoid, which was used to orient the cilia. **(B)** Cilia orientations are represented by two angles: θ (tilt angle from the surface normal e_n) and φ (angle between the surface projection of the ciliary vector and the meridional direction). The cell surface is represented in grey, e_m direction in blue, e_f direction in red and the normal e_n in green. **(C)** Representation of the average cilium of each vesicle as the 3D mean resultant vector of all cilia unit vectors in the same local basis: 3D representation on the left panel, with a 3D view from the tip of each cilium; K plots displaying the values of θ and φ of the average cilium for each vesicle but also the average θ and φ per condition studied, in the same 2D graph (right panel). To draw the K plots we used the *kent_sp function* of the SPAK Matlab package (http://www.physiol.usyd.edu.au/~simonc/) – for more details please see (Leong and Carlile, 1998). For each case, the ellipse describes the distribution of individual vesicles and shows how concentrated the data is about the mean (cross). The lengths of the minor and major axes of the ellipse correspond to the standard deviation in each direction.
e_D= dorsal direction; e_L= left direction; e_A= anterior direction; e_m = aligned along a meridian from the ventral to the dorsal pole of the KV; e_f = follows a KV parallel (has the same direction as the typical flow observed within the vesicle); e_n = vector normal to the KV surface and pointing towards the center of the vesicle; D=dorsal pole; V= ventral pole; P = posterior pole; A = anterior pole

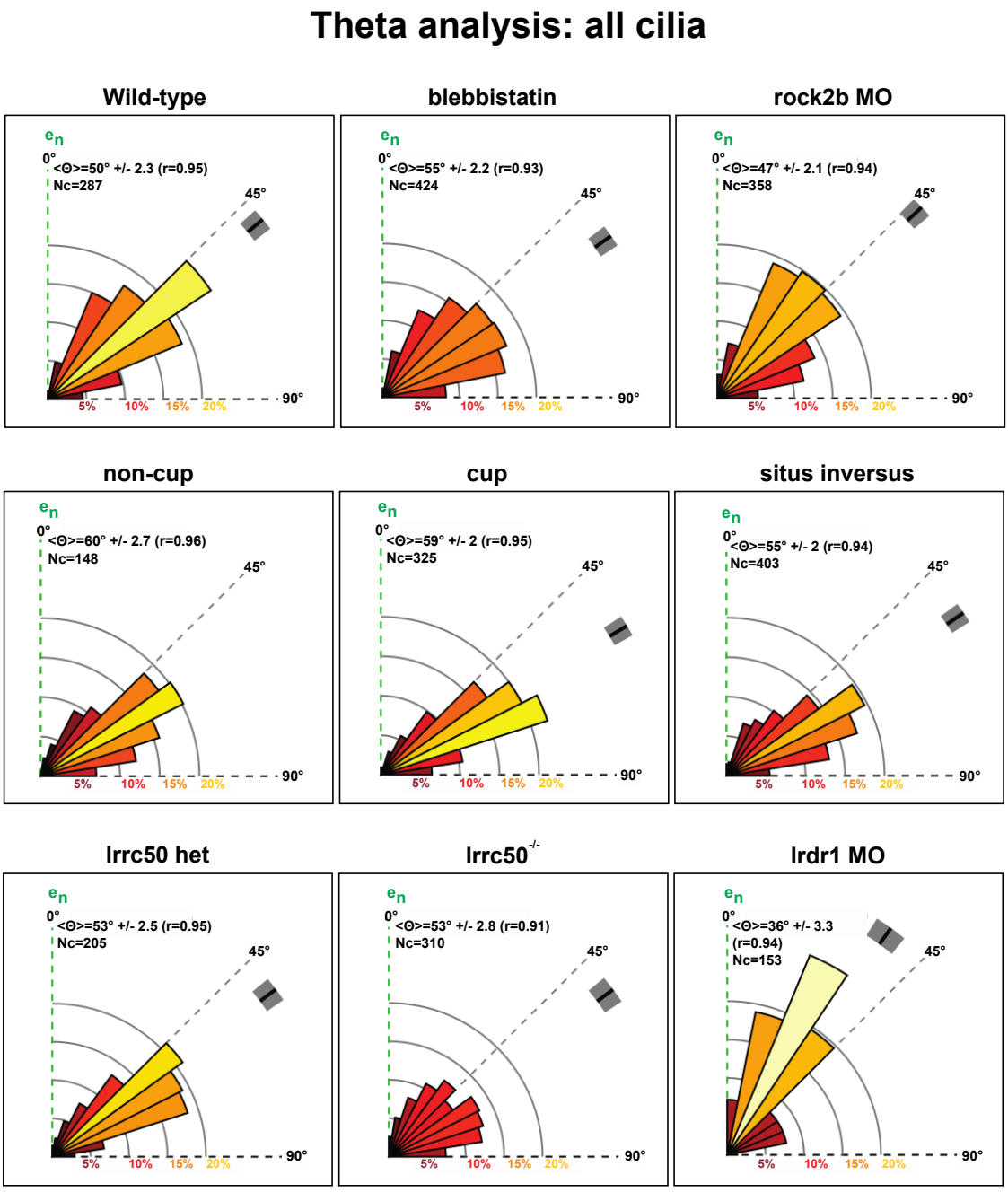

Manuscript 4 - Fig. 5: Distributions of θ at 8-SS for all cilia (motile + immotile) for all cases: Tilt angle (θ) distributions with the mean (black tick) and the 95% confidence interval (grey strip). For all conditions, the mean values of θ are higher than 0°. N_c= number of cilia; r = dispersion of the vector; e_m= aligned along a meridian from the ventral to the dorsal pole of the KV; e_f= follows a KV parallel (has the same direction as the typical flow observed within the vesicle); e_n= vector normal to the KV surface and pointing towards the centre of the vesicle. Cases code: lrdr1 MO = lrdr1-morphant; rock2b MO = rock2b-morphant; cup = cup$^{-/-}$; non cup = cup$^{+/+}$ or cup$^{+/-}$ siblings; situs inversus = spaw$^{-/-}$

wild-type, the *lrdr1*-MO revealed a very low value of θ, almost orthogonal to the cell surface (**Fig. 5**). Regarding the φ angle, we found most candidates have an average value of φ close to zero (**Fig. 6** and **Supplemental Fig. 9B** and **Supplemental Tables 2-4**), as expected for the meridional tilt (by definition: φ close to 0°). Yet, the two conditions in which cilia motility was impaired presented negative values of φ (**Fig. 6** and **Supplemental Fig. 9** and **Supplemental Tables 2-4**). For both *lrdr1*-MO and *lrrc50*$^{-/-}$, our results show their immotile cilia populations are randomly oriented in the KV (**Fig. 5-6**) and that the meridional tilt is lost.

Altogether, our results show that only the conditions in which motility was impaired caused a loss in the meridional tilt (**Fig. 5-6**). All the other candidates kept the meridional tilt observed in wild-type embryos at 8-SS. It is noteworthy, however, that in all those cases a small fraction of immotile cilia existed and those appear randomly oriented, reinforcing the idea that cilia motility is needed to properly orient cilia to reach the meridional tilt (**Supplemental Fig. 10-13**).

Next, we determined the θ and φ angles of the average cilium, with a special focus on the cilia motility-disrupted cases in which the meridional tilt was lost. The study of θ and φ values of the average cilium from 3-, 8-, and 9-14-SS wild-type embryos confirmed our previous conclusions about the increase in θ and φ over time (**Fig. 7**), which results in a meridional tilt that strengthens the directional flow in the KV. For 3-SS, we analyzed motile and immotile cilia separately. Motile cilia at 3-SS already have a meridional orientation (φ close to 0°), while immotile cilia are far from the meridional orientation (φ=20.7°, **Fig. 7** and **Supplemental Table 5**). Cilia in *lrrc50*$^{-/-}$ embryos, our average cilium results confirmed a total loss of the meridional tilt (**Fig. 8A** – yellow vs. green). Whereas, *lrrc50*$^{+/-}$ siblings have similar values of θ and φ compared to the wild-type 8-SS (**Fig. 8A** - brown vs. green), thus keeping the meridional tilt. In comparison with immotile cilia at 3-SS, *lrrc50*$^{-/-}$ cilia have much lower values for φ (φ=-33.9: **Fig.8B** and **Supplemental Table 5**), revealing a stronger misorientation.

In the absence of cilia motility (and flow) (Essner et al., 2005) we would expect that θ would be zero for both *lrrc50*$^{-/-}$ and *lrdr1*-morphant embryos, which was surprisingly not the case, particularly for the *lrrc50*$^{-/-}$ (θ=17.7º: **Fig.8B** and **Supplemental Table 5**). Having θ angle different from zero and very negative values of φ angle (φ=-36.9º, **Supplemental Table 5**), we conclude that *lrrc50*$^{-/-}$ embryos present a strongly disrupted KV cilia orientation. For the *lrdr1*-morphant (**Fig.8B**), we found less negative values for φ (φ=-13.9º, **Supplemental Table 5**) but with very low θ (θ=4.47, **Supplemental Table 5**). In fact, immotile cilia in the *lrdr1*-morphant embryos are very close of being orthogonal to the cell surface, which was not the case for *lrrc50*$^{-/-}$ immotile cilia as mentioned previously (**Fig.5**). Thus, despite both having immotile cilia populations, impaired expression of *lrdr1* and *lrrc50* impair cilia meridional tilt in different ways.

Analysis of the average cilium angles in the other pre-selected candidates, in which the meridional tilt was not affected, revealed very similar values of θ and φ as those seen in the wild-type 8-SS (**Supplemental Fig. 14** and **Supplemental Table 5**). The only exception was the *rock2b*-morphant cases that had lower values of θ and φ compared to wild-type 8-SS (**Supplemental Fig. 14C** and **Supplemental Table 5**), although the biological relevance of this remains unknown.

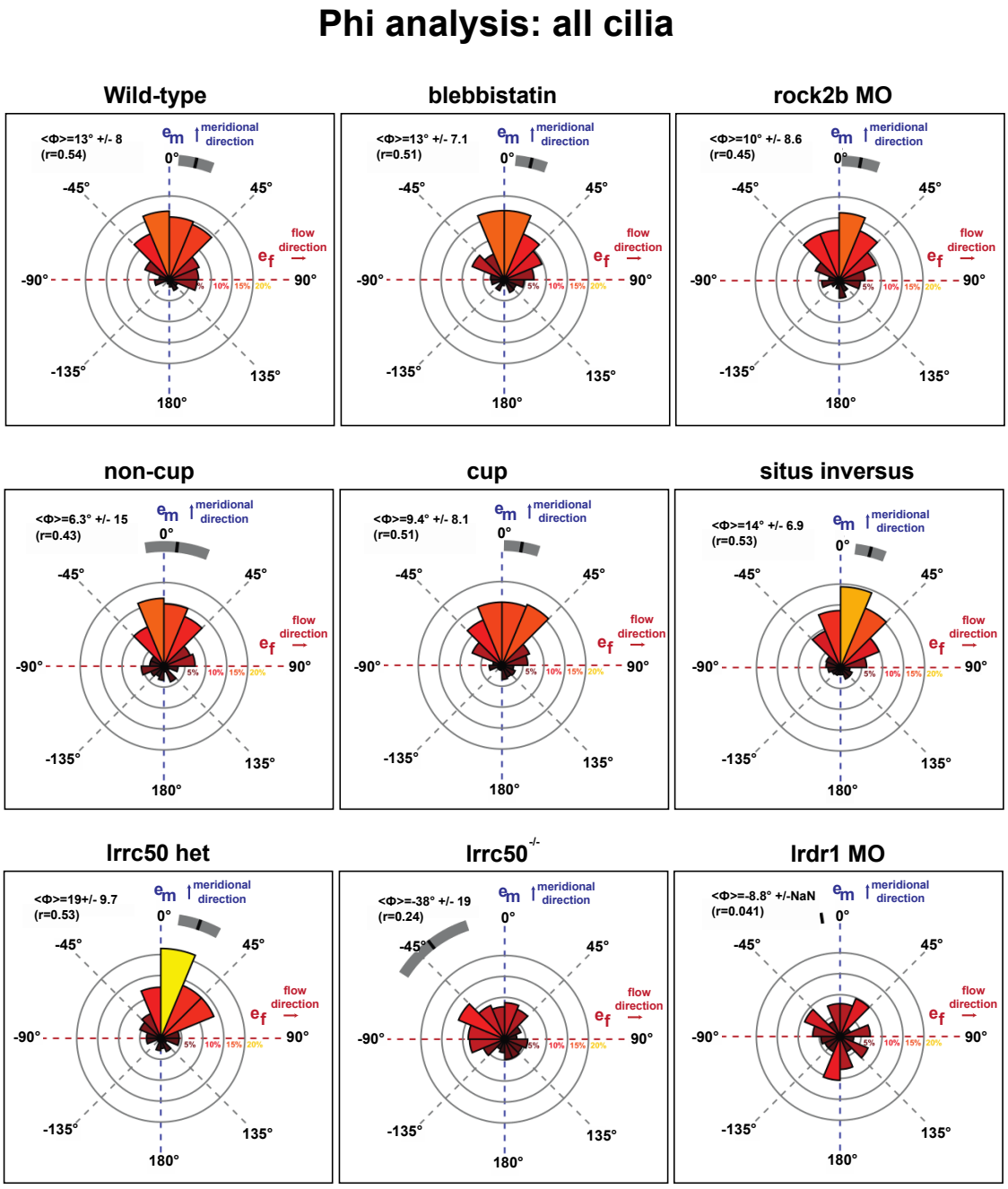

Manuscript 4 - Fig. 6: Distributions of φ at 8-SS for all cilia (motile + immotile) for all cases: Rosette plots showing the φ angle distribution values and the mean (black tick) with a 95% confidence interval (grey strip). In each rosette plot, 0° means the meridional direction and 90° the direction of the flow. In the absence of motility, the meridional orientation is lost. r = dispersion of the vector; e_m= aligned along a meridian from the ventral to the dorsal pole of the KV; e_f= follows a KV parallel (has the same direction as the typical flow observed within the vesicle). Cases code: lrdr1 MO = lrdr1-morphant; rock2b MO = rock2b-morphant; cup = cup$^{-/-}$; non cup = cup$^{+/+}$ or cup$^{+/-}$ siblings; situs inversus = spaw$^{-/-}$

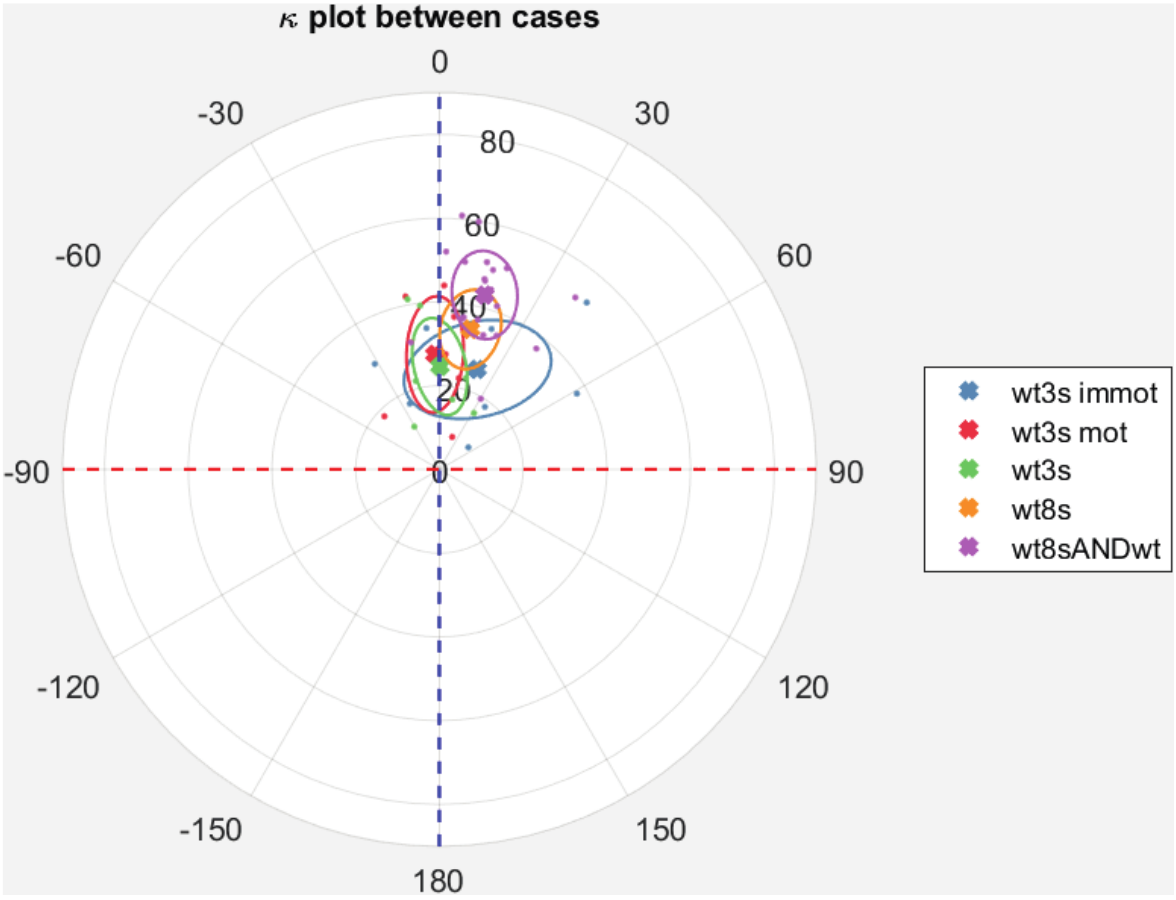

Manuscript 4 - Fig. 7: Average θ and φ values increased with developmental time: K plots displaying the average θ and φ for the wild-type embryos analysed. The three wild-type developmental stages (3-SS in green; 8-SS in orange, 8SS and later stages in purple). At 3-SS, the motile and immotile cilia were also represented separately (blue and red respectively). For all cases, each dot represents the average value of θ and φ per embryo, and each cross the average θ and φ per condition: φ values can be read around the rosette, while θ values on the grey lines going from the centre to the periphery. The circles around each cross display the standard deviation (see also Supplemental Table 4). Cases code: wt3s = wild-type 3-SS; wt8s = wild-type 8-SS; wt8sANDwt = wild-type 8-SS and 9-14-SS merged

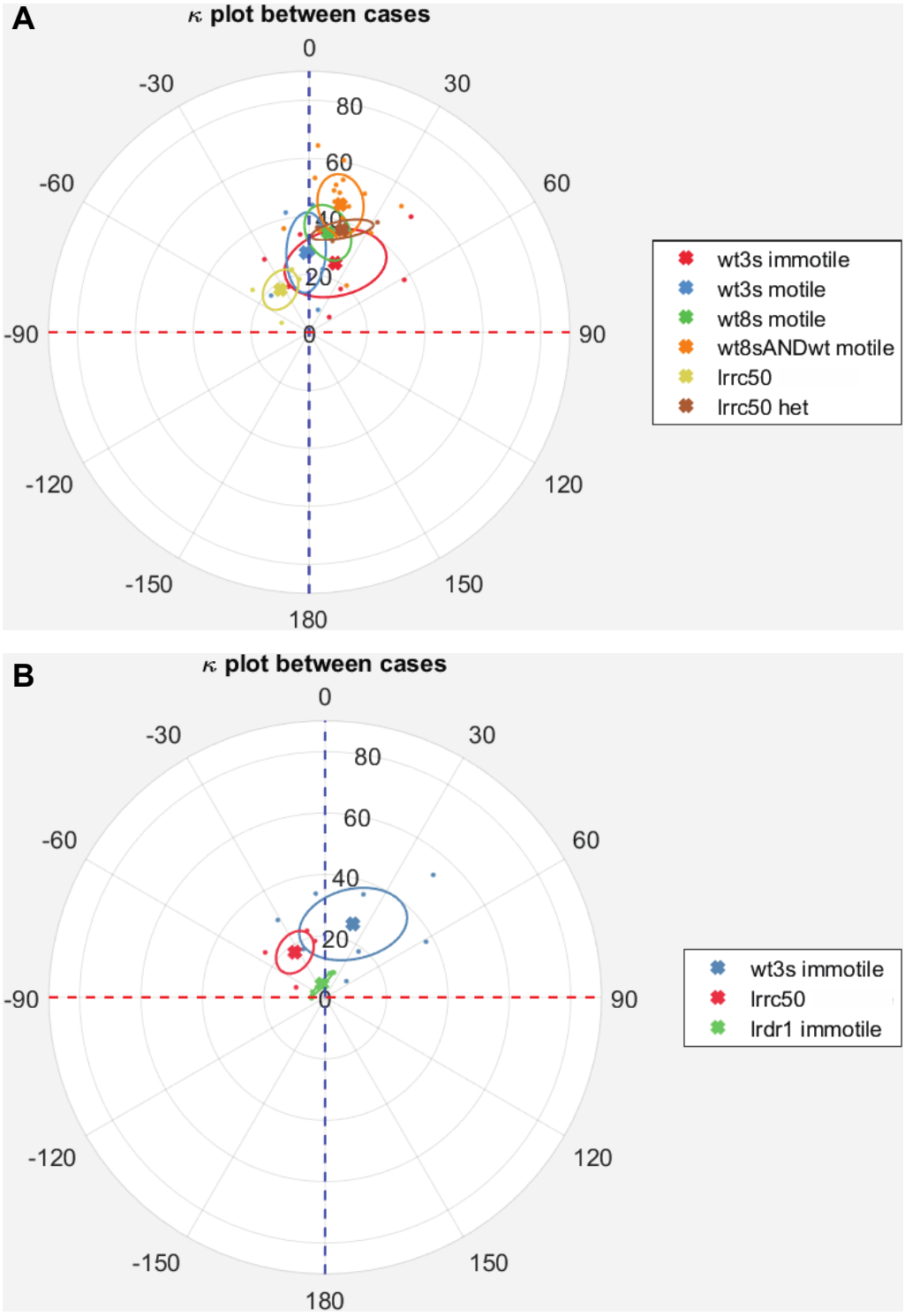

Manuscript 4 - Fig. 8: *lrrc50*$^{-/-}$ has a much more disrupted cilia orientation in comparison with wild-type controls and *lrrc50*$^{+/-}$ siblings, while *lrdr1* MO are very close of being orthogonal to the cell surface: K plots displaying the average θ and φ for the wild-type embryos analysed in comparison with the *lrrc50*$^{-/-}$ and *lrrc50*$^{+/-}$ siblings **(A)** and all the three cases with a significant number of immotile cilia **(B). (A)** Comparison between the three wild-type developmental stages (3-SS immotile cilia in red and motile cilia in blue; 8-SS in green, 8SS and later stages in orange), with the *lrrc50*$^{-/-}$ (in dark yellow) and *lrrc50*$^{+/-}$ (in brown) embryos; **(B)** comparison between the immotile cilia at 3-SS (blue), all population of immotile cilia of *lrrc50*$^{-/-}$ and all population of immotile cilia in the *lrdr1* (green). For all cases, each dot represents the average value of θ and φ per embryo, and each cross the average θ and φ per condition: φ values can be read around the rosette, while θ values on the grey lines going from the centre to the periphery. The circles around each cross display the standard deviation (see also Supplemental Table 4). Cases code: wt3s = wild-type 3-SS; wt8s = wild-type 8-SS; wt8sANDwt = wild-type 8-SS and 9-14-SS merged; lrdr1 = *lrdr1*-morphant; lrrc50 = *lrrc50*$^{-/-}$; lrrc50 het = *lrrc50*$^{+/-}$ siblings.

Altogether, our results show that from all the pre-selected candidates, only the conditions in which cilia motility was impaired the meridional tilt was lost (**Fig. 5-6** and **Fig. 8**). Also cilia 3D orientation analyses should be based on θ and φ angles distributions for a first estimation of cilia orientation but mainly in the analysis of the average cilium for each KV. Together both readouts provide a more comprehensive analysis of the 3D cilia orientation in the KV, even though the study of the average cilium for each KV allows to predict the cilia-generated flow profiles, since it is assumed that in the physical environment of the KV the amplitude and direction of the average flow will result from the θ and φ angles of the average cilium for each KV.

KV cilia implantation is not symmetrical along the LR axis at later stages

Having addressed our main question on the regulation of the meridional tilt observed *in vivo* in the KV (Manuscript 3), and given our *3D-Cilia Map* method allows cilia from the right and left hemispheres of the KV to be studied separately, we decided to investigate any potential asymmetry in cilia orientation in the KV. Thus, we tested two asymmetric features for cilia 3D orientation ($< \varphi > \neq 0$ and $| < \varphi >_{left} | \neq | < \varphi >_{right} |$), in 3-, 8-, and 9-14-SS wild-type (Manuscript 3) and embryos from the pre-selected conditions.

As described previously, all the conditions (wild-type and pre-selected candidates) showed an average value of φ different from zero at the 8-SS stage, even the *lrrc50*$^{-/-}$ and *lrdr1*-morphant embryos in which immotile cilia have negative average values of φ (**Fig. 9A** and **Supplemental Table 2-4**). Moreover, the average value of φ is systematically higher for those cilia on the left side of the KV compared to those on the right side (**Fig. 9B** and **Supplemental Fig. 15**), even in *lrrc50*$^{-/-}$ which cilia lost the meridional tilt (**Fig. 9B** and **Supplemental Fig. 16**). Intriguingly, in the *lrrc50*$^{-/-}$ there is a clear difference between left and right φ values, which is even stronger when compared to wild-type or the other pre-selected candidates (**Fig. 9B** and **Supplemental Fig. 15-16**). Leading to the hypothesis that a trend of asymmetric φ between the left and right hemispheres of the KV is present already at 8-SS. We performed a similar analysis regarding the θ angle but no differences were observed between the cilia on the left and right sides of the KV (**Supplemental Fig. 17**), including in the motility-disrupted conditions (**Supplemental Fig. 18**).

Next, we determined the φ angle distributions in the left and right-sided cilia of the wild-type embryos at 3-SS, when immotile cilia are present as well as in later stages. The φ angle distributions at later stages revealed a 30° difference between φ-values of left and right cilia, indicating an overall posterior bias. Strikingly, while right-sided cilia become perfectly oriented along the meridional direction (φ=2°, **Fig. 10C**), the left-sided cilia exhibit a strong tilt following the direction of the flow away from the meridional direction (φ=29°, **Fig. 10C**). In the wild-type embryos at 8-SS this asymmetry is less pronounced (**Fig. 10B**), as seen in the pre-selected candidates analyzed the trend of asymmetry is already present.

In wild-type embryos at 3-SS, we observed a difference on the average value of φ between the left and the right-sided cilia **(Fig. 10A)**. Importantly, this difference seems to be a mirror-symmetric bias between the left and right hemispheres (+18° on the left and -19° on the right; **Fig. 10A**), corresponding to a posterior bias of cilia orientation on both sides. If both left and right-sided cilia balance their φ angles to result in an average value of φ=0, we could conclude KV cilia at 3-SS have a symmetrical orientation and thus, $| < \varphi >_{left} | = | < \varphi >_{right} |$. Our current results indicate that left and right cilia implantation is not completely symmetrical after 3-SS and this difference increases with time (**Fig. 10B-C**). We performed a similar analysis regarding the θ angle but no difference was observed between the left and right-sided cilia, meaning θ maintains LR symmetry over time (**Supplemental Fig. 19**).

Altogether, our results demonstrate that the meridional tilt is maintained in most conditions studied (by definition: θ > 0° and φ close to 0°) as observed in wild-type embryos at 8-SS. Control of cilia orientation was only lost in motility-disrupted cases (**Fig. 5-8**). Thus, our study highlights the need of motility to properly orient cilia along the meridians during KV development (**Fig. 7**). Finally, we uncovered a LR asymmetry trend in the average value of the φ angle, which is always higher on the left side, even when cilia motility is affected and the 3D cilia orientations are defective (**Fig. 9**). Our observations suggest that this LR asymmetric cilia implantation trend begins after 3-SS and then increases over time (**Fig. 10**).

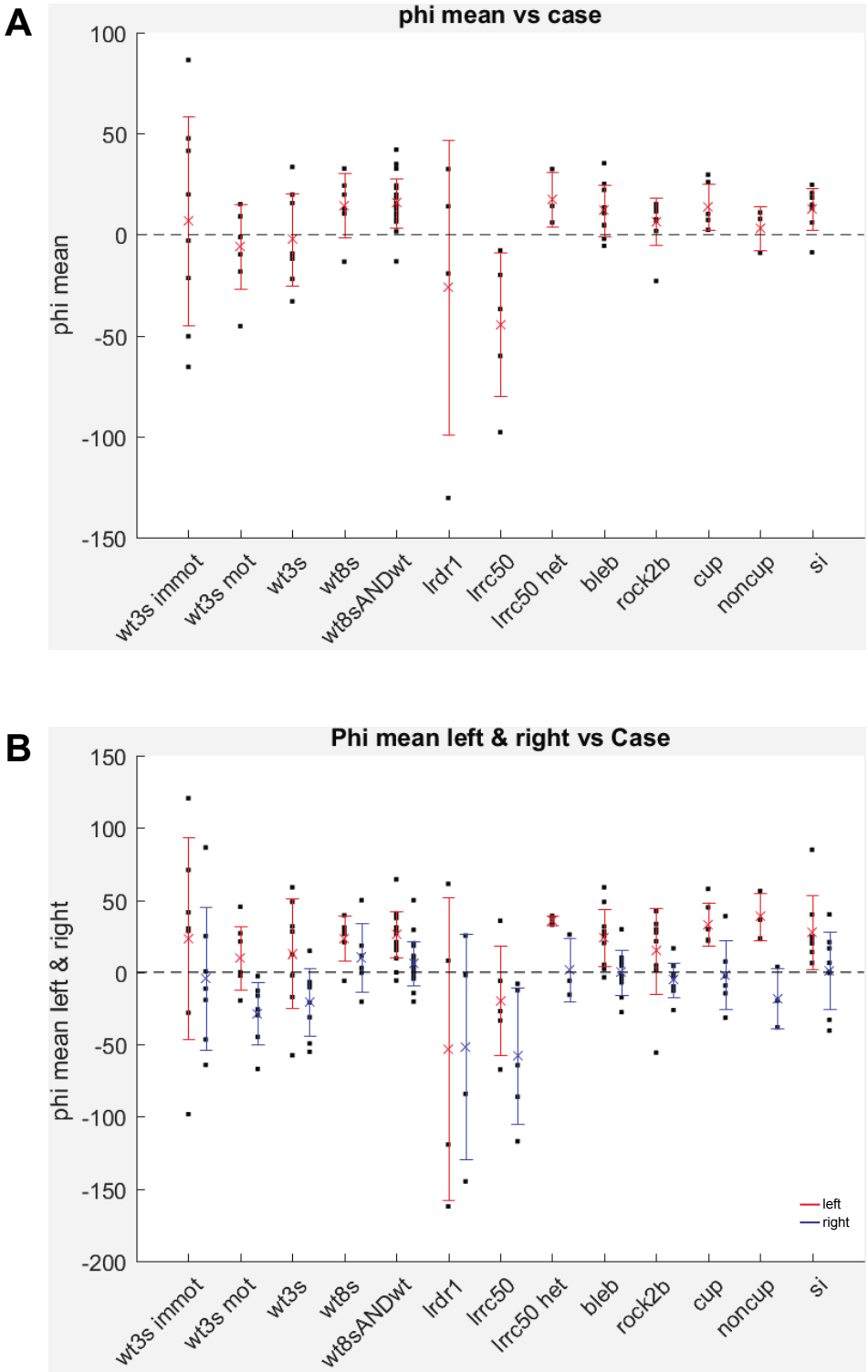

Manuscript 4 - Fig. 9: Quantification of the mean value for φ of individual KV at different stages and conditions: (A-B) Dot plots displaying the mean values of φ versus case **(A)** and the mean values of φ on the left and on the right sides of the KV versus case **(B)**. For all conditions in **(A)** and **(B)**, each black dot represents the mean values for one individual KV, the red cross displays the average value for all KVs of the respective condition and the red line the standard deviation of the mean (see the values in Supplemental Table 2-4). The Y axis in both **(A)** and **(B)** is displayed in degrees. The mean values of φ are always higher than zero, except for the conditions with immotile cilia. Also the mean values of φ are always higher for cilia on the left side of the KV. Cases code: wt3s = wild-type 3-SS; wt8s = wild-type 8-SS; wt8sANDwt = wild-type 8-SS and 9-14-SS merged; lrdr1 = lrdr1-morphant; lrrc50 = lrrc50$^{-/-}$; lrrc50 het = lrrc50$^{+/-}$ siblings, bleb = blebbistatin-treated; rock2b = rock2b-morphant; cup = cup$^{-/-}$; noncup = cup$^{+/+}$ or cup$^{+/-}$ siblings; si = situs inversus (spaw$^{-/-}$)

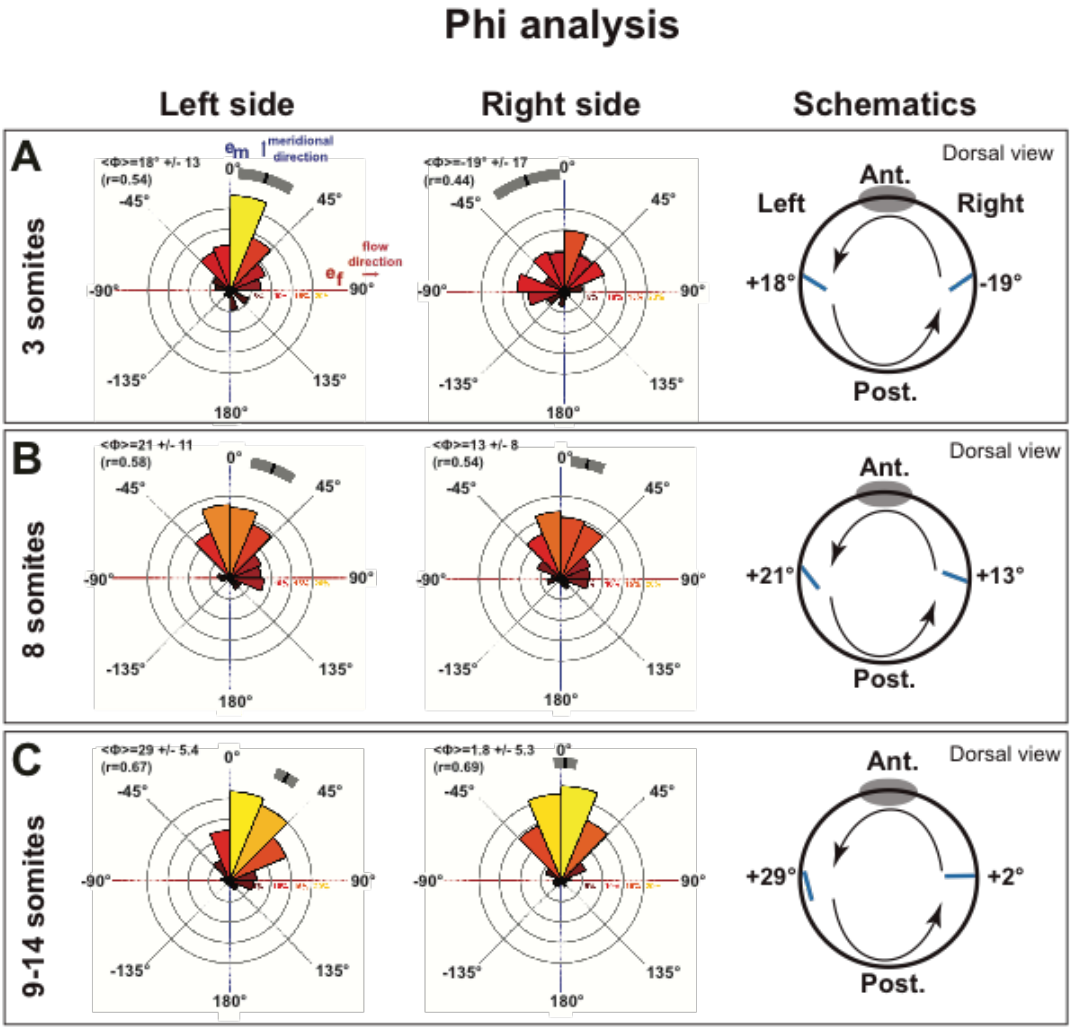

Manuscript 4 - Fig. 10: Motile cilia orientation becomes asymmetric over time between left and right sides considering φ angle quantification: Quantification of the φ angle distribution on left-sided cilia (left) and right-sided cilia (middle), and a schematics of the KV in dorsal view summarizing the average φ angle observed on the left and right hemispheres of the KV (left). Rosette plots showing the distribution of angle φ. The black tick and the grey strip indicate the mean with its 95% confidence interval. **(A)** 3 somites, **(B)** 8somites and **(C)** 9-14 somites. N_c= number of cilia; r = dispersion of the vector; e_m= aligned along a meridian from the ventral to the dorsal pole of the KV; e_f= follows a KV parallel (has the same direction as the typical flow observed within the vesicle).

Discussion

In a previous study we demonstrated that spatial orientation is a key functional feature of motile cilia in LR symmetry breaking, as it determines the strength and directionality of the induced flow (Manuscript 3). We also proposed that the meridional tilt is the main 3D orientation of KV cilia *in vivo*. However, the mechanism setting the meridional tilt remained unclear. Here, we used the *3D-Cilia Map* methodology to analyze the key biophysical parameters of KV cilia (such as cilia density and 3D orientation) in a group of five pre-selected conditions previously reported to impact LR determination, such as rock2b-myosin II pathway, cilia motility, PCP pathway, cilia mechanosensor and Nodal-related signaling (**Fig. 1B-C**). In our study, we combined gene expression analysis (ISH) and visceral organ *situs* scoring, with live-imaging and large-scale analysis of the biophysical features of cilia using *3D-Cilia Map*.

Several studies have focused on cilia orientation and density to explain the flow directionality in fish (Borovina et al., 2010; Montenegro-Johnson et al., 2016; Nonaka et al., 2005; Okabe et al., 2008; Okada et al., 2005; Sampaio et al., 2014). Additionally, different types of cilia orientation have been observed *in vivo* such as posterior tilt (Borovina et al., 2010), dorsal tilt (Supatto et al., 2008), or a mix of the two (Okabe et al., 2008). In mouse and rabbit, posterior tilting of cilia in the ventral node is thought to occur passively (Okada et al., 2005), while in zebrafish it is more likely to be achieved 'actively', by the action of the PCP pathway (Borovina et al., 2010; Hashimoto et al., 2010; Okabe et al., 2008), or the flow itself (Guirao et al., 2010). Differences in shape and in flow-profiles between the different animal models, however, could hide other mechanisms involved in the 3D orientation of cilia. Our approach allowed us to gain insights into the potential mechanism behind the meridional tilt observed *in vivo*, thus making our work the most comprehensive study to date of cilia orientation in the zebrafish KV.

All the pre-selected candidates revealed defects in the LR axis determination, whether in the abnormal propagation of the *southpaw* in the LPM or in the *situs* of the internal organs. Only the *rock2b*$^{-/-}$ embryos did not show LR defects and were excluded from the pre-selected candidates for 3D cilia orientation analysis. We are currently analyzing this *rock2b* mutant allele in more detail to better understand the differences between this mutant embryos and the morpholino used to knock-down the same gene (*rock2b*-MO). Next, we plan to analyze the expression pattern of *charon*, antagonist of *southpaw*, which remains unknown. Given that *charon* was suggested to be the first asymmetric flow target gene in several vertebrates (Hojo et al., 2007; Lopes et al., 2010; Nakamura and Hamada, 2012; Schweickert et al., 2007), and is also known to be flow-responsive in the KV (Sampaio et al., 2014), we expect that potential asymmetries in the expression pattern of this gene bring novel insights into the involvement of the selected pathways, especially in the motility-disrupted conditions, in the process of LR determination.

Considering the 3D cilia orientation analysis of our candidates, we concluded that even though all the pathways studied are implicated in LR axis determination, not all impact the meridional tilt observed *in vivo*. Our results showed that the meridional tilt was strikingly affected in cases in which cilia motility

was impaired, and not in any other condition studied in this work. Thus, we can conclude LR axis determination can be affected at different levels and independently of cilia-orientation **(Fig.11)**. There are differences between the two conditions in which motility is affected: in the *lrrc50*$^{-/-}$ the main angle affected is φ (average value of θ is similar to the controls, even though with a wider distribution) (**Fig.11**), while in the *lrdr1*-morphants, θ is almost orthogonal to the cell surface **(Fig.5)** and this impacts the φ angle that has a random distribution **(Fig.11)**. In both cases we expected cilia to be as close to orthogonal as possible to the cell surface, and since that was not the case for the *lrrc50*$^{-/-}$, we could speculate that earlier in development the immotile cilia of those mutants experience other influences that sets this orientation independently of motility (e.g. intrinsic cell chirality). Although we suggest cilia motility is necessary to set the final meridional orientation of cilia (supported by the rising in θ and φ with developmental time), it may not be needed to set the primary orientation before cilia starts beating. In the future we will further explore this hypothesis by obtaining experimental data for the *lrrc50*$^{-/-}$ at 3-SS and earlier, when lumenization of the KV begins. We anticipate that these experiments will give us insights in to the initial 3D orientation of cilia. We would also like to test the intrinsic chirality of the KV cells and its impact on cilia orientation. This is likely to be significantly more challenging, however, since experiments are more difficult to perform given the accessible tools, which are mainly drug treatments and it will be extremely difficult to exclude its side effects on the whole embryo.

We demonstrated for the first time that 3D cilia orientation in the KV varies at different developmental stages. At later stages (after 8-SS) of the KV development cilia are asymmetrically oriented between the right and left hemispheres of the KV, with an overall posterior bias (**Fig. 10**). At 8-SS there is already a trend that suggests this asymmetry may already be set at an earlier stage. However, the experimental number need to be increase for statistical significance and confirm this trend, $|< \varphi >_{left}| \neq |< \varphi >_{right}|$, at 8-SS for all the conditions studied. Surprisingly, our results revealed a potential symmetry already at 3-SS: the average value of φ=0 because the side-asymmetry observed is a result of a mirror-symmetric bias between both sides **(Fig. 10)**. This indicates that the KV cilia at 3-SS have a symmetrical orientation and thus $| < \varphi >_{left} | = | < \varphi >_{right} |$. We are currently collecting more experimental data to statistically confirm the observed trend. Also it would be very interesting to acquire experimental data using embryos at the onset of KV lumen formation. Overall, our results revealed that cilia organization, and in particular motile cilia orientation, is highly dynamic between early and late stages.

Even though all the other pre-selected candidates seem not to interfere with the meridional tilt, we would like to discuss them briefly. The Rock2b-Myosin II and Nodal-related gene (*spaw*) pathways impacted mainly the morphogenesis of the KV, disrupting the anterior cluster of ciliated cells, without having an effect in cilia orientation. These results support the hypothesis that cilia positioning may not follow the AP axis as in the mouse node but the DV axis as previously reported (Supatto et al., 2008). Also, it will be of great interest to further explore the potential role of *spaw* in the KV morphogenesis given our surprising observation that the formation of the anterior cluster is disrupted in the situs

inversus$^{-/-}$ (*spaw*) embryos. Regarding the PCP/*Vangl2* mutants, we confirmed the severe defects in the determination of the LR axis. The involvement of PCP in setting up the cilia posterior tilt was reported in the mouse node (Hashimoto et al., 2010) and the zebrafish KV (Borovina et al., 2010). However, if the PCP has a role in setting up the meridional tilt in the KV remains unknown. We are currently analyzing data from the *vangl2* mutants which will enable us to address this question in the near future. The cup (*pkd2/trpp2*) mutants had severe defects in LR axis determination, however neither the anterior cluster of ciliated cells nor the 3D orientation of cilia seemed to be affected. Thus, we conclude *pkd2/trpp2* should act downstream of KV morphogenesis and cilia orientation.

In conclusion, the study presented here brings robust and novel insights on the role of cilia during LR determination in zebrafish. Altogether, our results demonstrate that in conditions which cilia motility is impaired, the meridional tilt observed *in vivo* for KV cilia was strikingly lost. Thus, our study also suggests that cilia motility is needed to properly orient cilia during development of the KV. In addition we demonstrated 3D cilia orientation in the KV varies at different developmental stages, with a surprising trend of asymmetric cilia implantation after 3-SS that increases over time. In the future, we would like to explore the role of cell chirality in this system, as it could work in parallel with the motile cilia and fluid-flow to break the initial symmetry in the zebrafish KV.

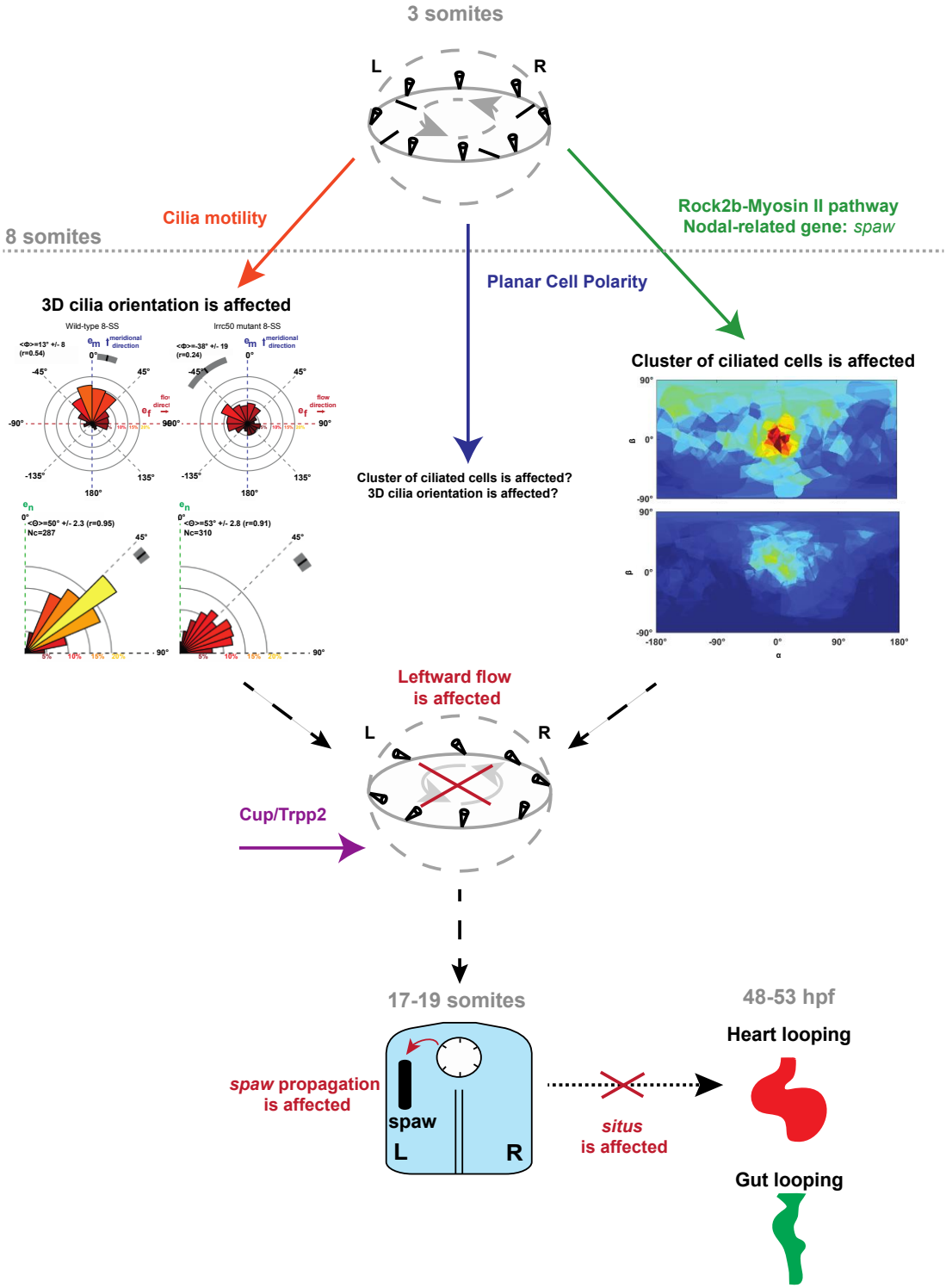

Manuscript 4 - Fig. 11: Schematics summarizing the main results from 3-SS to late organogenesis. All the pre-selected conditions revealed laterality defects regarding either the expression pattern of *spaw* in the LPM or the internal organ *situs*, in comparison with wild-type transgenic embryos. Altogether, our results demonstrate most pre-selected conditions studied kept the meridional tilt. Only in the conditions cilia motility was impaired, the meridional tilt was lost (left side on the scheme). Also, the Rock2b-Myosin II and Nodal-related gene (*spaw*) pathways impacted mainly the morphogenesis of the KV, disrupting the anterior cluster of ciliated cells, without having an effect in cilia orientation (right side on the scheme). However, if the PCP has a role in setting up the meridional tilt in the KV remains unknown. We are currently analysing data from the *vangl2* mutants, which will enable us to address this question in the near future. The cup (*pkd2/trpp2*) mutants had severe defects in LR axis determination, however neither the anterior cluster of ciliated cells nor the 3D orientation of cilia seemed to be affected. Thus, we conclude *pkd2/trpp2* should act downstream of KV morphogenesis and cilia orientation.

Materials and Methods

Zebrafish strains

The zebrafish (*Danio rerio*) lines used in the study of cilia orientation and position were: *Tg(actb2:Mmu.Arl13b-GFP)*(Borovina et al., 2010), *Tg(dnaaf1^{tm317b}; actb2:Mmu.Arl13b-GFP*)(Sullivan-Brown et al., 2008), *Tg(rock2b^{Sa17708}; actb2:Mmu.Arl13b-GFP)(Kettleborough et al., 2013), Tg(trilobite^{tc240a}; actb2:Mmu.Arl13b-GFP)* (Heisenberg and Nusslein-Volhard, 1997), *Tg(spaw^{s457}; actb2:Mmu.Arl13b-GFP) (Beis et al., 2005; Kalogirou et al., 2014)*, *Tg(cup^{tc241}; actb2:Mmu.Arl13b-GFP)* (Schottenfeld et al., 2007). All zebrafish strains were maintained at the IGBMC fish facility under standard husbandry conditions (14h light/10h dark cycle). The Animal Experimentation Committee of the Institutional Review Board of IGBMC approved all animal experiments performed in this project.

Morpholino (MO) knockdown

MO designed to block the *rock2b* RNA splicing site (Wang et al., 2011) and a MO directed against the *lrdr1* translation start codon (Essner et al., 2005), were obtained from *Gene Tools, LLC* and dissolved in water to a stock concentration of 3M (*rock2b*-MO: 5'-GCACACACTCACTCACCAGCTGCAC-3' and *lrdr1*-MO: 5'-GCGGTTCCTGCTCCTCCATCGCGCC-3'). To deliver MO to all embryonic cells, embryos were injected at 1-cell stage with 0,66ng of rock2b-MO and 2ng of lrdr1-MO. Non-injected embryos were kept as controls.

Blebbistatin treatment

Embryos at bud-stage were dechorionated and treated with 35µM of blebbistatin (SIGMA B0560)/DMSO at 32ºC in the dark. Non-treated embryos were used to stage the development of the treated ones. When reaching the 3-somite-stage (SS), the treated embryos were washed carefully in 0.3% Danieau medium and kept at 32ºC until the desired developmental stage for imaging was reached (see the following section). 1%-DMSO treated embryos were used as drug-control effects.

Experimental use of zebrafish embryos

For live imaging experiments, embryos were raised at 32°C in the dark and imaged between 3- and 14- somite-stages (SS). Embryos were soaked in with Bodipy TR (Molecular Probes) for 60 minutes prior the desired developmental stage, and were subsequently embedded in 0.8% low melting point agarose (Sigma Aldrich) in 0.3% Danieau medium. After imaging, and in order to be able to score the heart *situs*, the embryos were released from the agarose mold and kept separate at 28.5ºC. For LR read-out experiments, zebrafish embryos were collected after 20 min of contact between the mating pairs to guarantee homogeneity of the egg population. For heart and gut *situs* scoring experiments, embryos were raised at 28.5ºC in the dark in 0.3% Danieu medium supplemented with 0.003% (wt/v) 2-phenylthiourea to inhibit pigment formation and staged according to hours post-fertilization (hpf). For spaw expression patterns, embryos were raised at 25ºC in the dark in 0.3% Danieu medium and staged according to the number of somites. For both LR scoring experiments, whole clutches were used in order to perform robust population studies.

Genotyping strategies of adult fish and single embryos

Adult fish were anesthetized in 80µg/mL Tricaine before cutting 1/3 of the caudal fin, and kept separated until the end of the genotyping experiments. Each piece of fin was kept in Lysis buffer at 55°C over-night (ON) with agitation. DNA extraction was performed using NaCl, isopropanol and 70%-Ethanol. DNA extracted from embryos follows a protocol using NaOH and Tris-HCl (Appendix 1). DNA samples were stored at -20ºC. PCR was performed in order to amplify the DNA fragments of interest for genotyping. All primers were design using the program ApE (http://biologylabs.utah.edu/jorgensen/wayned/ape/) and using the sequences available on Ensemble (Ensembl genome browser 84). The designed primers are listed below: *cup*^{tc241}: PF: 5'-CCATTAGCCTGCACATTCAATC-3'; PR: 5'-ATCGCACTGCTCATCTGAAG-3'; sequencing with PF; *dnaaf1*^{tm317b}: PF: 5'-CTAGTTTGAGCGACTTGTCCA-3'; PR2: 5'-CACCCGCTGGAAAGATCAAG-3'; Sequencing PR: 5'-CACTGATGCGGTTGTGGGAC-3'; *rock2b*^{Sa17708}: PF: 5'-AGGAGTCGGAGAGGCTGAAG-3'; PR: 5'-ACAGGCCAGAACTTAACACAGG-3'; Sequencing PF: 5'-GCCTTTAGACAGTCCCAGCAG-3'; *spaw*^{s457}: PF1: 5'-GCTCTCTGATGTGCCTGACG-3'; PR1: 5'-TCGATCCACACGCAATCAAC-3'; sequencing with PF.

2-photon excitation fluorescence microscopy (2PEF)

To image deep enough into the zebrafish embryo and capture the entire Kupffer's vesicle (KV), each live embryo of the different conditions was imaged using 2PEF microscopy with a SP8 direct microscope (Leica Inc.) at 930nm wavelength (Chameleon Ultra laser, Coherent Inc.) using a low magnification high numerical aperture (NA) water immersion objective (Leica, 25x, 0.95 NA). We imaged the KV of embryos labeled with both *Arl13b*-eGFP and BodipyTR at 8-somite stages (SSs): 100 x 100 x 50 µm^3 3D-stacks with 0.2 x 0.2 x 0.8 µm^3 voxel size and 2.4 µs pixel dwell time were typically acquired in order to maximize the scanning artifact allowing to properly reconstruct cilia orientation in 3D as described in (Supatto and Vermot, 2011). The fluorescence signal was collected using Hybrid internal detectors at 493-575 nm and 594-730 nm in order to discriminate the GFP signal labeling cilia from the signal labeling the KV cell surface. To uncover the orientation of the KV within the body axes, the midline was also imaged. We typically imaged a volume of 600 µm × 600 µm × 150 µm comprising the midline and the KV from top to bottom with a voxel size of 1.15 µm laterally and 5 µm axially. During live imaging, numbers were given to the embryos in order to identify them afterwards. After live imaging, embryos were carefully removed from the mold of agarose and let grow in separate and numbered wells at 28.5°, in order to access the heart laterality at 30hpf. Only embryos presenting defects in heart laterality were selected for the following cilia analysis. The same kind of method was used to genotype embryos after imaging.

3D-Cilia Map: quantitative 3D cilia feature mapping

We used *3D-Cilia Map*, a quantitative imaging strategy to visualize and quantify the 3D biophysical features of all endogenous cilia in the KV in live zebrafish embryos, as described in Manuscript 2 and Manuscript 3.

Whole-mount *in situ* hybridization (WISH)

Whole-mount *in situ* hybridization was performed as described previously (Thisse and Thisse, 2008). Digoxigenin RNA probes were synthesized from DNA templates of *spaw* (Long et al., 2003) and *foxA3* (Monteiro et al., 2008). Embryos for *spaw* and *foxA3* ISH were fixed at 17-SS and 53hpf respectively. After WISH embryos were scored and then kept in 20%-Glycerol/PBS at 4°C or genotyped.

Scoring of *spaw* expression, heart and gut looping

Spaw expression patterns in the LPM can be classified according to four main categories: left, bilateral, right or absent (**Supplemental Fig.1A**) (Long et al., 2003). The zebrafish heart looping was accessed at 48hpf when the heart is already beating. Due to its transparency, the zebrafish heart can be visible under a regular binocular using brightfield illumination, and its *situs* can be evaluated according to the midline of the embryo. Embryos were categorized according to the heart looping at 48hpf: dextral-loop (normal loop), no loop or sinistral-loop (reserved loop). We performed WISH for *foxA3* at 53hpf in order to visualize the gut (liver and pancreas) *situs* (**Supplemental Fig.1B**) (Monteiro et al., 2008) in the same embryos we accessed the heart looping at 48hpf. Embryos were evaluated after WISH under a binocular using brightfield illumination and scored according to the curvature between the liver and the pancreas: left curvature (liver on the left, pancreas on the right), no curvature (liver and pancreas in the midline and most of the times bilateral) and right curvature (liver on the right and pancreas on the left). For the sake of simplicity, we merged the laterality information of heart and gut looping and described it according to the clinical terminology used: *situs solitus* (describes the normal condition: heart with a rightward loop and the gut showing the liver is on the left and the pancreas on the right), *situs inversus* (pathological condition characterized by a complete reversal of the organ laterality) and *heterotaxy* (pathological condition described by any combination of abnormal LR asymmetries that cannot be strictly classified as *situs solitus* or *situs inversus*) (Fliegauf et al., 2007; Ramsdell, 2005; Shapiro et al., 2014; Sutherland and Ware, 2009).

Quantifications and statistical analysis

Spaw expression and organ *situs* patterns in the different populations were statistically compared using a Chi-square test using *GraphPad Prism 7.0*, as in (Borovina et al., 2010). Results were considered highly significant when $p<0.0001$ (****), very significant when $p=0.001$ (***), and significant when $p=0.0015$ (**). Error bars depict SEM. Values in the Fig. legends present just the Mean.

Supplemental Figures, Tables and Movie

Supplemental Figures 1-19, Tables 1-5 and Movie 1 are in the following pages.

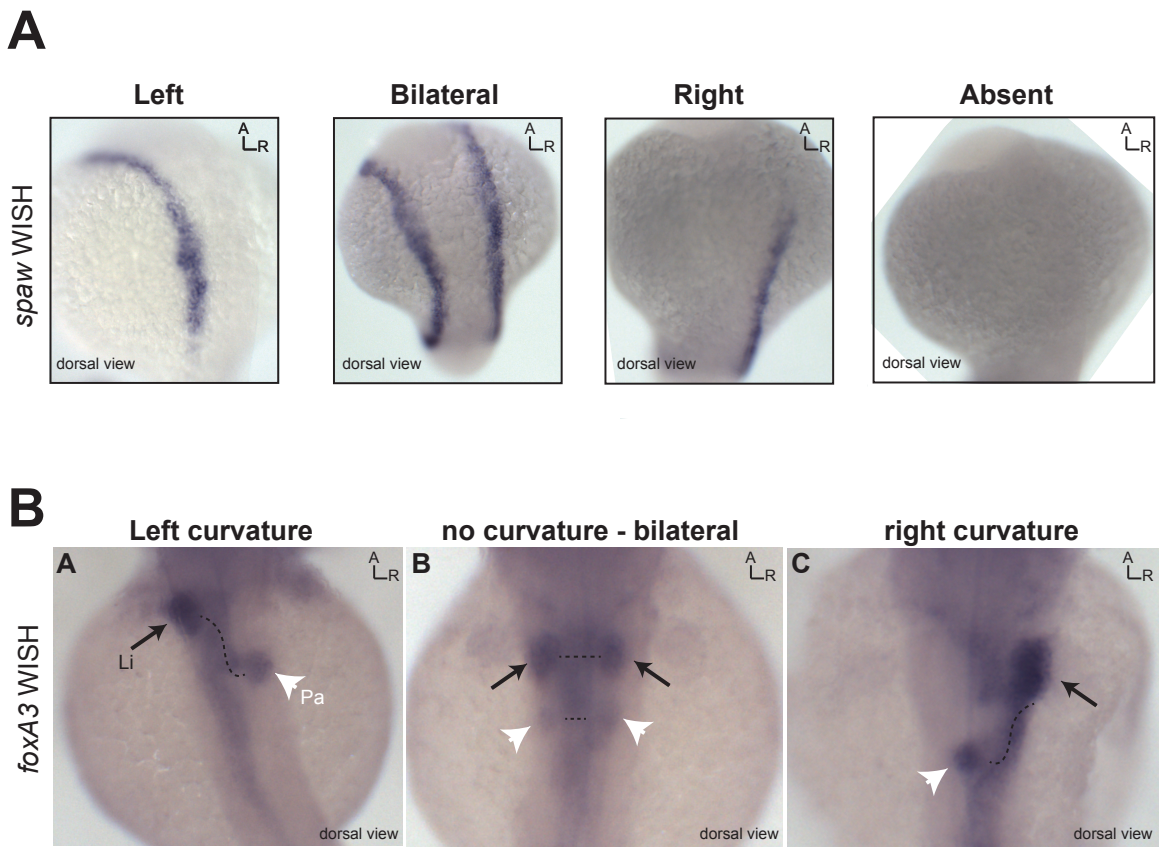

Manuscript 4 - Supplemental Fig. 1: Read-out quantification of the LR axis determination: *spaw* expression patterns in the LPM **(A)** and 53hpf gut laterality visible by the *foxA3* probe for ISH **(B)** from *lrrc50*$^{-/-}$ embryos. We used these embryos to illustrate the different patterns possible for each ISH. *Spaw* patterns in the LPM were classified in left, bilateral, right or absent. Embryos were evaluated after *foxA3* WISH under a binocular using brightfield illumination and scored according to the curvature between the liver and the pancreas: left curvature (liver on the left, pancreas on the right – B left panel), no curvature (liver and pancreas in the midline and most of the times bilateral – B middle panel) and right curvature (liver on the right and pancreas on the left – B right panel).
Li = liver ; Pa= Pancreas

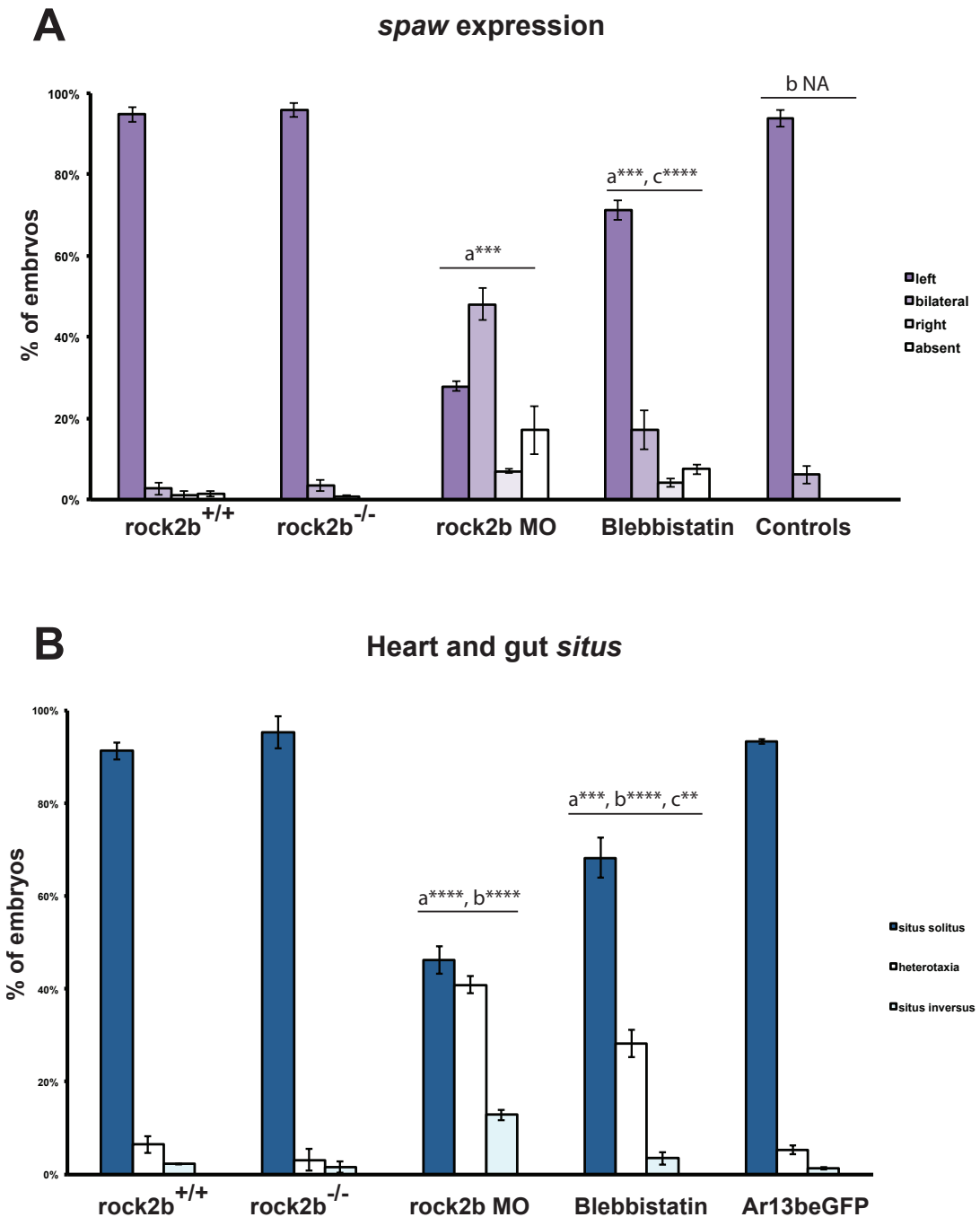

Manuscript 4 - Supplemental Fig. 2: Quantification of the *spaw* expression patterns in the LPM and the heart and gut *situs* for the conditions of the Rock2b-Myosin II pathway. 2D 100% stacked column plots depicting the expression patterns of *spaw* in the LPM for the conditions of the Rock2b-Myosin II pathway (*rock2b*$^{+/+}$, *rock2b*$^{-/-}$, *rock2b* MO, Blebbistatin), and also non-treated drug controls **(A)**, and the *situs* phenotypes for the same conditions **(B)**. The percentage of embryos can be read on the X axis. *Spaw* expression patterns in the LPM can be divided in left, bilateral, right or absent (A). *Situs* phenotypes can be divided in *situs solitus*, *heterotaxia* and *situs inversus*, the clinical terminology (B). The number of experiments performed and the total number of embryos for all conditions can be accessed in Supplemental Table 1. Statistical analyses were performed using a Chi-square test: p<0.0001 (****), p=0.001 (***) and p=0.0015 (**) - "a" indicates statistically significant difference from *rock2b*$^{+/+}$ and *rock2b*$^{-/-}$; "b" indicates statistically significant difference from Arl13beGFP/Controls; "c" indicates statistically significant difference from rock2b-MO; NA means the test was not possible to be performed since one (or more) category was equal to zero. Error bars depict SEM.

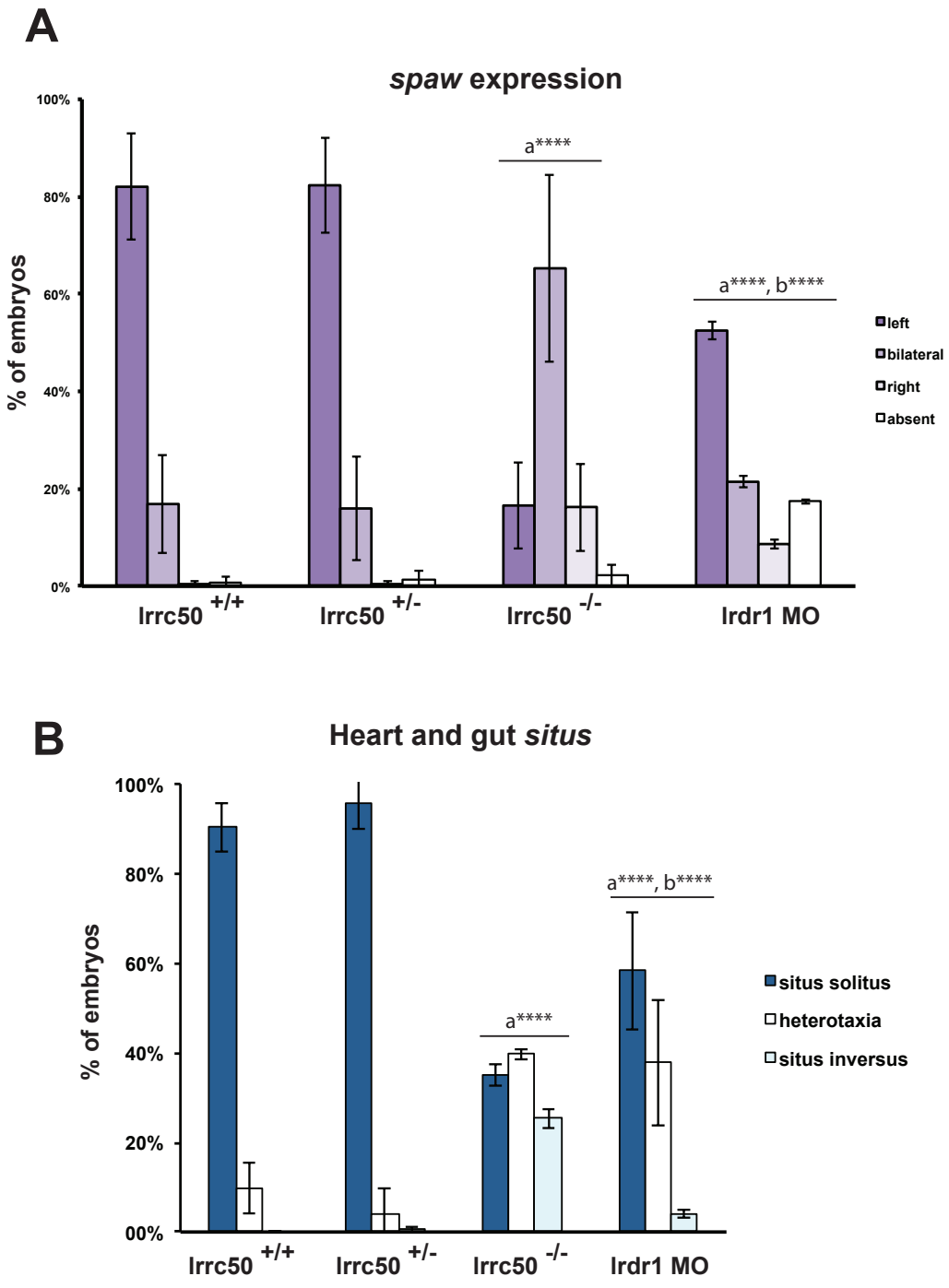

Manuscript 4 - Supplemental Fig. 3: Quantification of the *spaw* expression patterns in the LPM and the heart and gut *situs* for the conditions of absence of cilia motility. 2D 100% stacked column plots depicting the expression patterns of *spaw* in the LPM for the conditions of absence of cilia motility (*lrrc50*$^{+/+}$, *lrrc50*$^{+/-}$, *lrrc50*$^{-/-}$ and *lrdr1* MO) **(A)**, and the *situs* phenotypes for the same conditions **(B)**. The percentage of embryos can be read on the X axis. *Spaw* expression patterns in the LPM can be divided in left, bilateral, right or absent (A). *Situs* phenotypes can be divided in *situs solitus*, *heterotaxia* and *situs inversus*, the clinical terminology (B). The number of experiments performed and the total number of embryos for all conditions can be accessed in Supplemental Table 1. Statistical analyses were performed using a Chi-square test: p<0.0001 (****), p=0.001 (***) and p=0.0015 (**) - "a" indicates statistically significant difference from *lrrc50*$^{+/+}$ and *lrrc50*$^{+/-}$; "b" indicates statistically significant difference from *lrdr1*-MO. Error bars depict SEM.

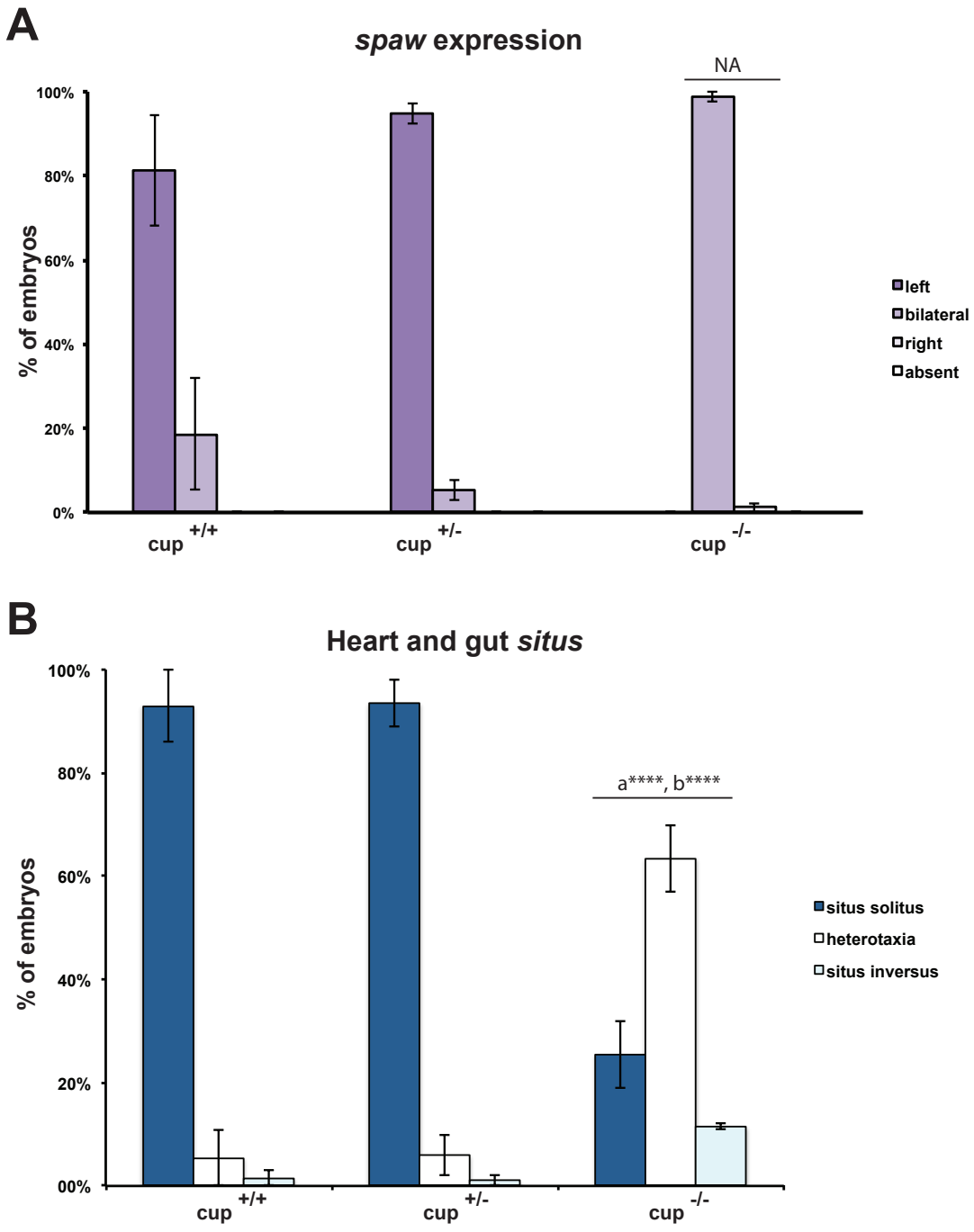

Manuscript 4 - Supplemental Fig. 4: Quantification of the *spaw* expression patterns in the LPM and the heart and gut *situs* for the conditions of the potential mechanosensor of the KV, cup/trpp2. 2D 100% stacked column plots depicting the expression patterns of *spaw* in the LPM for the conditions of the potential mechanosensor of the KV, *cup/trpp2* (*cup*$^{+/+}$, *cup*$^{+/-}$, *cup*$^{-/-}$) **(A)**, and the *situs* phenotypes for the same conditions **(B)**. The percentage of embryos can be read on the X axis. *Spaw* expression patterns in the LPM can be divided in left, bilateral, right or absent (A). *Situs* phenotypes can be divided in *situs solitus*, *heterotaxia* and *situs inversus*, the clinical terminology (B). The number of experiments performed and the total number of embryos for all conditions can be accessed in Supplemental Table 1. Statistical analyses were performed using a Chi-square test: p<0.0001 (****), p=0.001 (***) and p=0.0015 (**) - "a" indicates statistically significant difference from *cup*$^{+/+}$; "b" indicates statistically significant difference from *cup*$^{+/-}$; NA means the test was not possible to be performed since one (or more) category was equal to zero. Error bars depict SEM.

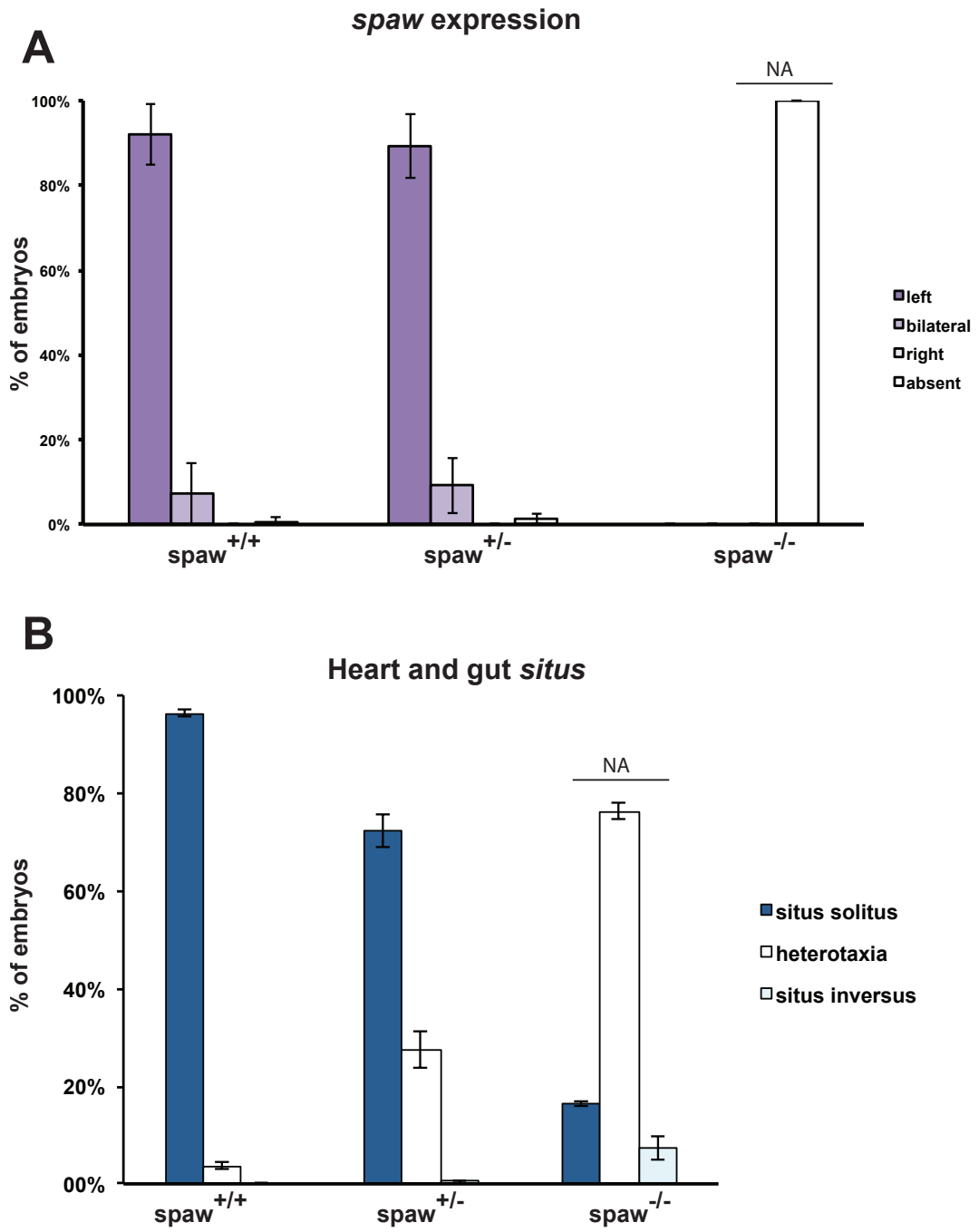

Manuscript 4 - Supplemental Fig. 5: Quantification of the *spaw* expression patterns in the LPM and the heart and gut *situs* for the conditions of the Nodal-related gene *spaw*. 2D 100% stacked column plots depicting the expression patterns of *spaw* in the LPM for the conditions of the Nodal-related gene *spaw* (*spaw*$^{+/+}$, *spaw*$^{+/-}$, *spaw*$^{-/-}$) **(A)**, and the *situs* phenotypes for the same conditions **(B)**. The percentage of embryos can be read on the X axis. *Spaw* expression patterns in the LPM can be divided in left, bilateral, right or absent (A). *Situs* phenotypes can be divided in *situs solitus*, *heterotaxia* and *situs inversus*, the clinical terminology (B). The number of experiments performed and the total number of embryos for all conditions can be accessed in Supplemental Table 1. Statistical analyses were performed using a Chi-square test: p<0.0001 (****), p=0.001 (***) and p=0.0015 (**) - "a" indicates statistically significant difference from *spaw*$^{+/+;}$ "b" indicates statistically significant difference from *spaw*$^{+/-}$; NA means the test was not possible to be performed since one (or more) category was equal to zero. Error bars depict SEM.

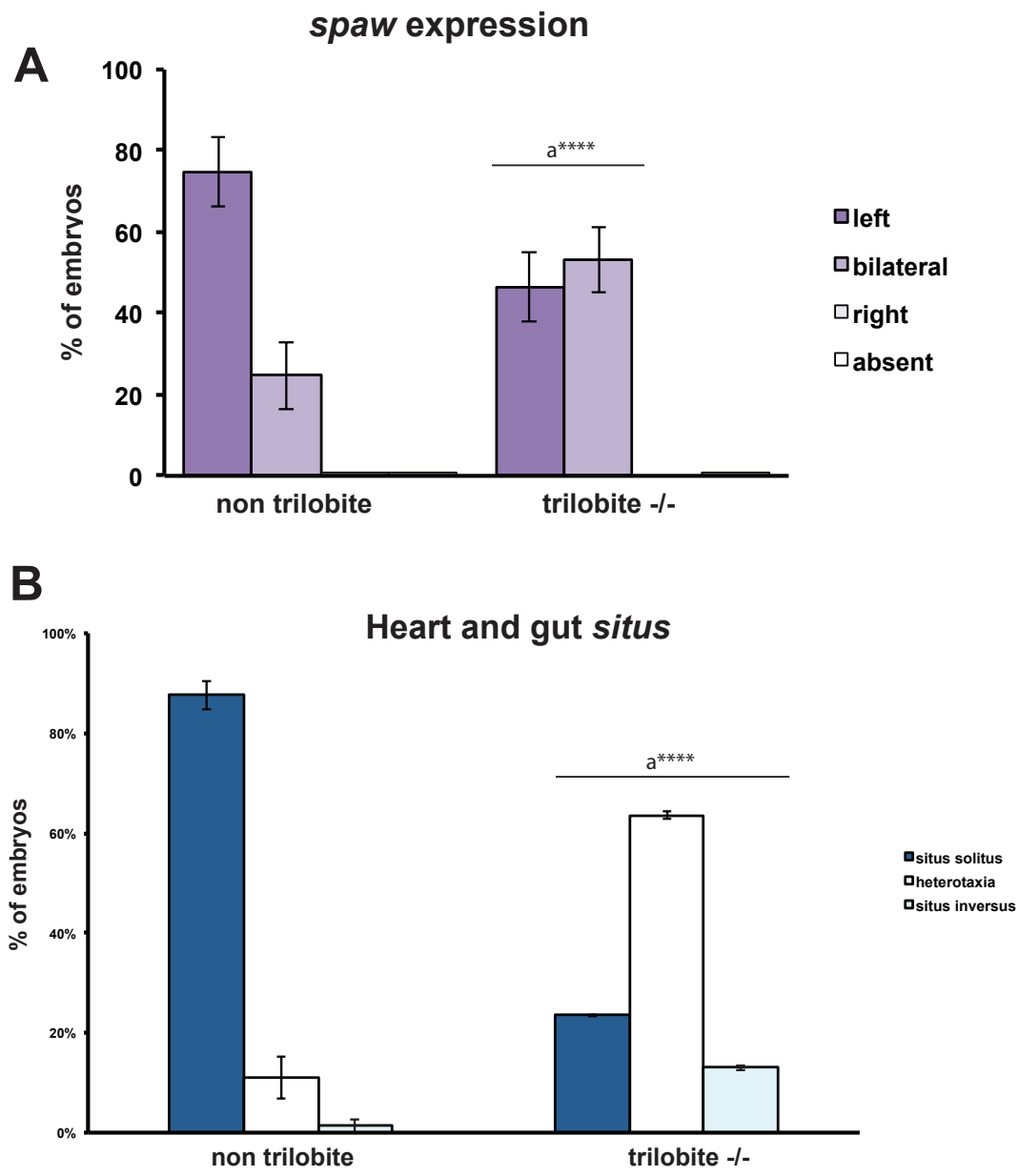

Manuscript 4 - Supplemental Fig. 6: Quantification of the *spaw* expression patterns in the LPM and the heart and gut *situs* for the conditions of the PCP pathway. 2D 100% stacked column plots depicting the expression patterns of *spaw* in the LPM for the conditions of the PCP pathway (non-trilobite and *trilobite*$^{-/-}$) **(A)**, and the *situs* phenotypes for the same conditions **(B)**. The percentage of embryos can be read on the X axis. *Spaw* expression patterns in the LPM can be divided in left, bilateral, right or absent (A). *Situs* phenotypes can be divided in *situs solitus*, *heterotaxia* and *situs inversus*, the clinical terminology (B). The number of experiments performed and the total number of embryos for all conditions can be accessed in Supplemental Table 1. Statistical analyses were performed using a Chi-square test: p<0.0001 (****), p=0.001 (***) and p=0.0015 (**) - "a" indicates statistically significant difference from non-trilobite. Error bars depict SEM.

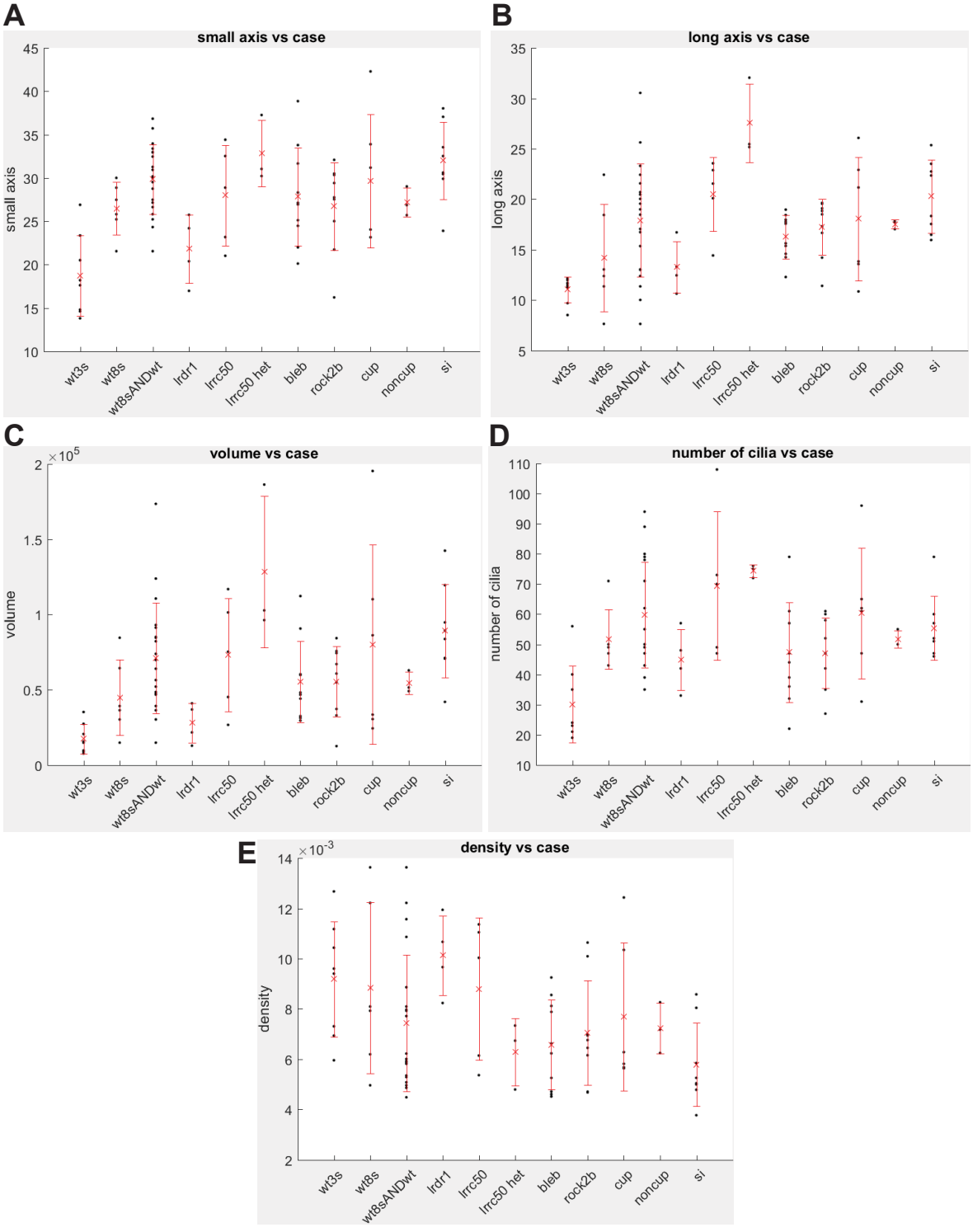

Manuscript 4 - Supplemental Fig. 7: Quantification of the morphological parameters of individual KVs at different developmental stages and different conditions: Dot plots displaying the small **(A)** and long axes **(B)** of the oblate spheroid of the KV, but also the volume **(C)**, number of cilia **(D)** and density **(E)**. For all conditions, each black dot represents one individual KV, the red cross displays the average value for all KVs of the respective condition and the red line the standard deviation of the mean (see the values in Supplemental Table 2-4). The Y axis is displayed in µm for **(A-B),** in pL for **(C)**, absolute numbers for **(D)** and for cilia/µm^3 in **(E)**. Despite all the individual variability in the morphological parameters of the KV, the average embryo per pre-selected condition presented similar values as the wild-type at the same developmental stage, and thus potential differences in 3D cilia orientation do not come from defects at the level of the overall KV morphogenesis. Cases code: wt3s = wild-type 3-SS; wt8s = wild-type 8-SS; wt8sANDwt = wild-type 8-SS and 9-14-SS merged; lrdr1 = *lrdr1*-morphant; lrrc50 = *lrrc50*$^{-/-}$; lrrc50 het = *lrrc50*$^{+/-}$ siblings, bleb = blebbistatin-treated; rock2b = *rock2b*-morphant; cup = *cup*$^{-/-}$; noncup = *cup*$^{+/+}$ or *cup*$^{+/-}$ siblings; si = situs inversus (*spaw*$^{-/-}$)

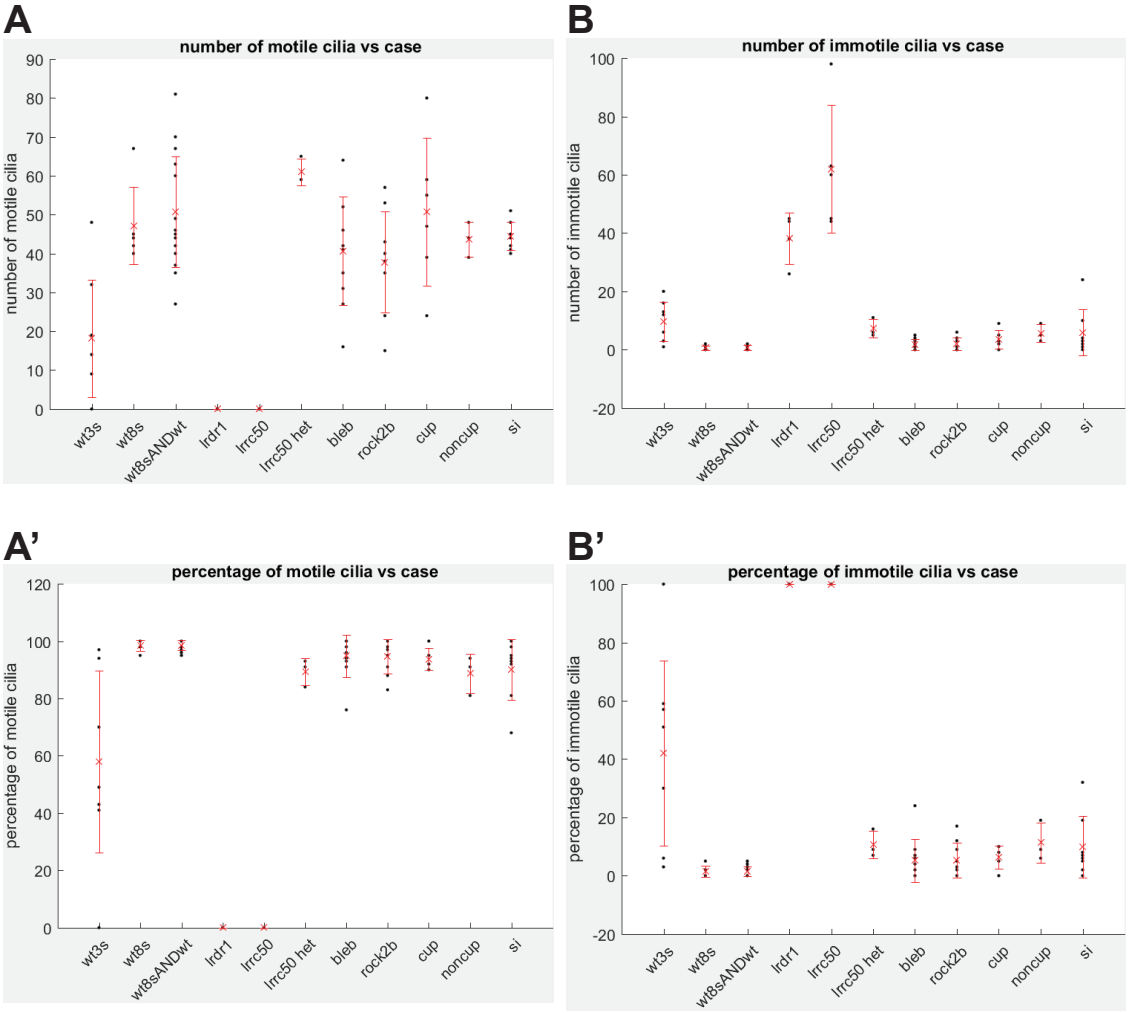

Manuscript 4 - Supplemental Fig. 8: Quantification of the number and percentage of motile and immotile cilia of individual KV at different stages and conditions: Dot plot displaying the values of the number **(A)** and percentage **(A')** of motile cilia versus case and number **(B)** and percentage **(B')** of immotile cilia versus case. For all conditions, each black dot represents one individual KV, the red cross displays the average value for all KVs of the respective condition and the red line the standard deviation of the mean (see the values in Supplemental Table 2-4). For **(A)** and **(B)**, the Y axis is displayed in absolute numbers and for **(A')** and **(B')** in percentages. Overall, for all candidates at 8-SS, the number of immotile cilia is almost insignificant (B-B'). Only wild-type embryos at 3-SS had a significant number of immotile cilia (≈40%, B-B'). Conversely, in the cases which cilia motility was disrupted, the number of motile cilia was reduced to zero (A-A'). In both lrdr1-morphant and lrrc50$^{-/-}$ embryos, all cilia were unable to beat. Despite all the individual variability in the morphological parameters of the KV, the average embryo per pre-selected condition presented similar values as the wild-type at the same developmental stage, and thus potential differences in 3D cilia orientation do not come from defects at the level of the overall KV morphogenesis. Cases code: wt3s = wild-type 3-SS; wt8s = wild-type 8-SS; wt8sANDwt = wild-type 8-SS and 9-14-SS merged; lrdr1 = *lrdr1*-morphant; lrrc50 = *lrrc50*$^{-/-}$; lrrc50 het = *lrrc50*$^{+/-}$ siblings, bleb = blebbistatin-treated; rock2b = *rock2b*-morphant; cup = *cup*$^{-/-}$; noncup = *cup*$^{+/+}$ or *cup*$^{+/-}$ siblings; si = situs inversus (*spaw*$^{-/-}$).

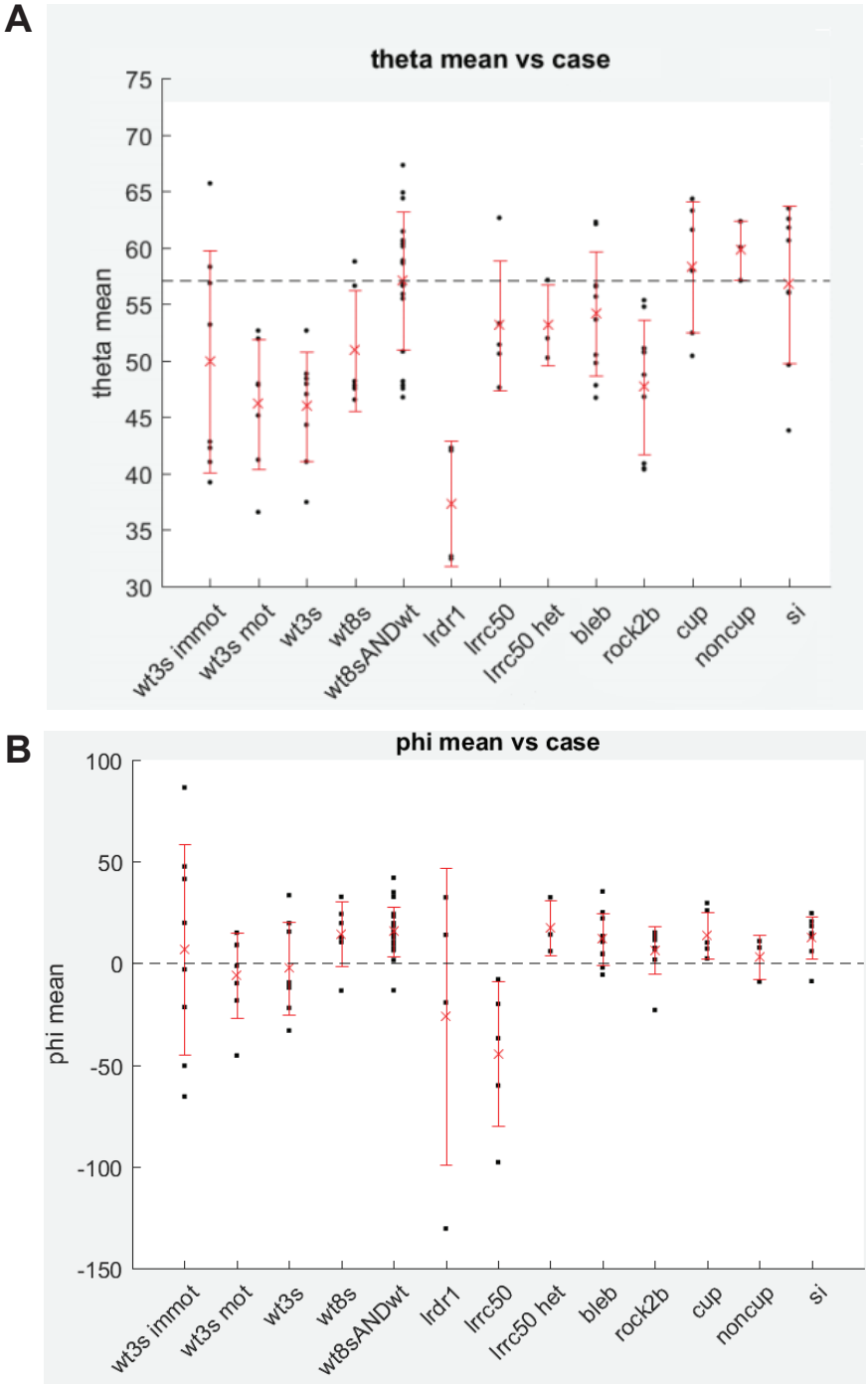

Manuscript 4 - Supplemental Fig. 9: Quantification of the mean value for θ and φ for individual KV at different stages and conditions: Dot plot displaying the mean values of θ **(A)** and mean values of φ **(B)** versus case. For all conditions, each black dot represents the mean values for one individual KV, the red cross displays the average value for all KVs of the respective condition and the red line the standard deviation of the mean (see the values in Supplemental Table 2-4). The Y-axis is displayed in degrees. For all conditions, the mean values of θ are higher than 0° **(A)**. The mean values of φ are always higher than zero, except for the conditions with immotile cilia **(B)**. Cases code: wt3s = wild-type 3-SS; wt8s = wild-type 8-SS; wt8sANDwt = wild-type 8-SS and 9-14-SS merged; lrdr1 = *lrdr1*-morphant; lrrc50 = *lrrc50*$^{-/-}$; lrrc50 het = *lrrc50*$^{+/-}$ siblings, bleb = blebbistatin-treated; rock2b = *rock2b*-morphant; cup = *cup*$^{-/-}$; noncup = *cup*$^{+/+}$ or *cup*$^{+/-}$ siblings; si = situs inversus (*spaw*$^{-/-}$)

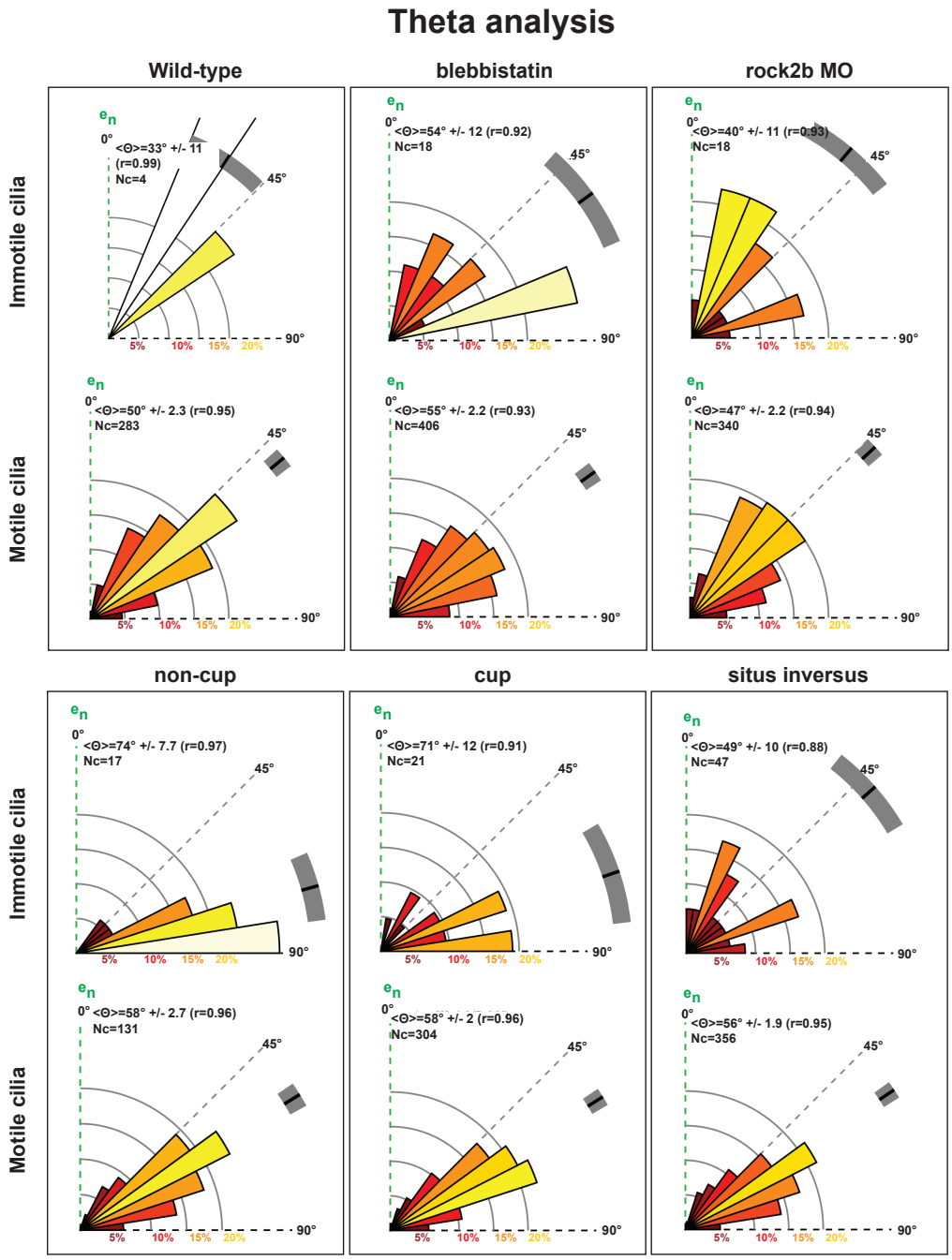

Manuscript 4 - Supplemental Fig. 10: Distributions of θ at 8-SS for immotile and motile cilia for all cases: Tilt angle (θ) distributions with the mean (black tick) and the 95% confidence interval (grey strip). Immotile cilia are not properly oriented in comparison with motile cilia.

N_c= number of cilia; r = dispersion of the vector; e_m= aligned along a meridian from the ventral to the dorsal pole of the KV; e_f= follows a KV parallel (has the same direction as the typical flow observed within the vesicle); e_n= vector normal to the KV surface and pointing towards the centre of the vesicle. Cases code: rock2b MO = *rock2b*-morphant; cup = *cup*$^{-/-}$; non cup = *cup*$^{+/+}$ or *cup*$^{+/-}$ siblings; situs inversus = *spaw*$^{-/-}$

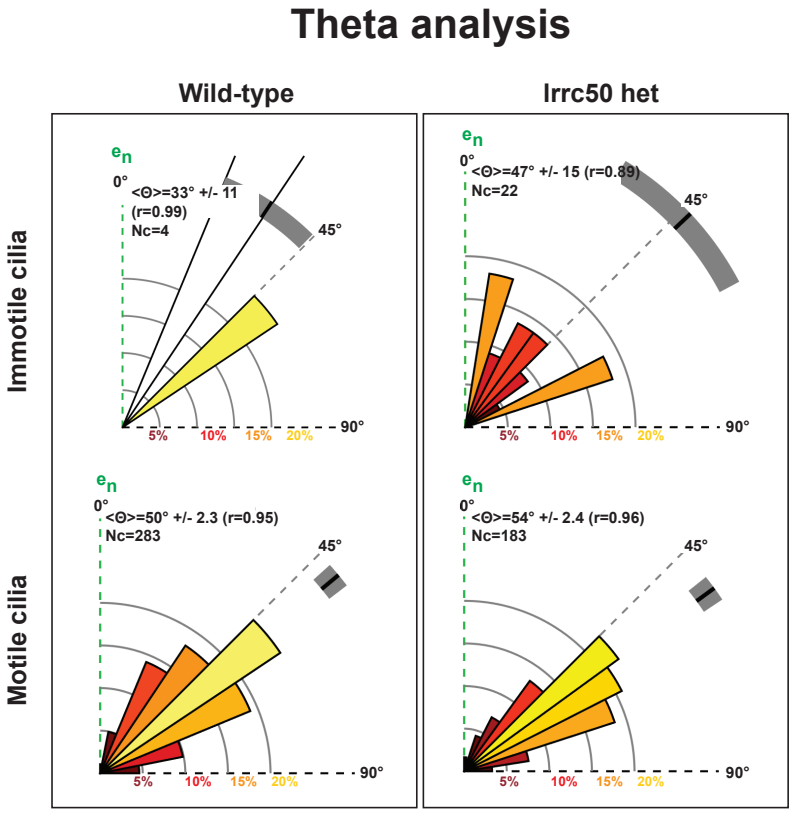

Manuscript 4 - Supplemental Fig. 11: Distributions of θ at 8-SS for immotile and motile cilia: Tilt angle (θ) distributions with the mean (black tick) and the 95% confidence interval (grey strip). Immotile cilia have a wider distribution of values and are not properly oriented in comparison with motile cilia. N_c= number of cilia; r = dispersion of the vector; e_m= aligned along a meridian from the ventral to the dorsal pole of the KV; e_f= follows a KV parallel (has the same direction as the typical flow observed within the vesicle); e_n= vector normal to the KV surface and pointing towards the centre of the vesicle.

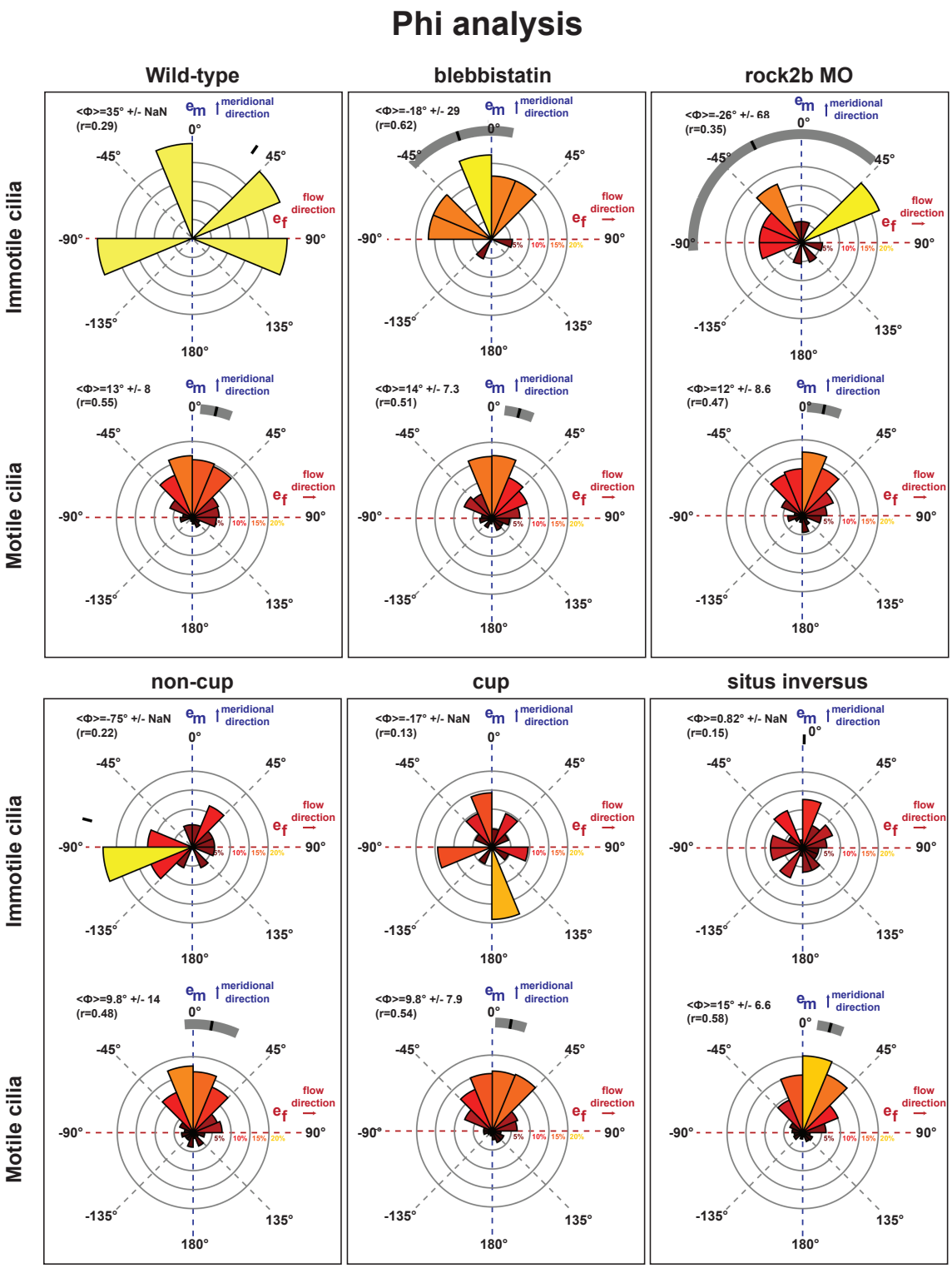

Manuscript 4 - Supplemental Fig. 12: Distributions of φ at 8-SS for immotile and motile cilia: Rosette plots showing the φ angle distribution values and the mean (black tick) with a 95% confidence interval (grey strip). In each rosette plot, 0° means the meridional direction and 90° the direction of the flow. Immotile cilia are not properly oriented compared to motile cilia. r = dispersion of the vector; e_m= aligned along a meridian from the ventral to the dorsal pole of the KV; e_f= follows a KV parallel (has the same direction as the typical flow observed within the vesicle). Cases code: lrdr1 MO = *lrdr1*-morphant; rock2b MO = *rock2b*-morphant; cup = *cup*$^{-/-}$; non cup = *cup*$^{+/+}$ or *cup*$^{+/-}$ siblings; situs inversus = *spaw*$^{-/-}$

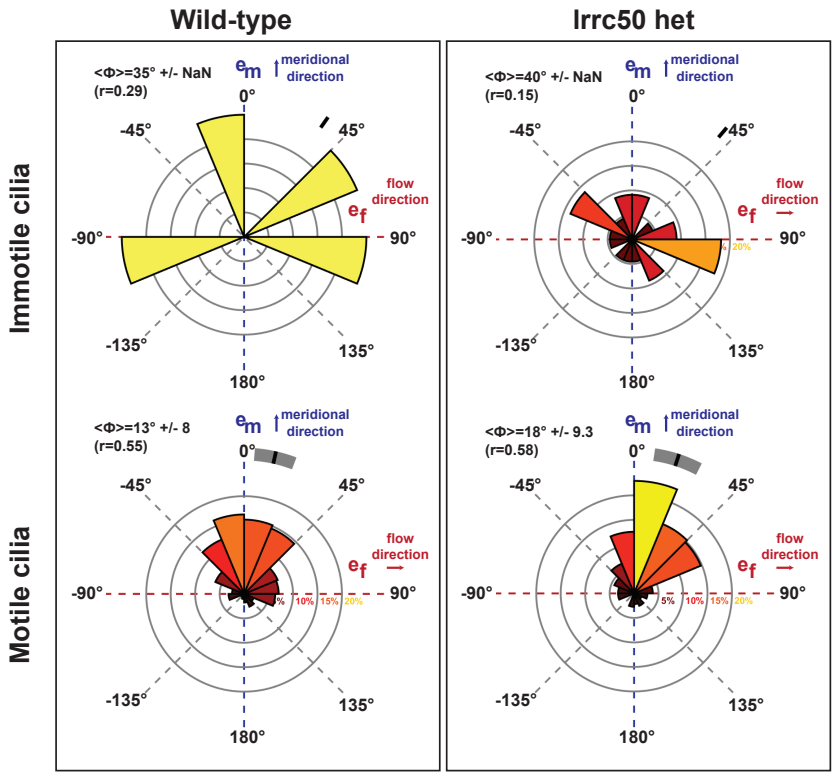

Manuscript 4 - Supplemental Fig. 13: Distributions of φ at 8-SS for immotile and motile cilia for Irrc50 het: Rosette plots showing the φ angle distribution values and the mean (black tick) with a 95% confidence interval (grey strip). In each rosette plot, 0° means the meridional direction and 90° the direction of the flow. Immotile cilia are randomly oriented compared to the motile cilia. r = dispersion of the vector; e_m= aligned along a meridian from the ventral to the dorsal pole of the KV; e_f= follows a KV parallel (has the same direction as the typical flow observed within the vesicle).

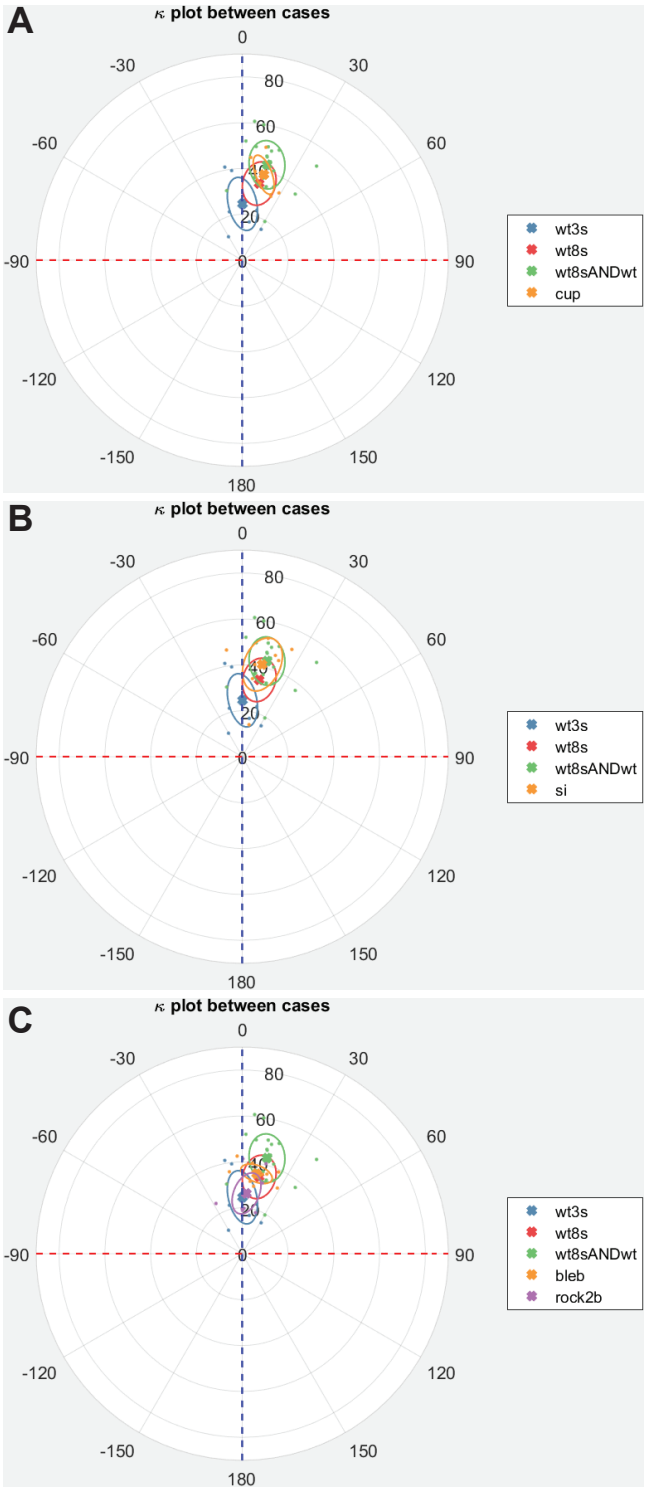

Manuscript 4 - Supplemental Fig. 14: cup$^{-/-}$, situs inversus (spaw$^{-/-}$), blebbistatin-treated and rock2b-morphant embryos have very similar cilia orientations compared to wild-type controls: K plots displaying the average θ and φ for the wild-type embryos analysed in comparison with the *cup*$^{-/-}$ **(A)**, *situs inversus*$^{-/-}$ **(B)** and blebbistatin-treated and *rock2b*-morphants embryos **(C)**. Comparisons between the three wild-type developmental stages (3-SS in blue; 8-SS in red, 8SS and later stages in green) with the *cup*$^{-/-}$ (orange in **A**), the situs inversus (*spaw*$^{-/-}$) (orange in **B**), blebbistatin-treated and *rock2b*-morphants embryos (orange and purple in **C** respectively). For all cases, each dot represents the average value of θ and φ per embryo, and each cross the average θ and φ per condition: φ values can be read around the rosette, while θ values on the grey lines going from the centre to the periphery. The circles around each cross display the standard deviation (see also Supplemental Table 4). Cases code: wt3s = wild-type 3-SS; wt8s = wild-type 8-SS; wt8sANDwt = wild-type 8-SS and 9-14-SS merged; cup = *cup*$^{-/-}$; si = situs inversus (*spaw*$^{-/-}$); bleb = blebbistatin-treated; rock2b = *rock2b*-morphant

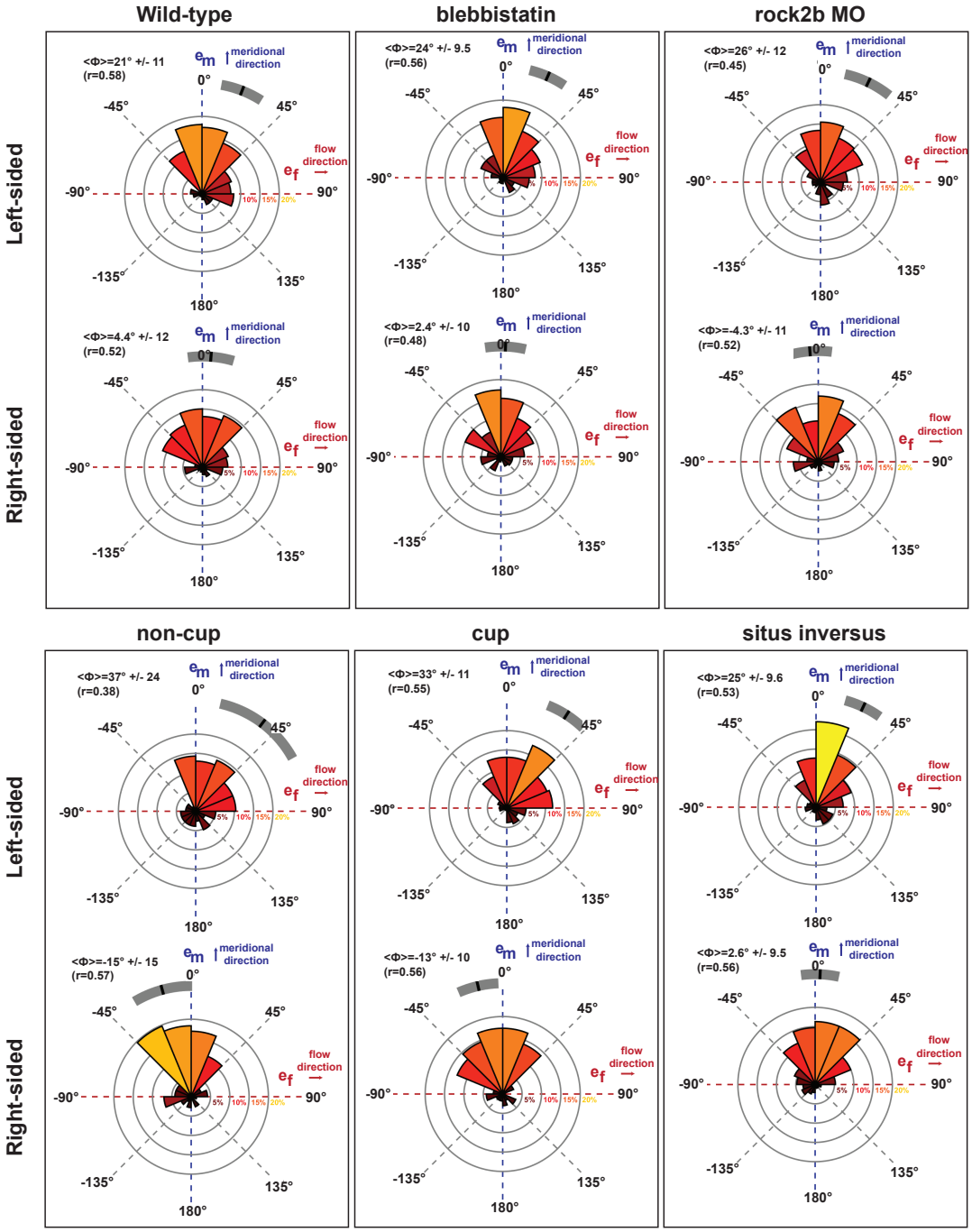

Manuscript 4 - Supplemental Fig. 15: Distributions of φ at 8-SS for all cilia on the left-side and right-side of the KV: Rosette plots showing the φ angle distribution values and the mean (black tick) with a 95% confidence interval (grey strip). In each rosette plot, 0° means the meridional direction and 90° the direction of the flow. Values of φ are always higher on the left-sided cilia in comparison with the right-sided. r = dispersion of the vector; e_m= aligned along a meridian from the ventral to the dorsal pole of the KV; e_f= follows a KV parallel (has the same direction as the typical flow observed within the vesicle). Cases code: rock2b MO = *rock2b*-morphant; cup = *cup*$^{-/-}$; non cup = *cup*$^{+/+}$ or *cup*$^{+/-}$ siblings; situs inversus = *spaw*$^{-/-}$

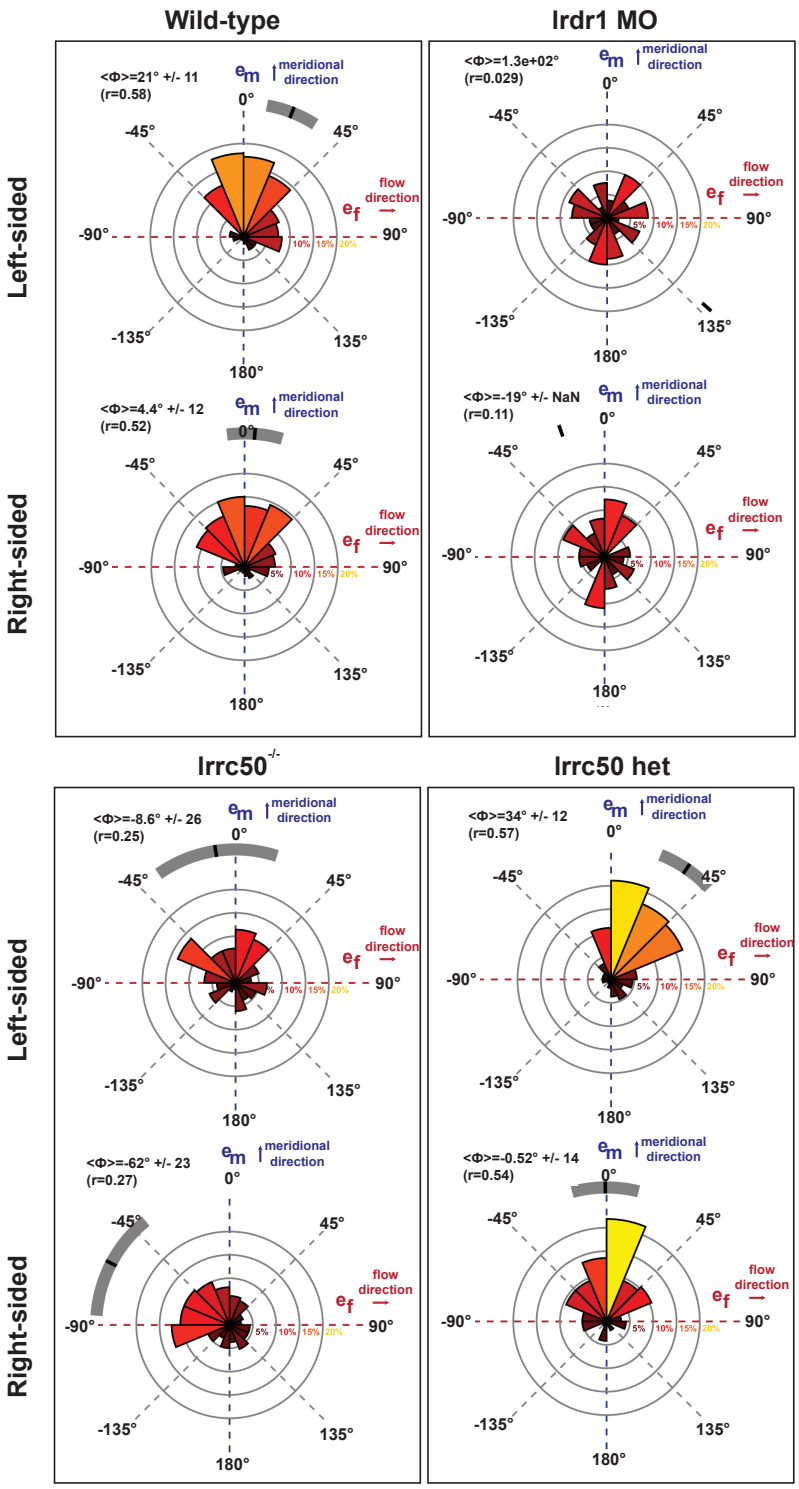

Manuscript 4 - Supplemental Fig. 16: Distributions of φ at 8-SS for all cilia on the left-side and right-side of the KV for motility-disrupted cases: Rosette plots showing the φ angle distribution values and the mean (black tick) with a 95% confidence interval (grey strip). In each rosette plot, 0° means the meridional direction and 90° the direction of the flow. Values of φ are always higher on the left-sided cilia in comparison with the right-sided. r = dispersion of the vector; e_m= aligned along a meridian from the ventral to the dorsal pole of the KV; e_f= follows a KV parallel (has the same direction as the typical flow observed within the vesicle). Cases code: Irdr1 MO = *Irdr1*-morphant

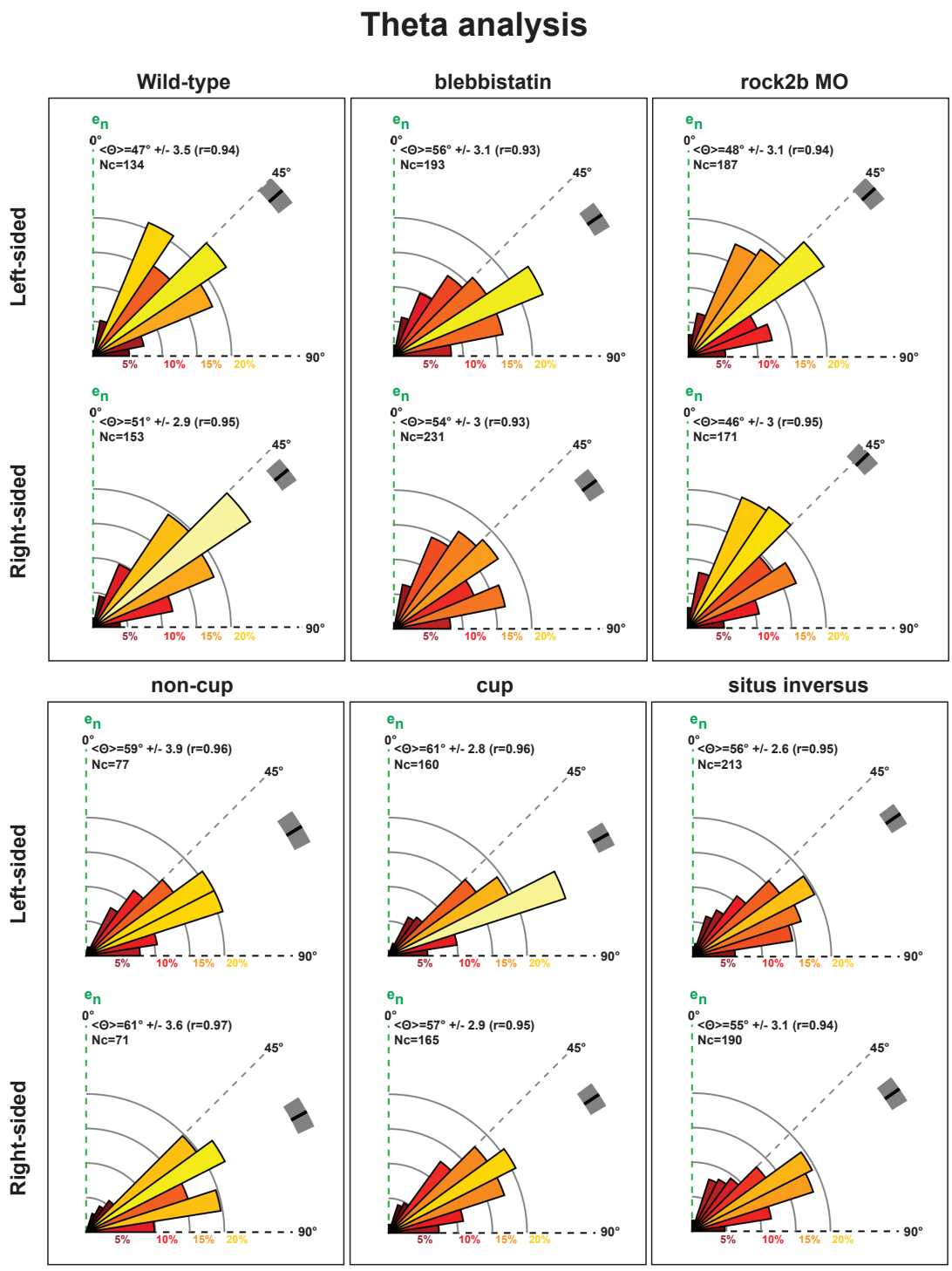

Manuscript 4 - Supplemental Fig. 17: Distributions of θ at 8-SS for all cilia on the left and right sides of the KV: Tilt angle (θ) distributions with the mean (black tick) and the 95% confidence interval (grey strip). Each rosette plot shows the distribution between 0° (orthogonal to the cell surface) and 90° (parallel to the cell surface). There is no LR difference of the θ values. N_c= number of cilia; r = dispersion of the vector; e_m= aligned along a meridian from the ventral to the dorsal pole of the KV; e_f= follows a KV parallel (has the same direction as the typical flow observed within the vesicle); e_n= vector normal to the KV surface and pointing towards the centre of the vesicle. Cases code: rock2b MO = *rock2b*-morphant; cup = cup$^{-/-}$; non cup = *cup*$^{+/+}$ or *cup*$^{+/-}$ siblings; situs inversus = *spaw*$^{-/-}$

Theta analysis

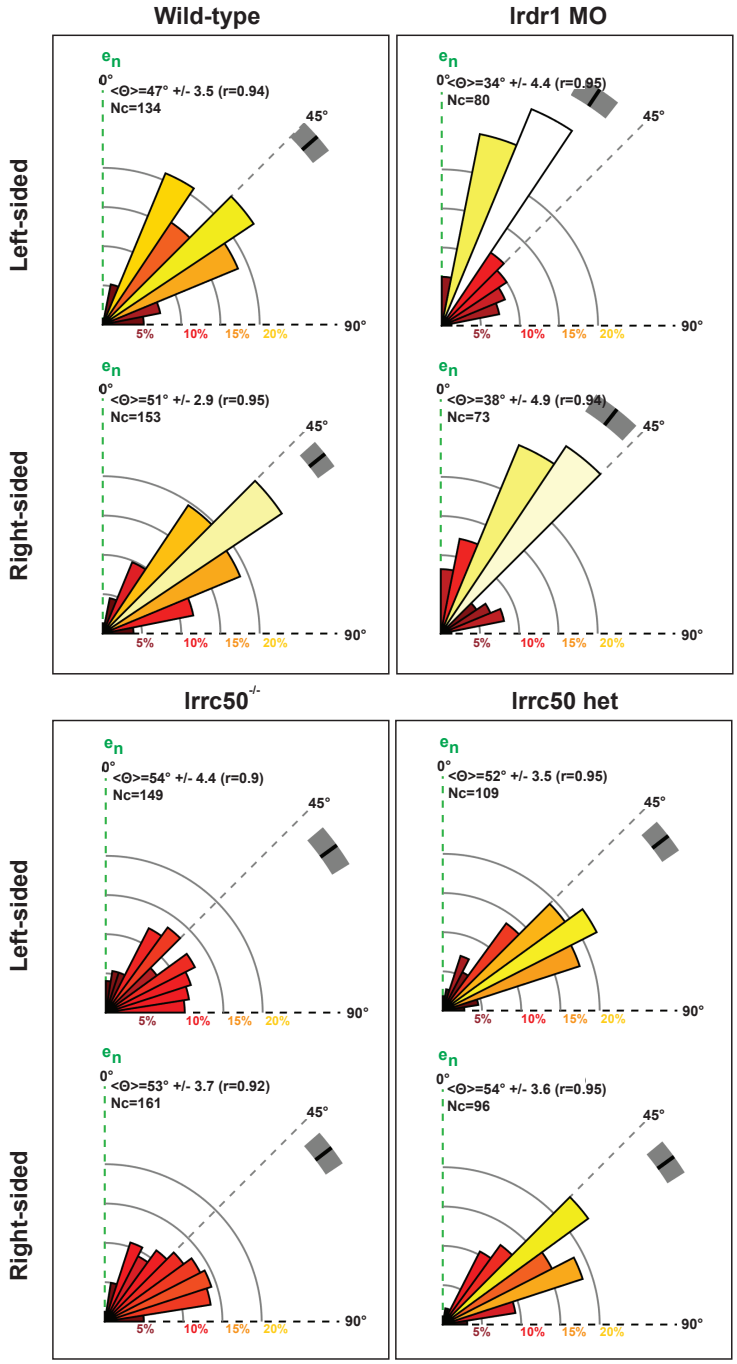

Manuscript 4 - Supplemental Fig. 18: Distributions of θ at 8-SS for all cilia on the left-side and right-side of the KV: Tilt angle (θ) distributions with the mean (black tick) and the 95% confidence interval (grey strip). Each rosette plot shows the distribution between 0° (orthogonal to the cell surface) and 90° (parallel to the cell surface). N_c= number of cilia; r = dispersion of the vector; e_m= aligned along a meridian from the ventral to the dorsal pole of the KV; e_f= follows a KV parallel (has the same direction as the typical flow observed within the vesicle); e_n= vector normal to the KV surface and pointing towards the centre of the vesicle. Cases code: Irdr1 MO = *Irdr1*-morphant

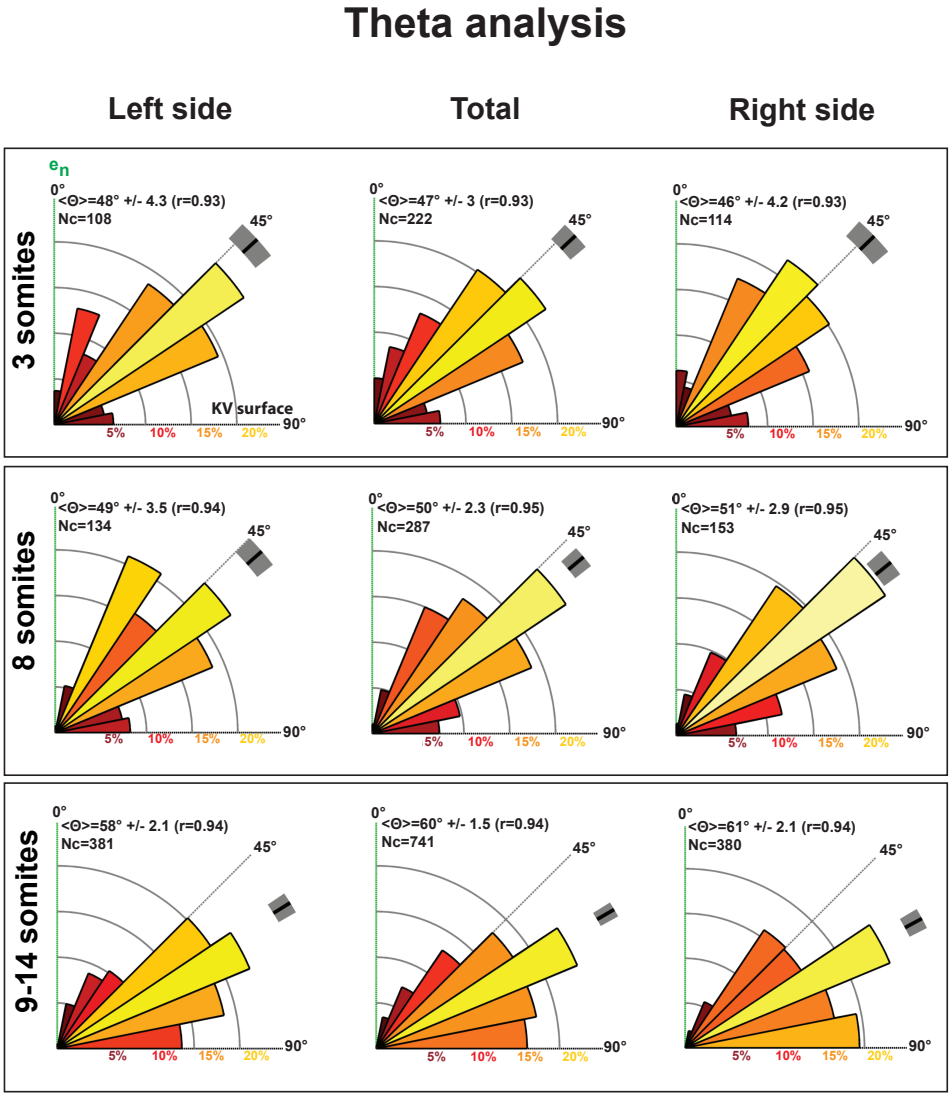

Manuscript 4 - Supplemental Fig. 19: Distribution of θ at different stages for cilia in the left side of the KV and the right side: Tilt angle (θ) distributions with the mean (black tick) and the 95% confidence interval (grey strip). The plots in the middle show the distribution for the whole KV. There is no difference between the left and right sides at any developmental stage. N_c= number of cilia; r = dispersion of the vector; e_m= aligned along a meridian from the ventral to the dorsal pole of the KV; e_f= follows a KV parallel (has the same direction as the typical flow observed within the vesicle).

spaw expression	Arl13b-GFP		blebbistatin		rock2b MO		rock2b +/+		rock2b -/-		lrdr1 MO		lrrc50 +/+		lrrc50 +/-		lrrc50 -/-	
	average	StDev.P	average	StDev.P	average	StDev.P	average	StDev.P	average	StDev.P	average	StDev.P	average	StDev.P	average	StDev.P	average	StDev.P
left	92,3%	6,9%	71,2%	2,5%	27,9%	1,3%	94,8%	1,9%	95,7%	1,7%	52,47%	1,77%	82,11%	10,91%	82,34%	9,85%	16,51%	8,77%
bilateral	7,7%	6,9%	17,1%	4,8%	48,1%	4,0%	2,7%	1,5%	3,4%	1,5%	21,53%	1,22%	16,83%	10,04%	15,98%	10,63%	65,17%	19,20%
right	0,0%	0,0%	4,2%	1,1%	6,9%	0,5%	1,1%	1,1%	0,8%	0,3%	8,66%	1,03%	0,35%	0,61%	0,41%	0,47%	16,14%	8,91%
absent	0,0%	0,0%	7,5%	1,3%	17,1%	5,9%	1,4%	0,7%	0,0%	0,0%	17,34%	0,38%	0,70%	1,22%	1,28%	1,94%	2,18%	2,25%
n_experiments	4		2		2		2		2		3		4					
n_embryos	386		242		297		565		537		356		1298					

spaw expression	AB		cup +/+		cup +/-		cup -/-		spaw +/+		spaw +/-		spaw -/-		non trilobite		trilobite -/-	
	average	StDev.P	average	StDev.P	average	StDev.P	average	StDev.P	average	StDev.P	average	StDev.P	average	StDev.P	average	StDev.P	average	StDev.P
left	99,0%	1,0%	81,36%	13,18%	94,67%	2,36%	0,00%	0,00%	92,08%	7,18%	89,40%	7,61%	0,00%	0,00%	74,80%	8,53%	46,50%	8,47%
bilateral	1,0%	1,0%	18,64%	13,18%	5,33%	2,36%	98,84%	1,16%	7,22%	7,40%	9,26%	6,56%	0,00%	0,00%	24,60%	8,21%	53,20%	8,02%
right	0,0%	0,0%	0,00%	0,00%	0,00%	0,00%	1,16%	1,16%	0,00%	0,00%	0,00%	0,00%	0,00%	0,00%	0,20%	0,24%	0,00%	0,00%
absent	0,0%	0,0%	0,00%	0,00%	0,00%	0,00%	0,00%	0,00%	0,71%	1,00%	1,35%	1,29%	100,00%	0,00%	0,30%	0,47%	0,30%	0,47%
n_experiments	2		2						3						3			
n_embryos	257		302						612						577			

Heart and Gut situs	Arl13b-GFP		blebbistatin		rock2b MO		rock2b +/+		rock2b -/-		lrdr1 MO		lrrc50 +/+		lrrc50 +/-		lrrc50 -/-	
	average	StDev.P	average	StDev.P	average	StDev.P	average	StDev.P	average	StDev.P	average	StDev.P	average	StDev.P	average	StDev.P	average	StDev.P
situs solitus	93,4%	0,6%	68,3%	4,3%	46,3%	3,0%	91,3%	1,8%	95,3%	3,5%	58,28%	13,08%	90,33%	5,43%	95,50%	5,68%	35,09%	2,46%
heterotaxy	5,3%	0,9%	28,3%	2,9%	40,9%	1,8%	6,4%	1,8%	3,1%	2,3%	37,69%	13,91%	9,79%	5,63%	4,16%	5,74%	39,65%	1,11%
situs inversus	1,3%	0,3%	3,5%	1,3%	12,9%	1,2%	2,3%	0,1%	1,6%	1,2%	4,02%	0,82%	0,00%	0,00%	0,34%	0,59%	25,26%	2,06%
n_experiments	2		2		2		2		2		2		4					
n_embryos	257		419		292		753		484		477		893					

Heart and Gut situs	AB		cup +/+		cup +/-		cup -/-		spaw +/+		spaw +/-		spaw -/-		non trilobite		trilobite -/-	
	average	StDev.P	average	StDev.P	average	StDev.P	average	StDev.P	average	StDev.P	average	StDev.P	average	StDev.P	average	StDev.P	average	StDev.P
situs solitus	96,6%	0,6%	93,00%	7,00%	93,50%	4,50%	25,50%	6,50%	96,36%	0,70%	72,13%	3,28%	16,47%	0,60%	87,62%	2,85%	23,47%	0,26%
heterotaxy	3,4%	0,6%	5,50%	5,50%	6,00%	4,00%	63,50%	6,50%	3,64%	0,70%	27,46%	3,69%	76,33%	1,72%	11,02%	4,21%	63,50%	0,79%
situs inversus	0,0%	0,0%	1,50%	1,50%	1,00%	1,00%	11,50%	0,50%	0,00%	0,00%	0,41%	0,41%	7,20%	2,32%	1,36%	1,36%	13,03%	0,53%
n_experiments	2		2						2						2			
n_embryos	361		372						370						298			

Manuscript 4 - Supplemental Table 1: Table summarizing the average and stdev.p for the quantification of the *spaw* expression patterns in the LPM and the heart and gut *situs* for all the conditions studied in this manuscript. The number of experiments performed and the total number of embryos for all conditions are also depicted in this table.

wild-type 3SS (wt3s)																							
Vesicle #	EllipsoidAxisa (µm)	AEllipsoidAxisb (µm)	Radius (µm)	Ell. Volume (pL)	Average Cilium	Phi Mean	R Phi	Phi confidence	Theta Mean	R Theta	Theta confidence	Theta Average	Phi Average	Ellipsoid fit RMS residue (µm)	Mean density (cilia/µm²)	Nb Total cilia	Nb Motile cilia	% Motile cilia	Nb Immotile cilia	% Immotile cilia
1	26,90	11,62	22,00	35,00	0,75	15,55	0,59	16,76	48,40	0,94	5,68	33,66	11,37	2,07	0,01	56,00	48,00	86,00	3,00	5,00
2	20,51	11,70	18,00	21,00	0,81	-11,98	0,62	25,32	48,82	0,95	8,07	39,37	-6,73	1,56	0,01	23,00	14,00	61,00	6,00	26,00
3	23,36	11,99	20,00	27,00	0,74	-11,53	0,66	18,65	52,64	0,91	8,72	41,32	-10,61	2,38	0,01	35,00	32,00	91,00	1,00	3,00
4	17,62	11,41	16,00	15,00	0,75	19,73	0,40	48,16	41,03	0,92	11,08	22,68	16,24	2,14	0,01	21,00	14,00	67,00	6,00	29,00
5	14,60	8,52	13,00	8,00	0,75	-33,11	0,30		37,45	0,93	10,94	11,83	-30,34	1,50	0,01	19,00	0,00	0,00	16,00	84,00
6	14,79	9,70	13,00	9,00	0,65	-9,49	0,26		47,01	0,92	10,37	16,96	10,44	1,78	0,01	24,00	9,00	38,00	13,00	54,00
7	13,80	12,15	13,00	10,00	0,65	-21,97	0,39	46,28	47,93	0,90	11,75	21,86	-14,92	1,92	0,01	23,00	9,00	39,00	12,00	52,00
8	18,19	11,27	16,00	16,00	0,68	33,49	0,27	54,79	44,29	0,92	7,95	15,78	31,55	2,05	0,01	40,00	19,00	48,00	20,00	50,00
All Vesicles	18,72	11,05	16,00	17,00	0,71	1,37	0,43	11,35	46,69	0,92	3,06	26,48	2,68	1,92	0,01	30,00	18,00	60,00	10,00	32,00

wild-type 8SS (wt8s)																							
Vesicle #	EllipsoidAxisa (µm)	AEllipsoidAxisb (µm)	Radius (µm)	Ell. Volume (pL)	Average Cilium	Phi Mean	R Phi	Phi confidence	Theta Mean	R Theta	Theta confidence	Theta Average	Phi Average	Ellipsoid fit RMS residue (µm)	Mean density (cilia/µm²)	Nb Total cilia	Nb Motile cilia	% Motile cilia	Nb Immotile cilia	% Immotile cilia
1	28,87	18,44	25,00	64,00	0,77	-13,46	0,49	22,05	46,53	0,95	5,17	31,13	-12,51	1,21	0,01	50,00	40,00	80,00	2,00	4,00
2	21,54	7,64	17,00	15,00	0,79	10,39	0,63	16,36	47,51	0,93	6,28	36,78	9,05	1,11	0,01	49,00	45,00	92,00	1,00	2,00
3	25,22	11,36	21,00	30,00	0,71	12,68	0,64	17,31	58,76	0,94	6,38	46,35	13,61	2,25	0,01	43,00	42,00	98,00	0,00	0,00
4	27,48	12,39	22,00	39,00	0,67	24,28	0,55	19,35	56,62	0,92	6,87	41,33	19,46	2,46	0,01	50,00	44,00	88,00	1,00	2,00
5	25,81	13,04	21,00	36,00	0,78	19,73	0,58	15,03	47,80	0,96	3,76	33,73	18,09	1,76	0,01	71,00	67,00	94,00	0,00	0,00
6	30,00	22,43	27,00	85,00	0,68	32,67	0,27	47,47	48,17	0,95	5,22	19,54	30,41	1,66	0,00	47,00	45,00	96,00	0,00	0,00
All Vesicles	26,49	14,22	22,00	45,00	0,72	13,69	0,52	8,13	50,50	0,94	2,27	34,08	12,33	1,74	0,01	52,00	47,00	91,00	1,00	1,00

wild-type 8-14SS (wt8sANDwt)																							
Vesicle #	EllipsoidAxisa (µm)	AEllipsoidAxisb (µm)	Radius (µm)	Ell. Volume (pL)	Average Cilium	Phi Mean	R Phi	Phi confidence	Theta Mean	R Theta	Theta confidence	Theta Average	Phi Average	Ellipsoid fit RMS residue (µm)	Mean density (cilia/µm²)	Nb Total cilia	Nb Motile cilia	% Motile cilia	Nb Immotile cilia	% Immotile cilia
1	28,76	18,47	25,00	64,00	0,76	-13,32	0,49	22,08	46,74	0,95	5,20	31,07	-12,62	1,24	0,01	50,00	40,00	80,00	2,00	4,00
2	21,54	7,64	17,00	15,00	0,79	10,39	0,63	16,36	47,51	0,93	6,28	36,78	9,05	1,11	0,01	49,00	45,00	92,00	1,00	2,00
3	25,22	11,36	21,00	30,00	0,71	12,68	0,64	17,31	58,76	0,94	6,38	46,35	13,61	2,25	0,01	43,00	42,00	98,00	0,00	0,00
4	27,48	12,39	22,00	39,00	0,67	24,28	0,55	19,35	56,62	0,92	6,87	41,33	19,46	2,46	0,01	50,00	44,00	88,00	1,00	2,00
5	25,81	13,04	21,00	36,00	0,78	19,73	0,58	15,03	47,80	0,96	3,76	33,73	18,09	1,76	0,01	71,00	67,00	94,00	0,00	0,00
6	30,00	22,43	27,00	85,00	0,68	32,67	0,27	47,47	48,17	0,95	5,22	19,54	30,41	1,66	0,00	47,00	45,00	96,00	0,00	0,00
7	36,84	30,54	35,00	174,00	0,61	14,34	0,42	19,77	58,62	0,94	4,49	36,90	14,37	2,06	0,01	89,00	70,00	79,00	0,00	0,00
8	27,15	15,36	23,00	47,00	0,68	13,18	0,57	14,80	60,11	0,94	4,87	46,66	13,35	1,99	0,01	78,00	63,00	81,00	0,00	0,00
9	32,95	20,46	29,00	93,00	0,71	15,14	0,65	12,22	61,43	0,94	4,53	50,77	12,83	2,15	0,01	80,00	67,00	84,00	0,00	0,00
10	32,98	20,04	29,00	91,00	0,71	15,77	0,59	17,62	56,74	0,92	6,72	44,69	15,98	2,64	0,00	50,00	44,00	88,00	0,00	0,00
11	31,27	17,05	26,00	70,00	0,72	23,14	0,55	15,29	50,79	0,94	4,65	34,08	23,08	2,01	0,01	78,00	67,00	86,00	2,00	3,00
12	35,72	20,70	31,00	111,00	0,69	15,30	0,60	12,44	69,64	0,92	4,87	49,32	15,06	1,69	0,01	94,00	81,00	86,00	2,00	2,00
13	33,97	25,63	31,00	124,00	0,66	6,41	0,49	20,02	55,48	0,94	5,44	36,37	8,63	1,78	0,01	62,00	46,00	74,00	2,00	3,00
14	24,33	19,56	23,00	48,00	0,75	42,08	0,72	15,64	60,34	0,92	7,67	52,34	38,34	4,35	0,01	39,00	35,00	90,00	1,00	3,00
15	30,93	13,00	25,00	52,00	0,74	9,46	0,68	17,78	58,86	0,93	7,96	49,91	7,04	2,58	0,00	35,00	27,00	77,00	0,00	0,00
16	32,46	16,74	27,00	74,00	0,74	1,53	0,71	14,03	60,61	0,93	6,54	52,05	1,76	2,30	0,01	49,00	37,00	76,00	0,00	0,00
17	30,17	21,57	27,00	82,00	0,82	7,17	0,82	11,31	64,87	0,94	5,87	60,84	5,12	2,86	0,01	50,00	44,00	88,00	1,00	2,00
18	29,52	23,31	27,00	85,00	0,73	9,66	0,71	13,27	67,30	0,95	4,81	59,86	9,05	2,60	0,01	55,00	49,00	89,00	1,00	2,00
19	33,38	10,02	26,00	47,00	0,67	34,97	0,50	21,93	55,88	0,95	5,49	37,00	38,75	2,08	0,01	49,00	40,00	82,00	2,00	4,00
20	26,63	19,00	24,00	56,00	0,63	18,44	0,56	14,75	64,37	0,93	5,26	50,67	18,55	1,75	0,01	79,00	60,00	76,00	0,00	0,00
All Vesicles	29,86	17,92	26,00	71,00	0,69	15,09	0,57	3,69	57,27	0,93	1,26	43,18	14,37	2,17	0,01	60,00	51,00	85,00	1,00	1,00

Manuscript 4 - Supplemental Table 2: Table summarizing some of the cilia features collected from the 3D-CiliaMap for individual wild-type KV at 3-, 8- and 9-14-SS. The last row of each table represents the Mean values for each category.

rock2b MO (rock2b)

Vesicle #	EllipsoidAxisa (µm)	AEllipsoidAxisb (µm)	Radius (µm)	Ell. Volume (pL)	Average Cilium	Phi Mean	R Phi	Phi confidence	Theta Mean	R Theta	Theta confidence	Theta Average	Phi Average	Ellipsoid fit RMS residue (µm)	Mean density (cilia/µm²)	Nb Total cilia	Nb Motile cilia	% Motile cilia	Nb Immotile cilia	% Imotile cilia
1	25,01	14,21	21,00	37,00	0,67	15,12	0,48	20,34	51,08	0,90	7,02	31,97	15,98	2,27	0,01	61,00	43,00	70,00	6,00	10,00
2	27,54	17,30	24,00	55,00	0,69	7,55	0,45	25,30	48,73	0,94	6,11	26,56	4,61	2,44	0,01	47,00	38,00	81,00	0,00	0,00
3	32,08	19,55	28,00	84,00	0,68	11,55	0,32	33,76	46,78	0,94	5,16	18,78	17,90	3,86	0,01	60,00	57,00	95,00	1,00	2,00
4	21,73	16,67	20,00	33,00	0,63	-22,99	0,31	48,89	50,71	0,91	9,08	24,67	-27,65	1,83	0,01	35,00	15,00	43,00	3,00	9,00
5	30,34	19,63	27,00	76,00	0,77	13,88	0,35	37,13	40,34	0,95	5,54	19,79	2,25	2,35	0,00	42,00	35,00	83,00	0,00	0,00
6	30,50	19,10	27,00	74,00	0,77	11,52	0,35	36,80	40,45	0,95	5,75	19,73	-0,24	1,99	0,00	42,00	35,00	83,00	1,00	2,00
7	16,21	11,41	15,00	13,00	0,75	6,92	0,34	51,72	40,87	0,94	8,01	18,82	0,36	1,23	0,01	27,00	24,00	89,00	0,00	0,00
8	27,75	18,84	25,00	61,00	0,71	1,73	0,60	16,94	54,76	0,92	6,88	41,34	0,37	2,19	0,01	52,00	40,00	77,00	4,00	8,00
9	29,41	18,51	26,00	67,00	0,72	12,90	0,59	16,41	55,33	0,96	4,29	40,52	14,81	2,39	0,01	58,00	53,00	91,00	3,00	5,00
All Vesicles	26,73	17,25	24,00	56,00	0,70	8,27	0,43	8,59	48,41	0,93	2,14	27,37	6,09	2,28	0,01	47,00	38,00	80,00	2,00	4,00

blebbistatin (bleb)

Vesicle #	EllipsoidAxisa (µm)	AEllipsoidAxisb (µm)	Radius (µm)	Ell. Volume (pL)	Average Cilium	Phi Mean	R Phi	Phi confidence	Theta Mean	R Theta	Theta confidence	Theta Average	Phi Average	Ellipsoid fit RMS residue (µm)	Mean density (cilia/µm²)	Nb Total cilia	Nb Motile cilia	% Motile cilia	Nb Immotile cilia	% Imotile cilia
1	38,86	17,75	32,00	112,00	0,54	25,06	0,42	21,05	62,27	0,90	7,77	38,97	24,08	3,12	0,01	79,00	64,00	81,00	4,00	5,00
2	27,13	15,63	23,00	48,00	0,64	10,59	0,39	37,54	53,62	0,94	7,30	29,78	9,59	1,77	0,00	32,00	27,00	84,00	0,00	0,00
3	33,79	18,97	29,00	91,00	0,64	22,10	0,46	24,92	56,65	0,93	6,54	36,29	17,24	3,38	0,00	47,00	42,00	89,00	0,00	0,00
4	24,47	17,58	22,00	44,00	0,70	13,45	0,56	17,61	50,48	0,90	9,18	35,68	14,27	1,83	0,01	57,00	46,00	81,00	2,00	4,00
5	20,11	18,43	20,00	31,00	0,64	35,32	0,40	32,76	55,66	0,95	5,85	32,44	28,20	1,97	0,01	39,00	35,00	90,00	0,00	0,00
6	28,31	17,97	25,00	60,00	0,59	-2,08	0,44	22,64	62,08	0,92	6,12	42,56	2,99	2,23	0,01	61,00	52,00	85,00	1,00	2,00
7	26,94	15,37	23,00	47,00	0,73	11,12	0,57	17,21	49,77	0,92	6,25	35,67	10,56	2,14	0,01	57,00	52,00	91,00	0,00	0,00
8	31,67	14,25	26,00	60,00	0,67	4,76	0,56	20,15	56,56	0,94	6,21	39,67	6,39	2,12	0,01	44,00	41,00	93,00	3,00	7,00
9	25,12	12,29	21,00	32,00	0,76	4,45	0,54	23,94	47,80	0,96	5,30	31,71	6,23	2,31	0,01	36,00	31,00	86,00	3,00	8,00
10	21,99	14,59	19,00	30,00	0,81	-5,59	0,69	22,50	46,70	0,95	7,92	36,11	-8,95	1,53	0,00	22,00	16,00	73,00	5,00	23,00
All Vesicles	27,84	16,28	24,00	56,00	0,65	12,15	0,48	7,12	55,23	0,92	2,16	35,95	11,20	2,24	0,01	47,00	41,00	86,00	2,00	4,00

lrrc50 -/- (lrrc50)

Vesicle #	EllipsoidAxisa (µm)	AEllipsoidAxisb (µm)	Radius (µm)	Ell. Volume (pL)	Average Cilium	Phi Mean	R Phi	Phi confidence	Theta Mean	R Theta	Theta confidence	Theta Average	Phi Average	Ellipsoid fit RMS residue (µm)	Mean density (cilia/µm²)	Nb Total cilia	Nb Motile cilia	% Motile cilia	Nb Immotile cilia	% Imotile cilia
1	23,17	20,10	22,00	45,00	0,66	7,92	0,30	42,88	47,80	0,92	5,95	20,44	4,71	2,79	0,01	49,00	0,00	0,00	49,00	100,00
2	21,01	14,43	19,00	27,00	0,67	-19,99	0,29	42,48	53,27	0,93	9,85	20,87	-16,13	4,42	0,01	49,00	0,00	0,00	45,00	92,00
3	29,88	21,55	26,00	75,00	0,60	-97,87	0,15		50,69	0,93	6,79	20,83	-97,01	1,54	0,01	47,00	0,00	0,00	44,00	94,00
4	32,53	21,88	29,00	101,00	0,45	-36,87	0,17	52,07	62,63	0,92	4,70	19,23	-34,24	3,22	0,01	108,00	0,00	0,00	98,00	91,00
5	34,41	23,56	31,00	117,00	0,65	-60,14	0,41	22,54	51,40	0,93	5,39	22,43	-58,90	2,43	0,01	73,00	0,00	0,00	60,00	82,00
All Vesicles	28,00	20,50	25,00	73,00	0,56	-39,27	0,23	18,34	54,27	0,91	2,70	18,71	-36,82	2,28	0,01	69,00	0,00	0,00	62,00	89,00

lrdr1 MO (lrdr1)

Vesicle #	EllipsoidAxisa (µm)	AEllipsoidAxisb (µm)	Radius (µm)	Ell. Volume (pL)	Average Cilium	Phi Mean	R Phi	Phi confidence	Theta Mean	R Theta	Theta confidence	Theta Average	Phi Average	Ellipsoid fit RMS residue (µm)	Mean density (cilia/µm²)	Nb Total cilia	Nb Motile cilia	% Motile cilia	Nb Immotile cilia	% Imotile cilia
1	25,73	13,30	22,00	37,00	0,80	-19,32	0,05		32,44	0,94	5,78	4,57	-67,00	2,24	0,01	48,00	0,00	0,00	44,00	92,00
2	24,19	16,72	22,00	41,00	0,69	-130,59	0,13		42,03	0,92	6,30	4,41	-94,66	3,16	0,01	57,00	0,00	0,00	45,00	79,00
3	20,38	12,46	18,00	22,00	0,70	13,99	0,13		42,25	0,93	6,92	8,01	10,56	1,56	0,01	42,00	0,00	0,00	38,00	90,00
4	16,97	10,64	15,00	13,00	0,81	32,45	0,29	56,66	32,64	0,96	6,14	8,53	19,62	0,95	0,01	33,00	0,00	0,00	26,00	79,00
All Vesicles	21,82	13,28	19,00	28,00	0,74	0,83	0,06		37,75	0,93	3,23	4,08	-23,17	1,98	0,01	45,00	0,00	0,00	38,00	85,00

Manuscript 4 - Supplemental Table 3: Table summarizing some of the cilia features collected from the 3D-CiliaMap for individual KV at 8-SS for rock2b-MO, blebbistatin-treated, lrrc50$^{-/-}$ and lrdr1-MO embryos. The last row of each table represents the Mean values for each category.

cup -/- (cup)

Vesicle #	EllipsoidAxisa (µm)	AEllipsoidAxisb (µm)	Radius (µm)	Ell. Volume (pL)	Average Cilium	Phi Mean	R Phi	Phi confidence	Theta Mean	R Theta	Theta confidence	Theta Average	Phi Average	Ellipsoid fit RMS residue (µm)	Mean density (cilia/µm²)	Nb Total cilia	Nb Motile cilia	% Motile cilia	Nb Immotile cilia	% Immotile cilia
1	33,89	22,91	30,00	110,00	0,65	2,35	0,56	16,62	61,57	0,97	3,75	44,99	4,78	1,67	0,01	65,00	55,00	85,00	3,00	5,00
2	42,29	26,08	37,00	195,00	0,64	10,19	0,60	12,39	64,32	0,94	4,25	50,34	11,88	3,00	0,01	96,00	80,00	83,00	9,00	9,00
3	23,15	10,86	19,00	24,00	0,70	29,66	0,48	23,31	52,43	0,96	4,99	33,44	28,66	1,24	0,01	47,00	39,00	83,00	2,00	4,00
4	23,16	13,58	20,00	31,00	0,65	7,23	0,49	19,62	57,94	0,96	4,43	39,11	8,30	1,68	0,01	62,00	59,00	95,00	0,00	0,00
5	24,04	13,84	21,00	34,00	0,70	25,98	0,44	32,80	50,40	0,94	7,53	30,49	24,16	1,30	0,01	31,00	24,00	77,00	2,00	6,00
6	31,19	21,17	28,00	86,00	0,51	7,17	0,35	29,74	63,27	0,94	5,39	34,55	13,12	1,64	0,01	61,00	47,00	77,00	5,00	8,00
All Vesicles	29,62	18,07	26,00	80,00	0,63	11,36	0,50	7,89	59,81	0,95	2,03	40,69	12,91	1,76	0,01	60,00	51,00	84,00	4,00	6,00

cup +/+ or +/- (non cup)

Vesicle #	EllipsoidAxisa (µm)	AEllipsoidAxisb (µm)	Radius (µm)	Ell. Volume (pL)	Average Cilium	Phi Mean	R Phi	Phi confidence	Theta Mean	R Theta	Theta confidence	Theta Average	Phi Average	Ellipsoid fit RMS residue (µm)	Mean density (cilia/µm²)	Nb Total cilia	Nb Motile cilia	% Motile cilia	Nb Immotile cilia	% Immotile cilia
1	26,86	17,04	24,00	52,00	0,71	10,91	0,61	17,11	62,32	0,97	4,32	50,55	8,52	1,16	0,01	50,00	44,00	88,00	3,00	6,00
2	25,71	17,73	23,00	49,00	0,64	7,70	0,44	23,73	57,08	0,96	4,26	35,36	4,76	1,29	0,01	55,00	48,00	87,00	5,00	9,00
3	29,02	17,84	25,00	63,00	0,51	-9,10	0,22	63,09	60,02	0,95	5,16	20,56	-12,07	1,99	0,01	50,00	39,00	78,00	9,00	18,00
All Vesicles	27,20	17,54	24,00	55,00	0,61	6,42	0,42	14,86	59,72	0,96	2,63	36,83	3,95	1,48	0,01	52,00	44,00	85,00	6,00	11,00

situs inversus -/- (si)

Vesicle #	EllipsoidAxisa (µm)	AEllipsoidAxisb (µm)	Radius (µm)	Ell. Volume (pL)	Average Cilium	Phi Mean	R Phi	Phi confidence	Theta Mean	R Theta	Theta confidence	Theta Average	Phi Average	Ellipsoid fit RMS residue (µm)	Mean density (cilia/µm²)	Nb Total cilia	Nb Motile cilia	% Motile cilia	Nb Immotile cilia	% Immotile cilia
1	29,90	22,35	27,00	84,00	0,66	18,31	0,56	19,63	61,77	0,97	4,51	46,43	18,19	1,99	0,00	47,00	40,00	85,00	2,00	4,00
2	30,44	18,33	26,00	71,00	0,69	24,66	0,63	16,05	63,47	0,96	4,78	51,51	24,90	1,49	0,01	51,00	48,00	94,00	0,00	0,00
3	30,61	22,75	28,00	89,00	0,69	13,74	0,17	66,88	43,80	0,93	5,19	14,24	12,09	2,52	0,01	79,00	51,00	65,00	24,00	30,00
4	37,05	16,48	30,00	95,00	0,67	5,91	0,55	17,65	56,06	0,92	6,42	40,62	7,81	1,80	0,01	60,00	44,00	73,00	10,00	17,00
5	38,03	23,51	33,00	142,00	0,68	-8,79	0,54	19,55	60,63	0,95	5,42	46,99	8,40	2,40	0,00	52,00	45,00	87,00	3,00	6,00
6	23,89	17,54	22,00	42,00	0,75	13,07	0,57	18,30	49,61	0,96	4,66	34,27	7,48	0,58	0,01	51,00	41,00	80,00	3,00	6,00
7	33,54	25,36	31,00	124,00	0,76	20,57	0,67	13,95	66,00	0,96	4,20	44,78	20,80	1,28	0,00	57,00	45,00	79,00	4,00	7,00
8	32,52	15,96	27,00	71,00	0,73	14,75	0,67	15,67	62,55	0,95	5,55	32,77	12,40	1,87	0,01	46,00	42,00	91,00	1,00	2,00
All Vesicles	32,00	20,29	28,00	89,00	0,68	13,19	0,51	6,87	65,86	0,94	1,94	39,31	12,24	1,74	0,01	55,00	45,00	80,00	6,00	11,00

Manuscript 4 - Supplemental Table 4: Table summarizing some of the cilia features collected from the 3D-CiliaMap for individual KV at 8-SS for cup$^{-/-}$, non-cup and situs inversus (spaw$^{-/-}$) embryos. The last row of each table represents the Mean values for each category.

	K	β	Φ	Θ
wt3s immotile	20	3,9	20,7	25,5
wt3s motile	52	16	-2,22	27,5
wt3s	63	18	0,298	24,6
wt8s	64	11	12,4	34,2
wtsANDwt	48	8,5	14,6	43
lrdr1 (MO)	5,00E+03	2,40E+03	-13,9	4,47
lrrc50 (mutant)	72	11	-36,9	17,8
lrrc50 het	3,00E+02	1,30E+02	17,9	37,2
lrrc50 het immotile	17	6,4	49,6	20,2
lrrc50 het motile	1,90E+02	56	17,3	40
bleb	1,80E+02	50	10,2	35,4
rock2b (MO)	83	21	3,96	26,3
cup	2,00E+02	72	14,2	38,5
non cup	8,10E+02	3,90E+02	3,03	35,2
situs inversus (si)	46	10	12,2	41,1

Manuscript 4 - Supplemental Table 5: Table summarizing some of the cilia features collected from the K plots for all conditions analysed. K values describe the standard deviation in a Gaussian, while β values describe the anisotropy between two orthogonal axes. θ and φ values are also displayed.

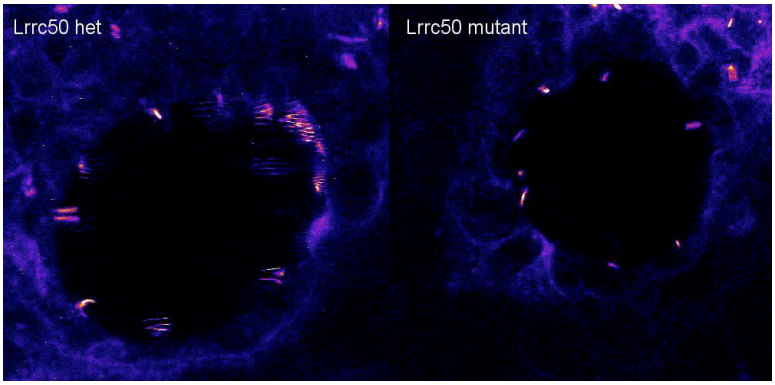

Manuscript 4 - Supplemental Movie 1: Visualization of KV cilia from the lrrc50 het and lrrc50 mutant. Embryos from the transgenic background (actb2:Arl13b-GFP) (Borovina et al., 2010), were crossed with the lrrc50 line (Sullivan-Brown et al., 2008), which allowed us to image cilia *in vivo*. Embryos were soaked for 60 minutes in Bodipy TR (Molecular Probe) prior imaging and 2PEF microscopy at 930 nm wavelength was used. A full z-stack of the KV can be seen for both cases. On the left panel, is depicted a KV from a lrrc50 het embryo, showing the cilia are motile (cone shape artefact), whereas on the right panel is shown the KV of a lrrc50 mutant embryo, with only immotile cilia (straight lines). Movie displayed at 15fps.

References

Beis, D., Bartman, T., Jin, S.W., Scott, I.C., D'Amico, L.A., Ober, E.A., Verkade, H., Frantsve, J., Field, H.A., Wehman, A., *et al.* (2005). Genetic and cellular analyses of zebrafish atrioventricular cushion and valve development. Development *132*, 4193-4204.

Borovina, A., Superina, S., Voskas, D., and Ciruna, B. (2010). Vangl2 directs the posterior tilting and asymmetric localization of motile primary cilia. Nat Cell Biol *12*, 407-412.

Boucher, C., and Sandford, R. (2004). Autosomal dominant polycystic kidney disease (ADPKD, MIM 173900, PKD1 and PKD2 genes, protein products known as polycystin-1 and polycystin-2). Eur J Hum Genet *12*, 347-354.

Colantonio, J.R., Vermot, J., Wu, D., Langenbacher, A.D., Fraser, S., Chen, J.N., and Hill, K.L. (2009). The dynein regulatory complex is required for ciliary motility and otolith biogenesis in the inner ear. Nature *457*, 205-209.

Delling, M., Indzhykulian, A.A., Liu, X., Li, Y., Xie, T., Corey, D.P., and Clapham, D.E. (2016). Primary cilia are not calcium-responsive mechanosensors. Nature *531*, 656-660.

Essner, J.J., Amack, J.D., Nyholm, M.K., Harris, E.B., and Yost, H.J. (2005). Kupffer's vesicle is a ciliated organ of asymmetry in the zebrafish embryo that initiates left-right development of the brain, heart and gut. Development *132*, 1247-1260.

Essner, J.J., Vogan, K.J., Wagner, M.K., Tabin, C.J., Yost, H.J., and Brueckner, M. (2002). Conserved function for embryonic nodal cilia. Nature *418*, 37-38.

Ferreira, R.R., and Vermot, J. (2016). The balancing roles of mechanical forces during left-right patterning and asymmetric morphogenesis. Mech Dev.

Field, S., Riley, K.L., Grimes, D.T., Hilton, H., Simon, M., Powles-Glover, N., Siggers, P., Bogani, D., Greenfield, A., and Norris, D.P. (2011). Pkd1l1 establishes left-right asymmetry and physically interacts with Pkd2. Development *138*, 1131-1142.

Fliegauf, M., Benzing, T., and Omran, H. (2007). When cilia go bad: cilia defects and ciliopathies. Nat Rev Mol Cell Biol *8*, 880-893.

Francescatto, L., Rothschild, S.C., Myers, A.L., and Tombes, R.M. (2010). The activation of membrane targeted CaMK-II in the zebrafish Kupffer's vesicle is required for left-right asymmetry. Development *137*, 2753-2762.

Gonzalez-Perrett, S., Kim, K., Ibarra, C., Damiano, A.E., Zotta, E., Batelli, M., Harris, P.C., Reisin, I.L., Arnaout, M.A., and Cantiello, H.F. (2001). Polycystin-2, the protein mutated in autosomal dominant polycystic kidney disease (ADPKD), is a Ca2+-permeable nonselective cation channel. Proc Natl Acad Sci U S A *98*, 1182-1187.

Guirao, B., Meunier, A., Mortaud, S., Aguilar, A., Corsi, J.M., Strehl, L., Hirota, Y., Desoeuvre, A., Boutin, C., Han, Y.G., *et al.* (2010). Coupling between hydrodynamic forces and planar cell polarity orients mammalian motile cilia. Nat Cell Biol *12*, 341-350.

Hamada, H., Meno, C., Watanabe, D., and Saijoh, Y. (2002). Establishment of vertebrate left-right asymmetry. Nat Rev Genet *3*, 103-113.

Hanaoka, K., Qian, F., Boletta, A., Bhunia, A.K., Piontek, K., Tsiokas, L., Sukhatme, V.P., Guggino, W.B., and Germino, G.G. (2000). Co-assembly of polycystin-1 and -2 produces unique cation-permeable currents. Nature *408*, 990-994.

Hashimoto, M., Shinohara, K., Wang, J., Ikeuchi, S., Yoshiba, S., Meno, C., Nonaka, S., Takada, S., Hatta, K., Wynshaw-Boris, A., *et al.* (2010). Planar polarization of node cells determines the rotational axis of node cilia. Nat Cell Biol *12*, 170-176.

Heisenberg, C.P., and Nusslein-Volhard, C. (1997). The function of silberblick in the positioning of the eye anlage in the zebrafish embryo. Dev Biol *184*, 85-94.

Heisenberg, C.P., Tada, M., Rauch, G.J., Saude, L., Concha, M.L., Geisler, R., Stemple, D.L., Smith, J.C., and Wilson, S.W. (2000). Silberblick/Wnt11 mediates convergent extension movements during zebrafish gastrulation. Nature *405*, 76-81.

Hirokawa, N., Tanaka, Y., and Okada, Y. (2012). Cilia, KIF3 molecular motor and nodal flow. Curr Opin Cell Biol *24*, 31-39.

Hojo, M., Takashima, S., Kobayashi, D., Sumeragi, A., Shimada, A., Tsukahara, T., Yokoi, H., Narita, T., Jindo, T., Kage, T., *et al.* (2007). Right-elevated expression of charon is regulated by fluid flow in medaka Kupffer's vesicle. Dev Growth Differ *49*, 395-405.

Hong, H., Kim, J., and Kim, J. (2015). Myosin heavy chain 10 (MYH10) is required for centriole migration during the biogenesis of primary cilia. Biochem Biophys Res Commun *461*, 180-185.

Jaffe, K.M., Grimes, D.T., Schottenfeld-Roames, J., Werner, M.E., Ku, T.S., Kim, S.K., Pelliccia, J.L., Morante, N.F., Mitchell, B.J., and Burdine, R.D. (2016). c21orf59/kurly Controls Both Cilia Motility and Polarization. Cell Rep *14*, 1841-1849.

Jessen, J.R., and Solnica-Krezel, L. (2004). Identification and developmental expression pattern of van gogh-like 1, a second zebrafish strabismus homologue. Gene Expr Patterns *4*, 339-344.

Kalogirou, S., Malissovas, N., Moro, E., Argenton, F., Stainier, D.Y., and Beis, D. (2014). Intracardiac flow dynamics regulate atrioventricular valve morphogenesis. Cardiovasc Res *104*, 49-60.

Kamura, K., Kobayashi, D., Uehara, Y., Koshida, S., Iijima, N., Kudo, A., Yokoyama, T., and Takeda, H. (2011). Pkd1l1 complexes with Pkd2 on motile cilia and functions to establish the left-right axis. Development *138*, 1121-1129.

Kawakami, Y., Raya, A., Raya, R.M., Rodriguez-Esteban, C., and Izpisua Belmonte, J.C. (2005). Retinoic acid signalling links left-right asymmetric patterning and bilaterally symmetric somitogenesis in the zebrafish embryo. Nature *435*, 165-171.

Kettleborough, R.N., Busch-Nentwich, E.M., Harvey, S.A., Dooley, C.M., de Bruijn, E., van Eeden, F., Sealy, I., White, R.J., Herd, C., Nijman, I.J., *et al.* (2013). A systematic genome-wide analysis of zebrafish protein-coding gene function. Nature *496*, 494-497.

Kilian, B., Mansukoski, H., Barbosa, F.C., Ulrich, F., Tada, M., and Heisenberg, C.P. (2003). The role of Ppt/Wnt5 in regulating cell shape and movement during zebrafish gastrulation. Mech Dev *120*, 467-476.

Kramer-Zucker, A.G., Olale, F., Haycraft, C.J., Yoder, B.K., Schier, A.F., and Drummond, I.A. (2005). Cilia-driven fluid flow in the zebrafish pronephros, brain and Kupffer's vesicle is required for normal organogenesis. Development *132*, 1907-1921.

Kreiling, J.A., Prabhat, Williams, G., and Creton, R. (2007). Analysis of Kupffer's vesicle in zebrafish embryos using a cave automated virtual environment. Dev Dyn *236*, 1963-1969.

Lindemann, C.B., and Lesich, K.A. (2010). Flagellar and ciliary beating: the proven and the possible. J Cell Sci *123*, 519-528.

Long, S., Ahmad, N., and Rebagliati, M. (2003). The zebrafish nodal-related gene southpaw is required for visceral and diencephalic left-right asymmetry. Development *130*, 2303-2316.

Lopes, S.S., Lourenco, R., Pacheco, L., Moreno, N., Kreiling, J., and Saude, L. (2010). Notch signalling regulates left-right asymmetry through ciliary length control. Development *137*, 3625-3632.

Marlow, F., Zwartkruis, F., Malicki, J., Neuhauss, S.C., Abbas, L., Weaver, M., Driever, W., and Solnica-Krezel, L. (1998). Functional interactions of genes mediating convergent extension, knypek and trilobite, during the partitioning of the eye primordium in zebrafish. Dev Biol *203*, 382-399.

Marshall, W.F., and Kintner, C. (2008). Cilia orientation and the fluid mechanics of development. Curr Opin Cell Biol *20*, 48-52.

McGrath, J., Somlo, S., Makova, S., Tian, X., and Brueckner, M. (2003). Two populations of node monocilia initiate left-right asymmetry in the mouse. Cell *114*, 61-73.

Monteiro, R., van Dinther, M., Bakkers, J., Wilkinson, R., Patient, R., ten Dijke, P., and Mummery, C. (2008). Two novel type II receptors mediate BMP signalling and are required to establish left-right asymmetry in zebrafish. Dev Biol *315*, 55-71.

Montenegro-Johnson, T.D., Baker, D.I., Smith, D.J., and Lopes, S.S. (2016). Three-dimensional flow in Kupffer's Vesicle. J Math Biol.

Nakamura, T., and Hamada, H. (2012). Left-right patterning: conserved and divergent mechanisms. Development *139*, 3257-3262.

Nonaka, S., Yoshiba, S., Watanabe, D., Ikeuchi, S., Goto, T., Marshall, W.F., and Hamada, H. (2005). De novo formation of left-right asymmetry by posterior tilt of nodal cilia. PLoS Biol *3*, e268.

Okabe, N., Xu, B., and Burdine, R.D. (2008). Fluid dynamics in zebrafish Kupffer's vesicle. Dev Dyn *237*, 3602-3612.

Okada, Y., Takeda, S., Tanaka, Y., Izpisua Belmonte, J.C., and Hirokawa, N. (2005). Mechanism of nodal flow: a conserved symmetry breaking event in left-right axis determination. Cell *121*, 633-644.

Pennekamp, P., Karcher, C., Fischer, A., Schweickert, A., Skryabin, B., Horst, J., Blum, M., and Dworniczak, B. (2002). The ion channel polycystin-2 is required for left-right axis determination in mice. Curr Biol *12*, 938-943.

Pitaval, A., Tseng, Q., Bornens, M., and Thery, M. (2010). Cell shape and contractility regulate ciliogenesis in cell cycle-arrested cells. J Cell Biol *191*, 303-312.

Ramsdell, A.F. (2005). Left-right asymmetry and congenital cardiac defects: getting to the heart of the matter in vertebrate left-right axis determination. Dev Biol *288*, 1-20.

Sampaio, P., Ferreira, R.R., Guerrero, A., Pintado, P., Tavares, B., Amaro, J., Smith, A.A., Montenegro-Johnson, T., Smith, D.J., and Lopes, S.S. (2014). Left-right organizer flow dynamics: how much cilia activity reliably yields laterality? Dev Cell *29*, 716-728.

Sarmah, B., Latimer, A.J., Appel, B., and Wente, S.R. (2005). Inositol polyphosphates regulate zebrafish left-right asymmetry. Dev Cell *9*, 133-145.

Schottenfeld, J., Sullivan-Brown, J., and Burdine, R.D. (2007). Zebrafish curly up encodes a Pkd2 ortholog that restricts left-side-specific expression of southpaw. Development *134*, 1605-1615.

Schweickert, A., Weber, T., Beyer, T., Vick, P., Bogusch, S., Feistel, K., and Blum, M. (2007). Cilia-driven leftward flow determines laterality in Xenopus. Curr Biol *17*, 60-66.

Shapiro, A.J., Davis, S.D., Ferkol, T., Dell, S.D., Rosenfeld, M., Olivier, K.N., Sagel, S.D., Milla, C., Zariwala, M.A., Wolf, W., *et al.* (2014). Laterality defects other than situs inversus totalis in primary ciliary dyskinesia: insights into situs ambiguus and heterotaxy. Chest *146*, 1176-1186.

Sullivan-Brown, J., Schottenfeld, J., Okabe, N., Hostetter, C.L., Serluca, F.C., Thiberge, S.Y., and Burdine, R.D. (2008). Zebrafish mutations affecting cilia motility share similar cystic phenotypes and suggest a mechanism of cyst formation that differs from pkd2 morphants. Dev Biol *314*, 261-275.

Supatto, W., Fraser, S.E., and Vermot, J. (2008). An all-optical approach for probing microscopic flows in living embryos. Biophys J *95*, L29-31.

Supatto, W., and Vermot, J. (2011). From cilia hydrodynamics to zebrafish embryonic development. Curr Top Dev Biol *95*, 33-66.

Sutherland, M.J., and Ware, S.M. (2009). Disorders of left-right asymmetry: heterotaxy and situs inversus. Am J Med Genet C Semin Med Genet *151C*, 307-317.

Thisse, C., and Thisse, B. (2008). High-resolution in situ hybridization to whole-mount zebrafish embryos. Nat Protoc *3*, 59-69.

Vassilev, P.M., Guo, L., Chen, X.Z., Segal, Y., Peng, J.B., Basora, N., Babakhanlou, H., Cruger, G., Kanazirska, M., Ye, C., *et al.* (2001). Polycystin-2 is a novel cation channel implicated in defective intracellular Ca(2+) homeostasis in polycystic kidney disease. Biochem Biophys Res Commun *282*, 341-350.

Wang, G., Cadwallader, A.B., Jang, D.S., Tsang, M., Yost, H.J., and Amack, J.D. (2011). The Rho kinase Rock2b establishes anteroposterior asymmetry of the ciliated Kupffer's vesicle in zebrafish. Development *138*, 45-54.

Wang, G., Manning, M.L., and Amack, J.D. (2012). Regional cell shape changes control form and function of Kupffer's vesicle in the zebrafish embryo. Dev Biol *370*, 52-62.

Wu, M., and Yu, S. (2016). New Insights into the Molecular Mechanisms Targeting Tubular Channels/Transporters in PKD Development. Kidney Dis (Basel) *2*, 128-135.

Yoshiba, S., Shiratori, H., Kuo, I.Y., Kawasumi, A., Shinohara, K., Nonaka, S., Asai, Y., Sasaki, G., Belo, J.A., Sasaki, H., *et al.* (2012). Cilia at the node of mouse embryos sense fluid flow for left-right determination via Pkd2. Science *338*, 226-231.

Yuan, S., Zhao, L., Brueckner, M., and Sun, Z. (2015). Intraciliary calcium oscillations initiate vertebrate left-right asymmetry. Curr Biol *25*, 556-567.

General discussion and Perspectives

My PhD project focused on the connection between the biophysical basis of directional flow generation, cilia implantation and the biological mechanism that controls left-right (LR) symmetry breaking in the zebrafish LR organizer (LRO). More specifically, I analyzed the three-dimensional organization of ciliary implantation in order to extract the key parameters modulating the directional flow involved in breaking the axis of symmetry in the zebrafish LRO, the Kupffer's vesicle (KV). Our results were then compiled in three different manuscripts. Here, I will discuss the main achievements and conclusions of this work, and in addition, I will propose some future perspectives that could help to shed light to some questions that remained unanswered.

1. 3D-Cilia Map, a tool to use in spheroid ciliated systems

The optical clarity of zebrafish embryos, coupled with its small size, makes zebrafish ideal for live imaging-based studies. Zebrafish embryos have very little autofluorescence and scattering, and in addition are very resistant to phototoxicity. However, imaging the zebrafish LRO in its total volume was a challenge since it is not easily accessible with regular confocal microscopy given its deep localization inside the embryo. However, with the methodology we developed in collaboration with the group of Dr. Supatto (Ecole Polytechnique, Palaiseau, France), called *3D-Cilia Map*, we can now perform *in vivo* imaging of the KV without altering the integrity of the embryo and its native environment. The workflow of the method was described in Manuscript 2, and even though the methodology is well optimized for the zebrafish KV, we are still trying to improve the process of data registration and cilia analysis. Dr. Supatto and his student Guillaume Pakula are continuing to develop tools that will allow a more automated analysis in critical steps such as: definition of the three orthogonal axes to set the reference frames using the low magnification live acquisition of the whole embryos; definition of the surface mask of the KV; and more importantly, set the cilium base and the respective vector to be able to extract cilia features. The manual analysis as it was performed during this PhD project was laborious and time-consuming. In addition, the group of Dr. Supatto is now developing new scripts that will allow the extraction of more cilia features from experimental datasets such as cilia beat frequency, cilia length, cilia cone angle and amplitude. Overall, it will also make 3D-Cilia Map a user-friendly tool that will allow the scientific community to use it in other spheroid ciliated systems, such as 3D models of cultured ciliated cells to study ciliopathies (Giles et al., 2014), or induced multi-ciliated airway 3D spheroids to study the pluripotency of human stem cells (Konishi et al., 2016).

2. Meridional tilt is the main cilia orientation *in vivo* in the zebrafish KV

We made use of the developed 3D-Cilia Map to analyze the biophysical parameters of cilia across the entire KV in wild-type embryos at three distinct embryonic stages in order to extract the behaviors of cilia orientation through time. This quantitative description of the KV morphology and cilia in the wild-type condition allowed us to generate accurate quantitative data *in vivo*. Through large-scale monitoring of biophysical features of cilia in 3D and theoretical considerations (Manuscript 3), we found that meridional tilt is the dominant mechanism generating the rotational flow within the KV. Furthermore, single-embryo analysis revealed a significant variability between embryos within the

parameters we studied. However the rotational flow was the most robust asymmetric parameter in the KV, in contrast with the local flows that were very variable. Thus, local flow amplitude itself should not be used as a robust predictor of the left and right side of the KV as reported in (Sampaio et al., 2014). In addition, our results showed the high density of cilia at the anterior pole of the KV only results in higher flow amplitude, but cannot explain the rotational flow responsible for breaking the LR symmetry in the zebrafish embryo.

In contrast to the zebrafish KV, cilia in the mouse node are distributed on a flat epithelial surface orthogonal to the dorsoventral (DV) axis and exhibit a posterior tilt (Nonaka et al., 2005; Okada et al., 2005). Some of the previous studies in zebrafish suggested that cilia are tilted towards the posterior side of the KV along the anteroposterior (AP) axis (Borovina et al., 2010; Kreiling et al., 2007; Okabe et al., 2008) and others that they are tilted towards the dorsal side (Supatto and Vermot, 2011). This confusion is to some extent caused by the spheroidal shape of the KV, resulting in a cilium orientation that depends on its position on the spheroid surface. In addition, the orientation towards the posterior or dorsal direction in the KV is topologically impossible for posterior and dorsal cilia, respectively.

To understand the potential mechanism(s) behind the meridional tilt observed *in vivo* using the 3D-Cilia Map methodology, we performed a comprehensive analysis of the main biophysical parameters of cilia, in a group of pre-selected conditions known to impact LR axis determination (Manuscript 4). Altogether, our results demonstrate that most of the pre-selected conditions studied had no dramatic impact on the meridional tilt. In the conditions where cilia motility was impaired, however, the meridional tilt is lost. These results suggest that motility is needed to set up the proper orientation of cilia in the KV. Interestingly, lack of cilia motility in the *lrdr1* MO leads to complete loss of cilia orientation where cilia are pointing orthogonally to the cell surface. By comparison, we found that *lrrc50*$^{-/-}$ cilia, which also lack motility, still display an angle. Thus we conclude that cilia motility is important for proper cilia positioning but may not be completely needed to set the first orientations cilia experience in the KV, before they start beating. One possible explanation is immotile cilia might experience other influences that set this orientation independently of motility (e.g. intrinsically cell chirality – see (Ferreira and Vermot, 2017; Inaki et al., 2016). Understanding the mechanism of cilia positioning will be key to better understand the impact of dyneins on cilia orientation. There is a lot to bet that the connection between cilia basis and the cytoskeleton is part of the answer.

3. Cilia orientation in the KV is highly dynamic and is not symmetrical along the LR axis at later stages

Our work suggests that cilia orientation is dynamic in the KV. Even though more work need to be done to consolidate this observation, it looks like cilia reach their meridional orientation when becoming motile and also progressively reorient to become LR asymmetric. This is interesting because this is a feature that has never been observed in the node (Hashimoto et al., 2010). Previous studies of multiciliated cells have underlined the importance of flow in modulating ciliary orientations (Guirao et al., 2010), and shown that synergistic influences from the planar cell polarity and flow can induce a

self-regulating polarized field. So far, it has been difficult to perform experiments in which the role of cilia motility and flow could be addressed separately, making it difficult to conclude if the meridional tilt is achieved by the influence of cilia motility gained over time or by the amplitude of the global flow. However, given our numerical simulations from Manuscript 3, we do not expect this reorientation to be caused by flow but either be a result from a torque of a moving cilium. We can conclude the meridional orientation is definitely set by the fact cilia gain motility and not by the increase in amplitude of the directional global flow over time, which imposed torque is not capable of modulating cilia orientation of motile cilia. To address this question experimentally we planned to do chimeric KVs, by making use of cell transplantation. The dorsal forerunner cells (DFCs), precursors of the KV, can be easily distinguishable using a transgenic (sox17:GFP)^{s870} line available in the lab, and transplanted prior the formation of the KV to another embryo. Our plan would be to transplant DFCs between wild-type and lrrc50$^{-/-}$ embryos, and try to generate KVs with a mixed population of wild-type motile cilia and mutant immotile cilia. This way we might demonstrate if the meridional orientation we observed is cell-autonomous, and thus independent of flow forces generated inside the KV.

This dynamic in cilia orientation to progressively become LR asymmetric lead us to speculate about the possibility of an existing cell-intrinsic mechanism that dictate this LR asymmetric cilia orientation in the LRO. At the molecular scale, asymmetries of sub cellular components has long been thought to provide the initial asymmetry necessary to initiate an asymmetric gene cascade (Brown and Wolpert, 1990; Levin and Mercola, 1998a), which perfectly fits this hypothesis since the internal organization of motile cilia is chiral (Hilfinger and Julicher, 2008). Microtubules and actin filaments are the two main cytoskeleton networks supporting intracellular architecture and cell polarity (Satir, 2016). With the recent discovery that the centrosome acts as an actin organizer (Farina et al., 2016) and the mechanism that position cilium at the cell surface could be microtubule dependent, the role of actin, microtubules and centrosomes in this system should be better characterized. Also, the intriguing structure of centrioles, and the role of microtubules in generating asymmetries, gives strength to the theory that the centrosome could itself be a symmetry-breaking chiral structure (Bornens, 2012).

Cell chirality can generate LR positional information that can be used to guide ciliated cells as they develop into a functional LRO (Vandenberg et al., 2013). We would like to test the intrinsic chirality of the KV cells and its impact on cilia orientation but the accessible tools are mainly drug treatments. The potential drawback is that it might be difficult to control its side effects on the whole embryo. We will work on more targeted and efficient tools to address cell chirality without disrupting the embryos. This will help address the question if cell chirality and cilia motility are part of the same pathway to set the final cilia orientation in the LRO

4. Testing the physical limits of flow detection favors the chemical sensing hypothesis

By making use of the information gained from *3D-Cilia Map*, we developed numerical simulations to investigate the physical limits of the system to discriminate left from right giving the flow irregularities

and intrinsic noise. Thus, we tested the reliability of each of the proposed hypothesis to happen in the symmetry breaking mechanism in zebrafish. Currently, two competing hypotheses have been proposed for asymmetric flow detection: the direction of flows generated by beating cilia is detected either through mechanosensation (McGrath et al., 2003; Tabin and Vogan, 2003), or via the detection of chemical signals transported in the flow (Okada et al., 2005; Tanaka et al., 2005). Our work showed the physical limits of the chemical sensing are weaker compared to the mechanosensing hypothesis, thus concluding the transport of a chemical signal by the flow would provide a simple and reliable mechanism for the initial LR axis determination in zebrafish.

It is known motile cilia can sense the external chemical environment (Shah et al., 2009). The big question about the chemical sensing hypothesis is naturally which could be the chemical that would be secreted and driven by the flow. Our numerical model allowed to limit the size of the signaling molecule for its reliable asymmetric distribution in the KV (above the lower limit of 2nm), which will help others searching for possible candidates. The size range of membrane bound extra-cellular vesicles (ECVs) with important roles in cell biology and pathological processes (Cocucci et al., 2009; Hogan et al., 2009; Raposo and Stoorvogel, 2013; Wood et al., 2013) is within the limit size of our predicting model. ECVs are released from most mammalian cell types and carry specific signaling molecules, such as morphogens (retinoic acid - RA and Sonic hedgehog - Shh) (Tanaka et al., 2005), RNA and micro RNA (Alqadah et al., 2013; Ma et al., 2016; Schier, 2009) that may be transferred between donor and a recipient cells through low Reynolds number flow and without direct contact (Raposo and Stoorvogel, 2013). Vesicular trafficking at the cilia base has important roles in cilia-transduced cell signaling (Clement et al., 2013; Sung and Leroux, 2013), however attention has shifted to the idea that several types of ECVs transmit signals from one cell to another from the tip of the cilium (Matusek et al., 2014; Nager et al., 2017; Phua et al., 2017). Importantly, recent work in cell culture has shown that primary cilia can release vesicles by a process described as “cilia decapitation” (Phua et al., 2017), based on a mechanism of membrane excision that occurs at the tip of the cilium, which dependent of F-actin polymerization (Nager et al., 2017) and actomyosin contractility (Phua et al., 2017). The tip of the cilia is thus a local of actin-mediated release of proteins and signaling molecules to the extracellular space (Nager et al., 2017). This is interesting in the context of my work as I found that perturbing some elements of the actin cytoskeleton can affect LR patterning without dramatically changing the cilia orientation and, as a consequence, the flow. Potentially, the mechanism by which actin modulate LR patterning involves the membrane excision.

For the mouse node it has been shown that fibroblast growth factor (FGF) signaling triggers the secretion of membrane-sheathed objects (0.3–5mm in diameter), called ‘nodal vesicular parcels’ (NVPs) – currently called ECVs (Tanaka et al., 2005). Same report claimed these NVPs carry Shh and RA, that are then transported to the left side of the node by the cilia-mediated flow and there, burst and be sensed by the sensory cilia. Different set of experiments suggested FGF-signaling triggers NVP secretion of these NVPs that then create the LR asymmetric gradient. NVPs were observed live using lipophilic fluorescent dyes and electron microscopy but since this report (Tanaka et al., 2005),

no other has shown the presence of NVPs in other model organisms, including zebrafish. RA and Shh have very important roles in development and can act as morphogens inside ECVs (Matusek et al., 2014; Tanaka et al., 2005). In addition, it seems that Hedgehog (HH) signaling is not required within the node for the establishment of LR asymmetry, which argues against this model (Tsiairis and McMahon, 2009). Rather, this report shows the HH signaling acts directly within the LPM and not at the level of the node (Tsiairis and McMahon, 2009). In zebrafish, native particles can be seen in the KV and tracked to calculate flow velocities and profiles (Lopes et al., 2010; Sampaio et al., 2014), however these particles are not seen in every embryos and the number per vesicle is relatively low. In addition, the origin of these native particles is not totally understood: some have hypothesize that they are made of cell debris or parts of broken cilia that then travel in the fluid. Whether they could also be parcels containing signaling molecules as suggested by (Tanaka et al., 2005) remains thus an open question. Recently, several studies have shown that cilia can secrete ECVs (Nager et al., 2017; Phua et al., 2017). Further studies are needed to understand if these particles are at the size range of ECVs. Interestingly, our modeling predicts that low frequency of vesicle release increases the robustness of the mechanism of LR symmetry breaking in the KV. In addition, other groups are currently working in deciphering the role ECVs in the zebrafish KV, through a similar mechanism already described in Drosophila (Matusek et al., 2014). It is clear that identifying the chemical(s) that travel inside these ECVs and are involved in symmetry breaking would be a major breakthrough in the field.

To conclude, we proposed the transport of chemical signals by the flow can provide a simple and reliable mechanism of LR symmetry breaking, if the particle size is bigger than 2 nm, which is in agreement with the size range of ECVs. Furthermore, it will be interesting to identify the signaling factors carried by the ECVs and explore the impact of the ECV machinery in the process of LR patterning.

Altogether, the data of my PhD thesis suggest the initial mechanism to break the LR symmetry is most likely to be based on the transport of a chemical signal, while later, cells intrinsically provide their cilia the cues to orient asymmetrically. Together our results predict a succession of events in the KV, with cell chirality as a “ground-state” mechanism intrinsic of KV cells: (i) asymmetric transport of a chemical molecule that can start at the early stages of cilia motility, based on the cilia-driven flow, (ii) which is then followed by an asymmetric reorientation of cilia at later stages.

5. Developing a new tool for flow-profile measurements *in vivo*

The experimental investigation of cilia-driven flow and its function during embryonic development needs the measuring of parameters characterizing both motile cilia and fluid flow *in vivo*. As describe in this work, key information for the LR axis determination is detained in the fluid flow profiles as well as in the cilia features as cilia positioning, beating pattern and orientation. Even though 3D-Cilia Map is an excellent method to extract the biophysical features of cilia in the zebrafish KV, and other spheroid ciliated systems, it was not designed to measure the cilia-driven flow in the KV. We tried

different approaches in the lab but we were not completely convinced they would retrieve the outcomes we needed. We tried live imaging and tracking of the native particles present in the KV as described by (Lopes et al., 2010; Sampaio et al., 2014), however the success rate of observing this particles was relatively low and not compatible with the large-scale analysis we aimed to do in our study.

We are currently trying in a new methodology to measure KV flow *in vivo*, which consists in injecting inside the KV a highly fluorescent lipid-dye and track at high speed its diffusive motion using fast microscopy. We will also implement in the lab the methodology described in (Supatto et al., 2008). By combining femtosecond laser ablation, fast acquisition and 3D-particle tracking, it is possible to measure the flow profiles generated by cilia in the KV. Embryos are soaked in BodipyTR (Molecular Probes) was for cilia 3D orientation live imaging, and a single cell lining the KV is ablated with a tight focus illumination pulse at 820nm wavelength. The single cell ablation will promote the generation of microdebris that will travel in the directional flow and after fast 3D confocal acquisition, these particles can be tracked and estimated the flow profile of the embryo (Supatto et al., 2008). Further work will be needed to characterize flow. We will do the first analysis in the wild-type conditions and the ones which motility was impaired to optimize the system, which we hope in a near future we will regularly use to study KV flow profiles. In addition, the KV is a very dynamic organ, with large-scale morphogenetic movements, at the scale of the cilium, and this also made it difficult to plan other kind of experiments such as time-lapse imaging or optogenetics, even though we are still planning to find ways of solving these challenges.

6. Relevance of multidisciplinary approaches to address question regarding LR

To address the hydrodynamics involved in the LR symmetry breaking during early embryo development, efforts have been made to combine experimental data and numerical key predictions, in order to get a global view of this system. As described in the introduction of this thesis, the first models and simulations were done based on mouse node experimental data (Cartwright et al., 2004; Smith et al., 2007; Vilfan and Julicher, 2006). More recent models were done based on zebrafish experimental data, but still with some parameters inferred from the mouse node (Montenegro-Johnson et al., 2016; Sampaio et al., 2014). That is also why our project will give a major contribution to the LR field because it defined the KV and cilia biophysical features that govern the flow in a highly quantitative way, helping future models to be more accurate (Manuscript 3). With the growing input of mechanical forces and cell chirality as key elements at different levels of the LR symmetry breaking pathway, the role of multidisciplinary approaches to address questions in this context is of extreme importance. My PhD project is the perfect example of how a multi-disciplinary approach can work to achieve such a complex aim as exploring the connection between the biophysical basis of directional flow generation and the biological mechanism that controls LR symmetry breaking and cilia implantation in the zebrafish LRO. LROs illustrates well the interplay between fluid mechanics, numerical modeling, and experimental investigation in live embryos, only possible with the collaboration between developmental biologists and physicists. The theory for the numerical simulations of the flow patterns

was crucial to generate predictions that can then be tested experimentally or conversely to do *in silico* experiments that could not be done *in vivo* due to limitations of the system. Thus, the LR pathway is an exceptional example of the interplay between physics and genetics, and that is also why it is so fascinating.

References

Adams, D.S., Robinson, K.R., Fukumoto, T., Yuan, S.P., Albertson, R.C., Yelick, P., Kuo, L., McSweeney, M., and Levin, M. (2006). Early, H+-V-ATPase-dependent proton flux is necessary for consistent left-right patterning of non-mammalian vertebrates. Development *133*, 1657-1671.

Afzelius, B.A. (1976). A human syndrome caused by immotile cilia. Science *193*, 317-319.

Alqadah, A., Hsieh, Y.W., and Chuang, C.F. (2013). microRNA function in left-right neuronal asymmetry: perspectives from C. elegans. Front Cell Neurosci *7*, 158.

Amack, J.D. (2014). Salient features of the ciliated organ of asymmetry. Bioarchitecture *4*, 6-15.

Amack, J.D., Wang, X., and Yost, H.J. (2007). Two T-box genes play independent and cooperative roles to regulate morphogenesis of ciliated Kupffer's vesicle in zebrafish. Dev Biol *310*, 196-210.

Antic, D., Stubbs, J.L., Suyama, K., Kintner, C., Scott, M.P., and Axelrod, J.D. (2010). Planar cell polarity enables posterior localization of nodal cilia and left-right axis determination during mouse and Xenopus embryogenesis. PLoS One *5*, e8999.

Anton, H., Harlepp, S., Ramspacher, C., Wu, D., Monduc, F., Bhat, S., Liebling, M., Paoletti, C., Charvin, G., Freund, J.B.*, et al.* (2013). Pulse propagation by a capacitive mechanism drives embryonic blood flow. Development *140*, 4426-4434.

Badano, J.L., Mitsuma, N., Beales, P.L., and Katsanis, N. (2006). The ciliopathies: an emerging class of human genetic disorders. Annu Rev Genomics Hum Genet *7*, 125-148.

Bajoghli, B., Aghaallaei, N., Soroldoni, D., and Czerny, T. (2007). The roles of Groucho/Tle in left-right asymmetry and Kupffer's vesicle organogenesis. Dev Biol *303*, 347-361.

Battle, C., Ott, C.M., Burnette, D.T., Lippincott-Schwartz, J., and Schmidt, C.F. (2015). Intracellular and extracellular forces drive primary cilia movement. Proc Natl Acad Sci U S A *112*, 1410-1415.

Beis, D., Bartman, T., Jin, S.W., Scott, I.C., D'Amico, L.A., Ober, E.A., Verkade, H., Frantsve, J., Field, H.A., Wehman, A.*, et al.* (2005). Genetic and cellular analyses of zebrafish atrioventricular cushion and valve development. Development *132*, 4193-4204.

Bell, E., Munoz-Sanjuan, I., Altmann, C.R., Vonica, A., and Brivanlou, A.H. (2003). Cell fate specification and competence by Coco, a maternal BMP, TGFbeta and Wnt inhibitor. Development *130*, 1381-1389.

Belo, J.A., Silva, A.C., Borges, A.C., Filipe, M., Bento, M., Goncalves, L., Vitorino, M., Salgueiro, A.M., Texeira, V., Tavares, A.T.*, et al.* (2009). Generating asymmetries in the early vertebrate embryo: the role of the Cerberus-like family. Int J Dev Biol *53*, 1399-1407.

Berbari, N.F., O'Connor, A.K., Haycraft, C.J., and Yoder, B.K. (2009). The primary cilium as a complex signaling center. Curr Biol *19*, R526-535.

Berens, P. (2009). CircStat: A MATLAB Toolbox for Circular Statistics. Journal of Statistical Software *31*.

Bisgrove, B.W., and Yost, H.J. (2006). The roles of cilia in developmental disorders and disease. Development *133*, 4131-4143.

Bloodgood, R.A. (2010). Sensory reception is an attribute of both primary cilia and motile cilia. J Cell Sci *123*, 505-509.

Blum, M., Andre, P., Muders, K., Schweickert, A., Fischer, A., Bitzer, E., Bogusch, S., Beyer, T., van Straaten, H.W., and Viebahn, C. (2007). Ciliation and gene expression distinguish between node and posterior notochord in the mammalian embryo. Differentiation *75*, 133-146.

Blum, M., Beyer, T., Weber, T., Vick, P., Andre, P., Bitzer, E., and Schweickert, A. (2009). Xenopus, an ideal model system to study vertebrate left-right asymmetry. Dev Dyn *238*, 1215-1225.

Blum, M., Feistel, K., Thumberger, T., and Schweickert, A. (2014a). The evolution and conservation of left-right patterning mechanisms. Development *141*, 1603-1613.

Blum, M., Schweickert, A., Vick, P., Wright, C.V., and Danilchik, M.V. (2014b). Symmetry breakage in the vertebrate embryo: when does it happen and how does it work? Dev Biol *393*, 109-123.

Boettger, T., Wittler, L., and Kessel, M. (1999). FGF8 functions in the specification of the right body side of the chick. Curr Biol *9*, 277-280.

Bornens, M. (2012). The centrosome in cells and organisms. Science *335*, 422-426.

Borovina, A., Superina, S., Voskas, D., and Ciruna, B. (2010). Vangl2 directs the posterior tilting and asymmetric localization of motile primary cilia. Nat Cell Biol *12*, 407-412.

Boucher, C., and Sandford, R. (2004). Autosomal dominant polycystic kidney disease (ADPKD, MIM 173900, PKD1 and PKD2 genes, protein products known as polycystin-1 and polycystin-2). Eur J Hum Genet *12*, 347-354.

Brown, N.A., and Wolpert, L. (1990). The development of handedness in left/right asymmetry. Development *109*, 1-9.

Brueckner, M. (2007). Heterotaxia, congenital heart disease, and primary ciliary dyskinesia. Circulation *115*, 2793-2795.

Brummett, A.R., and Dumont, J.N. (1978). Kupffer's vesicle in Fundulus heteroclitus: a scanning and transmission electron microscope study. Tissue Cell *10*, 11-22.

Capdevila, J., Vogan, K.J., Tabin, C.J., and Izpisua Belmonte, J.C. (2000). Mechanisms of left-right determination in vertebrates. Cell *101*, 9-21.

Cartwright, J.H., Piro, N., Piro, O., and Tuval, I. (2007). Embryonic nodal flow and the dynamics of nodal vesicular parcels. J R Soc Interface *4*, 49-55.

Cartwright, J.H., Piro, N., Piro, O., and Tuval, I. (2008). Fluid dynamics of nodal flow and left-right patterning in development. Dev Dyn *237*, 3477-3490.

Cartwright, J.H., Piro, O., and Tuval, I. (2004). Fluid-dynamical basis of the embryonic development of left-right asymmetry in vertebrates. Proc Natl Acad Sci U S A *101*, 7234-7239.

Cartwright, J.H., Piro, O., and Tuval, I. (2009). Fluid dynamics in developmental biology: moving fluids that shape ontogeny. HFSP J *3*, 77-93.

Caspary, T., Larkins, C.E., and Anderson, K.V. (2007). The graded response to Sonic Hedgehog depends on cilia architecture. Dev Cell *12*, 767-778.

Castleman, V.H., Romio, L., Chodhari, R., Hirst, R.A., de Castro, S.C., Parker, K.A., Ybot-Gonzalez, P., Emes, R.D., Wilson, S.W., Wallis, C.*, et al.* (2009). Mutations in radial spoke head protein genes RSPH9 and RSPH4A cause primary ciliary dyskinesia with central-microtubular-pair abnormalities. Am J Hum Genet *84*, 197-209.

Clement, C.A., Ajbro, K.D., Koefoed, K., Vestergaard, M.L., Veland, I.R., Henriques de Jesus, M.P., Pedersen, L.B., Benmerah, A., Andersen, C.Y., Larsen, L.A.*, et al.* (2013). TGF-beta signaling is associated with endocytosis at the pocket region of the primary cilium. Cell Rep *3*, 1806-1814.

Cocucci, E., Racchetti, G., and Meldolesi, J. (2009). Shedding microvesicles: artefacts no more. Trends Cell Biol *19*, 43-51.

Colantonio, J.R., Vermot, J., Wu, D., Langenbacher, A.D., Fraser, S., Chen, J.N., and Hill, K.L. (2009). The dynein regulatory complex is required for ciliary motility and otolith biogenesis in the inner ear. Nature *457*, 205-209.

Collignon, J., Varlet, I., and Robertson, E.J. (1996). Relationship between asymmetric nodal expression and the direction of embryonic turning. Nature *381*, 155-158.

Compagnon, J., Barone, V., Rajshekar, S., Kottmeier, R., Pranjic-Ferscha, K., Behrndt, M., and Heisenberg, C.P. (2014). The notochord breaks bilateral symmetry by controlling cell shapes in the zebrafish laterality organ. Dev Cell *31*, 774-783.

Cooper, M.S., and D'Amico, L.A. (1996). A cluster of noninvoluting endocytic cells at the margin of the zebrafish blastoderm marks the site of embryonic shield formation. Dev Biol *180*, 184-198.

Coutelis, J.B., Gonzalez-Morales, N., Geminard, C., and Noselli, S. (2014). Diversity and convergence in the mechanisms establishing L/R asymmetry in metazoa. EMBO Rep *15*, 926-937.

Cui, C., Little, C.D., and Rongish, B.J. (2009). Rotation of organizer tissue contributes to left-right asymmetry. Anat Rec (Hoboken) *292*, 557-561.

Dasgupta, A., and Amack, J.D. (2016). Cilia in vertebrate left-right patterning. Philos Trans R Soc Lond B Biol Sci *371*.

Delling, M., Indzhykulian, A.A., Liu, X., Li, Y., Xie, T., Corey, D.P., and Clapham, D.E. (2016). Primary cilia are not calcium-responsive mechanosensors. Nature *531*, 656-660.

Erter, C.E., Solnica-Krezel, L., and Wright, C.V. (1998). Zebrafish nodal-related 2 encodes an early mesendodermal inducer signaling from the extraembryonic yolk syncytial layer. Dev Biol *204*, 361-372.

Essner, J.J., Amack, J.D., Nyholm, M.K., Harris, E.B., and Yost, H.J. (2005). Kupffer's vesicle is a ciliated organ of asymmetry in the zebrafish embryo that initiates left-right development of the brain, heart and gut. Development *132*, 1247-1260.

Essner, J.J., Vogan, K.J., Wagner, M.K., Tabin, C.J., Yost, H.J., and Brueckner, M. (2002). Conserved function for embryonic nodal cilia. Nature *418*, 37-38.

Farina, F., Gaillard, J., Guerin, C., Coute, Y., Sillibourne, J., Blanchoin, L., and Thery, M. (2016). The centrosome is an actin-organizing centre. Nature Cell Biology *18*, 65-+.

Feldman, B., Gates, M.A., Egan, E.S., Dougan, S.T., Rennebeck, G., Sirotkin, H.I., Schier, A.F., and Talbot, W.S. (1998). Zebrafish organizer development and germ-layer formation require nodal-related signals. Nature *395*, 181-185.

Ferrante, M.I., Romio, L., Castro, S., Collins, J.E., Goulding, D.A., Stemple, D.L., Woolf, A.S., and Wilson, S.W. (2009). Convergent extension movements and ciliary function are mediated by ofd1, a zebrafish orthologue of the human oral-facial-digital type 1 syndrome gene. Hum Mol Genet *18*, 289-303.

Ferreira, R.R., and Vermot, J. (2017). The balancing roles of mechanical forces during left-right patterning and asymmetric morphogenesis. Mech Dev *144*, 71-80.

Field, S., Riley, K.L., Grimes, D.T., Hilton, H., Simon, M., Powles-Glover, N., Siggers, P., Bogani, D., Greenfield, A., and Norris, D.P. (2011). Pkd1l1 establishes left-right asymmetry and physically interacts with Pkd2. Development *138*, 1131-1142.

Fliegauf, M., Benzing, T., and Omran, H. (2007). When cilia go bad: cilia defects and ciliopathies. Nat Rev Mol Cell Biol *8*, 880-893.

Francescatto, L., Rothschild, S.C., Myers, A.L., and Tombes, R.M. (2010). The activation of membrane targeted CaMK-II in the zebrafish Kupffer's vesicle is required for left-right asymmetry. Development *137*, 2753-2762.

Freund, J.B., Goetz, J.G., Hill, K.L., and Vermot, J. (2012). Fluid flows and forces in development: functions, features and biophysical principles. Development *139*, 1229-1245.

Fukumoto, T., Kema, I.P., and Levin, M. (2005). Serotonin signaling is a very early step in patterning of the left-right axis in chick and frog embryos. Curr Biol *15*, 794-803.

Giles, R.H., Ajzenberg, H., and Jackson, P.K. (2014). 3D spheroid model of mIMCD3 cells for studying ciliopathies and renal epithelial disorders. Nat Protoc *9*, 2725-2731.

Goetz, J.G., Steed, E., Ferreira, R.R., Roth, S., Ramspacher, C., Boselli, F., Charvin, G., Liebling, M., Wyart, C., Schwab, Y.*, et al.* (2014). Endothelial cilia mediate low flow sensing during zebrafish vascular development. Cell Rep *6*, 799-808.

Goetz, S.C., and Anderson, K.V. (2010). The primary cilium: a signalling centre during vertebrate development. Nat Rev Genet *11*, 331-344.

Gokey, J.J., Ji, Y., Tay, H.G., Litts, B., and Amack, J.D. (2016). Kupffer's vesicle size threshold for robust left-right patterning of the zebrafish embryo. Dev Dyn *245*, 22-33.

Gomez-Lopez, S., Lerner, R.G., and Petritsch, C. (2014). Asymmetric cell division of stem and progenitor cells during homeostasis and cancer. Cell Mol Life Sci *71*, 575-597.

Gonzalez-Perrett, S., Kim, K., Ibarra, C., Damiano, A.E., Zotta, E., Batelli, M., Harris, P.C., Reisin, I.L., Arnaout, M.A., and Cantiello, H.F. (2001). Polycystin-2, the protein mutated in autosomal dominant polycystic kidney disease (ADPKD), is a Ca2+-permeable nonselective cation channel. Proc Natl Acad Sci U S A *98*, 1182-1187.

Gros, J., Feistel, K., Viebahn, C., Blum, M., and Tabin, C.J. (2009). Cell movements at Hensen's node establish left/right asymmetric gene expression in the chick. Science *324*, 941-944.

Guirao, B., Meunier, A., Mortaud, S., Aguilar, A., Corsi, J.M., Strehl, L., Hirota, Y., Desoeuvre, A., Boutin, C., Han, Y.G.*, et al.* (2010). Coupling between hydrodynamic forces and planar cell polarity orients mammalian motile cilia. Nat Cell Biol *12*, 341-350.

Hamada, H. (2008). Breakthroughs and future challenges in left-right patterning. Dev Growth Differ *50 Suppl 1*, S71-78.

Hamada, H., Meno, C., Watanabe, D., and Saijoh, Y. (2002). Establishment of vertebrate left-right asymmetry. Nat Rev Genet *3*, 103-113.

Hamada, H., and Tam, P.P. (2014). Mechanisms of left-right asymmetry and patterning: driver, mediator and responder. F1000Prime Rep *6*, 110.

Hanaoka, K., Qian, F., Boletta, A., Bhunia, A.K., Piontek, K., Tsiokas, L., Sukhatme, V.P., Guggino, W.B., and Germino, G.G. (2000). Co-assembly of polycystin-1 and -2 produces unique cation-permeable currents. Nature *408*, 990-994.

Hashimoto, H., Rebagliati, M., Ahmad, N., Muraoka, O., Kurokawa, T., Hibi, M., and Suzuki, T. (2004). The Cerberus/Dan-family protein Charon is a negative regulator of Nodal signaling during left-right patterning in zebrafish. Development *131*, 1741-1753.

Hashimoto, M., Shinohara, K., Wang, J., Ikeuchi, S., Yoshiba, S., Meno, C., Nonaka, S., Takada, S., Hatta, K., Wynshaw-Boris, A.*, et al.* (2010). Planar polarization of node cells determines the rotational axis of node cilia. Nat Cell Biol *12*, 170-176.

Heisenberg, C.P., and Nusslein-Volhard, C. (1997). The function of silberblick in the positioning of the eye anlage in the zebrafish embryo. Dev Biol *184*, 85-94.

Heisenberg, C.P., Tada, M., Rauch, G.J., Saude, L., Concha, M.L., Geisler, R., Stemple, D.L., Smith, J.C., and Wilson, S.W. (2000). Silberblick/Wnt11 mediates convergent extension movements during zebrafish gastrulation. Nature *405*, 76-81.

Hellman, N.E., Liu, Y., Merkel, E., Austin, C., Le Corre, S., Beier, D.R., Sun, Z., Sharma, N., Yoder, B.K., and Drummond, I.A. (2010). The zebrafish foxj1a transcription factor regulates cilia function in response to injury and epithelial stretch. Proc Natl Acad Sci U S A *107*, 18499-18504.

Hildebrandt, F., Benzing, T., and Katsanis, N. (2011). Ciliopathies. N Engl J Med *364*, 1533-1543.

Hilfinger, A., and Julicher, F. (2008). The chirality of ciliary beats. Phys Biol *5*, 016003.

Hirokawa, N., Tanaka, Y., and Okada, Y. (2009). Left-right determination: involvement of molecular motor KIF3, cilia, and nodal flow. Cold Spring Harb Perspect Biol *1*, a000802.

Hirokawa, N., Tanaka, Y., and Okada, Y. (2012). Cilia, KIF3 molecular motor and nodal flow. Curr Opin Cell Biol *24*, 31-39.

Hirokawa, N., Tanaka, Y., Okada, Y., and Takeda, S. (2006). Nodal flow and the generation of left-right asymmetry. Cell *125*, 33-45.

Hogan, M.C., Manganelli, L., Woollard, J.R., Masyuk, A.I., Masyuk, T.V., Tammachote, R., Huang, B.Q., Leontovich, A.A., Beito, T.G., Madden, B.J*., et al.* (2009). Characterization of PKD protein-positive exosome-like vesicles. J Am Soc Nephrol *20*, 278-288.

Hojo, M., Takashima, S., Kobayashi, D., Sumeragi, A., Shimada, A., Tsukahara, T., Yokoi, H., Narita, T., Jindo, T., Kage, T*., et al.* (2007). Right-elevated expression of charon is regulated by fluid flow in medaka Kupffer's vesicle. Dev Growth Differ *49*, 395-405.

Hong, H., Kim, J., and Kim, J. (2015). Myosin heavy chain 10 (MYH10) is required for centriole migration during the biogenesis of primary cilia. Biochem Biophys Res Commun *461*, 180-185.

Hove, J.R., Koster, R.W., Forouhar, A.S., Acevedo-Bolton, G., Fraser, S.E., and Gharib, M. (2003). Intracardiac fluid forces are an essential epigenetic factor for embryonic cardiogenesis. Nature *421*, 172-177.

Inacio, J.M., Marques, S., Nakamura, T., Shinohara, K., Meno, C., Hamada, H., and Belo, J.A. (2013). The dynamic right-to-left translocation of Cerl2 is involved in the regulation and termination of Nodal activity in the mouse node. PLoS One *8*, e60406.

Inaki, M., Liu, J., and Matsuno, K. (2016). Cell chirality: its origin and roles in left-right asymmetric development. Philos Trans R Soc Lond B Biol Sci *371*.

Inoue, M., Tanimoto, M., and Oda, Y. (2013). The role of ear stone size in hair cell acoustic sensory transduction. Sci Rep *3*, 2114.

Ishikawa, H., and Marshall, W.F. (2011). Ciliogenesis: building the cell's antenna. Nat Rev Mol Cell Biol *12*, 222-234.

Jaffe, K.M., Grimes, D.T., Schottenfeld-Roames, J., Werner, M.E., Ku, T.S., Kim, S.K., Pelliccia, J.L., Morante, N.F., Mitchell, B.J., and Burdine, R.D. (2016). c21orf59/kurly Controls Both Cilia Motility and Polarization. Cell Rep *14*, 1841-1849.

Jessen, J.R., and Solnica-Krezel, L. (2004). Identification and developmental expression pattern of van gogh-like 1, a second zebrafish strabismus homologue. Gene Expr Patterns *4*, 339-344.

Jones, C.M., Kuehn, M.R., Hogan, B.L., Smith, J.C., and Wright, C.V. (1995). Nodal-related signals induce axial mesoderm and dorsalize mesoderm during gastrulation. Development *121*, 3651-3662.

Joseph, E.M., and Melton, D.A. (1997). Xnr4: a Xenopus nodal-related gene expressed in the Spemann organizer. Dev Biol *184*, 367-372.

Kalogirou, S., Malissovas, N., Moro, E., Argenton, F., Stainier, D.Y., and Beis, D. (2014). Intracardiac flow dynamics regulate atrioventricular valve morphogenesis. Cardiovasc Res *104*, 49-60.

Kamura, K., Kobayashi, D., Uehara, Y., Koshida, S., Iijima, N., Kudo, A., Yokoyama, T., and Takeda, H. (2011). Pkd1l1 complexes with Pkd2 on motile cilia and functions to establish the left-right axis. Development *138*, 1121-1129.

Kartagener, M. (1933). Zur Pathogenese der Bronchiektasien. I. Mitteilung Bronchiektasien bei Situs viscerum inversus. Beitr Klin Tuberk Spezif Tuberkuloseforsch, 498-501.

Kawakami, Y., Raya, A., Raya, R.M., Rodriguez-Esteban, C., and Izpisua Belmonte, J.C. (2005). Retinoic acid signalling links left-right asymmetric patterning and bilaterally symmetric somitogenesis in the zebrafish embryo. Nature *435*, 165-171.

Kawasumi, A., Nakamura, T., Iwai, N., Yashiro, K., Saijoh, Y., Belo, J.A., Shiratori, H., and Hamada, H. (2011). Left-right asymmetry in the level of active Nodal protein produced in the node is translated into left-right asymmetry in the lateral plate of mouse embryos. Dev Biol *353*, 321-330.

Kettleborough, R.N., Busch-Nentwich, E.M., Harvey, S.A., Dooley, C.M., de Bruijn, E., van Eeden, F., Sealy, I., White, R.J., Herd, C., Nijman, I.J.*, et al.* (2013). A systematic genome-wide analysis of zebrafish protein-coding gene function. Nature *496*, 494-497.

Kilian, B., Mansukoski, H., Barbosa, F.C., Ulrich, F., Tada, M., and Heisenberg, C.P. (2003). The role of Ppt/Wnt5 in regulating cell shape and movement during zebrafish gastrulation. Mech Dev *120*, 467-476.

Kimmel, C.B., Ballard, W.W., Kimmel, S.R., Ullmann, B., and Schilling, T.F. (1995). Stages of embryonic development of the zebrafish. Dev Dyn *203*, 253-310.

King, S.M. (2016). Axonemal Dynein Arms. Cold Spring Harb Perspect Biol *8*.

Konishi, S., Gotoh, S., Tateishi, K., Yamamoto, Y., Korogi, Y., Nagasaki, T., Matsumoto, H., Muro, S., Hirai, T., Ito, I.*, et al.* (2016). Directed Induction of Functional Multi-ciliated Cells in Proximal Airway Epithelial Spheroids from Human Pluripotent Stem Cells. Stem Cell Reports *6*, 18-25.

Kramer-Zucker, A.G., Olale, F., Haycraft, C.J., Yoder, B.K., Schier, A.F., and Drummond, I.A. (2005). Cilia-driven fluid flow in the zebrafish pronephros, brain and Kupffer's vesicle is required for normal organogenesis. Development *132*, 1907-1921.

Kreiling, J.A., Prabhat, Williams, G., and Creton, R. (2007). Analysis of Kupffer's vesicle in zebrafish embryos using a cave automated virtual environment. Dev Dyn *236*, 1963-1969.

Lee, J.D., and Anderson, K.V. (2008). Morphogenesis of the node and notochord: the cellular basis for the establishment and maintenance of left-right asymmetry in the mouse. Dev Dyn *237*, 3464-3476.

Leong, P., and Carlile, S. (1998). Methods for spherical data analysis and visualization. J Neurosci Methods *80*, 191-200.

Levin, M. (2005). Left-right asymmetry in embryonic development: a comprehensive review. Mech Dev *122*, 3-25.

Levin, M., Johnson, R.L., Stern, C.D., Kuehn, M., and Tabin, C. (1995). A molecular pathway determining left-right asymmetry in chick embryogenesis. Cell *82*, 803-814.

Levin, M., and Mercola, M. (1998a). The compulsion of chirality: toward an understanding of left-right asymmetry. Genes Dev *12*, 763-769.

Levin, M., and Mercola, M. (1998b). Gap junctions are involved in the early generation of left-right asymmetry. Dev Biol *203*, 90-105.

Levin, M., and Mercola, M. (1999). Gap junction-mediated transfer of left-right patterning signals in the early chick blastoderm is upstream of Shh asymmetry in the node. Development *126*, 4703-4714.

Levin, M., Pagan, S., Roberts, D.J., Cooke, J., Kuehn, M.R., and Tabin, C.J. (1997). Left/right patterning signals and the independent regulation of different aspects of situs in the chick embryo. Dev Biol *189*, 57-67.

Levin, M., Thorlin, T., Robinson, K.R., Nogi, T., and Mercola, M. (2002). Asymmetries in H+/K+-ATPase and cell membrane potentials comprise a very early step in left-right patterning. Cell *111*, 77-89.

Li, Y., Klena, N.T., Gabriel, G.C., Liu, X., Kim, A.J., Lemke, K., Chen, Y., Chatterjee, B., Devine, W., Damerla, R.R.*, et al.* (2015). Global genetic analysis in mice unveils central role for cilia in congenital heart disease. Nature *521*, 520-524.

Li, Y., Yagi, H., Onuoha, E.O., Damerla, R.R., Francis, R., Furutani, Y., Tariq, M., King, S.M., Hendricks, G., Cui, C.*, et al.* (2016). DNAH6 and Its Interactions with PCD Genes in Heterotaxy and Primary Ciliary Dyskinesia. PLoS Genet *12*, e1005821.

Lindemann, C.B., and Lesich, K.A. (2010). Flagellar and ciliary beating: the proven and the possible. J Cell Sci *123*, 519-528.

Lodish H, B.A., Zipursky SL, Matsudaira P, Baltimore D and Darnell J. (2000). Molecular Cell Biology. 4th edition. New York: W H Freeman.

Logan, M., Simon, H.G., and Tabin, C. (1998). Differential regulation of T-box and homeobox transcription factors suggests roles in controlling chick limb-type identity. Development *125*, 2825-2835.

Long, S., Ahmad, N., and Rebagliati, M. (2003). The zebrafish nodal-related gene southpaw is required for visceral and diencephalic left-right asymmetry. Development *130*, 2303-2316.

Lopes, S.S., Lourenco, R., Pacheco, L., Moreno, N., Kreiling, J., and Saude, L. (2010). Notch signalling regulates left-right asymmetry through ciliary length control. Development *137*, 3625-3632.

Lourenço, R.a.S., L. (2010). Symmetry OUT, Asymmetry IN. Symmetry *2*, 1033-1054.

Lowe, L.A., Supp, D.M., Sampath, K., Yokoyama, T., Wright, C.V., Potter, S.S., Overbeek, P., and Kuehn, M.R. (1996). Conserved left-right asymmetry of nodal expression and alterations in murine situs inversus. Nature *381*, 158-161.

Ma, H., Lin, Y., Zhao, Z.A., Lu, X., Yu, Y., Zhang, X., Wang, Q., and Li, L. (2016). MicroRNA-127 Promotes Mesendoderm Differentiation of Mouse Embryonic Stem Cells by Targeting Left-Right Determination Factor 2. J Biol Chem *291*, 12126-12135.

Malicki, J.J., and Johnson, C.A. (2017). The Cilium: Cellular Antenna and Central Processing Unit. Trends Cell Biol *27*, 126-140.

Manner, J. (2001). Does an equivalent of the "ventral node" exist in chick embryos? A scanning electron microscopic study. Anat Embryol (Berl) *203*, 481-490.

Marjoram, L., and Wright, C. (2011). Rapid differential transport of Nodal and Lefty on sulfated proteoglycan-rich extracellular matrix regulates left-right asymmetry in Xenopus. Development *138*, 475-485.

Marlow, F., Zwartkruis, F., Malicki, J., Neuhauss, S.C., Abbas, L., Weaver, M., Driever, W., and Solnica-Krezel, L. (1998). Functional interactions of genes mediating convergent extension, knypek and trilobite, during the partitioning of the eye primordium in zebrafish. Dev Biol *203*, 382-399.

Marques, S., Borges, A.C., Silva, A.C., Freitas, S., Cordenonsi, M., and Belo, J.A. (2004). The activity of the Nodal antagonist Cerl-2 in the mouse node is required for correct L/R body axis. Genes Dev *18*, 2342-2347.

Marshall, W.F., and Kintner, C. (2008). Cilia orientation and the fluid mechanics of development. Curr Opin Cell Biol *20*, 48-52.

Matusek, T., Wendler, F., Poles, S., Pizette, S., D'Angelo, G., Furthauer, M., and Therond, P.P. (2014). The ESCRT machinery regulates the secretion and long-range activity of Hedgehog. Nature *516*, 99-103.

Maul, C., and Kim, S. (1994). Image systems for a Stokeslet inside a rigid spherical container Physics of Fluids *6*, 2221-2223.

McGrath, J., and Brueckner, M. (2003). Cilia are at the heart of vertebrate left-right asymmetry. Curr Opin Genet Dev *13*, 385-392.

McGrath, J., Somlo, S., Makova, S., Tian, X., and Brueckner, M. (2003). Two populations of node monocilia initiate left-right asymmetry in the mouse. Cell *114*, 61-73.

Melby, A.E., Warga, R.M., and Kimmel, C.B. (1996). Specification of cell fates at the dorsal margin of the zebrafish gastrula. Development *122*, 2225-2237.

Mendes, R.V., Martins, G.G., Cristovao, A.M., and Saude, L. (2014). N-cadherin locks left-right asymmetry by ending the leftward movement of Hensen's node cells. Dev Cell *30*, 353-360.

Meno, C., Shimono, A., Saijoh, Y., Yashiro, K., Mochida, K., Ohishi, S., Noji, S., Kondoh, H., and Hamada, H. (1998). lefty-1 is required for left-right determination as a regulator of lefty-2 and nodal. Cell *94*, 287-297.

Mercola, M. (2003). Left-right asymmetry: nodal points. J Cell Sci *116*, 3251-3257.

Mercola, M., and Levin, M. (2001). Left-right asymmetry determination in vertebrates. Annu Rev Cell Dev Biol *17*, 779-805.

Mitchison, H.M., and Valente, E.M. (2017). Motile and non-motile cilia in human pathology: from function to phenotypes. J Pathol *241*, 294-309.

Monteiro, R., van Dinther, M., Bakkers, J., Wilkinson, R., Patient, R., ten Dijke, P., and Mummery, C. (2008). Two novel type II receptors mediate BMP signalling and are required to establish left-right asymmetry in zebrafish. Dev Biol *315*, 55-71.

Montenegro-Johnson, T.D., Baker, D.I., Smith, D.J., and Lopes, S.S. (2016). Three-dimensional flow in Kupffer's Vesicle. J Math Biol.

Morrow, S.M., Bissette, A.J., and Fletcher, S.P. (2017). Transmission of chirality through space and across length scales. Nat Nanotechnol *12*, 410-419.

Muller, M., Heeck, K., and Elemans, C.P. (2016). Semicircular Canals Circumvent Brownian Motion Overload of Mechanoreceptor Hair Cells. PLoS One *11*, e0159427.

Naganathan, S.R., Furthauer, S., Nishikawa, M., Julicher, F., and Grill, S.W. (2014). Active torque generation by the actomyosin cell cortex drives left-right symmetry breaking. Elife *3*, e04165.

Naganathan, S.R., Middelkoop, T.C., Furthauer, S., and Grill, S.W. (2016). Actomyosin-driven left-right asymmetry: from molecular torques to chiral self organization. Curr Opin Cell Biol *38*, 24-30.

Nager, A.R., Goldstein, J.S., Herranz-Perez, V., Portran, D., Ye, F., Garcia-Verdugo, J.M., and Nachury, M.V. (2017). An Actin Network Dispatches Ciliary GPCRs into Extracellular Vesicles to Modulate Signaling. Cell *168*, 252-263 e214.

Nakamura, T., and Hamada, H. (2012). Left-right patterning: conserved and divergent mechanisms. Development *139*, 3257-3262.

Nakamura, T., Mine, N., Nakaguchi, E., Mochizuki, A., Yamamoto, M., Yashiro, K., Meno, C., and Hamada, H. (2006). Generation of robust left-right asymmetry in the mouse embryo requires a self-enhancement and lateral-inhibition system. Dev Cell *11*, 495-504.

Nakamura, T., Saito, D., Kawasumi, A., Shinohara, K., Asai, Y., Takaoka, K., Dong, F., Takamatsu, A., Belo, J.A., Mochizuki, A.*, et al.* (2012). Fluid flow and interlinked feedback loops establish left-right asymmetric decay of Cerl2 mRNA. Nat Commun *3*, 1322.

Nauli, S.M., Alenghat, F.J., Luo, Y., Williams, E., Vassilev, P., Li, X., Elia, A.E., Lu, W., Brown, E.M., Quinn, S.J.*, et al.* (2003). Polycystins 1 and 2 mediate mechanosensation in the primary cilium of kidney cells. Nat Genet *33*, 129-137.

Nauli, S.M., Kawanabe, Y., Kaminski, J.J., Pearce, W.J., Ingber, D.E., and Zhou, J. (2008). Endothelial cilia are fluid shear sensors that regulate calcium signaling and nitric oxide production through polycystin-1. Circulation *117*, 1161-1171.

Nonaka, S., Shiratori, H., Saijoh, Y., and Hamada, H. (2002). Determination of left-right patterning of the mouse embryo by artificial nodal flow. Nature *418*, 96-99.

Nonaka, S., Tanaka, Y., Okada, Y., Takeda, S., Harada, A., Kanai, Y., Kido, M., and Hirokawa, N. (1998). Randomization of left-right asymmetry due to loss of nodal cilia generating leftward flow of extraembryonic fluid in mice lacking KIF3B motor protein. Cell *95*, 829-837.

Nonaka, S., Yoshiba, S., Watanabe, D., Ikeuchi, S., Goto, T., Marshall, W.F., and Hamada, H. (2005). De novo formation of left-right asymmetry by posterior tilt of nodal cilia. PLoS Biol *3*, e268.

Norris, D.P. (2012). Cilia, calcium and the basis of left-right asymmetry. BMC Biol *10*, 102.

Odate, T., Takeda, S., Narita, K., and Kawahara, T. (2016). 9 + 0 and 9 + 2 cilia are randomly dispersed in the mouse node. Microscopy (Oxf) *65*, 119-126.

Okabe, N., Xu, B., and Burdine, R.D. (2008). Fluid dynamics in zebrafish Kupffer's vesicle. Dev Dyn *237*, 3602-3612.

Okada, Y., Nonaka, S., Tanaka, Y., Saijoh, Y., Hamada, H., and Hirokawa, N. (1999). Abnormal nodal flow precedes situs inversus in iv and inv mice. Mol Cell *4*, 459-468.

Okada, Y., Takeda, S., Tanaka, Y., Izpisua Belmonte, J.C., and Hirokawa, N. (2005). Mechanism of nodal flow: a conserved symmetry breaking event in left-right axis determination. Cell *121*, 633-644.

Oteiza, P., Koppen, M., Concha, M.L., and Heisenberg, C.P. (2008). Origin and shaping of the laterality organ in zebrafish. Development *135*, 2807-2813.

Pagan-Westphal, S.M., and Tabin, C.J. (1998). The transfer of left-right positional information during chick embryogenesis. Cell *93*, 25-35.

Park, T.J., Mitchell, B.J., Abitua, P.B., Kintner, C., and Wallingford, J.B. (2008). Dishevelled controls apical docking and planar polarization of basal bodies in ciliated epithelial cells. Nat Genet *40*, 871-879.

Peeters, H., and Devriendt, K. (2006). Human laterality disorders. Eur J Med Genet *49*, 349-362.

Pennekamp, P., Karcher, C., Fischer, A., Schweickert, A., Skryabin, B., Horst, J., Blum, M., and Dworniczak, B. (2002). The ion channel polycystin-2 is required for left-right axis determination in mice. Curr Biol *12*, 938-943.

Pennekamp, P., Menchen, T., Dworniczak, B., and Hamada, H. (2015). Situs inversus and ciliary abnormalities: 20 years later, what is the connection? Cilia *4*, 1.

Phua, S.C., Chiba, S., Suzuki, M., Su, E., Roberson, E.C., Pusapati, G.V., Setou, M., Rohatgi, R., Reiter, J.F., Ikegami, K.*, et al.* (2017). Dynamic Remodeling of Membrane Composition Drives Cell Cycle through Primary Cilia Excision. Cell *168*, 264-279 e215.

Pitaval, A., Tseng, Q., Bornens, M., and Thery, M. (2010). Cell shape and contractility regulate ciliogenesis in cell cycle-arrested cells. J Cell Biol *191*, 303-312.

Pourquie, O. (2011). Vertebrate segmentation: from cyclic gene networks to scoliosis. Cell *145*, 650-663.

Purcell, E.M. (1977). Life at low Reynolds number. Am J Phys *45*, 3-11.

Ramsdell, A.F. (2005). Left-right asymmetry and congenital cardiac defects: getting to the heart of the matter in vertebrate left-right axis determination. Dev Biol *288*, 1-20.

Raposo, G., and Stoorvogel, W. (2013). Extracellular vesicles: exosomes, microvesicles, and friends. J Cell Biol *200*, 373-383.

Raya, A., and Izpisua Belmonte, J.C. (2004a). Sequential transfer of left-right information during vertebrate embryo development. Curr Opin Genet Dev *14*, 575-581.

Raya, A., and Izpisua Belmonte, J.C. (2004b). Unveiling the establishment of left-right asymmetry in the chick embryo. Mech Dev *121*, 1043-1054.

Rebagliati, M.R., Toyama, R., Fricke, C., Haffter, P., and Dawid, I.B. (1998a). Zebrafish nodal-related genes are implicated in axial patterning and establishing left-right asymmetry. Dev Biol *199*, 261-272.

Rebagliati, M.R., Toyama, R., Haffter, P., and Dawid, I.B. (1998b). cyclops encodes a nodal-related factor involved in midline signaling. Proc Natl Acad Sci U S A *95*, 9932-9937.

Ryan, A.K., Blumberg, B., Rodriguez-Esteban, C., Yonei-Tamura, S., Tamura, K., Tsukui, T., de la Pena, J., Sabbagh, W., Greenwald, J., Choe, S.*, et al.* (1998). Pitx2 determines left-right asymmetry of internal organs in vertebrates. Nature *394*, 545-551.

Rydholm, S., Zwartz, G., Kowalewski, J.M., Kamali-Zare, P., Frisk, T., and Brismar, H. (2010). Mechanical properties of primary cilia regulate the response to fluid flow. Am J Physiol Renal Physiol *298*, F1096-1102.

Sampaio, P., Ferreira, R.R., Guerrero, A., Pintado, P., Tavares, B., Amaro, J., Smith, A.A., Montenegro-Johnson, T., Smith, D.J., and Lopes, S.S. (2014). Left-right organizer flow dynamics: how much cilia activity reliably yields laterality? Dev Cell *29*, 716-728.

Sampath, K., Rubinstein, A.L., Cheng, A.M., Liang, J.O., Fekany, K., Solnica-Krezel, L., Korzh, V., Halpern, M.E., and Wright, C.V. (1998). Induction of the zebrafish ventral brain and floorplate requires cyclops/nodal signalling. Nature *395*, 185-189.

Sarmah, B., Latimer, A.J., Appel, B., and Wente, S.R. (2005). Inositol polyphosphates regulate zebrafish left-right asymmetry. Dev Cell *9*, 133-145.

Sarmah, B., and Wente, S.R. (2010). Zebrafish inositol polyphosphate kinases: new effectors of cilia and developmental signaling. Adv Enzyme Regul *50*, 309-323.

Satir, P. (2016). Chirality of the cytoskeleton in the origins of cellular asymmetry. Philos Trans R Soc Lond B Biol Sci *371*.

Satir, P., and Christensen, S.T. (2007). Overview of structure and function of mammalian cilia. Annu Rev Physiol *69*, 377-400.

Schier, A.F. (2009). Nodal morphogens. Cold Spring Harb Perspect Biol *1*, a003459.

Schottenfeld, J., Sullivan-Brown, J., and Burdine, R.D. (2007). Zebrafish curly up encodes a Pkd2 ortholog that restricts left-side-specific expression of southpaw. Development *134*, 1605-1615.

Schreiner, C.M., Scott, W.J., Jr., Supp, D.M., and Potter, S.S. (1993). Correlation of forelimb malformation asymmetries with visceral organ situs in the transgenic mouse insertional mutation, legless. Dev Biol *158*, 560-562.

Schwabe, G.C., Hoffmann, K., Loges, N.T., Birker, D., Rossier, C., de Santi, M.M., Olbrich, H., Fliegauf, M., Failly, M., Liebers, U.*, et al.* (2008). Primary ciliary dyskinesia associated with normal axoneme ultrastructure is caused by DNAH11 mutations. Hum Mutat *29*, 289-298.

Schweickert, A., Vick, P., Getwan, M., Weber, T., Schneider, I., Eberhardt, M., Beyer, T., Pachur, A., and Blum, M. (2010). The nodal inhibitor Coco is a critical target of leftward flow in Xenopus. Curr Biol *20*, 738-743.

Schweickert, A., Weber, T., Beyer, T., Vick, P., Bogusch, S., Feistel, K., and Blum, M. (2007). Cilia-driven leftward flow determines laterality in Xenopus. Curr Biol *17*, 60-66.

Shah, A.S., Ben-Shahar, Y., Moninger, T.O., Kline, J.N., and Welsh, M.J. (2009). Motile cilia of human airway epithelia are chemosensory. Science *325*, 1131-1134.

Shapiro, A.J., Davis, S.D., Ferkol, T., Dell, S.D., Rosenfeld, M., Olivier, K.N., Sagel, S.D., Milla, C., Zariwala, M.A., Wolf, W.*, et al.* (2014). Laterality defects other than situs inversus totalis in primary ciliary dyskinesia: insights into situs ambiguus and heterotaxy. Chest *146*, 1176-1186.

Shen, M.M. (2007). Nodal signaling: developmental roles and regulation. Development *134*, 1023-1034.

Shinohara, K., Chen, D., Nishida, T., Misaki, K., Yonemura, S., and Hamada, H. (2015). Absence of Radial Spokes in Mouse Node Cilia Is Required for Rotational Movement but Confers Ultrastructural Instability as a Trade-Off. Dev Cell *35*, 236-246.

Shinohara, K., and Hamada, H. (2017). Cilia in Left-Right Symmetry Breaking. Cold Spring Harb Perspect Biol.

Shinohara, K., Kawasumi, A., Takamatsu, A., Yoshiba, S., Botilde, Y., Motoyama, N., Reith, W., Durand, B., Shiratori, H., and Hamada, H. (2012). Two rotating cilia in the node cavity are sufficient to break left-right symmetry in the mouse embryo. Nat Commun *3*, 622.

Shiratori, H., and Hamada, H. (2006). The left-right axis in the mouse: from origin to morphology. Development *133*, 2095-2104.

Singh, G., Supp, D.M., Schreiner, C., McNeish, J., Merker, H.J., Copeland, N.G., Jenkins, N.A., Potter, S.S., and Scott, W. (1991). legless insertional mutation: morphological, molecular, and genetic characterization. Genes Dev *5*, 2245-2255.

Singla, V., and Reiter, J.F. (2006). The primary cilium as the cell's antenna: signaling at a sensory organelle. Science *313*, 629-633.

Sloboda, R.D. (2005). Intraflagellar transport and the flagellar tip complex. J Cell Biochem *94*, 266-272.

Smith, D.J., Blake, J.R., and Gaffney, E.A. (2008). Fluid mechanics of nodal flow due to embryonic primary cilia. J R Soc Interface *5*, 567-573.

Smith, D.J., Gaffney, E.A., and Blake, J.R. (2007). Discrete cilia modelling with singularity distributions: application to the embryonic node and the airway surface liquid. Bull Math Biol *69*, 1477-1510.

Smith, D.J., Montenegro-Johnson, T.D., and Lopes, S.S. (2014). Organized chaos in Kupffer's vesicle: how a heterogeneous structure achieves consistent left-right patterning. Bioarchitecture *4*, 119-125.

Song, H., Hu, J., Chen, W., Elliott, G., Andre, P., Gao, B., and Yang, Y. (2010). Planar cell polarity breaks bilateral symmetry by controlling ciliary positioning. Nature *466*, 378-382.

Sulik, K., Dehart, D.B., Iangaki, T., Carson, J.L., Vrablic, T., Gesteland, K., and Schoenwolf, G.C. (1994). Morphogenesis of the murine node and notochordal plate. Dev Dyn *201*, 260-278.

Sullivan-Brown, J., Schottenfeld, J., Okabe, N., Hostetter, C.L., Serluca, F.C., Thiberge, S.Y., and Burdine, R.D. (2008). Zebrafish mutations affecting cilia motility share similar cystic phenotypes and suggest a mechanism of cyst formation that differs from pkd2 morphants. Dev Biol *314*, 261-275.

Sung, C.H., and Leroux, M.R. (2013). The roles of evolutionarily conserved functional modules in cilia-related trafficking. Nat Cell Biol *15*, 1387-1397.

Supatto, W., Fraser, S.E., and Vermot, J. (2008). An all-optical approach for probing microscopic flows in living embryos. Biophys J *95*, L29-31.

Supatto, W., and Vermot, J. (2011). From cilia hydrodynamics to zebrafish embryonic development. Curr Top Dev Biol *95*, 33-66.

Supp, D.M., Brueckner, M., Kuehn, M.R., Witte, D.P., Lowe, L.A., McGrath, J., Corrales, J., and Potter, S.S. (1999). Targeted deletion of the ATP binding domain of left-right dynein confirms its role in specifying development of left-right asymmetries. Development *126*, 5495-5504.

Supp, D.M., Witte, D.P., Potter, S.S., and Brueckner, M. (1997). Mutation of an axonemal dynein affects left-right asymmetry in inversus viscerum mice. Nature *389*, 963-966.

Sutherland, M.J., and Ware, S.M. (2009). Disorders of left-right asymmetry: heterotaxy and situs inversus. Am J Med Genet C Semin Med Genet *151C*, 307-317.

Tabin, C.J., and Vogan, K.J. (2003). A two-cilia model for vertebrate left-right axis specification. Genes Dev *17*, 1-6.

Takahashi, S., Yokota, C., Takano, K., Tanegashima, K., Onuma, Y., Goto, J., and Asashima, M. (2000). Two novel nodal-related genes initiate early inductive events in Xenopus Nieuwkoop center. Development *127*, 5319-5329.

Tanaka, Y., Okada, Y., and Hirokawa, N. (2005). FGF-induced vesicular release of Sonic hedgehog and retinoic acid in leftward nodal flow is critical for left-right determination. Nature *435*, 172-177.

Theegarten, D., and Ebsen, M. (2011). Ultrastructural pathology of primary ciliary dyskinesia: report about 125 cases in Germany. Diagn Pathol *6*, 115.

Thisse, C., and Thisse, B. (2008). High-resolution in situ hybridization to whole-mount zebrafish embryos. Nat Protoc *3*, 59-69.

Tsiairis, C.D., and McMahon, A.P. (2009). An Hh-dependent pathway in lateral plate mesoderm enables the generation of left/right asymmetry. Curr Biol *19*, 1912-1917.

Tsikolia, N., Schroeder, S., Schwartz, P., and Viebahn, C. (2012). Paraxial left-sided nodal expression and the start of left-right patterning in the early chick embryo. Differentiation *84*, 380-391.

Tuazon, F.B., and Mullins, M.C. (2015). Temporally coordinated signals progressively pattern the anteroposterior and dorsoventral body axes. Semin Cell Dev Biol *42*, 118-133.

Vandenberg, L.N., Lemire, J.M., and Levin, M. (2013). It's never too early to get it Right: A conserved role for the cytoskeleton in left-right asymmetry. Commun Integr Biol *6*, e27155.

Vassilev, P.M., Guo, L., Chen, X.Z., Segal, Y., Peng, J.B., Basora, N., Babakhanlou, H., Cruger, G., Kanazirska, M., Ye, C.*, et al.* (2001). Polycystin-2 is a novel cation channel implicated in defective intracellular Ca(2+) homeostasis in polycystic kidney disease. Biochem Biophys Res Commun *282*, 341-350.

Vilfan, A. (2012). Generic flow profiles induced by a beating cilium. Eur Phys J E Soft Matter *35*, 72.

Vilfan, A., and Julicher, F. (2006). Hydrodynamic flow patterns and synchronization of beating cilia. Phys Rev Lett *96*, 058102.

Vincensini, L., Blisnick, T., and Bastin, P. (2011). 1001 model organisms to study cilia and flagella. Biol Cell *103*, 109-130.

Vonica, A., and Brivanlou, A.H. (2007). The left-right axis is regulated by the interplay of Coco, Xnr1 and derriere in Xenopus embryos. Dev Biol *303*, 281-294.

Wagnière, G.H. On Chirality and the Universal Asymmetry: Reflections on Image and Mirror Image

Wang, G., Cadwallader, A.B., Jang, D.S., Tsang, M., Yost, H.J., and Amack, J.D. (2011). The Rho kinase Rock2b establishes anteroposterior asymmetry of the ciliated Kupffer's vesicle in zebrafish. Development *138*, 45-54.

Wang, G., Manning, M.L., and Amack, J.D. (2012). Regional cell shape changes control form and function of Kupffer's vesicle in the zebrafish embryo. Dev Biol *370*, 52-62.

Wang, J.S., Wang, G., Feng, X.Q., Kitamura, T., Kang, Y.L., Yu, S.W., and Qin, Q.H. (2013). Hierarchical chirality transfer in the growth of Towel Gourd tendrils. Sci Rep *3*, 3102.

Wang, X., and Yost, H.J. (2008). Initiation and propagation of posterior to anterior (PA) waves in zebrafish left-right development. Dev Dyn *237*, 3640-3647.

Ware, S.M., Aygun, M.G., and Hildebrandt, F. (2011). Spectrum of clinical diseases caused by disorders of primary cilia. Proc Am Thorac Soc *8*, 444-450.

Wolpert, L. (2014). Revisiting the F-shaped molecule: is its identity solved? Genesis *52*, 455-457.

Wood, C.R., Huang, K., Diener, D.R., and Rosenbaum, J.L. (2013). The cilium secretes bioactive ectosomes. Curr Biol *23*, 906-911.

Wu, M., and Yu, S. (2016). New Insights into the Molecular Mechanisms Targeting Tubular Channels/Transporters in PKD Development. Kidney Dis (Basel) *2*, 128-135.

Yokouchi, Y., Vogan, K.J., Pearse, R.V., 2nd, and Tabin, C.J. (1999). Antagonistic signaling by Caronte, a novel Cerberus-related gene, establishes left-right asymmetric gene expression. Cell *98*, 573-583.

Yoshiba, S., and Hamada, H. (2014). Roles of cilia, fluid flow, and Ca2+ signaling in breaking of left-right symmetry. Trends Genet *30*, 10-17.

Yoshiba, S., Shiratori, H., Kuo, I.Y., Kawasumi, A., Shinohara, K., Nonaka, S., Asai, Y., Sasaki, G., Belo, J.A., Sasaki, H.*, et al.* (2012). Cilia at the node of mouse embryos sense fluid flow for left-right determination via Pkd2. Science *338*, 226-231.

Yu, X., Ng, C.P., Habacher, H., and Roy, S. (2008). Foxj1 transcription factors are master regulators of the motile ciliogenic program. Nat Genet *40*, 1445-1453.

Yuan, S., Zhao, L., Brueckner, M., and Sun, Z. (2015). Intraciliary calcium oscillations initiate vertebrate left-right asymmetry. Curr Biol *25*, 556-567.

Zhou, X., Sasaki, H., Lowe, L., Hogan, B.L., and Kuehn, M.R. (1993). Nodal is a novel TGF-beta-like gene expressed in the mouse node during gastrulation. Nature *361*, 543-547.

Appendix

Appendix 1: Other projects

During my PhD I also collaborate with two former colleagues of the lab in their projects: Dr. Goetz and Dr. Ramspacher. Essentially, I used my skills performing live imaging, zebrafish embryo manipulation and molecular biology to give my contribution to their projects during the revision period of both manuscripts. Their manuscripts are attached in this Appendix 1.

- **Developmental Alterations in Heart Biomechanics and Skeletal Muscle Function in Desmin Mutants Suggest an Early Pathological Root for Desminopathies.**

Ramspacher C., Steed E., Boselli F., Ferreira R., Faggianelli N., Roth S., Spiegelhalter C., Messaddeq N., Trinh L., Liebling M., Chacko N., Tessadori F., Bakkers J., Laporte J., Hnia K., Vermot J.
Cell Rep. 2015 doi: 10.1016/j.celrep.2015.05.010.

- **Endothelial cilia mediate low flow sensing during zebrafish vascular development.**

Goetz JG, Steed E, Ferreira RR, Roth S, Ramspacher C, Boselli F, Charvin G, Liebling M, Wyart C, Schwab Y, Vermot J.
Cell Rep. 2014 doi: 10.1016/j.celrep.2014.01.032.

Cell Reports

Article

Developmental Alterations in Heart Biomechanics and Skeletal Muscle Function in Desmin Mutants Suggest an Early Pathological Root for Desminopathies

Graphical Abstract

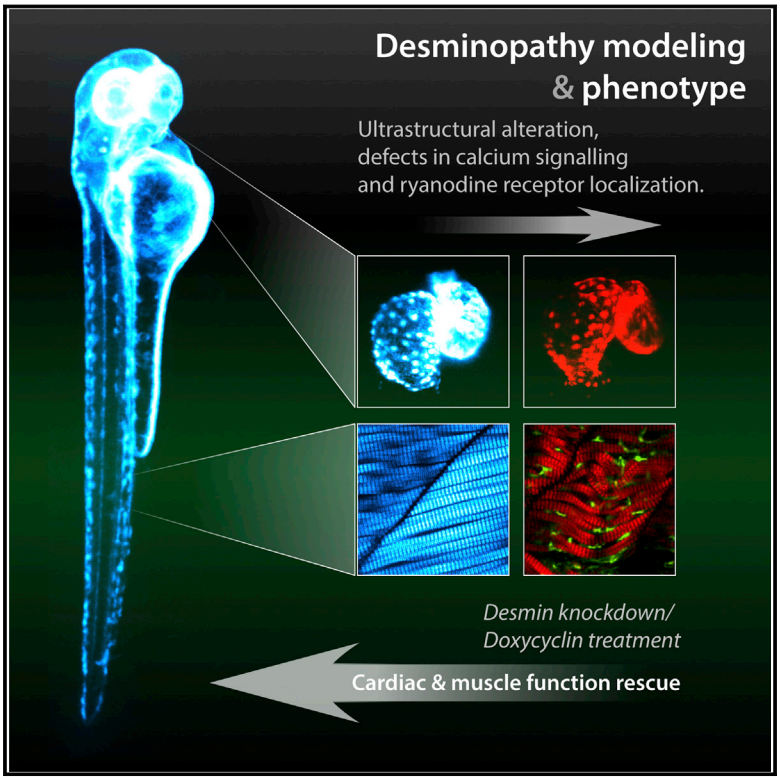

Authors

Caroline Ramspacher, Emily Steed, Francesco Boselli, ..., Jocelyn Laporte, Karim Hnia, Julien Vermot

Correspondence

julien@igbmc.fr

In Brief

Desminopathies are myopathies and cardiomyopathies associated with Desmin mutations leading to protein aggregates. Ramspacher et al. demonstrate that altered Desmin function or expression affect the EC coupling machinery and calcium dynamics. They show that aggregates are more toxic than the loss of function and can be rescued by knockdown and pharmacological treatment.

Highlights

- A knockin in the *Desmin* gene allows in vivo imaging of Desmin aggregates
- Knockout and knockin of Desmin alters skeletal muscle and cardiomyocyte function
- Excitation-contraction coupling is affected in Desmin knockout and knockin
- Doxycycline and decreased Desmin expression rescue muscle and cardiac function

Ramspacher et al., 2015, Cell Reports *11*, 1564–1576
June 16, 2015 ©2015 The Authors
http://dx.doi.org/10.1016/j.celrep.2015.05.010

CellPress

OPEN ACCESS
CellPress

Cell Reports
Article

Developmental Alterations in Heart Biomechanics and Skeletal Muscle Function in Desmin Mutants Suggest an Early Pathological Root for Desminopathies

Caroline Ramspacher,[1,2,3,4] Emily Steed,[1,2,3,4] Francesco Boselli,[1,2,3,4] Rita Ferreira,[1,2,3,4] Nathalie Faggianelli,[1,2,3,4] Stéphane Roth,[1,2,3,4] Coralie Spiegelhalter,[1,2,3,4] Nadia Messaddeq,[1,2,3,4] Le Trinh,[5] Michael Liebling,[6] Nikhil Chacko,[6] Federico Tessadori,[7] Jeroen Bakkers,[7] Jocelyn Laporte,[1,2,3,4] Karim Hnia,[1,2,3,4] and Julien Vermot[1,2,3,4,*]

[1]Institut de Génétique et de Biologie Moléculaire et Cellulaire, 67404 Illkirch, France
[2]Centre National de la Recherche Scientifique, UMR7104, 67404 Illkirch, France
[3]Institut National de la Santé et de la Recherche Médicale, U964, 67404 Illkirch, France
[4]Université de Strasbourg, 67404 Illkirch, France
[5]Molecular and Computational Biology, University of Southern California, Los Angeles, CA 90089, USA
[6]Department of Electrical and Computer Engineering, University of California Santa Barbara, Santa Barbara, CA 93106, USA
[7]Hubrecht Institute-KNAW and University Medical Center Utrecht, Utrecht 3584 CT, the Netherlands
*Correspondence: julien@igbmc.fr
http://dx.doi.org/10.1016/j.celrep.2015.05.010

SUMMARY

Desminopathies belong to a family of muscle disorders called myofibrillar myopathies that are caused by Desmin mutations and lead to protein aggregates in muscle fibers. To date, the initial pathological steps of desminopathies and the impact of desmin aggregates in the genesis of the disease are unclear. Using live, high-resolution microscopy, we show that Desmin loss of function and Desmin aggregates promote skeletal muscle defects and alter heart biomechanics. In addition, we show that the calcium dynamics associated with heart contraction are impaired and are associated with sarcoplasmic reticulum dilatation as well as abnormal subcellular distribution of Ryanodine receptors. Our results demonstrate that desminopathies are associated with perturbed excitation-contraction coupling machinery and that aggregates are more detrimental than Desmin loss of function. Additionally, we show that pharmacological inhibition of aggregate formation and Desmin knockdown revert these phenotypes. Our data suggest alternative therapeutic approaches and further our understanding of the molecular determinants modulating Desmin aggregate formation.

INTRODUCTION

Proteinopathies form a group of diseases with well-recognized features mainly hallmarked by protein aggregation. Desminopathies belong to the myofibrillar myopathies and comprise primary Desmin Related Myopathy and Cardiomyopathy (DRM and DRCM). Both DRM and DRCM are characterized by intracellular accumulation of misfolded proteins and the presence of desmin-positive insoluble granulofilamentous aggregates. Desmin-related diseases lead to progressive skeletal muscle weakness, cardiomyopathy, and conduction defects (van Spaendonck-Zwarts et al., 2011). The first symptoms of desminopathies in humans generally occur in the third decade, but the disease onset and the rate of progression of desminopathies are highly variable. Interestingly, numerous muscular disorders have been characterized as secondary DRM by the presence of desmin aggregates (Griggs et al., 2007; Hnia et al., 2011). The kinetics of aggregate formation in vivo remains unclear, and the contribution of these aggregates to developmental defects is still unknown. Thus, developing a model organism in which aggregate formation can be visualized in vivo will help elucidate the developmental defects underlying desminopathies and understand the dynamics of desmin aggregation and its impact on muscle function during embryogenesis.

Desmin is a muscle-specific type III intermediate filament protein essential for proper muscular function (Li et al., 1996; Milner et al., 1996). Mutations affecting desmin function or promoting desmin aggregation can promote skeletal or cardiac muscle phenotypes or both. Desmin knockout (KO) mice (Li et al., 1996; Milner et al., 1996) exhibit a loss of lateral alignment of myofibrils from the second week after birth. This phenotype is more severe in the heart and leads to progressive degeneration, calcification, and necrosis of the myocardium. Desmin was proposed to act as a scaffolding protein providing viscoelastic properties in the vascular wall (Lacolley et al., 2001) and stiffness to myocytes (Anderson et al., 2001), the lung airways (Shardonofsky et al., 2006), as well as the cardiomyocytes (Balogh et al., 2002; Costa et al., 2004; Rezniczek et al., 2007). The embryonic heart pumping is dependent on the biomechanical properties of cardiomyocytes (Forouhar et al., 2006), yet the role of desmin on heart biomechanics in vivo remains largely unexplored. Therefore, addressing whether there are mechanical mechanisms associated with desmin function that influence heart pumping and whether desmin aggregates affect these biomechanical mechanisms would help to solve this issue. To date, several mouse models of

desmin-related myopathy, consisting of knockin mice carrying specific patient's point mutations, were generated, yet most of them did not present clear aggregate structures, and subsequent phenotypes were often associated to dominant-negative effects on the desmin network rather than to aggregate formation (Joanne et al., 2013; Kostareva et al., 2008; Raats et al., 1996). So far, desmin aggregation was observed in mouse cardiomyocytes carrying a specific desmin mutation (Wang et al., 2001a) or *CRYAB* mutation (Wang et al., 2001b). Similarly, morpholino (MO)-mediated knockdown in zebrafish leads to cardiac and skeletal muscle phenotype (Li et al., 2013; Vogel et al., 2009). Yet, the role of desmin in heart function is still not well known, but it has been suggested that desmin impacts the mechanical properties of the cardiomyocytes (Hnia et al., 2014). Nevertheless, the sequence of events leading to these cellular alterations and their temporal relationship with protein aggregation have not yet been investigated. Thus, a comparison between desmin loss of function and pathological desmin aggregation would help to identify the cellular defects associated with either desmin depletion or aggregate formation alone.

In this study, we used genetically engineered zebrafish models allowing the comparative study of the effect of desmin aggregate formation and desmin loss of function to answer these questions. We found that desmin loss of function and the formation of desmin aggregates participate in multiple defects affecting skeletal and cardiac muscles, as well as vascular development and function in the zebrafish larvae. These defects are associated with abnormal calcium flux due to the disruption of excitation-contraction (EC) coupling machinery and to an abnormal subcellular localization of Ryanodine receptor (RyR) in both types of mutants. We further demonstrated that the majority of pathological phenotypes could be rescued by doxycycline treatment or desmin knockdown (MO), which could be of high interest for future treatment of desminopathies. Altogether, our results identify Desmin as an essential element in controlling embryonic cardiovascular and skeletal muscle function, due to its role in controlling myocardial cell contractile properties and calcium signaling. Furthermore, despite desmin being essential for heart function, its reduction is beneficial when aggregates are present and represents a potential therapeutic approach for patients.

RESULTS

Generation and Characterization of the *desma* Citrine (*desma*^{Ct122aGt}) and *desma* mCherry (*desma*^{Ct122aRGt}) Zebrafish Lines

Desmin intermediate filaments polymerize to form polymers following gradual steps of the classical assembly of intermediate filaments (Herrmann et al., 2009). The zebrafish *desmin a* (*desma*) gene is homologous to human desmin with 81% similarity in the protein sequences. *desmin b (desmb)*, a second homolog of human Desmin sharing 83% similarity, also exists in zebrafish (Figure S1). qPCR experiments and in situ hybridization showed that the expression level of *desmb* is low at early times of development (around 2,500-fold lower than the level of *desma* in 48 hpf wild-type embryos), and no overexpression of *desmb* was observed upon *desma* depletion (Figure S1). Accordingly, we conclude that the uncovered desmin protein distribution is reminiscent of Desma and that the expression of *desmb* can be neglected before 96 hpf.

Several desmin mutations have been shown to interfere with proper filament assembly when tested in vitro (Bär et al., 2005a, 2010). Such mutations could also promote aggregate formation when transfected into cultured cells (Bär et al., 2005b). However, these observations are at the steady-state level and do not provide information on aggregate formation and dynamics. In order to address the role of desmin aggregates in vivo, we used a knockin line where citrine has been inserted between amino acids 460 and 461 in the C terminus of *desmin a.* This line, named *desma*^{Ct122aGt} (or *ct122aGt*), was obtained from a gene trap screen. In this genetic context, the *desma* gene contains an artificial exon intercalating the citrine fluorescent protein coding sequence within the gene. This method enables in vivo expression of labeled Desmin at endogenous levels (Trinh et al., 2011). For the second line, we made use of the FlipTrap capability in the *desma*^{ct122aGt} line to undergo Cre-lox recombination. Upon Cre-lox recombination, the *desma*^{ct122aGt} is converted to a mCherry fusion that truncates the Desma protein, leading to a mCherry tag followed by a stop codon in the case of the reverted *desma*^{Ct122aRGt} (or *ct122aRGt*) line, leading to the deletion of 13 C-terminal amino acids in the tail domain (Figure 1A). We analyzed the global shape of the embryo and larvae as well as the viability of the *ct122aGt* and found they display no overall defects and develop normally (Figure 1B). The insertion of the fluorescent tag leads to Desmin aggregation in both lines in myocardial and skeletal muscles at 48 hpf (Figures 1C and 1D). Correlative light and electron microscopy (CLEM) using tomography showed that *ct122aGt* aggregates are positioned throughout the cytoplasm and have a fibrous structure and an average size of 9.7 ± 0.4 μm at 48 hpf (Figures 1E and 1F; Movie S1). We segmented the aggregates in 3D, and analysis of the reconstructions shows that the core structure of the aggregates is a cluster of Desmin filaments packed into a disorganized network (Movie S1).

Similar to *ct122aGt*, aggregates were observed both in the heart and skeletal muscles in the *ct122aRGt* line. Subsequent analysis of the Desma aggregate size and structure revealed that *ct122aRGt* aggregates are positioned throughout the cytoplasm similarly to what is observed in *ct122aGt*, but they are more electron dense and have a more granular structure than the *ct122aGt* aggregates (Figure 1E). Their average size was also smaller (1.4 ± 0.05 μm). In the myocardium, these aggregates were found preferentially close to cardiomyocyte membranes (Figure S1G). The differences observed between the *ct122aGt* and *ct122aRGt* lines suggest that Desma aggregation properties depend on its sequence integrity. This highlights the heterogeneity of aggregate size and shape reminiscent of *desmin* mutations, which is also observed in different human mutations (Bär et al., 2005b; Brodehl et al., 2012).

Desmin Loss or Aggregation Leads to Muscle Disorganization and Altered Organelles

Desminopathies are characterized by accumulation of granulofilamentous material leading to progressive muscle weakness with specific histological hallmarks, such as misshaped and mislocalized mitochondria, z-band streaming, and myofibrillar

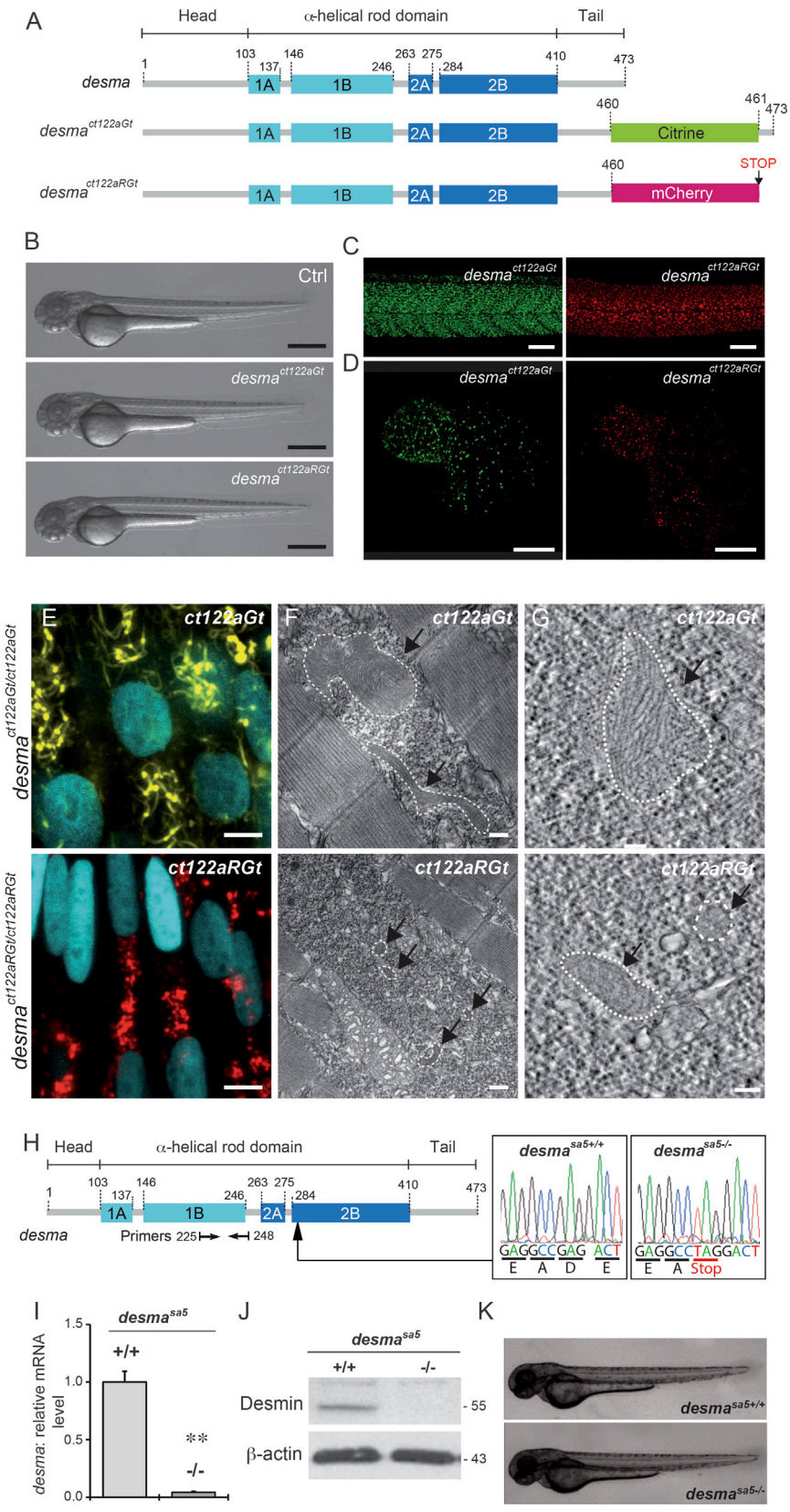

Figure 1. Desmin Flip Trap Fish Lines, *desma*^{ct122aGt} and *desma*^{ct122aRGt}, Enable Formation and Visualization of Desmin Aggregates while the *desma*$^{sa5-/-}$ Allele Leads to a Loss of *desma* Transcripts

(A) Schematic drawing of the *desma* gene in WT, *desma*^{ct122aGt} or *ct122aGt* (with citrine fusion), and *desma*^{ct122aRGt} or *Ct122aRGt* (with mCherry fusion) fish lines. The *ct122aRGt* line presents a 13-amino-acid deletion at the end of the tail domain, and the *ct122aGt* line presents a full *desma* sequence containing the citrine fluorescent protein.

(B) Side views of *ct122aGt* and *ct122aRGt* zebrafish embryos at 55 hpf. Scale bar, 500 μm.

(C and D) Desmin aggregates are observed in skeletal muscles (scale bar, 100 μm) (C) and in the myocardium (scale bar, 50 μm) (D) in *ct122aGt* and *ct122aRGt* 48-hpf embryos.

(E–G) Semicorrelative light and electron microscopy of skeletal muscles of *ct122aGt* and *ct122aRGt* 48-hpf embryos. (E) Confocal micrograph at high magnification of ct122aGt and *ct122aRGt* embryos. Nuclei are labeled with H2B-Cerulean. Scale bar, 5 μm. (F) Electron micrograph analyses of the same region showed cytosolic aggregates (the black arrows are pointing to the aggregates circled by the dotted lines) in *ct122aGt* and *ct122aRGt* embryos. Scale bar, 200 nm. (G) Electron tomography at high magnification showing filamentous aggregate structures in ct122aGt and compact aggregates with regular condensed structure in the *ct122aRGt* (the black arrows are pointing to the aggregates circled by the dotted lines). Scale bar, 100 nm. *ct122aGt* and *ct122aRGt* refers to homozygous embryos.

(H) Scheme of the WT *desma* gene in zebrafish. Arrow indicates the position of the mutation in the *desma* gene sequence. Sequencing of genomic DNA from *desma*$^{sa5+/+}$ and *desma*$^{sa5-/-}$ larvae reveals a G to T mutation resulting in a stop codon that leads to truncated Desma in *desma*$^{sa5-/-}$ mutants.

(I) Reverse transcriptase qPCR on RNA extracted from pools of WT and *desma*$^{sa5-/-}$ mutants demonstrates defective amplification of the mutant transcripts of exons 3–4 demonstrating that the corresponding mRNA is degraded. The primers used for qPCR are highlighted in (A).

(J) Immunoblot of 2 dpf WT and *desma*$^{sa5-/-}$ mutants demonstrating full knockdown of Desma protein.

(K) Side views of zebrafish *desma*$^{sa5+/+}$ and *desma*$^{sa5-/-}$ embryos at 55 hpf.

Scale bar, 500 μm. The error bars correspond to the SEM.

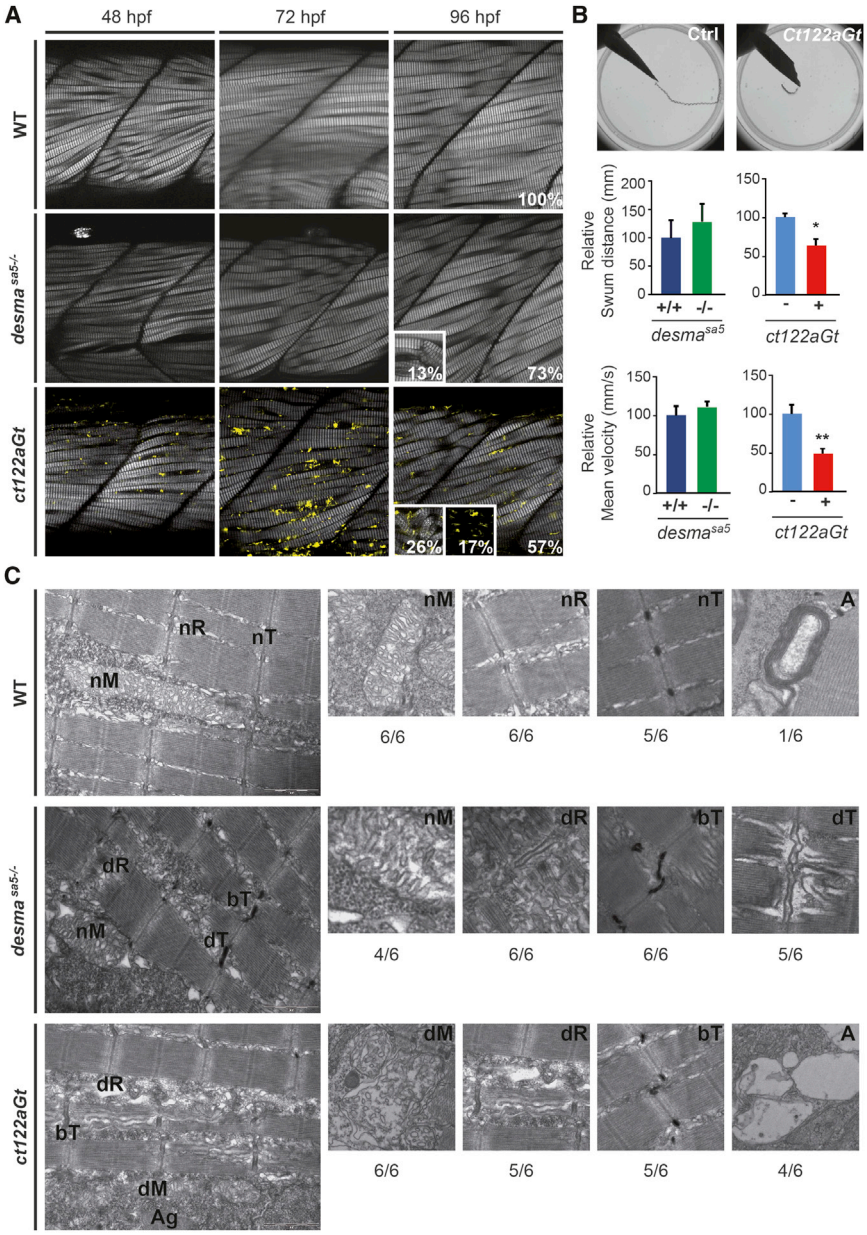

Figure 2. Aggravation of the Skeletal Muscle Phenotype Is Observed in *desma*^{ct122aGt} Embryos Compared to *desma*$^{sa5-/-}$

(A) Optical sections of the mid trunk region using SHG imaging show misalignment of muscle fibers in *desma*$^{sa5-/-}$ and *desma*^{ct122aGt} homozygous embryos compared to WT siblings at 48, 72, and 96 hpf. In *ct122aGt* mutants, muscle fiber misalignment is often accompanied by fiber breaks and degeneration from 48 hpf. At 96 hpf, phenotypes are separated in to three categories: weak *(W)* with misalignment only; strong *(S)* (see inset at 96 hpf for the *desma*^{ct122aGt} and *desma*$^{sa5-/-}$) with misalignment accompanied with breaks, degenerations, and/or general decrease of the SHG intensity; and extreme *(E)* (see inset at 96 hpf for the *desma*^{ct122aGt}) where the SHG signal is absent because of the complete disorganization of sarcomeric structures. Scale bar, 20 μm.

(B) Touch-evoke response assays show reduced swimming distance and velocity in *ct122aGt* embryos compared to controls, while the locomotion capacity of *desma*$^{sa5-/-}$ is similar to *desma*$^{sa5+/+}$.

(C) Electron micrograph of mitochondria (M), sarcoplasmic reticulum (R), T-Tubules (T), and autophagy structures (A) in controls, *desma*$^{sa5-/-}$, and *ct122aGt* mutants. Note the sarcomeric reticulum dilatation (dR) T-tubule dilation (dT) and T-tubule bending (bT) in *desma*$^{sa5-/-}$ and the dilated mitochondria in the *ct122aGt* (dM), while these structures are normal in wild-type animals. The ratio indicates the respective frequencies (n = 6). *ct122aGt* indicates *desma*^{ct122aGt} homozygous embryos. Scale bar, 100 nm.

The error bars correspond to the SEM.

degeneration (Schröder and Schoser, 2009). In mouse, desmin knockout (KO) leads to several histological hallmarks commonly observed in desminopathy patients despite the absence of desmin aggregates. A desmin KO line *desma*$^{sa5-/-}$ was obtained from the Sanger Institute ENU-mutagenesis screen. The *desma*^{sa5} allele is a point mutation leading to a premature stop codon at the beginning of the 2B alpha helix (Figure 1H). This leads to a complete depletion of *desmin* expression as verified by *desma* mRNA quantification (Figure 1I) and further validated by western blot (Figure 1J). This suggests that the mutation leads to mRNA decay and that *desma*^{sa5} is a null allele. When analyzing the viability of the *desma*$^{sa5-/-}$, we found that *desma* depletion does not affect early embryonic overall morphology (Figure 1K); however, we noted that a significant fraction of mutants died before adult stages (25%) (Figure S2A). Similar lethality percentage was observed for the *ct122aGt* (Figure S2A).

To assess the organization of muscle fibers in the tails of embryos from both *desma*$^{sa5-/-}$ and *ct122aGt*, we used second harmonic generation (SHG) microscopy. Second harmonic light can be generated when two photons with the same frequency interact with non-centrosymmetric structures and are effectively combined to generate a new photon with twice the energy (Mojzisova and Vermot, 2011). This approach allows muscle fibers imaging without any exogenous labeling at high resolution (Plotnikov et al., 2006). From 48 hpf onward, *desma*-null embryos present perturbed organization of myofibrils with a misalignment of fibers (Figure 2A). Further investigation of *desma* loss of function was performed using two MOs, one translation blocking and one splice blocking, with a mismatch MO used as a control. Our results show that both *desma* morphants lead to similar skeletal muscle phenotypes observed for *desma*$^{sa5-/-}$ (data not shown). The same phenotype is observed in *ct122aGt* embryos from 48 hpf and is accompanied by breaks in myofibril organization in 43% of embryos at 96 hpf (n = 35) (Figure 2A). In some cases, characterized

as "extreme phenotypes," the sarcomere organization was completely lost as no SHG signal was observed (17%). The classification of our phenotype based on SHG (from weak to strong) is also correlated with the specific labeling of actin filaments in the skeletal muscle of the somite using phalloidin (Figure S3). A touch evoke assay was performed to obtain functional insight into the observed phenotypes. *ct122aGt* embryos showed a decreased swimming capacity compared to their corresponding controls with lower swimming distance and velocity, while *desma*$^{sa5-/-}$ behaved in a similar manner to *desma*$^{sa5+/+}$ (Figure 2B). The ultrastructure obtained by transmission electron microscopy (TEM) analysis of *desma*$^{sa5-/-}$ and *ct122aGt* skeletal muscles at 52 hpf (Figure 2C) showed misalignment of muscle fibers, a concomitant misalignment of T-tubules and dilatation/disorganization of the sarcoplasmic reticulum (SR), while the ER seemed unaffected in both lines. Moreover, abnormal mitochondria and mitophagy were only observed in *ct122aGt* embryos at 52 hpf. Additionally, these embryos displayed degenerating cells with loss of material and the presence of autophagosomes. Taken together, these data validate previously reported observations made in other models of desminopathies and suggest that our lines are appropriate models to study desmin function in vivo. Furthermore, our data indicate that Desmin aggregates lead to a more severe muscle phenotype than Desmin loss at the ultrastructural, cellular, and functional level.

Desma Is Required for Early Heart Function

Desmin aggregates lead to a large spectrum of phenotypes in both skeletal and cardiac muscle. The variability of phenotypes is often observed in cardiomyopathies and includes dilated, hypertrophic, and restrictive cardiomyopathy. Also in certain cases additional conduction defects are observed in adult patients (Clemen et al., 2013). Nevertheless the impact of desmin on early heart function remains unclear. Therefore, we investigate heart function in the embryo by assessing cardiac contractility using high temporal imaging of the beating heart. We found that *ct122aGt*, *ct122aRGt*, and *desma*$^{sa5-/-}$ all display an increased heart rate at 30 and 48 hpf compared to corresponding controls (Figure S4A) as well as cardiac arrhythmia (2% of the *desma*$^{sa5-/-}$ and 7% of the *ct122aGt*) (Figure S2B). We next addressed heart function by measuring the difference between diastolic and systolic chamber diameter over the corresponding diastolic diameter (also known as atrial and ventricular fractional shortening (FS%) in *desma*$^{sa5-/-}$ embryos and noted a significantly lower atrial but a significantly higher ventricular FS at 48 hpf compared to *desma*$^{sa5+/+}$. Importantly, rescue of the heart function was observed at 48 hpf in *desma*$^{sa5-/-}$ by overexpressing the zebrafish *desma* full-length mRNA, demonstrating that the abnormal heart function is specifically due to the loss of Desma in the *desma*$^{sa5-/-}$ (Figure S4A). Furthermore, *ct122aGt* and *ct122aRGt* embryos present higher atrial and lower ventricular FS at 48 hpf than the controls and the *desma* mutants. As heart dysfunction could lead to vascular defects, we measured flow velocity in the dorsal aorta of *desma*$^{sa5-/-}$, *ct122aGt*, and *ct122aRGt* embryos and found that *desma*$^{sa5-/-}$ displayed an increased arterial blood flow in contrast to *ct122aGt* and *ct122aRGt* embryos, which have lower blood flow velocities compared to controls. We also found that the blood vessel diameter was more variable than the controls, which might be associated with the somitic defects (Figures S4B–S4E). These data suggest that both desmin aggregates and levels impact wall motion in the early embryonic heart and that desminopathies can lead to early cardiac defects and abnormal vascular flow.

Heart Biomechanics Are Perturbed upon *desma* Depletion or Desmin Aggregation

To further characterize the requirement of desmin on cardiomyocyte function in vivo, we addressed the contribution of desmin to the biomechanics of the heart by monitoring key parameters defining heart-wall motion in vivo. We investigated the heart-contraction pattern in 4D in order to precisely quantify heart-wall motion during a typical heartbeat (Forouhar et al., 2006). To do so, we used the myocardial-specific *Tg(myl7:EGFP)* transgenic line. 4D reconstructions were obtained for 48 hpf *Tg(myl7:egfp) desma*$^{sa5+/+}$ (n = 5), *desma*$^{sa5-/-}$ (n = 5), and *ct122aGt* (n = 6) embryos (Figure 3A; Movies S2, S3, and S4). Quantification of the heart-wall motion in both heart chambers showed that *ct122aGt*, *ct122aRGt*, and *desma*$^{sa5-/-}$ embryos display abnormal ventricular contraction profile (Figure 3B). As the heart pumping depends on a contraction wave going from the atrium to the ventricle, we used the atrioventricular canal (AVC) displacement as a readout of the global contraction pattern. The AVC serves as a hinge, which is passively subjected to constraint due to the contraction of the atrium and ventricle. Thus, the AVC lateral motion is a mark of the synchronization between both chamber contractions (Figure 3C). To quantify the chamber synchronization, we specifically tracked the motion of the AVC cells in relation to myocardial contraction and extracted the velocity profiles of the AVC cells in the different conditions. As expected, in control embryos, the propagation of regular wave leads to a single velocity peak when the contraction wave traverses the AVC. In the absence of functional desmin (*ct122aRGt* and *desma*$^{sa5-/-}$ embryos), two velocity peaks were typically observed, demonstrating that the contraction wave does not spread uniformly along the length of the heart (Figure 3D). Together, these data show that *desma* is required to maintain proper synchronization of heart-wall motion and has an important role in coordinating the contraction wave of the heart.

Desma$^{sa5-/-}$ and *Ct122aRGt* Display Alterations in the Embryonic Heart Conduction System

It was reported that some desminopathy patients have arrhythmias associated with defects in the cardiac conduction system including calcifications (Yuri et al., 2007). Given that heart contraction waves are directly controlled by Ca^{2+} propagation in the myocardium, we tested the dynamics of Ca^{2+} propagation in our models. We used GCaMP3.0, a genetically encoded Ca^{2+} indicator (Warp et al., 2012), which reveals Ca^{2+} dynamics in the heart and the activity of the conduction system in vivo (Chi et al., 2010). We characterized the Ca^{2+} transient generation in the myocardium from *desma*$^{sa5-/-}$ and *ct122aRGt* embryos being double transgenic for *Tg(myl7:galFF)* and *Tg(UAS:GCaMP3.0)*. This permits imaging of Ca^{2+} using fast confocal microscopy and subsequent 4D reconstruction of the heartbeat and enables

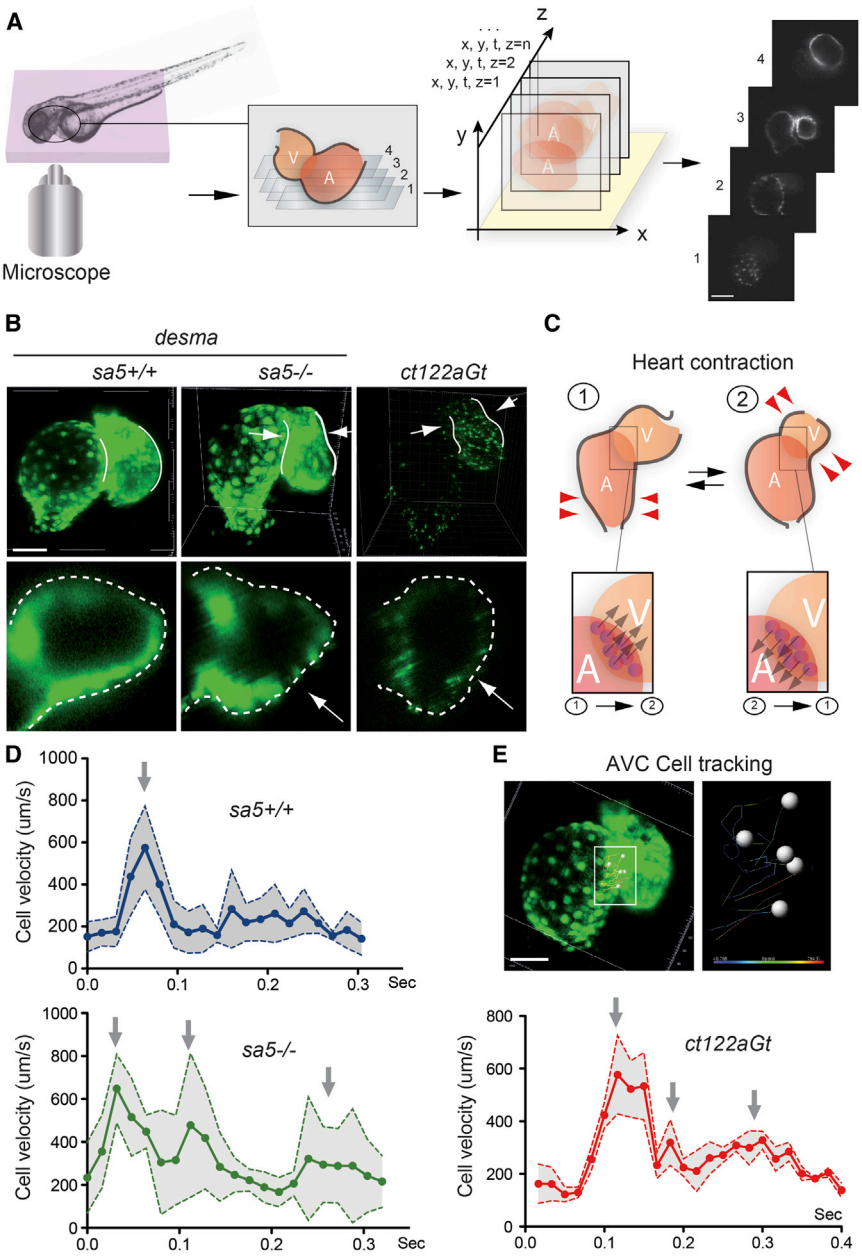

Figure 3. Heart Biomechanics Are Altered in the Absence of *desma* and in the Presence of Desmin Aggregates

(A) 4D reconstructions of the heart-wall dynamics were obtained from 2D series recorded at a rate of 120 frames/s (fps) in successive planes. Periodic contractions were reconstructed in three dimensions using post acquisition synchronization of 48-hpf embryonic hearts. Scale bar, 30 μm.

(B) Comparison of myocardial wall shape in *desma*$^{sa5+/+}$, *desma*$^{sa5-/-}$, and *ct122aGt* 4D reconstructed hearts shows a squeezing of the ventricle in both mutants (Movies S2, S3, and S4). The lower panels show a zoom of an optical transverse section through the middle of the ventricle of *desma*$^{sa5+/+}$, *desma*$^{sa5-/-}$, and *ct122aGt* revealing the squeezing in absence of functional Desma (red arrows). Scale bar, 30 μm.

(C) Schematic drawing recapitulating the myocardial movements associated with heart contraction and the subsequent movement of the atrioventricular canal (AVC). Examples of AVC cells tracks are shown in the lower panel. Their velocity was used as readout of the global contraction pattern of the heart. Scale bar, 30 μm.

(D) Graph representing the velocity of myocardial cell motion in the AVC region following 3D cell tracking in *desma*$^{sa5+/+}$, *desma*$^{sa5-/-}$, and *ct122aGt*.

(E) Individual nuclei were tracked automatically and their speed was extracted. *ct122aGt* indicates *desma*^{ct122aGt} homozygous embryos.

The error bars correspond to the SEM.

the intra-cardiac calcium fluxes to be recorded concomitantly with the native heart-wall motion (Figure 4A; Movies S5, S6, and S7). To quantify the Ca^{2+} wave, the relative fluorescence intensity was measured locally over time at the base of the atrium (1), the top of the atrium (2), the tip of the ventricle (3), and the middle of the ventricular outer curvature (4). In controls, the peaks of calcium intensity followed the contraction wave exactly and clear oscillations of fluorescence matching the contraction wave were recorded in all of the analyzed regions. By contrast, the calcium amplitude observed at the tip of the ventricle (region 3) was lower in *desma*$^{sa5-/-}$ and *ct122aRGt* embryos (1.32 ± 0.082 and 1.33 ± 0.021, respectively) compared to their corresponding controls (1.52 ± 0.082 for *desma*$^{sa5+/+}$ and 1.51 ± 0.091 for *ct122aRGt*$^{-/-}$). Similar observations were made in the region corresponding to the outer curvature of the ventricle in the *ct122aRGt* embryos (1.34 ± 0.051 compared to control 1.61 ± 0.078) (Figure 4B). These data suggest that the absence of functional desmin filaments leads to locally decreased Ca^{2+} amplitude. These observations provide the physiological basis for the aberrant contraction wave observed in the absence of functional desmin filaments as well as the abnormal synchronization between atrium and ventricle during the contraction cycles.

RyR Distribution and Localization Is Altered in *Desma*$^{sa5-/-}$ and *Ct122aRGt* Heart

Ca^{2+} flux is mostly regulated by channels that allow a fine spatio-temporal regulation of Ca^{2+} turnover. Ryanodine receptor (RyR) is a master calcium channel, which modulates the spontaneous heartbeat during development (Wu et al., 2011). Given the fact that SR shape is altered in our models, we asked whether the abnormal Ca^{2+} flux observed in our model could be linked to RyR distribution. At 48 hpf, RyR is expressed and localized on the SR membranes, while the junction of SR and T-tubules called

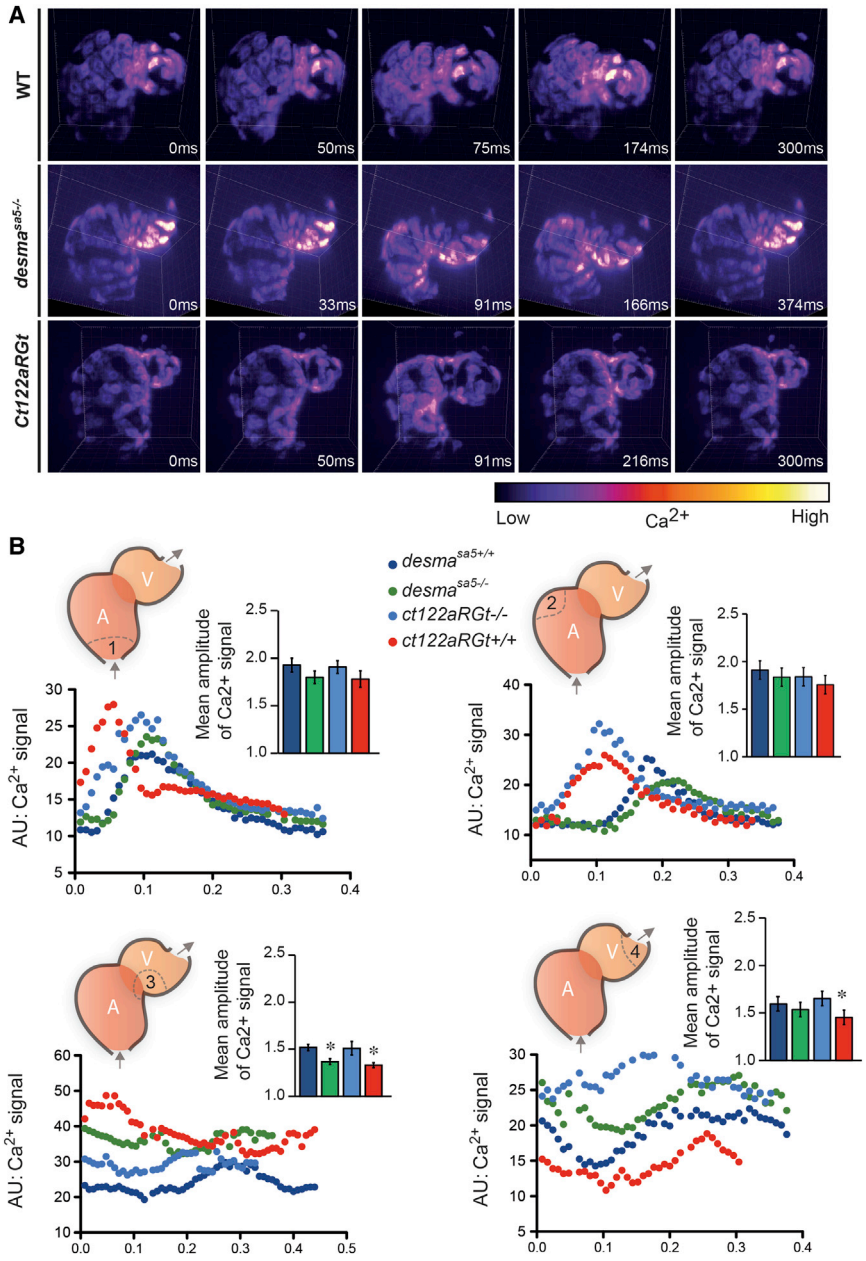

Figure 4. Ca^{2+} Propagation in the Beating Heart Is Deficient in the Absence of Functional Desmin

(A) Snapshots from videos corresponding to the 4D reconstructions of a single heartbeat in *Tg(myl7: GalFF; UAS:Gcamp3.0)* WT, *desma*$^{sa5-/-}$, and *ct122aRGt* 48-hpf embryos (Movies S5, S6, and S7) show perturbations in the Ca^{2+} signal at the ventricle tip in the absence of functional Desma. Scale bar, 30 μm.

(B) Ca^{2+} intensity plots and quantification of the amplitude of the Ca^{2+} peak upon contraction in four different regions of the heart: (1) inflow tract; (2) atrium outer curvature; (3) ventricle proximal outer curvature; and (4) ventricle distal outer curvature. The amplitude is significantly reduced in region 3 of the *desma*$^{sa5-/-}$ and in regions 3 and 4 of the *ct122aRGt* (n = 5 embryos, n ≥ 10 cells for each condition). Plots correspond to a representative example of each condition. Note that the heart-contraction sequences for each condition are not starting at the same moment of the contraction cycle. Gray arrows indicate the direction of blood flow through the heart. *ct122aRGt* indicates *desma*^{ct122aRGt} homozygous embryos. The error bars correspond to the SEM.

"the triad" (RyR localization in adult muscle) is not formed yet. However, even in the absence of mature triad compartment, RyR is expressed and functionally regulates the entry of calcium in the SR to coordinate myocardial contraction (Jurynec et al., 2008). We analyzed RyR distribution in control and in the *ct122aGt* embryos (Figure 5A). We found that RyR localization in *ct122aGt* is aberrantly accumulating and clustering in the myocardial cells (Figure 5A). We next assessed the composition of the desmin aggregates by performing solubility assay. Along with RyR, we tested for the αB-crystallin chaperone that pellets with desmin in the X100-Triton insoluble fraction (Wang et al., 2001b). We found that the insoluble (Pellet) fractions contained both αB-crystallin and RyR, along with Desmin in the *ct122aGt* embryos, while these proteins were mainly present in the soluble fractions in controls (Figure 5B). Also, we found that RyR localization and solubility were also altered in absence of Desmin in *desma*$^{sa5-/-}$ heart at 48 and 72 hpf, albeit to a lesser extent than in *ct122aGt* embryos (Figure 5C; Figures S5A and S5B). These results suggest that RyR distribution and function is affected in absence of functional desmin, which could interfere with gradual establishment of functional EC coupling machinery in muscle cells (Figure 5D).

desma Knockdown in *ct122aGt* Restores Muscle Morphology

A key step toward obtaining novel therapies of proteinopathies is the development of approaches allowing the decrease of the size and the number of aggregates. Hence, targeting desmin aggregates by decreasing *desma* level in the *ct122aGt* line will give us clues about the contribution of misfolded desmin in the muscle phenotypes. To do so, we used a MO-based approach to knockdown desmin in *ct122aGt* line. Injection of two different MO concentrations, 33 and 100 μM, lead to a drastic reduction of skeletal muscles phenotypes as assessed at 48, 72, and 96 hpf using SHG and categorized into normal (N), weak (W), strong (S), and extreme (E). We defined a scale of SHG phenotypes in which weak phenotype corresponds to the situation where muscle fibers are misaligned or present abnormal curvatures (Figure 6A). A strong phenotype is attributed when muscles display degenerated and/or broken

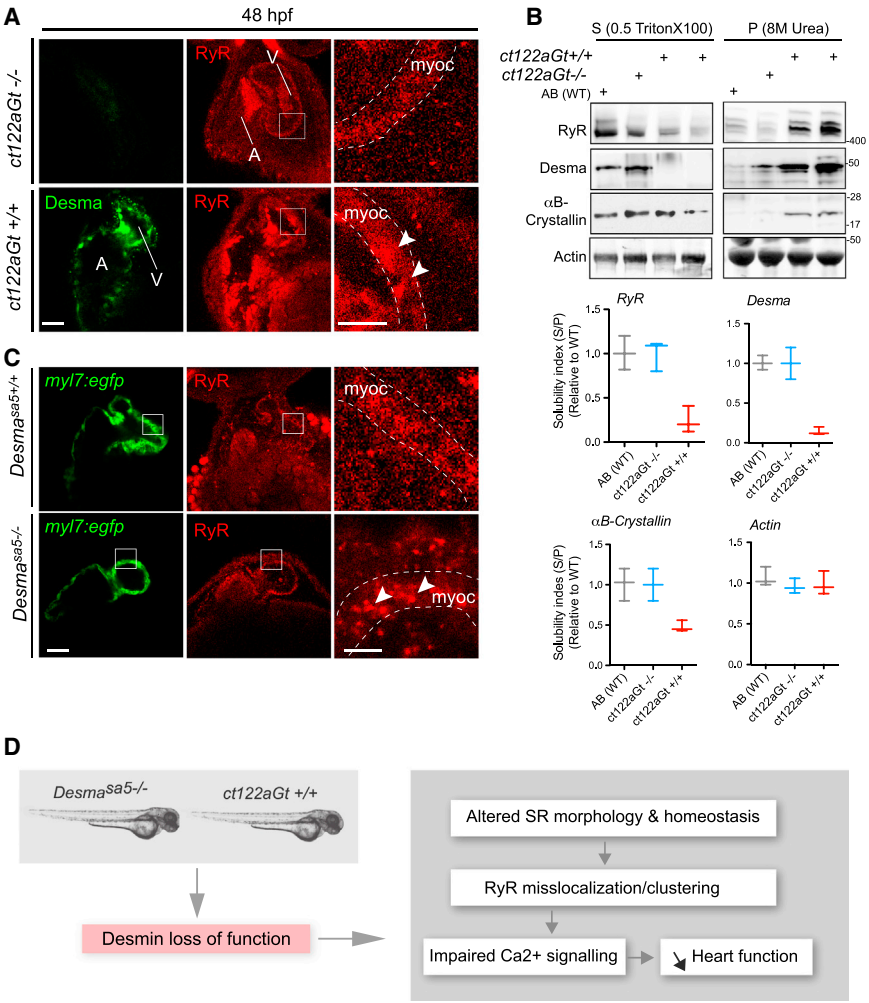

Figure 5. Desma Aggregation or Loss of Function Impact on Ryanodine Receptor Localization

(A) Confocal images of RyR (red) in cardiac muscle from 48-hpf embryos showed homogenous and regular labeling mostly in the myocardium (myoc, highlighted with the white dotted lines) in control fish (*ct122aRGt*$^{-/-}$), while in desma *ct122aRGt*$^{+/+}$ mutant hearts RyR display irregular localization and clustering (white arrowheads). Scale bar, 30 μm.

(B) In support of (A), RyR solubility was reduced in *ct122aRGt*$^{+/+}$ mutant fish extracts compared to control where the majority of RyR fraction remains in the Triton X-100 fractions. αB-crystallin solubility is also affected in *ct122aRGt*$^{+/+}$ embryos. Actin is the loading control. Bars showed quantification from two independent experiments, and each sample contains a mixture of 50–100 fish.

(C) Similar to (A), confocal images of cardiac muscle from 48-hpf embryos in *desma*$^{sa5-/-}$ animals crossed with the myocardium-specific *Tg(myl7:egfp)* (green) line compared to controls (*Tg(myl7:egfp; desma*$^{sa5+/+}$*)*) showing mislocalization and clustering (white arrowheads) of RyR in the myocardium (myoc, highlighted with the white dotted lines). Scale bar, 30 μm. myoc, myocardium

(D) Schematic drawing of how *desma* loss of function (knockout or aggregation) could impact sarcoplasmic reticulum shape and EC-coupling machinery particularly on RyR localization.

The error bars correspond to the SEM.

fibers, a global decrease in the size of the musculature or a global decrease in the intensity of the SHG signal. A phenotype is called extreme when the muscle disorganization is such that no SHG signal is observed anymore (Figure 6A). Using this scale, we found that *desma* knockdown (MO-33 and 100 μM) rescues *ct122aGt* muscle phenotypes with a complete disappearance of the strong phenotype (Figure 6B). Only weak phenotypes were observed in embryos injected with the MOs, which correlates with the drastic decrease in both the size and number of aggregates, respectively (Figure 6C). Interestingly, the effect observed is dose- dependent both in terms of aggregate size, number, and swimming distance (but not the swimming speed) and in terms of total protein decrease when additional MO concentrations were used (Figures 6D–6I). Finally the knockdown was sufficient to restore normal heart function as revealed by the rescue of the ventricular and atrial fractional shortening, whereas heart rate remained unchanged (Figure 6I). Our data show that the presence of aggregates is the main cause of pathological features in zebrafish models of desminopathies and that decreased desmin levels can reduce aggregate formation and, concomitantly, the pathology affecting the skeletal and cardiac muscles.

Doxycycline Treatment Decreases Aggregates and Ameliorates the Skeletal Muscle Phenotype in the *ct122aGt* Line

To further validate our model, we next tested compounds or drugs with the potential to act negatively on protein aggregates in the *ct122aGt* line. Doxycycline (Doxy) (Zheng et al., 2010) has raised lots of interest in the last few years and is likely the most appropriate therapeutic approach for ameliorating desminopathies. Doxy treatment lowers the aggregate content in many proteinopathies (e.g., Huntington disease) and can partially rescue the desmin-related cardiomyopathy phenotype in the αB-crystallin mouse model (Wang et al., 2001b; Zheng et al., 2010). We treated *ct122aGt* embryos with Doxy from 12 hpf and measured aggregate size and number using confocal microscopy after 36 hr of treatment (Figure 7A). We performed CLEM on Doxy-treated embryos to address the structure of the aggregates and clearance activity. The analysis revealed a more condensed and spherical structure of aggregates lacking filamentous extensions compared to vehicle-treated embryos (Figure 7A). Moreover, the size of the aggregates was found to be dramatically

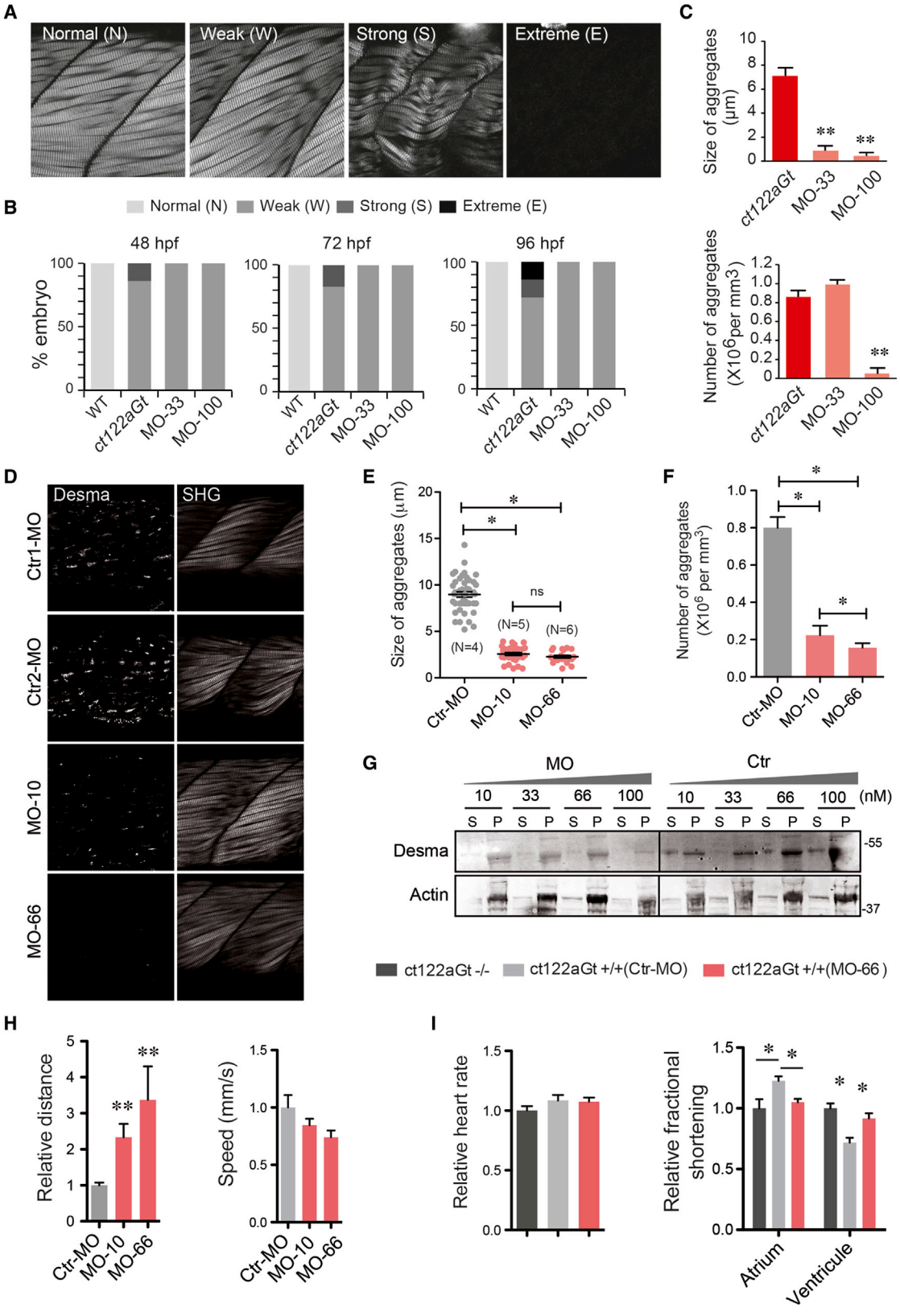

(legend on next page)

smaller in Doxy-treated embryos (3.2 ± 0.5 μm versus 9.7 ± 0.4 μm in untreated *ct122aGt*), while their number is increased (Figure 7B). We also found that Doxy-*ct122aGt* embryos displayed a weak phenotype according to our SHG analysis (100% versus 50% in corresponding controls at 72 hpf) (Figure 7C) suggesting that Doxy could fragment or/and inhibit the formation of big aggregates, which impact muscle phenotype. Doxy could also restore normal swimming distance suggesting that cellular distribution of aggregates as well as their size may have a direct impact on the severity of the phenotypes (Figure 7D). Furthermore, we found that Doxy restored normal ventricular heart rate and fractional shortening by comparison to the untreated embryos (Figure 7E). Interestingly, the atrial fractional shortening is higher in the mutants (treated and non-treated) suggesting that the rescue is heart compartment specific and that desmin affects the fractional shortening differently in the atrium and ventricle. We further addressed the impact of Doxy on desmin solubility in a dose-dependent manner. By performing solubility assays, we found that Doxy treatment dramatically increases the desmin soluble fraction comparable to that observed for controls using increased concentrations (Figure 7F). However, the beneficial impact in terms of solubility reaches a plateau when high Doxy concentration was used (50 μg/ml) (Figure 7F; Figures S6A and S6B). We also found that the effect of the Doxy could act on established aggregates as size and numbers of aggregates could also be reduced following Doxy treatment after aggregate formation (from 24 hpf) (Figure S7A). We tested Doxy activity once aggregates are formed by starting the treatment at 24 hpf and found that it still leads to a significant decrease of aggregate size and increase in their number in Doxy-*ct122aGt* lines (Figure S7B). The treated embryos developed at the same pace as controls suggesting that reduction in aggregate size is mostly due to its specific action on aggregates. We conclude that Doxy could target desmin aggregates even once they are formed and consequently could rescue muscular defects in the *ct122aGt* line. Together, these data validate the use of our line to study drugs affecting aggregate formation in vivo. It also unambiguously confirms that desmin aggregates are linked to several pathological hallmarks observed in skeletal and cardiac muscle from desminopathies.

DISCUSSION

Although the zebrafish has been used extensively to identify new regulators of cardiac and skeletal muscle function by conducting forward genetic screens, there has been very limited success in identifying novel mutants displaying aggregation phenotypes and proteinopathies using endogenously tagged proteins. By analyzing these mutant embryos, we observed the presence of aggregates when the protein is truncated or fused with fluorescent proteins. This strategy leads to aggregates that are morphologically similar to those observed in humans, unlike previous animal models in which there are no (or few) desmin aggregates (Hnia et al., 2014). Here, we took advantage of the zebrafish to analyze desmin function and desmin aggregation in the heart muscles in vivo. We found that heart defects are visible in zebrafish at embryonic stages and as the myocardium matures. The first signs of desminopathies are most frequently observed in adulthood in both mouse models and patients (Goldfarb and Dalakas, 2009). We found that embryonic heart contractility and blood flow is abnormal in the absence of desmin and in the presence of desmin aggregates in zebrafish. Desmin-null mice present arterial defects attributed to altered smooth muscle cells function where desmin is well expressed (Li et al., 1996). In the zebrafish embryo, smooth muscle cells appear at larvae stage. Considering that *desma* is not detectable in endothelial cells, our results suggest that the reported vascular phenotypes could result from an indirect impact of blood flow alterations. Although infrequent or poorly diagnosed in human desminopathies, subtle vascular abnormalities should be further investigated in relation to heart and muscle function.

The altered cardiovascular physiology observed in desmin mutants is accompanied with conduction defects leading to abnormal ventricular contraction. Remodeling of gap junctions and mislocalization of Cx43 and other mechanical junction proteins like desmoplakin, plakoglobin, and N-cadherin were shown previously in a mouse model of desmin-related cardiomyopathy (Gard et al., 2005). Mislocalization of intercellular junction components is commonly observed in arrhythmogenic cardiomyopathies and triggers a loss of mechanical and electrical coupling of cardiomyocytes (Agullo-Pascual et al., 2014; Asimaki et al., 2014). We found that distribution of RyR, an essential element

Figure 6. Reduction of Desma Level Ameliorates Skeletal and Cardiac Muscle Phenotypes Observed in *desma*^{ct122aGt} Homozygous Embryos

(A) Classification of the skeletal muscle phenotypes obtained with SHG. Normal phenotype is attributed to embryos with similar muscle shape as the controls. Weak phenotype corresponds to the situation where muscle fibers are misaligned or present abnormal curvatures. A strong phenotype is attributed when embryonic muscle display degenerated and/or broken fibers, a global decrease in the size of the musculature or a global decrease in the intensity of the SHG signal. A phenotype is called extreme when the muscle disorganization is such that no SHG signal is observed anymore. Scale bar, 30 μm.

(B) Evaluation of phenotypes in *ct122aGt* injected with the 33 and 100 μM MO, uninjected, and WT embryos from 48 to 96 hpf. The assessment of a phenotype is based on the scale presented in (A) after SHG imaging.

(C) Size and number of aggregates in *ct122aGt* injected with two different concentrations of MO (33 and 100 μM). Embryos injected with 100 μM present a high reduction in aggregate numbers, while 33 μM of MO did not reduce the aggregate number.

(D) Images of aggregates and corresponding SHG in *ct122aGt* embryos treated with 10- and 66-nM concentrations of MO or the corresponding control (Ctr). Scale bar, 30 μm.

(E and F) Two additional concentration of MO showed a dose-dependent reduction in size and number of aggregates.

(G) All the tested concentration were employed to monitor desmin solubility index = Triton X-100 soluble desmin (S)/insoluble or pellet (P) in whole zebrafish extracts. Actin is the loading control.

(H) Decreased *desma* level by MO treatment improves fish mobility but does not impact speed.

(I) MO-mediated *desma* knockdown restore normal cardiac fractional shortening in *ct122aGt* line. *ct122aGt* indicates *desma*^{ct122aGt} homozygous embryos. The error bars correspond to the SEM.

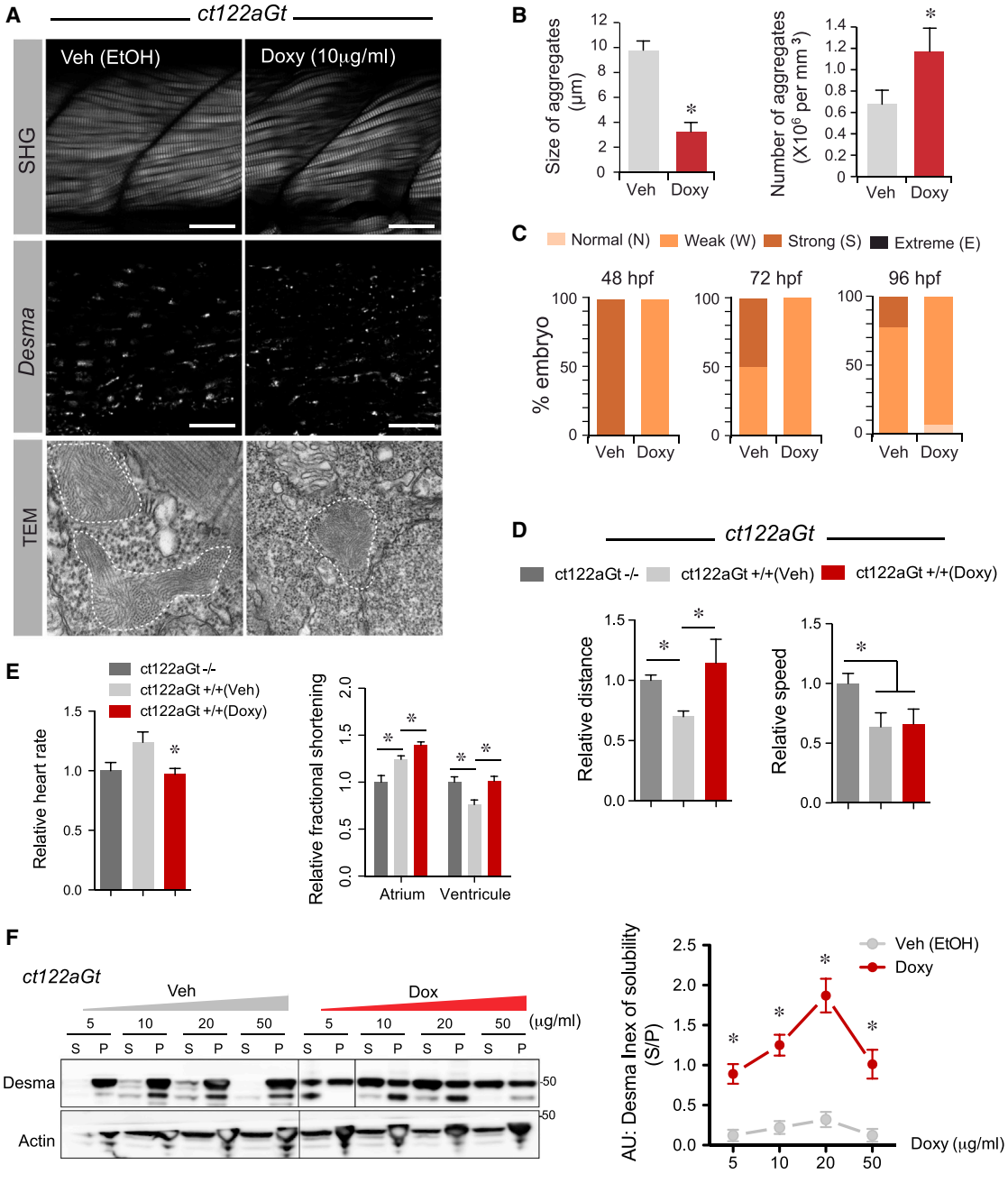

Figure 7. Pharmacological Targeting of Desma Aggregates Rescue *ct122aGt* Phenotype

(A) Confocal and electron microscopy images showing the impact of Doxycycline (Doxy) treatment on *ct122aGt* muscle. Doxy-treated embryos showed more condensed and smaller aggregates compared to the controls. Scale bar, 20 μm (SHG). Scale bar, 100 nm (TEM)

(B) Quantification of aggregate size and number in Doxy-treated embryos compared to the corresponding vehicle-treated embryos.

(C) Evaluation of the phenotypes of Doxy and vehicle-treated embryos using SHG and the scale defined in (C) show that only weak and normal phenotypes were observed after Doxy treatment, while strong phenotypes are present in the controls. Note that the vehicle contains ethanol, which is leading to a stronger phenotype than in the non-vehicle-treated *ct122aGt* line.

(D) Touch-evoke response assays showing that Doxy treatment improves swimming distance but not speed in *ct122aGt*.

(E) Doxy-treated *ct122aGt* showed increased fractional shortening (FS) in the atrium but could re-establish FS in the ventricle.

(F) Doxy treatment increases *desma* solubility (index of solubility) in dose-dependent manner. Actin is the loading control. *ct122aRGt* indicates *desma*^{ct122aRGt} homozygous embryos.

The error bars correspond to the SEM.

of the excitation contraction coupling machinery, was affected in our models. We speculate that this could explain conduction phenotypes in our models and observed in 62% of desminopathy patients (van Spaendonck-Zwarts et al., 2011). As morphogenesis of cardiomyocytes can be influenced by endogenous electrical currents in the embryonic heart (Chi et al., 2010), it is possible that desmin indirectly controls the final steps of heart development and morphogenesis through the regulation of Ca^{2+} conduction in cardiomyocytes. As our data show that the physiological mechanism of cardiac defects in desminopathies is associated with abnormal calcium dynamics in cardiomyocytes, further analysis in mouse embryos or juveniles could highlight similar features in higher vertebrates.

Finally, we employed a strategy to decrease the amount of endogenous desmin (MO) or to target the desmin aggregates (doxycycline treatment) to analyze the effects of drugs as well as to modulate the severity of the phenotype. While biochemical and cellular characterization of desmin aggregates was extremely helpful to understand properties and dynamics of these aggregates in vitro (Herrmann et al., 2009), this work should help to clarify the details of the cellular basis of desminopathies in vivo. Our data also validate the use of a knockdown strategy to decrease desmin level during early embryonic stages, which was sufficient to restore parts of the cardiac and muscular defects. Similarly, we showed that Doxy is likely acting as a chemical chaperone to interfere with existent desmin aggregates and could also inhibit gradual aggregate formation and size. We propose that future use of our desmin aggregation models *ct122aGt* and *ct122aRGt* might help to apply screening strategies for the identification of chemical compounds inhibiting desmin aggregation. As new and powerful strategies are now emerging for drug screening using whole zebrafish embryos, this will allow the potential of chemicals that could be applied in humans to be investigated. In conclusion, we have identified desmin as a potential therapeutic target for desminopathies and generated several useful zebrafish lines for modeling desminopathies.

EXPERIMENTAL PROCEDURES

Zebrafish Husbandry and Embryo Treatments

Animal experiments were approved by the Animal Experimentation Committee of the Institutional Review Board of the IGBMC. The following lines were used in this study: wild-type AB, *desma*^{ct122Gta} and *desma*^{ct122aRGt} lines (Trinh et al., 2011), *desma*^{sa5}(Kettleborough et al., 2013), *Tg(myl7:egfp)* (Huang et al., 2003), *Tg(myl7:ras-eGFP)*^{s883} (D'Amico et al., 2007), *Tg(fli1a:neGFP)*^{y7} (Roman et al., 2002), *Tg(fli:gal4FF*^{ubs}*; UAS:kaede)* (Herwig et al., 2011), *Tg(myl7:GalFF; UAS:RFP)*^{hu6228} (Strate et al., 2015), and *Tg(UAS:gcamp3.0; Gal4s1020t)* (Warp et al., 2012) and were described previously. Embryos were staged according to hours (hpf) and days postfertilization (dpf). They were incubated at 28.5°C in 0.3% Danieau medium supplemented with 0.003% (w/v) 2-phenylthiourea to inhibit pigment formation.

desma^{sa5} fish were genotyped using the following primers: FP: ACACA CACTCGCCAAACAAA and RP: GTCTCAGCAACTTCCGGTTC. For imaging, embryos were anesthetized with 0.02% Tricaine (Sigma-Aldrich) and were mounted on glass bottom Petri dishes embedded in 0.8% low melting point agarose (Sigma-Aldrich). Before fixation for electron microscopy and still heart imaging, embryos were treated for 10 min with 40 mM 2,3-butanedione monoxime (BDM) as a myosin inhibitor to have their muscle in a constant relaxed state. Doxycycline (Sigma-Aldrich) was supplemented in the fish medium from 12 hpf at 10 μg/ml.

Morpholino Knockdown and mRNA Rescue

One translation start site blocking and one splice site blocking MO were designed to knockdown *desma* (Gene Tools). *desma* ATG MO: GGCTGAAT ATTTCGTGCTCATGACT, *desma* splice MO (exon 2-intron 2): ATGACATAA AGTACATACAGCTCTG. *desma* ATG mismatched MO (GGCTCAAAATT TGGTCCTCATCACT) was used as control. 2.3 nl of MO (100 μM) was injected into embryos at one-cell stage. For rescue experiments in *desma*$^{sa5-/-}$, full-length zebrafish *desma* cDNA was obtained in pME18SFL3 (Source Bioscience) and amplified using TAATACGACTCACTATAGGGACCATGAGCACGA AATATTCAGC and GGATCCAGACATGATAAGATAC primers. The resulting fragments were transcribed in vitro using mMessage mMachine T7 Kit (Ambion). 0.25 ng of the mRNA was injected into embryos at the one-cell stage.

SUPPLEMENTAL INFORMATION

Supplemental Information includes Supplemental Experimental Procedures, seven figures, and seven movies and can be found with this article online at http://dx.doi.org/10.1016/j.celrep.2015.05.010.

ACKNOWLEDGMENTS

We thank D. Paulin for thoughtful comments on the manuscript. We thank S. Abdelilah-Seyfried, M. Affolter, and C. Wyart for providing fish stocks. We thank the IGBMC fish facility (S. Geschier and S. Gredler) and the IGBMC imaging center, in particular B. Gurchenkov, P. Kessler, M. Koch, and D. Hentsch. This work was supported by HFSP, INSERM, AFM, FRM, and the seventh framework program (MC-IRG256549 to J.V.). C.R. was supported by the AFM. This study was supported by grant ANR-10-LABX-0030-INRT, a French State fund managed by the Agence Nationale de la Recherche under the frame program Investissements d'Avenir labeled ANR-10-IDEX-0002-02.

Received: July 25, 2014
Revised: April 3, 2015
Accepted: May 5, 2015
Published: June 4, 2015

REFERENCES

Agullo-Pascual, E., Cerrone, M., and Delmar, M. (2014). Arrhythmogenic cardiomyopathy and Brugada syndrome: diseases of the connexome. FEBS Lett. *588*, 1322–1330.

Anderson, J., Li, Z., and Goubel, F. (2001). Passive stiffness is increased in soleus muscle of desmin knockout mouse. Muscle Nerve *24*, 1090–1092.

Asimaki, A., Kapoor, S., Plovie, E., Karin Arndt, A., Adams, E., Liu, Z., James, C.A., Judge, D.P., Calkins, H., Churko, J., et al. (2014). Identification of a new modulator of the intercalated disc in a zebrafish model of arrhythmogenic cardiomyopathy. Sci. Transl. Med. *6*, 40ra74.

Balogh, J., Merisckay, M., Li, Z., Paulin, D., and Arner, A. (2002). Hearts from mice lacking desmin have a myopathy with impaired active force generation and unaltered wall compliance. Cardiovasc. Res. *53*, 439–450.

Bär, H., Fischer, D., Goudeau, B., Kley, R.A., Clemen, C.S., Vicart, P., Herrmann, H., Vorgerd, M., and Schröder, R. (2005a). Pathogenic effects of a novel heterozygous R350P desmin mutation on the assembly of desmin intermediate filaments in vivo and in vitro. Hum. Mol. Genet. *14*, 1251–1260.

Bär, H., Mücke, N., Kostareva, A., Sjöberg, G., Aebi, U., and Herrmann, H. (2005b). Severe muscle disease-causing desmin mutations interfere with in vitro filament assembly at distinct stages. Proc. Natl. Acad. Sci. USA *102*, 15099–15104.

Bär, H., Schopferer, M., Sharma, S., Hochstein, B., Mücke, N., Herrmann, H., and Willenbacher, N. (2010). Mutations in desmin's carboxy-terminal "tail" domain severely modify filament and network mechanics. J. Mol. Biol. *397*, 1188–1198.

Brodehl, A., Hedde, P.N., Dieding, M., Fatima, A., Walhorn, V., Gayda, S., Šarić, T., Klauke, B., Gummert, J., Anselmetti, D., et al. (2012). Dual color photoactivation localization microscopy of cardiomyopathy-associated desmin mutants. J. Biol. Chem. *287*, 16047–16057.

Chi, N.C., Bussen, M., Brand-Arzamendi, K., Ding, C., Olgin, J.E., Shaw, R.M., Martin, G.R., and Stainier, D.Y. (2010). Cardiac conduction is required to preserve cardiac chamber morphology. Proc. Natl. Acad. Sci. USA *107*, 14662–14667.

Clemen, C.S., Herrmann, H., Strelkov, S.V., and Schröder, R. (2013). Desminopathies: pathology and mechanisms. Acta Neuropathol. *125*, 47–75.

Costa, M.L., Escaleira, R., Cataldo, A., Oliveira, F., and Mermelstein, C.S. (2004). Desmin: molecular interactions and putative functions of the muscle intermediate filament protein. Braz. J. Med. Biol. Res. *37*, 1819–1830.

D'Amico, L., Scott, I.C., Jungblut, B., and Stainier, D.Y. (2007). A mutation in zebrafish hmgcr1b reveals a role for isoprenoids in vertebrate heart-tube formation. Curr. Biol. *17*, 252–259.

Forouhar, A.S., Liebling, M., Hickerson, A., Nasiraei-Moghaddam, A., Tsai, H.J., Hove, J.R., Fraser, S.E., Dickinson, M.E., and Gharib, M. (2006). The embryonic vertebrate heart tube is a dynamic suction pump. Science *312*, 751–753.

Gard, J.J., Yamada, K., Green, K.G., Eloff, B.C., Rosenbaum, D.S., Wang, X., Robbins, J., Schuessler, R.B., Yamada, K.A., and Saffitz, J.E. (2005). Remodeling of gap junctions and slow conduction in a mouse model of desmin-related cardiomyopathy. Cardiovasc. Res. *67*, 539–547.

Goldfarb, L.G., and Dalakas, M.C. (2009). Tragedy in a heartbeat: malfunctioning desmin causes skeletal and cardiac muscle disease. J. Clin. Invest. *119*, 1806–1813.

Griggs, R., Vihola, A., Hackman, P., Talvinen, K., Haravuori, H., Faulkner, G., Eymard, B., Richard, I., Selcen, D., Engel, A., et al. (2007). Zaspopathy in a large classic late-onset distal myopathy family. Brain *130*, 1477–1484.

Herrmann, H., Strelkov, S.V., Burkhard, P., and Aebi, U. (2009). Intermediate filaments: primary determinants of cell architecture and plasticity. J. Clin. Invest. *119*, 1772–1783.

Herwig, L., Blum, Y., Krudewig, A., Ellertsdottir, E., Lenard, A., Belting, H.G., and Affolter, M. (2011). Distinct cellular mechanisms of blood vessel fusion in the zebrafish embryo. Curr. Biol. *21*, 1942–1948.

Hnia, K., Tronchere, H., Tomczak, K.K., Amoasii, L., Schultz, P., Beggs, A.H., Payrastre, B., Mandel, J.L., and Laporte, J. (2011). Myotubularin controls desmin intermediate filament architecture and mitochondrial dynamics in human and mouse skeletal muscle. The Journal of clinical investigation *121*, 70–85.

Hnia, K., Ramspacher, C., Vermot, J., and Laporte, J. (2014). Desmin in muscle and associated diseases: beyond the structural function. Cell Tissue Res.

Huang, C.J., Tu, C.T., Hsiao, C.D., Hsieh, F.J., and Tsai, H.J. (2003). Germ-line transmission of a myocardium-specific GFP transgene reveals critical regulatory elements in the cardiac myosin light chain 2 promoter of zebrafish. Dev. Dyn. *228*, 30–40.

Joanne, P., Chourbagi, O., Hourdé, C., Ferry, A., Butler-Browne, G., Vicart, P., Dumonceaux, J., and Agbulut, O. (2013). Viral-mediated expression of desmin mutants to create mouse models of myofibrillar myopathy. Skelet Muscle *3*, 4.

Jurynec, M.J., Xia, R., Mackrill, J.J., Gunther, D., Crawford, T., Flanigan, K.M., Abramson, J.J., Howard, M.T., and Grunwald, D.J. (2008). Selenoprotein N is required for ryanodine receptor calcium release channel activity in human and zebrafish muscle. Proc. Natl. Acad. Sci. USA *105*, 12485–12490.

Kettleborough, R.N., Busch-Nentwich, E.M., Harvey, S.A., Dooley, C.M., de Bruijn, E., van Eeden, F., Sealy, I., White, R.J., Herd, C., Nijman, I.J., et al. (2013). A systematic genome-wide analysis of zebrafish protein-coding gene function. Nature *496*, 494–497.

Kostareva, A., Sjöberg, G., Bruton, J., Zhang, S.J., Balogh, J., Gudkova, A., Hedberg, B., Edström, L., Westerblad, H., and Sejersen, T. (2008). Mice expressing L345P mutant desmin exhibit morphological and functional changes of skeletal and cardiac mitochondria. J. Muscle Res. Cell Motil. *29*, 25–36.

Lacolley, P., Challande, P., Boumaza, S., Cohuet, G., Laurent, S., Boutouyrie, P., Grimaud, J.A., Paulin, D., Lamazière, J.M., and Li, Z. (2001). Mechanical properties and structure of carotid arteries in mice lacking desmin. Cardiovasc. Res. *51*, 178–187.

Li, Z., Colucci-Guyon, E., Pinçon-Raymond, M., Mericskay, M., Pournin, S., Paulin, D., and Babinet, C. (1996). Cardiovascular lesions and skeletal myopathy in mice lacking desmin. Dev. Biol. *175*, 362–366.

Li, M., Andersson-Lendahl, M., Sejersen, T., and Arner, A. (2013). Knockdown of desmin in zebrafish larvae affects interfilament spacing and mechanical properties of skeletal muscle. J. Gen. Physiol. *141*, 335–345.

Milner, D.J., Weitzer, G., Tran, D., Bradley, A., and Capetanaki, Y. (1996). Disruption of muscle architecture and myocardial degeneration in mice lacking desmin. J. Cell Biol. *134*, 1255–1270.

Mojzisova, H., and Vermot, J. (2011). When multiphoton microscopy sees near infrared. Curr. Opin. Genet. Dev. *21*, 549–557.

Plotnikov, S.V., Millard, A.C., Campagnola, P.J., and Mohler, W.A. (2006). Characterization of the myosin-based source for second-harmonic generation from muscle sarcomeres. Biophys. J. *90*, 693–703.

Raats, J.M., Schaart, G., Henderik, J.B., van der Kemp, A., Dunia, I., Benedetti, E.L., Pieper, F.R., Ramaekers, F.C., and Bloemendal, H. (1996). Muscle-specific expression of a dominant negative desmin mutant in transgenic mice. Eur. J. Cell Biol. *71*, 221–236.

Rezniczek, G.A., Konieczny, P., Nikolic, B., Reipert, S., Schneller, D., Abrahamsberg, C., Davies, K.E., Winder, S.J., and Wiche, G. (2007). Plectin 1f scaffolding at the sarcolemma of dystrophic (mdx) muscle fibers through multiple interactions with beta-dystroglycan. J. Cell Biol. *176*, 965–977.

Roman, B.L., Pham, V.N., Lawson, N.D., Kulik, M., Childs, S., Lekven, A.C., Garrity, D.M., Moon, R.T., Fishman, M.C., Lechleider, R.J., and Weinstein, B.M. (2002). Disruption of acvrl1 increases endothelial cell number in zebrafish cranial vessels. Development *129*, 3009–3019.

Schröder, R., and Schoser, B. (2009). Myofibrillar myopathies: a clinical and myopathological guide. Brain Pathol. *19*, 483–492.

Shardonofsky, F.R., Capetanaki, Y., and Boriek, A.M. (2006). Desmin modulates lung elastic recoil and airway responsiveness. Am. J. Physiol. Lung Cell. Mol. Physiol. *290*, L890–L896.

Strate, I., Tessadori, F., and Bakkers, J. (2015). Glypican4 promotes cardiac specification and differentiation by attenuating canonical Wnt and Bmp signaling. Development *142*, 1767–1776.

Trinh, A., Hochgreb, T., Graham, M., Wu, D., Ruf-Zamojski, F., Jayasena, C.S., Saxena, A., Hawk, R., Gonzalez-Serricchio, A., Dixson, A., et al. (2011). A versatile gene trap to visualize and interrogate the function of the vertebrate proteome. Genes Dev. *25*, 2306–2320.

van Spaendonck-Zwarts, K.Y., van Hessem, L., Jongbloed, J.D., de Walle, H.E., Capetanaki, Y., van der Kooi, A.J., van Langen, I.M., van den Berg, M.P., and van Tintelen, J.P. (2011). Desmin-related myopathy. Clin. Genet. *80*, 354–366.

Vogel, B., Meder, B., Just, S., Laufer, C., Berger, I., Weber, S., Katus, H.A., and Rottbauer, W. (2009). In-vivo characterization of human dilated cardiomyopathy genes in zebrafish. Biochem. Biophys. Res. Commun. *390*, 516–522.

Wang, X., Osinska, H., Dorn, G.W., 2nd, Nieman, M., Lorenz, J.N., Gerdes, A.M., Witt, S., Kimball, T., Gulick, J., and Robbins, J. (2001a). Mouse model of desmin-related cardiomyopathy. Circulation *103*, 2402–2407.

Wang, X., Osinska, H., Klevitsky, R., Gerdes, A.M., Nieman, M., Lorenz, J., Hewett, T., and Robbins, J. (2001b). Expression of R120G-alphaB-crystallin causes aberrant desmin and alphaB-crystallin aggregation and cardiomyopathy in mice. Circ. Res. *89*, 84–91.

Warp, E., Agarwal, G., Wyart, C., Friedmann, D., Oldfield, C.S., Conner, A., Del Bene, F., Arrenberg, A.B., Baier, H., and Isacoff, E.Y. (2012). Emergence of patterned activity in the developing zebrafish spinal cord. Curr. Biol. *22*, 93–102.

Wu, H.H., Brennan, C., and Ashworth, R. (2011). Ryanodine receptors, a family of intracellular calcium ion channels, are expressed throughout early vertebrate development. BMC Res. Notes *4*, 541.

Yuri, T., Miki, K., Tsukamoto, R., Shinde, A., Kusaka, H., and Tsubura, A. (2007). Autopsy case of desminopathy involving skeletal and cardiac muscle. Pathol. Int. *57*, 32–36.

Zheng, H., Tang, M., Zheng, Q., Kumarapeli, A.R., Horak, K.M., Tian, Z., and Wang, X. (2010). Doxycycline attenuates protein aggregation in cardiomyocytes and improves survival of a mouse model of cardiac proteinopathy. J. Am. Coll. Cardiol. *56*, 1418–1426.

Cell Reports
Report

Endothelial Cilia Mediate Low Flow Sensing during Zebrafish Vascular Development

Jacky G. Goetz,[1,2,3,4,11] Emily Steed,[1,2,3,4] Rita R. Ferreira,[1,2,3,4] Stéphane Roth,[1,2,3,4] Caroline Ramspacher,[1,2,3,4] Francesco Boselli,[1,2,3,4] Gilles Charvin,[1,2,3,4] Michael Liebling,[5] Claire Wyart,[6,7,8,9] Yannick Schwab,[10] and Julien Vermot[1,2,3,4,*]

[1]Institut de Génétique et de Biologie Moléculaire et Cellulaire, 67400 Illkirch, France
[2]Centre National de la Recherche Scientifique, UMR7104, 67404 Illkirch, France
[3]Institut National de la Santé et de la Recherche Médicale, U964, 67404 Illkirch, France
[4]Université de Strasbourg, 67404 Illkirch, France
[5]Department of Electrical and Computer Engineering, University of California, Santa Barbara, Santa Barbara, CA 93106, USA
[6]Institut du Cerveau et de la Moelle Épinière (ICM), Hôpital de la Pitié-Salpêtrière, 75013 Paris, France
[7]Inserm UMRS 1127, 75013 Paris, France
[8]CNRS UMR 7225, 75013 Paris, France
[9]UPMC University of Paris 06, 75005 Paris, France
[10]Electron Microscopy Core Facility, Cell Biology and Biophysics Unit, European Molecular Biology Laboratory, Meyerhofstrasse 1, 69117 Heidelberg, Germany
[11]Present address: Inserm U1109, The Microenvironmental Niche in Tumorigenesis and Targeted Therapy, 67200 Strasbourg, France; LabEx Medalis, Fédération de Médecine Translationnelle de Strasbourg (FMTS), 67000 Strasbourg, France
*Correspondence: julien@igbmc.fr
http://dx.doi.org/10.1016/j.celrep.2014.01.032

SUMMARY

The pattern of blood flow has long been thought to play a significant role in vascular morphogenesis, yet the flow-sensing mechanism that is involved at early embryonic stages, when flow forces are low, remains unclear. It has been proposed that endothelial cells use primary cilia to sense flow, but this has never been tested in vivo. Here we show, by non-invasive, high-resolution imaging of live zebrafish embryos, that endothelial cilia progressively deflect at the onset of blood flow and that the deflection angle correlates with calcium levels in endothelial cells. We demonstrate that alterations in shear stress, ciliogenesis, or expression of the calcium channel PKD2 impair the endothelial calcium level and both increase and perturb vascular morphogenesis. Altogether, these results demonstrate that endothelial cilia constitute a highly sensitive structure that permits the detection of low shear forces during vascular morphogenesis.

INTRODUCTION

The formation of a functional cardiovascular system relies on a complex interplay among a genetic program, fluid mechanics, and processes of cellular reorganization (Potente et al., 2011; Herbert and Stainier, 2011). Although the genetics of flow-inducible genes have been extensively analyzed over the last few years (Buschmann et al., 2010; Bussmann et al., 2011; Chen et al., 2012; Corti et al., 2011; le Noble et al., 2004; Nicoli et al., 2010), much less is known about the blood-flow-sensing mechanisms used during vascular development. Numerous in vitro studies have demonstrated that vascular endothelial cells (ECs) can both sense and transduce biomechanical stimuli, such as wall shear stress, through primary cilia (Hierck et al., 2008; Nauli et al., 2008). However, a quantitative understanding of the flow conditions sensed by cilia and an assessment of their function within the intact developing vascular network are still lacking. Moreover, the potential involvement of cilia in sensing flow forces of small amplitude, such as those observed in early embryonic stages, remains unclear.

RESULTS

Because we expected flow forces to vary greatly at the onset of flow, we first characterized the flow conditions generated over time during the early embryonic stages when flow begins (Forouhar et al., 2006). The flow features in the vascular network directly depend on heart function. We thus followed heart morphology (Figure 1A; Movie S1) and contraction between 24 and 28 hr postfertilization (hpf). At 24 hpf, we could not detect the opening of the endocardial lumen. To quantitate this, we measured the linear deformation of both the endocardium and myocardium, and found they remained low (90%) and very low (18%), respectively (Figures 1A–1C and S1A–S1C; Movies S1, S2, and S5). This means that even though the myocardium contracts significantly, the endocardium does not open properly and strongly limits flow forces. By comparison, the inner structure of the endocardial lumen displayed a clear opening of the

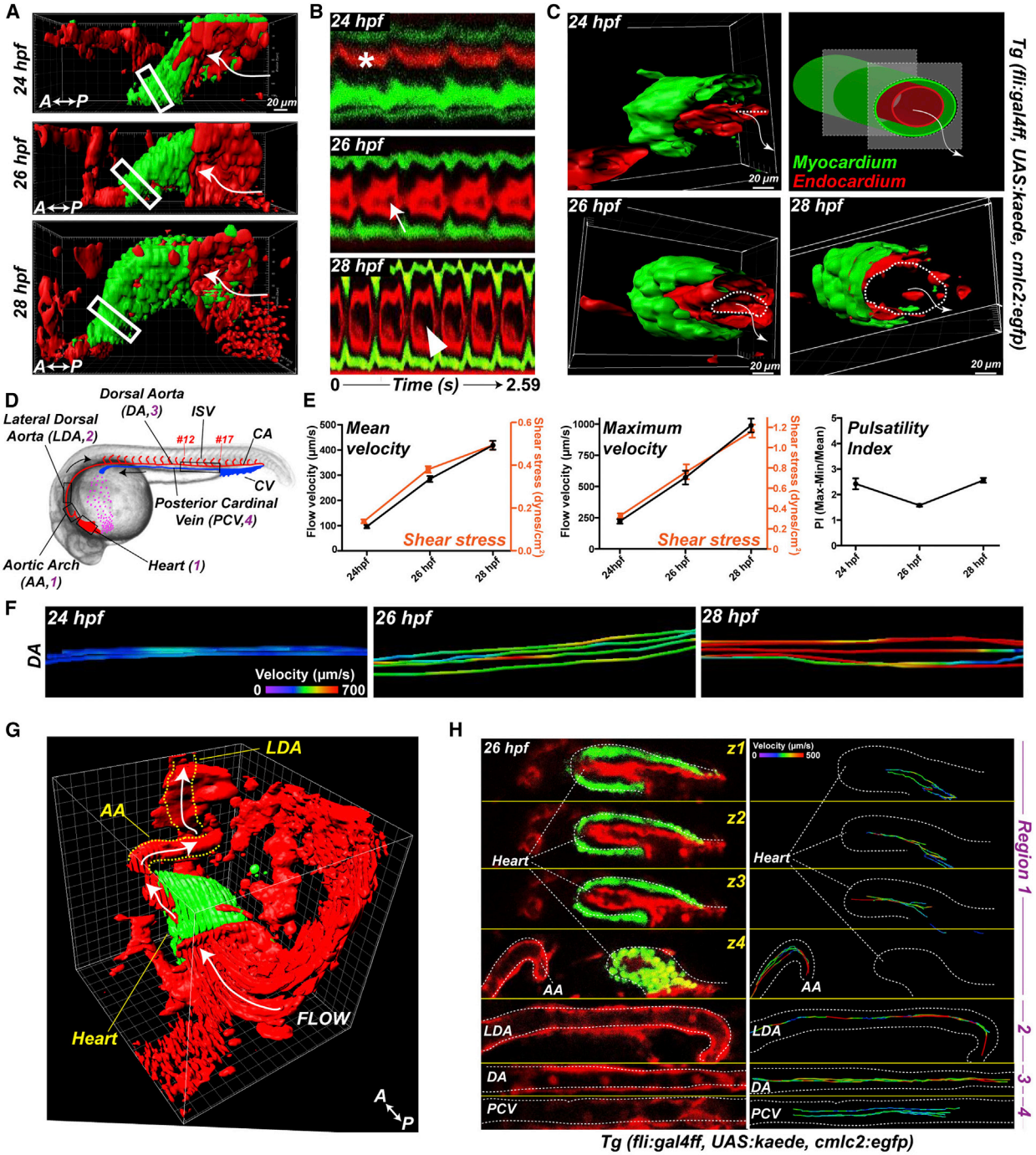

(legend on next page)

endocardium (dashed lines) at 26 hpf (Figures 1A–1C, S1B, and S1C; Movies S3 and S5). Consistently, the linear deformation of the endocardium reached 197% at 26 hpf, whereas the myocardium displayed only a mild increase to 40% (Figure S1C; Movies S3 and S5). At 28 hpf, the heartbeat significantly increased (2.63 ± 0.17 Hz), as did the endocardial linear deformation to 283% (75% for the myocardium; Figures 1A–1C and S1A–S1C; Movies S1, S4, and S5). Altogether, these data show that endocardial deformation is the major factor controlling heart pumping efficiency at these early stages.

Because the vascular network is complex and flow forces directly depend on the anatomy of the network, we next characterized the flow along the network. Between 24 and 28 hpf, we found that flow increased almost linearly in the dorsal aorta (DA), whereas pulsatility remained steady (Figures 1E and 1F; Movie S6). We also analyzed the flow velocities at the heart exit and further downstream in the network at 26 hpf. Blood cells exit the heart into the ventral aorta, which branches into the mandibular aortic arches (AAs) (Isogai et al., 2001; Figures 1D, 1G, S1D, and S1E; Movie S7). The arches empty directly into the two (left and right) lateral dorsal aortas (LDAs), draining blood into the medial DA (Isogai et al., 2001; Figures 1D, 1G, S1D, and S1E; Movie S7). Blood-flow velocity peaks in the AA and LDA reached 883 ± 118 and 1159 ± 187 μm/s, respectively, although the mean velocities were 192 ± 13 and 170 ± 15 μm/s, respectively (Figures 1G–1I and S1E; Movie S7). Altogether, these data demonstrate that flow profiles vary extensively along the vascular network and with the developmental stage due to heart remodeling. It also suggests that every area of the network is in contact with unique flow profiles during the onset of flow.

Detecting such variability in intravascular flow necessitates a very sensitive mechanism of flow sensing. Flow velocity is considerably slower along the vessel wall than at its center, because viscous friction prevents fluid from slipping on the vessel wall (Freund et al., 2012; Supatto and Vermot, 2011). In this context, cilia protrusion allows flow to be sensed away from the cell membrane, and therefore constitutes an advantageous structure for low-amplitude flow sensing. To determine the distribution of endothelial cilia in vivo, we analyzed a double-transgenic line, *Tg(β-actin:arl13b-egfp; flk1:mCherry)*, labeling cilia and ECs, respectively. We found that most ECs displayed cilia protruding into the aorta and vein lumen between 24 and 28 hpf (at 28 hpf, 76% [934/1,271 cells] of the ECs in the caudal artery [CA] and vein [CV] are ciliated; Figures 2A–2D; see also Movie S8, left panel). Cilia were reduced in number at later stages and almost absent in the CA and CV at 48 hpf (4%, 31/996 cells), suggesting that cilia are necessary when flow forces are low, during the time of vascular morphogenesis. To confirm this hypothesis, we analyzed cilia distribution in *tnnt2a* morphants, which lack a functional *troponin T2a* gene, a key component of the heart muscle thin filaments specific to the myocardium (Sehnert et al., 2002), thus resulting in noncontractile hearts. We found that 68% of ECs (742/1,091) remained ciliated in the absence of flow. These observations are consistent with earlier in vitro studies suggesting that high shear stress can disassemble cilia (Iomini et al., 2004).

Using correlative microscopy approaches, we next characterized the 3D ultrastructure of endothelial cilia by electron microscopy (EM) coupled to electron tomography in order to precisely assess the endothelial cilia deformation in conjunction with its ultrastructure. Using a set of anatomical landmarks, we focused on different cilia, located in the CA (arterial; Figures 2A–2D, 2F–2M, and S2B–S2D; Movies S8, S9, S10, and S11) and the CV (venous; Figures 2E and S2A). We then generated thick (~250 nm) serial sections of the region of interest and reassembled 16 consecutive tomograms to reconstruct 4 μm of the protruding cilia near the cell surface (Figures 2F–2L and S2B–S2D; Movies S9 and S10). We found that the basal body displayed a canonical 9-fold symmetry and was composed of nine microtubule triplets regularly spaced and linked to transition fibers in the region most proximal to the plasma membrane (Figures 2F and 2I–2L; Movies S9 and S10). Remarkably, we observed the rapid disappearance of some microtubules (red, Figure 2M; Movie S11) in the most distal extracellular region of the axoneme. Given that microtubules are known to confer stiffness to the structures they shape (Hoey et al., 2012), we reasoned that this unusual arrangement could give endothelial cilia unique stiffness profiles. To test this hypothesis, we modeled the cilium as a beam and computed the hydrodynamic load by the local slender-body theory. The bending stiffness is defined as $E_b = M/k$, with k being the curvature and M the moment at a cross-section of the cilium. Using our in vivo measurements, we estimated the bending stiffness (E_b) of endothelial cilia to be in the range of $0.5 < E_b < 1 \times 10^{-23}$ Nm^2, making them softer than kidney cilia previously examined in vitro ($1 < E_b < 5 \times 10^{-23}$ Nm^2) (Young et al., 2012), possibly due to their

Figure 1. Early Cardiac Morphometrics and Subsequent Hemodynamics at Blood Flow Onset

(A) 3D imaging of the heartbeat in *Tg(fli:gal4FF; UAS:kaede; cmlc2:egfp)* embryos. Heart myocardium is labeled in green (GFP), and endocardium and blood cells are in red (photoconverted Kaede).

(B) Kymographs of a section (boxed region) of the heart tube. The asterisk indicates the absence of a visible endocardial lumen at 24 hpf. The arrows indicate the progressive opening of the lumen at 26 and 30 hpf.

(C) 3D sections of the boxed regions in (A). The dashed lines underline the endocardium opening and the arrows show the flow direction.

(D) Simplified view of the cardiovascular system of 24–28 hpf embryos. CA, caudal artery; CV, caudal vein; ISV, intersomitic vessels.

(E) Blood cell tracking in the developing DA (see box in D). Graphs show the mean and maximum flow velocity in the DA (see box in D) and the pulsatility index (PI) at 24, 26, and 28 hpf.

(F) Tracks in the DA are color-coded for their instantaneous velocity over time.

(G) 3D anatomy of a 26 hpf heart and its neighboring vasculature and flow direction. See also Movies S5 and S7.

(H) Vascular hemodynamics in a single embryo. Three sections of the same heart are displayed (see corresponding regions in D). Tracks are color-coded for their instantaneous velocity over time.

(I) Plots of the velocity and PI observed in a single embryo.

Error bars depict SEM. Statistical significance was determined by unpaired Student's t test; *$p < 0.05$, **$p < 0.01$, ***$p < 0.001$. See also Figure S1.

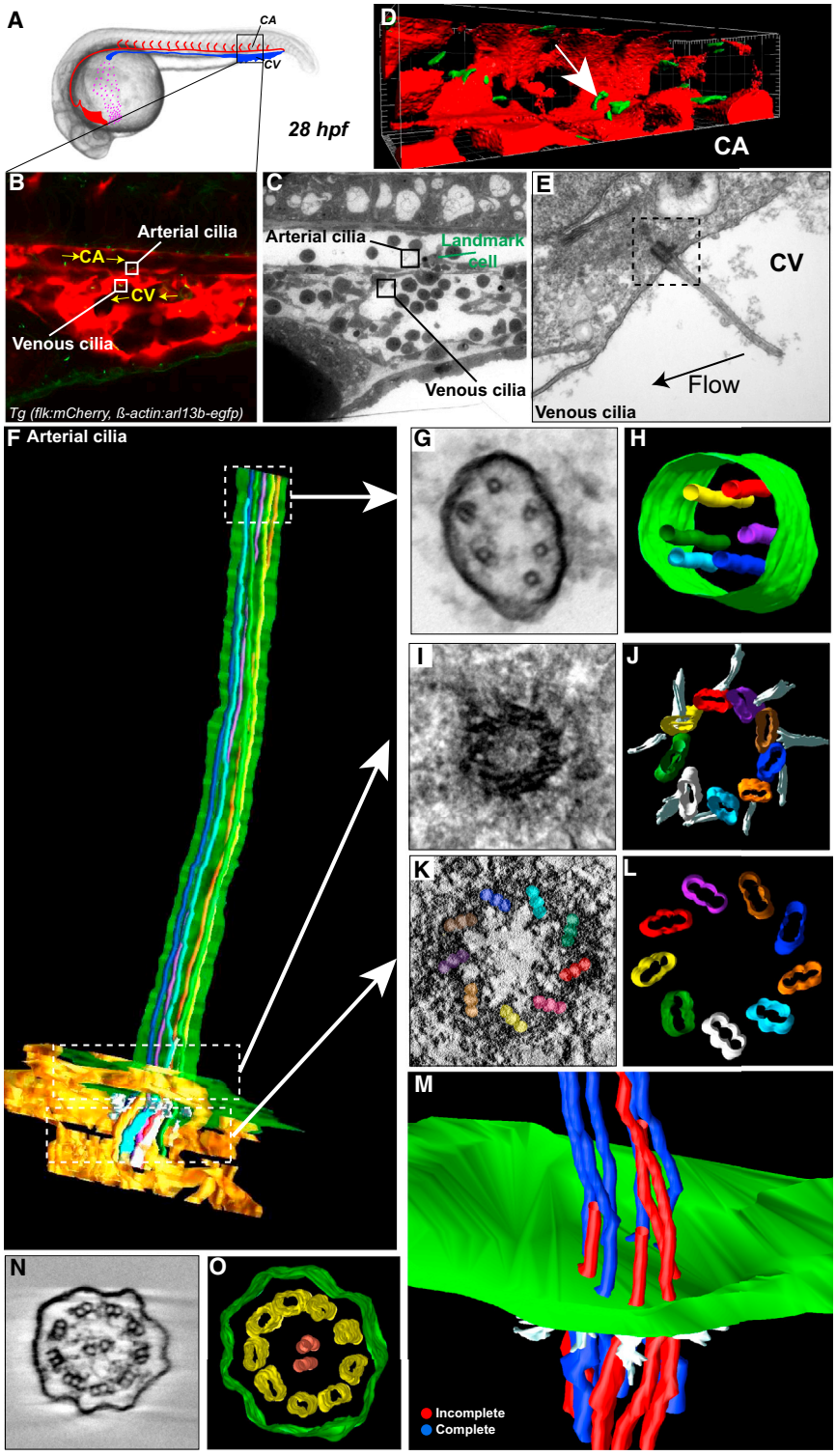

Figure 2. Early Embryonic Vessels Are Ciliated

(A) Global view of a 28 hpf embryo.

(B) Single confocal section of the region of interest in the CA; endothelium is in red, primary cilia are in green. Boxes define two cilia of interest located in the CA (arterial) and CV (venous). Flow direction is indicated. See also Movie S8.

(C) Transmission electron microscopy (TEM) image of the region shown in (B).

(D) 3D reconstruction of the region of interest (arrow points to cilium of interest).

(E) TEM image of the venous cilia highlighted in (B) and (C).

(F–M) Electron tomography of the arterial cilia outlined in (B)–(D).

(F) Reconstruction of the portion of the protruding cilia near the cell surface.

(G–L) Single tomograms and modeling of regions located in the axoneme (G and H) and the basal body (I–L) are presented. Microtubules were color-labeled along the whole cilia. Note that the light blue microtubule is incomplete over the tomogram presented in (G) and (H). See also Movies S8, S9, and S10.

(M) A portion of the cilia proximal to the plasma membrane. Microtubules that disappear along the cilia axis are labeled in red. See also Movie S11.

(N and O) Single tomogram and modeling of a motile cilia located in the pronephros. Note the characteristic 9+2 microtubule doublet architecture.

See also Figure S2 and Movie S12.

unique microtubule content. This low-microtubule feature was seen in all of the observed cilia regardless of vessel identity and position in the network (Figure S2). As expected, pronephric motile cilia of the same animal displayed the conventional 9+2 microtubule doublets in the axoneme (Figures 2N and 2O; Movie S12), demonstrating that the sample preparation did not affect the native cilia ultrastructure. We also tested whether blood flow is involved in controlling the endothelial cilia microtubule content by characterizing the endothelial cilia ultrastructure in controls at 24 hpf, when flow forces are extremely low, and in the silent heart mutants (*sih*), which lack a functional *tnnt2a* gene (Sehnert et al., 2002; Figure S2E). In the absence of flow, the observed cilia ultrastructure was similar to that of controls, suggesting that flow does not affect the microtubule content of endothelial cilia. Together, these results suggest that endothelial cilia have a unique ultrastructure, which by dictating rigidity and bending properties may render the cilia deformable in response to small flow variations.

To examine this, we tested the sensitivity of cilia deflection at the earliest stages of flow generation and characterized the relationship between blood flow and cilia bending. We segmented cilia based on their GFP signal and plotted the most acute value

of the angle between the cilia and the endothelial surface over time (Figures 3A–3C; Movie S13), while simultaneously imaging flow (Figure 3C; Movie S13). At 24 hpf, we found the average cilia angle in the DA lumen to be close to 84° (Figures 3D, 3F, and S3; Movie S14). This angle progressively decreased with time, reaching 41.5° ± 2° at 28 hpf (Figures 3D, 3F, and S3A; Movie S14), when cilia are highly deflected by flow. We also found that the frequency of cilia bending resembled that of the blood flow in response to heart contraction (2.41 Hz and 2.63 ± 0.17 Hz, respectively (Figures S1A, S3A, and S3B). Without flow in the *tnnt2a* morphants, endothelial cilia were not deflected (average angle 96° ± 2.2°; Figures 3H and 3I; Movie S15). Furthermore, although the absence of blood cells in *gata1* morphants did not affect the mean flow velocity (Figure 3J; Movie S16) or frequency of cilia deflection (Figure S3H), the cilia angle was less acute (58° versus 42° for controls), showing that cilia deflection also depends on blood viscosity (Figures 3H, 3I, and S3H; Movie S17). We conclude that cilia can be deflected by subtle changes in hemodynamic forces in the vascular network.

Because cilia deflection has been proposed to increase calcium signaling in vitro in kidney epithelial (Nauli et al., 2003) and EC cultures (Nauli et al., 2008), we next investigated whether endothelial cilia bending correlated with increased calcium signaling in vivo. Using the endothelial-specific expression of a genetically encoded calcium indicator, *Tg(fli:gal4ff; UAS:gcamp3.0)* (Warp et al., 2012), we observed a progressive increase in calcium levels in the DA during blood flow onset from 24 to 28 hpf (Figures 3E and 3G), consistent with the progressive flow-mediated cilia deflection between these stages (Figures 3D and 3F). At 28 hpf, we also observed a gradation in both cilia deflection and calcium content along the DA anteroposterior axis (Figures S3C–S3G), as well as a clear difference in both parameters between arterial cilia (located in the DA) and venous cilia (located in the PCV) (Figures S3C–S3G). These results indicate that changes in vascular flow velocities correlate with a specific cilia deflection angle and calcium level at every point in the vascular network. We also found that the absence of flow in *sih* mutants, as well as a strong reduction in heart contractility in *cmlc1* morphants (Meder et al., 2009), led to a dramatic decrease in EC calcium levels (Figures 3K and S4A–S4D), showing that cilia and flow are necessary to control intracellular calcium entry in ECs. We observed similar defects when blood viscosity was reduced in *gata1* morphants. The absence of *gata1* stopped red blood cell production, and plasma flow had the same average speed as observed in controls (Figure 3J). This allowed us to test the impact of decreased viscosity on cilia bending (Figures 3H and 3I). We observed similar defects in these conditions (Figure 3K). Cilia deflection is thus extremely sensitive to low-shear forces and enables subtle changes in hemodynamic forces to be transduced into differential calcium levels inside the EC.

Cilia mechanodetection and calcium signaling depend on the calcium-permeable channel PKD2/PC2/TRPP2 in several ciliated structures, such as the left-right organizer (McGrath et al., 2003; Yoshiba et al., 2012), kidney epithelial cells (Nauli et al., 2003), and cultured ECs (mouse and human) (AbouAlaiwi et al., 2009). We found that *pkd2* was expressed in the developing vascular network and that PKD2 was located in membranous structures close to the base of the cilia (Figure S4E). As in *sih* embryos, depletion of *pkd2* reduced endothelial calcium levels (Figures 3K, S4A, and S4D). These phenotypes were also observed upon spatiotemporal knockdown of *pkd2* using a photo-morpholino (photo-MO) to specifically initiate knockdown of *pkd2* in the caudal plexus at 22 hpf (Figures 3K and S4H–S4L). We additionally tested the role of cilia in the process by knocking down *ift88* (Kramer-Zucker et al., 2005; Tsujikawa and Malicki, 2004), a protein that is critical for ciliogenesis, using regular and photo-MOs (Figures S4M–S4U). Similar reductions in calcium levels were observed in the absence of endothelial cilia in both *ift88* morphants and *ift88* photomorphants when activated at 21 hpf (Figures S4N–S4U), further suggesting that flow acts through endothelial cilia to control calcium increase (Figure 3I). In all cases, loss of *pkd2* and endothelial cilia led to impaired calcium influx (Figures 3K, S4A–S4D, S4L, and S4T) but had no effect on the average blood flow velocity (Figures 3J, S4K, S4Q, and S4U) or cilia deflection in the case of *pkd2* morphants (Figure 3H). These results suggest that endothelial cilia-mediated mechanodetection depends on PKD2.

Flow function is highly diverse during angiogenesis and can induce vessel remodeling (Nicoli et al., 2010) or stabilization according to the vessel type (Potente et al., 2011). To test the possible influence of flow and endothelial cilia on the development of embryonic blood vessels, we studied the effects of the absence of blood flow at the primitive heart stage by knocking down *tnnt2a*. We then analyzed the formation of the caudal plexus, which is highly remodeled to form a functional CV during the time period in which endothelial cilia are visible. We observed that the absence of flow dramatically impaired remodeling of the CV. This morphological defect was associated with a decreased protrusive activity and reduced numbers of venous sprouts, vascular loops, and total ECs (Figures 4A–4C; Movies S18 and S19). Furthermore, we found that the absence of flow also led to a significant reduction in overall EC numbers in both the CA and CV (Figures 4C and S4C). Absence of flow did not affect intersomitic vessel (ISV) formation, confirming the fact that flow is not absolutely required for tip cell specification and migration (Isogai et al., 2003). Importantly, low blood viscosity in the *gata1* morphants led to intermediate phenotypes in terms of protrusive activity (Figure 4A), number of vascular loops (Figure 4B; Movie S19), and EC numbers in the CV (Figure 4C). This correlates with the intermediate values observed for calcium levels in these morphants (Figures 3K and S4A) and further suggests that there is a tight correlation between cilia deflection levels and the extent of vascular remodeling. Furthermore, these results confirm that the observed phenotypes are not due to perturbations in the circulating plasma factors involved in vascular development; plasma flow can still carry important diffusible molecules such as S1P1 and BMP10 (Gaengel et al., 2012; Jung et al., 2012; Laux et al., 2013; Ben Shoham et al., 2012). Similarly, loss of *pkd2* and *ift88* through regular and conditional knockdown all led to impaired morphogenesis of the CV (Figures 4A–4C, S4F, S4G, S4I, S4N, and S4S). Indeed, the defects were associated with a decreased number and activity of venous sprouts (Figure 4A), vascular loops (Figures 4B, S4F, S4I, S4N, S4O, S4S, S4T; Movie S19), and EC numbers (Figure 4C), but without altering the blood flow (Figures 3J, S4K, S4Q, and S4U) or ISV development.

Cell PRESS
Open ACCESS

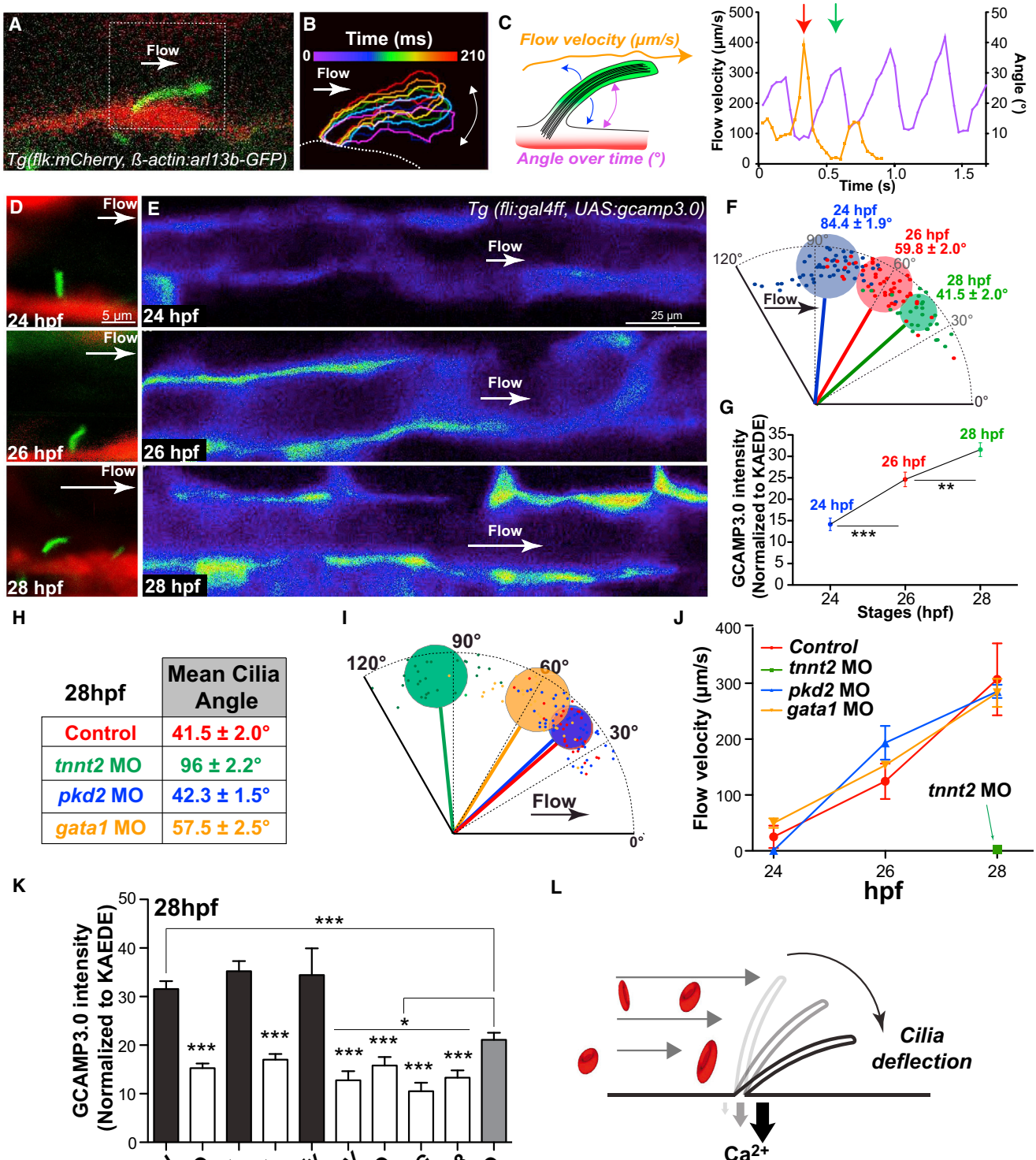

(legend on next page)

DISCUSSION

Through the use of primary cilia, ECs can sense extraordinarily low flow forces and discriminate between the very subtle variations in flow regimes generated along the developing vascular network. The relative simplicity of the zebrafish vascular network provides an ideal system in which to elucidate mechanotransduction mechanisms that could also be of significance in more complex organisms, such as humans. Although published work in mammalian systems has not identified a specific requirement for PKD2 signaling in venous angiogenesis (Garcia-Gonzalez et al., 2010), mammalian vascular systems are more complex, and the requirement for cilia during early development makes specific interrogation of later time points difficult (Oh and Katsanis, 2012). Given that we demonstrate the involvement of cilia in the sensing of low flow forces, it would be particularly interesting to study developmental programs that rely on such flow profiles, such as early cardiogenesis, lymphatic-valve formation, hematopoiesis, and tumor angiogenesis. In addition, vascular defects, such as atherosclerosis (Rydholm et al., 2010), have been linked to cilia and the detection of disturbed flow in humans, implying a pathological relevance to cilia-mediated flow sensing. Furthermore, specific loss of function of PKD2 in ECs has been implicated in angiogenesis defects in the placenta, which is an area of low flow forces (Garcia-Gonzalez et al., 2010). Thus, determining the precise role of cilia and PKD2 during angiogenesis could advance our understanding of pathological angiogenic processes.

EXPERIMENTAL PROCEDURES

Zebrafish Husbandry, Embryo Treatments, and MOs

The zebrafish lines used in this study were *Tg(cmlc2:egfp)* (Huang et al., 2003), *Tg(fli:gal4FF^{ubs}; UAS:kaede)* (Herwig et al., 2011), *Tg(flk1:mCherry)* (Bertrand et al., 2010), *Tg(β-actin:arl13b-egfp)* (Borovina et al., 2010), *Tg(UAS:gcamp3.0; Gal4s1020t)* (Warp et al., 2012), *Tg(fli1a:neGFP)^{y7}* (Roman et al., 2002), and *cup^{tc321}* (Schottenfeld et al., 2007), and were described previously. Morpholinos (MOs) were injected at the one-cell stage and animals were incubated at 28.5°C for 5 hr before treatment with 1-phenyl-2-thiourea (PTU; Sigma Aldrich) to prevent pigment formation. The MOs are further described in Supplemental Experimental Procedures. All zebrafish strains were maintained at the IGBMC under standard husbandry conditions. Animal experiments were approved by the Animal Experimentation Committee of the Institutional Review Board of the IGBMC.

In Vivo Imaging and Correlative Light and Electron Microscopy

Zebrafish embryos were staged, anesthetized with 0.02% tricaine solution (except for Figure 1), mounted in drops of 0.8% low-melting-point agarose (Sigma Aldrich), and imaged with various imaging modalities as described in Supplemental Experimental Procedures.

Heart Imaging and Image Processing

Heart myocardium (*Tg(cmlc2:egfp)*), endocardium, and blood cells (*Tg(fli:gal4FF; UAS:kaede)*) were imaged at 77 frames per second (fps). 4D imaging was performed using consecutive xy(c)tz time-lapse acquisitions. Time series were acquired at a random time in the cardiac cycle and 200–250 frames were acquired. Both channels were acquired simultaneously. Upon completion of a 2D time series at one z section, the optical plane was moved 5 μm and the acquisition was repeated. 4D data sets contained 20–35 z sections and ranged from 100 to 200 μm in total depth. Time series of 2D sections were temporally analyzed using custom-made MATLAB software (Liebling et al., 2005). Realigned 4D data sets were displayed and analyzed using Imaris software (Bitplane AG). Linear deformation of the outflow tract region was performed upon kymograph analysis. The kymograph line was drawn from the center of the cardiac tube perpendicular to the cardiac tube axis (see scheme in Figure S1C). Myocardium and endocardium deformation was quantified by measuring the variation (Δl/l) of length from the outer surface of the cell layer to the center of the cardiac tube.

Blood Cell Imaging and Velocity Measurements

Blood flow was imaged at 77 fps (Figure 1), 29 fps (Figures 3A–3C), 10 fps (Figure 3J), and 250 fps (Figure S4). Blood cells were tracked manually using Fiji or ImageJ. Mean flow velocity values were obtained by averaging instantaneous velocities over a single track. The pulsatility index (PI) was obtained using the following formula ($PI = (Velocity^{Max} - Velocity^{Min})/Velocity^{Mean}$). 3D data sets were analyzed, color-coded, and displayed using Imaris software (Bitplane AG). Maximum projections of ultrafast acquisitions (250 fps; Figure S4G) were used to map flow-carrying vessels and reveal vessel architecture.

Cilia Deflection and Image Processing

Cilia located in the central region of the dorsal aorta were imaged at 29 fps (*Tg(β-actin:Arl13b-GFP)*). Cilia and endothelium (*Tg(β-actin:Arl13b-GFP; flk:mCherry)*) were acquired simultaneously. The GFP signal was used to

Figure 3. Blood Flow Onset Is Mechanically Detected by Primary Cilia and Transduced via a *pkd2*-Dependent Calcium Increase

(A) High-speed confocal imaging at 29 fps and digital tracking in a *Tg (flk1:mCherry; β-actin:Arl13b-egfp)* embryo at 28 hpf. Note the cilium deflection and flow direction (white arrow). See also Movies S13 and S14.

(B) Digital tracking permits the segmentation of cilium outlines. Consecutive outlines were color-coded over time during one deflection phase (210 ms).

(C) Cilia deflection angle and flow velocity (see scheme) were quantified overtime and plotted. Note the correlation between maximum and minimum flow velocity and maximum and minimum flow deflection, respectively (red and green arrows).

(D) Cilia deflection in the DA of 24, 26, and 28 hpf embryos.

(F) Quantification of (D).

(E and G) Calcium content in the developing DA was evaluated and quantified using the endothelial-specific expression of GCAMP3.0 in *Tg(fli:gal4FF; UAS:gcamp3.0)* embryos. GCAMP3.0 intensity was normalized to the average KAEDE intensity observed in distinct embryos.

(H and I) Table and graphical display showing the average cilia deflection observed in 28 hpf control and indicated morphant embryos. See also Movie S15, which presents high-speed confocal imaging at 29 fps and digital tracking in a *Tg(β-actin:Arl13b-egfp)* embryo at 28 hpf injected with the *tnnt2a* MO. Note the absence of cilium deflection over a 210 ms period and random particle movement (blue track). The cilium is not deflected and remains perpendicular to the vessel wall.

(J) Blood flow velocity was quantified using transmission of light in embryos carrying the *Tg(fli:gal4FF; UAS:gcamp3.0)* transgene quantified in (K). Note the absence of flow in *tnnt2a* morphants. See an example in Movie S16.

(K) Calcium content in the developing DA was evaluated in different conditions and quantified using the endothelial-specific expression of GCAMP3.0 in *Tg(fli:gal4FF; UAS:gcamp3.0)* embryos.

(L) Summary graphical representation. The diagram shows that the early developing ECs are sensitive to low flow forces. Protruding and highly sensitive primary cilia behave as flow sensors and allow a fine detection of low but increasing flow forces during blood flow onset. Flow-mediated cilia deflection allows a PKD2-dependent calcium influx in the endothelium.

Error bars depict SEM. Statistical significance was determined by unpaired Student's t test; *$p < 0.05$, **$p < 0.01$, ***$p < 0.001$. See also Figures S3 and S4.

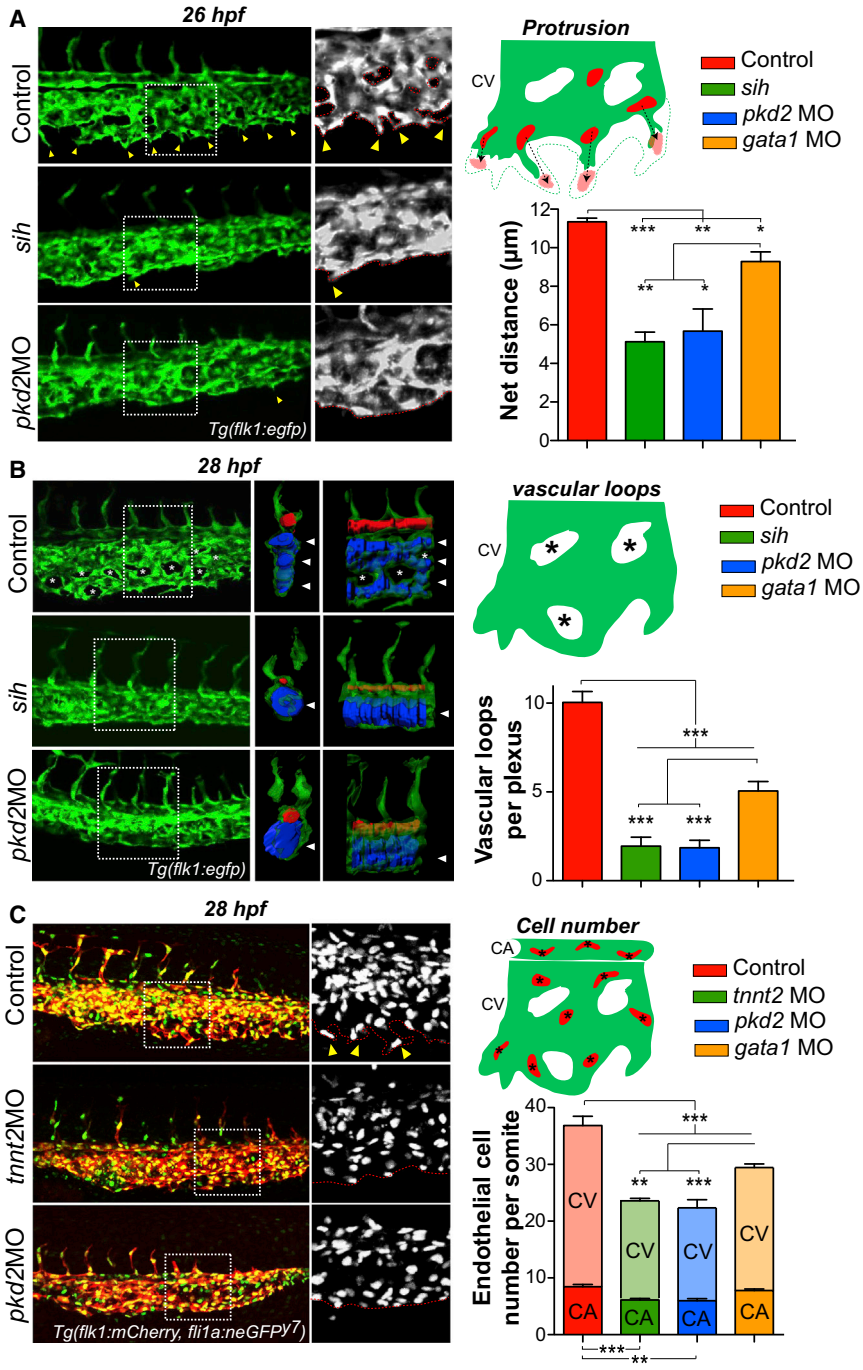

Figure 4. Early Hemodynamics Control Embryonic Angiogenesis

(A) The protrusive activity of the CV was assessed in controls, *sih* mutants, and *pkd2* morphants at 26 hpf. Yellow arrowheads point to vascular sprouts of the CV. Note the absence of such sprouts in both the *sih* mutants and *pkd2* morphants. Using the *Tg(fli1a:neGFP)*^{y7} transgenic line, we tracked the nuclei of ECs at the migration front of the CV (scheme) and followed their movement over a 1 hr period. See also Movie S18. The graph shows the average net distance covered by the tracked cells in control, mutant (*sih*), and morphant (*pkd2* and *gata1*) embryos (between three and four embryos were imaged per condition).

(B) Vascular morphogenesis of the CV was assessed in controls, *sih* mutants, and *pkd2* morphants at 28 hpf. Asterisks point to vascular loops, which are mostly absent in *sih* mutants and *pkd2* morphants (see scheme). 3D models of the vascular lumens of a delimited region (two somites) of the caudal plexus were created and are displayed as orthogonal and side views. The CA is colored in red and the CV is in blue. Images are representative of three to eight embryos imaged per condition. See also Movie S19. Arrowheads point to distinct vessels of the CV. Note that a single vessel is observed in both *sih* mutants and *pkd2* morphants. The graph shows the number of vascular loops present in the CV at 28 hpf.

(C) The overall number of ECs in the caudal plexus (CA+CV) was assessed in controls and *tnnt2a* and *pkd2* morphants at 28 hpf. Yellow arrowheads point to sprouting regions of the CV. Cell number was quantified in the caudal plexus of 28 hpf embryos and normalized per somite (between 6 and 11 embryos were imaged per condition; CA/V, caudal artery/vein).

Error bars depict SEM. Statistical significance was determined by unpaired Student's t test; *$p < 0.05$, **$p < 0.01$, ***$p < 0.001$. See also Figure S4.

retrieve cilia contours using custom MATLAB segmentation software, based on image thresholding and morphological features. The program calculated the most acute angle between the segmented cilia outline and the endothelial surface for each acquired image. Frequency analysis was performed using discrete Fourier transforms of ciliary movement.

Calcium Imaging

For endothelial-specific expression of Gcamp3.0, Tg(fli:gal4FF; UAS:kaede) embryos were crossed with Tg(UAS:GCaMP3; Gal4s1020t), and GCcamp3.0 was imaged as described in Supplemental Experimental Procedures.

Photo-MO Knockdown of *pkd2* and *ift88*

Photo-cleavable MOs were purchased from Genetools. The sense photo-MO (pMO-*pkd2*: 3′-CTT GCGCpGACCTCGAGTA-5′; pMO-*ift88: 3′-ATG GAGAATGTGpATCTTGTCC-5′*) was mixed with a translation-blocking anti-sense MO (MO3-*pkd2*MO: 5′-AGGACGAACGCGACTGGAGCTCA TC-3′; MO1-*ift88: 5′- CTGGGACAAGATGCACAT TCTCCAT-3′*) at a 1.1:1 molar ratio (see Figure S4 for the photo-MO strategy) and injected at the one- to two-cell stage into either *Tg(flk1:egfp)* or *Tg(β-actin:arl13b-egfp)* embryos. Photo-cleavage was performed at 21 hpf (pMO-*ift88*) or 22 hpf (pMO-*pkd2*). A detailed protocol is provided in Supplemental Experimental Procedures.

Immunolabeling

Whole-mount immunocytochemistry was performed as previously described (Obara et al., 2006). More detailed information is provided in Supplemental Experimental Procedures.

Bending Stiffness Estimation

The endothelial cilia biomechanics was modeled as previously described (Young et al., 2012). The cilium was modeled as a beam and the hydrodynamic

load was computed by the local slender-body theory. The bending stiffness was defined as $E_b = M/k$, with k being the curvature and M the moment at a cross-section of the cilium. Several simulations were repeated using flow conditions observed in 26 hpf embryos (Figure 1) by varying the value of E_b until the angle between the cilia tip and the cell base matched the angle measured in vivo (roughly 60°; Figure 3). A range of values for E_b were obtained to cover the variability of the angle between the cilia base and the cell surface (measured and imposed as a boundary condition).

Shear Stress Measurements

Shear stress was calculated as previously described (Vermot et al., 2009).

Statistics

Error bars depict SEM. Statistical significance was determined with GraphPad Prism by unpaired Student's t test (*$p < 0.05$, **$p < 0.01$, ***$p < 0.001$).

Movie Crafting and 3D Modeling

Movie crafting was performed using ImageJ. 3D modeling was performed using Imaris (Bitplane AG).

SUPPLEMENTAL INFORMATION

Supplemental Information includes Supplemental Experimental Procedures, four figures, and 19 movies and can be found with this article online at http://dx.doi.org/10.1016/j.celrep.2014.01.032.

ACKNOWLEDGMENTS

We thank P. Schultz and C. Crucifix for sharing equipment and help with electron tomography. We thank D. Acehan for help with electron tomography. We thank I. Drummond for providing the PKD2 antibody and the pkd2 mutant line (*cup*^{tc321}). We thank M. Affolter, H. Belting, J. Essner, P. Herbomel, and B. Ciruna for providing fish stocks. We thank the staff of the IGBMC imaging center, in particular C. Spiegelhalter, N. Messaddeq, P. Kessler, M. Koch, and D. Hentsch. We thank S. Geschier and S. Gredler of the IGBMC fish facility. We thank D. Wu, W. Supatto, D. Riveline, I. Kulic, and J.B. Freund for critical inputs during the study. This work was supported by HFSP, INSERM, La Ligue Contre le Cancer, FRM, and the Seventh Framework Program (MC-IRG256549 to J.V. and MC-IEF254951 to J.G.G.).

Received: November 15, 2013
Revised: December 20, 2013
Accepted: January 23, 2014
Published: February 20, 2014

REFERENCES

AbouAlaiwi, W.A., Takahashi, M., Mell, B.R., Jones, T.J., Ratnam, S., Kolb, R.J., and Nauli, S.M. (2009). Ciliary polycystin-2 is a mechanosensitive calcium channel involved in nitric oxide signaling cascades. Circ. Res. *104*, 860–869.

Ben Shoham, A., Malkinson, G., Krief, S., Shwartz, Y., Ely, Y., Ferrara, N., Yaniv, K., and Zelzer, E. (2012). S1P1 inhibits sprouting angiogenesis during vascular development. Development *139*, 3859–3869.

Bertrand, J.Y., Chi, N.C., Santoso, B., Teng, S., Stainier, D.Y., and Traver, D. (2010). Haematopoietic stem cells derive directly from aortic endothelium during development. Nature *464*, 108–111.

Borovina, A., Superina, S., Voskas, D., and Ciruna, B. (2010). Vangl2 directs the posterior tilting and asymmetric localization of motile primary cilia. Nat. Cell Biol. *12*, 407–412.

Buschmann, I., Pries, A., Styp-Rekowska, B., Hillmeister, P., Loufrani, L., Henrion, D., Shi, Y., Duelsner, A., Hoefer, I., Gatzke, N., et al. (2010). Pulsatile shear and Gja5 modulate arterial identity and remodeling events during flow-driven arteriogenesis. Development *137*, 2187–2196.

Bussmann, J., Wolfe, S.A., and Siekmann, A.F. (2011). Arterial-venous network formation during brain vascularization involves hemodynamic regulation of chemokine signaling. Development *138*, 1717–1726.

Chen, Q., Jiang, L., Li, C., Hu, D., Bu, J.W., Cai, D., and Du, J.L. (2012). Haemodynamics-driven developmental pruning of brain vasculature in zebrafish. PLoS Biol. *10*, e1001374.

Corti, P., Young, S., Chen, C.Y., Patrick, M.J., Rochon, E.R., Pekkan, K., and Roman, B.L. (2011). Interaction between alk1 and blood flow in the development of arteriovenous malformations. Development *138*, 1573–1582.

Forouhar, A.S., Liebling, M., Hickerson, A., Nasiraei-Moghaddam, A., Tsai, H.J., Hove, J.R., Fraser, S.E., Dickinson, M.E., and Gharib, M. (2006). The embryonic vertebrate heart tube is a dynamic suction pump. Science *312*, 751–753.

Freund, J.B., Goetz, J.G., Hill, K.L., and Vermot, J. (2012). Fluid flows and forces in development: functions, features and biophysical principles. Development *139*, 1229–1245.

Gaengel, K., Niaudet, C., Hagikura, K., Laviña, B., Muhl, L., Hofmann, J.J., Ebarasi, L., Nyström, S., Rymo, S., Chen, L.L., et al. (2012). The sphingosine-1-phosphate receptor S1PR1 restricts sprouting angiogenesis by regulating the interplay between VE-cadherin and VEGFR2. Dev. Cell *23*, 587–599.

Garcia-Gonzalez, M.A., Outeda, P., Zhou, Q., Zhou, F., Menezes, L.F., Qian, F., Huso, D.L., Germino, G.G., Piontek, K.B., and Watnick, T. (2010). Pkd1 and Pkd2 are required for normal placental development. PLoS ONE *5*, 5.

Herbert, S.P., and Stainier, D.Y. (2011). Molecular control of endothelial cell behaviour during blood vessel morphogenesis. Nat. Rev. Mol. Cell Biol. *12*, 551–564.

Herwig, L., Blum, Y., Krudewig, A., Ellertsdottir, E., Lenard, A., Belting, H.G., and Affolter, M. (2011). Distinct cellular mechanisms of blood vessel fusion in the zebrafish embryo. Curr. Biol. *21*, 1942–1948.

Hierck, B.P., Van der Heiden, K., Alkemade, F.E., Van de Pas, S., Van Thienen, J.V., Groenendijk, B.C., Bax, W.H., Van der Laarse, A., Deruiter, M.C., Horrevoets, A.J., and Poelmann, R.E. (2008). Primary cilia sensitize endothelial cells for fluid shear stress. Dev. Dyn. *237*, 725–735.

Hoey, D.A., Downs, M.E., and Jacobs, C.R. (2012). The mechanics of the primary cilium: an intricate structure with complex function. J. Biomech. *45*, 17–26.

Huang, C.J., Tu, C.T., Hsiao, C.D., Hsieh, F.J., and Tsai, H.J. (2003). Germ-line transmission of a myocardium-specific GFP transgene reveals critical regulatory elements in the cardiac myosin light chain 2 promoter of zebrafish. Dev. Dyn. *228*, 30–40.

Iomini, C., Tejada, K., Mo, W., Vaananen, H., and Piperno, G. (2004). Primary cilia of human endothelial cells disassemble under laminar shear stress. J. Cell Biol. *164*, 811–817.

Isogai, S., Horiguchi, M., and Weinstein, B.M. (2001). The vascular anatomy of the developing zebrafish: an atlas of embryonic and early larval development. Dev. Biol. *230*, 278–301.

Isogai, S., Lawson, N.D., Torrealday, S., Horiguchi, M., and Weinstein, B.M. (2003). Angiogenic network formation in the developing vertebrate trunk. Development *130*, 5281–5290.

Jung, B., Obinata, H., Galvani, S., Mendelson, K., Ding, B.S., Skoura, A., Kinzel, B., Brinkmann, V., Rafii, S., Evans, T., and Hla, T. (2012). Flow-regulated endothelial S1P receptor-1 signaling sustains vascular development. Dev. Cell *23*, 600–610.

Kramer-Zucker, A.G., Olale, F., Haycraft, C.J., Yoder, B.K., Schier, A.F., and Drummond, I.A. (2005). Cilia-driven fluid flow in the zebrafish pronephros, brain and Kupffer's vesicle is required for normal organogenesis. Development *132*, 1907–1921.

Laux, D.W., Young, S., Donovan, J.P., Mansfield, C.J., Upton, P.D., and Roman, B.L. (2013). Circulating Bmp10 acts through endothelial Alk1 to mediate flow-dependent arterial quiescence. Development *140*, 3403–3412.

le Noble, F., Moyon, D., Pardanaud, L., Yuan, L., Djonov, V., Matthijsen, R., Bréant, C., Fleury, V., and Eichmann, A. (2004). Flow regulates arterial-venous differentiation in the chick embryo yolk sac. Development *131*, 361–375.

Liebling, M., Forouhar, A.S., Gharib, M., Fraser, S.E., and Dickinson, M.E. (2005). Four-dimensional cardiac imaging in living embryos via postacquisition synchronization of nongated slice sequences. J. Biomed. Opt. *10*, 054001.

McGrath, J., Somlo, S., Makova, S., Tian, X., and Brueckner, M. (2003). Two populations of node monocilia initiate left-right asymmetry in the mouse. Cell *114*, 61–73.

Meder, B., Laufer, C., Hassel, D., Just, S., Marquart, S., Vogel, B., Hess, A., Fishman, M.C., Katus, H.A., and Rottbauer, W. (2009). A single serine in the carboxyl terminus of cardiac essential myosin light chain-1 controls cardiomyocyte contractility in vivo. Circ. Res. *104*, 650–659.

Nauli, S.M., Alenghat, F.J., Luo, Y., Williams, E., Vassilev, P., Li, X., Elia, A.E., Lu, W., Brown, E.M., Quinn, S.J., et al. (2003). Polycystins 1 and 2 mediate mechanosensation in the primary cilium of kidney cells. Nat. Genet. *33*, 129–137.

Nauli, S.M., Kawanabe, Y., Kaminski, J.J., Pearce, W.J., Ingber, D.E., and Zhou, J. (2008). Endothelial cilia are fluid shear sensors that regulate calcium signaling and nitric oxide production through polycystin-1. Circulation *117*, 1161–1171.

Nicoli, S., Standley, C., Walker, P., Hurlstone, A., Fogarty, K.E., and Lawson, N.D. (2010). MicroRNA-mediated integration of haemodynamics and Vegf signalling during angiogenesis. Nature *464*, 1196–1200.

Obara, T., Mangos, S., Liu, Y., Zhao, J., Wiessner, S., Kramer-Zucker, A.G., Olale, F., Schier, A.F., and Drummond, I.A. (2006). Polycystin-2 immunolocalization and function in zebrafish. J. Am. Soc. Nephrol. *17*, 2706–2718.

Oh, E.C., and Katsanis, N. (2012). Cilia in vertebrate development and disease. Development *139*, 443–448.

Potente, M., Gerhardt, H., and Carmeliet, P. (2011). Basic and therapeutic aspects of angiogenesis. Cell *146*, 873–887.

Roman, B.L., Pham, V.N., Lawson, N.D., Kulik, M., Childs, S., Lekven, A.C., Garrity, D.M., Moon, R.T., Fishman, M.C., Lechleider, R.J., and Weinstein, B.M. (2002). Disruption of acvrl1 increases endothelial cell number in zebrafish cranial vessels. Development *129*, 3009–3019.

Rydholm, S., Zwartz, G., Kowalewski, J.M., Kamali-Zare, P., Frisk, T., and Brismar, H. (2010). Mechanical properties of primary cilia regulate the response to fluid flow. Am. J. Physiol. Renal Physiol. *298*, F1096–F1102.

Schottenfeld, J., Sullivan-Brown, J., and Burdine, R.D. (2007). Zebrafish curly up encodes a Pkd2 ortholog that restricts left-side-specific expression of southpaw. Development *134*, 1605–1615.

Sehnert, A.J., Huq, A., Weinstein, B.M., Walker, C., Fishman, M., and Stainier, D.Y. (2002). Cardiac troponin T is essential in sarcomere assembly and cardiac contractility. Nat. Genet. *31*, 106–110.

Supatto, W., and Vermot, J. (2011). From cilia hydrodynamics to zebrafish embryonic development. Curr. Top. Dev. Biol. *95*, 33–66.

Tsujikawa, M., and Malicki, J. (2004). Intraflagellar transport genes are essential for differentiation and survival of vertebrate sensory neurons. Neuron *42*, 703–716.

Vermot, J., Forouhar, A.S., Liebling, M., Wu, D., Plummer, D., Gharib, M., and Fraser, S.E. (2009). Reversing blood flows act through klf2a to ensure normal valvulogenesis in the developing heart. PLoS Biol. *7*, e1000246.

Warp, E., Agarwal, G., Wyart, C., Friedmann, D., Oldfield, C.S., Conner, A., Del Bene, F., Arrenberg, A.B., Baier, H., and Isacoff, E.Y. (2012). Emergence of patterned activity in the developing zebrafish spinal cord. Current biology: CB *22*, 93–102.

Yoshiba, S., Shiratori, H., Kuo, I.Y., Kawasumi, A., Shinohara, K., Nonaka, S., Asai, Y., Sasaki, G., Belo, J.A., Sasaki, H., et al. (2012). Cilia at the node of mouse embryos sense fluid flow for left-right determination via Pkd2. Science *338*, 226–231.

Young, Y.N., Downs, M., and Jacobs, C.R. (2012). Dynamics of the primary cilium in shear flow. Biophys. J. *103*, 629–639.

Appendix 2: Extended Protocols

Tail-Clipping adult zebrafish

In the laboratory:

- Prepare the SDS Lysis buffer and fill 1.5mL tubes with a final volume of 200µL.
- **SDS lysis buffer solution** (for 100mL):

  1mL of Tris-HCl pH8.0 (stock = 10mM)

  4mL of NaCl (stock = 200mM)

  2mL of EDTA (stock = 10mM)

  2.5mL of SDS (stock = 0.5%)

  1mL of Proteinase K (stock = 100µg/ml)

  89,5mL MiliQ water

In the fish room:

- Prepare the water tanks in the fish facility, putting a divider in the middle and labeling each side with a number. The same numbers should be written in the 1.5mL tubes.
- Anesthetize the fish to genotype: put one fish at the time in a water tank containing 200mL of fish water supplemented with 200µL of Tricaine (stock at 80µg/ml).
- Put the fish in your hand and with a surgery scissor cut ⅓ of its caudal fin. With the help of a surgical tweezer, put the piece of fin in a 1.5mL tube containing Lysis buffer. Put the fish back in the isolated water tank prepared previously. Wear gloves during all the tail-clipping and clean surgery material in 100%-Ethanol before repeating the procedure with another fish.

In the laboratory:

- Digest fins overnight at 55C in a Thermomixer (Eppendorf) or water-bath.

Genotyping: DNA extraction of zebrafish caudal fins

- Add 80µL of 5M NaCl and mix vigorously.
- Centrifuge at 13000rpm for 10 minutes.
- Transfer the intermediate phase (approximately 200µL) to a new tube.
- Add 200µL of isopropanol.
- Mix vigorously.
- Centrifuge at 13000rpm for 1 minute.
- Remove supernatant.
- Add 500µL of 70%-Ethanol.
- Centrifuge at 13000rpm for 10 minutes.
- Remove supernatant (maximum possible) and let the pellet dry in the air.
- Re-suspend in 50µL of autoclaved water.

Genotyping: DNA extraction of single embryos

- Put single embryos in numbered 1.5mL tubes or in a 96-well plate.
- Add 100µL (53hpf embryo) or 50µL (tail or 16-19SS embryos) of 50mM NaOH.
- Digest for 10 min at 95ºC in a Thermomixer (Eppendorf) or water-bath.
- Cool down at 4ºC for 5 min.
- Add 1/10 volume of 1M Tris-HCl, ph8.0.
- Carry on with PCR or store at -20ºC.

PCR settings

Reaction for PCR (per sample):

10µL of Phusion High-Fidelity PCR Master Mix (Ref. F-531L from Thermo Scientific)

1µL of primer forward

1µL of primer reverse

7µL of MiliQ water

1µL DNA

PCR settings:

	98°C	3min		
	98°C	10sec		
x31	Tm	20sec		
	72°C	ExtT	goto2	loops 30
	72°C	8min		
	4°C	∞		

Electrophoresis

- Prepare a 2% agarose gel (1 drop of ethidium bromide each 100mL)
- Run at 120 volts and 400mA for 45 to 60 min.
- Check the gel under a UV lamp

Sequencing

The sequencing of the DNA samples was performed by a company named GATC (https://www.gatc-biotech.com/fr), following the principles below:

- Add 10µL of miliQ water to each DNA sample after PCR (20µL).
- Send a tube with the sequencing primers at a 1:10 concentration (3µL of 100µM stock primer + 27µL MiliQ water).

Fixation of embryos

- Put selected embryos in 1.5mL tubes properly labeled.
- Change Danieu medium to 4% paraformaldehyde PBS (PFA-PBS).
- Fix overnight at 4°C.
- Wash 2x5min in PBS at room temperature (RT).
- Transfer embryos to a Petri dish and dechorionate the embryos using forceps.
- Transfer embryos again to the 1.5mL tubes and add 100%-Methanol (MeOH).
- Replace with fresh 100%-MeOH after 5 min rocking.
- Store the embryos in -20°C.

Whole mount *in situ* hybridization

WISH Day 1

Rehydration

- Bring the embryos back to RT.
- Rehydrate embryos through 75%MeOH-25%PBS, 50%MeOH-50%PBS and 25%MeOH-75%PBS for 5 min each at RT.
- Wash 4x 5min in PBST (1X PBS + 0.1% Tween 20).

Permeabilisation

- Incubate in 10µg/ml Proteinase K in PBST for: 30 min at 53hpf and 3 sec for 16-19SS.
- Refix in 4% PFA-PBS for 20 min.
- Wash 5x 5min in PBST.

Prehybridization

- Remove as much PBST as possible.
- Add 500µl hybridization buffer and place the tubes in a polystyrene rack at 70°C (in a water bath) for 2 to 5 hours.

Hybridization

- Prepare probe in hybridization buffer (2µl probe / 200µl hybridization buffer per sample) and heat at 70ºC.
- Remove hybridization buffer from samples and add probe:hyb mix (200µl).
- Incubate at 70ºC overnight.

Before leaving, prepare wash solutions for Day 2 and leave at 70°C overnight so can begin immediately in the morning.

WISH Day 2

Washing

- Remove probe:hyb mix and keep for some
- Wash once in MH wash buffer and leave 2min at 70ºC (quick wash).
- Wash in 75%MH-25% 2X SSC for 10min at 70ºC.
- Wash in 50%MH-50% 2X SSC for 10min at 70ºC.
- Wash in 25%MH-75% 2X SSC for 10min at 70ºC.
- Wash in 100% 2X SSC for 10min at 70ºC.
- Wash 2x in 0.2X SSC for 30min at 70ºC;
- Wash in 75% 0.2X SSC-25% MABT for 10min at RT

- Wash in 50% 0.2X SSC-50% MABT for 10min at RT.
- Wash in 25% 0.2X SSC-75% MABT for 10min at RT.
- Wash in 100% MABT for 10min at RT.

Incubation with anti-DIG

- Dilute the 10%-Blocking Reagent (BR) stock (Roche) to 2% in MABT.
- Incubate embryos with 2%-BR for 3h at RT, with gentle rocking.
- Dilute the anti-DIG to 1:4000 in 2%-BR and incubate at 4ºC overnight, with gentle rocking.

WISH Day 3

Washes

3) Wash 6x 15 min in PBS at RT with gentle rocking.
4) Wash 3x 5 min in Revelation Solution.

Revelation

1) Centrifuge BM Purple for 2 min at maximum speed (enough to put 2mL per well)
2) Transfer embryos to a 6-well plate carefully ensuring they don't dry out.
3) Add 2mL of BM-Purple and leave in the dark at RT for signal to develop.
4) To stop the reaction, wash 4x in PBST and fix in 4% PFA-PBS for 20min.
5) Remove the 4%PFA-PBS and wash 4x in PBS.
6) Put embryos in 20% glycerol-PBS and store at 4ºC.

WISH Solutions

Hybridisation buffer (stored at -20ºC):

25mL of Formamide (stock = 50% FA)

12.5mL of 20X SSC (stock = 5X)

0.5mL of Heparin 5mg/ml (stock = 500mg/ml)

0.5mL of tRNA 50mg/ml (stock = 500mg/ml)

0.25mL of 20% Tween 20 (stock = 0.1%)

0.46mL 1M Citric Acid pH6.0

MiliQ water to 50mL

MH wash buffer (for 500mL):

250mL of Formamide (stock = 50% FA)

125mL of 20X SSC (stock = 5X)

2.5mL of 20% Tween 20 (stock = 0.1%)

4.6mL 1M Citric Acid pH6.0

MiliQ water to 500mL

Stock solutions: 2XSSC, 0.2X SSC, PBST

Revelation solution (for 100mL):

10mL of 100mM Tris-HCl pH9.5 (stock = 1M)

5mL of 50mM $MgCl_2$ (stock = 1M)

2mL of 100mM NaCl (stock = 5M)

0.5mL of 0.1% Tween 20 (stock = 20%)

MiliQ water to 100mL

BM Purple AP Substrate precipitating (Ref. 11 442 074 001 from Roche)

Appendix 3: Extended summary in French

INTRODUCTION

Les cils sont impliqués dans de nombreux processus, en particulier, la mécano-détection qui confère aux cellules la capacité de ressentir physiquement les variations de leur environnement. Les cellules de l'embryon en développement font faces à de multiples forces extracellulaires, celles-ci, résultant de flux microscopiques au sein de l'organisateur de l'axe gauche-droite. Les flux créés par les cils organisent l'axe embryonnaire gauche-droite chez la plupart des vertébrés. Les modèles les plus répandus concernant la spécification gauche-droite chez la majorité des vertébrés (Blum et al., 2009; Gros et al., 2009) impliquent un groupe de cellules (l'organisateur gauche-droite, OGD) du mésoderme pré-somitique (mésoderme para-axial) qui coordonnent l'établissement de l'asymétrie sous contrôle d'un flux lent (flux nodal) (Nonaka et al., 1998) et d'une amplification intercellulaire du signal d'asymétrie au sein et autour des cellules de l'OGD (Nakamura et al., 2006). Ce flux lent est généré par la rotation de multiples cils motiles localisés à la surface des cellules de l'OGD. Ce flux mène à une réponse collective des cellules qui a lieu spécifiquement du côté droit de l'OGD, ceci est associé à une libération asymétrique de calcium dans les cellules (McGrath et al., 2003; Yuan et al., 2015).

Chez le poisson zèbre, l'organisateur gauche-droite est appelé vésicule de Kupffer (VK) et n'est visible que transitoirement durant la somitogenèse (Essner et al., 2005). Les cils génèrent un flux unidirectionnel en décrivant un mouvement asymétrique dans l'espace (Satir and Christensen, 2007). Le mouvement circulaire du cil est composé de deux phases: la première est un mouvement de grande amplitude pendant laquelle le cil se trouve loin de la surface de la cellule de manière à déplacer le plus de liquide possible; la seconde phase consiste en un mouvement de faible amplitude pour retourner à la position initiale en frôlant la surface de la cellule, de cette manière la force du flux inverse est réduite (Marshall and Kintner, 2008). Les cils de l'OGD sont relativement courts et leurs battements décrivent un cône incliné (Hirokawa et al., 2006; Nonaka et al., 2005; Okada et al., 2005). Cette inclinaison est effectivement responsable des deux phases qui composent le mouvement de rotation du cil: la phase de large amplitude et la phase de faible amplitude. De plus, l'orientation spatiale des cils motiles est une caractéristique fonctionnelle clé impliquée dans la mise en place de l'asymétrie, étant donné qu'elle détermine la force et la direction du flux induit. L'orientation spatiale des cils peut être définie par les angles *Phi* et *Theta*, ce sont les déterminants majeurs de la force et de la direction du flux créé par les cils. Les mécanismes moléculaires gouvernant l'orientation des cils impliquent des éléments de la voie de signalisation de la polarité planaire cellulaire (Borovina et al., 2010; Hashimoto et al., 2010; Song et al., 2010) ainsi que le flux lui-même (Guirao et al., 2010).

BUT

La finalité de ma thèse était de connecter les bases biophysiques d'un flux directionnel aux mécanismes biologiques potentiels permettant la sensation du flux ainsi que l'identification de facteurs contrôlant le positionnement des cils. Pour apporter des réponses à cette question, nous avons défini plusieurs objectifs:

- Développer une méthode d'imagerie *in vivo* et un protocole d'analyse d'images pour d'extraire les informations concernant les caractéristiques biophysiques des cils (orientation 3D et densité) qui influencent l'établissement d'un flux directionnel.
- Analyser le comportement des cils à plusieurs niveaux en cartographiant les paramètres biophysiques des cils à travers toute la VK dans des embryons sauvages à trois stades de développement distincts. Puis, extraire les paramètres clés de l'implantation des cils amenant au flux directionnel observé dans la VK.
- Déterminer une possible corrélation entre l'orientation des cils et la mise en place de l'axe GD dans la VK du poisson zèbre.

Ces objectifs sont retrouvés dans la structure de cette thèse:

1. Le manuscrit 2 (Chapitre « méthode ») décrit le travail expérimental du cheminement d'analyse à différents niveaux que nous avons développé avec la collaboration du groupe de Dr. Supatto (Ecole Polytechnique, Palaiseau, France), appelé *3D-Cilia Map*. Pour cela, j'ai d'abord du optimiser cet outil (Objectif 1). Il faut noter que l'OGD n'est pas facile d'accès en expérimentation in vivo d'abord parce qu'il est localiser en profondeur dans l'embryon et aussi par la nécessité de systèmes de culture ex vivo complexes. Pour contourner ceci, nous nous avons étudié la VK du poisson zèbre qui nous permet d'imager in vivo l'embryon sans altérer son intégrité et son environnement naturel.

2. Le manuscrit 3 (Chapitre « résultats » I) présente notre analyse à différents niveaux des paramètres biophysiques des cils dans la VK d'embryons sauvages à trois stades de développement distincts afin extraire le comportement du mouvement des cils au cours du temps. Cette description quantitative de la morphologie de la VK et des cils dans des conditions «sauvage» nous on permis de générer des données quantitatives, in vivo, pour alimenter des modèles mathématiques permettant de simuler un profil de flux générer dans la VK. Aussi, en intégrant nos données expérimentales dans une étude physique de génération du flux, nous avons testé l'efficacité des cils à propager le signal asymétrique responsable du mécanisme de rupture de la symétrie (Objectif 2).

3. Le manuscrit 4 (Chapitre « résultats » II) décrit comment, à l'aide *3D-Cilia Map*, nous avons analysé un groupe de conditions présélectionnées (*knock-downs*, mutants et drogues) connues pour avoir un impact sur l'établissement de l'axe GD. En faisant cela, nous avons pu valider une méthodologie pour l'utilisation de *3D-Cilia Map* et nouvelles perspectives d'étude du lien pouvant exister entre l'orientation des cils et la détermination de l'axe GD. (Objectif 3)

RESULTATS PRINCIPAUX ET CONCLUSIONS

Manuscrit 2

Pour explorer les liens entre les bases biophysiques de la création du flux directionnel et les mécanismes biologique contrôlant la rupture de la symétrie gauche-droite ainsi que l'implantation des cils dans la VK du poisson zèbre, nous avons développé *3D-Cilia Map*, un système de cartographie des cils et de leur caractéristiques de haute précision en 3D. Cette méthode est basée sur l'analyse de données d'imagerie *in vivo* pour pouvoir cartographier les paramètres biophysiques des cils en 3D. Une telle approche adresse des questions relatives à l'orientation en 3D des cils motiles de la VK.

Le flux expérimental donné par *3D-Cilia Map* combine l'imagerie 3D *in vivo*, le traitement d'images et l'enregistrement de données pour quantifier, afficher et comparer les caractéristiques biophysiques de la VK et des cils. Ce système a été créé pour quantifier des paramètres tels que la taille, la forme et le volume de la VK, ainsi que la distribution spatiale, la densité de surface, la motilité et l'orientation de l'axe de rotation des cils. Les données expérimentales provenant de différents embryons sont combinées pour effectuer des analyses statistiques et comparer les conditions expérimentales. *3D-Cilia Map* est basé sur des protocoles d'imagerie *in vivo* rationalisés optimisés pour l'imagerie des cils permettant la visualisation de tous les cils endogènes dans les 50 à 80 cellules constituant la VK dans des embryons de poisson zèbre en développement, la VK est visible dans l'embryon (1- à 14- Somite stage (SS)), permettant une cartographie spatiale précise des cils dans de grands ensembles d'échantillons. L'approche utilise une lignée de poisson zèbre où les cils sont marqués par fluorescence - *actb2:Mmu.Arl13b-GFP* (Borovina et al., 2010) -, l'acquisition d'image 3D en microscopie à fluorescence deux photons, le traitement d'images et l'enregistrement de données ainsi qu'une analyse consciencieuse et précise des images obtenues. *3D-Cilia Map* résout la variabilité inhérente de la forme de la VK à travers des algorithmes après acquisition et génère une carte ciliotopique précise grâce à une reconstruction de coordonnées sphériques basée sur l'orientation de l'échantillon en 3D. Dans le pipeline d'analyse personnalisé, les caractéristiques expérimentales sont utilisées pour alimenter un modèle mathématique de dynamique des cils et de génération de flux de fluide pour obtenir des informations supplémentaires, tels que le profil du flux généré dans la VK pour un seul d'embryon, ou la force générée par les cils individuels.

Le flux de travail expérimental de *3D-Cilia Map* peut être divisé en six étapes décrites ci-dessous:

- Étape 1: imagerie 3D *in vivo* de la VK (Fig.1A-B)
- Étape 2: Estimation de l'orientation du plan du corps de l'embryon par rapport à l'emplacement de la VK (Fig.1A1-1A3).
- Étape 3: position et orientation des cils (Fig. 1B1-B6).
- Étape 4: enregistrement spatial 3D: coordonnées du plan du corps et raccord à l'ellipsoïde (Fig. 2A1-A3).
- Étape 5: orientation des angles des cils *Phi* (φ) et *Theta* (θ) en 3D: estimation et histogramme (Fig. 2B1-C2).
- Étape 6: carte 2D des caractéristiques des cils et mesure de la densité de surface des cils (Fig. 3A1-C2).

En résumé, *3D-Cilia Map* est une analyse multiscalaire quantitative puissante et rigoureuse des caractéristiques biophysiques des cils (orientation 3D, localisation spatiale et densité), qui pourrait être utilisées dans l'étude d'autres systèmes sphériques ciliés.

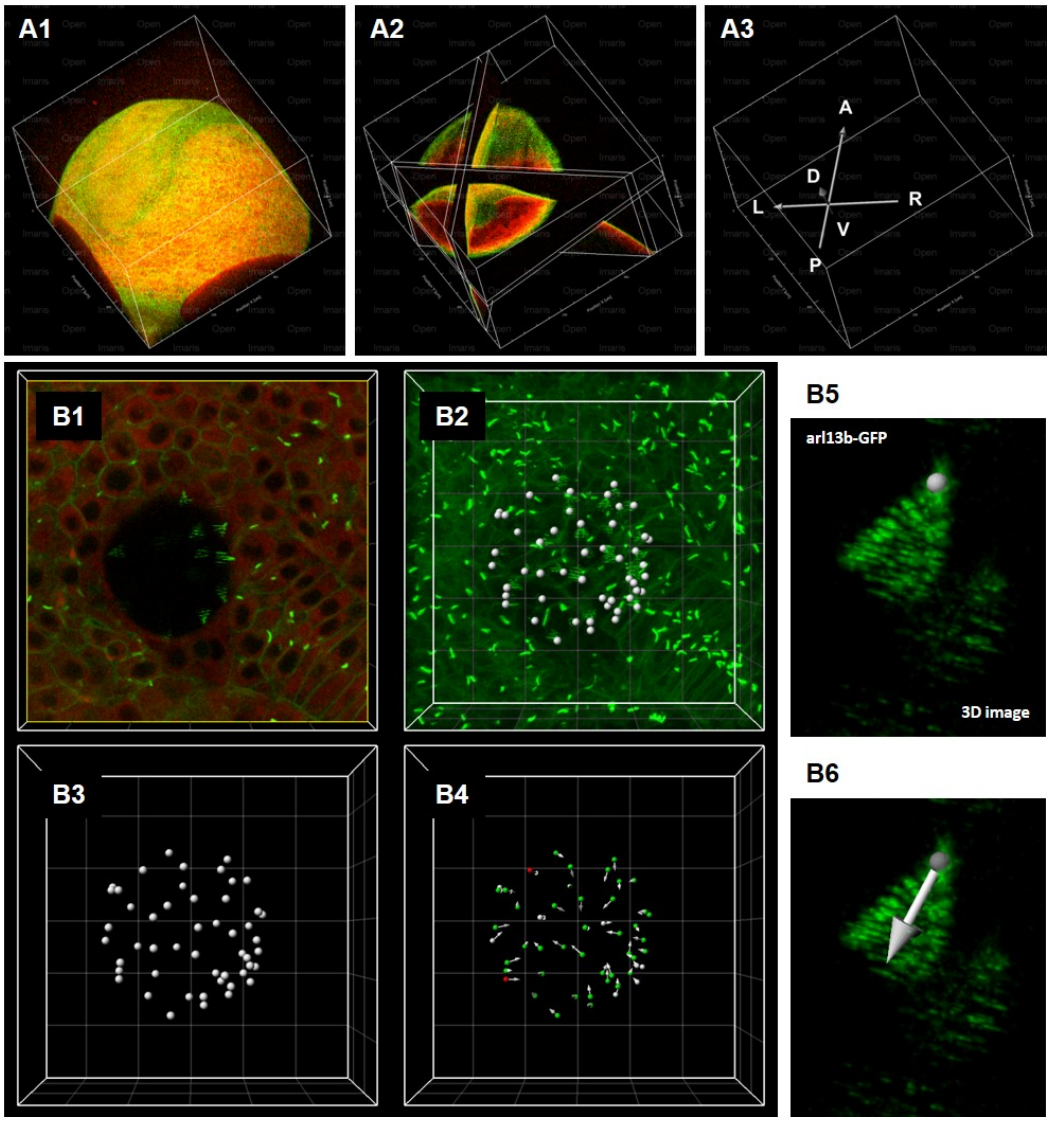

Manuscrit 2 - Fig. 1: Imagerie *in vivo* et traitement d'image pour extraire la position et l'orientation des cils: Pour obtenir une image suffisamment profonde de l'embryon du poisson zèbre et capturer la vésicule de Kupffer (VK) entière, chaque embryon a été imagé à l'aide d'un microscope SP8 2PEF direct (Leica Inc.) à une longueur d'onde de 930 nm (Chameleon Ultra Laser, Coherent Inc.) à l'aide d'un objectif d'immersion à eau à grande ouverture numérique (ON) et à faible grossissement (Leica, 25x, 0,95 ON). Nous avons utilisé les embryons transgéniques (*actb2:Mmu.Arl13b-GFP*) (Borovina et al., 2010) incubés pendant 60 minutes dans du Bodipy TR (Molecular Probe) avant l'étape d'imagerie in vivo: le signal de fluorescence a été capté à l'aide de détecteurs hybrides internes à 493-575 nm et 594-730 nm afin de distinguer les cils GFP du signal GFP de la surface des cellules de la VK. **(A1)** L'ensemble de l'embryon a été imagé à faible résolution spatiale pour estimer les axes embryonnaires: volume de 600µm × 600µm × 150µm comprenant la ligne médiane et la VK de haut en bas avec une taille de voxel de 1,15µm latéralement et 5µm axialement. L'estimation des coordonnées du plan du corps par rapport à l'emplacement de la VK a été effectuée en utilisant le dispositif illustré en **(A1)** et les trois axes orthogonaux ont été ajustés en 3D à l'aide d'Imaris (Bitplane), lequel point d'intersection est au sein de la VK **(A2)**. L'intersection de chaque axe orthogonal a été utilisé pour concevoir des vecteurs 3D **(A3)**. **(B1-2 et B5-6)** La VK a été imagé à une résolution spatiale élevée pour quantifier la distribution et l'orientation des cils en 3D: des coupes 3D de 100 x 100 x 50µm3 avec une taille de voxel de 0.2 x 0.2 x 0.8µm3 et une durée d'exposition de pixel de 2.4µs ont été acquises afin de maximiser l'artefact de balayage permettant de reconstituer correctement l'orientation des cils en 3D (Supatto and Vermot, 2011). Les bases des cils ont été segmentées manuellement à partir de la surface des cellules KV (marques grises dans B2-B3) et son orientation 3D a été estimée **(B4)**. Utilisant une fonction ImarisXT sur mesure de Matlab, l'orientation du cil a été estimée automatiquement à partir de la base segmentée **(B5-B6)**.

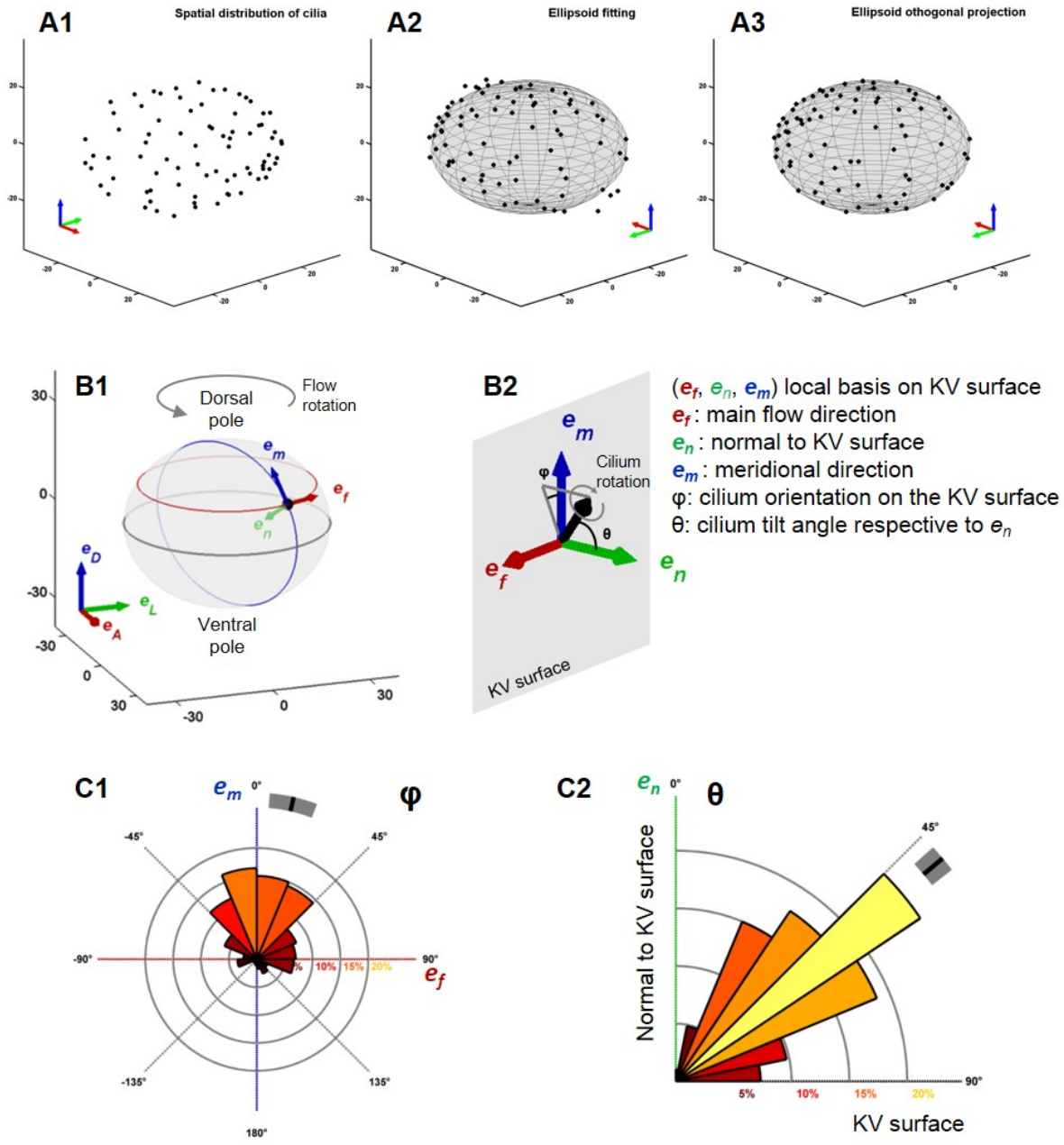

Manuscrit 2 - Fig. 2: Estimation de l'angle d'orientation des cils φ et θ: Transformation des coordonnées spatiales selon le plan du corps embryonnaire **(A1-A3)**: répartition spatiale de la position des cils dans le cadre de référence du plan du corps **(A1)**; Concordance d'un sphéroïde aplati avec la répartition des bases de cils, afin d'enregistrer les données de la VK provenant de différents embryons dans le même cadre **(A2)**; Projection orthogonale de cils à la surface du sphéroïde ajusté **(A3)**. Définition orthogonale locale des bases des cils (e_f, e_n, e_m) à chaque point de la surface du sphéroïde **(B1)** et définition des angles φ et θ **(B2)**. Combinaison de données à partir d'embryons différents et affichés dans des histogrammes "rosette" à l'aide de Matlab: rosette de 0 à 360 ° pour φ **(C1)** et rosette de 0 à 90 ° pour θ **(C2)**. Les cadres de référence dans A1-A3 sont identiques à ceux de B1: e_D, e_L et e_A.

Abréviations: e_D = direction dorsale; e_L = direction de gauche; e_A = direction antérieure.

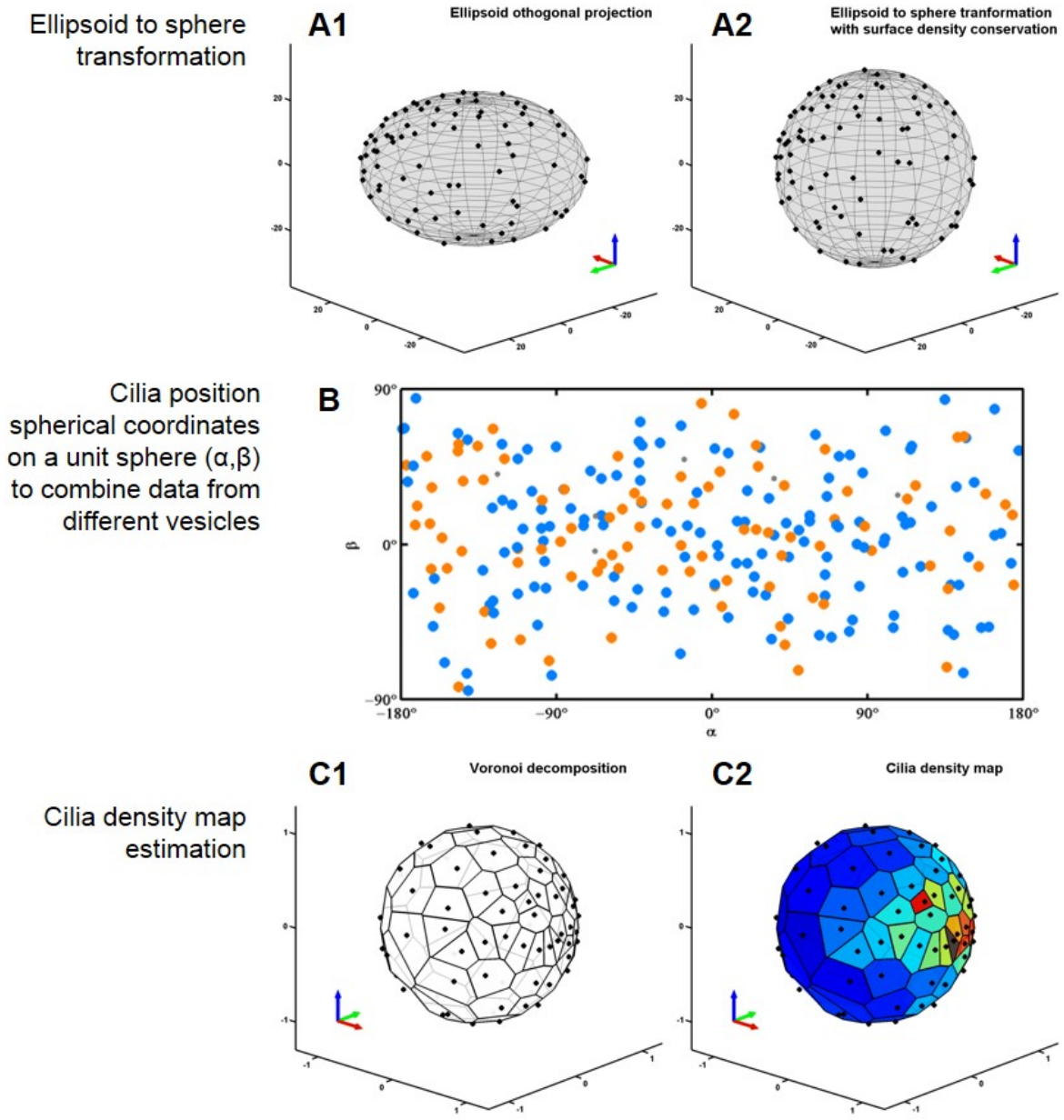

Manuscrit 2 - Fig. 3: Enregistrement des données et représentation sphérique du diagramme de *Voronoi* pour combiner les caractéristiques des cils de différents embryons et estimer la carte de densité des cils. **(A1-A2)** Transformation de l'ellipsoïde à la sphère: projection orthogonale de l'ellipsoïde **(A1)** et sa transformation avec conservation de la densité de surface **(A2)**. **(B)** L'état de motilité des cils de différents embryons est représenté dans une carte 2D (cils motiles et immobiles représentés par des points bleues et oranges, respectivement). **(C1-2)** Estimation de la carte de densité des cils: représentation des distributions des cils dans un diagramme sphérique de Voronoi **(C1)** à partir duquel on a estimé la surface occupée par le cil individuel et on a obtenu la densité locale des cils **(C2)**. Repères pour A1-A2 et C1-C2: e_D (bleu), e_L (vert) et e_A (rouge).

Abréviations: e_D = direction dorsale; e_L = direction de gauche; e_A = direction antérieure

Manuscrit 3

Nous nous sommes aidé de *3D-Cilia Map* pour analyser les paramètres biophysiques des cils à travers toute la VK chez des embryons sauvages à trois stades de développement distincts afin d'extraire le comportement de l'orientation des cils au fil du temps. Grâce à *3D-Cilia Map*, nous avons découvert que les cils sont orientés vers le pôle dorsal de la VK le long de l'axe méridional de celle-ci. En considérant que le processus de mise en place de l'asymétrie gauche-droite a lieu dans un organe dynamique dans l'espace et dans le temps (Compagnon et al., 2014; Yuan et al., 2015), nous avons ensuite exploré les variations au niveau de la position des cils pendant les évènements précoces de l'établissement de l'asymétrie gauche-droite. Cette description quantitative de la morphologie et des cils de la VK chez l'embryon sauvage nous a permis de générer des données précises en conditions *in vivo*. En contrôlant à grande échelle les caractéristiques biophysiques des cils en 3D et en s'appuyant sur des théories, nous avons établi que les cils sont majoritairement orientés le long des méridiens de la VK et que c'est cette orientation qui est le principal mécanisme générant le flux rotationnel au sein de la VK. Aussi, nous avons trouvé au stade 3-somites une orientation méridionale des cils mobiles dans la VK pas entièrement totalement formée. De plus, nous avons noté la présence d'un flux directionnel même à faible amplitude.

Une autre question à laquelle nous voulions apporter des réponses était comment l'inclinaison des cils et leur fonction agissent sur la mise en place de l'axe gauche-droite. En collaboration avec Dr. Andrej Vilfan, nous essayons de comprendre la dichotomie existant entre les signaux chimiques et la détection du signal physique, en modélisant les résultats obtenus par nos équipes et de déterminer quelles sont les conditions nécessaires pour l'un ou l'autre mécanisme. Notre modelé suggère qu'un mécanisme de signalisation chimique serait le plus plausible pour induire la rupture de la symétrie GD, que l'implication d'une force mécanique.

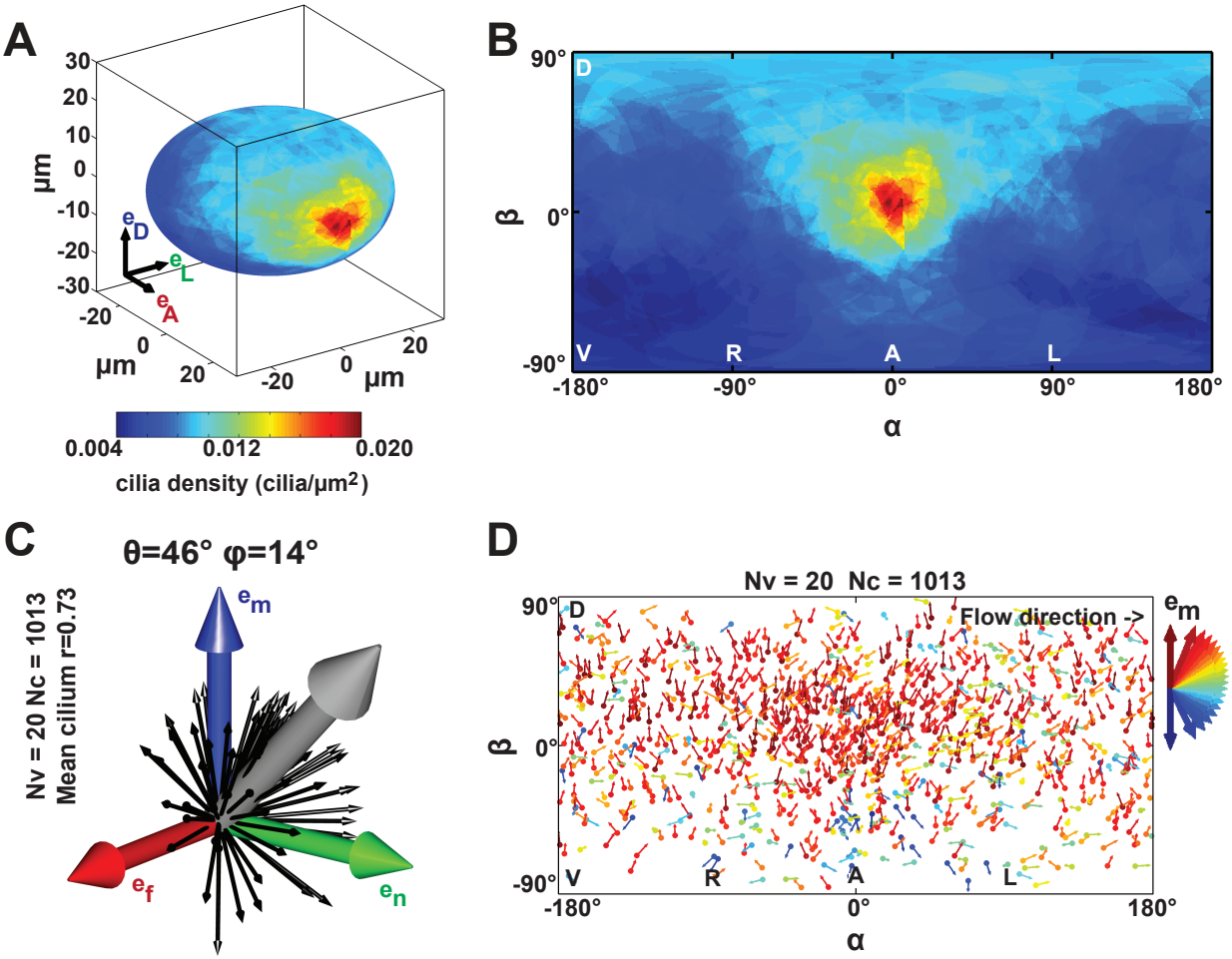

Figure 3

Manuscrit 3 - Fig. 3: Gradient antérieur de la densité des cils et leur inclinaison méridionale dans la vésicule de Kupffer (KV) à 8-14 somites (SS): **(A-B)** Moyenne de la densité des cils obtenue à partir de 20 vésicules représentées sur une carte 3D de la VK **(A)** ou sur un planisphère en 2D **(B)** révélant un gradient marqué de cils le long de l'axe AP et l'enrichissement en résultant au pôle antérieur (en rouge). **(B)** Outre l'enrichissement au pôle antérieur (α = 0 °, β = 0 °), un gradient de densité le long de l'axe DV est également visible (β≥0 ° vs β≤0 °). **(C)** Orientation des 1013 cils motiles analysés (e_m, e_n, e_f) sur l'ellipsoïde: le vecteur gris (pas à l'échelle) montre la moyenne vectorielle de toutes les orientations des cils motiles (θ = 46 ° et φ = 14 °; r = 0.73); pour des raisons de clarté, seules les orientations des cils d'une vésicule représentative sont matérialisés par des vecteurs noirs. **(D)** Orientation des cils (angles φ) sur un planisphère 2D. La majorité des cils pointent dans la direction méridionale (e_m en rouge).

Abréviations: N_v = nombre de vésicules; N_c = nombre de cils; R = longueur du vecteur resultant.

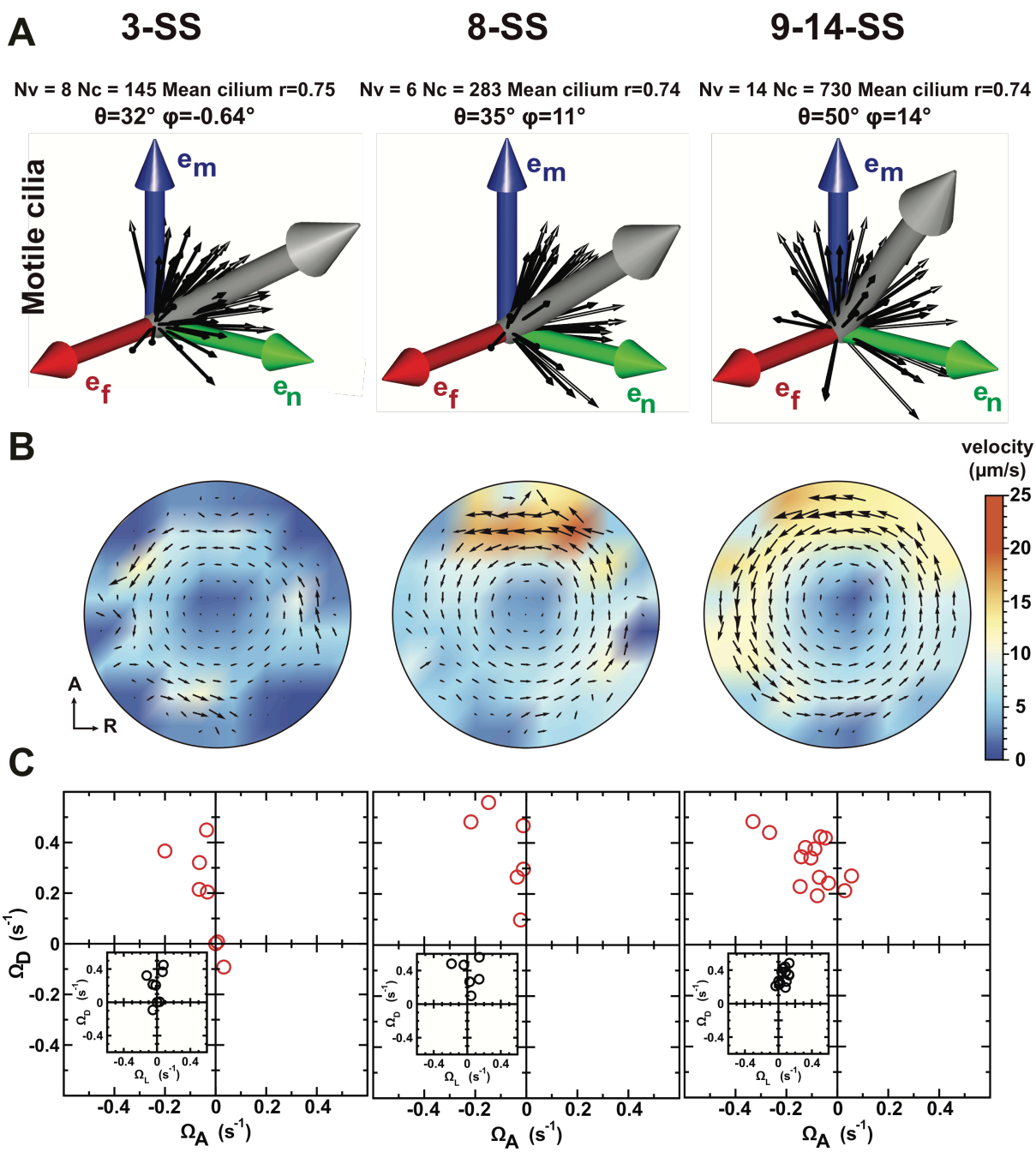

Figure 4

Manuscrit 3 - Fig. 4: Développement de profils de flux et orientation des cils au cours du temps de 3 à 9-14 somites (SS): **(A)** Orientation des cils sur le plan (e_m, e_n, e_f) au fil du temps (voir Figure 3C). Les vecteurs en noir montrent les orientations des cils d'une vésicule représentative. **(B)** Débit moyen dans le plan équatorial de la vésicule de Kupffer (KV) calculé à partir de cartes des cils à chaque étape du développement. Le débit moyen est en rotation autour de l'axe DV à tous les stades, devenant plus fort antérieurement à partir de 8-SS. Une visualisation 3D de ces flux est donnée dans la vidéo 2. **(C)** Vitesse angulaire effective ($\vec{\Omega}$) comme mesure du flux rotationnel à l'intérieur de la VK au cours temps. La vue de droite du vecteur ($\vec{\Omega}$) est illustrée dans les diagrammes principaux, la vue postérieure dans les inserts.

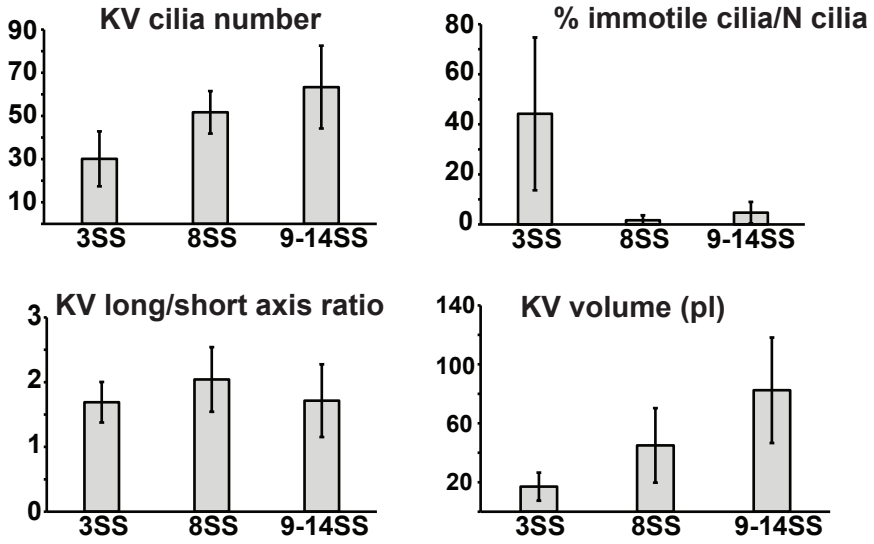

p value	KV cilia number		% immotile cilia		KV long/short axis ratio		KV volume (pl)	
	8SS	9-14SS	8SS	9-14SS	8SS	9-14SS	8SS	9-14SS
3SS	0.041	0.001	0.047	0.011	0.327	0.363	0.08	8.6×10^{-4}
8SS		0.018		0.1		0.079		0.009

Figure 4-figure supplement 1

Manuscrit 3 – Fig. 4-figure supplémentaire 1: Quantification de la VK et caractéristiques des cils en comparant les stades 3-, 8- and 9-14-somites (SS). Tableau des p-values (plus de caractéristiques dans le Tableau 1).

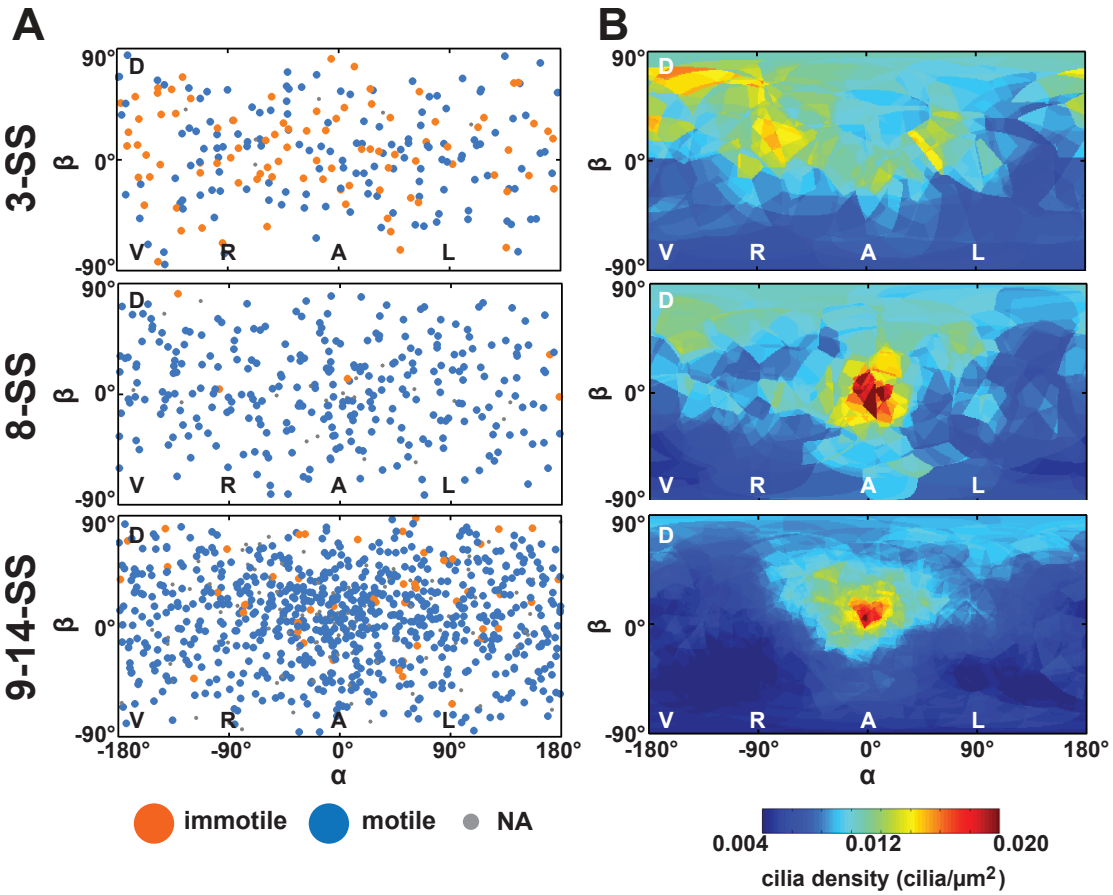

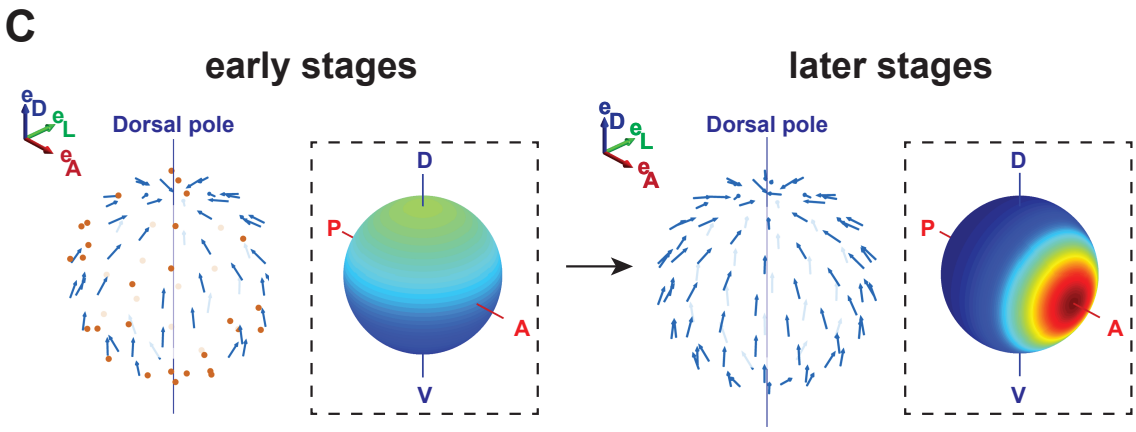

Figure 4-figure supplement 2

Manuscrit 3 - Fig.4- figure supplémentaire 2: Changements dans la répartition spatiale et l'orientation des cils dans le temps: **(A)** Distribution spatiale sur planisphère 2D des cils immobiles (bleus) et motiles (orange). Entre 3 et 9-14-somites (SS), la proportion de cils immobiles diminue de 44% à 5% (voir également le Tableau 1). **(B)** Les cartes de densité des cils montrent un enrichissement au pôle antérieur (α = 0 °) qui s'accentue au cours du temps (de 3 à 9-14-SS). **(C)** Schéma récapitulant les principales différences dans l'orientation des cils en 3D et la carte de densité (cadre en tiret) entre les étapes de développement précoces (3 SS, à gauche) et tardives (9 à 14 SS, à droite): les vésicules précoces comportent beaucoup de cils immobile (rouge), les cils mobiles (bleu) présentent toujours une inclinaison méridionale à la fois à des stades précoces et tardifs. La carte de densité des cils est d'abord dominée par un gradient dorsal avant de présenter un fort gradient antérieur à des stades plus tardifs (code couleur de bleu à rouge correspondant à une densité de cils faible à élevée, respectivement). Voir la figure 1 pour la définition du cadre de référence du plan du corps et des systèmes de coordonnées.

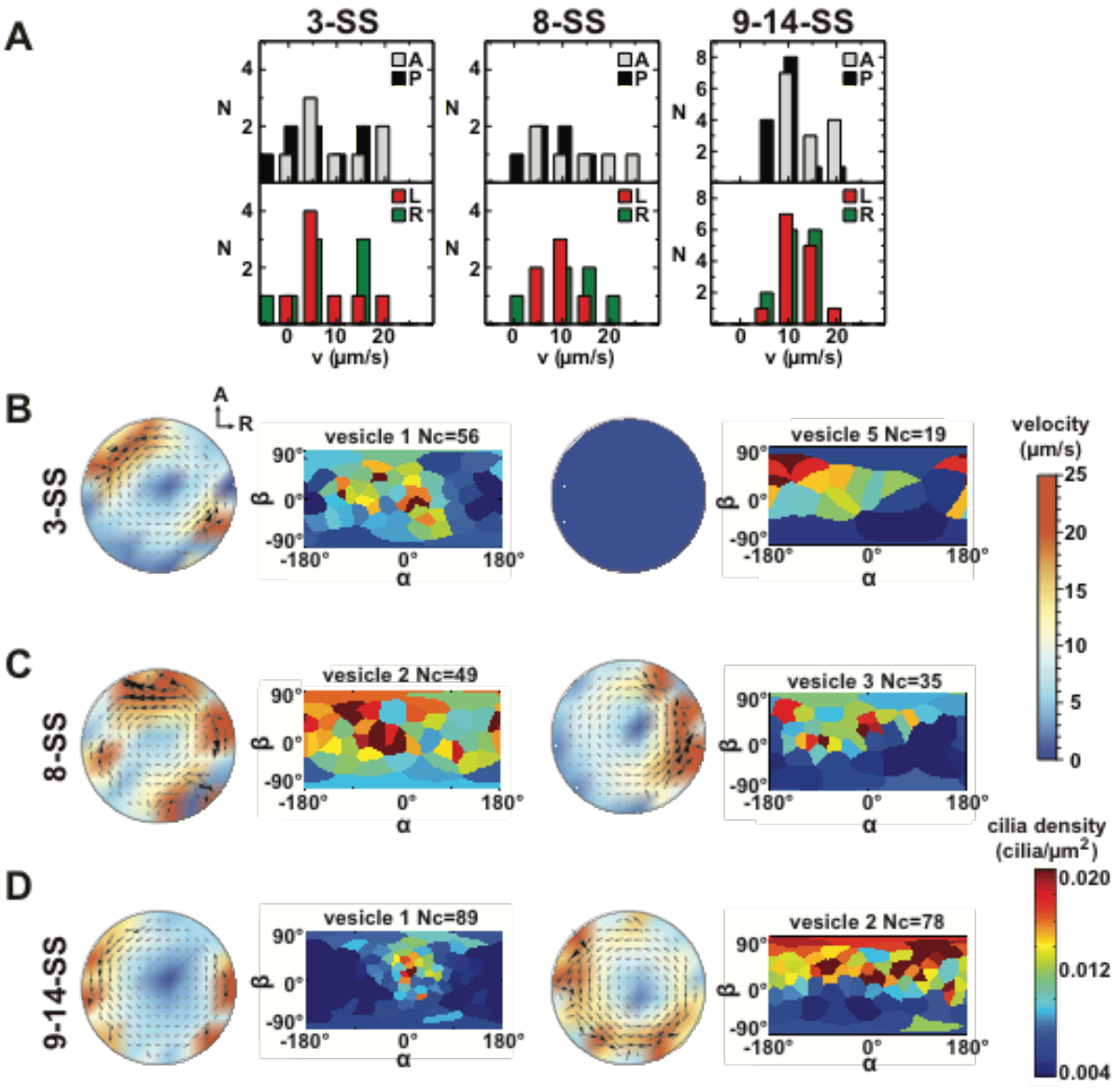

Figure 6

Manuscrit 3 - Fig. 6: Variabilité dans la distribution des cils et les profils du flux entre des VK individuelles à 3-, 8 et 9-14-somites (SS): (A) Distributions de la vitesse du flux dans les VK individuelles à 3-, 8 et 9-14-SS. Le panneau supérieur montre les vitesses moyennes dans les régions avoisinants les pôles A et P et le panneau inférieur celles autour des pôles L et R. **(B-D)** Profils de flux et cartes de densité des cils en 2D pour deux VK représentatives à 3-SS **(B)**, 8-SS **(C)** et 9-14-SS **(D)** (voir la figure 6-supplémentaire 1 pour toutes les VK individuelles).

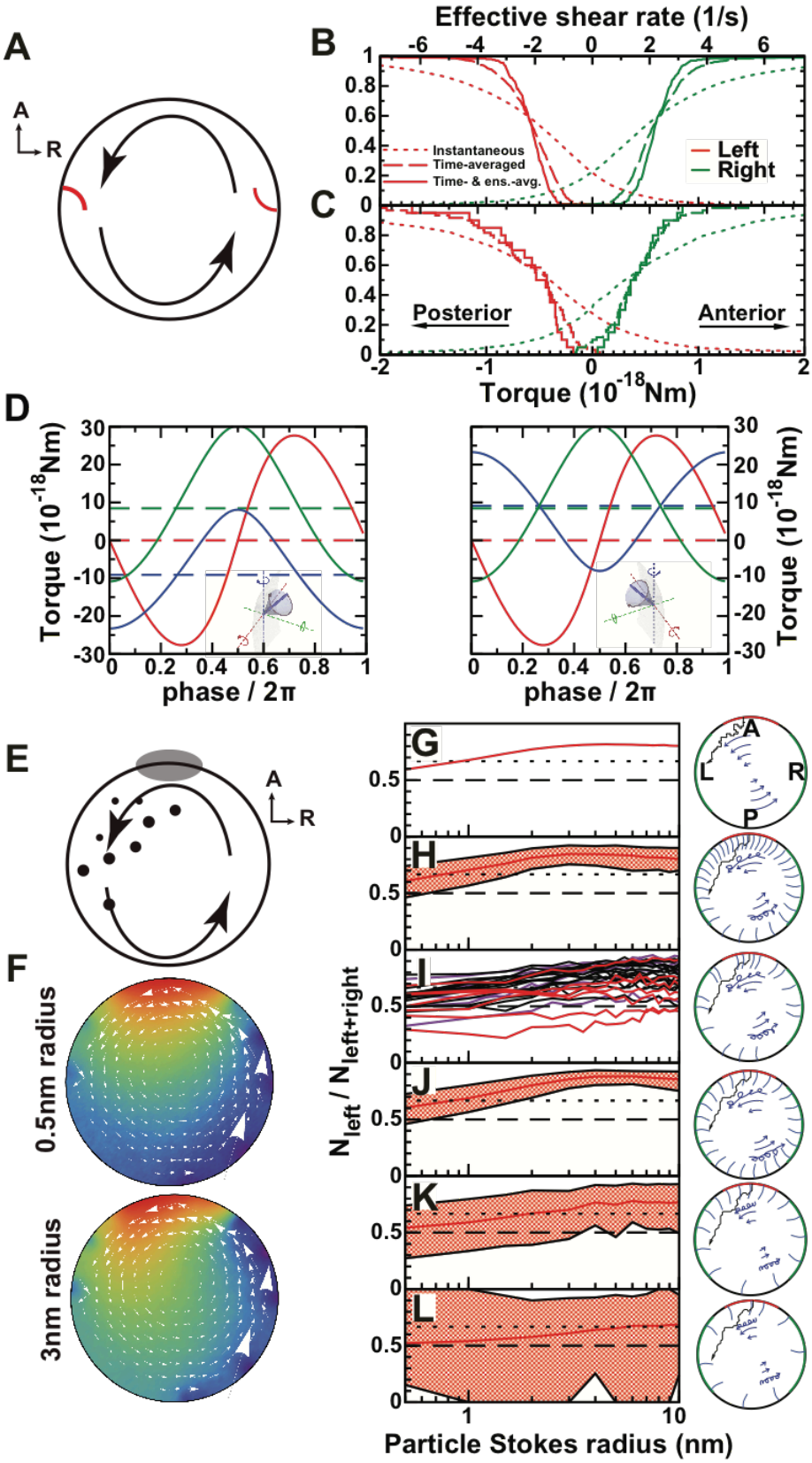

Figure 7

Manuscrit 3 - Fig. 7: Limites physiques d'un possible mécanisme de détection latéral. (A) Mécanisme mécanosensoriel 1: détection du flux directionnel. Les cils sensoriels (rouge) des côtés gauche et droit sont déviés par le flux rotationnel (flèches). Ils doivent être capables de distinguer les flux dirigés antérieurement et postérieurement. **(B-C)** Fraction cumulative de cils avec la force d'action antérieure en-dessous (droite, verte) ou au-dessus (gauche, rouge) de la valeur de l'abscisse. Les lignes

pointillées montrent des valeurs instantanées (floutées par les flux oscillants des cils adjacents), les lignes pointillées montrent la moyenne temporelle, et la ligne continue la moyenne temporelle et l'ensemble moyen des 3 cils immobiles pour chaque côté. Les diagrammes montrent les résultats sur les vésicules caractérisées aléatoirement **(B)** et expérimentalement **(C)**. Les résultats montrent qu'une détection fiable (<5% d'erreur) nécessiterait un seuil de sensibilité de 0.1 × 10^{-18} Nm. L'échelle supérieure montre le taux de cisaillement effectif au-dessus d'une surface plane qui induit le couple équivalent sur un cil passif isolé de même longueur. **(D)** Mécanisme mécanosensoriel 2: détection du mouvement du cil. Selon ce mécanisme, une cellule peut détecter la torsion provoquée par le mouvement de son propre cil actif à travers le fluide visqueux. Les lignes montrent la composante méridionale vers le postérieur (bleu), la composante parallèle vers le dorsal (rouge) et le composant normal (vert). La composante méridionale montre une moyenne temporelle de 10^{-18} Nm qui pourrait potentiellement permettre une discrimination entre le côté gauche (panneau gauche) et le côté droit (panneau droit). **(E)** Mécanisme chimiosensible, basé sur le transport des molécules de signalisation par le flux. Les particules sont sécrétées dans une région de 30° autour du pôle antérieur et se déplacent de façon diffuse à travers le flux rotatif. Elles sont absorbées lorsqu'elles rencontrent un cil en dehors de la région antérieure. Finalement, les particules absorbées dans une région de 45° autour des pôles LR sont comptées. **(F)** Concentration moyenne des particules (unités arbitraires) dans le plan équatorial pour les particules où la diffusion domine la circulation du fluide (rayon de Stokes = 0.5nm en haut) et celles où la "dérive" domine (3nm en bas). Dans le dernier cas, une asymétrie dans la distribution est clairement visible (Movie 3). **(G-L)** Fraction des particules comptées sur la gauche parmi le nombre total à gauche et à droite pour différents scénarii. La ligne pointillée montre un seuil de détection proposé avec un ratio gauche à droite de 2:1. La ligne rouge montre la vésicule moyenne et la région ombrée l'intervalle entre le 5ème et le 95ème percentile. **(G)** Modèle continu avec circulation uniforme ($\Omega = 0.5s^{-1}$). **(H)** Distribution des cils générée de manière aléatoire avec des paramètres naturels. **(I)** Simulation sur des vésicules individuelles à 3-SS (rouge), 8-SS (indigo) et 9-14-SS (noir). **(J)** Même cas que H, mais avec une répartition homogène des cils. K) Identique à H, mais avec un nombre réduit de cils (N_c = 35). **(L)** Nombre supplémentaire de cils (N_c = 20). Abréviation: N_c = nombre de cils.

stage	KV number	N cilia	% immotile cilia	Ellipsoid Axis a (µm)	Ellipsoid Axis b (µm)	ratio axis a / b	Volume (pl)	Average motile cilium: r	Average motile cilium: θ (°)	Average motile cilium: φ (°)	Ellipsoid fit RMS residue (µm)	Ω (s^{-1})
3-SS	1	56	11%	27	12	2.3	35	0.8	37	6	2.07	0.423
	2	23	39%	21	12	1.8	21	0.8	44	2	1.56	0.207
	3	35	3%	23	12	1.9	27	0.8	42	-11	2.38	0.457
	4	21	33%	18	11	1.6	15	0.8	22	12	2.14	0.350
	5	19	100%	15	9	1.7	8	NA	NA	NA	1.5	0.000
	6	24	54%	15	10	1.5	9	0.7	28	3	1.78	0.230
	7	23	61%	14	12	1.2	10	0.8	18	-46	1.92	0.110
	8	40	53%	18	11	1.6	16	0.7	8	22	2.05	0.034
	mean ± SD	**30±13**	**44% ± 31%**	**19 ± 5**	**11 ± 1**	**1.7 ± 0.3**	**17 ± 10**	**0.8 ± 0.1**	**28 ± 13**	**-2 ± 22**	**1.9 ± 0.3**	**0.226 ± 0.173**
8-SS	1	50	4%	29	18	1.6	64	0.8	37	-14	1.2	0.270
	2	49	2%	22	8	2.8	15	0.8	35	6	1.1	0.595
	3	43	0%	25	11	2.3	30	0.7	46	12	2.3	0.561
	4	50	4%	27	12	2.3	39	0.7	41	16	2.5	0.329
	5	71	0%	26	13	2.0	36	0.8	35	16	1.8	0.469
	6	47	0%	30	22	1.4	85	0.7	21	39	1.7	0.110
	mean ± SD	**52 ± 10**	**2% ± 2%**	**26 ± 3**	**14 ± 5**	**2.0 ± 0.5**	**45 ± 25**	**0.7 ± 0.1**	**36 ± 8**	**13 ± 17**	**1.7 ± 0.5**	**0.389 ± 0.186**
9-14-SS	1	89	16%	37	31	1.2	174	0.7	49	12	2.1	0.271
	2	78	6%	27	15	1.8	47	0.7	46	18	2.0	0.600
	3	80	3%	33	20	1.7	93	0.8	54	13	2.2	0.412
	4	50	0%	33	20	1.7	91	0.7	47	14	2.6	0.290
	5	78	6%	31	17	1.8	70	0.7	36	20	2.0	0.393
	6	94	4%	36	21	1.7	111	0.8	52	10	1.7	0.424
	7	62	11%	34	26	1.3	124	0.8	46	11	1.8	0.216
	8	39	3%	24	20	1.2	48	0.7	54	36	4.4	0.378
	9	35	0%	31	13	2.4	52	0.8	50	10	2.6	0.245
	10	49	4%	32	17	1.9	74	0.8	53	2	2.3	0.275
	11	50	2%	30	22	1.4	82	0.9	64	3	2.9	0.433
	12	55	2%	30	23	1.3	85	0.8	61	11	2.6	0.388
	13	49	4%	33	10	3.3	47	0.7	40	32	2.1	0.224
	14	79	5%	27	19	1.4	56	0.7	51	22	1.8	0.521
	mean ± SD	**63 ± 19**	**5% ± 4%**	**31 ± 4**	**19 ± 5**	**1.7 ± 0.6**	**82 ± 36**	**0.8 ± 0.05**	**50 ± 7**	**15 ± 10**	**2.3 ± 0.7**	**0.362 ± 0.114**

Table 1

Manuscrit 3 - Tableau 1: Propriétés statistiques de toutes les VK analysées. Tableau récapitulant certaines des caractéristiques des cils collectées à partir de *3D-Cilia Map* pour des VK individuelles à 3-, 8 et 9-14-somite (SS).

Symbol	Description	From 3D-CiliaMap	Value: standardized vesicle
$(\vec{e}_m, \vec{e}_f, \vec{e}_n)$	Cilium's coordinate system	+	
$(\vec{e}_A, \vec{e}_L, \vec{e}_D)$	KV coordinate system	+	
α	Coordinate	+	
β	Coordinate	+	
θ	Cilium tilt	+	$0 - 60°$
φ	Cilium orientation on the cell surface	+	0
ψ	Cilium, semi-cone angle		$25°$
ω	Cilium, angular frequency		$25 \times 2\pi\ \mathrm{s}^{-1}$
L	Cilium, length		$6\ \mu\mathrm{m}$
R	KV radius	+	$35\ \mu\mathrm{m}$
a	KV ellipsoid, equatorial radius	+	R
b	KV ellipsoid, height	+	R
N_c	Number of cilia	+	70
ρ	Surface density of cilia	+	
$\hat{\rho}$	Normalized surface density of cilia	+	See Figure 5
$g(\gamma)$	Cilia distribution, pair correlation	+	See Figure 5
η	Fluid viscosity	$0.001\ \mathrm{Pa\ s}$	
r_{Stokes}	Diffusive particle Stokes radius	$0.5 - 10\ \mathrm{nm}$	
D	Particle diffusion constant	$k_B T/(6\pi\eta\, r_{\mathrm{Stokes}})$	
$\vec{v}(\vec{x})$	Fluid velocity inside KV	calculated	
$\vec{\Omega}$	Effective flow angular velocity	calculated	
$N_{\mathrm{left}}, N_{\mathrm{right}}$	Number of particles captured on the left/right	simulated	

Manuscrit 3 - Tableau 2: Liste des symboles: Quantités et leurs valeurs avec des sources, le cas échéant.

Manuscrit 4

L'orientation spatiale des cils mobiles est un paramètre fonctionnel clé pour la rupture de la symétrie GD. Le rôle crucial des angles des cils *Phi* (φ) and *Theta* (θ) (déterminant respectivement la force et la direction du flux induit) amène la question de l'origine de ce flux in vivo. Pour comprendre le(s) potentiel(s) mécanisme(s) régissant l'inclinaison méridionale observée *in vivo* en utilisant la méthodologie mise en place avec *3D-Cilia Map*, nous avons réalisé une analyse complète des principaux paramètres biophysiques des cils dans un groupe de conditions présélectionnées connues pour avoir un impact sur la détermination de l'axe GD. Nos résultats démontrent que la plupart des conditions présélectionnées que nous avons étudiées n'avaient pas d'impact sur l'inclinaison méridionale des cils. Par contre, dans des conditions où la motilité des cils est altérée, l'orientation méridionale est remarquablement perdue. De plus, notre étude suggère que la motilité des cils est requise pour l'orientation correcte des cils au cours du développement de la VK. Pour la première fois nous avons montré une surprenante tendance des cils à s'implanter de façon asymétrique après le stade 3-somties qui s'accentue au cours du développement. En réalisant l'étude la plus complète à ce jour de l'orientation des cils dans la VK, nous avons mis en avant de nouveaux points de vue concernant le rôle des cils motiles dans la détermination de l'axe GD du poisson zèbre.

A

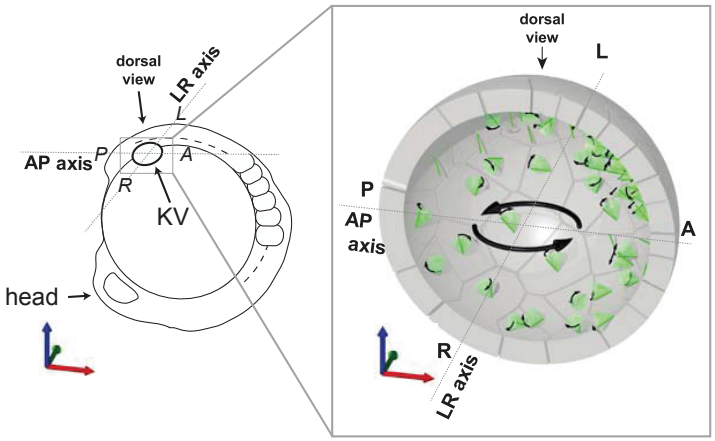

B

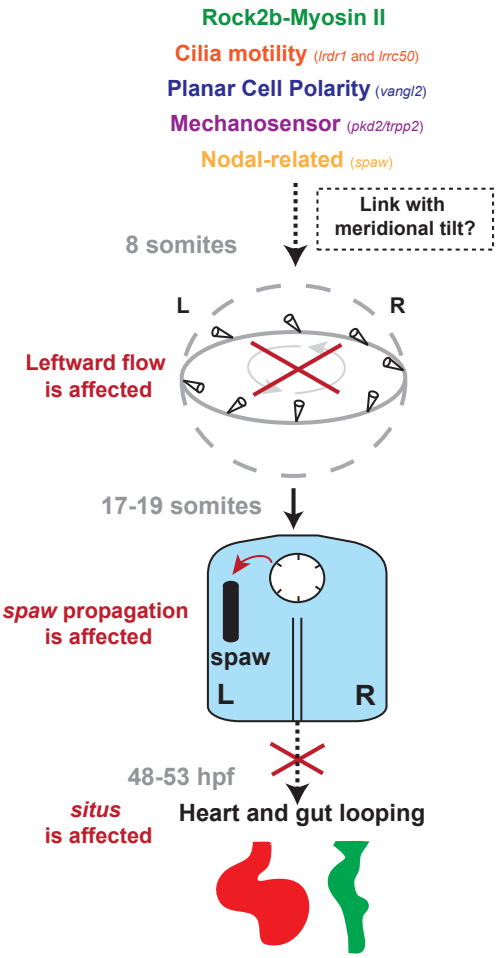

C

pre-selected conditions	Analysis tools		References
rock2b-Myosin II	*rock2b*-MO	MO designed to block the *rock2b* RNA splicing site	Wang et al., 2011
	blebbistatin drug	used to inhibit the ATPase activity of Myosin II	Wang et al., 2012
	rock2b mutant line	*rock2b* (Sa17708: point mutation)	Kettleborough et al., 2013
Cilia motility	*lrdr1*-MO	MO targeted against *dnah9* (*lrdr1*-MO) - motor dynein involved in cilia motility	Essner et al., 2005
	lrrc50 mutant line	*lrrc50* (tm317b: point mutation) - outer dynein subunit required for cilia motility	Sullivan-Brown et al., 2008 ; van Rooijen et al., 2008
Planar cell polarity	*trilobite/Vangl2* mutant line	Wnt/PCP mutants for *Vangl2*	Heisenberg et al., 2000
Cilia mechanosensor	*pkd2/trpp2* mutant line	*Pkd2/Trpp2*, called cup (tc241:point mutation)	Schottenfeld et al., 2007
Nodal-related gene	situs inversus/*spaw* mutant line	*spaw* (s457:point mutation)	Beis et al., 2005; Kalogirou et al., 2014

Manuscrit 4 - Fig. 1: schémas concernant la principale question de mon projet de doctorat et les outils d'analyse utilisés au cours du manuscrit: **(A)** Schéma de la position de la VK dans l'embryon, d'une coupe transversale de la VK et des 3 axes principaux utilisés pour localiser la position de chaque cil en 3D (AP, DV et LR) et en 2D - adaptées du Manuscrit 3. **(B)** Représentation schématique de la voie de détermination de l'axe LR dans le cadre de notre étude: les voies présélectionnées sont connues pour leur implication dans la détermination de l'axe LR, elle affectent plusieurs étapes de cette voie. Tous ont montré que cela affectait le flux anti-horaire créé par les cils dans la VK, ce qui affecterait par conséquent l'expression de spaw à gauche dans la LPM et la position asymétrique des organes internes. Un lien possible de ces voies avec l'inclinaison méridienne observée dans la VK reste inconnu et c'est la question principale que nous aimerions aborder dans ce manuscrit. **(C)** Tableau résumant les voies présélectionnées et les outils que nous avons utilisés pour traiter chaque voie, avec les références respectives.

Abréviations: AP = antérieur-postérieur; LR = gauche-droite; hpf = heures après la fertilisation; L = gauche, R = droite; MO = morpholino

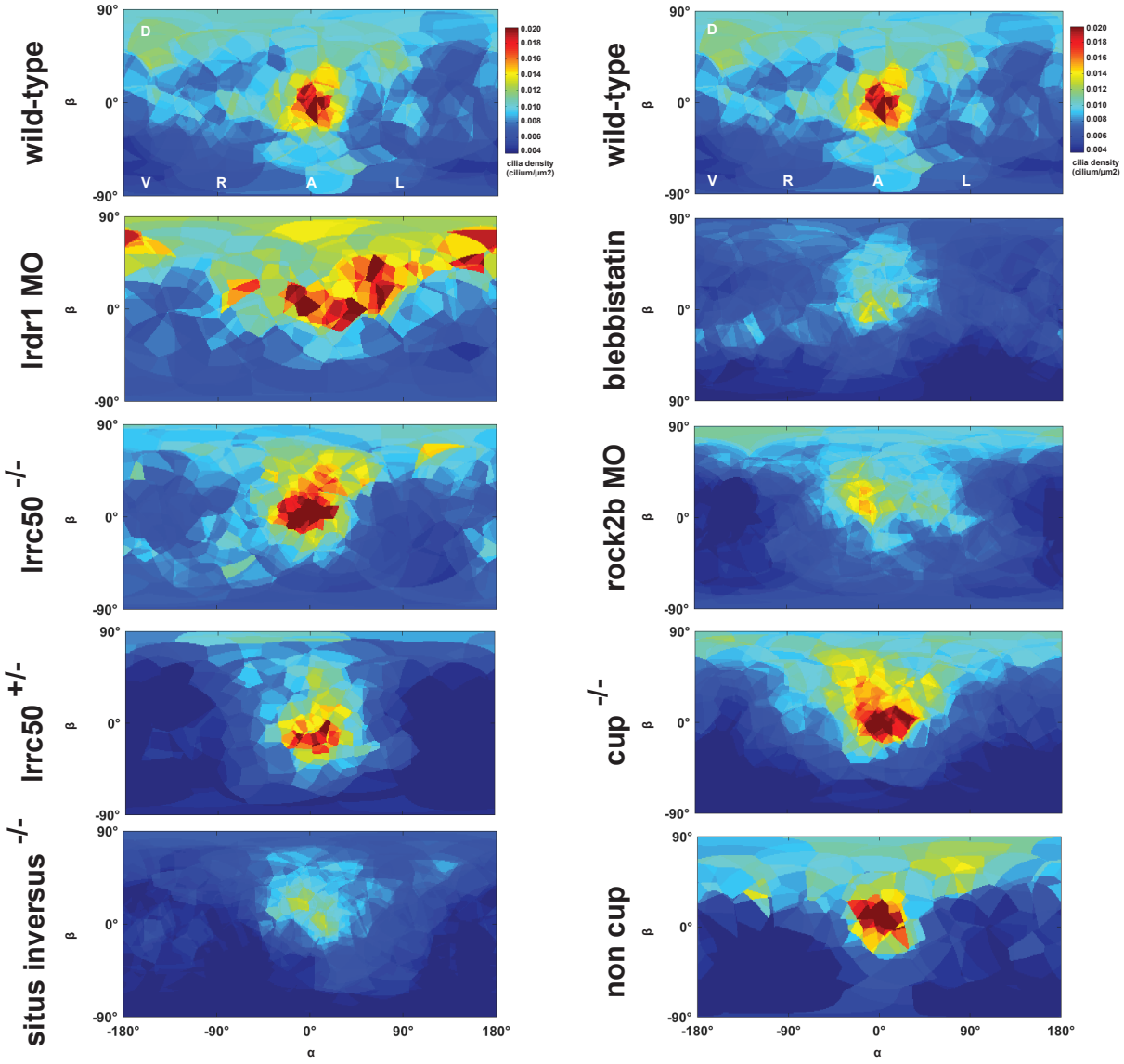

Manuscrit 4 - Fig. 3: Distribution moyenne de la densité en cils chez des embryons au stade 8-SS, représentée sur un planisphère en 2D (densité ciliaire en cil/µm^2). Les moyennes de densité de chaque condition pour toutes les vésicules ont été représentées sur un planisphère 2D avec des coordonnées sphériques. Toutes les cartes ont le même code de couleur. On considère qu'on a un groupement de cil en position antérieure lorsque la région est rouge α = 0 ° et β = 0 °. Les mutants traités à la blebibistatine, les morphants rock2b et les mutants situs inversus$^{-/-}$ (*spaw*) ne présentent pas ce regroupement antérieur de cellules ciliées. Toutes les autres conditions ont une concentration antérieure de cils comparables aux embryons de type sauvage.

Abréviations: *lrdr1* MO = *lrdr1*-morphant; *rock2b* MO = *rock2b*-morphant; cup = cup$^{-/-}$, non cup = embryons cup$^{+/+}$ ou cup$^{+/-}$; *situs inversus* = *spaw*$^{-/-}$

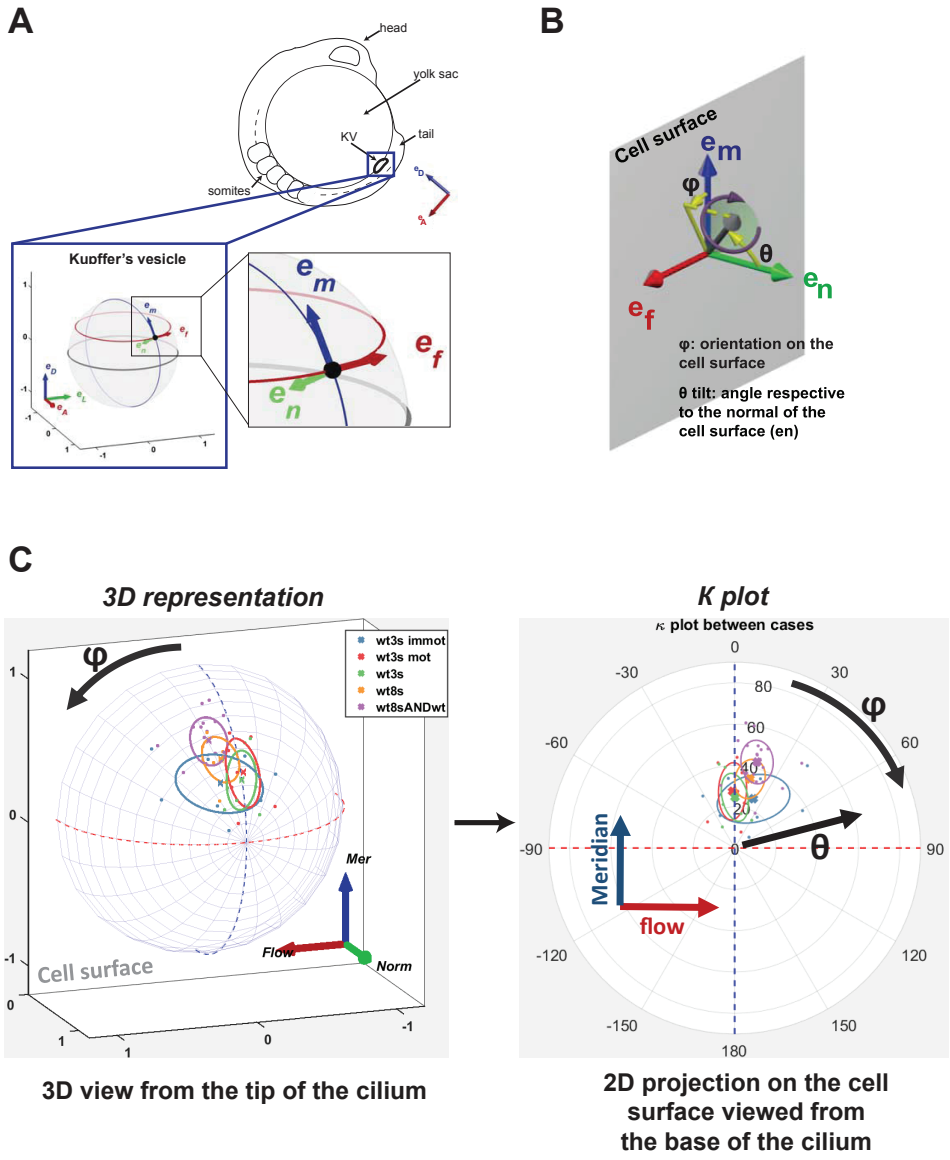

Manuscrit 4 - Fig. 4: Repères utilisés pour analyser l'orientation en 3D des cils dans la VK et nouvelle représentation du cil moyen (graphique K): (A) Vue latérale d'un dessin schématique d'un embryon de poisson zèbre à 5-SS, mettant en évidence la localisation de la vésicule de Kupffer (VK) (cadre bleu) et son orientation selon les coordonnées de référence (e_D et e_A). La zone agrandi (panneau inférieur) montre les schémas des deux systèmes de coordonnées utilisés (e_D, e_L et e_A; e_m, e_n et e_f). Le second agrandissement montre la base locale sur l'ellipsoide, qui a servi à orienter les cils. **(B)** L'orientation des cils est représentée par deux angles: θ (angle d'inclinaison de la surface normale en) et φ (angle entre la projection de surface du vecteur ciliaire et la direction méridienne). La surface de la cellule est représentée en gris, la direction de em en bleu, la direction de e_f est en rouge et en vert la normale en. **(C)** Représentation du cil moyen de chaque vésicule en un vecteur moyen en 3D regroupant tous les vecteurs unitaires des cils dans la même base de référence: représentation 3D sur le panneau gauche, avec une vue 3D à partir depuis l'extrémité de chaque cil. Les graphiques K montrent les valeurs de θ et φ d'un cil moyen pour chaque vésicule, mais aussi la moyenne θ et φ par condition étudiée, dans le même graphique 2D (panneau de droite). Pour dessiner les graphiques K, nous avons utilisé la fonction kent_sp du package SPAK Matlab (http://www.physiol.usyd.edu.au/~simonc/) pour plus de détails, voir (Leong and Carlile, 1998). Pour chaque cas, l'ellipse décrit la distribution des vésicules individuelles et montre à quel point les données sont concentrées sur la moyenne (croix). Les longueurs des axes mineurs et principaux de l'ellipse correspondent à l'écart type dans chaque direction. Abréviations: e_D = direction dorsale; e_L = direction vers la gauche; e_A = direction antérieure; em = aligné le long d'un méridien du pôle ventral au pôle dorsal de la VK; e_f = suit un parallèle de la VK (a la même direction que le flux typique observé dans la vésicule); e_n = vecteur étant normal à la surface de la VK et pointant vers le centre de la vésicule; D = pôle dorsal; V = pôle ventral; P = pôle postérieur; A = pôle antérieur

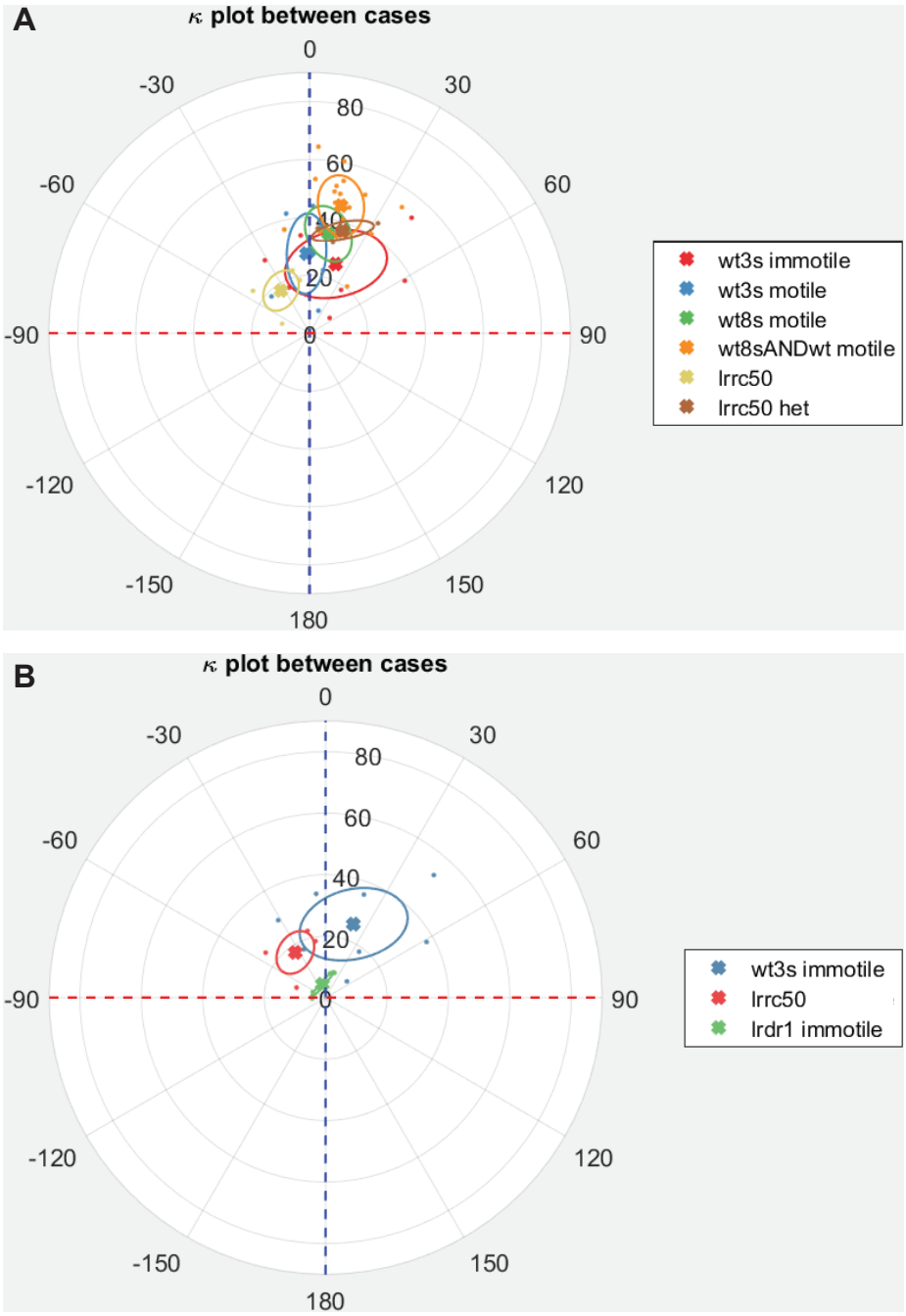

Manuscrit 4 - Fig. 8: lrrc50$^{-/-}$ a une orientation des cils beaucoup plus perturbée par rapport aux contrôles de type sauvage et aux *lrrc50*$^{+/-}$, tandis que les *lrdr1* MO sont très proche d'être orthogonaux à la surface de la cellule: les graphiques K montrent la moyenne θ et φ pour les embryons de type sauvage analysés par rapport aux embryons *lrrc50*$^{-/-}$ et *lrrc50*$^{+/-}$ **(A)** et pour les trois cas avec un nombre important de cils immobiles **(B)**. **(A)** comparaison entre les trois stades de développement chez les embryons de type sauvage (cils immobiles à 3-SS en rouge et motiles en bleu, 8-SS en vert, 8SS et stades ultérieures en orange), avec les embryons *lrrc50*$^{-/-}$ (en jaune foncé) et les *lrrc50*$^{+/-}$ (en brun); **(B)** comparaison entre les cils immobiles à 3-SS (bleu), toute la population de cils immobiles des embryons *lrrc50*$^{-/-}$ et toute la population de cils immobiles dans les embryons *lrdr1* (vert). Pour tous les cas, chaque point représente la valeur moyenne de θ et φ par embryon, et chaque croix les θ et φ moyens par condition: les valeurs φ peuvent être lues autour de la rosette, tandis que les valeurs θ sur les lignes grises qui vont du centre à la périphérie. Les cercles autour de chaque croix représentent l'écart type (voir également le Tableau supplémentaire 4). Abréviations: wt3s = type sauvage 3-SS; wt8s = type sauvage 8-SS; Wt8sANDwt = 8-SS sauvages et 9-14-SS regroupés; *lrdr1* = *lrdr1*-morphant; *lrrc50* = embryons *lrrc50*$^{-/-}$; *lrrc50* het = embryons *lrrc50*$^{+/-}$.

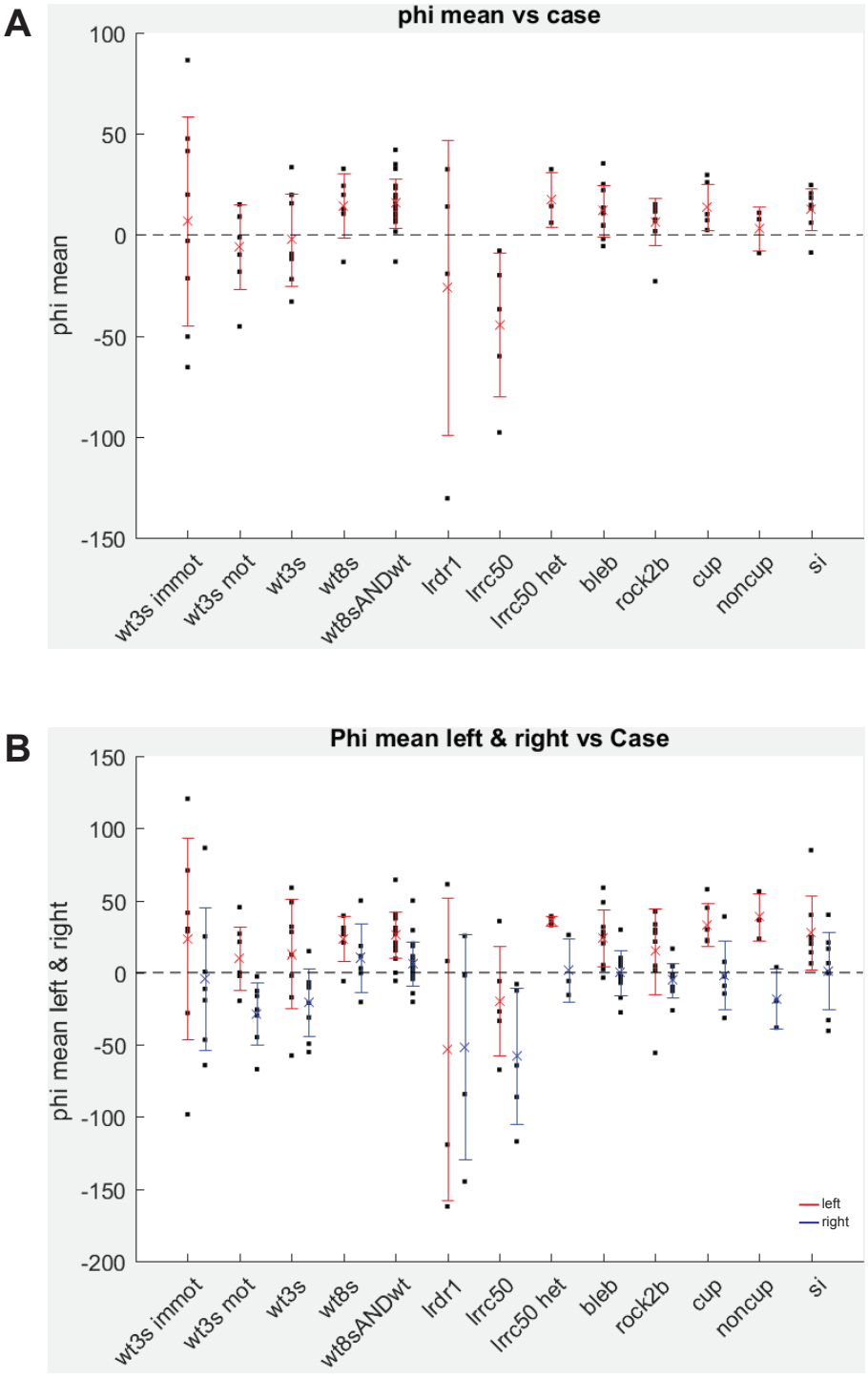

Manuscrit 4 - Fig. 9: Quantification de la valeur moyenne pour φ d'une VK individuelle à différents stades et conditions: **(A-B)** Les graphiques montrent les valeurs moyennes de φ par rapport aux cas **(A)** et les valeurs moyennes de φ des côtés gauche et droit des VK par rapport au cas **(B)**. Pour toutes les conditions dans **(A)** et **(B)**, chaque point noir représente la valeur moyenne pour une VK individuelle, la croix rouge affiche la valeur moyenne pour toutes les VK d'une condition précise et la ligne rouge l'écart type de la moyenne (voir les valeurs dans le Tableau supplémentaire 2-4). L'axe Y dans **(A)** et **(B)** est affiché en degrés. Les valeurs moyennes de φ sont toujours supérieures à zéro, à l'exception des conditions avec des cils immobiles. De même, les valeurs moyennes de φ sont toujours plus élevées pour les cils sur le côté gauche de la VK.

Abréviations: wt3s = type sauvage 3-SS; Wt8s = type sauvage 8-SS; Wt8sANDwt = 8-SS sauvages et 9-14-SS fusionnés; *lrdr1* = *lrdr1*-morphant; *lrrc50* = embryons *lrrc50*$^{-/-}$; *lrrc50* het = embryons *lrrc50*$^{+/-}$, bleb = traitement à la blebbistatine; *rock2b* = *rock2b*-morphant; *cup* = *cup*$^{-/-}$; non *cup* = embryons *cup*$^{+/+}$ ou *cup*$^{+/-}$; si = *situs inversus* (*spaw*$^{-/-}$).

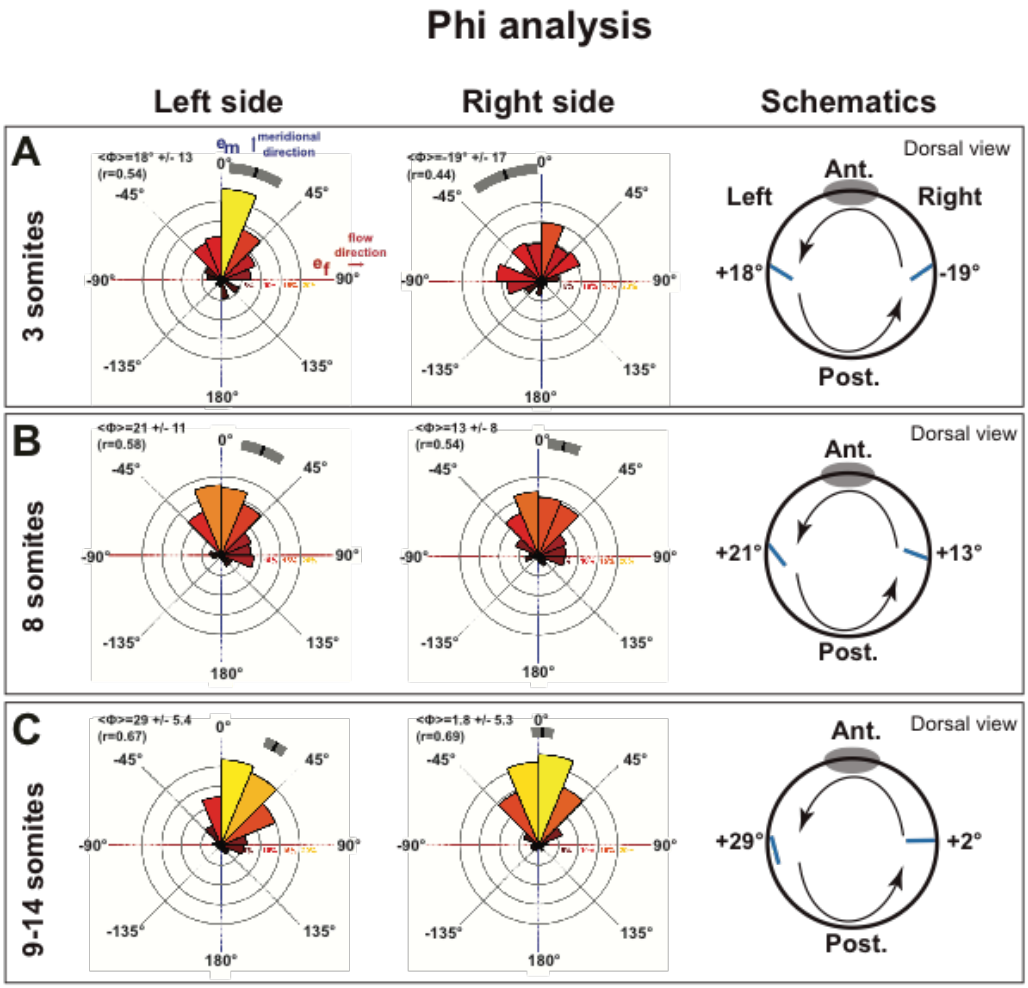

Manuscrit 4 - Fig. 10: L'orientation des cils motiles devient asymétrique au cours du temps entre les côtés gauche et droit de la VK en considérant la quantification de l'angle φ : quantification de la répartition de l'angle φ pour les cils de gauche (gauche) et les cils de droite (milieu), et schémas de la VK en vue dorsale qui résument l'angle φ moyen observé sur les hémisphères gauche et droit de la VK (gauche). Graphique en rosette montrant la répartition de l'angle φ. La marque noire et la bande grise indiquent la moyenne avec son intervalle de confiance de 95%. **(A)** 3 somites, **(B)** 8somites et **(C)** 9-14 somites. Abréviations: N_c = nombre de cils; R = dispersion du vecteur; e_m = aligné le long d'un méridien du pôle ventral au pôle dorsal de la VK; e_f = suit un parallèle KV (a la même direction que le flux typique observé dans la vésicule).

En résumé, dans mon projet de thèse, nous avons développé une méthode, appelée 3D-Cilia Map, et analysé l'organisation tridimensionnelle de l'implantation des cils afin d'extraire les paramètres clés responsables de la mise en place du flux directionnel et par conséquent de l'asymétrie GD. Aussi, nos résultats suggèrent qu'un mécanisme de signalisation chimique serait le plus plausible pour induire la rupture de la symétrie GD. Plus tard, les cellules réguleront intrinsèquement l'orientation asymétrique des cils à leur surface. Le travail présenté ici contribue de façon importante à nos connaissances actuelles concernant le comportement des cils et les mécanismes de sensation des flux dans l'établissement de l'axe gauche-droite au sein de l'organisateur gauche-droite du poisson zèbre.

Réferences

Blum, M., Beyer, T., Weber, T., Vick, P., Andre, P., Bitzer, E., and Schweickert, A. (2009). Xenopus, an ideal model system to study vertebrate left-right asymmetry. Dev Dyn *238*, 1215-1225.

Borovina, A., Superina, S., Voskas, D., and Ciruna, B. (2010). Vangl2 directs the posterior tilting and asymmetric localization of motile primary cilia. Nat Cell Biol *12*, 407-412.

Compagnon, J., Barone, V., Rajshekar, S., Kottmeier, R., Pranjic-Ferscha, K., Behrndt, M., and Heisenberg, C.P. (2014). The notochord breaks bilateral symmetry by controlling cell shapes in the zebrafish laterality organ. Dev Cell *31*, 774-783.

Essner, J.J., Amack, J.D., Nyholm, M.K., Harris, E.B., and Yost, H.J. (2005). Kupffer's vesicle is a ciliated organ of asymmetry in the zebrafish embryo that initiates left-right development of the brain, heart and gut. Development *132*, 1247-1260.

Gros, J., Feistel, K., Viebahn, C., Blum, M., and Tabin, C.J. (2009). Cell movements at Hensen's node establish left/right asymmetric gene expression in the chick. Science *324*, 941-944.

Guirao, B., Meunier, A., Mortaud, S., Aguilar, A., Corsi, J.M., Strehl, L., Hirota, Y., Desoeuvre, A., Boutin, C., Han, Y.G.*, et al.* (2010). Coupling between hydrodynamic forces and planar cell polarity orients mammalian motile cilia. Nat Cell Biol *12*, 341-350.

Hashimoto, M., Shinohara, K., Wang, J., Ikeuchi, S., Yoshiba, S., Meno, C., Nonaka, S., Takada, S., Hatta, K., Wynshaw-Boris, A.*, et al.* (2010). Planar polarization of node cells determines the rotational axis of node cilia. Nat Cell Biol *12*, 170-176.

Hirokawa, N., Tanaka, Y., Okada, Y., and Takeda, S. (2006). Nodal flow and the generation of left-right asymmetry. Cell *125*, 33-45.

Leong, P., and Carlile, S. (1998). Methods for spherical data analysis and visualization. J Neurosci Methods *80*, 191-200.

Marshall, W.F., and Kintner, C. (2008). Cilia orientation and the fluid mechanics of development. Curr Opin Cell Biol *20*, 48-52.

McGrath, J., Somlo, S., Makova, S., Tian, X., and Brueckner, M. (2003). Two populations of node monocilia initiate left-right asymmetry in the mouse. Cell *114*, 61-73.

Nakamura, T., Mine, N., Nakaguchi, E., Mochizuki, A., Yamamoto, M., Yashiro, K., Meno, C., and Hamada, H. (2006). Generation of robust left-right asymmetry in the mouse embryo requires a self-enhancement and lateral-inhibition system. Dev Cell *11*, 495-504.

Nonaka, S., Tanaka, Y., Okada, Y., Takeda, S., Harada, A., Kanai, Y., Kido, M., and Hirokawa, N. (1998). Randomization of left-right asymmetry due to loss of nodal cilia generating leftward flow of extraembryonic fluid in mice lacking KIF3B motor protein. Cell *95*, 829-837.

Nonaka, S., Yoshiba, S., Watanabe, D., Ikeuchi, S., Goto, T., Marshall, W.F., and Hamada, H. (2005). De novo formation of left-right asymmetry by posterior tilt of nodal cilia. PLoS Biol *3*, e268.

Okada, Y., Takeda, S., Tanaka, Y., Izpisua Belmonte, J.C., and Hirokawa, N. (2005). Mechanism of nodal flow: a conserved symmetry breaking event in left-right axis determination. Cell *121*, 633-644.

Satir, P., and Christensen, S.T. (2007). Overview of structure and function of mammalian cilia. Annu Rev Physiol *69*, 377-400.

Song, H., Hu, J., Chen, W., Elliott, G., Andre, P., Gao, B., and Yang, Y. (2010). Planar cell polarity breaks bilateral symmetry by controlling ciliary positioning. Nature *466*, 378-382.

Supatto, W., and Vermot, J. (2011). From cilia hydrodynamics to zebrafish embryonic development. Curr Top Dev Biol *95*, 33-66.

Yuan, S., Zhao, L., Brueckner, M., and Sun, Z. (2015). Intraciliary calcium oscillations initiate vertebrate left-right asymmetry. Curr Biol *25*, 556-567.

UNIVERSITÉ DE STRASBOURG

Rita RUA FERREIRA

igbmc institut de génétique et de biologie moléculaire et cellulaire

Etude du mécanisme de la sensation du flux ciliaire dans l'organiseur droite gauche du poisson zébre

Zebrafish left-right organizer: multi-scale analysis of cilia behaviors and flow-sensing mechanism for symmetry-breaking

Résumé

Les cils motiles et statiques jouent d'importants rôles dans la détermination de l'axe gauche-droite (GD) qui, en général, est mis en place par l'intermédiaire de flux directionnels générés dans des structures spécialisées appelées organisateurs gauche-droite (OGD). C'est ce point clé du développement qui dictera une organogenèse asymétrique. Dans mon projet de thèse, nous avons développé une méthode, appelée *3D-Cilia Map*, et analysé l'organisation tridimensionnelle de l'implantation des cils afin d'extraire les paramètres clés responsables de la mise en place du flux directionnel et par conséquent de l'asymétrie GD. En résumé, nos résultats suggèrent qu'un mécanisme de signalisation chimique serait le plus plausible pour induire la rupture de la symétrie GD. Plus tard, les cellules réguleront intrinsèquement l'orientation asymétrique des cils à leur surface. Le travail présenté ici contribue de façon importante à nos connaissances actuelles concernant le comportement des cils et les mécanismes de sensation des flux dans l'établissement de l'axe gauche-droite au sein de l'organisateur gauche-droite du poisson zèbre.

Mots-clés: détermination gauche-droite, vésicule de Kupffer du poisson-zèbre, flux directionnel, rupture de symétrie, inclinaison méridionale

Abstract

Both motile and immotile cilia play important roles in left-right (LR) axis determination, which generally involves cilia-mediated directional flows in organized structures (LR organizers, LRO) in which the LR symmetry is broken, thus driving asymmetric organogenesis in the developing embryos. In my PhD project we aimed to developed a method (*3D-Cilia Map*) and analyze the three-dimensional organization of ciliary implantation in order to extract the key parameters modulating the directional flow involved in breaking the axis of symmetry in the zebrafish LRO. Altogether, our results suggest the initial mechanism to break the LR symmetry is most likely to be based on the transport of a chemical signal, while later, cells intrinsically provide their cilia the cues to orient asymmetrically. The work presented here represents an important contribution to our current understanding of cilia behaviors and flow-sensing mechanisms in the establishment of the left-right axis in the zebrafish LRO.

Key-words: left-right determination; zebrafish Kupffer's vesicle; cilia; directional-flow; symmetry-breaking; meridional tilt

LABORATOIRE D'EXCELLENCE igbmc INRAT

INVESTISSEMENTS D'AVENIR

cnrs

Inserm